Sequential fluid migration along a fold and thrust belt: SE Pyrenees from Late Cretaceous to Oligocene

David Cruset Segura

Facultat de Ciències de la Terra
Departament de Mineralogia, Petrologia i Geologia aplicada
Universitat de Barcelona (UB)

SEQUENTIAL FLUID MIGRATION ALONG A FOLD AND THRUST BELT: SE PYRENEES FROM LATE CRETACEOUS TO OLIGOCENE

Memòria presentada per **David Cruset Segura** per optar al grau de Doctor en Geologia. Aquesta memòria ha estat desenvolupada dins del Programa de Doctorat de Ciències de la Terra sota la direcció de la Dra. **Anna Travé Herrero** i del Dr. J**aume Vergés Masip**.

David Cruset Segura

Barcelona, 2019

Dra. Anna Travé Herrero

Dr. Jaume Vergés Masip

Als meus pares i a la Gemma.

Thesis presentation and structure

This thesis constitutes the word that I have done to obtain the degree of PhD at the Department of Mineralogy, Petrology and Applied Geology of the Faculty of Earth Sciences of the University of Barcelona (UB). This dissertation is presented as a compendium of articles and is divided into twelve chapters.

Chapters 1, 2 and 3 consist of the general introduction, geological setting and the methodology, respectively.

Chapters 4 to 8 consist of the results and they include all the papers related to the research done during this thesis. Two of the papers are published, the third one is in review, the fourth one is submitted and the fifth one is in preparation:

Chapter 4:

Cruset, D., Cantarero, I., Travé, A., Vergés, J., John, C.M. (2016a). *Crestal graben fluid evolution during growth of the Puig-reig anticline (South Pyrenean fold and thrust belt).* Journal of Geodynamics 101, 30-50.

Chapter 5:

Cruset, D., Cantarero, I., Vergés, J., John, C.M., Muñoz-López, D., Travé, A. (2018). *Changes in fluid regime in syn-orogenic sediments during the growth of the south Pyrenean fold and thrust belt.* Global and Planetary Change 171, 207-224.

Chapter 6:

Cruset, D., Vergés, J., Albert, R., Gerdes, A., Benedicto, A., Cantarero, I., Travé, A. (in review in the journal Geology). *U-Pb geochronology applied to fracture-filling calcite cements to decipher emplacement and reactivation of SE Pyrenean thrust sheets*.

Chapter 7:

Cruset, D., Cantarero, I., Benedicto, A., John, C. M., Vergés, J., Travé, A. (submitted to Marine and Petroleum Geology). *From hydroplastic to brittle deformation: controls on fluid flow in the Lower Pedraforca thrust sheet (southern Pyrenees).*

Chapter 8:

Cruset, D., Vergés, J., Benedicto, A., Gómez-Rivas, E., Cantarero, I., John, C. M., Travé, A. (in preparation). *Fluid flow evolution from the Mesozoic extension to the Alpine orogeny in the Upper Pedraforca thrust sheet (southern Pyrenees).*

In this chapter the introduction, the geological setting, the methodology, the main results and part of the discussion are presented.

Chapters 9, 10 and 11 consists of the main discussion of the results presented in chapters 4 to 8, the main conclusions achieved in this thesis and all the references, respectively.

Chapter 12 includes the annexes of this thesis, which in addition to geochemical data, also include other publications and presentations in international congresses:

Annex 1: Geochemical data from Chapter 4 (Cruset et al., 2016).

Annex 2: Geochemical data from chapter 5 (Cruset et al., 2018).

Annex 3: Data repository from Chapter 6 (Cruset et al., in review).

Annex 4: Geochemical data from chapter 7 (Cruset et al., submitted).

Annex 5: Geochemical data from chapter 8 (Cruset et al., in preparation).

Annex 6: Other publications:

Cruset, D., Cantarero, I., Travé, A., Vergés, J. (2015). Evolución diagenética durante el crecimiento del anticlinal de Puig-reig (cinturón de pliegues y cabalgamientos surpirenaico). Geogaceta. 58, 27-30.

Cruset, D., Vergés, J., Cantarero, I., Travé, A. (2019) From rock-buffered to open fluid system during emplacement of the Lower Pedraforca thrust sheet (South Pyrenees). In: Doronzo D., Schingaro E., Armstrong-Altrin J., Zoheir B. (eds.) Petrogenesis and Exploration of the Earth's Interior. Proceedings of the 1st Springer Conference of the Arabian Journal of Geosciences (CAJG-1), Tunisia 2018. pp 215-217.

Annex 7: Oral presentations:

Cruset, D., Cantarero, I., Travé, A., Vergés, J., John, C. M. (2016b). *Fluid migration during the Cadí thrust sheet emplacement (South Pyrenean fold and thrust belt).* GEOFLUIDS VIII conference, Wuhan, China. June 22-27, 2016.

Cruset, D., Cantarero, I., Vergés, J., Travé, A. (2017) Fluid rock relationships during the formation and inversion of an extensional basin (Upper Pedraforca thrust sheet, South Pyrenean fold and thrust belt). International Meeting of Sedimentology 2007. Toulouse, France, October 10-12, 2017.

Acknowledgements/Agraïments

Després de quasi 5 anys em trobo escrivint els agraïments d'aquesta tesi. No em podia imaginar quan vaig començar la carrera de geologia que em ficaria en aquesta aventura, la qual ha estat una muntanya russa d'emocions.

Primer de tot voldria agrair als meus directors, l'Anna i el Jaume, per dirigir-me la tesi i haver-me introduït en el món de la recerca.

Anna, moltíssimes gràcies per proposar-me aquesta tesi. Gràcies sobretot per la teva confiança i perquè tot i les circumstàncies adverses que han anat sorgint al llarg d'aquesta tesi, sobretot al final, sempre has tingut un moment per atendre'm i un somriure per mi.

Jaume, t'agraeixo moltíssim el teu sentit crític i els teus consells. Sobretot la teva paciència als inicis d'aquesta tesi.

Aquesta tesi ha estat finançada pels projectes de recerca dirigits per l'Anna Travé (CGL2015-66335-C2-1-R i PGC2018-093903-B-C22), pel Jaume Vergés (ALPIMED Project PIE-CSIC-201530E082), el Grup Consolidat de Recerca "Geologia Sedimentària" (2014 SGR-251 i 2017 SGR824) i per l'Ajut de Personal Investigador predoctoral en Formació (APIF) finançat per la Universitat de Barcelona.

Agraeixo a tot el personal tècnic que m'ha ajudat al llarg d'aquesta tesi, sense la seva feina no hagués estat possible dur-la a terme:

Al Jordi Illa, perquè sempre troba una solució a qualsevol problema.

A tot el personal del servei de làmina prima de la facultat, la Dolors, la Montse, la Fadoua i el Vicenç, per la seva bona feina i per la seva comprensió quan hi havia poc temps per tindre llestes les mostres.

Al Joaquim Perona, pels centenars d'anàlisis d'isòtops estables que he encarregat al llarg de tota la tesi i perquè sempre ha estat disponible quan l'he necessitat.

Al Javier Garcia, del servei de Microscòpia Electrònica, a la Rosa Maria del Servei d'Isòtops estables, al Xavier Llobet del servei de Microsonda Electrònica i al Tariq del servei d'Espectroscòpia Raman. Gràcies a tots pels vostres consells i introduir-me en el funcionament de totes aquestes tècniques analítiques.

A Chema del "CAI de Geocronología" de la Universidad Complutense de Madrid, por estar siempre disponible cuando me ha surgido alguna duda sobre los resultados de isótopos de estroncio.

Gràcies al Jordi Bàguena i a la Marga de l'administració del departament per resoldre'm tots els problemes burocràtics que han anat sorgint tots aquests anys.

Gràcies a tots els companys que han passat i als que encara estan a la sala de becaris del departament, Irene, Ari, Sergi Valenzuela, Vito, Dani, Sergi Esteve, Guillem, Sedo, Damià, Luis, Nelson, Nicholas, Jun i Xiaolong, per tot el suport i els bons moments que hem passat (i encara passem) tots junts.

Gràcies sobretot a tu, Irene; m'has ajudat tant i m'has donat tanta tranquil·litat en els moments més difícils que mai podré agrair-t'ho suficient. Tot el que he après de tu no té preu, has estat com una tercera directora per mi.

Gràcies a tota la gent amb la que vaig coincidir durant la meva curta, però intensa, estada a l'Institut de Ciències de la Terra Jaume Almera ICTJA - CSIC:

Als companys de despatx, especialment a la Mar, l'Ángel i la Mireia per tot el recolzament que ens hem donat i encara ens donem entre nosaltres. Sobretot a tu Mar, ets una màquina i una de les persones més fortes que conec.

Al Max, per tot el que m'has fet riure (Cucciolotto).

Al Jordi Ibàñez, pel seu suport i per transmetre'm el seu entusiasme.

A l'Eduard Saura i a l'Emilio Casciello, pels seus consells.

A l'Enric, el Jorge, la Irene i la Ylènia del GDL (Group of Dynamics of the Lithosphere), per tot el viscut durant la campanya de camp a l'Argentina. Gràcies sobretot perquè no sabia que fos tan fàcil començar una estafa piramidal.

Gràcies a tots els professors del departament de Mineralogia, Petrologia i Geologia Aplicada per tot el coneixement i estima que m'han transmès. Espacialment al Lluís Gibert, al Juandi Martín i al Telm Bover pel seu positivisme contagiós.

Gràcies a l'Antonio Benedicto i a l'Enrique Gómez per les llargues discussions sobre deformació i fluids, ja que m'han ajudat a mirar-me els afloraments amb uns altres ulls. Sobretot, gràcies Antonio per interessar-te tant pel meu futur més enllà d'aquesta tesi.

Cédric, thank you very much for showing me the world of the clumped isotopes and for your kindness during my short stay at the Imperial College. Specially thank you for understanding me when I requested so often the results.

Thank you to all the people from the University of Frankfurt for making me feel at home. Axel, thank you very much for accepting me to come to Frankfurt, the results were one of the best findings of my thesis! Gracias especialmente a ti Richard, por aguantarme durante esas intensas jornadas de análisis.

Gràcies als meus companys de carrera, Uri, Maria, Pol, Jordi, Àxel, Guille, Dídac, Arantza, Rafa, Sergi, Dani i Mar, per acompanyar-me en una de les millors etapes de la meva vida.

Sobretot a l'Uri, que tot i els moments d'història que em compartit al llarg dels anys, hem arribat vius fins aquí.

Gràcies a tota la gent aliena a la meva feina i que és un pilar molt important a la meva vida, sense vosaltres el camí hagués estat molt més dur:

Gràcies als meus amics, Adri, Sancho, Àlex, Pau, "El mejorado", Alberto, Davan, Maria maña, Luís, Martín, Laura, Mireia, Belén, Sílvia, Carla, Diego, Dani Ruiz, Dani Bueno, Xavi, Hulio, "Ratón" i Pou "el mejor piloto de la galaxia", per fer-me desconnectar de la feina i entendre les meves absències.

Al meu germà, el Marc, a la seva parella, la Miriam, a l'Anna Mari i a la meva avia, pel seu suport i interès per la meva feina.

A la Gemma, el millor que m'ha passat a la vida. No hi ha cap terme que pugui descriure tot el que t'estimo. La meva feina consisteix en entendre el perquè de certes coses però no trobo explicació a com pots fer-me tan feliç. Gràcies per aguantar-me, sobretot els darrers mesos que han estat bastant intensos.

Als pares de la Gemma, el Jordi i la Montse, per tot el seu suport i facilitar-nos les coses sempre que ho hem necessitat.

Per últim, als meus pares, l'Amadeu i la Nieves. Gràcies per tota l'educació i l'amor que m'heu donat. Gràcies sobretot per inculcar-me les ganes de superar-me, d'anar més enllà i per creure en mi al llarg de tota la vida, sobretot en els moments que ni tan sols jo ho feia. Aquesta tesi també és vostra.

Table of contents

Summary

The south eastern Pyrenees allowed us to study the relationships between fluid flow and deformation in a complete section of a well-preserved fold and thrust belt. Furthermore, this study enables us to decipher the main controls on fluid flow and to perform a conceptual model of fluid migration in fold and thrust belts by comparing the southern Pyrenees with other orogens worldwide.

A combination of field-based and petrographic observations together with geochemical analyses was used to determine the origin of fluids from which these cements precipitated, the conditions of fluid migration and the fluid-rock relationships. These methods were applied to carbonate host rocks and calcite and dolomite cements precipitated in fractures and in intergranular and vug porosities.

The integration of the methodology allowed us to define up to 20 fluid flow events for the Upper Pedraforca thrust sheet, Eight for the Lower Pedraforca thrust sheet, seven for the Vallfogona thrust, which is the southern margin of the Cadí thrust sheet, and two for both the Abocador thrust and the Puig-reig anticline, which are located in the foreland Ebro basin.

During the late foreland stage of the south Pyrenean fold and thrust belt, the Puig-reig anticline formed. Structural and microstructural analysis developed in this fold demonstrate that at outcrop scale fracturing was controlled by rigidity contrasts between layers, diagenesis and structural position within the anticline, whereas grain size, cementation and porosity controlled deformation at the microscopic scale. Petrographic and geochemical studies of calcite precipitated in host rock porosity and fault planes reveal the presence of two migrating fluids, which represents two different stages of evolution of the Puig-reig anticline. During the layer-parallel shortening, hydrothermal fluids with temperatures between 92 and 130 ºC circulated through the main thrusts to the permeable host rocks, reverse and most of strike-slip faults precipitating as cement Cc1. During the fold growth, meteoric waters circulated downwards through normal and some strike-slip faults and mixed at depth with the previous hydrothermal fluid, precipitating as cement Cc2 at temperatures between 77 and 93 ºC. Integration of the results from the Puig-reig anticline in this work and the El Guix anticline indicates that hydrothermal fluids did not reach the El Guix anticline, in which only meteoric and evolved meteoric waters circulated along the fold.

In the south Pyrenean foreland basin, Hydrothermal fluids at temperatures up to 154 °C, migrated from the Axial zone to the foreland basin and mixed with connate fluids in equilibrium with Eocene sea-water during lower and middle Eocene (underfilled foreland basin). As the thrust front progressively emerged, low-temperature meteoric waters migrated downwards the foreland basin and mixed at depth with the hydrothermal fluids from middle Eocene to lower Oligocene (overfilled non-marine foreland basin). The comparison of the fluid flow models from the Southern Pyrenees with other orogens worldwide, seems to indicate that the presence or absence of thick

evaporitic units highly control fluid composition during the development of fold and thrust belts. Whereas in thrusts not detached along thick evaporite units, mixed fluids are progressively more depleted in $\delta^{18}O$ and have a lower temperature and lower Fe and Sr contents as the thrust front emerges, in thrust detachments through thick evaporite units, the mixed fluids are enriched in $\delta^{18}O$.

From U-Pb geochronology applied to calcite cements, 47 ages for the South Pyrenean fold and thrust belt are obtained. Results indicate that fluid migration took place during the Pyrenean compression and that deformation migrated from the upper thrust sheets to the lower thrust units and to the foreland from 70.5 ± 1.1 Ma to 25 ± 17 Ma. These U-Pb ages also indicate that each of the thrust sheets registers its own deformational history as well as the history of the underlying thrust units emplaced during tectonic stacking. For instance, the Upper Pedraforca thrust sheet records the entire compressional history of the SE Pyrenees. Likewise, the wide distribution of U-Pb ages within each tectonic unit indicates that deformation was continuous rather than episodic. Calcite veins with Neogene ages ranging from 18.9 ± 0.8 Ma to 2.6 ± 1.3 Ma are interpreted as having been formed during the Neogene rift and post-rift Western Mediterranean events stretching across NE Iberia. These ages are the first evidence demonstrating deformation within the SE Pyrenees during these post-compressional events.

In the Lower Pedraforca thrust sheet, during syn-sedimentary hydroplastic normal faulting affecting poorly-consolidated Upper Cretaceous sediments and Eocene syn-orogenic sediments, calcite cements did not precipitate. During the burial and the layer-parallel shortening, however, calcite cements Cc1 to Cc4 precipitated from fluids in a relatively paleohydrological system. Cc3 precipitated from high-salinity fluids (~+5.4 ‰ VSMOW) with $^{87}Sr/^{86}Sr$ ratios of 0.707922 and at temperatures around 70 ºC. Contrarily, during folding and thrusting, calcite cements Cc5 to Cc8 precipitated in a more open paleohydrological system. Cc6 precipitated from high-salinity fluids (~+5 ‰ VSMOW) with $^{87}Sr/^{86}Sr$ ratios 0.707817 and at temperatures around 75 ºC. The controls of deformation on the paleohydrological system observed in the Lower Pedraforca thrust sheet have strong similarities with that observed other areas worldwide under both compressional and extensional regimes.

In the Upper Pedraforca thrust sheet, brines at 125 and 145 ºC migrated through fractures during the Early Cretaceous extension. During the Late Cretaceous-Paleocene compression, formation waters at temperatures around 80 ºC and in equilibrium with Late Cretaceous seawater migrated through main thrust fault zones. As the Upper Pedraforca thrust sheet emplaced, the influence of meteoric waters increased, resulting in the slightly decrease of the salinity of migrating fluids. During the Eocene-Oligocene reactivation of this thrust unit, also formation waters at temperatures between 90 and 100 ºC migrated through main thrust fault zones. However, the influence of meteoric waters increased with respect to the Late Cretaceous-Paleocene compression, indicating exhumation of the Upper Pedraforca thrust sheet.

Stable, clumped and strontium isotopes together with elemental composition and rare earths and yttrium analysis indicate that during the emplacement of the Upper and Lower Pedraforca thrust sheets, from Late Cretaceous to middle Eocene, the fluid system was dominated by high-salinity formation fluids and meteoric waters at temperatures ranging between 70 and 90 ºC. In these thrust sheets, fluids migrated above evaporite detachments that acted as barriers for the input of deep sourced fluids. Contrarily, during the emplacement of the Cadí thrust sheet and during the deformation affecting the northern side of the Ebro foreland basin from middle Eocene to Oligocene, high-salinity hydrothermal fluids derived from the deeper parts of the Axial zone and at temperatures between 100 and 177 ºC, migrated through fractures to the thrust front. Hydrothermal fluid flow induced the development of thermal anomalies in the Vallfogonala and Abocador thrusts and in the Puig-reig anticline, which are structures rooted at depth with the basement. These fluid flow patterns observed during the growth of the south eastern Pyrenean fold and thrust belt are similar to that observed in the western side of this orogen.

The evolution of the fluid regime during the growth of the southern Pyrenees has strong similarities to that observed in other orogens worldwide such as the Sevier thrust belt, the western Alps, the Ionian zone in Albania, the Nuncios fold Complex in Mexico as some examples. From these similarities a conceptual model of fluid flow in fold and thrust belts in which the style of deformation is one of the main controlling parameters is performed. In this model, whereas in thin-skinned fold and thrust belts the fluid system is controlled by formation, marine and meteoric waters, in thick-skinned fold and thrust belts the system is controlled by the input of deep-sourced hydrothermal fluids, which induce the formation of thermal anomalies. In both situations, during the layer-parallel shortening stretching thrust sheets, the paleohydrological system was closed and the fluid-rock interaction was low. In contrast, during later folding and thrusting the system opened to the input external fluids and the interaction between fluids and their adjacent host rocks decreased progressively.

Chapter 1

Introduction

1. Introduction

1.1. Fluid flow and fold and thrust belts

Fluids interact with rocks during sedimentation, burial, deformation and metamorphism (Travé et al., 1998a, Schneider et al., 2008; Jamtveit and Aurstrheim, 2010; Cosgrove, 2015; Cantarero et al., 2018). These fluids are responsible of heat and matter transport (Gasparrini et al., 2013; Lu et al., 2017), are involved in ore deposition and hydrocarbon accumulations (Dewaele et al., 2004; Gasparrini et al., 2013; Perona et al., 2018), and induce seismically-induced slip and/or hydraulic fracturing (Aydin, 2000; Wiprut and Zoback, 2000; Rutqvist et al., 2013). Furthermore, the diagenetic products related to fluid flow (clay minerals and calcite and dolomite cements) can be aged using Ar-Ar and U-Pb geochronology to constrain the timing of fluid migration (Van der Pluijm et al., 2001; Hansman et al., 2018).

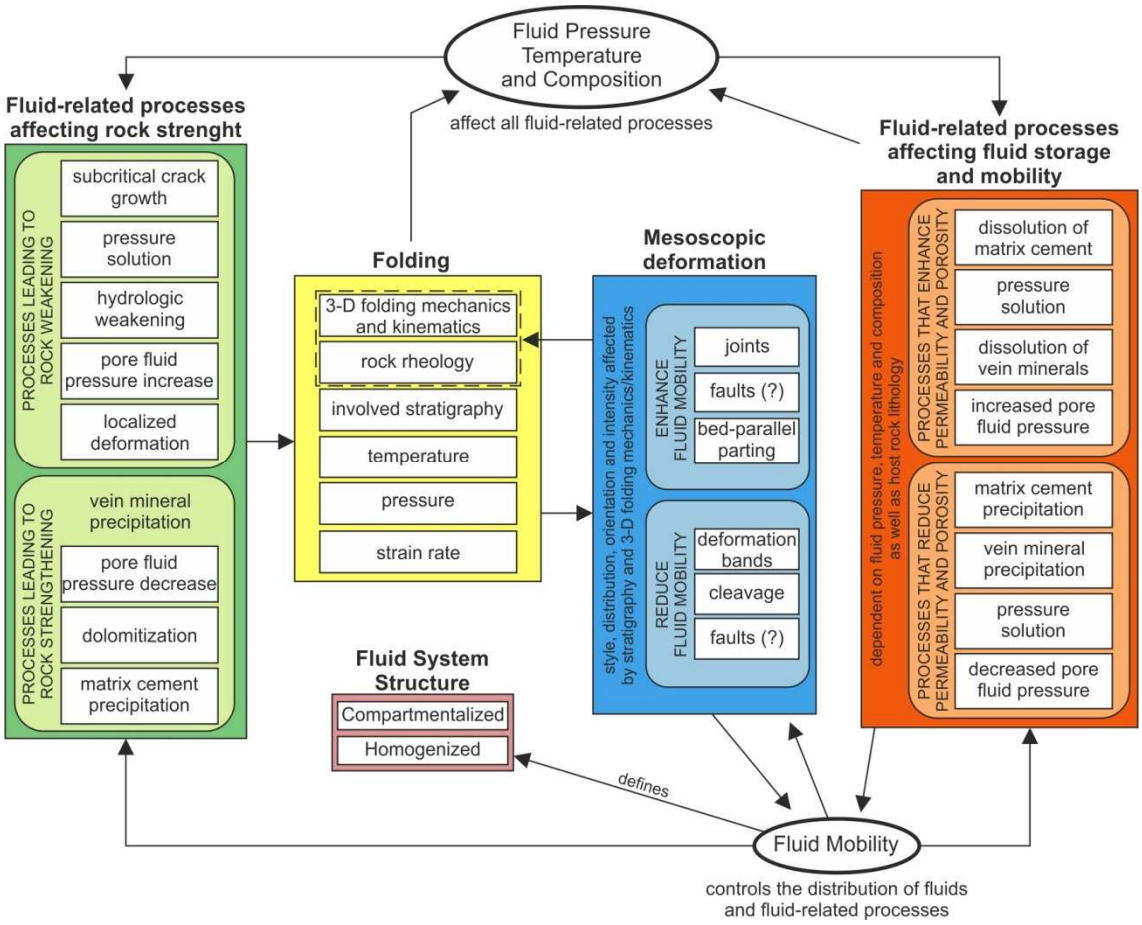

Fig. 1. Schematic representation of the variables, processes and feedback relationships comprising a deformation-related fluid system. Redrawn from Evans and Fischer (2012).

Fluid-related systems are constituted by different components and processes that interact among themselves defining a deformation-related fluid system (Fig. 1). Fluid pressure, temperature, composition and mobility have a feedback relationship with fluid-related processes affecting rock strength, fluid storage and mobility and mesoscopic deformation. The mobility of fluids defines the structure of the paleohydrological system (compartmentalized or homogenized).

Fluid-related processes affecting rock strength (such as pressure-solution, localized deformation, vein mineral precipitation, dolomitization, etc.) influences deformation (Fig. 1), which has a feedback relationship with mesoscopic deformation (e.g. fractures, deformation bands, cleavage). As a result of the relationships between these processes and feedbacks, the fluid-related system has a high complexity which can vary through time (Evans and Fischer, 2012).

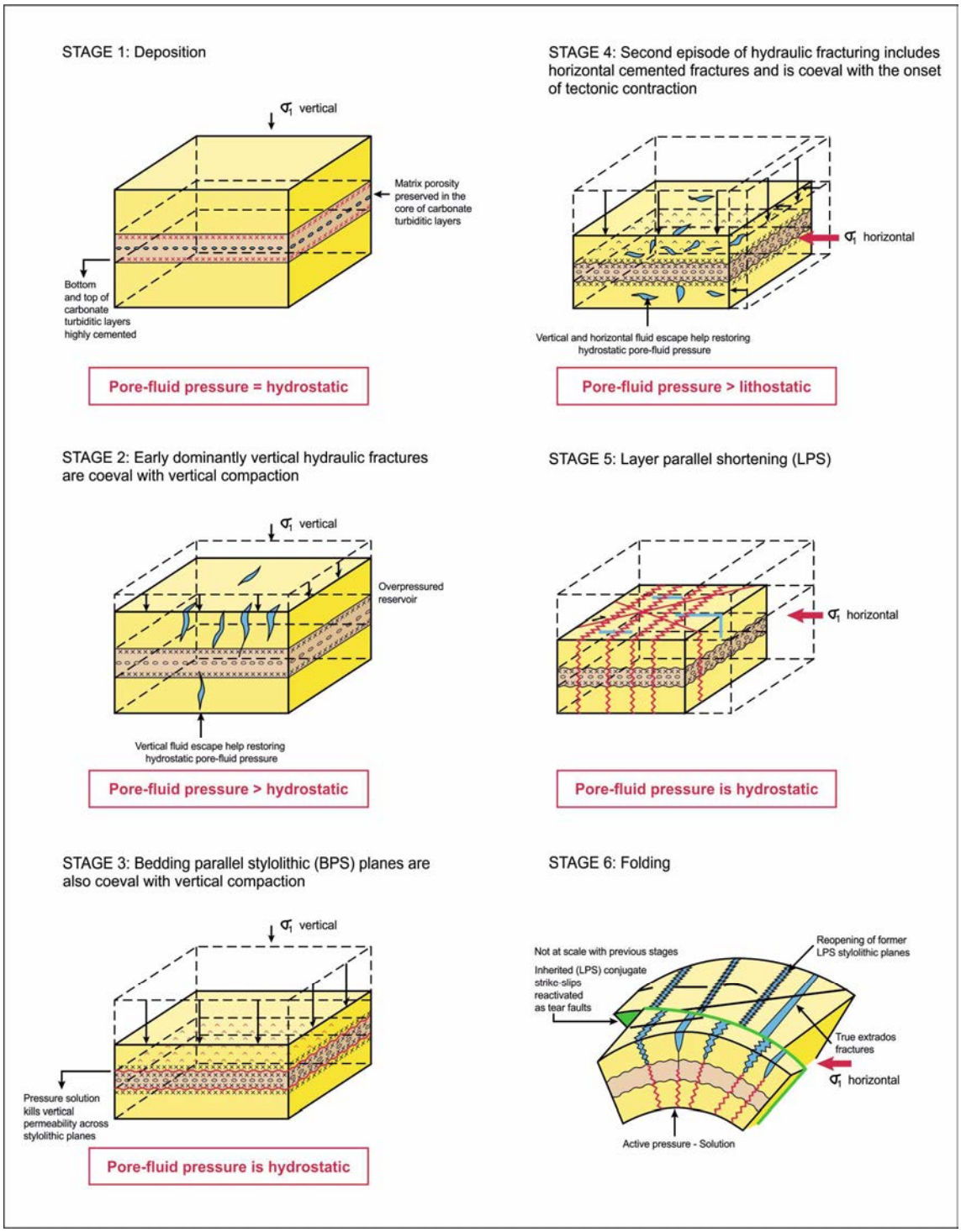

Fig. 2. Composite block diagram outlining the successive development of deformation structures in relation to the evolution of a carbonate-related fold and thrust belt (Roure et al., 2005).

In the past, the study of fluid flow was focused on specific diagenetic products and processes like hydrothermal dolomitization and dickite formation (Sibson et al., 1988; Lacombe et al. 2014). Nevertheless, nowadays diagenetic studies are also focused on to shed light on the geodynamic and paleohydrological evolution of deformed areas such as fold and thrust belts (Dewever, 2008; Vilasi, 2010; Beaudoin et al., 2014; Crognier et al., 2017).

Fold and thrust belts, especially when they are located in the onshore, have been considered difficult places to explore for many reasons. Seismic data is insufficient to allow good interpretations, reservoir development and charge history are difficult to unravel because of uncertainty of the burial history and the tectonic regime tends to lead to a high risk of seal breaching (Goffey et al., 2010). However, orogenic belts are a significant objective of research since they contain large amounts of resources, especially oil and gas, and give us information regarding to plate kinematics (Kendall et al., 2019). During the evolution of fold and thrust belts, the development of deformation structures such as bed-parallel and bed-perpendicular stylolite planes, conjugate fracture sets and hydraulic fracturing, exert a strong control on the permeability and porosity of the reservoir rocks (especially carbonates), and therefore, on fluid flow (Fig. 2). During compressional deformation, fluids are expelled into foreland basins through fractures and rock porosity induced by tectonics (squeegee-type) and/or topography during the successive stages of fold and thrust belts evolution (Oliver, 1986; Heydari, 1997; Bitzer et al., 2001; Pollyea et al., 2015) (Fig. 3).

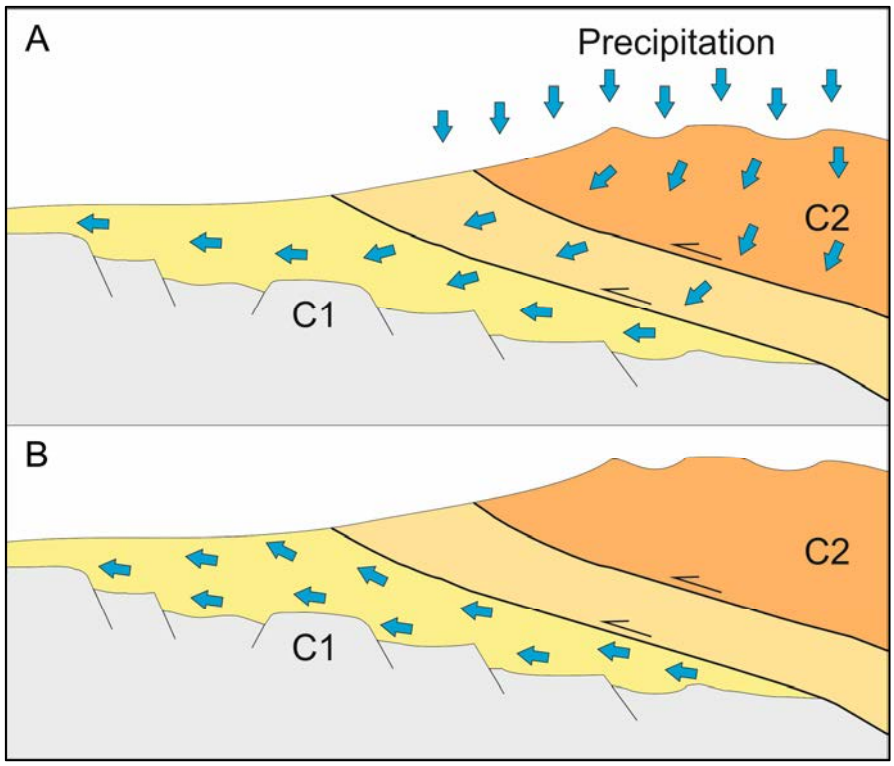

Fig. 3. Two dimensional flow systems hypothesized for mountain belts formed by collisional orogeny (continents C1 and C2): a) topography-driven flow orthogonal to the range front; b) tectonically-induced "squeegee" model for the expulsion of overpressured fluids from an overthrust passive margin. Redrawn from Sibson (2005).

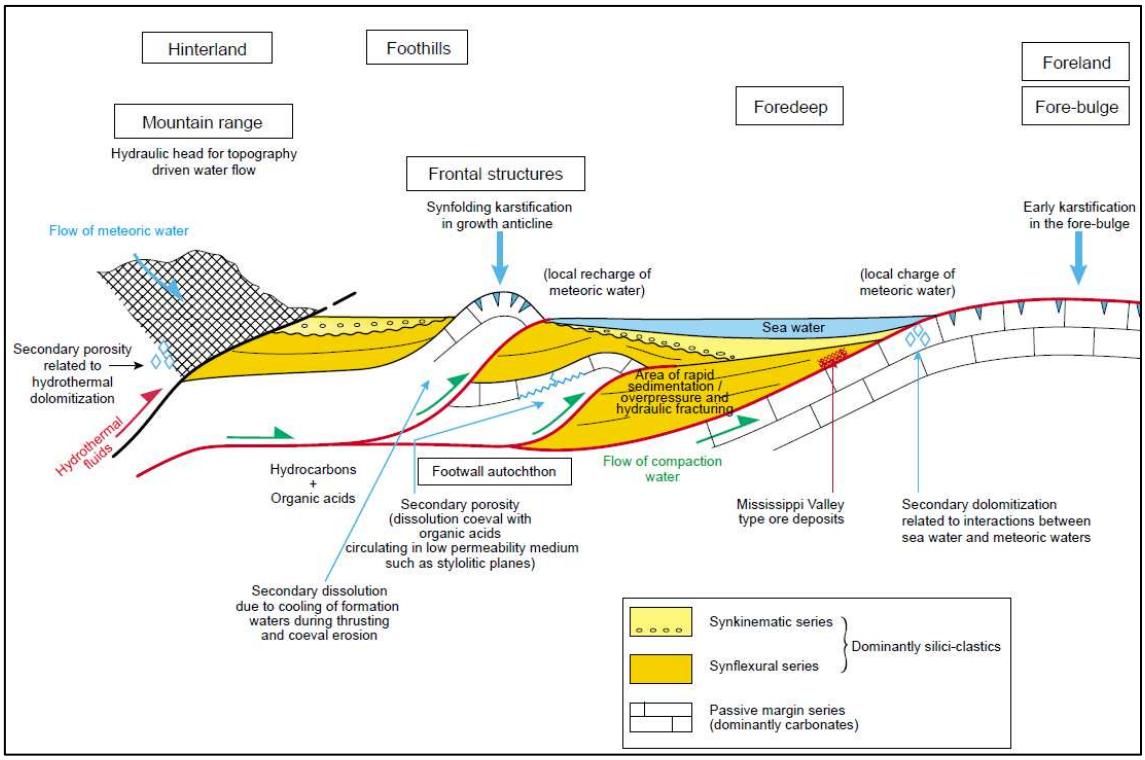

Fig. 4. Synthetic cross section of a fold and thrust belt summarizing the main structural domains as well as cementation habitats and carbonate dissolution areas (Roure et al., 2005).

Key elements such as the structural style and the stratigraphy of fold and thrust belts, as well as the petrology and geochemistry of diagenetic products related to fluid flow are easily studied in mountainous exposures since in core materials these elements are not always evident. Regarding to fluid flow, the challenges of this kind of research are to reconstruct the temperature, the chemical composition of the fluids and the prevailing paleohydrological system during the development of a compressional belt, as well as their evolution through time. These parameters are not homogeneous along the main structural domains of the thrust belt (Fig. 4) and must be studied separately and then integrated into an orogen-scale model (Travé et al., 2007).

1.2. Previous studies

Previous works on the relationships between fluid migration and deformation in fold and thrust belts exist related to fluid flow at orogen scale, such as those developed in the Bighorn Basin, in USA (Beaudoin et al., 2014), the Veracruz petroleum province (e.g. Ferket et al., 2006), The Mexican fold and thrust belt (Fitz-Díaz et al., 2011); in Northern Oman Mountains (e.g. Fontana et al., 2014), in the Spanish Linking Zone (Travé et al., 2004), in the Sicilian fold and thrust belt (Dewever, 2008), in the South Pyrenean fold and thrust belt (Travé et al., 2007) and in the Wessex Basin, UK (Worden et al., 2015), as some of the examples.

Detailed research in fluid flow related to compressional deformation has also been studied from diverse approaches, such as: 1) hydraulic behavior of fractures (e. g. Moretti et al., 2000; Labaume and Moretti, 2001; Breesch et al., 2009), 2) fluid overpressures and fracturing (e. g. Cobbold et al., 2013; Mackay, 2015), 3) fluid circulation during folding (e. g. Evans and Fischer,

2012; Beaudoin et al., 2015; Cosgrove, 2015) and 4) controls of the style of deformation on fluid flow (e. g. Beaudoin et al., 2011 and 2014; Travé et al., 2000 and 2007). Tables 1 to 5 summarizes some previous works developed from different approaches in fold and thrust belts worldwide. The locations of the studied fold and thrust belts in previous works are in Fig. 5.

Table 1. Summary of previous works of fluid flow at orogen scale.

Country	Area	Age	References
Canada	Canadian Rocky Mountains	Mesozoic-Tertiary	Vandenginste et al. (2012)
Mexico	Mexican fold and thrust belt	Late Cretaceous-Eocene	Ferket et al. (2006), Fitz-Díaz et al. (2011)
USA	Rocky Mountains	Mesozoic	Vandeginste et al. (2005)
USA	Bighorn Basin	Late Cretaceous	Beaudoin et al. (2014)
UAE	Northern Oman Mountains	Late Cretaceous-Miocene	Breesch (2008), Fontana et al. (2014)
Italy	Sicilian fold and thrust belt	Miocene	Dewever (2008)
Albania	Ionian fold and thrust belt	Tertiary	Swennen et al. (2000), Vilasi et al. (2009)
Belgium	Rhenohercynian fold belt	Late Carboniferous	Schroyen and Muchez (2000)
United Kingdom	Wessex Basin	Tertiary	Worden et al. (2015)
Spain	Linking Zone	Eocene-Miocene	Travé et al. (2004)
Spain	Catalan Coastal Ranges	Paleogene	Travé et al. (1998b)
Spain	South Pyrenean fold and thrust belt	Eocene-Oligocene	Travé et al. (2007)

Hydraulic behavior of fractures. The hydraulic behavior of faults and joints (Table 2) is of great importance since faults can act as paths or barriers for longitudinal and/or transversal fluid flow. Changes of this behavior controlled by depth have been studied in the Bolivian sub Andean zone by Moretti et al. (2000). These authors observed that at depths higher than 3 km, thrust faults can act as a barrier for fluid flow due to authigenic quartz cementation, whereas at shallower positions (< 2,5-3 km) act as fluid paths. Fluid compartmentalization in an orogen by thrust faults has been reported by Labaume and Moretti (2001) in the Bolivian sub Andean Zone, Breesch et al. (2009) in Northern Oman Mountains, Dewever et al. (2013) in the frontal part of the Sicilian fold and thrust belt, and by Travé et al. (1997, 1998a, 2000) and Lacroix et al. (2014) in the southern Pyrenees. These authors observed how thrust faults can act as barriers for transversal fluid flow allowing the development of different diagenetic histories both in the hanging and foot wall of these faults. The behavior of fracture corridors as seal-bypass systems has been studied in the Sevier thrust belt (Ogata et al., 2014). This work shows how fracture corridors develop large-scale networks of preferential fluid-flow pathways (Fig. 6). Similar behavior of fractures has

been reported in southwestern Lurestan province (Zagros Mountains, Iran) by Sharp et al. (2010). This work shows the controls of fracturing and facies architecture on dolomitization processes. In the Chrystalls Beach Complex of New Zealand, fracture mesh generation in underthrust sediments favored localized fluid flow and vein formation (Fagereng and Harris, 2014). Finally, Hausegger et al. (2009) studied the mechanisms of fault breccia formation in carbonate damage zones and its control on the hydraulic behavior of faults in Eastern Alps.

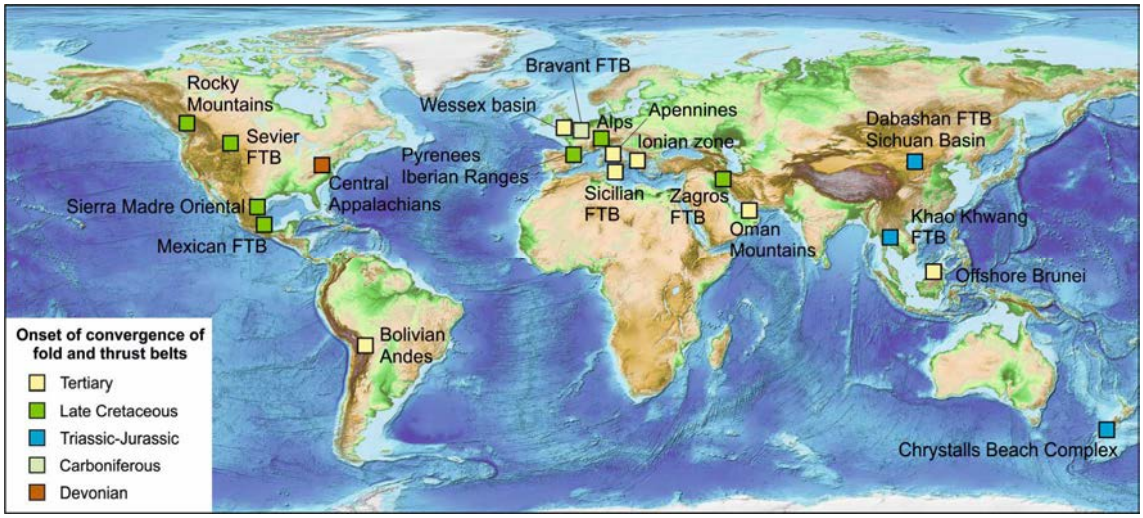

Fig. 5. Location of the fold and thrust belts presented in tables 1 to 5. The color of the boxes indicates the onset of convergence in these fold and thrust belts.

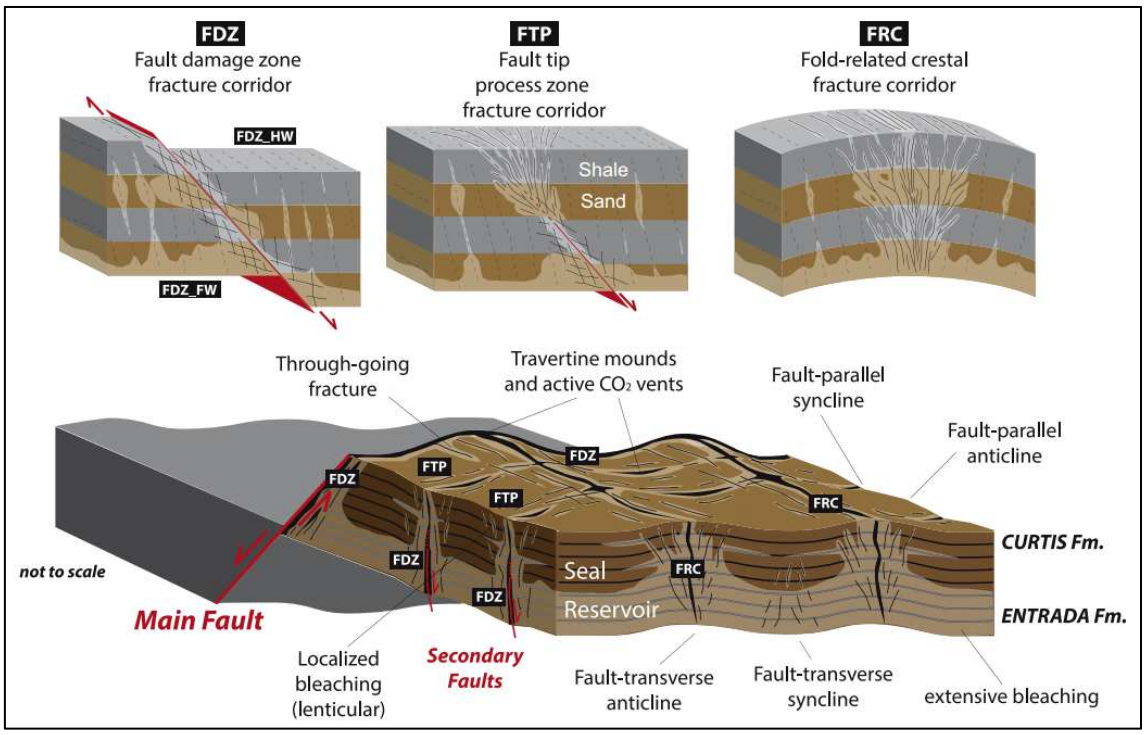

Fig. 6. Conceptual model showing the different fracture corridors types, and their relationships for developing a large-scale network of preferential fluid flow pathways (Ogata et al., 2014).

Table 2. Summary of previous works of the hydraulic behavior of faults.

Country	Area	Age	References
New Zealand	Chrystalls Beach Complex	Triassic-Jurassic	Fagereng and Harris (2014)
Bolivia	Sub Andean Zone	Neogene	Moretti et al. (2000), Labaume and Moretti (2001), Husson and Moretti (2002)
USA	Sevier thrust system	Mesozoic-Tertiary	Ogata et al. (2014)
Iran	Zagros fold and thrust belt	Mesozoic-Tertiary	Sharp et al. (2010), Shariatinia et al. (2014)
Thailand	Khao Khwang fold and thrust belt	Triassic	Hansberry et al. (2015)
UAE	Northern Oman Mountains	Late Cretaceous-Miocene	Breesch et al. (2009)
Austria	Eastern Alps	Mesozoic-Tertiary	Hausegger et al. (2009)
Belgium	Brabant Massif	Late Carboniferous	Piessens et al. (2002), Dewaele et al. (2004)
Italy	Northern Apennines	Miocene	Cello et al. (2001), Petracchini et al. (2012)
Italy	Sicilian fold and thrust belt	Oligocene-Miocene	Dewever et al. (2013)
Spain	Jaca and Ainsa basins (Pyrenees)	Eocene-Oligocene	Lacroix et al. (2013, 2014)
Spain	Ainsa Basin (Pyrenees)	Middle Eocene	Travé et al. (1997, 1998a)
Spain	Eastern Ebro Basin	Oligocene	Travé et al. (2000)
Switzerland	Western Alps	Mesozoic-Tertiary	Kirschner et al. (1999)

Fluid overpressures and fracturing. Other authors focused their research on the development of fractures due to fluid pressure built-up. (Table 3). Cobbold et al. (2013) studied several examples of bedding-parallel calcite, gypsum and quartz veins formed in different sedimentary basins worldwide. Mackay (2015) studied the role of fluids in the structural development of southern Canadian Rocky Mountains. Both authors concluded that overpressures are commonly related with the generation of hydrocarbons. Petroleum generation increases the fluid pressure within the rock driving the system into failure, allowing thrust reactivation and the development of bedding-parallel veins (Fig. 7). Li et al. (2013) document the development of fluid overpressures due to clay transformations in the Dabashan fold and thrust belt, in China. In this setting, overpressure fluids are the main carrier of oil and gas, which are trapped as fluid inclusions in calcite veins. Morley et al. (2014) compared two anticlines developed in different settings (deep

marine environment in Deepwater region offshore Brunei vs. arid continental environment in Central Basin of Iran, Zagros mountains) in order to decipher the main controls on overpressure development. These authors observed how the availability of water trapped in the pore-space and diagenetic processes like chemical compaction exert a strong influence on the development of overpressures. Turner and Williams (2004) highlighted the role of fluid overpressures during basin inversion. They document that overpressures induce reactivation of faults which are unfavorably oriented with respect to maximum principal stress. Besides, sudden fault reactivation is responsible of vertical fluid flow, which can transfer potentially very large volumes of hydrothermal fluids from deep to shallower parts of a compressional belt. These results have significant implications for the oil and ore industry, as well as for geothermal exploration.

Table 3. Summary of previous works of fluid overpressures and fracturing.

Country	Area	Age	References
USA	Rocky Mountains	Mesozoic	Mackay (2015)
China	Dabashan foreland belt	Jurassic-Cretaceous	Li et al. (2013)
China	Sichuan Basin	Late Triassic	Zeng (2010)
Iran	Zagros fold and thrust belt	Mesozoic-Tertiary	Morley et al. (2014)
Spain	Jaca and Ainsa basins (Pyrenees)	Eocene-Oligocene	Lacroix et al. (2013)

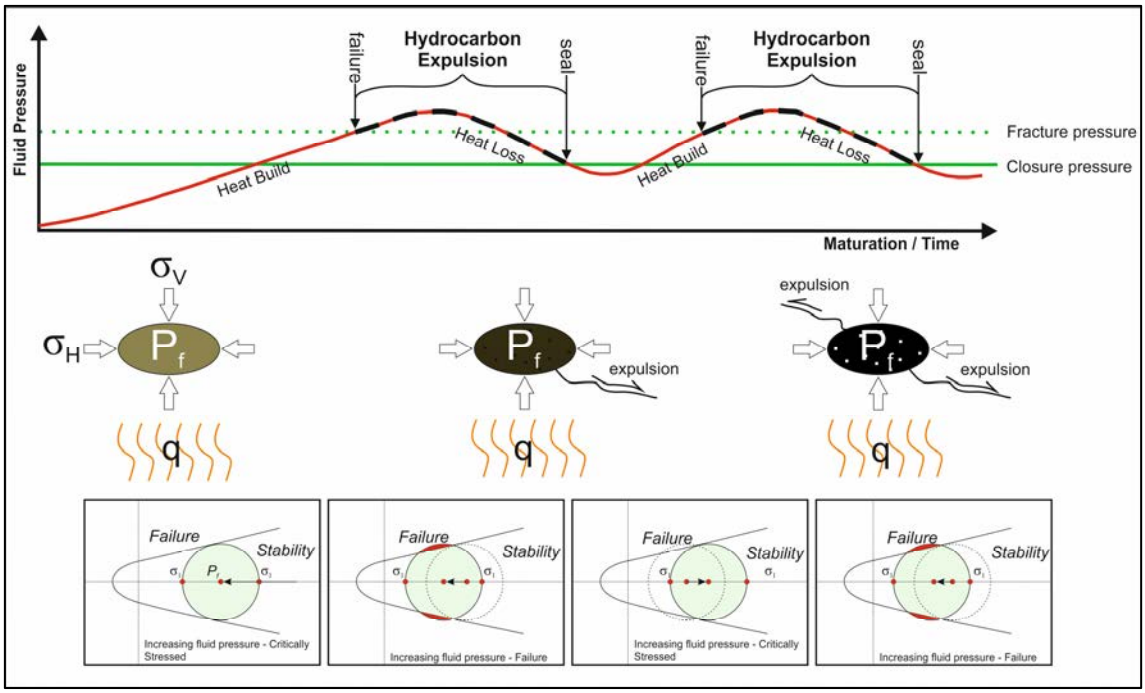

Fig. 7. Effect of fluid pressure in fracture development and later sealing. As organic matter is heated hydrocarbons volume increases in a confined pore space, resulting in a fluid pressure increase. The Mohr circle shifts into failure conditions and hydrocarbons are expelled from the pore space. Heat is lost with the expulsion of hydrocarbons as well as fluid pressure. This drives the system back into failure and the hydrocarbons are expelled, creating another loss of fluid pressure and heat (Mackay, 2015).

Fluid circulation during folding. Folds are one of the main structures investigated from different approaches since they are good traps for fluids of economic interest. However, fluid flow associated with folding (Table 4) has received less attention than fluid flow during faulting because folds are considered as one of the most complex systems in geology (Evans and Fischer, 2012). The importance of fluid flow in folds lies in the fact that temperature and pressure affect the folding process (Fig. 1). Recent studies focused on the relationships between fluid flow and folding have been done in the Southern Pyrenees (Beaudoin et al., 2015), Northern Apennines (Conti et al., 2010), Central Appalachians (Chandonais and Onasch, 2014; Evans et al., 2012), in the Nuncios Fold Complex, Sierra Madre Oriental (Fischer et al., 2009; Lefticariu et al., 2005) and in the North Pyrenean Saint-Jean-de-Luz basin (Tilhac et al., 2013). These authors concluded that the folding process can change the palaeohydrological behavior of sedimentary units, allowing the connection between different hydrostratigraphic units. Another process that occurs during folding is the development of overpressures in folds that allow fracture development and therefore can affect fluid mobility.

Table 4. Summary of previous works of fluid flow during folding.

Country	Area	Age	References
Mexico	Sierra Madre Oriental	Late Cretaceous-Eocene	Lefticaariu et al. (2005) Fischer et al. (2009) Fitz-Díaz et al. (2011)
USA	Central Appalachians	Devonian	Evans et al. (2012) Chandonais and Onasch (2014)
USA	Bighorn Basin	Late Cretaceous	Beaudoin et al. (2011, 2012, 2014)
France	Saint-Jean-de-Luz Basin	Eocene	Tilhac et al. (2013)
Italy	Northern Apennines	Miocene	Conti et al. (2010)
Spain	Sierras exteriores (Pyrenees)	Eocene-Oligocene	Beaudoin et al. (2015)
Spain	Eastern Ebro basin	Eocene-Oligocene	Travé et al. (2000)

Controls of the style of deformation on fluid flow. Another factor that can influence palaeohydrology in a basin or orogen is the structural style of deformation (Table 5). Beaudoin et al. (2011, 2014) discuss the effect of thick-skinned tectonics on fluid flow in the Bighorn Basin (Wyoming, USA). Their results suggest that basement-cored folds allow hydrothermal fluids to flow vertically from the crystalline basement to fractured cover sedimentary rocks. Travé et al. (2000, 2007) and Fischer et al. (2009) studied the fluid flow in a detachment fold in the South Pyrenean foreland basin and in the Nuncios Fold Complex (Sierra Madre Oriental), respectively. Their results indicate that fluids involved in detachment folds are mainly meteoric and formational

fluids mobilized at different depths and that detachments act as barriers for the input of deep-sourced fluids.

Table 5. Summary of previous works of controls of the style of deformation on fluid flow.

Country	Area	Age	References
Mexico	Sierra Madre Oriental	Late Cretaceous-Eocene	Fischer et al. (2009),
USA	Bighorn Basin	Late Cretaceous	Beaudoin et al. (2011, 2014)
France	External Alps	Eocene	Boutoux et al. (2014)
Spain	Eastern Ebro Basin	Oligocene	Travé et al. (2000)
Spain	South Pyrenean fold and thrust belt	Eocene-Oligocene	Travé et al. (2007)

1.3. Fluid flow in the south Pyrenean fold and thrust belt

The Pyrenees (Fig. 8) is a doubly-verging orogenic belt generated since the Late Cretaceous to the Oligocene due to the collision between the Iberian and European tectonic plates (Muñoz, 1992). This collision leads to the inversion of previous Mesozoic extensional basins and the development of an antiformal stack in the central part of this chain (Muñoz, 1988, 1992; Muñoz et al., 1986; Vergés et al., 2002a).

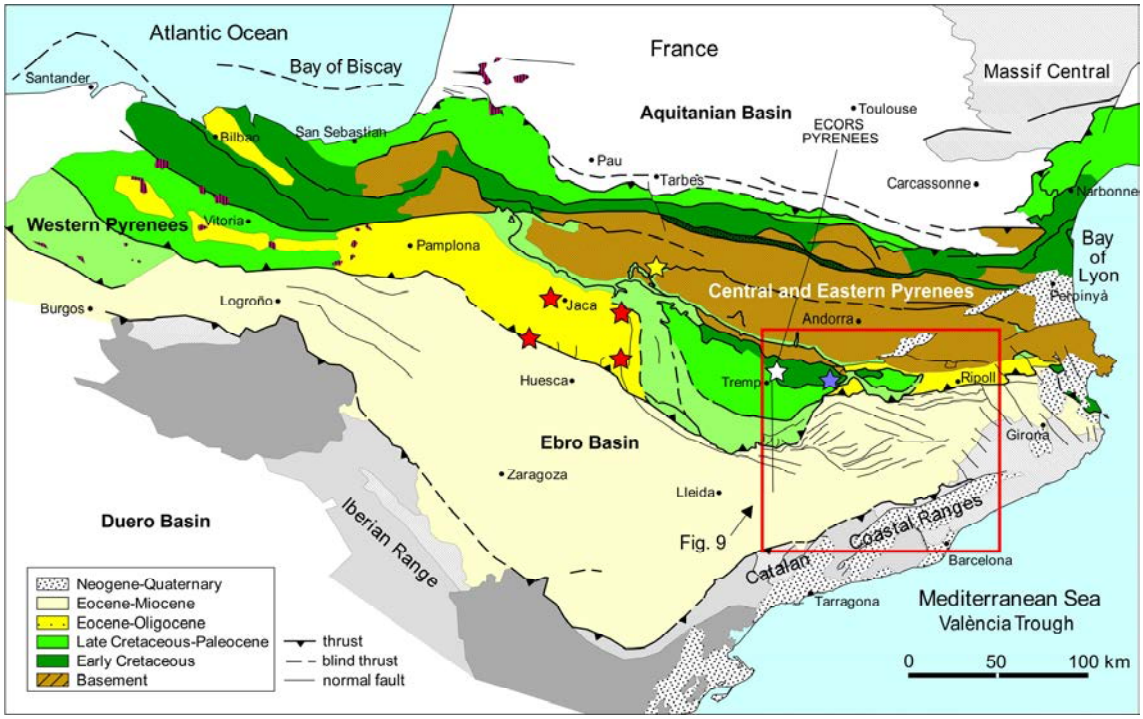

Fig. 8. Structural map of the NE sector of the Iberian Peninsula where are shown the main structural units of the Pyrenees (Vergés, 1993). The red stars represent the outcrops studied in the Jaca and Ainsa basins. The yellow star indicates the location of the outcrops studied in the Gavarnie thrust sheet, whereas white and blue stars show the outcrops studied in the south central Pyrenees. The red box shows the location of Fig. 9.

Studies about fluid flow during the formation of the South Pyrenean fold and thrust belt have been carried out in different locations of this orogen (Table 6). These studies represent different stages of evolution of the Pyrenees.

Table 6. Summary of previous works developed in the South Pyrenean fold and thrust belt.

Area	Age	Given information	References
Sierras Exteriores	Eocene-Oligocene	Fluid flow during folding	Beaudoin et al. (2015)
Jaca and Ainsa basins	Eocene-Oligocene	Fluid flow and overpressures and hydraulic behavior of faults	Lacroix et al. (2013, 2014, 2018) Crognier et al. (2017)
Ainsa Basin	Middle Eocene	Fluid flow controls on reservoir quality and hydraulic behavior of faults	Hoareau et al. (2015) Mansurbeg et al. (2009), Travé et al. (1997. 1998a)
Central Pyrenees	Late Eocene	Fluid source and mixing processes	Grant et al. (1990), Banks et al. (1991), McCaig et al. (2000a, b), Trincal et al. (2017).
	Upper Cretaceous	Sequence stratigraphy and Diagenesis	Booler and Tucker (2002)
		Fluid flow during folding	Nardini et al. (2019)
Southeastern Pyrenees	Late Eocene	Hydrocarbon migration and early diagenesis products	Giménez-Montsant et al. (1999), Caja et al. (2006a, b, 2007)
Eastern Ebro foreland basin	Eocene-Oligocene	Hydraulic behavior of faults	Travé et al. (2000)
South Pyrenean fold and thrust belt	Eocene-Oligocene	Thrust belt evolution	Travé et al. (2007)
	Paleocene-Oligocene	Fluid flow modelling	Bitzer et al. (2001)

In the Ainsa and Jaca basins (Fig. 8, red stars) there are some works of fluid circulation during the activity of the El Monte Perdido thrust under deep water conditions (Travé et al., 1997 and 1998a; Lacroix et al., 2013 and 2014). In the Hecho Group (Ainsa basin), Mansurbeg et al. (2009) studied the effect of diagenetic processes on reservoir quality, and Hoareau et al. (2015) studied the burial diagenesis in prodelta facies of the Sobrarbe deltaic complex. These authors concluded that the inherited detrital composition of the host rock can control the diagenetic evolution of a reservoir. In the Sierras Exteriores (southern margin of the Jaca Basin, Fig. 8, red stars), Beaudoin et al. (2015) documented the controls of fold-related fractures on fluid flow and its evolution during the development of the Pico del Aguila Anticline, a detachment fold developed during the middle Eocene to the Oligocene.

In the northwestern sector of the south central Pyrenees (Fig. 8, yellow star) some authors studied the chemical composition of high-salinity fluid inclusions in order to determine the source and behavior of fluids during the activity of the Gavarnie thrust sheet (Grant et al., 1990; Banks et al., 1991; McCaig et al., 2000a, b). The results highlight that these fluids were derived from Triassic brines and reveal the difficulty of expelling high-density fluids from the upper crust. This fact allowed these fluids to be involved in successive fluid flow events in the same zone over hundreds of millions of years. Trincal et al. (2017) studied in the same structure and documented the rock transformations by basement-derived fluids under low-grade metamorphism associated to thrusting. In the Southeastern sector of the Central Pyrenees (Fig. 8, white star) Booler and Tucker (2002) studied the controls of sea level changes on the early diagenesis in carbonate platforms in the Bóixols-Sant Corneli anticline. These Authors concluded that changes in the water table can control the development of different diagenetic products and therefore, it can give us further information during the sequence stratigraphy analysis of carbonate platforms. In the same anticline, Nardini et al. (2019) documented the fluid flow evolution from the early- to post-folding stage (Fig. 8, blue star). Their results reveal that during the early contraction the fluid system was dominated by Lower Cretaceous seawater, whereas during the main stage of folding, the system opened to meteoric waters which mixed at depth with the previous fluid. Finally, during the post-folding deformation stretching the Bóixols anticline, connate evaporated marine fluids migrated through newly-formed fractures.

In the south eastern Pyrenees (Fig. 9) fluid flow studies were mainly concentrated in the Cadí Thrust sheet, which is constituted of Permian, Triassic, Upper Cretaceous and lower to middle Eocene rocks (Vergés, 1993). The presence of oil shows made this structure an interesting target for oil companies (Clavell, 1992). Fluid flow studies in the Cadí thrust sheet have been focused especially on the oil-rich sedimentary units in the northern and southern margins of this structure. The main source rock in this area is the Armàncies formation, located in the northern margin of the Cadí thrust sheet. This sedimentary unit is composed of marine carbonates, marls and shales and was deposited during the middle Eocene (Giménez-Montsant, 1993). Works done by Caja et al. (2006a, b, 2007) (Fig. 9, blue stars) documented the relationships between oil migration and fracturing in the Armàncies and Corones formations, applying thermometry of oil and aqueous fluid inclusions within fracture-filling calcite cements. Other works in the Cadí thrust sheet reported the presence of organic matter-rich levels in the turbidite sediments of the Vallfogona formation in the southern margin of the Cadí thrust sheet (Permayer and Caja, 2007; Caja and Permayer, 2008) (Fig. 9, red star). However, these organic matter accumulations are not related with fluid flow through fractures, but with anoxic episodes during the deposition of the Vallfogona formation. Finally, Giménez-Montsant et al. (1999) studied the silica concretions developed within the carbonate facies of the Corones formation (Fig. 9, blue stars). These authors revealed the role of early mechanical compaction and sediment dewatering in silica supply derived from sponge spicule dissolution.

In the Ebro foreland Basin only one work has been done by Travé et al. (2000) (Fig. 9, green star). These authors studied the fluid circulation through pre-thrust veins and major thrust faults affecting the El Guix Anticline (eastern Ebro foreland basin). This anticline is a detachment fold generated during the last stages of deformation stretching the South Pyrenean foreland basin, which developed under endorheic conditions. This work documents the controls of the underlying saline Cardona formation on fluid composition and how faults act as regional fluid conduits when they are active.

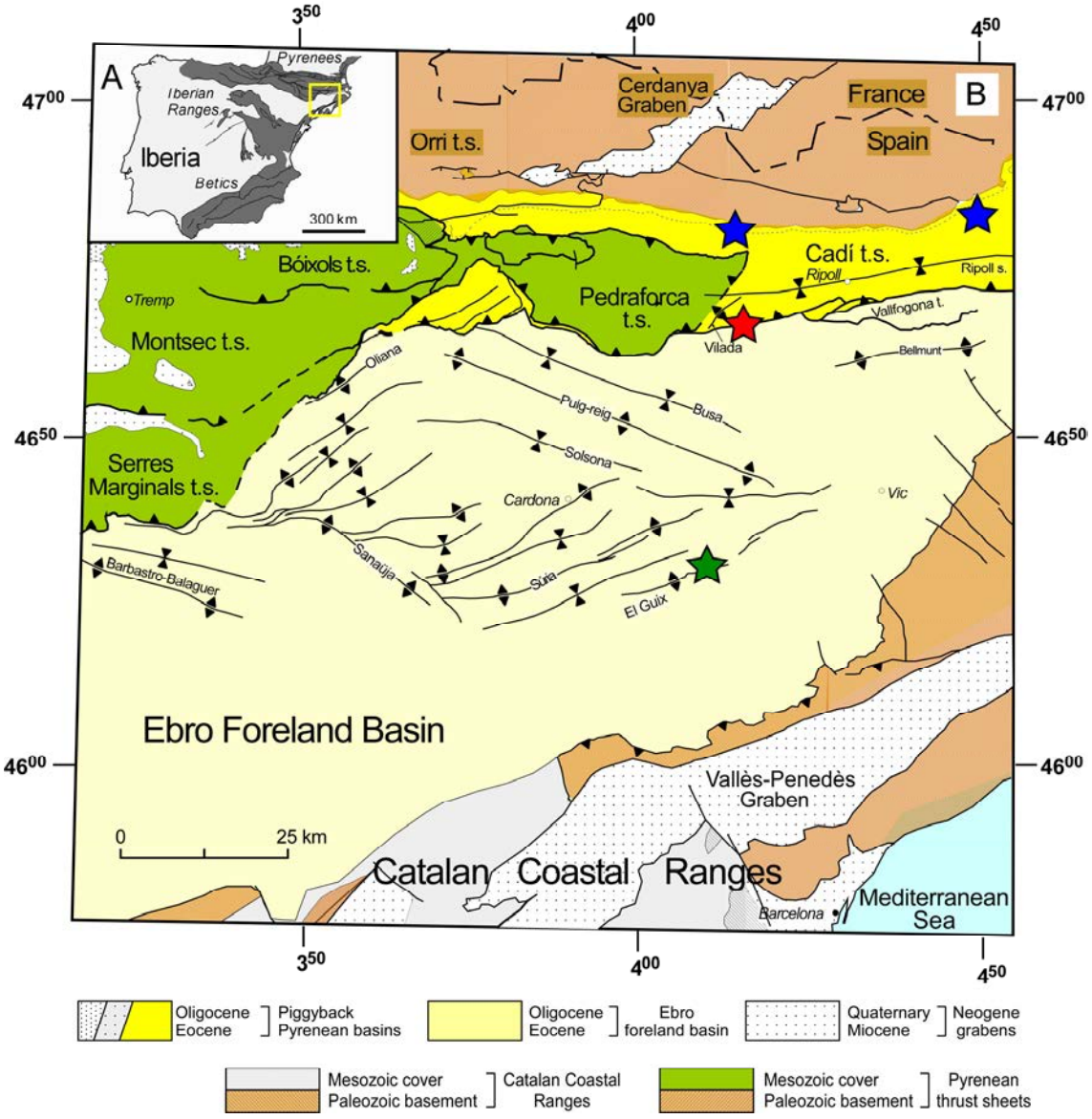

Fig. 9. A) Map of the Iberian Peninsula where is shown the location of the Pyrenees and Fig. 9 B. B) Structural map of the south eastern Pyrenees from Vergés (1993). The blue stars show the location of the outcrops studied by Caja et al. (2006a, b and 2007) and Giménez-Montsant et al. (1999). The red star shows the location of the outcrop studied by Permayer and Caja (2007) and Caja and Permayer (2008). The green star shows the location of the studied outcrop by Travé et al. (2000).

The work published by Travé et al. (2007) integrated fluid flow studies done in the Ainsa Basin (Fig. 8) and southeastern Pyrenees (Fig. 9) in order to perform an evolution model during the development of the South Pyrenean fold and thrust belt. However, not all the structural units

forming this orogen have been studied and therefore, a detailed study within the complete pile of superimposed south Pyrenean thrust sheets is needed to decipher evolution of the fluid regime during each stage of the evolution of this fold and thrust belt.

1.4. Problems to solve in this thesis

Considering the reported literature, there is a scarcity of studies documenting the evolution of fluids during the deformation of a whole section of a fold and thrust belt, since most of these previous works focused on the scale of individual folds and thrusts faults.

Another conflictive point is that the crosscutting relationships between diagenetic products related to fluid flow events (cements) are frequently unclear. It is because the tectonic evolution of fold and thrust belts is complex, and results in multiple stages of deformation and fluid flow events (Cosgrove, 2015). Additionally, the not preservation of syn-orogenic sediments in the thrust front in orogens with a high level of erosion makes difficult to constrain the absolute timing of the deformation and related fluid flow. Therefore, geochronological methods must be applied to fluid flow studies to constrain the timing of the migration of fluids and deformation in orogens.

Finally, there are relatively new analytical methods (e.g. Clumped isotopes, U-Pb geochronology, rare earth analysis) that are not extensively applied in the previous works. It would be interesting to apply these procedures to a case of study in order to reveal new proxies for fluid flow analysis.

1.5. Objectives of this thesis

The main objective of this thesis is to perform a conceptual model of fluid flow in fold and thrust belts, using a complete section of the south eastern Pyrenean fold and thrust belt as analogue. The southern Pyrenees have been selected as object of study due to: 1) the availability of an extensive geological data base (Garrido-Mejías, 1973; Puigdefàbregas et al., 1986; Sáez and Riba, 1986; Berástegui et al., 1990; Burbank et al., 1992; Vergés, 1993, 2002a); 2) the preservation of the structures; 3) the presence of oil shows (Caja et al., 2006a, b, 2007); and 4) the possibility to apply relatively new analytical methods not used in previous studies to study fluid flow. To deal with the main aim proposed, this thesis has been divided into four secondary objectives:

1) To study the evolution of the fluid regime during the development of the south eastern Pyrenean fold and thrust belt.

2) To constrain the absolute timing of syn-tectonic fluid migration in the south eastern Pyrenees.

3) To study the relationships between the evolution of the deformation and the paleohydrological system.

4) To perform a fluid flow model at the scale of the southern Pyrenees.

To generate the model of fluid flow at the scale of the southern Pyrenees proposed in objective 4 of this thesis, the results obtained in the objectives 1, 2 and 3 will be integrated with previous studies about fluid flow done in other areas of the Pyrenees (Travé et al. 1997, 1998a, 2000, 2007; Lacroix et al., 2011, 2014, 2018; Beaudoin et al., 2015; Crognier et al., 2017; Nardini et al., 2019). Finally, the Pyrenees will be compared with other orogens worldwide (Sevier thrust belt, Mexican fold and thrust belt, Ionian zone, Northern Oman Mountains and others) to stablish a conceptual model of fluid flow in fold and thrust belts.

The relationships between the objectives proposed and the articles mentioned in the presentation of this thesis are explained in the following lines:

Study the evolution of the fluid regime during the development of the south eastern Pyrenean fold and thrust belt. The evolution of the fluid regime during the growth of the south eastern Pyrenees is documented in detail in Cruset et al. (2015, 2016a and b, 2017, 2018, 2019) and in Chapters 4, 5 and 8. In these studies, composition, origin and temperature of the fluids migrating through the south Pyrenean thrust sheets will be deciphered integrating structural analyses, petrographic observations and geochemical methods applied to calcite and dolomite cements precipitated in fractures (e.g. carbon, oxygen and strontium isotopes, clumped isotopes thermometry, elemental composition analysis). The results document the evolution of the fluid regime during the change from an underfilled marine to an overfilled non-marine foreland basin.

Absolute timing of syn-orogenic fluid flow. U-Pb geochronology has been applied to fracture-filling calcite cements to constrain absolute ages for syn-tectonic fluid flow during the growth of the southern Pyrenees, as well as to improve the accuracy of the sequence of deformation within the south Pyrenean thrust sheets. The results indicate that compressional deformation ranged from the Late Cretaceous to the Oligocene and that deformation continued during the Neogene rift and post-rift Western Mediterranean events stretching across north east Iberia. This research has been included in Chapter 6 and in a scientific article that is in review in the journal Geology.

Relationships between the evolution of the deformation and the paleohydrological system. The study a whole history of fluid flow evolution from syn-sedimentary hydroplastic deformation to later brittle fracturing will allow us to characterize the controls of deformation on fluid regime as deformation of a studied structure evolves through time. Results of this research are included in Chapter 7 and in an article submitted to the journal Marine and Petroleum Geology. Geochemical analyses shed light on the changes in the paleohydrological system (open versus closed) during the compressional history of one of the thrust sheets forming the southern Pyrenees.

Chapter 2

Geology of the south eastern Pyrenees

2. Geology of the south eastern Pyrenees

2.1. Structure of the south eastern Pyrenees

The Pyrenees, formed within the framework of the Alpine orogeny and consist of a doubly verging orogenic belt generated during the continental collision between Iberia and Eurasia plates (Fig. 10), from Late Cretaceous to Miocene (Muñoz, 2002; Vergés et al., 2002a). This collision resulted from the partial subduction of the Iberian plate beneath the Eurasian plate (Choukroune, et al., 1989; Roure et al., 1989; Muñoz, 1992, 2002; Vergés et al., 1995, 2002a).

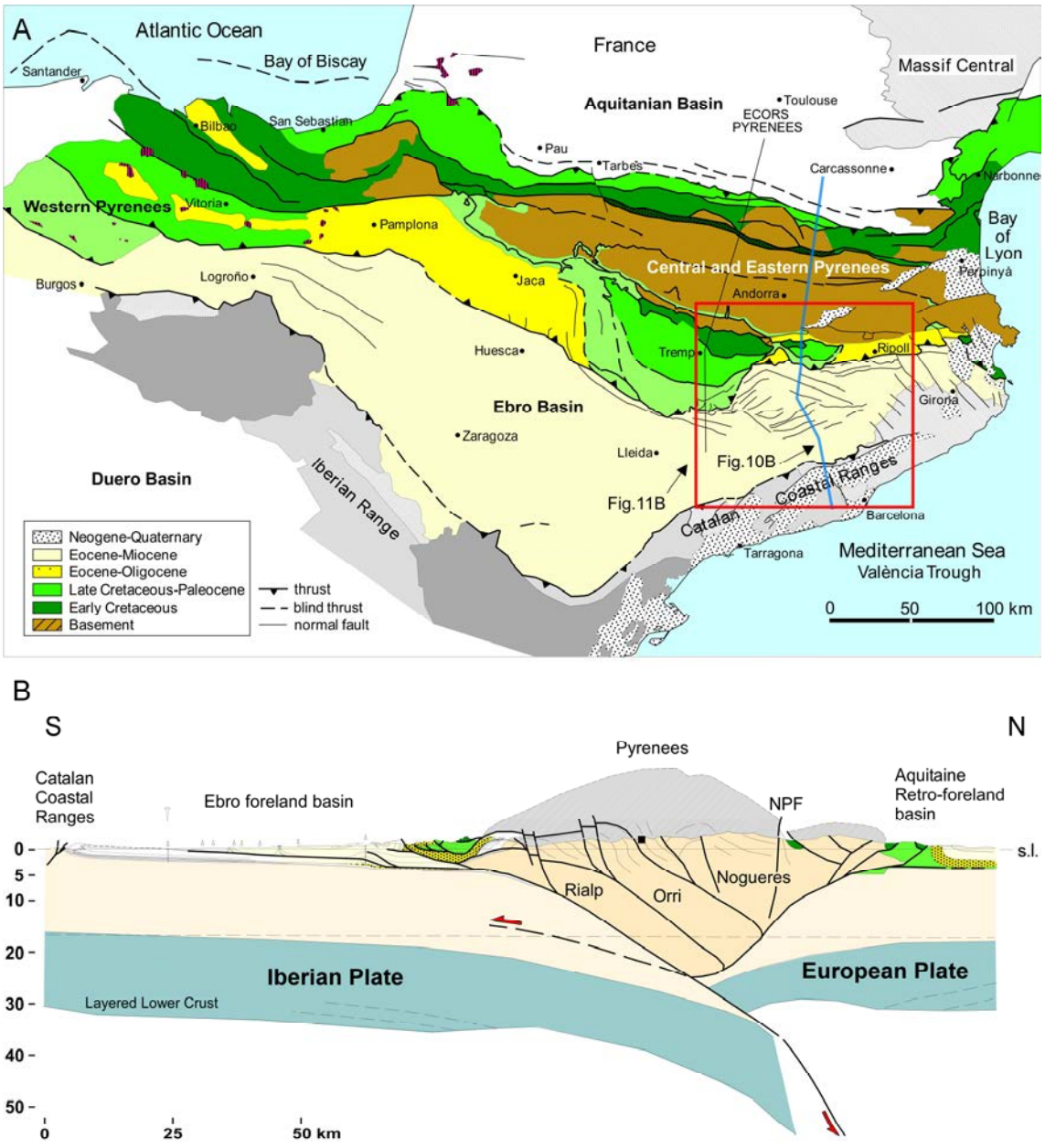

Fig. 10. A) Structural map of the NE sector of the Iberian Peninsula where are shown the main structural units of the Pyrenees (Vergés, 1993). The blue line indicates the location of Fig. 10B. The red box indicates the location of Fig. 11B. B) Eastern Pyrenees crustal-scale balanced cross-section from Vergés et al. (1995).

Prior to the Alpine compression, the north Iberian margin was affected by lithosphere extension during the Late Triassic and Early Jurassic, which favored the deposition of extensive carbonate sediments in platforms during the Jurassic (Mey et al., 1968; Peybernès, 1976; Vergés and García-Senz, 2001; Aurell et al., 2002; Martín-Chivelet, 2002). During the Late Jurassic and Early Cretaceous, the reactivation of the Pyrenean rifting resulted in the opening of the Bay of Biscay, which induced diapirism by the flow of Upper Triassic evaporites and the formation of salt-related basins (Rios, 1948; Brinkmann and Lögters, 1968; Serrano and Martínez del Olmo, 1990; McClay et al., 2004; Canérot et al., 2005; López-Mir et al., 2014; Poprawski et al., 2014; Saura et al., 2015; Tavani et al., 2018). In the north Pyrenean zone, however, this extension produced the extreme thinning of the continental crust and the exhumation of upper mantle rocks during the Late Aptian and the Albian-Cenomanian (Lagabrielle et al., 2010; Clerc and Lagabrielle, 2014; Clerc et al., 2016). After this rifting event and prior to the Pyrenean compression, moderate subsidence associated with post-rift thermal contraction affected the area (Martín-Chivelet, 2002). During the collision between Iberia and Eurasia plates, the previous Mesozoic extensional basins were inverted, and an antiformal stack constituted of basement-involved thrust sheets developed in the central part of the chain (Axial zone), acting as a boundary between the North and south Pyrenean fold and thrust belts (Muñoz, 1992).

The south Pyrenean fold and thrust belt (Fig. 11) consists of a sequence of south-verging thrusts sheets emplaced in a piggy-back thrust sequence (Puigdefàbregas et al., 1992) and detached predominantly above Triassic evaporites (Séguret, 1972) and Eocene evaporites deposited in the foreland basin (Vergés et al., 1992; Sans, 2003).

The structures studied in this thesis from top-and-older to bottom-and-younger consist of the complete stacking of south eastern Pyrenean thrust sheets (Upper Pedraforca, Lower Pedraforca and Cadí), and their related Ebro foreland basin (Fig. 11). These structures are described below:

Upper Pedraforca thrust sheet. It is the oldest cover thrust sheet of the eastern sector of the south Pyrenean fold-and-thrust belt. It consists of an extensional basin affected by diapirism, incorporated into the Pyrenean orogen during the Late Cretaceous-Palaeocene compression (Puigdefàbregas and Souquet, 1986; Vergés, 1993; Saura et al., 2015) and reactivated during the Eocene-Oligocene (Vergés, 1993). The Upper Pedraforca thrust sheet emplaces Upper Triassic, Jurassic and Cretaceous pre-compressive rocks over Upper Cretaceous to Palaeocene syn-orogenic sediments of the south Pyrenean foreland basin (Vergés, 1993; Martínez et al., 2001; García-Senz, 2002).

Lower Pedraforca thrust sheet. This structure consists of an allochthonous klippe detached in the Upper Triassic Keuper facies and emplaced from Lower to Middle Eocene (Puigdefàbregas et al., 1986; Burbank et al., 1992). The emplacement of this structural unit was under marine conditions, as attested by the syn-orogenic fan delta conglomerates of Queralt deposited at the thrust front (Vergés, 1993).

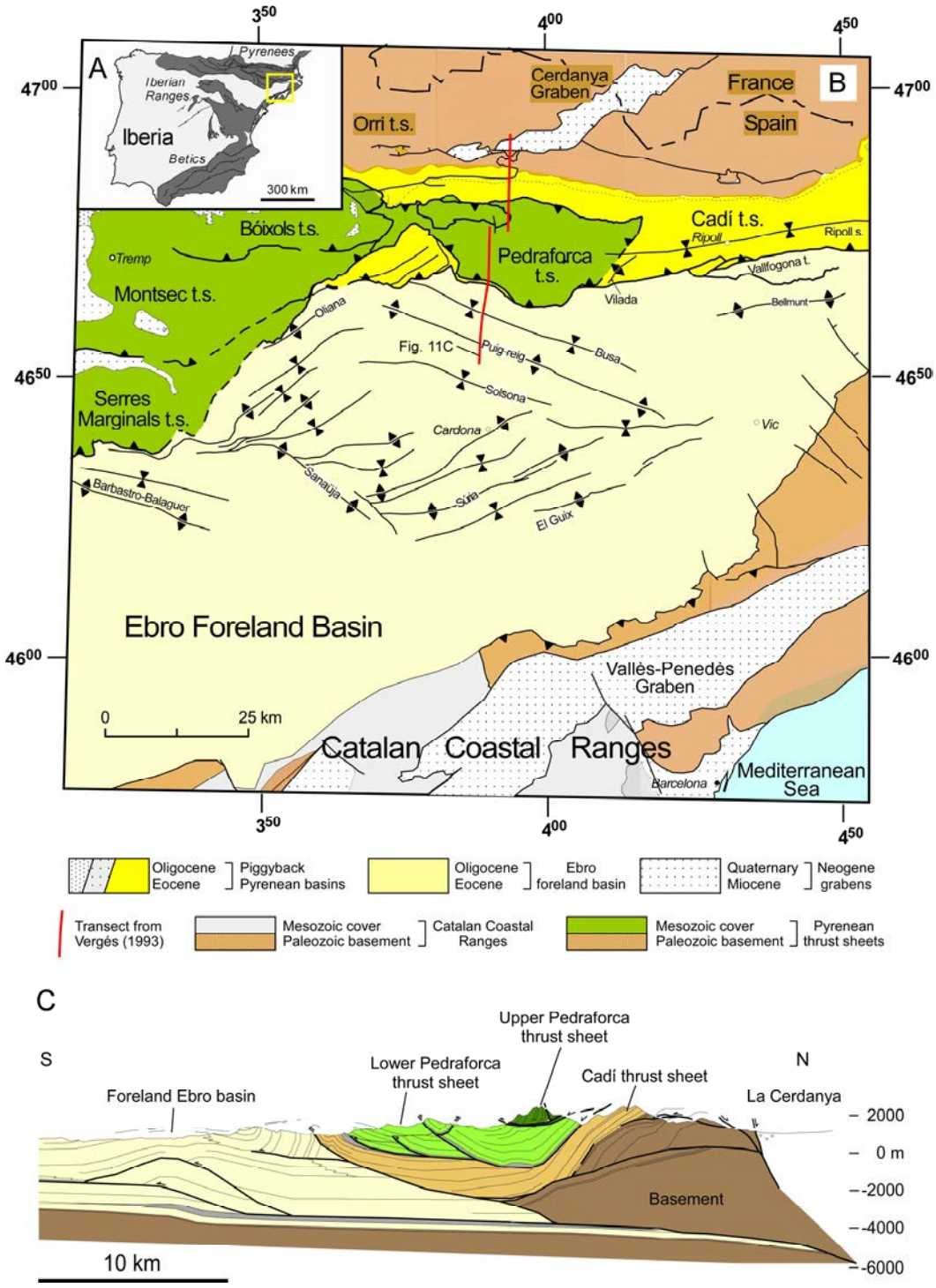

Fig.11. A) Regional map of the Iberian Peninsula showing the location of the south Pyrenean fold and thrust belt (yellow box). B) Simplified geological map showing the main structural units forming the south Pyrenean fold and thrust belt from Vergés (1993). C) Geological cross section of the South Pyrenean fold and thrust belt from Vergés (1993) where are shown the studied thrust sheets in this thesis. The location of the cross-section is located in Fig. 9.

Cadí thrust sheet. The lowermost Cadí thrust sheet is linked to the Axial Zone antiformal stack formed by the Orri and Rialp basement thrusted units (Muñoz, 1992), which are unconformably overlain by thin Mesozoic rocks and thick Paleogene rocks. The southern boundary of the Cadí thrust sheet is the Vallfogona thrust. The activity of this thrust fault started

in the middle Eocene under marine conditions and finished during the lower Oligocene under continental conditions (Burbank et al., 1992a, 1992b; Vergés, 1993; Vergés and Burbank, 1996; Cruset et al., in review).

Ebro foreland basin. It represents the non-marine stage of the South Pyrenean foreland basin (Vergés et al, 2002b), which developed from the middle Priabonian (Costa et al., 2010). The fold system deforming the eastern region of the Ebro foreland basin was detached above the Cardona evaporites (Sans et al.,1996; Sans, 2003).

2.2. Stratigraphy of the south eastern Pyrenees

The rocks forming the studied thrust sheets range in age from the Upper Triassic to the Oligocene and include pre-rift, syn-rift and post-rift marine rocks and marine to continental syn-orogenic sedimentary units.

The stratigraphy of the Upper Pedraforca thrust sheet is similar to that in its western equivalent, the Bóixols thrust sheet (García-Senz, 2002; Mencos et al., 2015) and is divided into pre-rift, syn-rift and post-rift marine sediments and marine to continental syn-orogenic sediments (Fig. 12). The pre-rift sequence is composed of Triassic and Jurassic rocks. Triassic units consist of evaporites and clays from the Keuper facies, which constitute the main detachment level in the Pyrenees, and laminated dolostones from the Isàvena Formation (Séguret, 1972; Calvet et al., 1993; Arnal et al., 2002). The Jurassic is represented by the Bonansa Formation and in the studied area consists of Lower Jurassic dolomitic breccias, laminated limestones and dark marls with brachiopods and ammonoids and Middle and Upper Jurassic dolostones (Peybernès 1976; Aurell et al., 2002). The syn-rift sequence comprises Lower Cretaceous rocks and consists of Berriasian breccias and Valanginian to Albian limestones and marls (García-Senz, 2002). Post-rift sediments in the UPTS are represented by limestones of the Cenomanian-Turonian Santa Fe Formation and Lower Santonian limestones with Lacazina from the Sant Corneli Formation (Mey et al., 1968; Skelton et al., 2003; Ullastre and Masriera, 2004). The Syn-orogenic sequence is constituted of Upper Cretaceous to Palaeocene sediments. The Upper Cretaceous units consist of marine marls, limestones and carbonate breccias of the Late Santonian to Maastrichtian Areny Formation. This unit is conformably overlain by the Maastrichtian to Danian marine dark marls, coastal siltstones and continental sandstones and conglomerates of Garumnian Facies (Puigdefàbregas and Souquet, 1986; Vicente et al., 2015).

In the Lower Pedraforca thrust sheet, the stratigraphy ranges in age from the Upper Triassic to the Oligocene and consists of pre- to syn-orogenic rocks (Fig. 13). Pre-compressive units consist of evaporites and red clays from the Keuper facies, Jurassic limestones and dolostones from the Bonansa Fm. and Coniacian to Lower Santonian limestones (Mey et al., 1968; Simó, 1985; Calvet et al., 1993). Syn-orogenic materials consist of Upper Santonian to Campanian marine sandstones and limestones from the Vallcarga Fm., Campanian-Maastrichtian coastal deposits of the Areny Fm., Maastrichtian-Thanetian continental deposits from the Garumnian

facies, Ilerdian limestones from the Cadí Fm., Lutetian-Bartonian marine conglomerates of the Coubet Fm. deposited in the thrust front and Oligocene continental conglomerates deposited during the reactivation of the Lower Pedraforca thrust sheet (Moeri, 1977; Vergés, 1993; López-Martínez et al., 1999; Rosell et al., 2001; Oms et al., 2007).

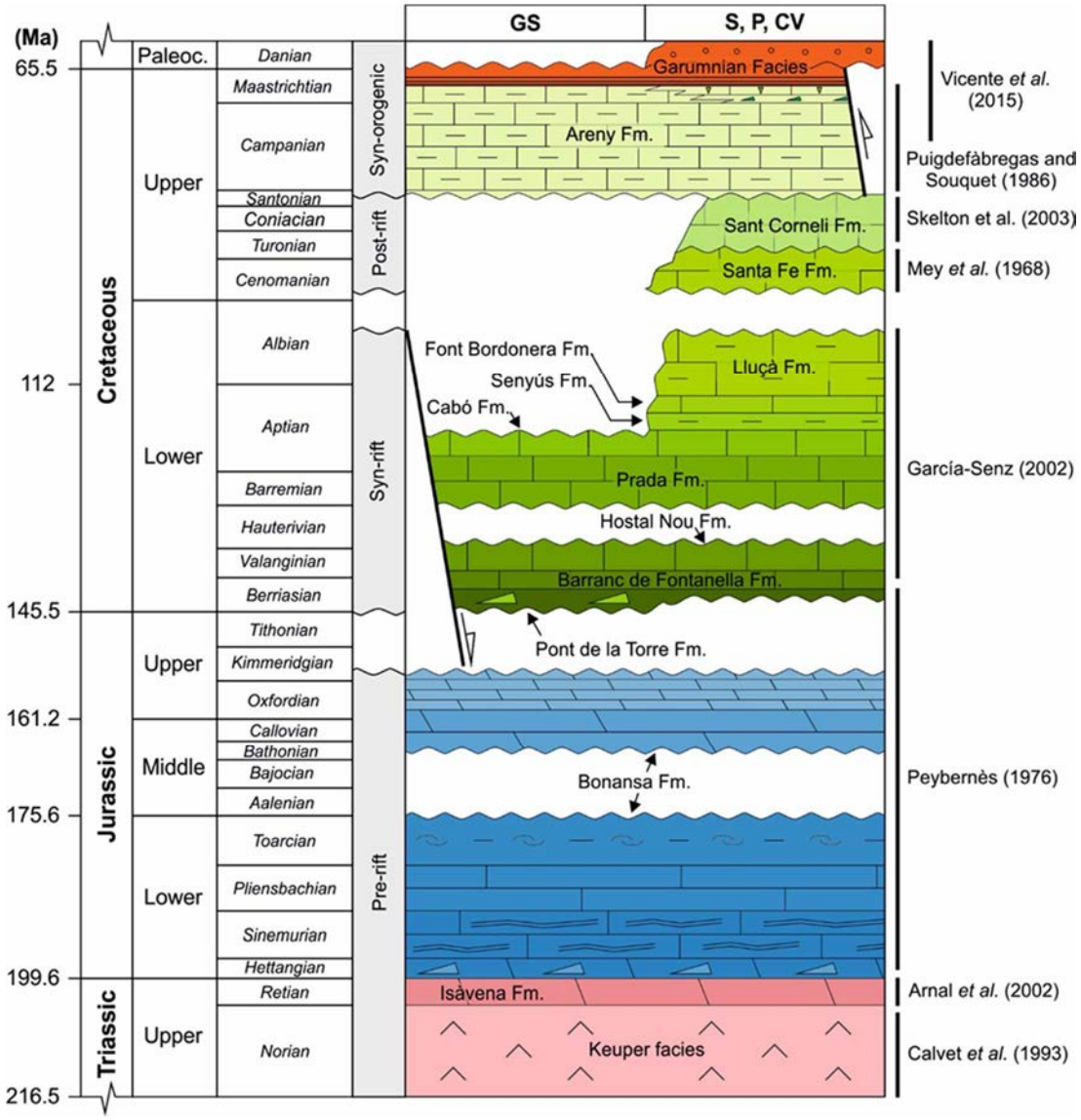

Figure 12. Chronostratigraphic diagram showing the main sedimentary units of the Upper Pedraforca thrust sheet and their related tectonic events. The age of sedimentary units has been defined according to Mey et al. (1968), Peybernès (1976), Puigdefàbregas and Souquet (1986), Calvet et al. (1993), Arnal et al. (2002), García-Senz (2002), Skelton et al. (2003) and Vicente et al. (2015).

The Cadí thrust sheet is constituted of Paleozoic, Mesozoic and Paleogene rocks (Fig. 13). Paleozoic rocks constitute the Orri and Rialp basement units and consist of pelitic rocks from the Ordovician, Devonian limestones and Permian volcanic and lacustrine rocks. This basement units are unconformably overlain by Triassic rocks from the fluvial Bundsandstein facies, marine limestones from the Muschlekalk and evaporites and red clays from the Keuper facies, Upper Cretaceous marine limestones from the Areny Formation, continental Paleocene deposits from the Garumnian, Eocene marine limestones from the Cadí, Corones and Armàncies formations, turbidite deposits from the Vallfogona Formation and foreland evaporites from the Beuda

Formation (Vergés et al., 1998). The turbidites of the Vallfogona formation are overthrusting the Lutetian to Bartonian marls of the Banyoles and Igualada formations. and Priabonian-Rupelian syn-tectonic alluvial sediments of the Berga formation, indicating that the Vallfogona thrust, the southern margin of the Cadí thrust sheet, was active until the lower Oligocene (Burbank et al., 1992b; Haines, 2008; Valero et al., 2014).

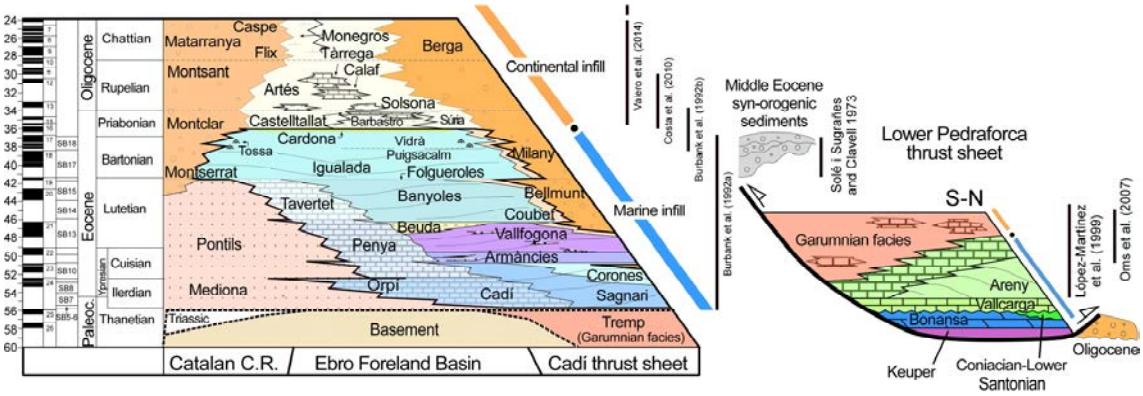

Fig. 13. N-S stratigraphic panel of the Lower Pedraforca thrust sheet, Cadí thrust sheet and eastern Ebro Foreland Basin modified from Vergés et al. (1998). The age of sedimentary units has been defined according to Burbank et al. (1992a, b), López-Martínez et al. (1999), Oms et al. (2007), Costa et al. (2010) and Valero et al. (2014). Shallow Benthic Zones (SBZ) are from Serra-Kiel et al. (1998a and b). The white boxes with references Q, G1, PEG, G2 and EST indicate the stratigraphic location of the studied outcrops.

The stratigraphy of the Ebro foreland basin consists of Lutetian and Bartonian marine marls (Banyoles and Igualada Formations; Serra-Kiel et al., 2003a, b) followed by the non-marine lower-middle Priabonian Berga and Solsona Formations (Riba,1973; Puigdefàbregas et al., 1986, 1992; Valero et al., 2014) (Fig. 13). These sedimentary units represent the endorheic infill of the Ebro foreland basin (Sáez et al., 2007; Costa et al., 2010).The Berga Formation consists of up to 2500 m thick alluvial con-glomerates, which grade to the south (study area) to finer fluvial sandstones, siltstones and claystones of the Solsona Formation (Williams et al., 1998; Barrier et al., 2010). In the studied area, The Berga and Solsona Formations show growth strata geometries, indicating coeval deposition during the growth of the Puig-reig anticline and emplacement of the Vallfogona thrust (Riba, 1973; Vergés,1993). The Berga Formation displays outstanding growth strata patterns in the Busa syncline, located between the Puig-reig anticline and the Vallfogona thrust (Riba, 1976; Suppe et al., 1997; Ford et al.,1997).

Chapter 3

Methodology

3. Methodology

In this chapter is presented the workflow followed to achieve the proposed objectives (Fig. 13). It consists of eight steps based on field-based and petrographic observations, as well as geochemical analyses.

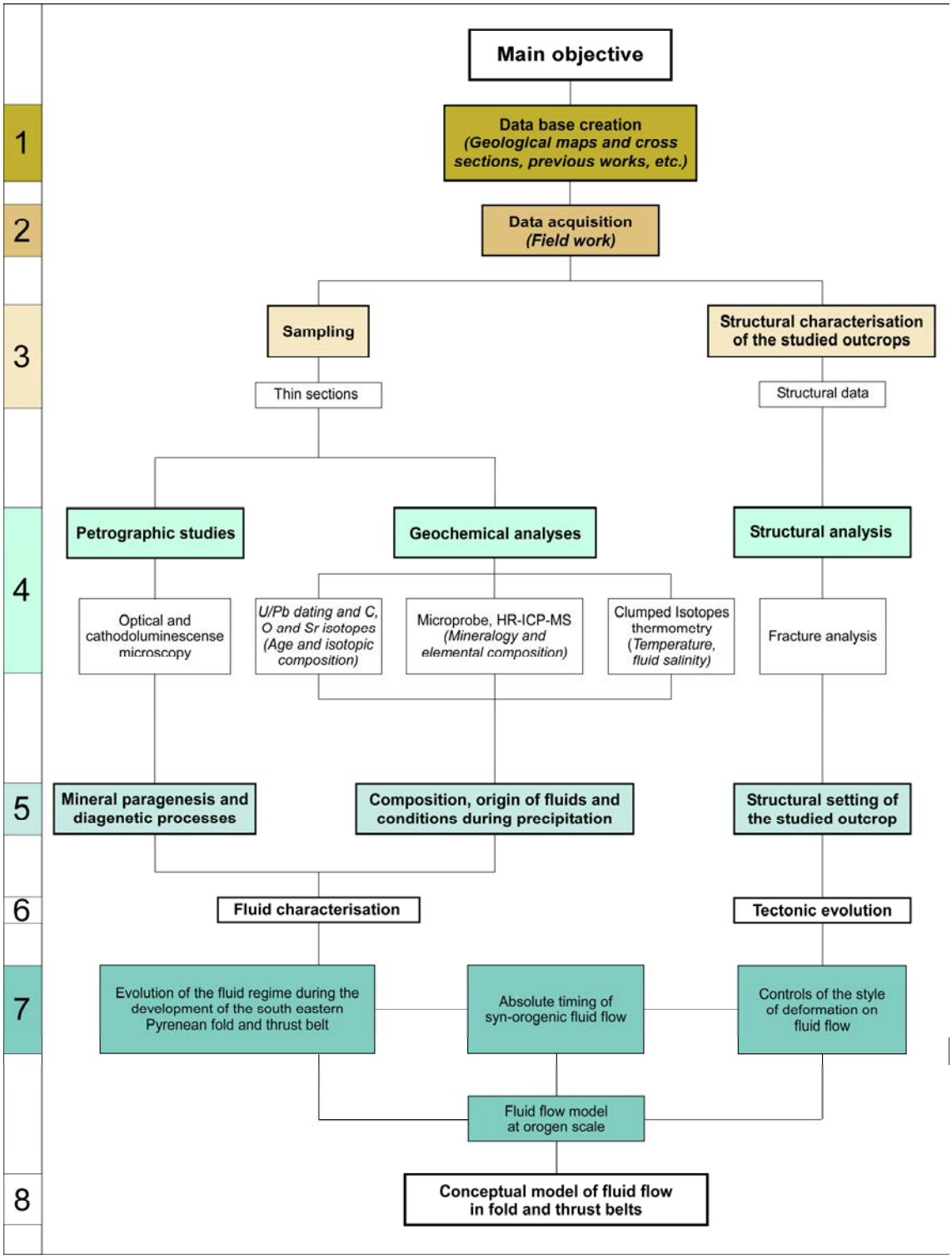

Fig. 13. Methodology followed to achieve the objectives proposed in this thesis.

3.1. Previous work

The previous step of the methodology consists of the creation of a data base including geological maps and cross sections of the study area and previous works from the south Pyrenean fold and thrust belt or worldwide (Fig. 13; Step 1). The aim of this early stage was to select adequate zones (outcrops) in order to develop the research.

3.2. Field work

Fourteen representative outcrops of the complete stacking of south Pyrenean thrust sheets were chosen because of their structural position and quality. For each one, structural data was acquired (fracture dips and orientations) (Fig. 13; Step 2). After data collection, the studied outcrops were characterized and sampled for petrological observations and geochemical analyses of calcite and dolomite cements (Fig. 13; Step 3). Each sample was oriented in the field, and the strike and dip of a planar surface of the specimen was measured.

3.3. Laboratory and office work

From data obtained in the field, a structural analysis of the studied outcrops, a structural analysis, petrographic study and geochemical analysis of the collected samples was undertaken (Fig. 13; Step 4). Structural data from the different studied outcrops was plotted in lower hemisphere Schmidt stereoplots to stablish the structural setting in which sampled structures formed. Petrographic observations of polished thin sections made from fracture-filling calcite and dolomite cements and host rocks were made using optical and cathodoluminescence microscopy. A CL Technosyn cathodoluminescence device Model 8200 MkII operating at 23 kV and 350 μA gun current was used to distinguish the different types of cements. Geochemical methods applied to calcite ad dolomite cements include carbon, oxygen and strontium isotopes, clumped isotopes thermometry, elemental characterization using electron microprobe, rare earths and yttrium analysis and U-Pb Geochronology. All these methods are described in detail below:

Carbon and oxygen isotopes. For carbon- and oxygen-isotope analysis, a 400 μm-thick dental drill was employed to extract 60 ± 10 μg of powder from trims containing calcite cements and carbonate host rocks. The calcite powder was reacted with 100% phosphoric acid for 2 minutes at 70 °C. The resultant CO_2 was analyzed using an automated Kiel Carbonate Device attached to a Thermal Ionization Mass Spectrometer Thermo Electron (Finnigan) MAT-252 following the method of McCrea (1950). The results were corrected using the standard technique from Craig and Gordon (1965) and Claypool et al. (1980), expressed in ‰ with respect to the VPDB (Vienna Pee Dee Belemnite) standard. Standard deviation is ± 0.02 ‰ for $\delta^{13}C$ and ± 0.05 ‰ for $\delta^{18}O$.

Strontium isotopes. To apply this method, 100% calcite or dolomite samples are fully dissolved in 5 ml of 10% acetic acid and introduced in an ultrasonic bath for 15 minutes. After this time, samples are dried after being centrifuged during 10 min at 4000 rpm. The resultant sample

is digested in 1 ml of 3 M HNO_3 and dried. Finally, the resultant product is digested again in 3 ml of 3 M HNO_3 and introduced in chromatographic columns. The chromatographic separation of Sr was done using an extraction resin type SrResinTM (Trisken International) (crown-ether (4.4' (5')-di-t-butylcyclohexano-18-crown-6). The Sr is recovered with HNO_3 0.05 M as eluent. The fraction where Sr is concentrated is dried, charged on a Re single filament with 1 µl of H_3PO_4 1 M and 2 µl of Ta_2O_5 and analyzed on a TIMS-Phoenix mass spectrometer. The method of acquisition of data consists of dynamic multicollection during 10 blocks of 16 cycles each one, with a beam intensity in the ^{88}Sr mass of 3 V. Analyses were corrected for possible interferences of ^{87}Rb. The $^{87}Sr/^{86}Sr$ ratios are normalized with respect to the measured mean value of the ratio $^{86}/Sr/^{88}Sr=0.1194$ in order to correct possible mass fractionation during filament charge and instrumental analyses. The precision of the analytical standard error or internal precision is 0.000009.

Clumped isotope thermometry. This method is applied to calcite and dolomite cements to calculate temperatures of cement precipitation as well as the $\delta^{18}O$ values of the fluids from which these they precipitated. To analyze the samples, 2–3 mg aliquots from cements were measured with the Imperial Batch Extraction system (IBEX), an automated line developed at Imperial College of London. Each sample was dropped in 105% phosphoric acid at 90 ºC and reacted for 30 min. The reactant CO_2 was separated using a poropak-Q column and transferred into the bellows of a Thermo Scientific MAT 253 mass spectrometer (Thermo Fisher GmbH, Bremen, Germany). The characterization of a replicate consisted of 8 acquisitions in dual inlet mode with 7 cycles per acquisition. The post-acquisition processing was completed with a software for clumped isotope analysis named Easotope (John and Bowen, 2016). Δ_{47} values were corrected for isotope fractionation during phosphoric acid digestion employing a phosphoric acid correction of 0.069 ‰ at 90 ºC for calcite (Guo et al., 2009). The data were also corrected for non-linearity applying the heated gas method (Huntington et al., 2009) and projected into the absolute reference frame of (Dennis et al., 2011). Carbonate $\delta^{18}O$ values were calculated with the acid fractionation factors of (Kim et al., 1997). Samples were measured three times and the average result was converted to temperatures using the calibration method of (Davies and John, 2019). Calculated $\delta^{18}O$ values of the fluid are expressed in ‰ with respect to the VSMOW standard (Vienna Standard Mean Ocean Water).

Electron microprobe. Carbon-coated polished thin sections were used to analyse major, minor and trace element concentrations on a CAMECA SX-50 electron microprobe. The microprobe was operated using 20 kV of excitation potential, 15 nA of current intensity and a beam diameter of 10 µm. The detection limits were 135 ppm for Mn, 127 ppm for Fe, 101 ppm for Ca, 146 ppm for Na, 180 ppm for Mg and 390 ppm for Sr. Precision on major element analyses averaged 0.64% standard error at 2σ confidence levels.

***Rare earth and yttrium analyses*.** To determine the rare earth and yttrium contents (REE+Y) of calcite and dolomite cements and carbonate host rocks, 2samples were analyzed by using high resolution inductively coupled plasma-mass spectrometry (HR-ICP-MS), using a Thermo

Scientific, model Element XR. Up to 100 mg of powder were sampled from trims using a 400/500 µm-diameter dental drill. Powdered samples were dried at 40ºC during 24 h and later 100 mg of sample were acid digested in closed PTFE vessels with a combination of HNO_3+HF+ $HClO_4$ (2.5 ml: 5 ml: 2.5 ml v/v). The samples were evaporated and, 1 ml of HNO_3 was added to make a double evaporation. Finally, the sample was re-digested and diluted with MilliQ water (18.2 MΩcm-1) and 1 ml of HNO_3 in a 100 ml volume flask. In order to improve the sensitivity of the ICP-MS, a tuning solution containing 1 µg.l-1 Li, B, Na, K, Sc, Fe, Co, Cu, Ga, Y, Rh, In, Ba, Tl, U was used, and as internal standard, 20 mg.l-1 of a monoelemental solution of 115In. Reference materials are the BCS-CRM nº 393 (ECRM 752-1) limestone, JA-2 Andesite and JB-3 Basalt. The precision of the results was expressed in terms of two standard deviations of a set of eight reference materials measurements (reference material JA-2), whereas accuracy (%) was calculated using the absolute value of the difference between the measured values obtained during the analysis and the certified values of a set of eight reference material analysis (reference material BCS-CRM nº 393 for major oxides and JA-2 for trace elements). The analysed elements and their detection limits expressed in ppm are: La (0.21), Ce (0.32), Pr (0.04), Nd (0.15), Sm (0.03), Eu (0.01), Gd (0.02), Tb (0.003), Dy (0.02), Y (0.20), Ho (0.003), Er (0.01), Yb (0.01) and Lu (0.01). The detection limit (DL) was calculated as three times the standard deviation of the average of ten blanks. A Multielemental Solution IV-CCS-1 Rare Earths Standard in HNO3, 125ml (100 µg/ml) of Inorganic Ventures was used in order to perform the calibration curves.REE and Y data are normalized to the Post-Archean Australian Shale (PAAS) from McLennan (1989).

U-Pb geochronology. The applied method is similar to that previously described by Ring and Gerdes (2016) and Burisch et al. (2017). U-Pb ages were acquired in situ in polished mounds (2 cm thick) made from hand samples of calcite and dolomite by laser ablation-inductively coupled plasma-mass spectrometry (LA-ICP-MS) at Goethe University Frankfurt, using a modified method described in Gerdes and Zeh (2006, 2009). A ThermoScientific Element 2 sector field ICP-MS was coupled to a Resolution S-155 (Resonetics) 193nm ArF excimer laser (CompexPro 102) equipped with a two-volume ablation cell (Laurin Technic). Samples were ablated in a helium atmosphere (0.3 L min-1) and mixed in the ablation funnel with 0.9 L min-1 argon and 0.05 L min-1 nitrogen. Signal strength at the ICP-MS was tuned for maximum sensitivity while keeping oxide formation (monitored as $^{248}ThO/^{232}Th$) below 0.2% and no fractionation of the Th/U ratio. Static ablation used a spot size of 213 µm and a fluence of about 2 J cm^{-2} at 12 Hz. This yielded for National Institute of Standards and Technology Standard Reference Material-614 (NIST SRM-614) a depth penetration of ~0.6 μms^{-1} and an average sensitivity of 350,000 c/s μg^{-1} for ^{238}U. The detection limit for ^{206}Pb and ^{238}U was ~0.2 and 0.03 ppb, respectively. Data were acquired in fully automated mode overnight in three sequences of 598 analyses each one. Each analysis consists of 20 s background acquisition followed by 20 s of sample ablation and 25 s washout. During 40 s of data acquisition, the signal of ^{206}Pb, ^{207}Pb. ^{208}Pb, ^{232}Th and ^{238}U were detected by peak jumping in pulse counting mode with a total integration time of 0.1s, resulting in 400 mass scans. Prior to analysis each spot was pre-ablated for 3 s to remove surface contamination. Soda-lime glass NIST SRM-614 was used as a reference glass together with two carbonate standards

to bracket sample analysis. Raw data were corrected offline using an in-house VBA spreadsheet program (Gerdes and Zeh, 2006, 2009). Following background correction, outliers (±2σ) were rejected based on the time-resolved $^{207}Pb/^{206}Pb$ and $^{206}Pb/^{238}U$ ratios. The mean $^{207}Pb/^{206}Pb$ ratio of each analysis was corrected for mass bias 0.3% and the $^{206}Pb/^{238}U$ ratio for interelement fractionation (~5%), including drift over the sequence time, using NIST SRM-614. Due to the carbonate matrix, additional offset factors of 1.061 in seq1 and 0.963 in seq2 have been applied, which was determined using WC-1 carbonate reference material (Roberts et al., 2017). The $^{206}Pb/^{238}U$ fractionation during 20s depth profiling was estimated to be 3%, based on the common Pb corrected WC-1 analyses, and has been applied as an external correction to all carbonate analyses. Repeated analyses of a Zechstein dolomite (Gypsum pit, Tettenborn, Germany) used as secondary (in-house) standard yielded a lower intercept age of 259.5 ± 5.2 Ma (MSWD = 0.99 and n = 17) for sequence 1 and 255.3 ± 5.8 Ma (MSWD = 1.4 and n = 18) for sequence 2. A stromatolitic limestone from the Cambrian-Precambrian boundary in South-Namibia, analysed during sequence 2, yielded a lower intercept ages of 543.8 ± 5.3 Ma (MSWD = 1.4). This is within uncertainty identical to the U/Pb zircon age of 543 ± 1 Ma from the directly overlying ash layer (Spitskopf formation; Bowring et al., 1993). Altogether the data imply an accuracy and repeatability of the method of ~2% or better. The analytical results are presented in Table DR2. Data were plotted in Tera-Wasserburg diagrams Fig. DR2 and ages calculated as lower intercepts using Isoplot 3.71 (Ludwig, 2009). All uncertainties are reported at the 2σ level.

From petrographic observations and geochemical analyses, a mineral paragenetic sequence of the studied cements, and the composition, origin and temperature of fluids, as well as the absolute age of fluid migration were well constrained (Fig. 13; Step 5). From the integration and interpretation of petrographic, geochemical and structural data, the tectonic evolution of the studied outcrops, as well as the characterization of the fluids from which calcite and dolomite cements precipitated is constrained (Fig. 13; Step 6). Then, from the combination of the fluid characterization and the tectonic evolution of the selected studied section of the south eastern Pyrenees, the timing of fluid migration and fluid flow evolution during the emplacement of the thrust sheets constituting the South Pyrenean fold and thrust belt is stablished, allowing us to achieve the secondary objectives of this thesis (Fig. 13; Step 7). To conclude, from the comparison of the obtained results in the southern Pyrenees with other orogens worldwide, a conceptual model of fluid flow in fold and thrust belts will be presented (Fig. 13; Step 8).

Chapter 4

Crestal graben fluid evolution during growth of the Puig-reig anticline (South Pyrenean fold and thust belt)

Journal of Geodynamics 101 (2016) 30–50

Contents lists available at ScienceDirect

Journal of Geodynamics

journal homepage: http://www.elsevier.com/locate/jog

Crestal graben fluid evolution during growth of the Puig-reig anticline (South Pyrenean fold and thrust belt)

David Cruset [a,b,*], Irene Cantarero [a], Anna Travé [a], Jaume Vergés [b], Cedric M. John [c]

[a] Departament de Mineralogia, Petrologia i Geologia Aplicada, Universitat de Barcelona, (UB), Martí i Franquès s/n, 08028 Barcelona, Spain
[b] Group of Dynamics of the Lithosphere, Institute of Earth Sciences Jaume Almera, ICTJA - CSIC, Lluís Solé i Sabaris s/n, 08028 Barcelona, Spain
[c] Qatar Carbonate and Carbon Storage Research Center and Department of Earth Science and Engineering, Imperial College London, SW7 2BP, UK

ARTICLE INFO

Article history:
Received 18 November 2015
Received in revised form 3 May 2016
Accepted 18 May 2016
Available online 19 May 2016

Keywords:
Fluids
Faults
Palaeohydrology
Growth anticline
South Pyrenean fold and thrust belt

ABSTRACT

The Puig-reig anticline, located in the South Pyrenean fold and thrust belt, developed during the Alpine compression, which affected the upper Eocene-lower Oligocene sediments of the Solsona and Berga Formations. In this study, we highlight the controls on formation of joints and reverse, strike-slip and normal faults developed in the crest domain of the Puig-reig anticline as well as the relationships between fluids and these fractures. We integrated structural, petrographic and geochemical studies, using for the first time in the SE Pyrenees the clumped isotopes thermometry to obtain reliable temperatures of calcite precipitation.

Structural and microstructural analysis demonstrate that at outcrop scale fracturing was controlled by rigidity contrasts between layers, diagenesis and structural position within the anticline, whereas grain size, cementation and porosity controlled deformation at the microscopic scale. Petrographic and geochemical studies of calcite precipitated in host rock porosity and fault planes reveal the presence of two migrating fluids, which represents two different stages of evolution of the Puig-reig anticline. During the layer-parallel shortening, hydrothermal fluids with temperatures between 92 and 130 °C circulated through the main thrusts to the permeable host rocks, reverse and most of strike-slip faults precipitating as cement Cc1. During the fold growth, meteoric waters circulated downwards through normal and some strike-slip faults and mixed at depth with the previous hydrothermal fluid, precipitating as cement Cc2 at temperatures between 77 and 93 °C.

Integration of the results from the Puig-reig anticline in this work and the El Guix anticline indicates that hydrothermal fluids did not reach the El Guix anticline, in which only meteoric and evolved meteoric waters circulated along the fold.

1. Introduction

A great variety of tectonic, sedimentary and fluid flow interactions take place during deformation of foreland basins at different scales and depths. Thus, fluid-rock interactions during deformation play a significant role during diagenesis, hydrocarbon migration and precipitation of ore deposits as it has been widely recognized (Oliver, 1986; Qing and Mountjoy, 1992; Machel and Cavell, 1999; Dewaele et al., 2004; Roure et al., 2005; Evans and Fischer, 2012; Vandeginste et al., 2012; Beaudoin et al., 2011, 2013, 2014; Lacombe et al., 2014). In addition, diagenetic processes related to fluid flow can control the fracture patterns of rocks (Shackleton et al., 2005; Laubach et al., 2009).

Fluids are expelled into foreland basins by tectonically-induced squeegee fluid flow, using major thrust faults and permeable rocks as paths (Oliver, 1986; Machel and Cavell, 1999; Sibson, 2005). Moreover, other driving forces such as topography and thermal gradients and changes in tectonic stresses and fluid pressures can control fluid flow at basin scale (Oliver, 1986; Heydari, 1997; Bitzer et al., 2001; Lyubetskaya and Ague, 2009). The palaeohydrological history of these fluids (e.g., fluid composition, pressure, temperature and burial) in deformed fold and thrust belts and foreland basins is recorded in the composition of the cements precipitated in rock porosity and fractures (Grant et al., 1990; Banks et al., 1991; McCaig et al., 2000a; Bitzer et al., 2001; Roure et al., 2005). Thus,

* Corresponding author at: Departament de Mineralogia, Petrologia i Geologia Aplicada, Universitat de Barcelona, (UB), Martí i Franquès s/n, 08028 Barcelona, Spain.
E-mail addresses: d.cruset@ub.edu (D. Cruset), i.cantarero@ub.edu (I. Cantarero), atrave@ub.edu (A. Travé), jverges@ictja.csic.es (J. Vergés), cedric.john@imperial.ac.uk (C.M. John).

http://dx.doi.org/10.1016/j.jog.2016.05.004
0264-3707/

the study of cements sheds light on the diagenetic and geodynamic evolution of fold and thrust belts.

Joints and faults related to folding in gently deformed foreland basins allow lateral and vertical migration of fluids across different hydrostratigraphic units (Travé et al., 2000; Lefticariu et al., 2005; Fischer et al., 2009; Beaudoin et al., 2011; Barbier et al., 2012; Evans et al., 2012; Evans and Fischer, 2012; Ogata et al., 2014). Previous work on the interactions between folding and fluid flow in fold and thrust belts worldwide have been conducted in many examples such as the Albanian fold and thrust belt (Vilasi et al., 2009), Northern Apennines (Conti et al., 2010), Sicilian fold and thrust belt (Dewever et al., 2013), Appalachians (Srivastava and Engelder, 1990; Evans et al., 2012; Chandonais and Onasch, 2014), Bighorn Basin (Beaudoin et al., 2011, 2013, 2014), Sevier thrust belt (Ogata et al., 2014), Nuncios Fold Complex (Lefticariu et al., 2005; Fischer et al., 2009) and the Zagros fold and thrust belt (Stephenson et al., 2007; Morley et al., 2014).

The South Pyrenean fold and thrust belt and its foreland Ebro basin constitute a well-known and well-preserved case study for tectonic and sedimentary interactions (Vergés et al., 2002a for a review). In this scenario, the study between fluid flow and deformation encompassing a pile of thrust sheets with different ages of emplacement (Vergés et al., 2002b), may contribute to better constrain the large-scale evolution of this fold and thrust belt as well as of its associated foreland basin (e.g., Van Geet et al., 2002; Travé et al., 2004; Ferket et al., 2006; Travé et al., 2007; Dewever et al., 2013; Beaudoin et al., 2014).

A first group of studies regarding the fluid evolution of the south Pyrenees mainly analysed the inner part of the thrust belt in the basement of the Axial Zone (McCaig, 1988; Grant et al., 1990; Banks et al., 1991; Knipe and McCaig, 1994; McCaig et al., 1995; Henderson and McCaig, 1996; McCaig et al., 2000a,b). Furthermore, fluid-rock interactions were analyzed in the cover thrust-sheets along the western side of the Central Pyrenees (Travé et al., 1997, 1998a, 2007; Lacroix et al., 2011; Beaudoin et al., 2015). A few more works report the fluid evolution of the southeastern Pyrenees thrusts sheets and foreland basin further east (Travé et al., 2000) as well as the relationships between fluid flow and hydrocarbon migration during the Eocene (Caja et al., 2006).

The Puig-reig anticline is located along the footwall of the SE Pyrenean outcropping basal thrust (the Vallfogona thrust). This anticline evolved during the late stages of deformation and thus, it was affected by the youngest generations of fluids within the fold and thrust belt system. This fact will permit further comparison with more complex fluid flow scenarios when studying older and piled thrust sheets (Cadí, Lower Pedraforca and Upper Pedraforca thrust sheets).

In this work, we report the fluid flow system evolution during the development of the Puig-reig anticline, located in the eastern sector and frontal most part of the South Pyrenean fold and thrust belt. We integrate structural, petrographic and geochemical data with the aim of determining the origin of the fluids from which cements precipitated in fractures and host rock porosity, and their relationships with deformation. We use for the first time in the southern Pyrenees the clumped isotopes thermometry (Ghosh et al., 2006; Eiler, 2007), which has been recently applied to other fault zones (Swanson et al., 2012; Bergman et al., 2013) allowing to obtain reliable precipitation temperatures when fluid inclusions in calcite does not allow to determine them. Finally, the results from the Puig-reig anticline are compared with the El Guix anticline along the tip-line of the Pyrenean front (Travé et al., 2000, 2007) in order to perform a fluid flow model for the frontal most part of the South Pyrenean fold and thrust belt.

2. Geological setting

The Pyrenees formed by the continental collision between Iberia and Eurasia plates and consist of a doubly verging orogenic belt generated from Late Cretaceous to Oligocene (Muñoz, 2002; Vergés et al., 2002a) (Fig. 1). This collision produced the underthrusting of the Iberian plate below the Eurasian plate as recognised in deep seismic profiles across the orogen (Choukroune and Team, 1989; Roure et al., 1989). As a result, the previous Mesozoic extensional basins were inverted and an antiformal stack constituted of basement-involved thrust sheets in the central part of the chain (Axial zone) developed (Muñoz, 1992). To the north of the Axial zone, the thick-skinned North Pyrenean fold and thrust belt was developed whereas to the south, the prevailing structural style was thin-skinned, resulting in the development of the South Pyrenean fold and thrust belt (Fig. 1), detached predominantly above Triassic evaporites (Séguret, 1972) and the Eocene evaporites deposited in the foreland basin (Vergés et al., 1992). During the emplacement of the successive thrust sheets, two foreland basins were formed: the Aquitaine Basin, related to the development of the North Pyrenean fold and thrust belt and the Ebro Basin, related to the emplacement of the South Pyrenean fold and thrust belt (Fig. 1). The Ebro Basin represents the non-marine stage of the South Pyrenean foreland basin (Vergés, 1993) developed from middle Priabonian time (Costa et al., 2010). The fold system deforming the eastern region of the Ebro Basin was detached above the Cardona evaporites (Sans et al., 1996; Sans, 2003). The Puig-reig anticline developed at the northern edge of the Cardona evaporitic basin, with an oblique trend to the Pyrenean direction, and represents a complex ramp anticline between the Beuda and the Cardona thrust flats (Figs. 1 and 2 a) (Vergés, 1993).

The Puig-reig anticline is located along the footwall of the SE Pyrenean basal thrust (the Vallfogona thrust) (Figs. 1 b and 2). It is a long-wavelength, south-verging and ESE/WNW trending anticline, slightly oblique to the main Pyrenean structures. The anticline is formed above a thrust ramp duplicating middle and upper Eocene marls (Banyoles and Igualada Formations) between the Beuda and the Cardona evaporitic detachment levels (Fig. 2a) (Vergés et al., 1992). The backlimb dips between 5 and 17 degrees towards the north, whereas the forelimb dips up to 40 degrees to the south, being subhorizontal in its frontal part (Fig. 2b). The Oliana anticline is the continuation of the Puig-reig anticline towards the west (Fig. 1), showing a much deeper erosion level, reaching the Igualada marls that are not exposed in the study area.

The stratigraphy of the Puig-reig anticline is composed of Lutetian and Bartonian marine marls (Banyoles and Igualada Formations; Serra-Kiel et al., 2003a,b) followed by non-marine lower-middle Priabonian Berga and Solsona Formations (Riba, 1973; Puigdefàbregas et al., 1986, 1992; Valero et al., 2014). These units represent the endorheic infill of the Ebro basin (García-Castellanos et al., 2003; Sáez et al., 2007; Costa et al., 2010; Fig. 3). The Berga Formation consists of up to 2500 m thick alluvial conglomerates, which grade to the south (study area) to finer fluvial sandstones, siltstones and claystones of the Solsona Formation (Williams et al., 1998; Barrier et al., 2010).

The Berga and Solsona Formations show growth strata geometries, observed in seismic lines (Vergés, 1993), indicating coeval deposition during the growth of the Puig-reig anticline and emplacement of the Vallfogona thrust (Fig. 2a) (Riba, 1973; Vergés, 1993). The Berga Formation displays outstanding growth strata patterns in the Busa syncline, located between the Puig-reig anticline and the Vallfogona thrust (Riba, 1976; Suppe et al., 1997; Ford et al., 1997) (Fig. 2a).

The study area, along the Cardener River, shows good and continuous exposures of the Berga and mostly Solsona syntectonic formations forming the Puig-reig anticline, cut by a system of

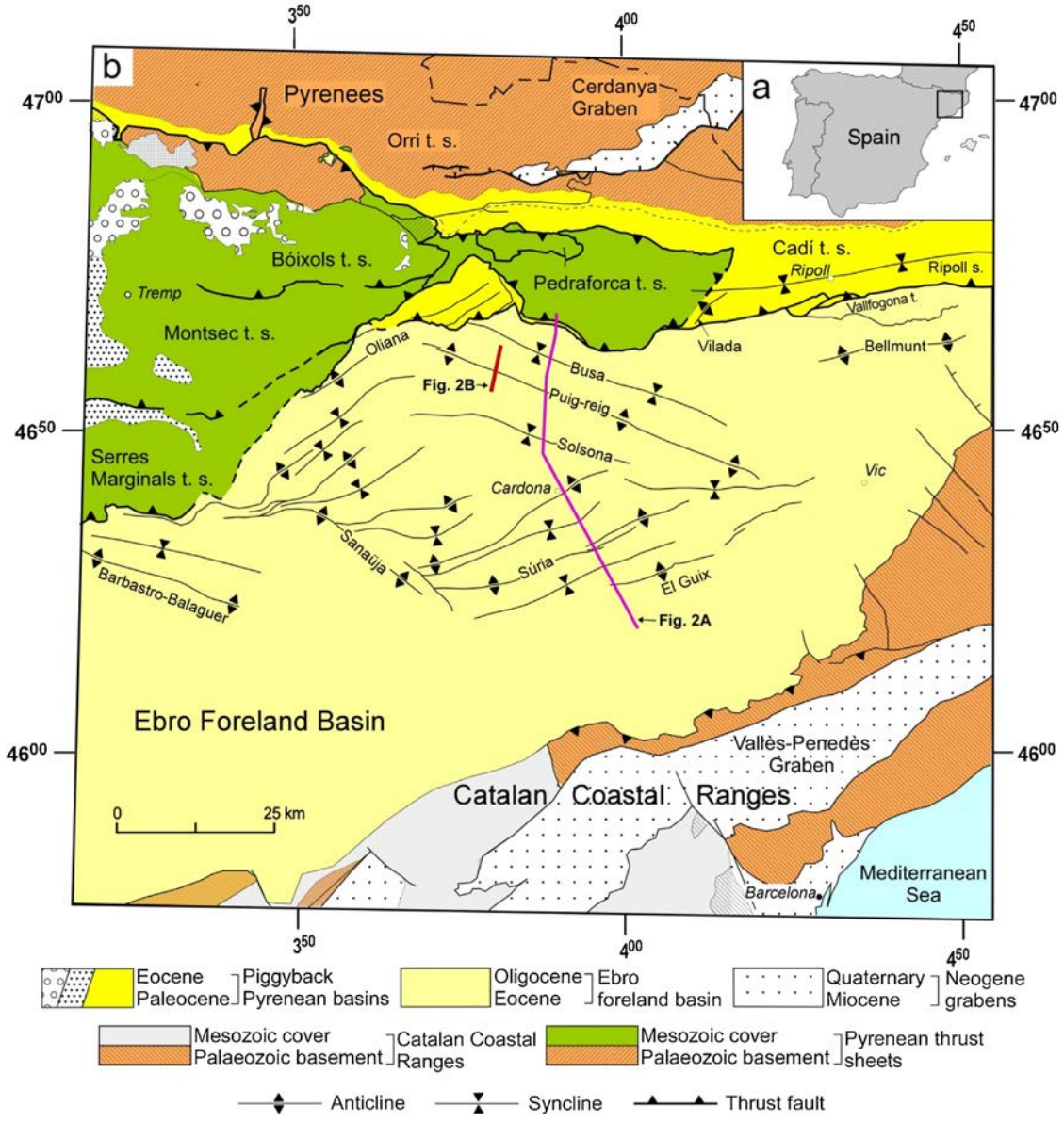

Fig. 1. (a) Regional map of the Iberian Peninsula showing the location of the South Pyrenean fold and thrust belt (black box; Fig. 1b). (b) Simplified geological map of the main structural units of the South Pyrenean fold and thrust belt (Vergés, 1993). The thick black line shows the trace of the geological cross section shown in Fig. 2a. The thick grey line shows the study area.

faults from which the antithetic normal faults extending its crestal domain are the most prominent.

3. Methodology

3.1. Sampling

The structure of the Puig-reig anticline displays a 10 km long geological cross section (Fig. 2b). To characterize the evolution of the fluids during the formation of this anticline, a structural analysis was combined with the petrographic and geochemical study of 32 polished thin sections made from 26 fracture-filling cements and host rocks (Fig. 4).

3.2. Petrography

Petrographic observations were made using optical and cathodoluminescence microscopy. A CITL Cathodoluminescence device Model 8200 Mk5-1 operating at 13.7 kV and 250 μA gun current was used to distinguish the different cements. Images from thin sections were analysed with the software J-Microvision in order to quantify the host rock components (clasts, cements, porosity). A random point-counting was done, using images of 5 mm^2 for coarse to medium sandstones, 1.5 mm^2 for fine sandstones, 0.5 mm^2 for lutites and 20 mm^2 for palustrine-lacustrine limestones. In addition, point-counting was applied in the matrix of host conglomerates using the same image size areas than in sandstones and lutites, depending on the grain size.

3.3. Fluid inclusions

Fluid inclusions were examined in vein calcite cements to determine composition and temperature conditions of the mineral-forming fluid. Thick sections were used for petrographic characterization of the fluid inclusions and for microthermometric

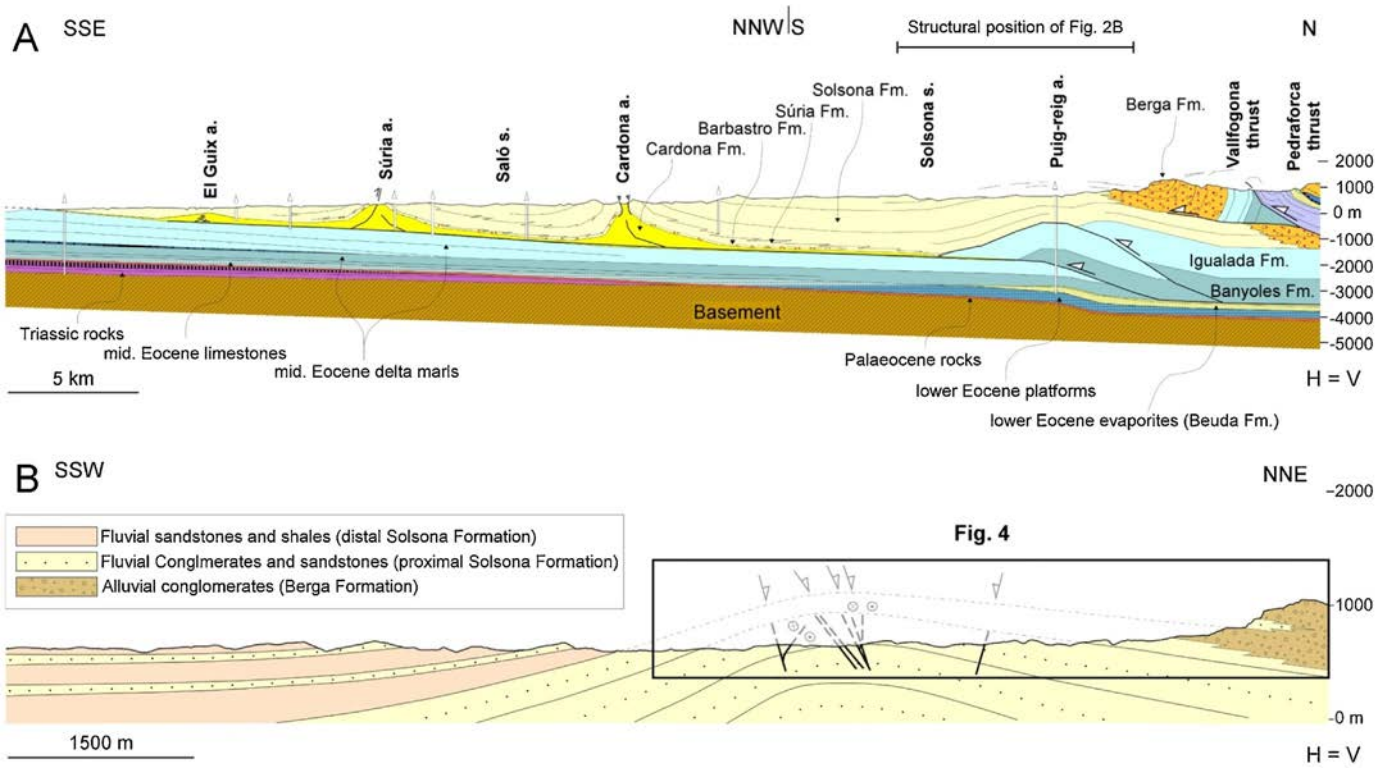

Fig. 2. (a) Geological cross section of the frontal part of the South Pyrenean fold and thrust belt (Vergés, 1993). The horizontal black line shows the structural position of Fig. 2b. (b) Geological cross section of the Puig-reig anticline performed in this work. Faults are drafted according to true dips. The black box indicates the location of Fig. 4.

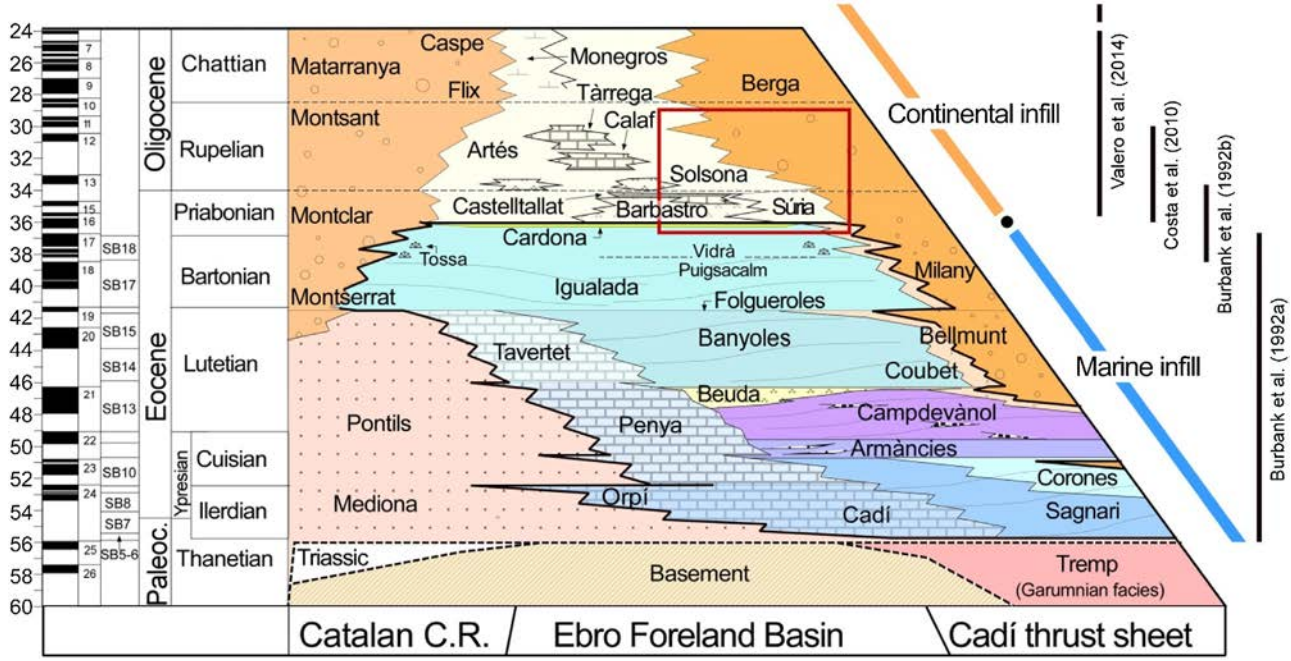

Fig. 3. N-S stratigraphic panel of the eastern Pyrenees and the eastern Ebro Foreland Basin modified from Vergés et al. (1998). The age of sedimentary units has been defined according to Burbank et al. (1992a,b), Costa et al. (2010) and Valero et al. (2014). The sedimentary record of the foreland basin is separated in Paleocene to upper Eocene marine sediments and upper Eocene to upper Oligocene continental sediments. The red box indicates the sedimentary units in the frontal part of the South Pyrenean fold and thrust belt.

determination. Measurements were made on a Linkam THMS-600 heating-freezing stage.

Raman microspectroscopy analyses were recorded with a LabRam HR800 Jobin-Yvon^{TM} microspectrometer equipped with 600 g/mm gratings and using 785 nm (red) and 532 nm (green) laser excitations. Acquisition timespan was 10 s during 10 accumulation spectra. Vapour bubbles were analysed in order to determine the presence of volatile species (CO_2, CH_4, N_2, H_2S).

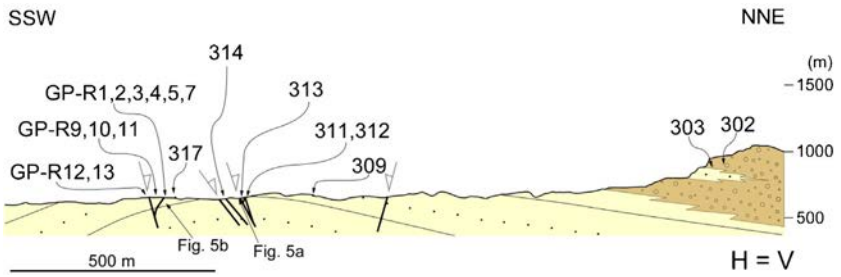

Fig. 4. Detail of Fig. 2b where are shown the sampled structures in this work.

3.4. Carbon and oxygen isotopes

Fracture-filling calcite and carbonate host rocks were sampled for carbon- and oxygen-isotope analysis employing a 400 μm-thick dental drill to extract 60 ± 10 μg of powder from trims. The calcite powder was reacted with 100% phosphoric acid for two minutes at 70 °C. The resultant CO_2 was analysed using an automated Kiel Carbonate Device attached to a Thermal Ionization Mass Spectrometer Thermo Electron (Finnigan) MAT-252 following the method of McCrea (1950). The results are precise to ±0.05‰ for $\delta^{18}O$ and ±0.01‰ for $\delta^{13}C$ and were corrected using the standard technique (Craig and Gordon, 1965; Claypool et al., 1980), expressed in ‰ with respect to the VPDB (Vienna Pee Dee Belemnite) standard.

3.5. Clumped isotope thermometry

Aliquots (replicates) of carbonate samples weighing 2–3 mg were measured using an automated line for clumped isotopes developed at Imperial College (The IBEX: Imperial Batch EXtraction system). The IBEX is a common acid bath device: individual samples are dropped in 105% phosphoric acid maintained at 90 °C, and reacted for 30 min. The reactant CO_2 is first continuously trapped during the phosphoric acid reaction by freezing it in a trap maintained at liquid nitrogen temperature. Subsequently, water is separated from the gas by heating up the water trap to −100 °C under helium flow, and the gas is then passed through a silver trap to remove sulfur, and through a trap densely packed with Porapak Q held at −35 °C. This has the effect of separating the clean CO_2 gas from potential contaminants, an essential step given that the analyte measured (mass 47 of CO_2) has a natural abundance of only 44 ppm (Eiler, 2007). Lastly, the CO_2 is captured in a second water trap maintained at liquid nitrogen temperature, transferred into a microvolume, and finally transferred into the bellows of the mass spectrometer. Mass spectrometric analyses were performed on a MAT 253 from Thermo Scientific following analytical protocols first described for the Imperial College lab in Dale et al. (2014), and more generally in Huntington et al. (2009) and Dennis et al. (2011). Full characterization of a replicate consists of 8 acquisitions in dual inlet mode with 7 cycles per acquisition. Each acquisition includes a peak centre, background measurements and an automatic bellows pressure adjustment aimed at a 15 V signal at mass 44. The sample gas is measured against an Oztech reference gas standard. Four inter-laboratory carbonate standards from Meckler et al. (2014) were measured to transfer the values into the absolute reference frame (CDES, Dennis et al., 2011), and a fifth standard (Carrara marble) was measured as a sample to ensure data consistency. Correction for non-linearity was performed following the background correction method of Bernasconi et al. (2013). Sample measurements were rejected based on elevated 48 and 49 signals, and the Δ47 values are corrected for isotope fractionation during phosphoric acid digestion using a phosphoric acid correction of 0.069‰ at 90 °C for calcite following Guo et al. (2009). This value is consistent with a recent empirical evaluation of the phosphoric acid reaction of calcite and aragonite (e.g., Wacker et al., 2013). Carbonate $\delta^{18}O$ values are calculated using the acid fractionation factors of Kim and O'Neil (1997). Each sample was measured at least three times, and the results averaged before being converted to temperatures using the calibration of Kluge et al. (2015).

3.6. Strontium isotopes

For $^{87}Sr/^{86}Sr$ analyses, four samples of 100% calcite from veins, a mudstone and a marly host rock were fully dissolved in 0.5 M acetic acid, dried and redissolved in 3 M HNO_3. To eliminate the solid residue resulting from reprecipitation after chemical dissolution, samples were centrifuged at 4000 rpm during 10 min before being charged in chromatographic columns. Samples were analysed on Re single filament with 1 μl of H_3PO_4 1 M and 2 μl of Ta_2O_5 on a TIMS-Phoenix mass spectrometer. The data acquisition method consists of dynamic multicollection during 10 blocks of 16 cycles each one, with a beam intensity in the ^{88}Sr mass of 3 V. Analyses have been corrected for possible interferences of ^{87}Rb. During the analyses, the NBS 987 standard was analysed 5 times obtaining a mean value of 0.710248 and a double standard deviation (STDEV 2σ) of 0.000008. The results were standardized with respect the $^{88}Sr/^{86}Sr$ value of 0.1194 in order to correct possible mass fractionations during sample analysis. Precision on major element analyses average 0.01% standard error at 2σ confidence levels.

3.7. Elemental composition

Carbon-coated polished thin sections were used to analyse major, minor and trace element concentrations on a CAMECA SX-50 electron microprobe. The microprobe was operated using 20 kV of excitation potential, 15 nA of current intensity and a beam diameter of 10 μm. The detection limits were 140 ppm for Mn, 198 ppm for Fe, 552 ppm for Ca, 128 ppm for Na, 500 ppm for Mg and 430 ppm for Sr. Precision on major element analyses averaged 0.64% standard error at 2σ confidence levels.

4. Structural observations

The studied section of the Puig-reig anticline is deformed by a system of fractures, which includes planar joints perpendicular to bedding and normal and strike-slip faults with displacements smaller than 20 m defining a crestal graben system (Fig. 2b). Few small low-angle thrusts are observed in the forelimb.

Normal faults, observed in the crest of the Puig-reig anticline, are trending NW-SE, oblique to the local fold axis but sub-parallel to the regional trend of the Puig-reig anticline (Fig. 1a). Normal faults dip from 40 to 70° either towards the foreland or the hinterland and intersect bedding at high angle (Fig. 5a). They show displacements from a few centimeters to 15 m. Kinematic indicators on fault planes show a pure strike-slip or oblique-slip set overprinted by a dip-slip set, pointing to the extensional reactivation of previous strike-slip faults. Fault cores are defined by

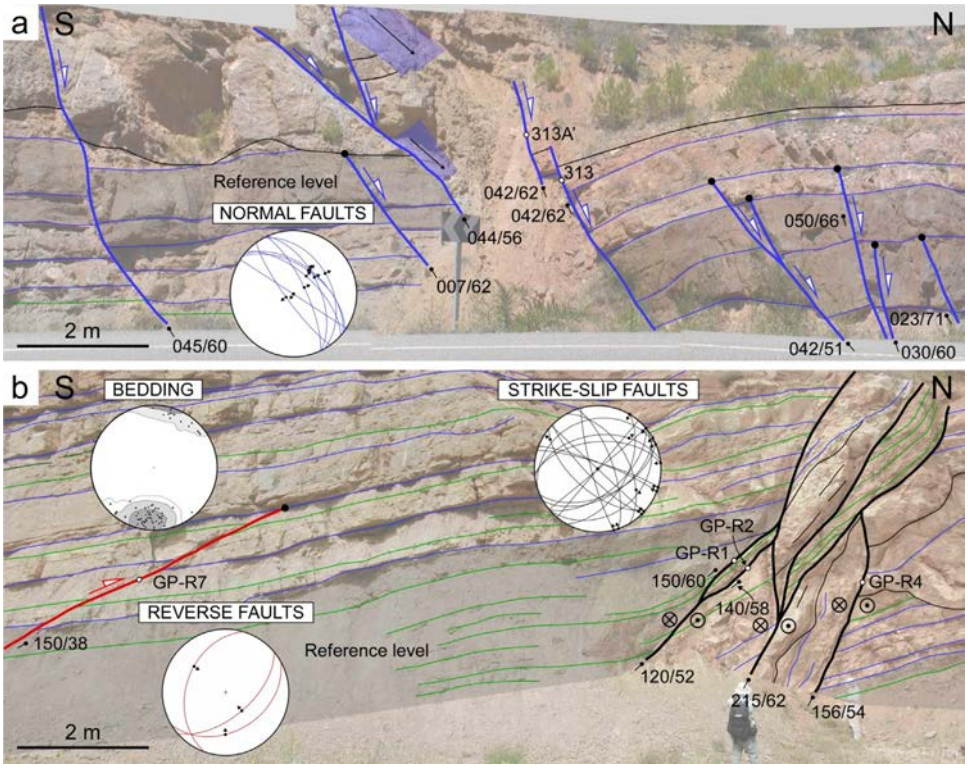

Fig. 5. Outcrop interpretation of the main structural features observed in the Puig-reig anticline. (a) Normal faults (thick blue lines) affecting the forelimb close to the hinge of the Puig-reig anticline. (b) Strike-slip (thick black lines) and reverse (thick red line) faults affecting the forelimb of the Puig-reig anticline. Thin black, blue and green lines represent conglomerates, sandstones and lutite layers, respectively. Dip directions and dips of faults are given. White points show sample locations. Stereograms for all bedding and fault dips and fault striae sets measured in the studied section of the Puig-reig anticline are given. Bedding dips are plotted as lines. (For interpretation of the references to colour in this figure caption, the reader is referred to the web version of this article.)

centimetre-thick discrete planes in normal faults with small displacements and by 2 m-thick gouges and cataclasites along normal faults showing larger displacements. The damage zone is constituted of non-cemented small normal faults and joints.

Dextral and less abundant sinistral strike-slip faults are planar or undulated. They display a high dispersion of trends, dipping from 40 to 90° either towards the foreland and the hinterland, and punctually develop conjugated fault sets (Fig. 5b). Strike-slip faults show high angle relative to bedding, although it is not constant along the studied section. Kinematic indicators on fault planes show a pure strike-slip or extensional oblique-slip motion. Fault cores are few centimetres thick discrete planes filled by calcite or up to 2 m thick fault gouges and cataclasites, whereas damage zones are constituted of small strike-slip faults filled by calcite.

Reverse faults, only observed in the forelimb, are NE-SW trending, nearly sub-perpendicular to the fold axis and are characterized by flat-ramp-flat geometries. Displacements are small, ranging from a few centimetres to 2 m (Fig. 5b). Reverse faults show low angle relative to bedding, regardless of structural position and bedding dip domain. Fault damage zones are not developed whereas discrete planes define fault cores. Slickenlines developed on fault planes indicate in most of cases dip-slip motion. Reverse faults are spatially related to layer-parallel faults, showing both faults detachment horizons at the contact between shales and sandstones.

Joints are stratabound fractures affecting the more competent layers (sandstones and conglomerates) all along the studied section of the Puig-reig anticline.

4.1. Microstructures

The microstructures in the reverse, strike-slip and normal faults zones are similar and consist of calcite shear veins, extension veins and stylolites.

4.1.1. Shear veins

Shear veins are up to 1 centimeter-thick tabular bodies extended along fault planes, bounded by striated shear surfaces and in most cases containing internal, mm-spaced shear surfaces. Shear veins are formed of several millimeter-thick bands of calcite parallel to the vein walls, locally showing rhomb-shaped veinlets separated by host rock bands (Fig. 6a). These veinlets were generated by a crack-seal mechanism and its obliquity with respect shear planes indicates the sense of shear (Ramsay, 1980; Labaume et al., 1991). In addition, sometimes shear veins define S-C patterns with cleavage planes (Fig. 6a). Locally, stylolites parallel to shear planes are present.

4.1.2. Extension veins

The extension veins observed in the studied host rock have been classified in four types according to their shapes, orientations and formation mechanisms: (1) microscopic feather fractures; (2) irregular veins; (3) dilational jogs; and (4) bedding-perpendicular veins. Microscopic feather fractures are formed perpendicular to the cleavage developing S-C structures by shearing (Fig. 6a). They are defined by tapered fractures that are thicker at the contact with shear veins thinning away from the fault. They have been interpreted to form after fault slip (Conrad and Friedman, 1976; Friedman and Logan, 1977; Blenkinsop, 2008). Irregular extension veins exhibit fuzzy contacts with the adjacent host rock (Fig. 6b). Fuzzy contacts may form by alteration of the host

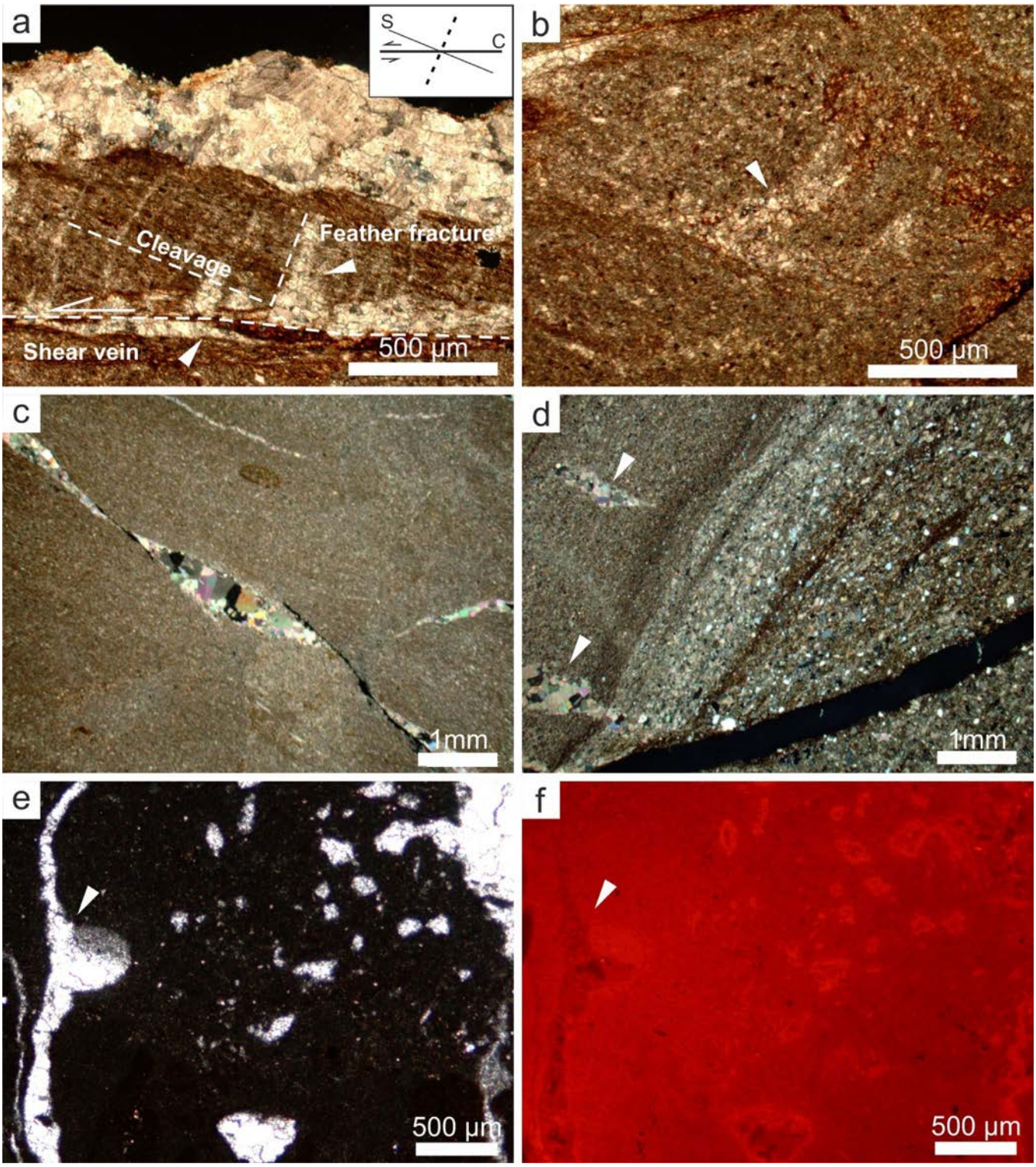

Fig. 6. Images from polarizing optical microscope and cathodoluminescence (CL) of the main features of the microstructures affecting the studied host rocks. (a) Sample GP-R11. Calcite shear vein with an associated microscopic feather fracture (crossed nicols). Note how cleavage perpendicular to the extensional fracture walls is developed in the host rock. (b) Sample GP-R11. Irregular extension vein (white triangle) affecting a siltstone layer (crossed nicols). Note how the contact of cement with the host rock is fuzzy. (c) Sample GP-R7. Dilational jog filled by blocky calcite (crossed nicols). (d) Sample GP-R2. Bedding-perpendicular veins (white triangles) (crossed nicols). (e) Sample GP-R4. Vein interconnected with a void filled by calcite cement displaying geopetal structures (white triangle). (f) Sample GP-R4. CL image of Fig. 6e (white triangle). Note how the vein and the void are filled by the same calcite cement.

rock wall or by deformation and recrystallization of veins with sharp boundaries (Passchier and Trouw, 2005). Dilational jogs are rhomb-shaped veins formed in relay zones between segments of non-cemented shear planes to form vein arrangements (Fig. 6c). Bedding-perpendicular veins are not related to shear planes and punctually show stylolite contacts with clayey host rocks (Fig. 6d). The contact between microscopic feather fractures, dilational jogs and bedding-perpendicular veins and host rock is sharp. Punctually,

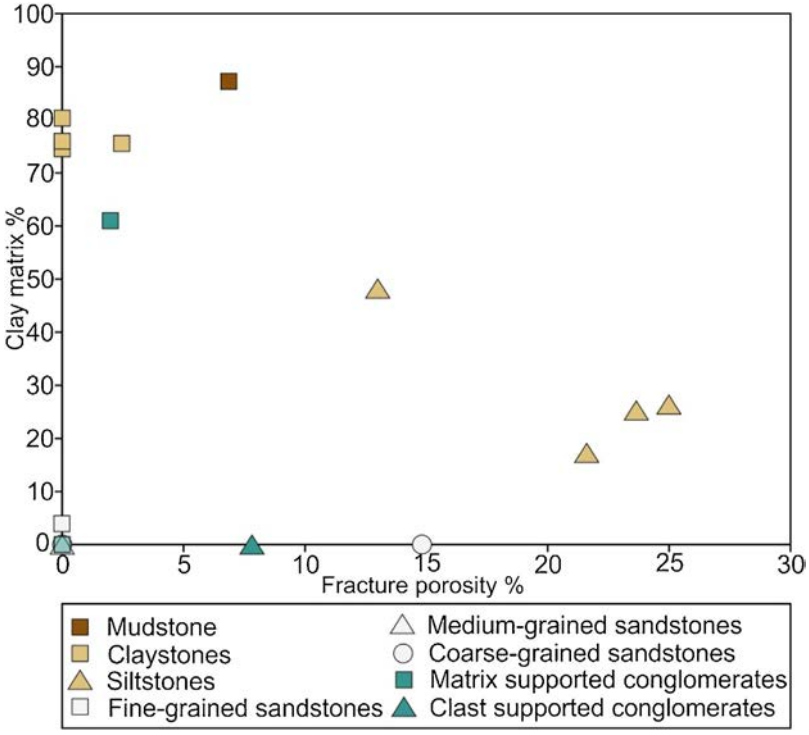

Fig. 7. Fracture porosity vs clay matrix content cross-plot. For each type of host rock the following samples have been analyzed by point counting: Mudstone (GP-R4); Claystones (GP-R2, 303 and 317); Siltstones (GP-R2, GP-R7, GP-R9 and GP-R10); Fine-grained sandstones (309A, 309B, 313A, 314D1 and 314D2); Medium-grained sandstones (311A, 311B, 312A and 314C); Coarse-grained sandstones (GP-R5 and GP-R12); Matrix supported conglomerates (GP-R13, 302 and 311F); Clast supported conglomerates (314A).

extension veins show irregular morphologies when are affected by a late stage of shear.

5. Petrology

5.1. Host rock

The Berga and Solsona Formations consist of alluvial and fluvial conglomerates, sandstones and lutites and thin intervals of lacustrine mudstones arranged in thickening and coarsening upward sequences.

Sandstones are stacked in tabular and channelized bodies with grain sizes ranging from fine to coarse. They are formed of mature sublitharenites constituted of 70–80% clasts, 0–5% clay matrix, 10–20% calcite cements and 5% porosity. Sandstones are well-sorted with subrounded clasts made of 80–90% quartz, 10–20% lithic fragments (limestones and metamorphic rocks) and traces of feldspar. In coarse-grained sandstones, some carbonate clasts have undergone ductile deformation to form pseudomatrix.

Conglomerates, which are stacked in channelized bodies, are grey in colour, heterometric, polymictic and present both matrix- and clast-supported fabrics. They are constituted of 50–80% clasts, 10–20% matrix, 10–20% calcite cement and 0–15% porosity. Clasts are rounded, with sizes ranging from 2 mm to 20 cm and consist of lithic fragments mainly derived from Mesozoic and Palaeogene dolostones and limestones in addition to less abundant Palaeozoic granitoids and metamorphic rocks. When clasts of different compositions are in contact, pressure solution processes occur. The matrix is formed by well sorted sandstones (mainly quartz grains) and red lutites.

Lutite layers are composed of red claystones and siltstones. Claystones are constituted of 90–100% of clay minerals and 0–10% of silt grains (mainly subhedral quartz) whereas siltstones are constituted of 50–80% of silt grains and 20–50% of clay minerals.

Carbonates are tabular bodies, up to 0.5 m thick, consisting of palustrine-lacustrine grey-yellow marlstones and brown mudstones. Sometimes they exhibit vug porosities cemented by calcite cement and displaying geopetal structures.

5.2. Host rock and fracture relationships

Point counting indicates that the abundance of fractures highly differs depending on the composition of the host rock (Fig. 7).

Lutite layers characterized by more than 70% of clay matrix are hardly affected by cemented fractures (Fig. 7). However, when the amount of silt increases the fracture porosity raises up to 13–25% (Fig. 7).

In fine and medium-grained mature sandstones, the intergranular porosity is totally occluded by calcite cement. In such cases, sandstones are not affected by fractures (Fig. 7). In contrast, in coarse-grained sandstones, grains are affected by small fractures, increasing up to a 15% the presence of microfractures filled by calcite cement (Fig. 7).

In conglomerates, the development of fractures differs depending on the fabric. In matrix supported conglomerates, calcite veins are less abundant than in clast supported conglomerates (Fig. 7). These fractures crosscut one or several clasts. The contact between clasts and matrix sometimes is open and filled by calcite cement (Fig. 8a).

Mudstones are slightly affected by fractures (Fig. 7), which locally are interconnected with vug porosities (Fig. 6e and f).

5.3. Calcite cements

Two generations of calcite cement have been recognized:

The first generation (Cc1) shows a zoned bright-orange to bright-red luminescence and is observed in the intergranular porosity of the clastic host rocks, vug porosity of host-carbonates

and in veins of reverse and most of strike-slip faults. In the intergranular porosity, Cc1 is formed of 5–10 μm in size euhedral blocky crystals that partially replace the host rock and previous cementation phases. Evidences of replacement include textures such as: (1) corroded borders of quartz and feldspar grains and protrusions of calcite cement (Fig. 8a and b); (2) pseudomorphs of sand and silt grains (Fig. 8c) and previous fibrous cements (Fig. 8d); and (3) patches of Cc1 microsparite within carbonate-derived conglomer-

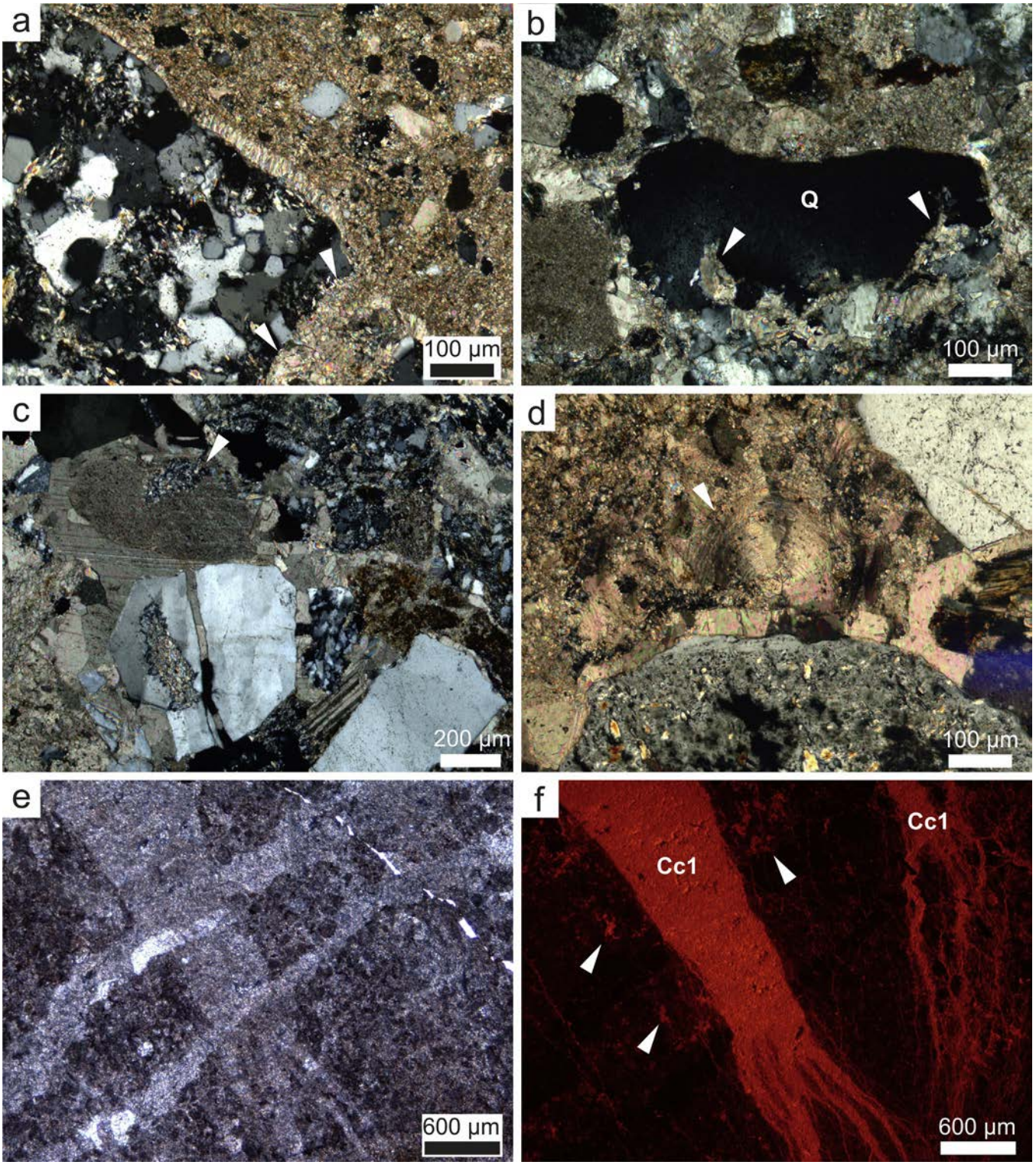

Fig. 8. Images from polarizing optical microscope and cathodoluminescence (CL) of the main replacement textures observed in host rocks. (a) Sample GP-R13. Calcite cement replacing partially a conglomerate clast made of polycrystalline quartz (white arrows). Note how the contact between silicic clast and conglomerate matrix is open and filled by calcite cement (crossed nicols). (b) Sample GP-R5. Protrusions of calcite (white triangles) into a quartz grain (Q) indicating replacement of detrital quartz (crossed nicols). (c) Sample GP-R12. Calcite cement Cc1 replacing a detrital grain (crossed nicols). Note how a remnant of de replaced grain is preserved (white triangle). (d) Sample GP-R12. Replacement of fibrous spherulite by calcite (crossed nicols). (e-f) Sample 302. CL image of a dolomite conglomerate clast (non-luminescent) affected by a vein filled by cement Cc1. Patches of microsparite with the same luminescence of Cc1 cement (white triangles) are developed in the conglomerate clast.

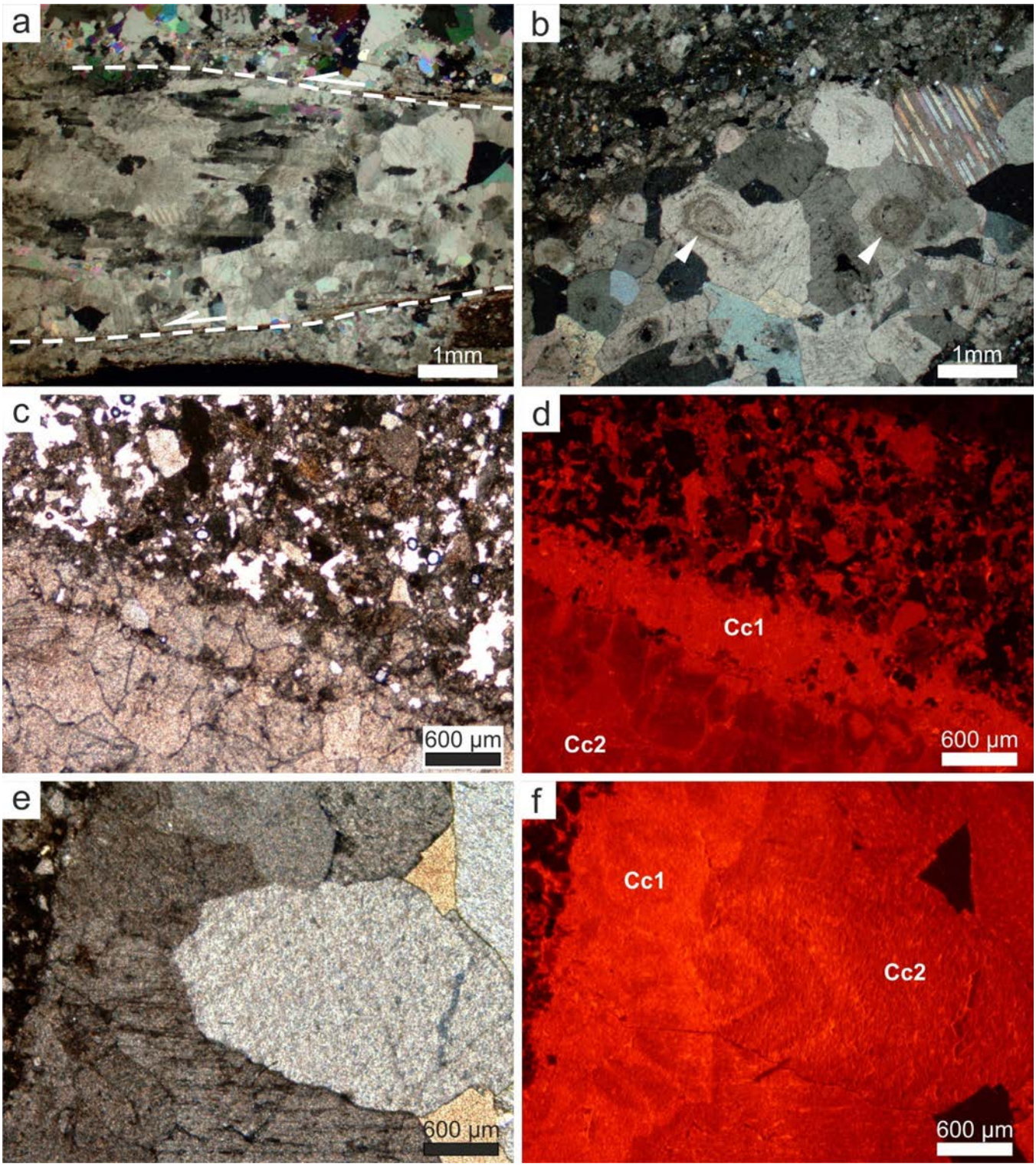

Fig. 9. Images from polarizing optical microscope and cathodoluminescence (CL) of the main features of calcite cements. (a) Sample GP-R1. Shear vein (white dashed line) filled by fibrous sparite passing laterally to blocky calcite (crossed nicols). (b) Sample 311A. Blocky calcite cement with growth zonation present in some crystals (white triangles). (c–d) Sample 311A. CL image where is shown the sharp contact between cements Cc1 and Cc2. (e–f) Sample 314D2. CL image where is shown the gradual change from calcite cement Cc1 to Cc2.

ate clasts (Fig. 8e and f). Contrarily, calcite cement Cc1 in veins shows a wider variety of morphologies, such as fibrous, blocky and bladed crystals. Fibrous crystals fill shear veins and change laterally to blocky sparite (Fig. 9a). They are arranged parallel to shear planes indicating a synkinematic growth. The size of fibrous calcite is around 1–1.5 mm long and 100–200 μm thick. Blocky crystals, with growth zonation in punctual cases (Fig. 9b), show differences depending on the type of veins where they precipitated. In shear veins, the size of blocky crystals ranges from 100 to 500 μm whereas in extension veins the size is smaller (from 5 to 10 μm). Bladed crystals, with widths and lengths up to 100 μm and 300 μm respectively, are developed in the margins of all vein types.

The second generation of calcite cement (Cc2) shows a zoned dull-orange to dull-red luminescence and it has been only observed in shear veins of all normal and some strike-slip faults. It consists of blocky crystals with sizes ranging from 100 μm to 5 mm.

The contact between Cc1 and Cc2 calcite cements within shear veins is sharp (Fig. 9c and d) or gradual (Fig. 9e and f). Moreover, all the cement textures in veins and the intergranular porosity show mechanical twinning, subgrain formation and serrated borders.

6. Fluid inclusion analysis

Fluid inclusions trapped in calcite cements have been studied by optical microscope and Raman spectroscopy.

Primary and secondary fluid inclusions have been observed in both calcite cement generations. However, their irregular shape and variable vapour/liquid ratios indicate that they were stretched as it is also attested by the wide range of temperatures of homogenization (between 130–210 °C for Cc1 and 120–280 °C for Cc2) (Fig. 10). Therefore, these fluid inclusions are unusable for microthermometry analysis. In addition, the salinity of the fluid could not be determined since the obtained elevated ice melting temperatures indicate the presence of clathrates (Goldstein and Reynolds, 1994), which hide the final disappearance of ice during melting (Diamond, 1994). It has not been possible to determine the eutectic temperature in this case. Raman spectroscopy was also applied in fluid inclusions trapped in calcite cements Cc1 and Cc2. However, in all samples, the strong fluorescence of calcite crystals did not allow to analyse their liquid and vapour phases.

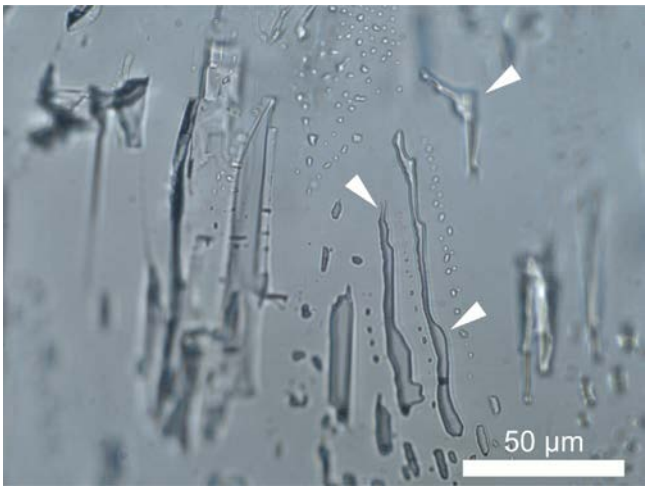

Fig. 10. Sample 311D. Image of optical microscope where is show a fluid inclusion assemblage. Note how fluid inclusions are stretched, showing an irregular shape (white triangles).

7. Geochemistry

7.1. Carbon and oxygen isotopes

Within the host rock, carbonate clasts of conglomerates show $\delta^{13}C$ values between −3.22 and +3.11‰ VPDB and $\delta^{18}O$ values between −8.91 and −3.43‰ VPDB (Fig. 11; Table 1). Palustrine-lacustrine limestones show $\delta^{13}C$ values between −3.3 and −2.4‰ VPDB and $\delta^{18}O$ values between −7.28 and −6.91‰ VPDB (Fig. 11; Table 1). These values are within the range of carbonates precipi-

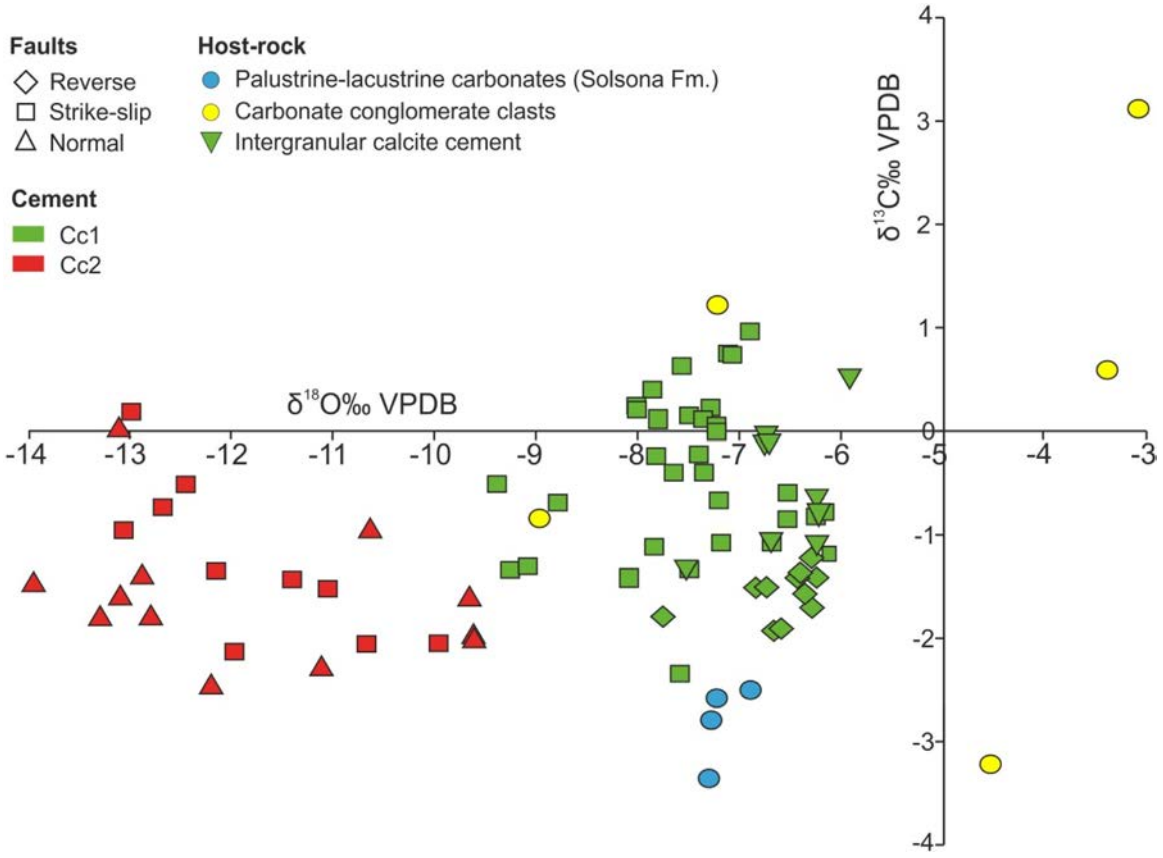

Fig. 11. $\delta^{18}O$ vs $\delta^{13}C$ cross-plot of carbonate host rocks and calcite cements of the Puig-reig anticline.

Table 1
$\delta^{18}O$ and $\delta^{13}C$ values of the host-carbonates and calcite cements Cc1 and Cc2. For the third and fourth columns, the blank spaces represent host rock samples which are not affected by faults and do not contain calcite cement, respectively.

Sample	Description	Fault type	Cement type	$\delta^{13}C$ VPDB	$\delta^{18}O$ VPDB
GP-R4	Palustrine-lacustrine carbonate	Strike-slip		−2.73	−7.26
302	Carbonate-derived clast	Strike-slip		−3.22	−4.70
303	Carbonate-derived clast	Strike-slip		3.11	−3.12
311F	Carbonate-derived clast	Strike-slip		1.22	−7.19
311G	Carbonate-derived clast	Strike-slip		−0.84	−8.91
312A	Carbonate-derived clast	Normal		0.59	−3.43
EM-1	Palustrine-lacustrine carbonate			−2.44	−6.92
PR-1A	Palustrine-lacustrine carbonate			−3.3	−7.28
PR-1B	Palustrine-lacustrine carbonate			−2.52	−7.22
GP-R1	Calcite shear vein	Strike-slip	Cc1	−1.51	−6.74
GP-R1	Calcite shear vein	Strike-slip	Cc1	−1.51	−6.85
GP-R1	Calcite shear vein	Strike-slip	Cc2	−1.44	−11.41
GP-R1	Calcite shear vein	Strike-slip	Cc2	−1.52	−11.06
GP-R1	Calcite shear vein	Strike-slip	Cc2	−1.34	−12.16
GP-R2	Calcite extension vein	Strike-slip	Cc1	−1.93	−6.67
GP-R2	Calcite extension vein	Strike-slip	Cc1	−1.91	−6.60
GP-R2	Intergranular cement	Strike-slip	Cc1	−1.07	−6.25
GP-R4	Vug porosity	Strike-slip	Cc1	−1.57	−6.37
GP-R4	Calcite shear vein	Strike-slip	Cc1	−1.22	−6.30
GP-R4	Calcite shear vein	Strike-slip	Cc1	−1.41	−6.25
GP-R5	Intergranular cement	Strike-slip	Cc1	0.53	−5.93
GP-R5	Calcite shear vein	Strike-slip	Cc2	−2.06	−10.67
GP-R5	Calcite shear vein	Strike-slip	Cc2	−2.05	−9.96
GP-R7	Calcite shear vein	Reverse	Cc1	−1.71	−6.29
GP-R7	Calcite shear vein	Reverse	Cc1	−1.79	−7.76
GP-R7	Intergranular cement	Reverse	Cc1	−0.62	−6.25
GP-R9A	Calcite extension vein	Strike-slip	Cc1	−0.59	−6.54
GP-R9A	Calcite shear vein	Strike-slip	Cc1	−0.78	−6.17
GP-R9A	Calcite shear vein	Strike-slip	Cc1	−0.82	−6.26
GP-R9A	Intergranular cement	Strike-slip	Cc1	−0.09	−6.72
GP-R9B	Calcite shear vein	Strike-slip	Cc1	−0.85	−6.54
GP-R9B	Intergranular cement	Strike-slip	Cc1	−0.02	−6.74
GP-R10	Calcite shear vein	Strike-slip	Cc1	−0.11	−6.76
GP-R11	Calcite shear vein	Strike-slip	Cc1	−1.08	−7.19
GP-R11	Calcite shear vein	Strike-slip	Cc1	−1.08	−6.69
GP-R11	Intergranular cement	Strike-slip	Cc1	−1.04	−6.69
GP-R11	Calcite shear vein	Strike-slip	Cc2	−1.61	−9.67
GP-R12	Intergranular cement	Normal	Cc1	−1.31	−7.53
GP-R12	Calcite shear vein	Normal	Cc2	−1.95	−9.63
GP-R12	Calcite shear vein	Normal	Cc2	−1.99	−9.62
GP-R13	Calcite shear vein	Strike-slip	Cc1	−1.37	−6.41
GP-R13	Calcite shear vein	Strike-slip	Cc1	−1.42	−6.44
GP-R13	Intergranular cement	Strike-slip	Cc1	−0.65	−6.23
302	Calcite extension vein	Strike-slip	Cc1	0.21	−8.02
302	Calcite shear vein	Strike-slip	Cc1	0.25	−8.02
302	Calcite shear vein	Strike-slip	Cc1	−0.51	−9.39
303	Calcite shear vein	Strike-slip	Cc1	0.10	−7.81
309A	Calcite shear vein	Strike-slip	Cc1	0.23	−7.29
309A	Calcite shear vein	Strike-slip	Cc1	0.11	−7.37
309B1	Calcite shear vein	Strike-slip	Cc1	−0.40	−7.36
309B1	Calcite shear vein	Strike-slip	Cc1	−0.40	−7.65
310	Calcite shear vein	Strike-slip	Cc1	0.96	−6.90
310	Calcite shear vein	Strike-slip	Cc1	0.75	−7.12
311A	Calcite shear vein	Strike-slip	Cc1	−0.69	−8.79
311A	Calcite shear vein	Strike-slip	Cc2	−0.73	−12.68
311A	Calcite shear vein	Strike-slip	Cc2	−2.13	−11.98
311B	Calcite shear vein	Strike-slip	Cc1	−0.67	−7.21
311B	Calcite shear vein	Strike-slip	Cc1	−1.30	−9.09
311D	Calcite shear vein	Strike-slip	Cc2	−0.95	−13.07
311D	Calcite shear vein	Strike-slip	Cc2	−0.51	−12.46
311F	Calcite shear vein	Strike-slip	Cc1	0.74	−7.05
311F	Calcite shear vein	Strike-slip	Cc1	0.74	−7.07
311G	Calcite shear vein	Strike-slip	Cc2	0.19	−12.99
312A	Calcite shear vein	Normal	Cc1	0.63	−7.57
312A	Calcite shear vein	Normal	Cc2	0.02	−13.11
313A	Calcite shear vein	Normal	Cc2	−1.40	−12.88
313A	Calcite shear vein	Normal	Cc2	−1.80	−13.30
313A'	Calcite shear vein	Normal	Cc1	−2.34	−7.59
313A'	Calcite shear vein	Normal	Cc2	−2.30	−11.14
314A	Small fracture affecting clasts	Normal	Cc1	0.15	−7.50
314A	Calcite shear vein	Normal	Cc2	−1.60	−13.10
314A	Calcite shear vein	Normal	Cc2	−0.95	−10.64
314B	Calcite shear vein	Strike-slip	Cc1	0.00	−7.23
314B	Calcite shear vein	Strike-slip	Cc1	0.05	−7.23

Table 1 (*Continued*)

Sample	Description	Fault type	Cement type	$\delta^{13}C$ VPDB	$\delta^{18}O$ VPDB
314C	Calcite shear vein	Strike-slip	Cc1	−0.22	−7.41
314C	Calcite shear vein	Strike-slip	Cc1	−0.23	−7.83
314D1	Calcite shear vein	Normal	Cc1	−1.11	−7.85
314D1	Calcite shear vein	Normal	Cc2	−1.79	−12.80
314D2	Calcite shear vein	Normal	Cc1	−1.34	−9.27
314D2	Calcite shear vein	Normal	Cc2	−1.47	−13.95
314D2	Calcite shear vein	Normal	Cc2	−2.46	−12.21
317	Calcite shear vein	Strike-slip	Cc1	−1.23	−8.09
317	Calcite shear vein	Strike-slip	Cc1	−1.34	−7.50

Table 2
Calcite cement $\delta^{13}C$, $\delta^{18}O$, Δ_{47} and $\delta^{18}O_{fluid}$. n represents the number of analyses per sample.

Sample	Cement type	n	$\delta^{13}C$ VPDB	$\delta^{18}O$ VPDB	Δ_{47}	T °C	$\delta^{18}O_{fluid}$ VSMOW
309B1	Cc1	3	−0.44	−7.77	0.548 ± 0.009	92 ± 5	4.7 ± 0.6
317	Cc1	3	−0.99	−6.95	0.494 ± 0.010	129 ± 8	9.2 ± 0.7
311A	Cc2	3	-0.77	-12.32	0.574 ± 0.010	77 ± 5	−1.7 ± 0.7
311D	Cc2	3	−0.73	−12.85	0.551 ± 0.004	90 ± 3	−0.7 ± 0.3

tated in lakes fed by rivers of Pyrenean provenance (Oberhänsli and Allen, 1987).

Calcite cement Cc1 shows $\delta^{13}C$ values between −2.5 and +1‰ VPDB and $\delta^{18}O$ values between −9 and −6‰ VPDB (Fig. 11, Table 1). Calcite cement Cc2, shows $\delta^{13}C$ values between −2 and +0.5‰ VPDB and $\delta^{18}O$ values between −14 and −9.5‰ VPDB (Fig. 11, Table 1).

7.2. Clumped isotope thermometry

For calcite cement Cc1, the measured Δ_{47} values by clumped isotope geochemistry are 0.548 ± 0.009‰ and 0.493 ± 0.0010‰, which translates into temperatures of 92 ± 5 °C and 129 ± 8 °C using the form of Kluge et al. (2015) (Table 2). In addition, the $\delta^{18}O_{fluid}$ composition for calcite cement Cc1 can be reconstructed using the clumped isotope temperatures, the $\delta^{18}O_{calcite}$ and the equation of Friedman and O'Neil (1977). Thus, the $\delta^{18}O_{fluid}$ for Cc1 is estimated to range between +4.7 ± 0.6 and +9.2 ± 0.7‰ VSMOW.

The measured Δ_{47} values for calcite cement Cc2 are 0.574 ± 0.010‰ and 0.551 ± 0.004‰, which translate to temperatures of 77 ± 5 °C and 93 ± 1 °C using the calibration of Kluge et al. (2015) (Table 2). The estimated $\delta^{18}O_{fluid}$ for calcite cement Cc2 ranges between −1.7 ± 0.7 and −0.7 ± 0.3‰ VSMOW.

7.3. Strontium isotopes

The host mudstone has a $^{87}Sr/^{86}Sr$ ratio of 0.708865 and the calcite fraction of the marls has a $^{87}Sr/^{86}Sr$ ratio of 0.708967 (Fig. 12; Table 3).

$^{87}Sr/^{86}Sr$ ratios for calcite cement Cc1 range between 0.709138 and 0.709246 and between 0.708947 and 0.709002 for calcite cement Cc2 (Fig. 12, Table 3).

7.4. Elemental composition

The elemental composition of calcite cement Cc1 (Fig. 13, Table 4) show values ranging from 600 to 4500 ppm in Mg and from 600 to 2800 ppm in Mn. Fe and Sr contents range from below the detection limit up to 3100 and up to 700 ppm, respectively.

Calcite cement Cc2 (Fig. 13, Table 4) show values from 300 to 2300 ppm in Mn and from 300 to 3200 ppm in Fe. Mg and Sr contents range from below detection limit up to 2400 and 3000 ppm, respectively.

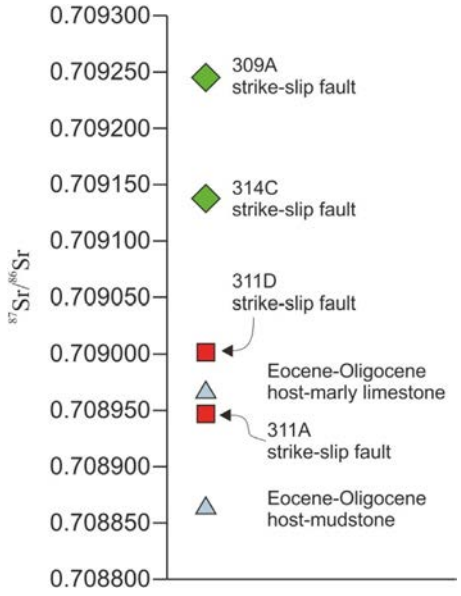

Fig. 12. $^{87}Sr/^{86}Sr$ composition of the calcite cements and carbonate host rocks. Grey diamonds represent veins with calcite cement Cc1. White squares represent veins with calcite cement Cc2. Black crosses represent palustrine-lacustrine carbonates.

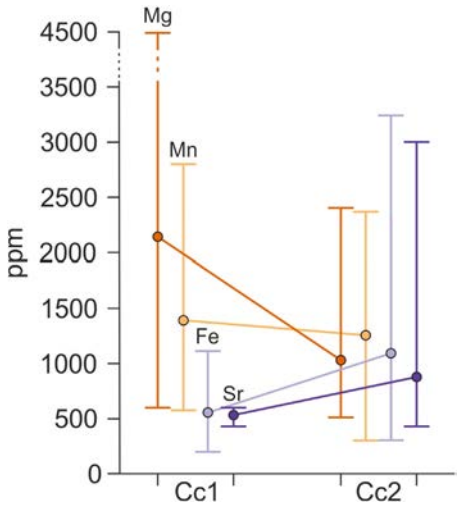

Fig. 13. Elemental composition of the calcite cements. For Mg, Mn, Fe and Sr. Minimum, maximum and mean contents are given.

Table 3
$^{87}Sr/^{86}Sr$ values of palustrine-lacustrine host-carbonates and calcite cements Cc1 and Cc2. For the third and fourth columns, the blank spaces represent host rock samples which are not affected by faults and do not contain calcite cement, respectively.

Sample	Description	Fault type	Cement type	$^{87}Sr/^{86}Sr$
GP-R4	Eocene-Oligocene host-mudstone	Strike-slip		0.708865
IP-R	Eocene-Oligocene host-marly limestone			0.708967
309A	Calcite shear vein	Strike-slip	Cc1	0.709246
311A	Calcite shear vein	Strike-slip	Cc2	0.708947
311D	Calcite shear vein	Strike-slip	Cc2	0.709002
314C	Calcite shear vein	Strike-slip	Cc1	0.709138

Table 4
Minimum, maximum and average values of the elemental composition of the calcite cements Cc1 and Cc2. n represents the number of analyses per calcite cement generation. For fault types affecting the analyzed samples see Table 1.

Filling stage	n	Analysed samples		Mg (ppm)	Mn (ppm)	Fe (ppm)	Sr (ppm)
Calcite cement Cc1	45	GP-R1GP-R4309A	Min.	600	600	<d.l.	<d.l.
		311A	Max.	4500	2800	1100	600
		314D2	Av.	2171	1406	544	537
Calcite cement Cc2	45	GP-R1 311A 311D	Min.	<d.l.	300	300	<d.l.
		312D2	Max.	2400	2300	3200	3000
			Av.	1038	1268	1080	886

8. Discussion

Discussion is organized in 5 main subsections discussing (1) the mechanical stratigraphy; (2) the type and origin of fluids across the Puig-reig anticline; (3) the mechanisms of calcite cement precipitation; (4) the relationships between fluid flow and the structural evolution of the Puig-reig anticline and (5) the evolution of fluid flow at the basin scale comparing the Puig-reig anticline results with the El Guix anticline (~32 km southwards), which is located along the SE Pyrenean deformation front within the Ebro basin.

8.1. Mechanical stratigraphy

Cementation during early burial mostly affected sandstone and conglomerate layers due to their higher porosity and permeability than clayey units. This early cementation, however, increased the relative mechanical strength of these layers and thus localizing the generation of stratabound joints across the entire anticline as described in other deformed basins (David et al., 1998; Shackleton et al., 2005; Laubach et al., 2009). Differences in rock mechanics between layers also controlled the development of bed-parallel slip surfaces and associated reverse faults in the forelimb of the Puig-reig anticline during compression, as was also observed in other thrust belts (Treagus, 1988; Bai and Pollard, 2000; Sanz et al., 2008).

Joints were reactivated as strike-slip and normal faults by shearing as evidenced by the high angle dips with respect to bedding and the stratabound character of some faults (like joints). Some of these faults crosscut competent and non-competent layers and they are mainly located in the crest and forelimb of the Puig-reig anticline. Thus, at outcrop scale, fracture patterns in the Puig-reig anticline were controlled by tectonic stress related to contraction, rock mechanics, diagenesis and structural position within the anticline. These controls on fracturation have been also observed in other foreland fold belts (Shackleton et al., 2005; Laubach et al., 2009; Watkins et al., 2015).

At the microscopic scale, the development of microstructures was controlled by grain size, host rock cementation and porosity. In fine to medium-grained sandstones and matrix-supported conglomerates, fractures are absent, whereas in coarse-grained sandstones and clast-supported conglomerates, grain crushing increases up to 15% and 8%, respectively (Fig. 7). In conglomerates in which carbonate and silicic clasts are in contact, stylolite contacts are developed instead of fractures. Intergranular porosity of all these sediments was occluded by calcite cement Cc1 indicating that cementation together with grain size exerted a strong control on fracture development. In this study, coarse-grained rocks are more prone to fracturing than finer rocks, as was also observed from experimental tests by Chuhan et al. (2002) in sandstones, reporting an increase of grain crushing during compaction related with an increase of grain size. In fine lutite units (claystone) and conglomerates supported by clay matrix fractures are hardly present (Fig. 7) because the absence of cements makes them to behave as ductile levels when are affected by deformation. Siltstone layers were more permeable, and are partially cemented, increasing their stiffness and facilitating brittle deformation. Therefore, development of fractures in lutite layers was controlled by cementation, which changed rock mechanics (Laubach et al., 2009). Fractures in palustrine-lacustrine mudstones were controlled by vug porosity (Fig. 6e and f), which probably facilitated fracture nucleation (Vajdova et al., 2010).

8.2. Type and origin of the fluids

The type of fluid that flowed through the intergranular porosity of host rocks and fault planes has been determined by using the isotopic and elemental composition of the carbonate cements (Meyers and Lohmann, 1985; Banner and Hanson, 1990).

8.2.1. Cement Cc1

Calcite cement Cc1, precipitated in the intergranular porosity, reverse and most of strike-slip faults. The temperatures from which cement Cc1 precipitated (between 92 °C and 129 °C) would imply burial depths between 4 and 5 km, assuming a geothermal gradient of 25 °C km^{-1}. These depths have never been attained according to previous works based on cross sections (Vergés, 1993), stratigraphic profiles (Barrier et al., 2010) and vitrinite reflectance data (Clavell, 1992; Vergés et al., 1998), which indicate a maximum depth of 1.7 km for the Solsona Formation in the Puig-reig anticline. Thus, with a thickness of 1.7 km and a geothermal gradient of 25 °C km^{-1}, the temperature reached at the base of the Solsona Formation was around 42 °C, which is lower than that obtained from clumped isotopes. These results account for the occurrence of hydrothermal fluids circulating channelized along the thrust faults from the Palaeozoic basement at depths of around 4–5 km upwards to the shallower Solsona Formation (Fig. 2a). This hydrothermal fluid should have flowed rapid enough to be at thermal disequilibrium with its adjacent host rock (Beaudoin et al., 2011).

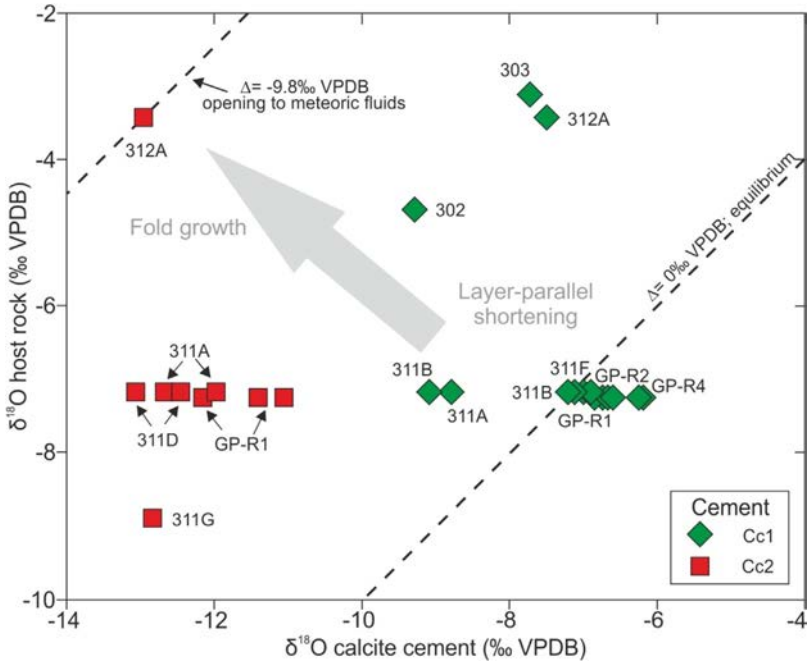

Fig. 14. $\delta^{18}O$ calcite cement vs $\delta^{18}O$ host rock cross plot. Grey diamonds represent veins with calcite cement Cc1. White squares represent veins with calcite cement Cc2. Δ represents the isotopic difference between calcite cements and carbonate host rocks.

Calcite cement Cc1 is characterized by a narrow range of $\delta^{18}O$ (from −7.53 to −5.93‰ VPDB) and $\delta^{13}C$ within the same range of the host carbonates (Fig. 11), probably a result of the buffering of the pore-water isotopic composition by the host carbonates (Marshall, 1992; Travé et al., 1998b; Fig. 14). $\delta^{18}O$ of strike-slip faults have a wider range of values (from −9.63 to −6.25‰ VPDB), with some veins in disequilibrium with their host carbonates (Fig. 14).

The calculated $\delta^{18}O_{fluid}$ from clumped isotope thermometry (Table 3) range between +4.7 and +9.2‰ VSMOW, within the range of formation, metamorphic and magmatic waters (Taylor, 1987). Magmatic waters are ruled out since magmatism is not developed during the formation of the Pyrenees. However, we have no evidences to discern between formation and metamorphic waters. The high $^{87}Sr/^{86}Sr$ values (between 0.709138 and 0.709246) indicate that the hydrothermal fluid interacted with a highly radiogenic source (Fig. 12, Table 2). The source for this highly radiogenic fluid can be the Palaeozoic basement located at depth and/or the Palaeozoic-derived silicic clasts of the Solsona and Berga Formations. The $^{87}Sr/^{86}Sr$ of Pyrenean Palaeozoic sedimentary rocks range between 0.709600 and 0.717000 and between 0.706633 and 0.715405 for granitic rocks (Bickle et al., 1988; Banks et al., 1991). The low radiogenic underlying evaporite units of the Cardona (between 0.70798 and 0.70800), Barbastro (0.70796) and Beuda (between 0.707739 and 0.707980) Formations (Travé et al., 2000; Carrillo, 2012; Carrillo et al., 2014), do not seem to be involved. The $\delta^{18}O$ of the Palaeozoic metamorphic rocks in the Pyrenees (between +10 and +16‰ VSMOW; Wickham and Taylor, 1985, 1987) and Hercynian granodiorites (up to +9‰ VSMOW; Wickham and Taylor, 1987; Losh, 1989; Tempest, 1991) is also consistent with a fluid highly interacted with the Palaeozoic basement.

8.2.2. Cement Cc2

The $\delta^{13}C$ of cement Cc2 is similar to that of cement Cc1 (Fig. 11). However, the $\delta^{18}O$ relationship between calcite cement and host rock indicates that the fluid from which Cc2 precipitated was not in equilibrium with its adjacent host carbonates (Fig. 14). The depletion in $\delta^{18}O$ of Cc2 with respect to Cc1 is interpreted as the progressive input of a meteoric external fluid (Travé et al., 1997), more evident in the crest of the anticline (Fig. 15). The lower $^{87}Sr/^{86}Sr$ of cement Cc2 with respect to Cc1 (Fig. 12) indicates not interaction of the fluid with a radiogenic source.

The $\delta^{18}O_{fluid}$ obtained from clumped isotopes (Table 3), between −1.7‰ and −0.7‰ VSMOW, are higher than those of modern rainfall in the same area (from −6.4 to −4.6‰ VSMOW; Travé and Calvet, 2001) and probably also of the upper Eocene and lower Oligocene rainwater, taking into account that during this time the Iberian plate was in similar latitude than present day (Rosenbaum et al., 2002). These values may result from mixing of meteoric waters with a more $\delta^{18}O$-enriched fluid. The wide range of $\delta^{18}O$ (Fig. 11), low Mg and Mn content and high Fe and Sr content (Fig. 13), also account for a mixing between fluids.

Temperatures obtained for calcite cement Cc2 (between 77 °C and 93 °C), although lower than those obtained for Cc1, they still account for hydrothermal fluid flow, taking into account the minimum burial depth of 1.7 km and assuming a geothermal gradient of 25 °C km^{-1}. This temperature decrease would also agree with Cc2 precipitation from the mixing between the hydrothermal fluid responsible of Cc1 precipitation and a low temperature meteoric fluid.

The increase in Fe and Sr content in cement Cc2 compared to Cc1 could be controlled by the progressive burial and compaction of shale units of the Solsona Formation, leading to ion expulsion from shales (Coplen and Hanshaw, 1973; Hanshaw and Coplen, 1973; Travé et al., 1997) and increasing the Fe content towards the deeper stratigraphic levels (Fig. 15).

8.3. Mechanisms of calcite cement precipitation

Calcite cements Cc1 and Cc2 are in thermal disequilibrium with the surrounding host rock. However, since calcite has a retrograde solubility, and preferentially precipitates when temperature increases, other parameters have to take into account when calcite precipitates from a hot ascending fluid (Segnit et al., 1962; Fein and Walther, 1987). According to Bons et al. (2012) and Beaudoin et al. (2014), controlling parameters such as changes in pH and in oxidation conditions as well as fluid mixing influence the Ca

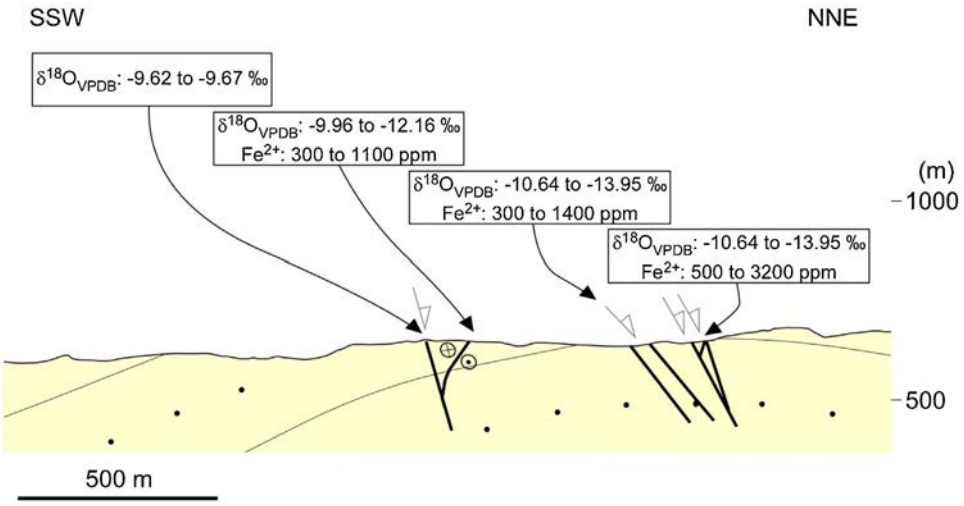

Fig. 15. Detail of the Puig-reig anticline showing the trends in $\delta^{18}O$ and Fe^{2+} content in calcite cement Cc2. The $\delta^{18}O$ decreases and the Fe^{2+} content increases downwards the stratigraphic record. Minimum and maximum values are given.

oversaturation of the fluid, which can promote precipitation of calcite cement, even when fluids are decreasing their temperature. Another controlling parameter is the decrease in pCO_2 during fracture opening. Moreover, during faulting, zones of low pCO_2 are developed, allowing fluid migration into fractures and precipitation of calcite cements Cc1 and Cc2 (Bons et al., 2012).

If calcite cement precipitation was coeval with fracture opening (as evidenced by veins with elongated blocky calcite), the $\delta^{18}O$ composition allows us to determine which specific parameters controlled calcite precipitation (Beaudoin et al., 2014). Thus, the narrow range of $\delta^{18}O$ values for calcite cement Cc1 present in the intergranular porosity and reverse and some strike-slip faults indicates that precipitation was controlled by pCO_2 drop related to fracturing. In contrast, the wide range in $\delta^{18}O$ in calcite cement Cc1 and Cc2 present in some strike-slip and in all normal faults may be indicative that the main controlling parameter of calcite precipitation was mixing of two fluids.

8.4. Relationship between fluid flow and structural evolution of the Puig-reig anticline

In the Puig-reig anticline, calcite cements Cc1 and Cc2 are related to two fluid flow stages during fold growth. Cement Cc1 is related to layer-parallel shortening whereas cement Cc2 relates to the fold growth. Earlier cements precipitated before the growth of the anticline and are totally replaced by calcite cement Cc1 (Fig. 8).

8.4.1. Fluid flow during layer-parallel shortening (time T1)

Relationships between fractures and calcite cement Cc1 in the Puig-reig anticline indicate precipitation during layer-parallel shortening as evidenced by the constant angular relations between reverse and most of the strike-slip faults with bedding (Fig. 16). The same relationships between bedding and fractures during layer-parallel shortening have been also observed in anticlines formed in the Zagros fold and thrust belt (Casini et al., 2011; Reif et al., 2012; Tavani et al., 2015). Reverse faults in the forelimb and strike-slip faults in the hinge of the Puig-reig anticline could have been formed due to an increase of fluid pressure, controlled by fluid migration to the fold crest and/or by syntectonic sedimentation, as pointed out in other fold-fluid systems (Evans and Fischer, 2012).

During T1, hydrothermal fluids migrated upwards, using faults as preferential paths. This fluid migrated along the blind thrust system responsible for the development of the Puig-reig anticline reaching the overlying Solsona and Berga Formations through

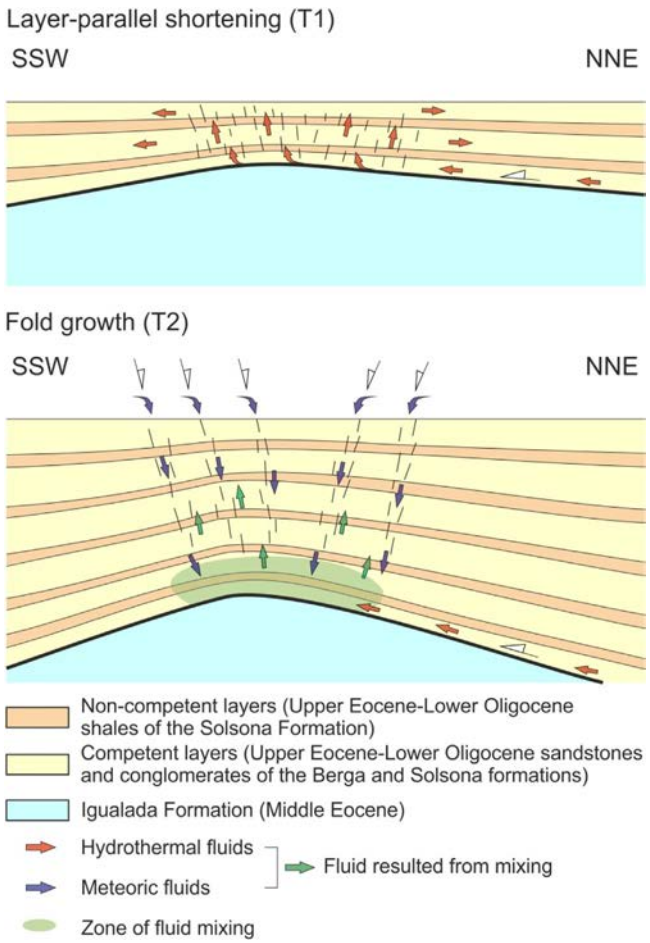

Fig. 16. Conceptual models of the structural and fluid flow evolution of the Puig-reig anticline. Red, blue and green arrows indicate fluid movement. No vertical exaggeration. Fluid flow during the layer-parallel shortening. Hydrothermal fluids migrated along the main faults and more permeable sedimentary units. Below, fluid flow during fold growth. During this event, meteoric fluids circulated downwards the normal faults formed by outer arc extension and mixed with the hydrothermal fluids at depth.

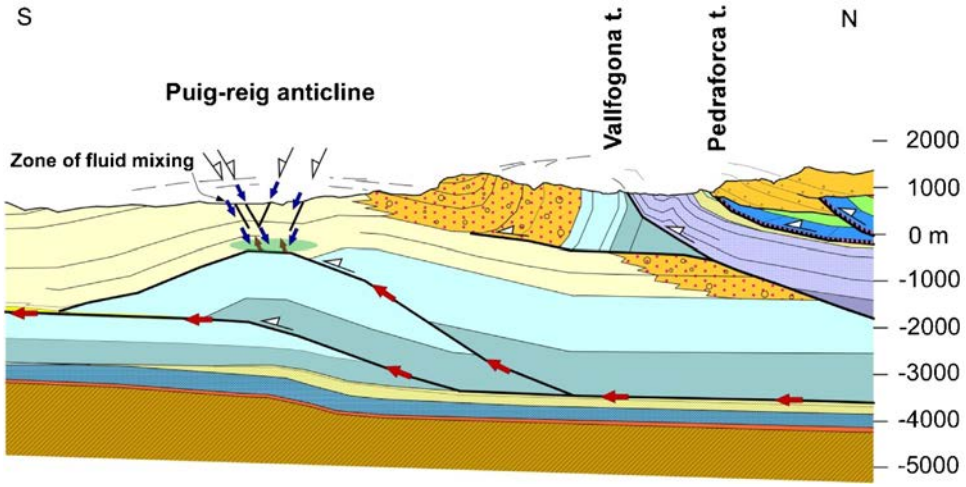

Fig. 17. Fluid flow model of the northern part of the Ebro Basin. Red arrows indicate fluid migration of deep formation waters during T1 and T2. Blue arrows indicate fluid migration of shallow meteoric waters during T2. For sedimentary units legend see Fig. 2a.

the reverse and strike-slip fault planes affecting these units (Figs. 16 and 17). These fractures allowed hydrothermal fluid circulation, cementing the permeable layers in the system (sandstones, conglomerate sand matrix and siltstones) and replacing earlier cements. Although the studied reverse and strike-slip faults are relatively small, they probably form a well-connected network allowing lateral and vertical fluid migration across different stratigraphic units, as already observed in the Bighorn Basin (Beaudoin et al., 2013).

8.4.2. Fluid flow during fold growth (time T2)

During the second stage of fluid flow, cement Cc2 precipitated (Fig. 16). Normal faults, which are sub-parallel to the regional fold axis, were formed due to the outer-arc extension of the Puig-reig anticline during fold growth. In addition, during T2, previous faults and bedding-perpendicular joints were passively rotated into the limbs and suitably oriented strike-slip faults were reactivated as normal faults, as observed by the presence of dip-slip striae overprinting strike-slip markers in the same fault planes.

Cement Cc2 is only present in fault planes due to the entire cementation of the more permeable units by cement Cc1 during T1. Small normal and strike-slip faults formed during T2 developed sufficient vertical connectivity to allow vertical fluid flow across the previously cemented sedimentary units. The newly formed normal and strike-slip faults changed the palaeohydrological system acting as paths for low-temperature, probably meteoric, fluids (Fig. 16). These fluids reached the interface between the Solsona and Igualada Formations in the core of the Puig-reig anticline (Fig. 17), in accordance with the fault-valve model (Sibson, 1981; Henderson and McCaig, 1996). According to this model, fluids migrate downwards through short-displacement faults by decrease in fluid pressure (P_f) at depth after the seismogenic cycle of an underlying thrust fault (Fig. 17). The low-temperature fluids were enriched at depth in Fe and Sr and mixed with the hydrothermal fluid from which cement Cc1 precipitated, according to the model of Bons et al. (2014). After mixing, fluids migrated upwards through normal and strike-slip faults (precipitating cement Cc2 by pCO_2 drop) due to an increase of P_f related to the build-up stresses developed during compression, as described in the central Pyrenees (Henderson and McCaig, 1996).

This evolution of the fluid flow model is consistent with previous works done in fold-fluid systems, reporting the opening of the fluid system to external fluids and mixing during development of fold-related fractures (Travé et al., 2000; Fischer et al., 2009; Beaudoin et al., 2011; Evans et al., 2012; Ogata et al., 2014).

8.5. Fluid flow at basin scale

8.5.1. The El Guix anticline

The El Guix anticline developed at the southern tip line of the South Pyrenean fold and thrust belt during the lower Oligocene (Sans and Vergés, 1995). This anticline is detached above the Cardona salt, which is the main detachment level between the deformed and non-deformed foreland basin (Figs. 1 b and 2 a). The El Guix anticline has a long wavelength (5.6 km), small amplitude and consists of two anticlines at the present erosion level (Sans, 2003). The sedimentary cover forming the El Guix anticline consists of the distal part of the Solsona Formation, the deltaic-lacustrine units of the Súria and Torà formations and the Barbastro gypsum (Travé et al., 2000). These sediments are located 300 m above the Cardona detachment horizon and are affected by a set of thrusts and backthrusts with dips ranging from 27 to 40° (Sans and Vergés, 1995).

8.5.2. Puig-reig anticline vs El Guix anticline

In the El Guix anticline, three fluid flow stages were established, whereas in the Puig-reig anticline only 2 fluid flow stages have been determined in this study.

The first fluid flow stage of the El Guix anticline was characterized by local migration of meteoric waters through microfractures developed by layer-parallel shortening in a relatively open system. In the Puig-reig anticline this stage has not been observed. However, the presence of early cements replaced by calcite cement Cc1 indicates the presence of a previous fluid flow stage.

The second fluid flow stage of the El Guix anticline took place during the folding and thrusting. During these events, external meteoric fluids flowed downwards to the detachment horizon located in the Cardona Formation and through the main backthrusts, which acted as effective channelized paths for these fluids (Travé et al., 2000). During their migration, these meteoric waters evolved to a formation water composition. In contrast, in the Puig-reig anticline, hydrothermal fluids circulated along the basal thrust of the South Pyrenean thrust system (Figs. 2 a and 17). These hydrothermal fluids were mixed at depth with meteoric waters that percolated downwards through normal and strike-slip faults. Cement Cc2 precipitated when the mixed fluids migrated upwards during compression. The lack of such cements in the El Guix anti-

cline reveals that hydrothermal fluids did not reach the frontal most part of the fold and thrust system, indicating that these fluids were probably diluted during their forward migration, as has been already pointed in other fold and thrust belts such as the Bighorn Basin (Beaudoin et al., 2014).

Formation waters in the El Guix anticline and hydrothermal fluids in the Puig-reig anticline circulated in a rock-buffered system, as evidenced by the $\delta^{13}C$ signal of calcite cements and carbonate host rocks. In both structures, fluids interacted with the upper Eocene-lower Oligocene lacustrine mudstones and marlstones (between −5.6 and −3.71‰ VPDB in the El Guix anticline and between −3.3 and −2.4‰ VPDB in the Puig-reig anticline). In addition, in the Puig-reig anticline, hydrothermal fluids also interacted with conglomerate clasts derived from Jurassic, Cretaceous and Paleogene marine carbonates (between −3.22 and +3.11‰ VPDB).

The last fluid flow stage of the El Guix anticline was interpreted to have developed during the extensional elastic rebound of the south eastern margin of the Ebro basin during the opening of the Valencia Trough in late Oligocene-early Miocene times (Lewis et al., 1996). During this extensional stage, local meteoric fluids flowed through fractures and through vug porosity developed within the cement of previous microstructures (Travé et al., 2000).

8.5.3. Migration paths

As discussed previously, hydrothermal fluids are only recognised in the Puig-reig anticline and not in the El Guix anticline. Two possible origins are pointed for these hydrothermal fluids: formation waters or metamorphic fluids. In both cases, large thrust faults would have acted as channelled paths for fluids that migrated from the inner part of the Pyrenees towards the thrust front, as was also stated in the Ainsa basin (Travé et al., 1997).

Later, low temperature meteoric waters were introduced into the palaeohydrological system in the frontal part of the South Pyrenean fold and thrust belt. In the El Guix anticline, local meteoric fluids, which evolved to formation waters, migrated downwards by lateral variations of the topography to the detachment level in the Cardona salts (Travé et al., 2000), whereas in the Puig-reig anticline, fluids percolated to deeper parts of this fold through the crestal graben fracture system reaching the Solsona-Igualada interface and the blind thrust system that created the anticline.

9. Conclusions

A multidisciplinary approach has been used in this study to determine controls on deformation and fluid interactions within a fault system (normal and strike-slip faults) cutting Eocene-Oligocene alluvial and fluvial deposits of the Berga and Solsona Formations, along the crestal domain of the Puig-reig anticline in the SE Pyrenees.

Structural analyses indicate the timing of fracture development, which consists first in the development of joints, small reverse and strike-slip faults and the later extensional reactivation of suitably oriented strike-slip faults as normal faults. At outcrop scale, development of these fractures was controlled by rigidity contrasts between layers, diagenesis and structural position within the anticline, whereas grain size, cementation and porosity controlled deformation at the microscopic scale.

Structural, petrographic and geochemical data from intergranular cements and calcite veins reveal the presence of two migrating fluids producing two cementation events: Cc1 related to the layer-parallel shortening and Cc2 linked to the anticline growth.

Cc1 cement precipitated from an ascending hydrothermal fluid at temperatures between 92 and 130 °C. This fluid had $\delta^{18}O_{fluid}$ between +4.7 and +9.2‰ VSMOW, relatively high $^{87}Sr/^{86}Sr$ ratio, and high Mn and Mg content and relatively low Sr and Fe content. This fluid was probably a result of the buffering of the pore-water isotopic composition by the host carbonates. Hydrothermal fluids migrated from around 4–5 km depth through the fracture system, including most of the strike-slip faults, to reach the Berga and Solsona Formations, during the layer-parallel shortening, partially replacing the host rocks by calcite. Cc1 precipitation was induced by pCO2 drop related to fracturing.

Cc2 cement precipitated from a fluid in disequilibrium with its adjacent host rock at a temperature between 77 and 93 °C. This fluid, with $\delta^{18}O_{fluid}$ between −1.7‰ and −0.7‰ VSMOW, relatively low $^{87}Sr/^{86}Sr$ and Mg, and high Sr and Fe content, resulted from the mixing at depth of the hydrothermal fluid from which Cc1 precipitated and low-temperature, probably meteoric, waters. Low-temperature fluids percolated through the crestal graben fault system according to the fault-valve model during the growth of the Puig-reig anticline.

Fluid flow patterns between the Puig-reig and the El Guix anticlines along the same transect reveal that hydrothermal fluids migrated from N to S but did not reach the El Guix anticline along the tip line of the South Pyrenean fold and thrust belt. In this anticline, local meteoric and evolved meteoric fluids circulated along the fold.

Hydrothermal fluids derived from the inner part of the Pyrenean Chain migrated forelandwards, whereas meteoric fluids in the Puig-reig and the El Guix anticlines were added into the fluid system along the frontal parts of the evolving Ebro foreland fold and thrust belt.

Acknowledgements

The Isotopic, Raman and electron microprobe analyses were carried out at “Centres Científics i Tecnològics” of the Universitat de Barcelona. Strontium analyses were done at the “CAI de Geocronología y Geoquímica Isotopica (UCM-CEI)” of the Universidad Complutense de Madrid. Fluid inclusion thermometry was performed at the facilities of the “Departament de Geologia” of the Universitat Autònoma de Barcelona. The clumped isotopes analyses were performed in the Qatar Stable Isotope Laboratory of Imperial College of London. We thank Mercè Corbella, Esteve Cardellach and Dídac Navarro for their support during fluid inclusion analysis. This research was performed within the framework of DGICYT Spanish ProjectCGL2015-66335-C2-1-R, Grup Consolidat de Recerca “Geologia Sedimentària” (2014SGR-251). The accurate and constructive comments from two anonymous reviewers and from the guest editor O. Lacombe helped to improve the original manuscript.

References

Bai, T., Pollard, D.D., 2000. Fracture spacing in layered rocks: a new explanation based on the stress transition. J. Struct. Geol. 22, 43–57.

Banks, D.A., Davies, G.R., Yardley, B.W.D., McCaig, A.M., Grant, N.T., 1991. The chemistry of brines from an Alpine thrust system in the Central Pyrenees: an application of fluid inclusion analysis to the study of fluid behavior in orogenesis. Geochimia et Cosmochimica Acta 55, 1021–1030.

Banner, J.L., Hanson, G.N., 1990. Calculation of simultaneous isotopic and trace element variations during water-rock interaction with applications to carbonate diagenesis. Geochimia et Cosmochimica Acta 54, 3123–3137.

Barbier, M., Leprêtre, R., Callot, J.P., Gasparrini, M., Daniel, J.M., Hamon, Y., Lacombe, O., Floquet, M., 2012. Impact of fracture stratigraphy on the paleo-hydrogeology of the Madison Limestone in two basement-involved folds in the Bighorn basin (Wyoming, USA). Tectonophysics 576–577, 116–132.

Barrier, L., Proust, J.N., Nalpas, T., Robin, C., Guillocheau, F., 2010. Control of alluvial sedimentation at foreland basin active margins, case study from the north-eastern Ebro basin (south-eastern Pyrenees, Spain). J. Sediment. Res. 80, 728–749.

Beaudoin, N., Bellahsen, N., Lacombe, O., Emmanuel, L., 2011. Fracture-controlled paleohydrogeology in a basement-cored fault-related fold: sheep mountain anticline, wyoming, United States. Geochem. Geophys. Geosyst. 12, 1–15.

Beaudoin, N., Lacombe, O., Bellahsen, N., Emmanuel, L., 2013. Contribution of studies of sub-seismic fracture populations to paleo-hydrological reconstructions (Bighorn basin, USA). Procedia Earth Planet. Sci. 7, 57–60.
Beaudoin, N., Bellahsen, N., Lacombe, O., Emmanuel, L., Pironon, J., 2014. Crustal-scale fluid flow during the tectonic evolution of the Bighorn Basin (Wyoming, USA). Basin Res. 26, 403–435.
Beaudoin, N., Huyghe, D., Bellahsen, N., Lacombe, O., Emmanuel, L., Mouthereau, F., Ouanhnon, L., 2015. Fluid systems and fracture development during syn-depositional fold growth: an example from the Pico del Aguila anticline, Sierras Exteriores, southern Pyrenees, Spain. J. Struct. Geol. 70, 23–38.
Bergman, S.C., Huntington, K.W., Crider, J.G., 2013. Tracing paleofluid sources using clumped isotope thermometry of diagenetic cements along the Moab Fault, Utah. Am. J. Sci. 313, 490–515.
Bernasconi, S.M., Hu, B., Wacker, U., Fiebig, J., Breitenbach, S.F.M., Rutz, T., 2013. Background effects on Faraday collectors in gas-source mass spectrometry and implications for clumped isotope measurements. Rapid Commun. Mass Spectrom. 27, 603–612.
Bickle, M.J., Wickham, S.M., Chapman, H.J., Taylor, H.P., 1988. A strontium, neodynium and oxygen study of hydrothermal metamorphism and crustal anatexis in the Trois Seignerus Massif, Pyrenees, France. Contrib. Mineral. Petrol. 100, 399–417.
Bitzer, K., Travé, A., Carmona, J.M., 2001. Fluid flow processes at basin scale. Acta Geologica Hispanica 36, 1–20.
Blenkinsop, T.G., 2008. Relationships between faults, extension fractures and veins, and stress. J. Struct. Geol. 30, 622–632.
Bons, P.D., Elburg, M.A., Gómez-Rivas, E., 2012. A review of the formation of tectonic veins and their microstructures. J. Struct. Geol. 43, 33–62.
Bons, P.D., Fusswinkel, T., Gómez-Rivas, E., Markl, G., Wagner, T., Walter, B., 2014. Fluid mixig from below in unconformity-related hydrothermal ore deposits. Geology 42, 1035–1038.
Burbank, D.W., Puigdefàbregas, C., Muñoz, J.A., 1992a. The chronology of the Eocene tectonic and stratigraphic development of the Eastern Pyrenean Foreland Basin. NE Spain. Geol. Soc. Am. Bull. 104, 1101–1120.
Burbank, D.W., Vergés, J., Muñoz, J.A., Bentham, P., 1992b. Coeval hinward- and forward-imbricating thrusting in the south-central Pyrenees: spain: timing and rates of shortening and deposition. Geol. Soc. Am. Bull. 104, 3–17.
Caja, M.A., Permanyer, A., Marfil, R., Al-Asm, I.S., Martín-Crespo, T., 2006. Fluid flow record from fracture-fill calcite in the Eocene limestones from the South-Pyrenean Basin (NE Spain) and its relationship to oil shows. J. Geochem. Explor. 89, 27–32.
Carrillo, E., Rosell, L., Ortí, F., 2014. Multiepisodic evaporite sedimentation as an indicator of palaeogeographical evolution in foreland basins (South-eastern Pyrenean basin, early–middle Eocene. Sedimentology 61, 2086–2112.
Carrillo, E., 2012. The Evaporites of the Southeastern Pyrenean Basin (Late Cuisian –Lutetian): Sedimentology and Structure. Phd Thesis. University of Barcelona, Barcelona, Spain, pp. 192.
Casini, G., Gillespie, P.A., Vergés, J., Romaire, I., Fernández, N., Casciello, E., Saura, E., Mehl, C., Homke, S., Embry, J.-C., Aghajari, L., Hunt, D.W., 2011. Sub-seismic fractures in foreland fold and thrust belts: insight from the lurestan province, zagros mountains, Iran. Pet. Geosci. 17, 263–282.
Chandonais, D.R., Onasch, C.M., 2014. Fluid history of the blue ridge anticlinorium in the central Appalachians. J. Struct. Geol. 69, 415–427.
Choukroune, P., Team, E., 1989. The ECORS Pyrenean deep seismic profile reflection data and the overall structure of an orogenic belt. Tectonics 8, 23–39.
Chuhan, F., Kjeldstad, A., BjØrlykke, K., HØeg, K., 2002. Porosity loss in sand by grain crushing—experimental evidence and relevance to reservoir quality. Mar. Petrol. Geol. 19, 39–53.
Clavell, E., 1992. Geologia Del Petroli De Les Conques Terciàries De Catalunya. Phd thesis. University of Barcelona, pp. 488.
Claypool, G.E., Kaplan, W.T., Kaplan, I.R., Sakai, H., Zak, I., 1980. The age curves of sulfur and oxygen isotopes in marine sulfate and their mutual interpretations. Chem. Geol. 28, 199–260.
Conrad, R.E., Friedman, M., 1976. Microscopic feather fractures in the faulting process. Tectonophysics 33, 187–198.
Conti, S., Fontana, D., Mecozzi, S., Panieri, G., Pini, G.A., 2010. Late Miocene seep-carbonates and fluid migration on top of the Montepetra intrabasinal high (Northern Apennines, Italy): relations with synsedimentary folding. Sediment. Geol. 231, 41–54.
Coplen, T.B., Hanshaw, B.B., 1973. Ultratitration by a compacted clay membrane-I: oxygen and hydrogen isotopic fractionation. Geochimia et Cosmochimica Acta 37, 2295–2310.
Costa, E., Garcés, M., López-Blanco, M., Beamud, E., Gómez-Paccard, M., Larrasoaña, J.C., 2010. Closing and continentalization of the South Pyrenean foreland basin (NE Spain): magnetochronological constraints. Basin Res. 22, 904–917.
Craig, H., Gordon, I.I., 1965. Deuterium and oxygen-18 variations in the ocean and the marine atmosphere. In: Tongiorgi, E. (Ed.), Proceedings of a Conference on Stable Isotopes in Oceanographic Studies and Paleotemperatures. Consiglio Nazionale delle Richerche, Laboratorio di Geologia Nucleare, Pisa, Italy, pp. 9–130.
Dale, A., John, C.M., Mozley, P.S., Smalley, P.C., Muggeridge, A.H., 2014. Time-capsule concretions: unlocking burial diagenetic processes in the Mancos Shale using carbonate clumped isotopes. Earth Planet. Sci. Lett. 394, 30–37.
David, C., Menendez, B., Bernabe, Y., 1998. The mechanical behavior of synthetic sandstone with varying brittle cement content. Int. J. Rock Mech. Min. Sci. Geomech. Abstr. 35, 759–770.
Dennis, K.J., Affeck, H.P., Passey, B.H., Schrag, D.P., Eiler, J.M., 2011. Defining an absolute reference frame for 'clumped' isotope studies of CO2. Geochimia et Cosmochimica Acta 75, 7117–7131.
Dewaele, D., Muchez, P., Banks, D.A., 2004. Fluid evolution along multistage composite fault systems at the southern margin of the lower Palaeozoic Anglo-Brabant fold belt, Belgium. Geofluids 4, 341–356.
Dewever, B., Swennen, R., Breesch, L., 2013. Fluid flow compartmentalization in the Sicilian fold and thrust belt: implications for the regional aqueous fluid flow and oil migration history. Tectonophysics 591, 194–209.
Diamond, L.W., 1994. Salinity of multivolatile fluid inclusions determined from clathrate hydrate stability. Geochimia et Cosmochimica Acta 58, 19–41.
Eiler, J.M., 2007. Clumped-isotope geochemistry—the study of naturally-occurring, multiply-substituted isotopologues. Earth Planet. Sci. Lett. 262, 309–327.
Evans, M.A., Fischer, M.P., 2012. On the distribution of fluids in folds: a review of controlling factors and processes. J. Struct. Geol. 44, 2–24.
Evans, M.A., Bebeout, G.E., Brown, C.H., 2012. Changing fluid conditions during folding: an example from the central Appalachians. Tectonophysics 576–577, 99–115.
Fein, J.B., Walther, J.V., 1987. Calcite solubility in supercritical CO2-H2O fluids. Geochimia et Cosmochimica Acta 51, 1665–1673.
Ferket, H., Swennen, R., Arzate, S.O., Roure, F., 2006. Fluid flow evolution in petroleum reservoirs with a complex diagenetic history: an example from Veracruz, Mexico. J. Geochem. Explor. 89, 108–111.
Fischer, M.P., Higuera-Díaz, I.C., Evans, M.A., Perry, E.C., Lefticariu, L., 2009. Fracture-controlled paleohydrology in a map-scale detachment fold: insights from the analysis of fluid inclusions in calcite and quartz veins. J. Struct. Geol. 31, 1490–1510.
Ford, M., Williams, E.A., Artoni, A., Vergés, J., Hardy, S., 1997. Progressive evolution of a fault-related fold pair from growth strata geometries, Sant Llorenç de Morunys, SE Pyrenees. J. Struct. Geol. 19, 413–441.
Friedman, M., Logan, J.M., 1977. Microscopic feather fractures. Bull. Soc. Am. 81, 3417–3420.
Friedman, I., O'Neil, J.R., 1977. Compilation of stable isotope fractionation factors of geochemical interest. In: Fleischer, M. (Ed.), Data of Geochemistry. U.S. Gov. Print. Off., Washington D. C, pp. 1–12.
García-Castellanos, D., Vergés, J., Gaspar-Escribano, J., Cloetingh, S., 2003. Interplay between tectonics, climate, and fluvial transport during the Cenozoic evolution of the Ebro Basin (NE Iberia). J. Geophys. Res. 108 (B7), 2347.
Ghosh, P., Adkins, J., Affek, H., Balta, B., Guo, W., Schauble, E.A., Schrag, D., Eiler, J.M., 2006. 13C—18O bonds in carbonate minerals: a new kind of paleothermometer. Geochimia et Cosmochimica Acta 70, 1439–1456.
Goldstein, R.H., Reynolds, T.J., 1994. Sysematics of fluid inclusions in diagenetic minerals. SEPM Short Course Notes.
Grant, N.T., Banks, D.A., McCaig, A.M., Yardley, B.W.D., 1990. Chemistry, source, and behavior of fluids involved in Alpine thrusting of the central Pyrenees. J. Geophys. Res. 95, 9123–9131.
Guo, W., Mosenfelder, J.L., Goddard, W.A., Eiler, J.M., 2009. Isotopic fractionations associated with phosphoric acid digestion of carbonate minerals: insights from first-principles theoretical modeling and clumped isotope measurements. Geochimia et Cosmochimica Acta 73, 7203–7225.
Hanshaw, B.B., Coplen, T.B., 1973. Ultrafiltration by a compacted clay membrane II—sodium ion exclusion at various ionic strengths. Geochimia et Cosmochimica Acta 37, 2311–2327.
Henderson, I.H.C., McCaig, A.M., 1996. Fluid pressure and salinity variations in shear zone-related veins central Pyrenees, France: implications for the fault-valve model. Tectonophysics 262, 321–348.
Heydari, E., 1997. Hydrotectonic models of burial diagenesis in platform carbonates based on formation water geochemistry in North American sedimentary basins. In: Montañez, I.P., Gregg, J.M., Shelton, K.L. (Eds.), Basin-wide Diagenetic Patterns: Integrated Petrologic, Geochemical, and Hydrologic Considerations. Society of Economic Paleontologists and Mineralogists, Special Publication 57, pp. 53–79.
Huntington, K.W., Eiler, J.M., Affeck, H.P., Guo, W., Bonifacie, M., Yeung, L.Y., Thiagarajan, N., Passey, B., Tripati, A., Daëron, M., Came, R., 2009. Methods and limitations of 'clumped' CO_2 isotope ($\Delta 47$) analysis by gas-source isotope ratio mass spectrometry. J. Mass Spectrom. 44, 1318–1329.
Kim, S.T., O'Neil, J.R., 1997. Equilibrium and nonequilibrium oxygen isotope effects in synthetic carbonates. Geochimia et Cosmochimica Acta 61, 3461.
Kluge, T., John, C.M., Jourdan, A.L., Davis, S., Crawshaw, J., 2015. Laboratory calibration of the calcium carbonate clumped isotope thermometer in the 25–250 °C temperature range. Geochimia et Cosmochimica Acta 157, 213–227.
Knipe, R.J., McCaig, A.M., 1994. Microstructural and microchemical consequences of fluid flow in deforming rocks. In: Parnell, J. (Ed.), Geofluids: Origin, Migration and Evolution of Fluids in Sedimentary Basins. Geological Society London, Special Publications, pp. 99–112.
Labaume, P., Berty, C., Laurent, P., 1991. Syn-digenetic evolution of shear structures in superficial nappes: an example from the Northern Apennines (NW Italy). J. Struct. Geol. 13, 385–398.
Lacombe, O., Swennen, R., Caracausi, A., 2014. Fluid–rock–tectonics interactions in basins and orogens. Mar. Petrol. Geol. 55, 332.
Lacroix, B., Buatier, M., Labaume, P., Travé, A., Dubois, M., Charpentier, D., Ventalon, S., Convert-Gaubier, D., 2011. Microtectonic and geochemical characterization of thrusting in a foreland basin: example of the South-Pyrenean orogenic wedge (Spain). J. Struct. Geol. 33, 1359–1377.
Laubach, S.E., Olson, J.E., Gross, M.R., 2009. Mechanical and fracture stratigraphy. AAPG Bull. 93, 1413–1426.

Lefticariu, L., Perry, E.C., Fischer, M.P., Banner, J.L., 2005. Evolution of fluid compartmentalization in a detachment fold complex. Geology 33, 69–72.
Lewis, C.J., Vergés, J., Marzo, M., Heller, P.L., 1996. Youthful topography indicating active surface uplift in NE Iberia: mantle upwelling along a leakly transform fault? Ann. Geophys. 14 (Suplement I), C-204.
Losh, S., 1989. Fluid-rock interaction in an evolving ductile shear zone and across the brittle-ductile transition, central Pyrenees, France. Am. J. Sci. 289, 601–648.
Lyubetskaya, T., Ague, J.J., 2009. Modeling the magnitudes and directions of regional metamorphic fluid flow in collisional orogens. J. Petrol. 50, 1505–1531.
Machel, H.G., Cavell, P.A., 1999. Low-flux, tectonically-induced sequeegee fluid flow (hot flash) into the Rocky Mountain Foreland Basin. Bull. Can. Petrol. Geol. 47, 510–533.
Marshall, J.D., 1992. Climatic and oceanographic isotopic signals from the carbonate rock record and their preservation. Geol. Mag. 129, 143–160.
McCaig, A.M., Wayne, D.M., Marshall, J.D., Banks, D., Henderson, I., 1995. Isotopic and fluid inclusion studies of fluid movement along the Gavarnie thrust, central Pyrenees: reaction fronts in carbonate mylonites. Am. J. Sci. 295, 309–343.
McCaig, A.M., Tritlla, J., Banks, D.A., 2000a. Fluid flow patterns during Pyrenean thrusting. J. Geochem. Explor. 69–70, 539–543.
McCaig, A.M., Tritlla, J., Banks, D.A., 2000b. Fluid mixing and recycling during Pyrenean thrusting: evidence from fluid inclusion halogen ratios. Geochimia et Cosmochimica Acta 64, 3395–3412.
McCaig, A.M., 1988. Deep fluid circulation in fault zones. Geology 16, 867–870.
McCrea, J.M., 1950. On the isotopic chemistry of carbonates and a paleotemperature scale. J. Chem. Phys. 18, 849–957.
Meckler, A.N., Ziegler, M., Millán, M.I., Breitenbach, S.F., Bernasconi, S.M., 2014. Long-term performance of the Kiel carbonate device with a new correction scheme for clumped isotope measurements. Rapid Commun. Mass Spectrom. 28, 1705–1715.
Meyers, W.J., Lohmann, K.C., 1985. Isotope geochemistry of regionally extensive calcite cement zones and marine components in Mississipian limestones, New Mexico. In: Harris, O.M., Schneidermann, N. (Eds.), Carbonate Cements SEPM. Special Publications, pp. 223–239.
Morley, C.K., Warren, J., Tingay, M., Boonyasaknanon, P., Julapour, A., 2014. Comparison of modern fluid distribution, pressure and flow in sediments associated with anticlines growing in deepwater (Brunei) and continental environments (Iran). Mar. Petrol. Geol. 51, 210–229.
Muñoz, J.A., 1992. Evolution of a continental collision belt: ECORS–Pyrenees crustal balanced section. In: McClay, K.R. (Ed.), Thrust Tectonics. Chapman & Hall, London, pp. 235–246.
Muñoz, J.A., 2002. The pyrenees. In: Gibbons, W., Moreno, T. (Eds.), The Geology of Spain. Geological Society, London, pp. 370–385.
Oberhänsli, H., Allen, P.A., 1987. Stable isotopic signatures of tertiary lake carbonates eastern Ebro Basin, Spain. Palaeogeogr. Palaeoclimatol. Palaeoecol. 60, 59–75.
Ogata, K., Senger, K., Braathen, A., Tveranger, J., 2014. Fracture corridors as seal-bypass systems in siliciclastic reservoir-cap rock successions: field-based insights from the Jurassic Entrada Formation (SE Utah, USA). J. Struct. Geol. 66, 162–187.
Oliver, J., 1986. Fluids expelled tectonically from orogenic belts: their role in hydrocarbon migration and other geologic phenomena. Geology 14, 99–102.
Passchier, C.W., Trouw, R.A.J., 2005. Microtectonics, 2 ed. Springer, Berlin, Heidelberg.
Puigdefàbregas, C., Muñoz, J.A., Marzo, M., 1986. Thrust belt development in the eastern pyrenees and related depositional sequences the southern foreland basin. In: Allen, P.A., Homewood, P. (Eds.), Foreland Basins. Blackwell Publishing Ltd., Oxford, UK, pp. 229–246.
Puigdefàbregas, C., Muñoz, J.A., Vergés, J., 1992. Thrusting and foreland basin evolution in the southern pyrenees. In: McClay, K.R. (Ed.), Thrust Tectonics. London, Chapman & Hall, pp. 247–254.
Qing, H., Mountjoy, E., 1992. Large-scale fluid flow in the middle devonian presqu'ile barrier, western Canada sedimentary basin. Geology 20, 903–906.
Ramsay, J.G., 1980. The crack-seal mechanism of rock deformation. Nature 284, 135–139.
Reif, D., Decker, K., Grasemann, B., Peresson, H., 2012. Fracture patterns in the Zagros fold-and-thrust belt: kurdistan region of Iraq. Tectonophysics 576–577, 46–62.
Riba, O., 1973. Las discordancias sintectónicas del Alto Cardener (prepirineo catalán): ensayo de interpretación evolutiva. Acta Geologica Hispanica 8, 90–99.
Riba, O., 1976. Syntectonic unconformities of the alto cardener, spanish pyrenees: a genetic interpretation. Sediment. Geol. 15, 213–233.
Rosenbaum, G., Lister, G.S., Duboz, C., 2002. Relative motions of africa, iberia and europe during alpine orogeny. Tectonophysics 359, 117–129.
Roure, F., Choukroune, P., Berastegui, J., Muñoz, J.A., Villien, A., Matheron, P., Bareyt, M., Seguret, M., Camara, P., Deramond, J., 1989. Ecors deep seismic data and balanced cross sections: geometric constraints on the evolution of the Pyrenees. Tectonics 8, 41–50.
Roure, F., Swennen, R., Schneider, F., Faure, J.L., Ferket, H., Guilhaumou, N., Osadetz, K., Robion, P., Vandeginste, V., 2005. Incidence and importance of tectonics and natural fluid migration on reservoir evolution in foreland fold-and-Thrust belts. Oil Gas Sci. Technol. 60, 67–106.
Sáez, A., Anadón, P., Herrero, M.J., Moscariello, A., 2007. Variable style of transition between Paleogene fluvial fan and lacustrine systems, southern Pyrenean foreland, NE Spain. Sedimentology 54, 367–390.
Séguret, M., 1972. Étude tectonique des nappes et séries décollées de la partie centrale du vesant sud des Pyrénées. Pub. USTELA, sér, Geol. Struct. n.2, Montpellier.
Sans, M., Vergés, J., 1995. Fold development related to contractional salt tectonics: southeastern pyrenean thrust front, Spain. In: Jackson, M.P.A., Roberts, D.G., Snelson, S. (Eds.), Salt Tectonics: a Global Perspective. AAPG Memoir, pp. 369–378.
Sans, M., Muñoz, J.A., Vergés, J., 1996. Triangle zone and thrust wedge geometries related to evaporitic horizons (Southern Pyrenees). Can. Pet. Geol. Bull. 4, 375–384.
Sans, M., 2003. From thrust tectonics to diapirism: the role of evaporites in the kinematic evolution of the eastern South Pyrenean front. Geologica Acta 1, 239–259.
Sanz, P., Pollard, D.D., Allwardt, P.F., Borja, R.I., 2008. Mechanical models of fracture reactivation and slip on bedding surfaces during folding of the asymmetric anticline at Sheep Mountain, Wyoming. J. Struct. Geol. 30, 1177–1191.
Segnit, E.R., Holland, H.D., Biscardi, C.J., 1962. The solubility of calcite in aqueous solutions-I. The solubility of calcite in water between 75 and 200° at CO_2 pressures up to 60 atm. Geochimia et Cosmochimica Acta 26, 1301–1331.
Serra-Kiel, J., Mató, E., Saula, E., Travé, A., Ferràndez-Cañadell, C., Àlvarez-Pérez, G., Franquès, J., Romero, J., 2003a. An inventory of the marine and transitional Middle/Upper eocene deposits of the southeastern pyrenean foreland basin (NE Spain). Geologica Acta 1, 201–229.
Serra-Kiel, J., Travé, A., Mató, E., Saula, E., Ferràndez-Cañadell, C., Busquets, P., Tosquella, J., Vergés, J., 2003b. Marine and transitional Middle/Upper eocene units of the southeastern pyrenean foreland basin (NE Spain). Geologica Acta 1, 177–200.
Shackleton, J.R., Cooke, M.L., Sussman, A.J., 2005. Evidence for temporally changing mechanical stratigraphy and effects on joint-network architecture. Geology 33, 101–104.
Sibson, R.H., 1981. Fluid flow accompanying faulting: field evidence and models. In: Simpson, D.W., Richards, P.G. (Eds.), Earthquake Prediction. American Geophysical Union, pp. 593–603.
Sibson, R.H., 2005. Hinge-parallel fluid flow in fold-thrust belts: how widespread? Proc. Geolo. Assoc. 116, 301–309.
Srivastava, D.C., Engelder, T., 1990. Crack-propagation sequence and pore-fluid conditions during fault-bend folding in the Appalachian valley and ridge, central Pennsylvania. Geol. Soc. Am. Bull. 102, 116–128.
Stephenson, B.J., Koopman, A., Hillgartner, H., McQuillan, H., Bourne, S., Noad, J., Rawnsley, K., 2007. Structural and stratigraphic controls on fold-related fracturing in the Zagros Mountains, Iran: implications for reservoir development. In: Lonergan, L., Jolly, R.J.H., Rawnsley, K., Sanderson, D.J. (Eds.), Fractured Reservoirs. Geological Society London, Special Publications, pp. 1–21.
Suppe, J., Sábat, F., Muñoz, J.A., Poblet, J., Roca, E., Vergés, J., 1997. Bed-by-bed fold growth by kink-band migration: sant Llorenç de Morunys, eastern Pyrenees. J. Struct. Geol. 19, 443–461.
Swanson, E.M., Wernicke, B.P., Eiler, J.M., Losh, S., 2012. Temperatures and fluids on faults based on carbonate clumped-isotope thermometry. Am. J. Sci. 312, 1–21.
Tavani, S., Storti, F., Lacombe, O., Corradetti, A., Muñoz, J.A., Mazzoli, S., 2015. A review of deformation pattern templates in foreland basin systems and fold-and-thrust-belts: implications for the state of stress in the frontal regions of thrust wedges. Earth Sci. Rev. 141, 82–104.
Taylor, B.E., 1987. Stable isotope geochemistry of ore-forming fluids. In: Kyser, T.K. (Ed.), Short Course in Stable Isotope Geochemistry of Low Temperature Fluids. Mineral Association of Canada, pp. 337–418.
Tempest, S.A., 1991. Fluid-rock Interaction in Ductile Shear Zones, Central-eastern Pyrenees. Phd thesis. Leeds University, pp. 202.
Travé, A., Calvet, F., 2001. Syn-rift geofluids in fractures related to the early-middle Miocene evolution of the Vallès-Penedès half-graben (NE Spain). Tectonophysics 336, 101–120.
Travé, A., Labaume, P., Calvet, F., Soler, A., 1997. Sediment dewatering and pore fluid migration along thrust faults in a foreland basin inferred from isotopic and elemental geochemical analyses (Eocene southern Pyrenees, Spain). Tectonophysics 282, 375–398.
Travé, A., Labaume, P., Calvet, F., Soler, A., Tritlla, J., Bautier, M., Potdevin, J.L., Séguret, M., Raynaud, S., Briqueu, L., 1998a. Fluid migration during Eocene thrust emplacement in the south Pyrenean foreland basin (Spain): an integrated structural, mineralogical and geochemical approach. In: Mascle, A., Puigdefàbregas, C., LuterBacher, H.P., Fernàndez, M. (Eds.), Cenozoic Foreland Basins of Western Europe. Geological Society, Special Publications, pp. 163–188.
Travé, A., Calvet, F., Soler, A., Labaume, P., 1998b. Fracturing and fluid migration during Paleogene compression and Neogene extension in the Catalan Coastal Ranges, Spain. Sedimentology 45, 1063–1082.
Travé, A., Calvet, F., Sans, M., Vergés, J., Thirlwall, M., 2000. Fluid history related to the Alpine compression at the margin of the south-Pyrenean Foreland basin: the El Guix anticline. Tectonophysics 321, 73–102.
Travé, A., Calvet, F., Salas, R., Playà, E., 2004. Fluid flow during paleogene compression in the linking zone fold and thrust belt (Northeast Spain). In: Swennen, R., Roure, F., Granath, J.W. (Eds.), Deformation, Fluid Flow, and Reservoir Araisal in Foreland Fold and Thrust Belts. AAPG Hedberg Series, pp. 215–243.
Travé, A., Labaume, P., Vergés, J., 2007. Fluid systems in Foreland Fold and thrust belts: an overview from the Southern Pyrenees. In: Lacombe, O., Lavé, J., Roure, F., Vergés, J. (Eds.), Thrust Belts and Foreland Basins: From Fold Kinematics to Hydrocarbon Systems. Springer, pp. 93–115.

Treagus, S.H., 1988. Strain refraction in layered systems. J. Struct. Geol. 19, 551–566.
Vajdova, V., Zhu, W., Chen, T.Z.N., Wong, T.F., 2010. Micromechanics of brittle faulting and cataclastic flow in Tavel limestone. J. Struct. Geol. 32, 1158–1169.
Valero, L., Garcés, M., Cabrera, L., Costa, E., Sáez, A., 2014. 20 Myr of eccentricity paced lacustrine cycles in the Cenozoic Ebro Basin. Earth Planet. Sci. Lett. 408, 183–193.
Van Geet, M., Swennen, R., Durmishi, C., Roure, F., Muchez, P., 2002. Paragenesis of Cretaceous to Eocene carbonate reservoirs in the Ionian fold and thrust belt (Albania): relation between tectonism and fluid flow. Sedimentology 49, 697–718.
Vandeginste, V., Swennen, R., Allaeys, M., Ellam, R.M., Osadetz, K., Roure, F., 2012. Challenges of structural diagenesis in foreland fold-and-thrust belts: a case study on paleofluid flow in the Canadian Rocky Mountains West of Calgary. Mar. Pet. Geol. 35, 235–251.
Vergés, J., Martínez, A., Muñoz, J.A., 1992. South Pyrenean fold and thrust belt: the role of foreland evaporitic levels in thrust geometry. In: McClay, K. (Ed.), Thrust Tectonics. London, Chapman & Hall, pp. 255–264.
Vergés, J., Marzo, M., Santaeulària, T., Serra-Kiel, J., Burbank, D.W., Muñoz, J.A., Giménez-Montsant, J., 1998. Quantified vertical motions and tectonic evolution of the SE Pyrenean foreland basin. In: Mascle, A., Puigdefàbregas, C., Luterbacher, H.P., Fernàndez, M. (Eds.), Cenozoic Foreland Basins of Western Europe. Geological Society Special Publications, pp. 107–134.
Vergés, J., Marzo, M., Muñoz, J.A., 2002a. Growth strata in foreland settings. Sediment. Geol. 146, 1–9.
Vergés, J., Fernàndez, M., Martínez, A., 2002b. The Pyrenean orogen: pre-, syn-, and post-collisional evolution. In: Rosenbaum, G., Lister, G. (Eds.), Reconstruction of the evolution of the Alpine-Himalayan Orogen, Journal of the Virtual Explorer, pp. 55-74.
Vergés, J., 1993. Estudi Geològic Del Vessant Sud Del Pirineu Oriental I Central. Evolució Cinemàtica En 3D. Universitat de Barcelona, Barcelona, Spain203 (PhD Thesis).
Vilasi, N., Malandain, J., Barrier, L., Callot, J.P., Amrouch, K., Guilhaumou, N., Lacombe, O., Muska, K., Roure, F., Swennen, R., 2009. From outcrop and petrographic studies to basin-scale fluid flow modelling: the use of the Albanian natural laboratory for carbonate reservoir characterisation. Tectonophysics 474, 367–392.
Wacker, U., Fiebig, J., Schoene, B.R., 2013. Clumped isotope analysis of carbonates: comparison of two different acid digestion techniques. Rapid Commun. Mass Spectrom. 27, 1631–1642.
Watkins, H., Butler, R.W.H., Bond, C.E., Healy, D., 2015. Influence of structural position on fracture networks in the Torridon Group, Achnashellach fold and thrust belt, NW Scotland. J. Struct. Geol. 74, 64–80.
Wickham, S.M., Taylor, H.P., 1985. Stable isotopic evidence for large-scale seawater infiltration in a regional metamorphic terrane; the Trois Seigneurs Massif Pyrenees, France. Contrib. Mineral. Petrol. 91, 122–137.
Wickham, S.M., Taylor, H.P., 1987. Stable isotope constraints on the origin and depth of penetration of hydrothermal fluids associated with Hercynian regional metamorphism and crustal anatexis in the Pyrenees. Contrib. Mineral. Petrol. 95, 255–268.
Williams, E.A., Ford, M., Vergés, J., Artoni, A., 1998. Alluvial gravel sedimentation in a contractional growth fold setting, Sant Llorenç de Morunys, southeastern Pyrenees. In: Mascle, A., Puigdefàbregas, C., Luterbacher, H.P., Fernàndez, M. (Eds.), Cenozoic Foreland Basins of Western Europe. Geological Society Special Publications, pp. 69–106.

Chapter 5

Changes in fluid regime in syn-orogenic sediments during the growth of the south Pyrenean fold and thrust belt

Global and Planetary Change 171 (2018) 207–224

Contents lists available at ScienceDirect

Global and Planetary Change

journal homepage: www.elsevier.com/locate/gloplacha

Changes in fluid regime in syn-orogenic sediments during the growth of the south Pyrenean fold and thrust belt

David Cruset[a,*], Irene Cantarero[a], Jaume Vergés[b], Cédric M. John[c], Daniel Muñoz-López[a], Anna Travé[a]

[a] Departament de Mineralogia, Petrologia i Geologia Aplicada, Facultat de Ciències de la Terra, Universitat de Barcelona (UB), Martí i Franquès s/n, 08028 Barcelona, Spain.
[b] Institut de Ciències de la Terra Jaume Almera, ICTJA-CSIC, Lluís Solé i Sabaris s/n, 08028 Barcelona, Spain
[c] Department of Earth Science and Engineering, Imperial College London, SW7 2BP, UK

ARTICLE INFO

Keywords:
Fluid regime
Syn-orogenic sediments
Fractures
South Pyrenean fold and thrust belt

ABSTRACT

The eastern sector of the south Pyrenean fold and thrust belt developed during the Alpine compression and affected Upper Cretaceous to lower Oligocene foreland basin deposits. In this study, we determine the changes in fluid regime and fluid composition during the growth of this fold and thrust belt, integrating petrographic and geochemical data obtained from fracture-filling cements.

Hydrothermal fluids at temperatures up to 154 °C, migrated from the Axial zone to the foreland basin and mixed with connate fluids in equilibrium with Eocene sea-water during lower and middle Eocene (underfilled foreland basin). As the thrust front progressively emerged, low-temperature meteoric waters migrated downwards the foreland basin and mixed at depth with the hydrothermal fluids from middle Eocene to lower Oligocene (overfilled non-marine foreland basin).

The comparison of the fluid flow models from the Southern Pyrenees with other orogens worldwide, seems to indicate that the presence or absence of thick evaporitic units highly control fluid composition during the development of fold and thrust belts. Whereas in thrusts not detached along thick evaporite units, mixed fluids are progressively more depleted in $\delta^{18}O$ and have a lower temperature and lower Fe and Sr contents as the thrust front emerges, in thrust detachments through thick evaporite units, the mixed fluids are enriched in $\delta^{18}O$.

1. Introduction

Geofluids interact with sediments during development of fold and thrust belts. These interactions are responsible of ore deposits precipitation and have an important role during hydrocarbon migration and diagenesis, which affects reservoir quality (Oliver, 1986; Qing and Mountjoy, 1992; Machel and Cavell, 1999; Bitzer et al., 2001; Dewaele et al., 2004; Roure et al., 2005; Evans and Fischer, 2012; Vandeginste et al., 2012; Rodríguez-Morillas et al., 2013).

The geochemical composition of the diagenetic products related to fluid flow (cements) depends on the type of fluid, fluid/rock ratios and host rock composition (Banner, 1995; Swennen et al., 2003; Travé et al., 2007; Swart, 2015). Furthermore, fluids favor propagation of fractures, which act as seals or paths (Reynolds and Lister, 1987; McCaig, 1988; Sibson et al., 1988; Carter et al., 1990; Shackleton et al., 2005). Fluid migration along fractures and rock porosity is induced by tectonics (squeegee-type) and/or topography during the successive stages of fold and thrust belts evolution (Oliver, 1986; Heydari, 1997; Bitzer et al., 2001; Pollyea et al., 2015). Thus, the study of fracture- and porosity-filling cements provide information about changes in fluid regime (e.g. temperature, pressure, burial and fluid composition) and in turn, sheds light on the tectonic history of compressional belts (Banks et al., 1991; Marker and Burkhard, 1992; Bitzer et al., 2001; Roure et al., 2005, 2010).

Studies of the relationships between fluids and deformation in fold and thrust belts worldwide report two general trends regarding fluid flow. The first trend consists of the progressive depletion in $\delta^{18}O$ of the fluids, which has been related to the increase of the temperature of fluids due to the progressive burial of the studied structures (Dewaele et al., 2004; Travé et al., 2004; Breesch et al., 2009; Vilasi et al., 2009; Vilasi, 2010; Evans et al., 2012; Vandeginste et al., 2012; Beaudoin et al., 2014; Fontana et al., 2014). However, other works relate this depletion to the progressive input of low-temperature meteoric waters into the fluid system, which mixed at depth with fluids with a higher

* Corresponding author.
E-mail addresses: d.cruset@ub.edu (D. Cruset), i_cantarero@ub.edu (I. Cantarero), jverges@ictja.csic.es (J. Vergés), cedric.john@imperial.ac.uk (C.M. John), munoz-lopez@ub.edu (D. Muñoz-López), atrave@ub.edu (A. Travé).

https://doi.org/10.1016/j.gloplacha.2017.11.001
Received 18 April 2017; Received in revised form 26 October 2017; Accepted 3 November 2017
Available online 07 November 2017
0921-8181/

temperature and salinity (Immenhauser et al., 2007; Hausegger et al., 2010; Cruset et al., 2016). The second trend consists of the enrichment in $\delta^{18}O$ of fluids along time due to their interaction with clays (Dewever, 2008; Dewever et al., 2013), although in the Larra/Eaux-chaudes thrust (Jaca Basin) and areas affected by salt tectonics, this enrichment is related to the increase of fluid salinity due to the influence of evaporites (Fischer et al., 2013; Crognier et al., 2017).

The South Pyrenean fold and thrust belt constitutes a well-known example in which the relationships between sequential emplacement of thrust sheets of different ages and *syn*-tectonic deposits are well-constrained (Muñoz et al., 1986; Vergés and Muñoz, 1990; Burbank et al., 1992a, 1992b; Vergés, 1993; Vergés et al., 2002a, 2002b; Beamud et al., 2010; Carrigan et al., 2016; Labaume et al., 2016). In addition, works already done on fluid regime evolution in the Southern Pyrenees show the same evolution trends regarding fluid flow than those observed in other fold and thrust belts worldwide (Travé et al., 1997, 1998, 2000, 2007; Caja et al., 2006; Caja and Permanyer, 2008; Lacroix et al., 2011, 2014; Beaudoin et al., 2015; Cruset et al., 2016; Crognier et al., 2017). Consequently, the southern Pyrenees represent an excellent laboratory for the study of the changes in fluid regime during progressive deformation in fold and thrust belts.

In this work we define the changes in fluid regime from the beginning of the emplacement of the South eastern Pyrenean thrust sheets to the end of contraction, using data from the entire pile of superposed thrust sheets (Lower Pedraforca, Vallfogona, L'Escala and Abocador thrusts) within the foreland basin (Vergés, 1993). We determine the origin of fluids from which cements precipitated in fractures and rock porosity, their evolution trends during each stage of deformation and controlling parameters using petrographic and geochemical data (carbon, oxygen and strontium isotopes, clumped isotopes thermometry and elemental composition). The results are integrated with previous studies done in the west central Pyrenees (Ainsa Basin, Travé et al., 1997; Castillo Mayor klippe and Jaca thrust, Lacroix et al., 2014; Larra/Eaux-chaudes thrust, Crognier et al., 2017) and the eastern Ebro Basin (El Guix anticline, Travé et al., 2000, and Puig-reig anticline, Cruset et al., 2016), to constrain the evolution of fluid regime at the scale of the south Pyrenean fold and thrust belt, which finally is compared to other compressional belts.

2. Geological setting

The Pyrenees consist of a doubly verging orogenic belt generated during the continental collision between Iberia and Eurasia plates, from Late Cretaceous to Miocene (Muñoz, 2002; Vergés et al., 2002a) (Fig. 1). This collision resulted from the partial subduction of the Iberian plate beneath the Eurasian plate (Choukroune, and team, E, 1989; Roure et al., 1989; Muñoz, 1992, 2002; Vergés et al., 2002a, 2002b). The previous Mesozoic extensional basins were inverted and an antiformal stack constituted of basement-involved thrust sheets developed in the central part of the chain (Axial zone), acting as a boundary between the North and south Pyrenean fold and thrust belts (Muñoz, 1992) (Fig. 1).

The south Pyrenean fold and thrust belt consists of a sequence of south-verging thrusts emplaced in a piggy-back thrust sequence (Puigdefàbregas et al., 1992) and detached predominantly above Triassic evaporites (Séguret, 1972) and Eocene evaporites deposited in the foreland basin (Vergés et al., 1992: Sans, 2003) (Fig. 2).

The four structures selected for this study are located in the south-eastern Pyrenees (Fig. 1) and are representative of the change from marine to continental conditions during thrust front migration. The oldest structure studied is the Lower Pedraforca thrust sheet (Figs. 2a, 3a), an allochthonous klippe detached in the Keuper facies and emplaced from lower to middle Eocene (Puigdefàbregas et al., 1986; Burbank et al., 1992a). The emplacement of the Lower Pedraforca thrust sheet was under marine conditions, as attested by the syn-orogenic conglomerates of Queralt related to this structure (Vergés, 1993). The second structure is the Vallfogona thrust (Figs. 2a, b, 3a), which is the southern boundary of the Cadí thrust sheet. The activity of this thrust fault started in the middle Eocene under marine conditions and finished during the lower Oligocene under continental conditions (Burbank et al., 1992a, 1992b; Vergés, 1993; Vergés and Burbank, 1996; Haines, 2008). The two youngest structures are the Abocador and L'Escala thrusts (Figs. 2b, 3a), active from middle to upper Eocene and from upper Eocene to lower Oligocene, respectively (Travé et al., 2007; Haines, 2008). These two structures affect the sediments of the Ebro foreland basin, which form the footwall of the Vallfogona thrust, and developed under marine-continental transitional conditions (Travé et al., 2007).

The sediments of the study area range in age between Upper Triassic and Oligocene and consist of pre- and syn-orogenic deposits related to the emplacement of the thrust sequence (Fig. 3b). The Lower Pedraforca thrust sheet is composed of the pre-orogenic Keuper facies, Lias and Dogger limestones and dolostones, Santonian limestones and the syn-orogenic Campanian-Maastrichtian coastal deposits of the Areny Fm., Maastrichtian-Thanetian continental deposits from the Garumnian facies, Ilerdian limestones from the Cadí Fm. and Lutetian-Bartonian conglomerates of the Coubet Fm. (Mey et al., 1968; Vergés, 1993; López-Martínez et al., 1999; Rosell et al., 2001; Oms et al., 2007). The hangingwall of the Vallfogona thrust consists of Cuisian-Lutetian turbiditic deposits of the Vallfogona Fm, which are overlain by the Lutetian evaporites of the Beuda Fm. (Vergés et al., 1998). These turbidites are overthrusting the Lutetian to Bartonian marls of the Banyoles and Igualada Fm. and Priabonian-Rupelian syn-tectonic alluvial sediments of the Berga Fm., indicating that the Vallfogona thrust was active until the lower Oligocene (Burbank et al., 1992b; Haines, 2008; Valero et al., 2014). Further south, two formations are involved in the Abocador and L'Escala thrusts. The hangingwalls of both thrusts are constituted of alluvial and fluvial deposits of the Bellmunt Fm. (upper Lutetian; Moya et al., 1991; Serra-Kiel et al., 2003), whereas the footwalls consist of the Bartonian deltaic deposits of the Puigsacalm Fm. (Mató et al., 1994; Serra-Kiel et al., 2003).

3. Methodology

In order to characterize the evolution of the fluids involved in the emplacement of the Lower Pedraforca, Vallfogona, Abocador and L'Escala thrusts, 107 polished thin sections made from host rocks and fracture-filling cements precipitated during the Alpine compression were studied using petrographic and geochemical methods.

Petrographic observations were made using optical and cathodoluminescence microscopy. A CL Technosyn cathodoluminescence device Model 8200 MkII operating at 23 kV and 350 μA gun current was used to distinguish the different generations of cements.

Fluid inclusions were examined in calcite cements to determine salinity and temperature conditions of the mineral-forming fluid. Thick sections were used for petrographic characterization of the fluid inclusions and for microthermometric analyses. Measurements were made on a Linkam THMS-600 heating-freezing stage. Fluid inclusions, with a size ranging between 2 and 5 μm, were cooled and heated to temperatures around −150 °C and 300 °C, respectively. However, the attempt to obtain ice melting and homogenization temperatures from two-phase fluid inclusions (liquid-gas) failed, since changes in bubble volume were not observed.

Carbon-coated polished thin sections were used to analyze major, minor and trace element concentrations on a JEOL JXA-8230 electron microprobe. The microprobe was operated using 20 kV of excitation potential, current intensity of 6 nA for Ca and Mg and 40 nA for Mn, Fe and Sr with a beam diameter of 10 μm. Detection limits are 236 ppm for Ca, 131 ppm for Na, 397 ppm for Mg, 226 ppm for Mn, 78 ppm for Fe and 291 ppm for Sr. Precision on major element analyses averaged a standard error of 6.15% at 2σ confidence levels.

Fracture-filling calcite and carbonate host rocks were sampled for

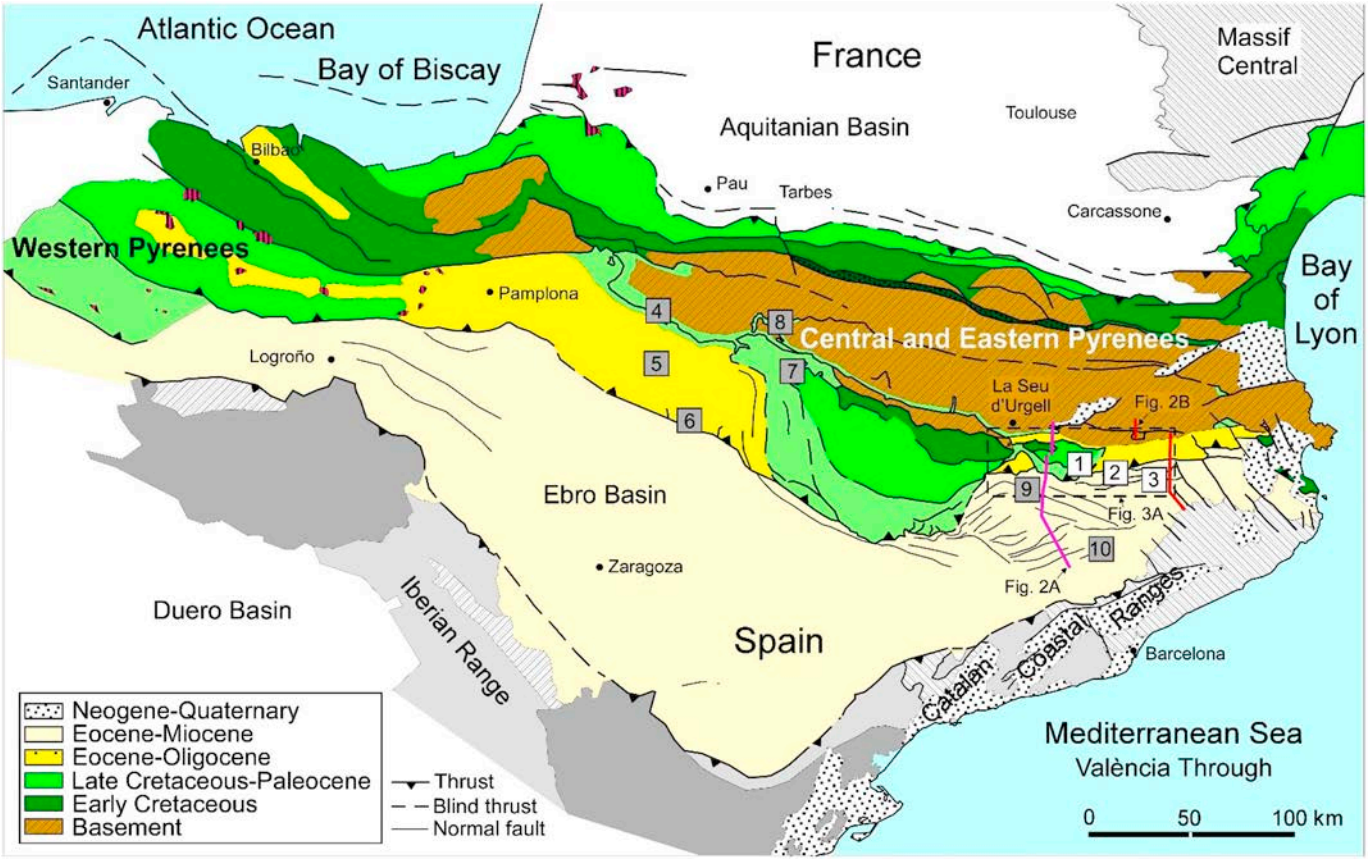

Fig. 1. Structural sketch of the Pyrenees from Vergés (1993). The white squares show the location of the studied structures in this work: 1) Lower Pedraforca thrust sheet; 2) Vallfogona thrust; 3) Abocador and L'Escala thrusts. The grey squares show the location of the structures previously studied by other authors that have been compared with our structures: 4) Larra/Eaux-chaudes thrust (Crognier et al., 2017); 5) Jaca Basin (Lacroix et al., 2014; Crognier et al., 2017); 6) Sierras Exteriores (Beaudoin et al., 2015; Crognier, 2016); 7) Ainsa Basin (Travé et al., 1997); 8) Gavarnie thrust (McCaig et al., 1995); 9) Puig-reig anticline (Cruset et al., 2016); 10) El Guix anticline (Travé et al., 2000). The purple and red lines indicate the location of cross-sections shown in Fig. 2a and b, respectively. (For interpretation of the references to color in this figure legend, the reader is referred to the web version of this article.)

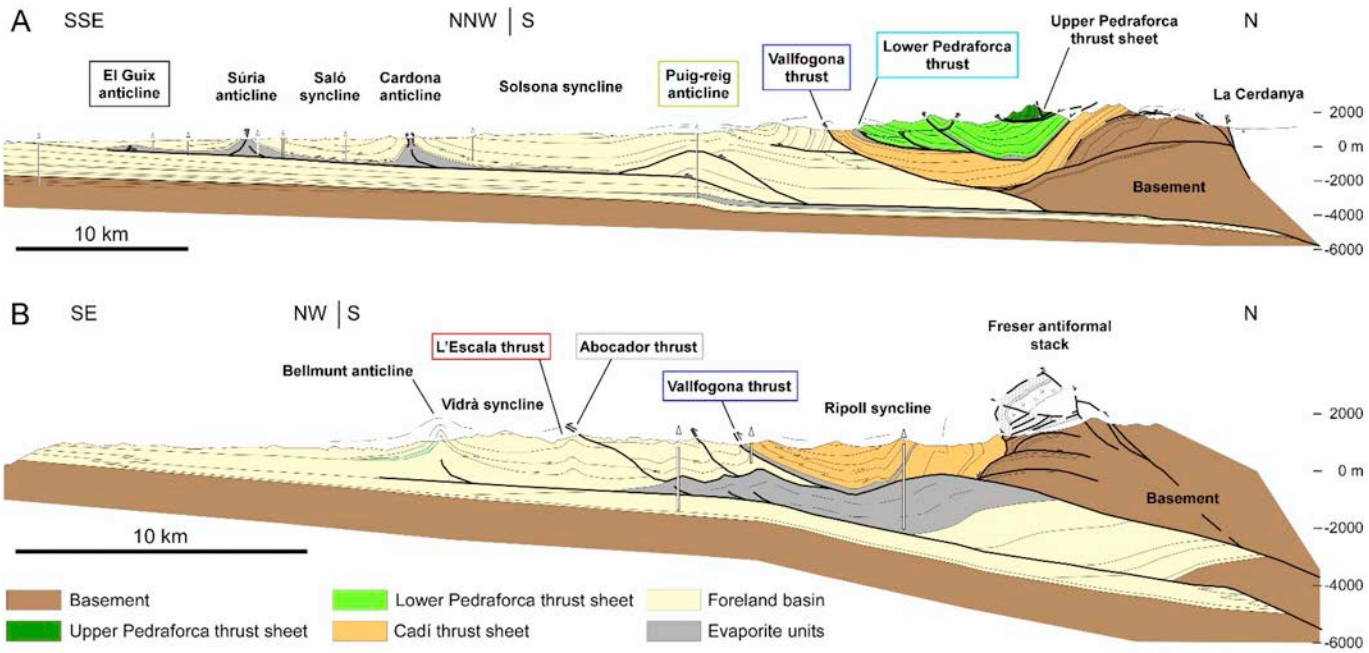

Fig. 2. Cross sections of the studied areas (Vergés, 1993). The color boxes indicate the structural position of the studied outcrops in SE Pyrenees also shown in Fig. 1. Each color is equivalent to the color of lines and boxes in Figs. 3, 4, 5, 6, 7, 8, 9 and 10. (For interpretation of the references to color in this figure legend, the reader is referred to the web version of this article.)

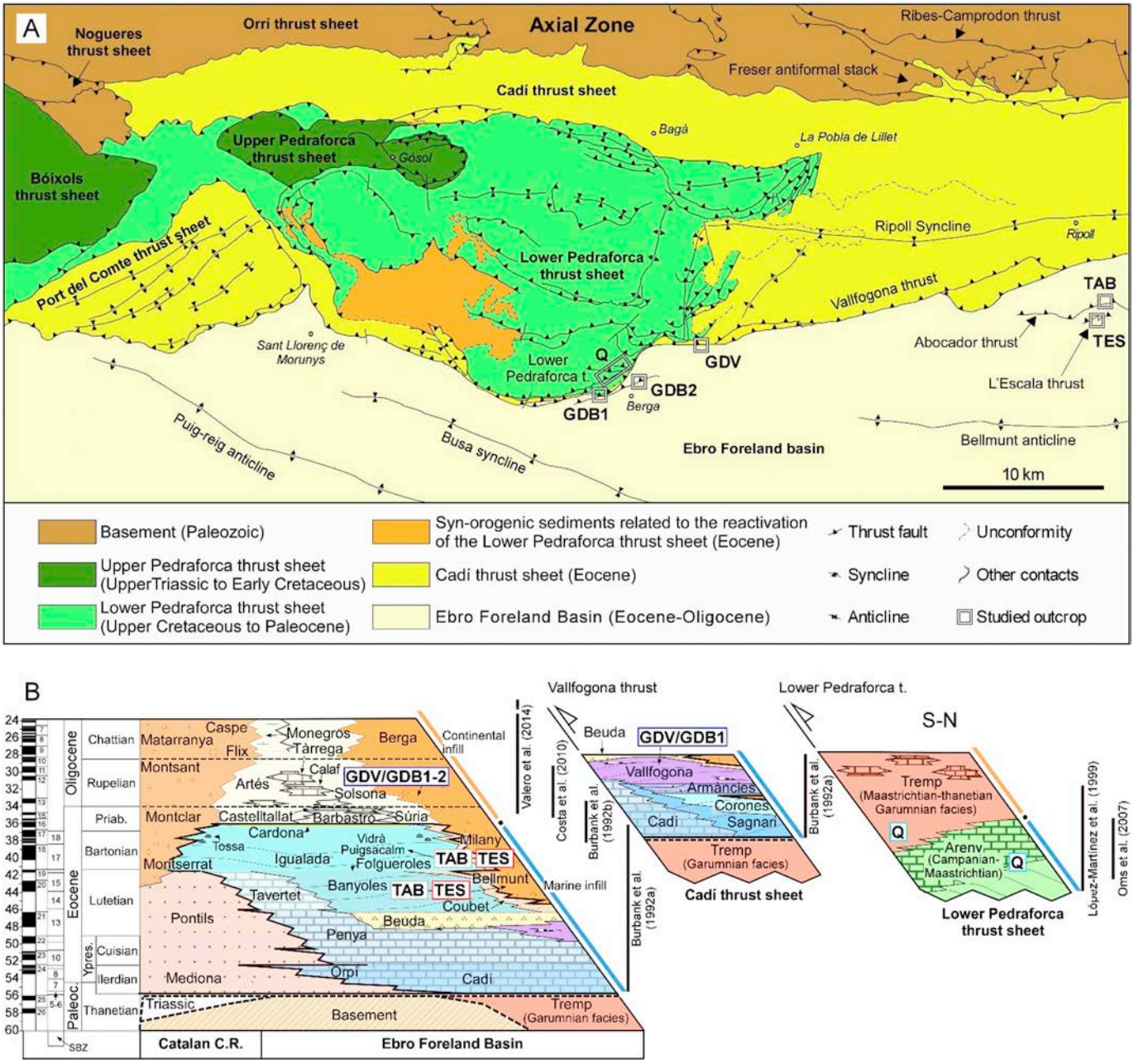

Fig. 3. A) Structural sketch of the studied area with outcrop locations. Q samples are referred to the Lower Pedraforca thrust sheet, GDV and GDB to the Vallfogona thrust and TAB and TES to the Abocador and L'Escala thrusts, respectively. B) N–S stratigraphic panel of the Lower Pedraforca thrust sheet, Cadí thrust sheet and eastern Ebro Foreland Basin modified from Vergés et al. (1998). The age of sedimentary units has been defined according to Burbank et al. (1992a, 1992b), López-Martínez et al. (1999), Oms et al. (2007), Costa et al. (2010) and Valero et al. (2014). Shallow Benthic Zones (SBZ) from Serra-Kiel et al. (1998a, 1998b). The color boxes with references Q, GDV, GDB, TAB and TES indicate the stratigraphic location of the studied outcrops.

carbon- and oxygen-isotope analysis employing a 400 μm-thick dental drill to extract 60 ± 10 μg of powder from trims. The calcite powder was reacted with 100% phosphoric acid for 2 min at 70 °C. The resultant CO_2 was analyzed using an automated Kiel Carbonate Device attached to a Thermal Ionization Mass Spectrometer Thermo Electron (Finnigan) MAT-252 following the method of McCrea (1950). The results were corrected using the standard technique (Craig and Gordon, 1965; Claypool et al., 1980), expressed in ‰ with respect to the VPDB (Vienna Pee Dee Belemnite) standard.

For clumped isotopes thermometry, aliquots (replicates) of three carbonate samples weighing 2–3 mg were measured for three out of five samples (GDV20, GDV30, GDV13, Table 1) using an automated line developed at Imperial College (the IBEX: Imperial Batch EXtraction system). In addition, two single measurements of two additional samples (TAB9, STn(3)(2), Table 1) were measured using a manual vacuum line described in Dale et al. (2014). In both cases, samples are dropped in 105% phosphoric acid maintained at 90 °C, and reacted for 10 min. The reactant CO_2 is separated from contaminants using a poropak-Q column, and transferred into the bellows of a MAT 253 mass spectrometer from Thermo Scientific. Full characterization of a replicate consists of 8 acquisitions in dual inlet mode with 7 cycles per acquisition. All post-acquisition processing were performed using Easotope, a dedicated software for clumped isotope analysis (John and Bowen, 2016). Δ_{47} values are corrected for isotope fractionation during phosphoric acid digestion using a phosphoric acid correction of 0.069‰ at 90 °C for calcite following Guo et al. (2009), the data is corrected for

non-linearity using the heated gas method (Huntington et al., 2009) and projected into the absolute reference frame of Dennis et al. (2011). Carbonate $\delta^{18}O$ values are calculated using the acid fractionation factors of Kim and O'Neil (1997). Most of the samples were measured at least three times, and the results averaged before being converted to temperatures using the calibration of Kluge et al. (2015); in this case, the error reported represents ± 1 standard error of the means. For two samples (TAB9, STn(3)(2), Table 1), only one measurement was performed and the error reported is ± 1 external standard deviation of a measurement.

For $^{87}Sr/^{86}Sr$ analyses, samples of 100% calcite from veins and host rocks were fully dissolved in 0.5 M acetic acid, dried and redissolved in 3 M HNO_3. The solid residue resulting from reprecipitation was centrifuged at 4000 rpm during 10 min before being charged in chromatographic columns. Samples were analyzed on Re single filament with 1 μl of H_3PO_4 1 M and 2 μl of Ta_2O_5 on a TIMS-Phoenix mass spectrometer. The data acquisition method consists of dynamic multicollection during 10 blocks of 16 cycles each one, with a beam intensity in the ^{88}Sr mass of 3 V. Analyses have been corrected for possible interferences of ^{87}Rb.

4. Structural and stratigraphic location of the samples

Seven outcrops were studied and sampled to determine the fluid flow regime in the Lower Pedraforca and Vallfogona thrusts and in the Abocador and L'Escala foreland thrusts (Fig. 3).

In the Lower Pedraforca thrust sheet, two different outcrops were sampled along a 1.5 km long transect composed of the Campanian-Maastrichtian coastal deposits of the Areny Fm. and Maastrichtian-Thanetian continental deposits from the Garumnian facies (Q, Fig. 3a, b). This transect consists of three south-verging anticlines formed in the southern sector of the imbricated thrust system forming the Lower Pedraforca thrust sheet. The limbs and hinges of these folds are affected by vug porosity and intense fracturing, which consists of bed-perpendicular joints and reverse and strike-slip faults formed as a result of the background deformation related to the Lower Pedraforca thrust sheet. Fault zones related to the major thrusts forming the imbricate system of the Lower Pedraforca thrust sheet do not outcrop in the studied area.

The Vallfogona thrust was sampled in three different outcrops along its strike (GDV, GDB1–2; Fig. 3). Outcrops GDV and GDB1 are formed of up to 450 m-thick fault zones affecting the Cuisian-Lutetian turbidites of the Vallfogona Fm. and the alluvial sediments of the Berga Fm. (Fig. 3b). Outcrop GDB2 is formed of an up to 40 m-thick fault zone affecting only the Berga Fm (Fig. 3b) and consists of a minor thrust fault related to the activity of the Vallfogona thrust. In the three outcrops, the fault zones are mainly composed of damage zones both in the hangingwall and footwall of the Vallfogona thrust in which vug porosity, bed-parallel slip surfaces and reverse and strike-slip faults are concentrated and filled with calcite cement. Sampled fault cores consist of cm-thick gouges with very scarce calcite veins.

The Abocador thrust (TAB) has been studied in a 200 m-thick fault zone with a 7 m thick fault core whereas the L'Escala thrust (TES) has been studied in a 150 m-thick fault zone, with less than 1 m thick fault core, in both cases cutting through the alluvial sediments of the Lutetian Bellmunt Fm. and Bartonian deltaic deposits of the Puigsacalm Fm (Fig. 3a, b). The fault cores of both thrusts are composed of clay-rich gouges with small calcite veins. Damage zones comprise almost all the volume of the sampled outcrops and are intensively affected by bed-perpendicular joints and reverse and strike-slip faults filled by calcite cement.

5. Fracture analysis

Rocks involved in the studied structures are affected by bed-parallel slip surfaces, joints, E-W to WSW-ENE trending reverse faults and predominantly NW-SE and NE-SW trending strike-slip faults (Fig. 4). Joints are mostly bed-perpendicular, indicating that they formed during layer-parallel shortening together with bed-parallel slip surfaces (Casini et al., 2011). However, some of the joints in L'Escala thrust cut the Bellmunt and Puigsacalm formations at a constant angle regardless bedding dips, indicating that these fractures formed after folding and thrusting. The high trend and dip dispersion of joints in the Lower Pedraforca thrust sheet in contrast to the Abocador and L'Escala thrusts (Fig. 4) are interpreted that deformation was more intense in the former structure or that it extended during a longer period. Reverse and strike-slip faults in the Lower Pedraforca thrust sheet and in the Vallfogona, Abocador and L'Escala thrusts cut stratification at a high angle regardless bedding dips, suggesting that these fractures formed once strata was already folded and therefore, after development of bed-perpendicular joints. The concentration of these faults in the fault zones of major thrusts and the striae sets measured on their planes (Fig. 4), indicating a tectonic displacement to the south in agreement with the regional trend (Vergés, 1993), suggest that they formed during the activity of the major thrusts.

6. Calcite cements

The integration of textural, petrographic and geochemical data obtained from fracture-filling cements allows to identify three generations of calcite cement for the Lower Pedraforca thrust sheet (Cc1 to Cc3), seven for the Vallfogona thrust (Cc1 to Cc7) and two for the Abocador thrust (Cc1 and Cc2) (Fig. 5). In the L'Escala thrust, three calcite cement generations (Cc1 to Cc3) were already identified (Travé et al., 2007) (Fig. 5).

6.1. Petrology

In the Lower Pedraforca thrust sheet, Cc1 cement is formed of up to 30 μm in size of non-luminescent blocky calcite crystals precipitated in the intergranular and intragranular porosity of the Upper Cretaceous Areny Fm. (Fig. 5). Cement Cc2 consists of up to 1 mm of non- to dull orange luminescent sparite calcite crystals precipitated in vug porosity, joints and reverse and strike-slip faults postdating Cc1 (Fig. 5) and affecting both the Areny Fm. and Paleocene Garumnian facies. Calcite cement Cc3 consists of up to 3 mm of zoned dull brown and dull orange blocky sparite calcite crystals precipitated in vug porosity, reverse and strike-slip faults cutting the previous fractures and vugs (Fig. 5).

In the Vallfogona thrust, calcite cements Cc1, Cc2, Cc3 and Cc4 consist of dull brown to non-luminescent calcite, precipitated in fractures and porosity of the Lutetian Vallfogona turbidites from the hangingwall (Fig. 5). Cement Cc1 is formed of 10–20 μm in size blocky sparite precipitated in the intergranular and intragranular porosity of the turbidite sandstones (Fig. 5). Cc2 is formed of 200 μm to 2 mm blocky and up to 1 mm long fibrous sparite precipitated in bed-parallel slip surfaces, bed-perpendicular joints and vug porosity postdating Cc1 (Fig. 5). Calcite cement Cc3 is formed of up to 1 mm long fibrous calcite precipitated parallel to the walls of thrust faults postdating Cc2 (Fig. 5). Cc4 is formed of 100 μm to 2 mm blocky and up to 1 mm long fibrous sparite precipitated in strike-slip and thrust faults postdating Cc3 (Fig. 5). Calcite cement Cc5 precipitated in strike-slip and reverse faults and intergranular porosity of Upper Eocene to Oligocene syn-orogenic alluvial sediments of the Berga Fm. from the thrust footwall (Fig. 5). This cement is formed of up to 100 μm blocky and up to 1 mm long fibrous sparite crystals of bright orange calcite (Fig. 5). The presence of Cc5 cement in sediments younger than those in the hangingwall accounts for a later precipitation with respect to Cc1 to Cc4 cements. Cements Cc6 and Cc7 are formed of up to 10 μm of zoned non-luminescent to bright blocky calcite crystals precipitated in vug porosity cross-cutting Cc4 and Cc5 cements, respectively (Fig. 5). The difference between these two last cements lies in their elemental composition (Fig. 6).

In the Abocador thrust, cement Cc1 precipitated in rock porosity

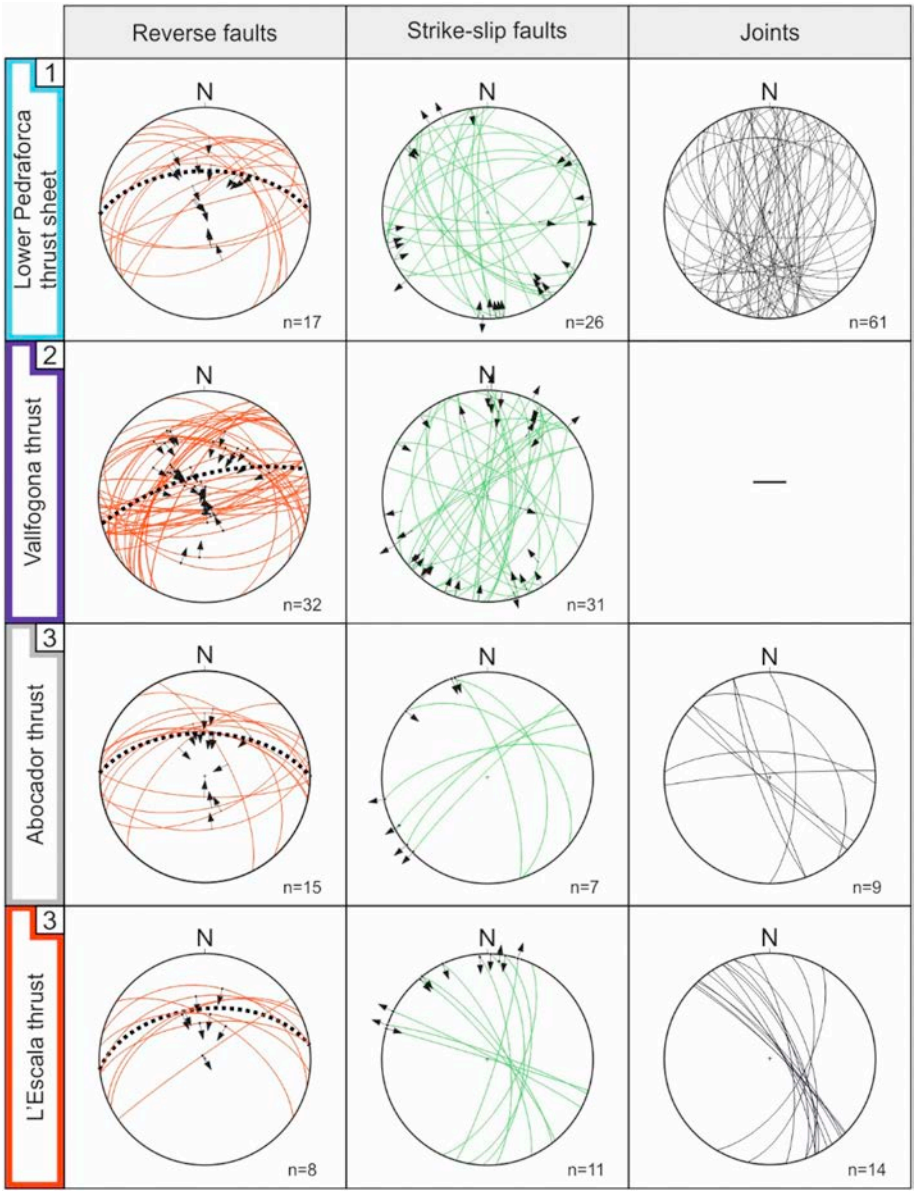

Fig. 4. Lower hemisphere Schmidt stereoplots representing fracture data from the different studied outcrops. The dotted thick black lines indicate the main plane orientation for thrust faults. The boxes with numbers represent the structure location in Fig. 1.

and strike-slip and thrust faults affecting the Lutetian alluvial sediments of the Bellmunt Fm. in the hangingwall and Bartonian marls of the Puigsacalm Fm. in the footwall. Cement Cc2 postdates cement Cc1 and precipitated in some reactivated thrust faults (Fig. 5). Both cements consist of orange to bright orange up to 6 μm blocky calcite and up to 10 μm long and 2 μm thick fibrous calcite associated with celestite and barite (Fig. 5).

In L'Escala thrust, calcite cements Cc1, Cc2 and Cc3 consist of orange to bright orange calcite precipitated in fractures affecting the Bellmunt and Puigsacalm Fms. (Fig. 5). Cc1 cement is formed of up to 2 mm blocky crystals and up to 0.7 mm long and 200 μm thick fibrous sparite precipitated in bed-perpendicular pre-thrust joints and thrust faults (Fig. 5). Calcite cements Cc2 and Cc3 are formed of up to 5 mm long and 2 mm thick fibrous sparite filling post-thrust strike-slip faults and post-thrust NW-SE joints respectively (Fig. 5).

6.2. Geochemistry

6.2.1. Elemental composition

Minimum, maximum and mean Fe, Mg, Sr and Mn contents of the calcite cements precipitated in fractures and rock porosity in the Vallfogona, Abocador and L'Escala thrusts, and together with already published data of the Ainsa Basin (Travé et al., 1997), El Guix anticline (Travé et al., 2000) and Puig-reig anticline (Cruset et al., 2016), are plotted in Fig. 6 (details in supplementary data), summarizing up to 39 analyzed samples and 747 measures.

The graphic (Fig. 6) shows that the Fe content decreases from the activity of the Molinos thrust (23,780 ppm) to the last stages of evolution of the Vallfogona thrust (below the detection limit in cement Cc7), that is, from lower Eocene to lower Oligocene (Fig. 6). However, a final increase in the Fe content (up to 7731 ppm) is observed during the lower Oligocene in calcite cements precipitated in the Guix anticline (Fig. 6). The Sr content also shows a depletion from lower Eocene to lower Oligocene, with values ranging from 8090 ppm in the Arro syncline and Atiart thrust to below the detection limit in the El Guix anticline (Fig. 6). Contrarily, the Mg and Mn contents do not show a specific trend during this time span, with values ranging from 4135 to 1452 ppm and from 4239 to below the detection limit, respectively (Fig. 6).

6.2.2. Carbon and oxygen isotopes

The carbon and oxygen composition of the calcite cements

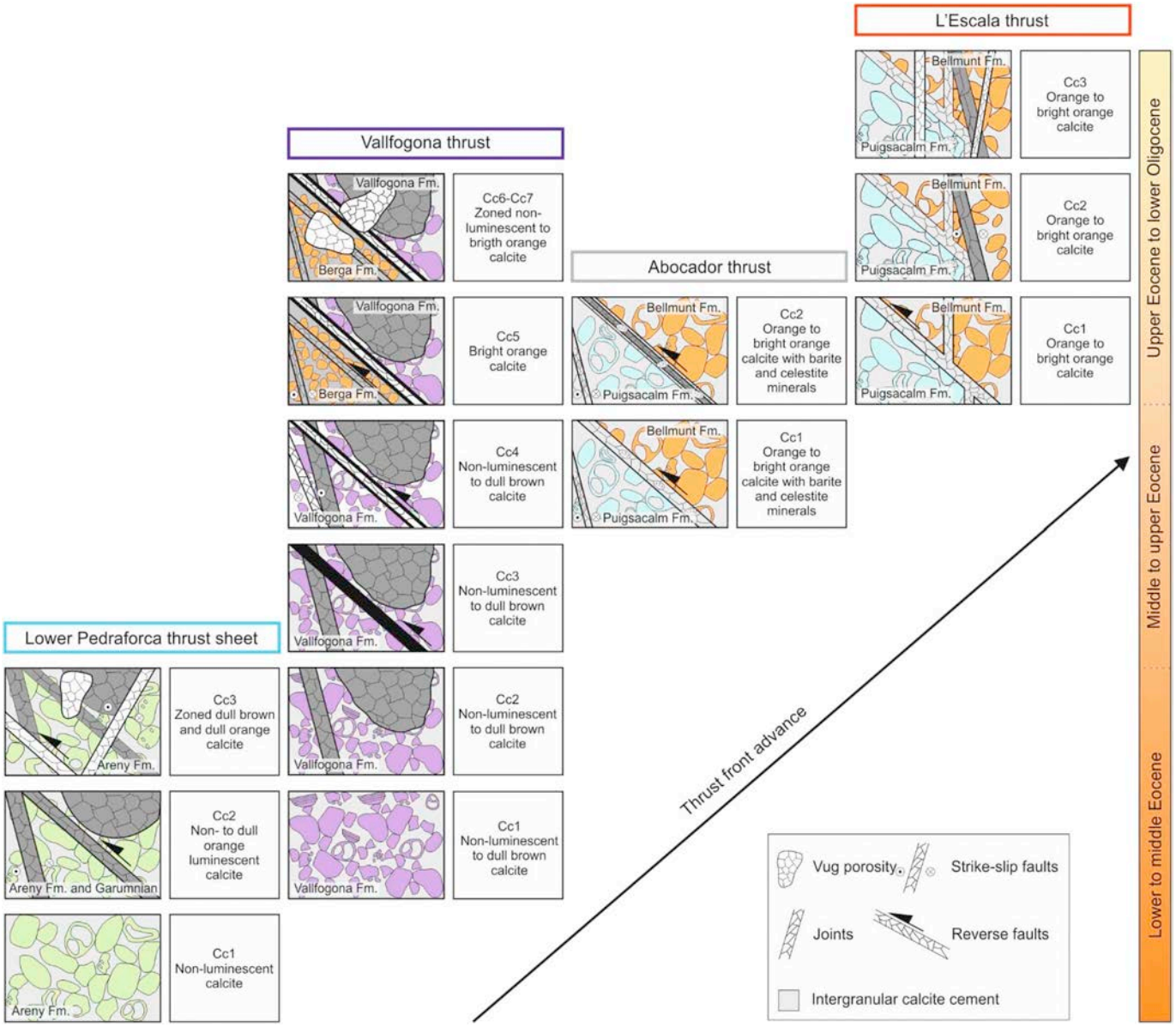

Fig. 5. Cross-cutting relationships between fractures and related calcite cements in the Lower Pedraforca thrust sheet and Vallfogona, Abocador and L'Escala thrusts. The different cement generations and their main petrographic features as well as host rock formations are indicated.

precipitated in the Lower Pedraforca thrust sheet, Vallfogona, Abocador and L'Escala thrusts, together with already published data from the Ainsa Basin (Travé et al., 1997), Castillo Mayor klippe and Jaca thrust (Lacroix et al., 2014), El Guix anticline (Travé et al., 2000) and Puigreig anticline (Cruset et al., 2016) is presented in Fig. 7, summarizing up to 153 analyzed samples.

6.2.2.1. Lower Pedraforca thrust sheet. Upper Cretaceous marine carbonates from the Areny Fm. show $\delta^{13}C$ values ranging between + 1.45 and + 1.68‰ VPDB and $\delta^{18}O$ values ranging between − 4.48 and ‰ − 3.20 VPDB (Fig. 7). Palustrine limestones from the Paleocene (Garumnian facies) show $\delta^{13}C$ values ranging between − 17.47 and − 3.65‰ VPDB and $\delta^{18}O$ values ranging between − 8.20 and − 4.77‰ VPDB (Fig. 7).

Due to the small size of calcite cement Cc1, only cements Cc2 and Cc3 were analyzed for carbon and oxygen isotopes analysis. Calcite cement Cc2 shows $\delta^{13}C$ values ranging between − 15.18 and − 0.38‰ VPDB and $\delta^{18}O$ values between − 9.21 and − 2.61‰ VPDB (Fig. 7), similar to its adjacent host rock (Fig. 8). Calcite cement Cc3 shows $\delta^{13}C$ values ranging between + 0.84 and + 1.71‰ VPDB and $\delta^{18}O$ values ranging between − 9.86 and − 4.39‰ VPDB (Fig. 7). Calcite cement Cc3 has $\delta^{13}C$ similar to the Upper Cretaceous Areny Fm. and the Paleocene Garumnian Facies, whereas it has $\delta^{18}O$ slightly depleted with respect these host rocks (Fig. 8).

6.2.2.2. Vallfogona thrust. Cuisian marine marls from the hangingwall of the Vallfogona thrust (Vallfogona Fm.) show $\delta^{13}C$ values between − 2.56 and − 0.26‰ VPDB and $\delta^{18}O$ values between − 6.94 and − 4.72‰ VPDB (Fig. 7). One sample of Priabonian-Rupelian palustrine limestones from the footwall of the Vallfogona thrust (Berga Fm.) shows $\delta^{13}C$ values of − 2.95‰ VPDB and $\delta^{18}O$ values of − 7.19‰ VPDB (Fig. 7).

Due to the small size of Cc1, Cc6 and Cc7 calcite cements, only Cc2, Cc3, Cc4 and Cc5 calcite cements were analyzed for carbon and oxygen isotopes (Fig. 7). These calcite cements show a progressive depletion in $\delta^{13}C$ and $\delta^{18}O$ from Cc2 to Cc5 (Fig. 7). Cc2 calcite cement shows $\delta^{13}C$ values ranging between − 3.86 and − 1.08‰ VPDB and $\delta^{18}O$ ranging between − 6.24 and − 4.74‰ VPDB. Cc3 shows $\delta^{13}C$ values ranging

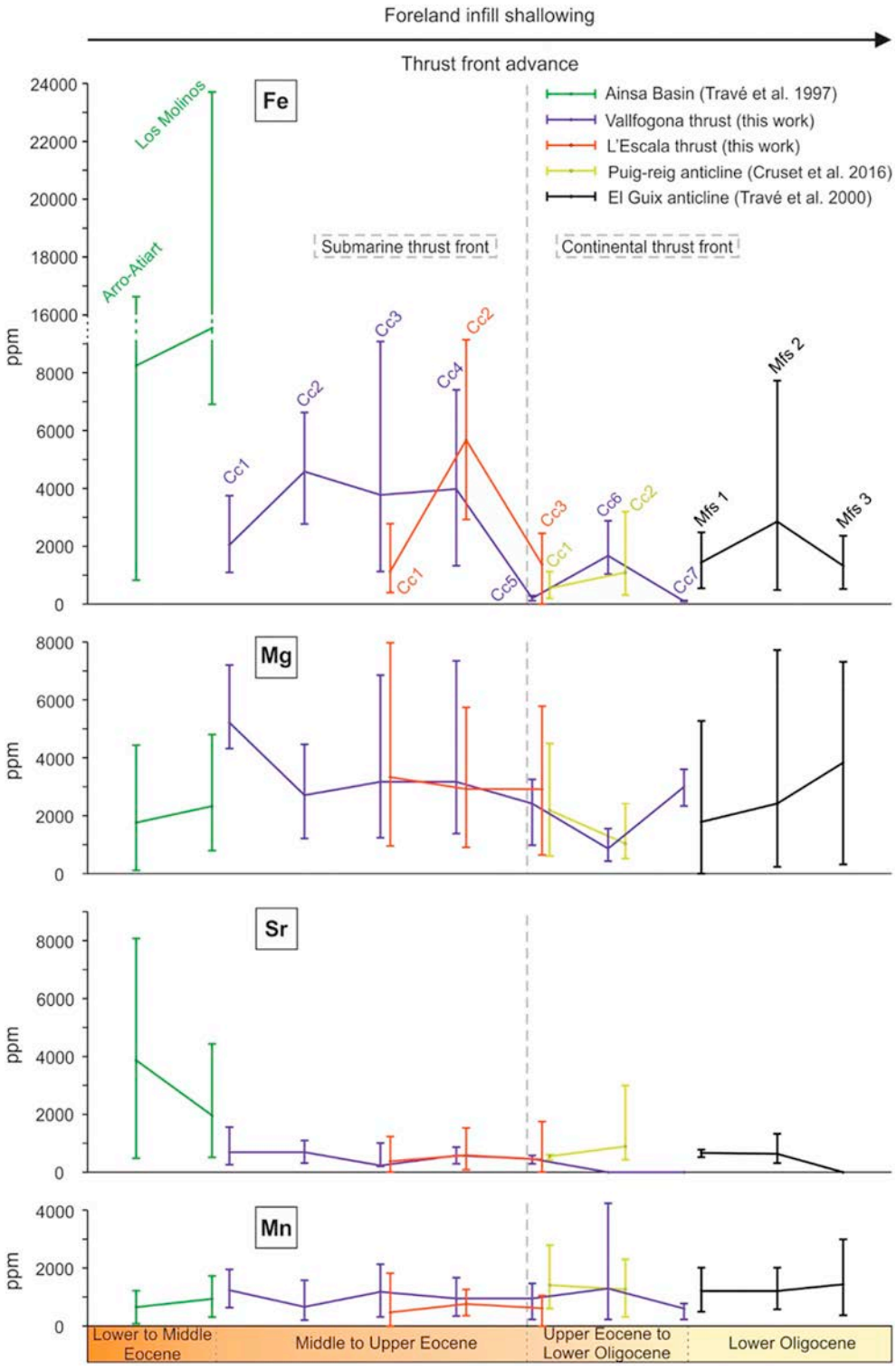

Fig. 6. Elemental composition of the calcite cements for the Vallfogona and L'Escala thrusts, Ainsa Basin (Travé et al., 1997), El Guix anticline (Travé et al., 2000) and Puig-reig anticline (Cruset et al., 2016). For each structure Mg, Mn, Fe and Sr minimum, maximum and mean contents are given. Each of the different color lines represent one single structure. Equivalent colors are used in Figs. 2, 3, 4, 5, 7, 8, 9 and 10. The dashed grey line indicates the change from marine to continental conditions of thrust emplacement. The age of each calcite cement generation is approximated. (For interpretation of the references to color in this figure legend, the reader is referred to the web version of this article.)

between −0.9 and +0.21‰ VPDB and $\delta^{18}O$ between −7.55 and −6.04‰ VPDB. Calcite cement Cc4 shows $\delta^{13}C$ values ranging between −1.74 and −1.38‰ VPDB and $\delta^{18}O$ between −7.34 and −6.74‰ VPDB. Calcite cement Cc5 has $\delta^{13}C$ values between −3.05 and −0.57‰ VPDB and $\delta^{18}O$ between −9.95 and −7.56‰ VPDB. Calcite cements Cc2 to Cc5 have $\delta^{18}O$ progressively more depleted with respect their adjacent host rocks, whereas the $\delta^{13}C$ do not show a clear trend (Fig. 8).

6.2.2.3. Abocador thrust. Due to their small size, carbonate clasts from the Bellmunt Fm. were not sampled. A detrital carbonate clast from the Bartonian Puigsacalm Fm. (footwall) shows $\delta^{13}C$ of −1.69‰ VPDB and $\delta^{18}O$ of −8.05‰ VPDB. The carbonate fraction from marls from the Puigsacalm Fm. shows $\delta^{13}C$ of +0.45‰ VPDB and $\delta^{18}O$ of −6.73‰ VPDB (Fig. 7).

Contrarily to the Vallfogona thrust, calcite cements show depletion in $\delta^{13}C$ and enrichment in $\delta^{18}O$ from Cc1 to Cc2 (Figs. 7, 8). Cc1 calcite cement has $\delta^{13}C$ values between −2.72 and −1.05‰ VPDB and $\delta^{18}O$ values between −8.81 and −7.61‰ VPDB (Fig. 7). Calcite cement Cc2 has $\delta^{13}C$ values between −4.19 and −1.46‰ VPDB and $\delta^{18}O$ values

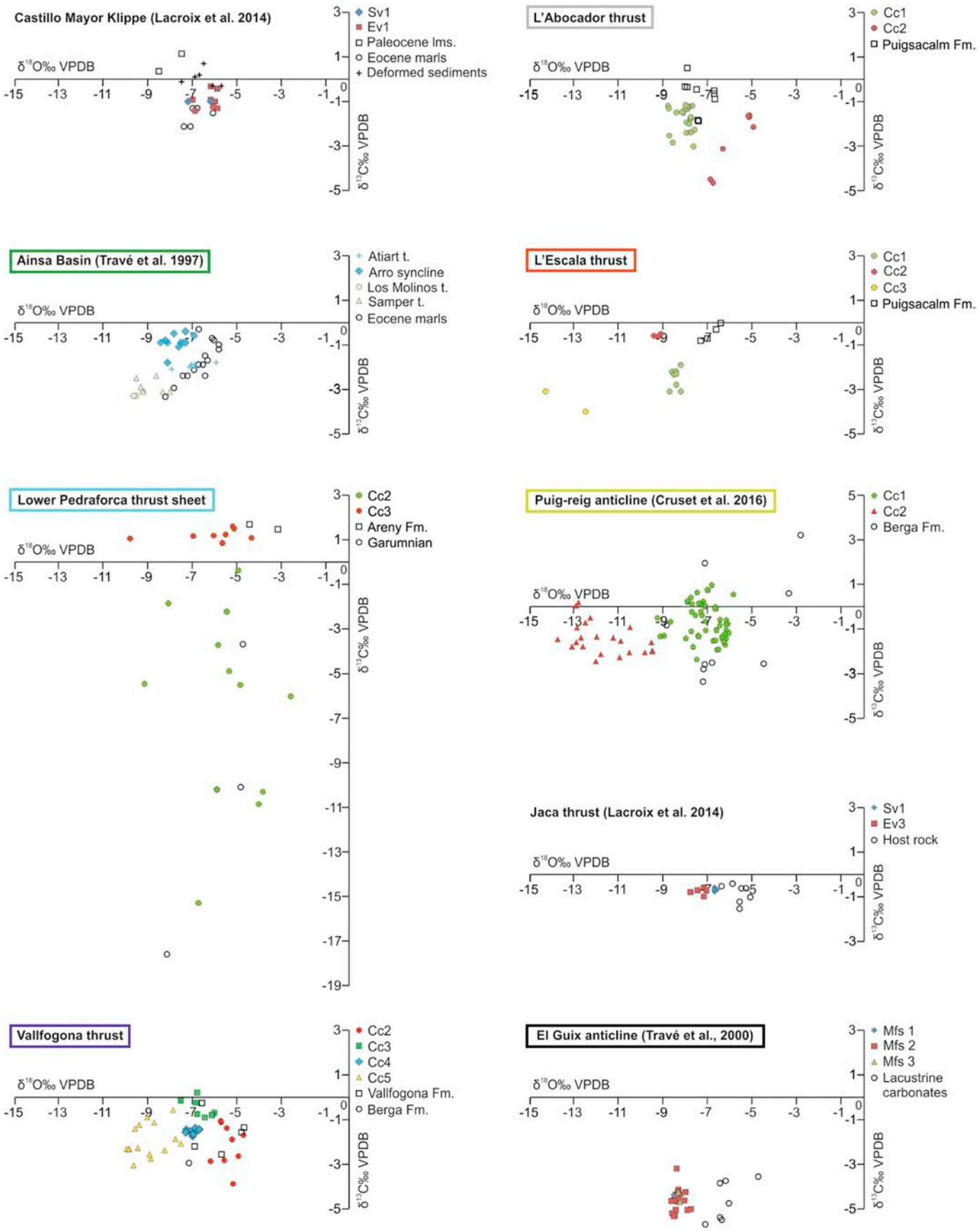

Fig. 7. $\delta^{18}O$ vs $\delta^{13}C$ cross-plots of carbonate host rocks and calcite cements from the Lower Pedraforca thrust sheet, Vallfogona, Abocador and L'Escala thrusts, Ainsa Basin (Travé et al., 1997), Castillo Mayor klippe and Jaca thrust (Lacroix et al., 2014), El Guix anticline (Travé et al., 2000) and Puig-reig anticline (Cruset et al., 2016). Empty symbols represent the different host rocks.

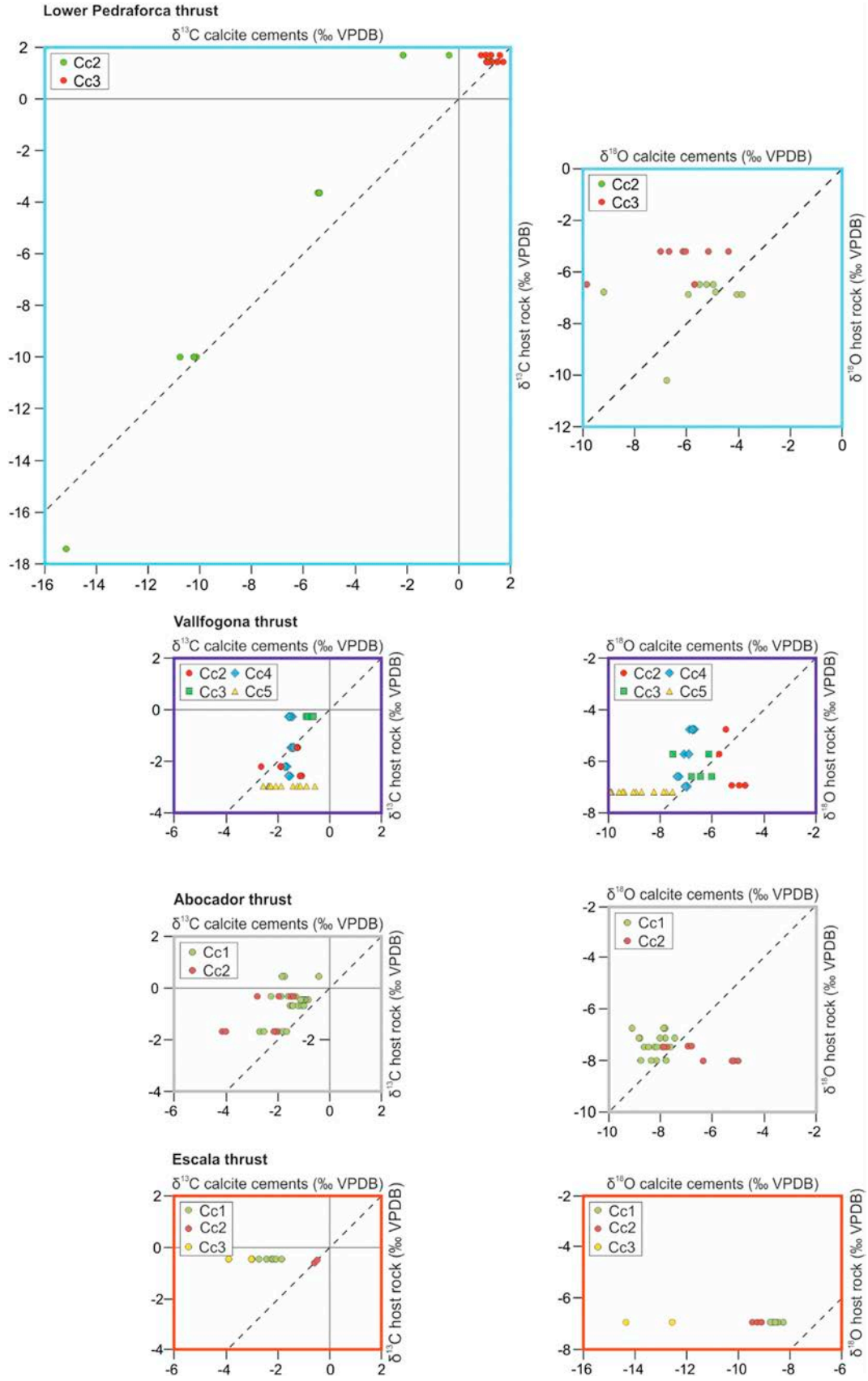

Fig. 8. $\delta^{13}C_{calcite\ veins}$ vs $\delta^{13}C_{host\ rocks}$ and $\delta^{18}O_{calcite\ veins}$ vs $\delta^{18}O_{host\ rocks}$ cross-plots from the Lower Pedraforca thrust sheet, Vallfogona, Abocador and L'Escala thrusts. The dashed black line represents the equilibrium between calcite veins and their adjacent host rocks.

between −6.9 and −4.98‰ VPDB (Fig. 7).

6.2.2.4. L'Escala thrust. The carbonate fraction of marls from the Puigsacalm Fm. (footwall) show $\delta^{13}C$ values between −0.80 and 0‰ VPDB and $\delta^{18}O$ values between −7.40 and −6.50‰ VPDB (Fig. 7).

In the L'Escala thrust, calcite cements show a progressive depletion in $\delta^{13}C$ and $\delta^{18}O$ from Cc1 to Cc3, like in the Vallfogona thrust (Figs.7, 8). Calcite cement Cc1 has $\delta^{13}C$ values between −2.8 and −1.90‰ VPDB and $\delta^{18}O$ values between −8.80 and −8.30‰ VPDB (Fig. 7). Calcite cement Cc2 has $\delta^{13}C$ values between −0.60 and −0.50‰ VPDB and $\delta^{18}O$ values between −9.50 and −9.20‰ VPDB (Fig. 7). Calcite cement Cc3 has $\delta^{13}C$ values between −4 and −3.10‰ VPDB and $\delta^{18}O$ values between −14.40 and −12.60‰ VPDB (Fig. 7).

6.2.3. Clumped isotopes

For this study, clumped isotopes thermometry has been measured in three calcite cements from the Vallfogona thrust (Fig. 9; Table 1). The results are presented together with data already published from the Puig-reig anticline (Cruset et al., 2016) and two preliminary data from the Abocador thrust and El Guix anticline (Fig. 9; Table 1).

Table 1
Calcite cement $\delta^{13}C$, $\delta^{18}O$, Δ_{47} and $\delta^{18}O_{fluid}$ of the Vallfogona thrust and Puig-reig anticline. Preliminary Δ_{47} and $\delta^{18}O_{fluid}$ for the Abocador thrust and El Guix anticline are also included. n represents the number of analyses per sample.

Structure	Sample	Cement type	*n*	$\delta^{13}C$ VPDB	$\delta^{18}O$ VPDB	Δ_{47}	T °C	$\delta^{18}O_{fluid}$ VSMOW
Vallfogona thrust	GDV20	Cc2	3	−1.06	−6.04	0.463 ± 0.002	154 ± 2	+12.12 ± 0.1434
	GDV30	Cc4	3	−1.66	−7.11	0.532 ± 0.010	101 ± 6	+6.37 ± 0.626
	GDV13	Cc5	3	−2.29	−9.64	0.527 ± 0.023	105 ± 14	+4.22 ± 1.37
Puig-reig anticline; Cruset et al. (2016)	309B1	Cc1	3	−0.44	−7.77	0.548 ± 0.009	92 ± 5	+4.7 ± 0.6
	317	Cc1	3	−0.99	−6.95	0.494 ± 0.010	129 ± 8	+9.2 ± 0.7
	311A	Cc2	3	−0.77	−12.32	0.574 ± 0.010	77 ± 5	−1.7 ± 0.7
	311D	Cc2	3	−0.73	−12.85	0.551 ± 0.004	90 ± 3	−0.7 ± 0.3
Abocador thrust	TAB9	Cc2	1	−1.69	−8.22	0.423 ± 0.03	177 ± 40	+14.1 ± 4.7
El Guix anticline	STn(3)(2)	Mfs2	1	−4.48	−8.62	0.487 ± 0.03	117 ± 25	+7.1 ± 2.5

For the Vallfogona thrust, the Δ_{47} values for calcite cements Cc2, Cc4 and Cc5 are 0.463 ± 0.002‰, 0.532 ± 0.010‰ and 0.527 ± 0.023‰, respectively. These values translate into temperatures of 154° ± 2 °C (Cc2), 101° ± 6 °C (Cc4) and 105° ± 14 °C (Cc5) using the equation of Kluge et al. (2015) (Fig. 9). Thus, from clumped isotopes temperatures and the equation of Friedman and O'Neil (1977), the $\delta^{18}O_{fluid}$ for Cc2, Cc4 and Cc5 is +12.12 ± 0.14‰, +6.37 ± 0.63‰ and +4.22 ± 1.37‰ VSMOW respectively (Fig. 9).

In the Puig-reig anticline, the measured Δ_{47} values in calcite cements Cc1 and Cc2 are between 0.548 ± 0.009‰ and 0.493 ± 0.0010‰ and between 0.574 ± 0.010‰ and 0.551 ± 0.004‰, respectively. With these values, and from the equations mentioned above, we obtain temperatures ranging between 92° ± 5 °C and 129° ± 8 °C for Cc1 and between 77 ± 5 °C and 93° ± 1 °C for Cc2 (Fig. 9) and $\delta^{18}O_{fluid}$ for Cc1 and Cc2 is between +4.7 ± 0.6 and +9.2 ± 0.7‰ VSMOW and between −1.7 ± 0.7 and −0.7 ± 0.3‰ VSMOW respectively (Fig. 9).

In the Abocador thrust, a preliminary measured Δ_{47} of 0.423 ± 0.03 is obtained for calcite cement Cc2, which translates into a temperature of 177 ± 40 °C and a $\delta^{18}O_{fluid}$ of +14.1 ± 4.7‰ VSMOW (Fig. 9).

In the El Guix anticline, a preliminary measured Δ_{47} of 0.487 ± 0.03 is obtained for calcite cement precipitated in a thrust fault affecting the sediments forming this fold (micro fracture stage 2 (mfs2) in Travé et al., 2000). This value translates into a temperature of 117 ± 25 °C and a $\delta^{18}O_{fluid}$ of +7.1 ± 2.5‰ VSMOW (Fig. 9).

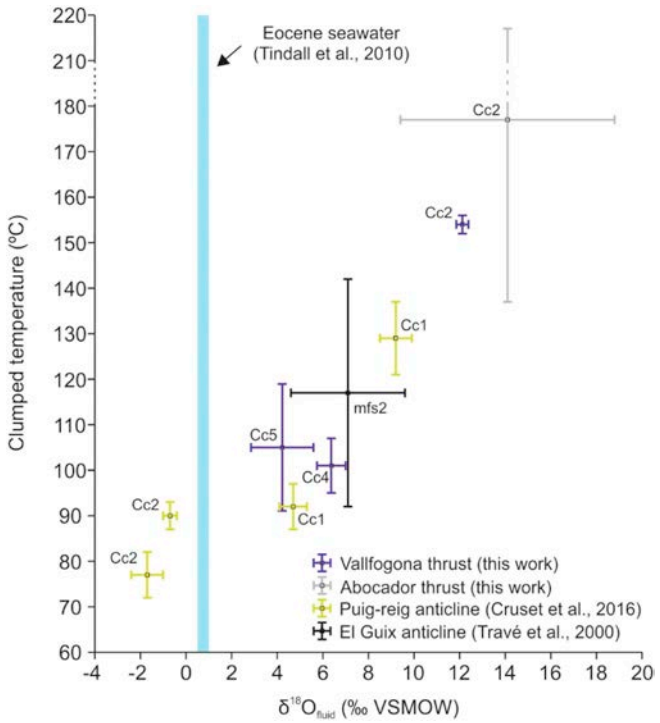

Fig. 9. Clumped isotopes temperatures (°C) vs calculated $\delta^{18}O_{fluid}$ (‰ VSMOW) for The Vallfogona and Abocador thrusts, Puig-reig anticline (Cruset et al., 2016) and El Guix anticline (Travé et al., 2000). $\delta^{18}O$ Eocene seawater in ‰ VSMOW is from Tindall et al. (2010).

6.2.4. Strontium isotopes

The $^{87}Sr/^{86}Sr$ ratios of the calcite cements, celestite, host carbonates and evaporites from the Ainsa Basin (Travé et al., 1997), Vallfogona and L'Escala thrusts, El Guix anticline (Travé et al., 2000) and Puig-reig anticline (Cruset et al., 2016) are presented in Fig. 10(for details see supplementary data). The $^{87}Sr/^{86}Sr$ ratios of the Cuisian evaporites of the eastern sector of the south Pyrenean foreland basin (Carrillo, 2012) and the LOWESS curve (McArthur et al., 2001) are also plotted.

From Lower Eocene to Lower Oligocene an increase of the $^{87}Sr/^{86}Sr$ ratios of calcite cements (from 0.707744 to 0.70933) is observed (Fig. 10). At outcrop scale, the $^{87}Sr/^{86}Sr$ ratios from older to younger cements in the Ainsa Basin and the Vallfogona and L'Escala thrusts also show an increment of the $^{87}Sr/^{86}Sr$ ratios (Fig. 10). In contrast, in the Puig-reig anticline this trend is overturned and in El Guix anticline trends are not observed (Fig. 10).

7. Discussion

In this section, we discuss 1) the type and origin of fluids from which calcite cements precipitated in each structure; 2) the changes of fluid regime at the scale of the south Pyrenean fold and thrust belt from lower Eocene to lower Oligocene; and 3) a conceptual model of fluid flow in fold and thrust belts.

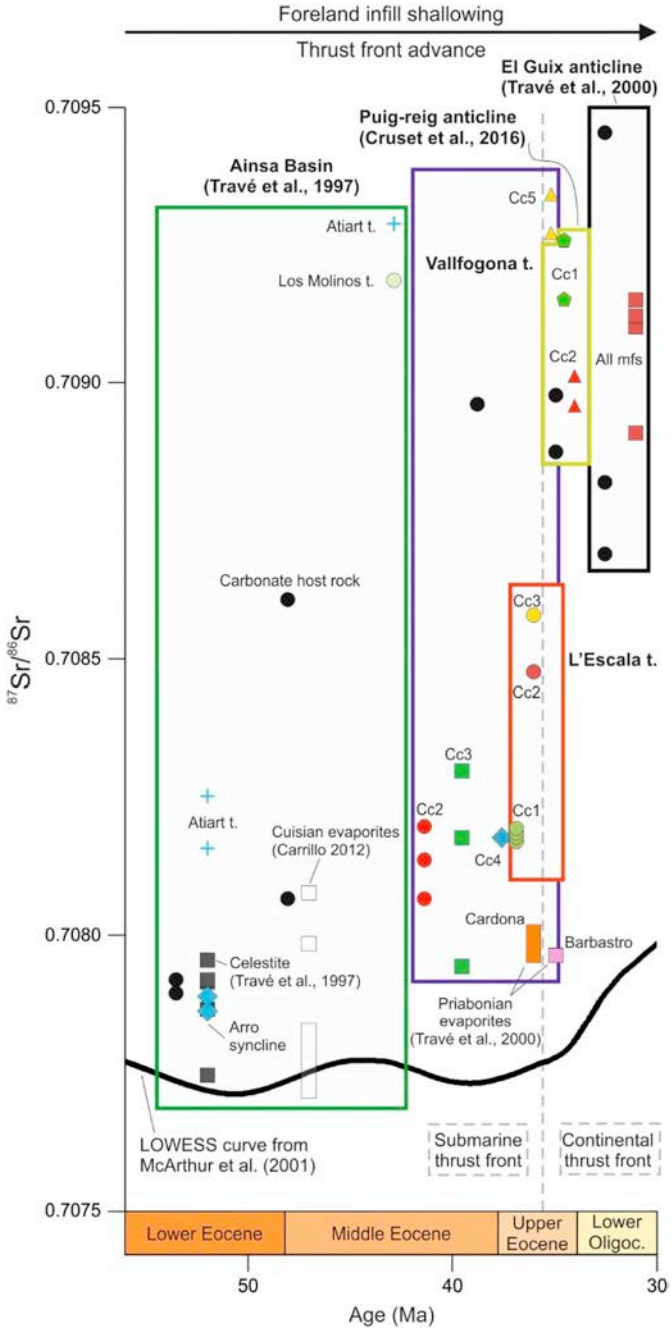

Fig. 10. $^{87}Sr/^{86}Sr$ composition of calcite cements, carbonate host rocks and celestite minerals from the Vallfogona and L'Escala thrusts, Ainsa Basin (Travé et al., 1997), El Guix anticline (Travé et al., 2000) and Puig-reig anticline (Cruset et al., 2016). The age of each calcite cement generation is approximated. The $^{87}Sr/^{86}Sr$ ratios of the Cuisian evaporites of the eastern sector of the south Pyrenean foreland basin from Carrillo (2012) and the LOWESS curve from McArthur et al. (2001) are also plotted. The dashed grey line indicates the change from marine to continental conditions of thrust emplacement.

7.1. Type of fluids

The type of fluids that flowed through rock porosity and fractures in the south Pyrenean fold and thrust belt can be determined by using the elemental and isotopic composition of the studied calcite cements (Meyers and Lohmann, 1985; Banner and Hanson, 1990).

The $\delta^{13}C$ of the calcite cements in the Lower Pedraforca thrust, Vallfogona thrust, cement Cc2 in L'Escala thrust, Ainsa Basin (Travé et al., 1997), El Guix anticline (Travé et al., 2000), Castillo Mayor klippe and Jaca thrust (Lacroix et al., 2014) and Puig-reig anticline (Cruset et al., 2016) are similar to their adjacent host rocks (Figs. 7, 8), indicating that the fluid system was rock-buffered. In contrast, in the Abocador thrust and in cements Cc1 and Cc3 in L'Escala thrust, the $\delta^{13}C$ of calcite cements shows depletion with respect to their adjacent host rocks up to 3.42‰ VPDB and 3.8‰ VPDB respectively (Figs. 7, 8). This depletion can be explained by the input of organogenic or soil-derived carbon into the fluid system (Irwin et al., 1977; Cerling et al., 1989).

The $\delta^{18}O_{fluid}$ calculated from clumped isotopes temperatures for the Vallfogona thrust (+12.12‰ VSMOW for Cc2, +6.37‰ VSMOW for Cc4 and +4.22‰ VSMOW for Cc5), calcite cement Cc1 in Puig-reig anticline (between +4.7 and +9.2‰ VSMOW), calcite cement Cc2 in the Abocador thrust (+14.083‰ VSMOW) and El Guix anticline (+7.09‰ VSMOW) are within the range of magmatic, metamorphic and formation waters (Taylor, 1987). In the Ainsa Basin, a $\delta^{18}O_{fluid}$ within the same range of composition (between +9.51 and +16‰ VSMOW) is calculated from fluid inclusion data of celestite formed within calcite cements precipitated in the Arro syncline (Travé et al., 1998) and from the equation of Friedman and O'Neil (1977). A magmatic origin for these fluids is discarded since magmatism did not develop during the formation of the Pyrenees. Nevertheless, we have no evidence to differentiate between metamorphic and formation waters. The sulfur isotope composition of celestite crystals formed within calcite cements in the Ainsa Basin indicates the influence of marine connate waters trapped in the rock porosity (Travé et al., 1997). This influence has also been reported in calcite veins in the Castillo Mayor klippe, which are time-equivalent to the first stages of deformation of the Ainsa basin (Lacroix et al., 2014). However, the $^{87}Sr/^{86}Sr$ ratios of all the studied calcite cements are higher than those of Eocene seawater (Fig. 10). This fact can be explained by fluids in contact with clay minerals, the input of an external fluid in contact with Paleozoic crystalline rocks located at depth of the Axial zone and diluted by connate marine waters with low $^{87}Sr/^{86}Sr$ ratios or from the dissolution of emerged rocks by meteoric fluids (McCaig et al., 1995; Travé et al., 1997). The temperatures measured in the Vallfogona thrust (154 °C for Cc2, 101 °C for Cc4 and 105 °C for Cc5), Puig-reig anticline (between 92 °C and 129 °C for Cc1 and between 77 °C and 90 °C for Cc2) and Arro syncline (between 157 °C and 183 °C) were never reached by burial according to cross sections (Vergés, 1993) and vitrinite reflectance data (Clavell, 1992; Vergés et al., 1998) assuming a geothermal gradient of 25 °C km^{-1}, thus indicating a thermal anomaly. Preliminary temperature data from the Abocador thrust (177 °C) and El Guix anticline (117 °C) also seem to point to the presence of high temperature fluids. These results suggest hydrothermal fluid flow along fault zones in the Vallfogona, Abocador and L'Escala thrusts, background fractures in the Lower Pedraforca thrust sheet and fold-related fractures and intergranular porosity in the Puig-reig and el Guix anticlines, which were connected at depth with basement-involved thrusts in the inner part of the Pyrenees, as has been already reported (Bradbury and Woodwell, 1987; McCaig et al., 1995; Travé et al., 2007). However, the progressive decrease in Sr content (Table 1; Fig. 6) and increase of the $^{87}Sr/^{86}Sr$ ratios (Fig. 10) in the thrust front from the lower Eocene to lower Oligocene, together with the depletion in $\delta^{18}O$ (Fig. 7) and decrease in temperature at outcrop scale in the Ainsa Basin, Vallfogona and L'Escala thrusts and Puig-reig anticline, account for the input of meteoric waters, which mixed at depth with the hydrothermal fluids. The depletion in Fe content and $\delta^{18}O$ from older to younger calcite cements related to the input of meteoric waters has been also observed in the Jaca thrust

(Lacroix et al., 2014). The progressive depletion in $\delta^{18}O$ is related to the mixing between hydrothermal and meteoric fluids (Immenhauser et al., 2007), whereas the decrease in Fe content (Fig. 6) could be related to the progressive input of oxidizing meteoric fluids into the system (Froelich et al., 1979; Tucker and Wright, 1990), which may have flowed downwards along faults and joints by topography-driven fluid flow (Bitzer et al., 2001).

By contrast, in the Abocador thrust, there is enrichment in the $\delta^{18}O_{calcite}$ from older to younger cements (Fig. 7). This trend has also been observed in the Santo Domingo anticline (Sierras Exteriores, south western Pyrenees) with $\delta^{18}O_{fluid}$ values between −5 and 0‰ VSMOW in Bartonian-Priabonian veins and between +5 and +10‰ VSMOW in upper Priabonian-lower Rupelian veins (Crognier, 2016). These authors interpret the highest $\delta^{18}O_{fluid}$ values as a strong interaction between meteoric waters and host rocks or by the input of strongly evaporated fluids. In the same area, in the Pico del Águila anticline, post-folding calcite veins precipitated from low-temperature meteoric waters (Beaudoin et al., 2015). From the $\delta^{18}O_{calcite}$ of these veins (from −2.2 to 0‰ VPDB) together with the temperatures reported by these authors (below 80 ± 20 °C) a $\delta^{18}O_{fluid}$ between −4 and +11‰ VSMOW is obtained, suggesting that these meteoric waters could be highly $\delta^{18}O$-enriched brines. In the Larra/Eaux-chaudes thrust (Jaca Basin), a positive correlation between the $\delta^{18}O_{fluid}$, temperature and salinity is observed from older to younger stages without enrichment in the $\delta^{18}O_{calcite}$ (Crognier et al., 2017). These authors suggest that hydrothermal fluids interacted with Triassic evaporites which acted as the detachment level of the Larra/Eaux-chaudes thrust. A positive correlation between the $\delta^{18}O_{calcite}$ and fluid salinity has also been observed in fracture-filling calcites precipitated in worldwide areas affected by salt tectonics (Fischer et al., 2013).

The same scenario could be suggested for: 1) the Abocador thrust, where preliminary results on clumped isotopes thermometry (177 ± 40 °C and $\delta^{18}O_{fluid}$ of +14.1‰ VSMOW) and the presence of barite and celestite associated to calcite cements favor the hypothesis of hydrothermal fluids interacting with brines released from the underlying Eocene evaporites of the Beuda Fm., which acted as the detachment of this structure (Fig. 2b); 2) the El Guix anticline, with calcite cements without systematic $\delta^{18}O$ variation, temperature around 117 ± 25 °C, $\delta^{18}O_{fluid}$ of +7.1‰ VSMOW and halite precipitation in thrust zones also favoring the hypothesis of a fluid derived from the underlying Eocene Cardona Salt Formation (Travé et al., 2000) and; 3) the Larra/Eaux chaudes thrust and Sierras Exteriores with Triassic evaporites acting as the detachment level of the major thrust faults (Labaume et al., 2016). Consequently, we suggest that when evaporitic units are present, the presence of high salinity fluids derived from them, highly controls the $\delta^{18}O$ of the calcite cements.

The presence of the thermal anomalies discussed above, with fluids in disequilibrium with their adjacent host rocks during millions of years, indicate the occurrence of thermal convection controlling fluid flow (Lipsey et al., 2016). According to this mechanism, large volumes of fluids are driven to the reaction site through fractures and permeable host rocks during long time periods (Person et al., 1996; Morrow, 1998). Other scenarios, which involve fluid release by heating or decompression of interstitial fluids by seal breaking are ruled out, since these mechanisms provide low volumes of fluids and they do not generate thermal anomalies (Gomez-Rivas et al., 2014).

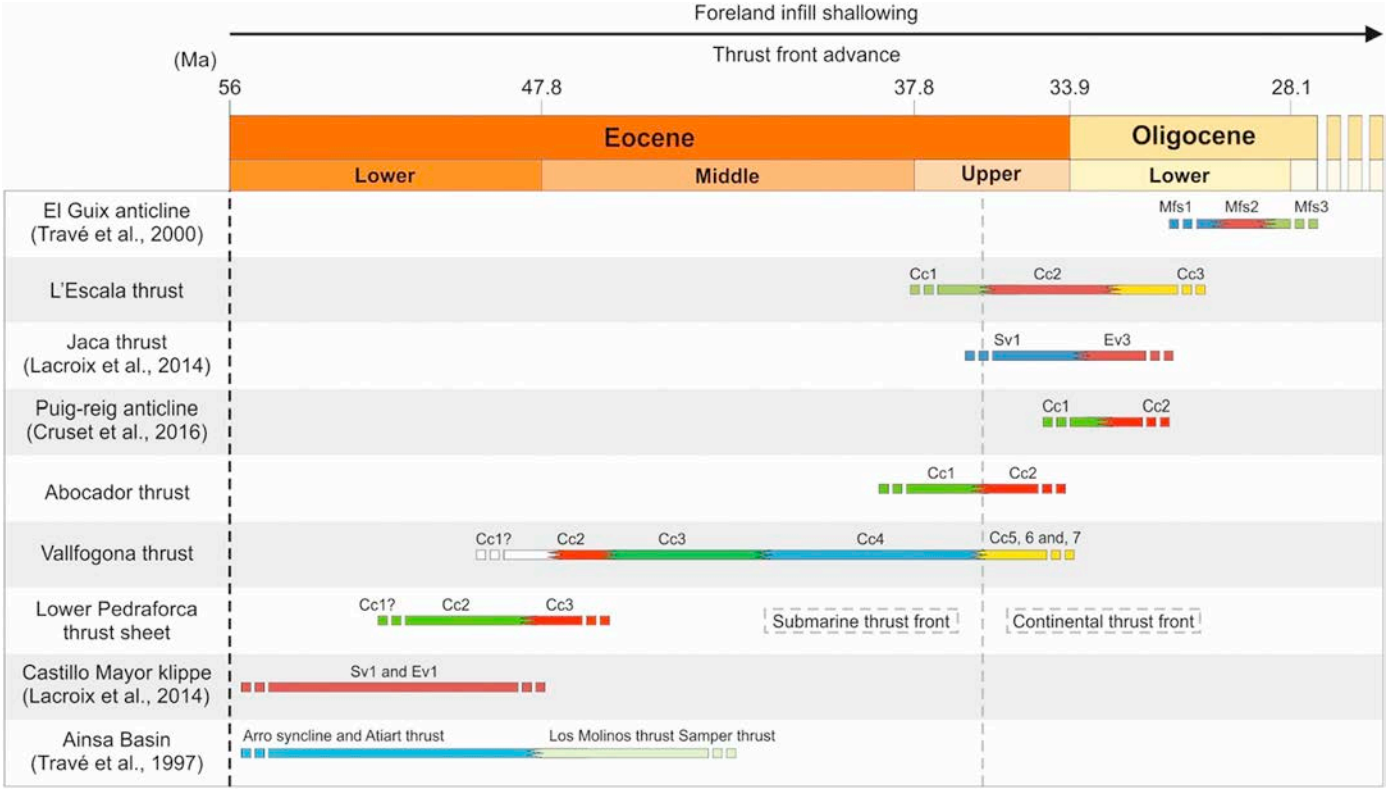

Fig. 11. Chronogram of the approximate ages of the different calcite cements in the Lower Pedraforca thrust sheet, Vallfogona, Abocador and L'Escala thrusts, Ainsa Basin (Travé et al., 1997), Castillo Mayor klippe and Jaca thrust (Lacroix et al., 2014), El Guix anticline (Travé et al., 2000) and Puig-reig anticline (Cruset et al., 2016). The dashed grey line indicates the change from marine to continental conditions of thrust emplacement.

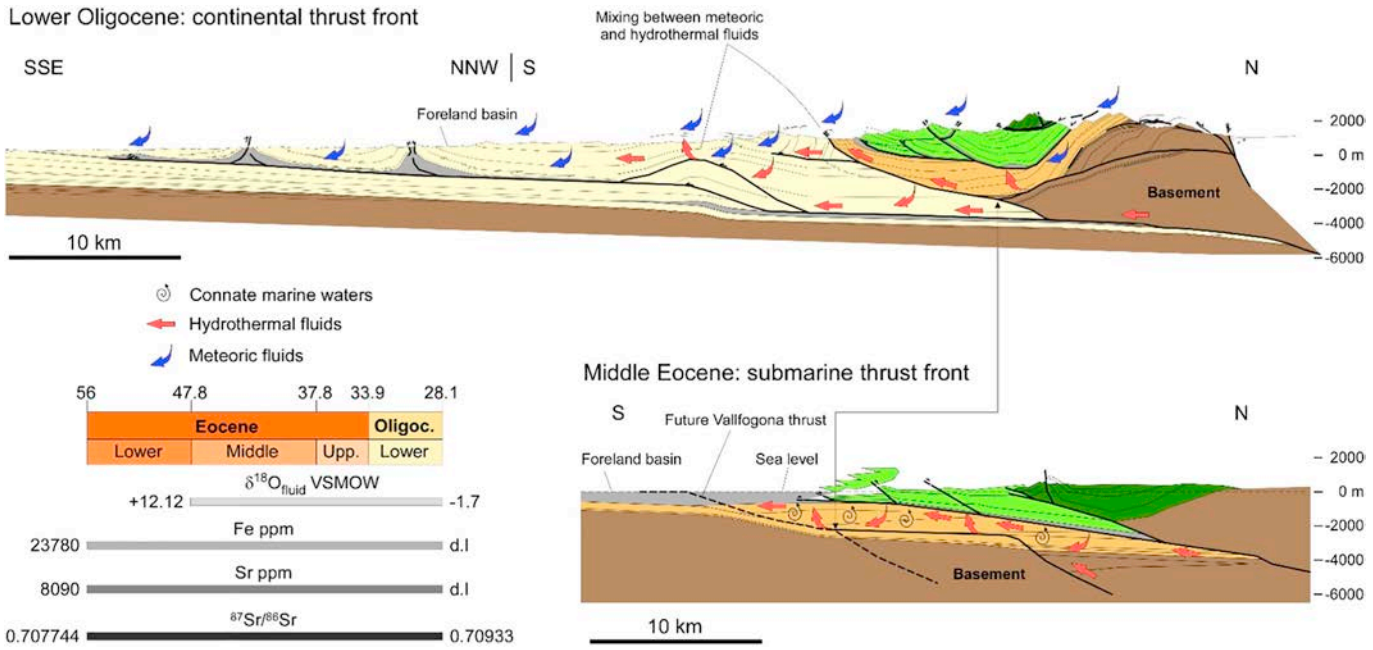

Fig. 12. Fluid flow evolution in the south Pyrenean fold and thrust belt from submarine to continental conditions during thrust front emplacement. The shifts in $\delta^{18}O_{fluid}$ VSMOW, Fe and Sr content and $^{87}Sr/^{86}Sr$ ratio from Lower Eocene to Lower Oligocene are also included. The middle Eocene stage is redrawn from Vergés et al. (1995) and the lower Oligocene stage is redrawn from Vergés (1993). Legend units are in Fig. 2.

7.2. Changes in fluid regime in the south Pyrenean fold and thrust belt from lower Eocene to lower Oligocene

The geochemical signatures of the calcite cements in the Lower Pedraforca thrust sheet, Vallfogona, Abocador and L'Escala thrusts, Ainsa Basin (Travé et al., 1997), Castillo Mayor klippe and Jaca thrust (Lacroix et al., 2014), El Guix anticline (Travé et al., 2000) and Puigreig anticline (Cruset et al., 2016) with respect to their timing of precipitation (Fig. 11) highlights that hydrothermal fluids have migrated along the south Pyrenean fold and thrust belt from the lower Eocene to lower Oligocene (Fig. 12).

From the lower to middle Eocene, hydrothermal fluids migrated during thrusting along reverse faults, strike-slip faults and joints from the crystalline basement to the syn-orogenic marine sediments deposited in the foreland basin (Fig. 12). During this period, hydrothermal fluids mixed with connate marine waters expelled from rock porosity by sediment compaction during the early stages of evolution of the foreland basin (Bitzer et al., 2001). The resultant fluid had a sulfur isotope composition in equilibrium with Eocene marine waters (Travé et al., 1997), high Fe and Sr contents (Fig. 6), enriched $\delta^{18}O$ (Fig. 7) and had $^{87}Sr/^{86}Sr$ ratios slightly higher than Eocene seawater (Fig. 10).

From the middle Eocene to lower Oligocene, as the foreland basin changed from underfilled to overfilled, the thrust front progressively emerged from deep water to endorheic domains (Figs. 11 and 12). The relative sea-level fall and related change in topographic elevation initiated topography-driven fluid flow (Bitzer et al., 2001) and as a consequence, the influence of meteoric waters, that mixed at depth with hydrothermal ascending fluids, increased progressively and changed the fluid composition (Fig. 12). This change in fluid flow conditions is reflected in the progressive decrease in Fe and Sr contents (Fig. 6), temperature (Table 1), depletion in $\delta^{18}O$ (Fig. 7) and high $^{87}Sr/^{86}Sr$ ratios with respect calcite cements precipitated previously (Fig. 10). However, in other areas such as the Abocador thrust, El Guix anticline (Travé et al., 2000) and the Sierras Exteriores and Larra/Eaux-chaudes thrust (Beaudoin et al., 2015; Crognier, 2016; Crognier et al., 2017), brines derived from the underlying thick evaporite units interacted with hydrothermal and meteoric fluids and controlled fluid composition even when these structures grew under continental conditions.

Assuming that hydrothermal fluid flow was continuous during the activity of the studied structures, the minimum fluid flow rate has been roughly estimated considering that fluids migrated from the basement hanging-wall cut-off to the frontal part of the Lower Pedraforca thrust sheet (30 km), the Vallfogona thrust (20 km where it has been studied; Fig. 2A), the Abocador thrust (24 km) and the L'Escala thrust (24 km) during 6, 11, 5 and 8 Ma, respectively. These ranges of time are based on magnetostratigraphy and $^{40}Ar/^{39}Ar$ dating on authigenic illite on fault planes (Vergés, 1993; Haines, 2008). Thus, for the Lower Pedraforca thrust sheet and the Abocador thrust, a minimum fluid flow rate of 5 km Ma^{-1} is obtained, whereas for the Vallfogona and the L'Escala thrusts the minimum calculated rate is 2 and 3 km Ma^{-1}, respectively. These values are consistent with the lowest rates calculated in other forelands such as in the Canadian and eastern Venezuelan foothills (Schneider, 2003) and in the Bighorn Basin (Beaudoin et al., 2014). This large-scale migration of hydrothermal fluids along the south Pyrenean fold and thrust belt was probably controlled by different driving forces such as squeegee-type fluid flow, which induces rates between 1 and 100 km Ma^{-1} (Ge and Garven, 1989) but only during short time periods (Schneider, 2003), coupled with topography and thermal gradients (Lyubetskaya and Ague, 2009).

7.3. Conceptual model of fluid flow in fold and thrust belts

The fluid flow model established for the southern Pyrenees in the previous section together with previous works done by other authors in other orogens worldwide (Ferket et al., 2000; Van Geet et al., 2002; Breesch, 2008; Vilasi, 2010; Vandeginste et al., 2012; Dewever et al., 2013), indicate that the presence or absence of thick evaporitic units highly control the final fluid composition. In all cases, ascending hydrothermal fluids mixed with low-temperature meteoric fluids (Fig. 13).

However, whereas in thrust sheets not detached along evaporite units (Fig. 13a), the mixed fluid was progressively more depleted in $\delta^{18}O$ and had lower Fe and Sr contents with respect to the former, not mixed, hydrothermal fluid (Fig. 13a), in thrust sheets detached along evaporite successions (Fig. 13b), brines derived from these evaporites were responsible for the $\delta^{18}O$ enrichment of the mixed fluid, without a systematic increase in Fe and Sr contents (Warren, 2006).

The trend from high $\delta^{18}O$ to more depleted values along with, where documented, the progressive decrease in Fe and Sr contents (Fig. 13a) during the emersion of the thrust front has been observed in the Vallfogona and L'Escala thrust, Ainsa Basin (Travé et al., 1997), Veracruz Basin (Ferket et al., 2000), North Oman Mountains (Breesch, 2008), south Ionian zone (Vilasi, 2010), Canadian Rocky Mountains (Vandeginste et al., 2012), Bighorn Basin (Beaudoin et al., 2011, 2014), Castillo Mayor klippe and Jaca thrust (Lacroix et al., 2014) and Puig-reig anticline (Cruset et al., 2016), which are structures not detached through thick evaporite units. As these structures emerged, the input of oxidizing meteoric waters depleted in Sr controlled the decrease in Fe content (Froelich et al., 1979; Tucker and Wright, 1990), whereas their mixing with hydrothermal fluids induced $\delta^{18}O$ depletion (Immenhauser et al., 2007). The trend from low $\delta^{18}O$ to more enriched values (Fig. 13b) has been observed in the Abocador thrust, El Guix anticline (Travé et al., 2000), Central Ionian Zone (Van Geet et al., 2002), Sicilian fold and thrust belt (Dewever et al., 2013), Sierras Exteriores (Beaudoin et al., 2015; Crognier et al., 2015; Crognier, 2016) and Larra/Eaux chaudes thrust (Crognier et al., 2017), where thrusts are detached along thick evaporitic units. In the Iudica-Scalpello area (Sicilian fold and thrust belt), based on the low salinity of the fluid inclusions, this trend is explained by smectite-illite transformations (Dewever et al., 2013).

8. Conclusions

A multidisciplinary study has been carried out to determine the changes in fluid regime and composition during the growth of the south Pyrenean fold and thrust belt from lower Eocene to lower Oligocene.

Integration of petrographic and geochemical data obtained from fracture-filling calcite cements reveals that hydrothermal fluids migrated from the Axial zone of the Pyrenees to its related foreland basin during Paleogene compression.

From Lower to Middle Eocene, ascending hydrothermal fluids migrated from the Axial zone to the foreland basin and mixed with connate marine waters trapped in rock porosity. The mixed fluid had temperatures up to 154 °C, enriched $\delta^{18}O$, $^{87}Sr/^{86}Sr$ slightly higher than Eocene seawater and high Fe and Sr contents. From Middle Eocene to Lower Oligocene, as the thrust front progressively emerged, meteoric waters migrated downwards the foreland basin by topography-driven fluid flow and mixed at depth with the hydrothermal fluids. The mixed fluid was progressively more depleted in $\delta^{18}O$, with temperatures between 77 and 129 °C, lower Fe and Sr contents and more radiogenic $^{87}Sr/^{86}Sr$ ratios than the former fluid.

The comparison of southern Pyrenees to other orogens worldwide, suggests that the presence or absence of thick evaporitic units had a fundamental role in the fluid composition during fold and thrust belt evolution. In all cases, hydrothermal fluids migrated along fractures within thrust sheets and mixed with low-temperature meteoric waters. When thrusts were not detached through thick evaporite units, the resultant fluid was progressively more radiogenic, more depleted in $\delta^{18}O$ and had a lower temperature and lower Sr and Fe content, as the thrust front emerged. In contrast, when thrusts were detached along thick evaporitic units, the resulting fluid was enriched in $\delta^{18}O$.

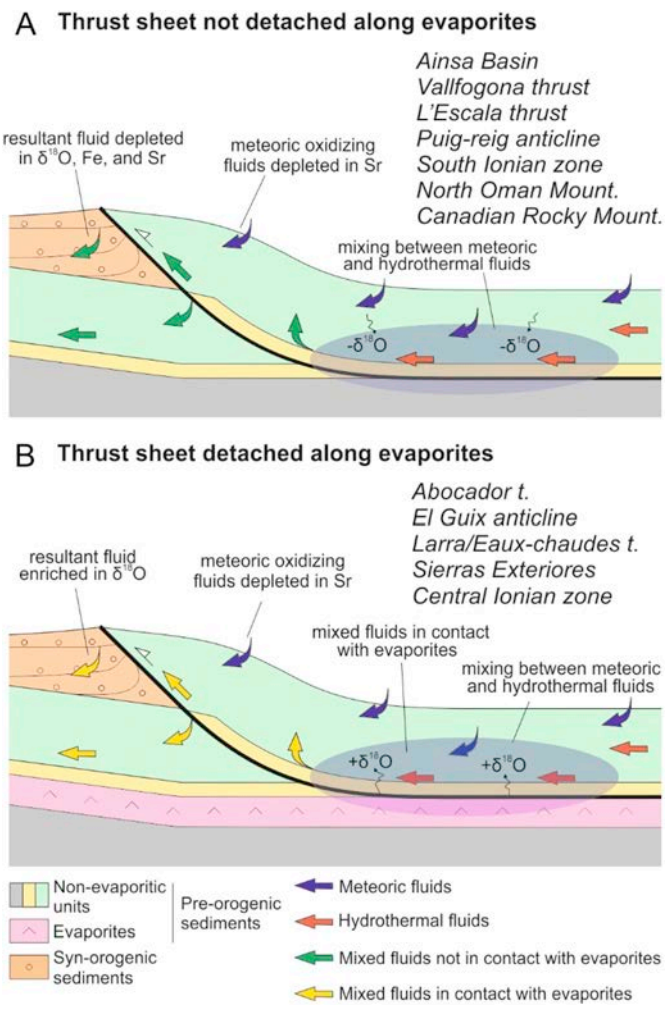

Fig. 13. Sketches of two possible scenarios for fluid flow regime in fold and thrust belts. A) Thrust sheet not detached through evaporites. B) Thrust sheet detached through evaporites. Not to scale.

Acknowledgements

The isotopic and electron microprobe analyses were carried out at "Centres Científics i Tecnològics" of the Universitat de Barcelona. Strontium analyses were done at the "CAI de Geocronología y Geoquímica Isotópica (UCM-CEI)" of the Universidad Complutense de Madrid. The clumped isotopes analyses were performed in the Qatar Stable Isotope Laboratory of Imperial College of London. This research was performed within the framework of DGICYT Spanish Project CGL2015-66335-C2-1-R and ALPIMED Project (PIE-CSIC-201530E082), Grup Consolidat de Recerca "Geologia Sedimentària" (2014SGR-251). We thank Pierre Labaume and Nicolas Beaudoin for their constructive reviews which highly improved the quality of the manuscript.

Appendix A. Supplementary data

Supplementary data to this article can be found online at https://doi.org/10.1016/j.gloplacha.2017.11.001.

References

Banks, D.A., Davies, G.R., Yardley, B.W.D., McCaig, A.M., Grant, N.T., 1991. The chemistry of brines from an Alpine thrust system in the Central Pyrenees: an application of fluid inclusion analysis to the study of fluid behavior in orogenesis. Geochim. Cosmochim. Acta 55, 1021–1030.

Banner, J.L., 1995. Application of the trace element and isotope geochemistry of strontium to studies of carbonate diagenesis. Sedimentology 42, 805–824.

Banner, J.L., Hanson, G.N., 1990. Calculation of simultaneous isotopic and trace element variations during water-rock interaction with applications to carbonate diagenesis. Geochim. Cosmochim. Acta 54, 3123–3137.

Beamud, E., Muñoz, J.A., Fitzgerald, P.G., Baldwin, S.L., Garcés, M., Cabrera, L., Metcalf,

J.R., 2010. Magnetostratigraphy and detrital apatite fission track thermochronology in syntectonic conglomerates: constraints on the exhumation of the South-Central Pyrenees. Basin Res. 23 (3), 309–331.
Beaudoin, N., Bellahsen, N., Lacombe, O., Emmanuel, L., 2011. Fracture-controlled paleohydrogeology in a basement-cored, fault-related fold: Sheep Mountain Anticline, Wyoming, United States. Geochem. Geophys. Geosyst. 12 (6), 1–15.
Beaudoin, N., Bellahsen, N., Lacombe, O., Emmanuel, L., Pironon, J., 2014. Crustal-scale fluid flow during the tectonic evolution of the Bighorn Basin (Wyoming, USA). Basin Res. 26 (3), 403–435.
Beaudoin, N., Huyghe, D., Bellahsen, N., Lacombe, O., Emmanuel, L., Mouthereau, F., Ouanhnon, L., 2015. Fluid systems and fracture development during syn-depositional fold growth: an example from the Pico del Aguila anticline, Sierras Exteriores, southern Pyrenees, Spain. J. Struct. Geol. 70, 23–38.
Bitzer, K., Travé, A., Carmona, J.M., 2001. Fluid flow processes at basin scale. Acta Geol. Hisp. 36 (1–2), 1–20.
Bradbury, H.J., Woodwell, G.R., 1987. Ancient fluid flow within foreland terrains. In: Goff, J.C., Williams, B.P.J. (Eds.), Fluid Flow in Sedimentary Basins and Aquifers. Geological Society Special Publicationpp. 87–102.
Breesch, L., 2008. Diagenesis and Fluid System Evolution in the Northern Oman Mountains, United Arab Emirates (PhD thesis). Katholieke Universiteit Leuven, Leuven, Belgium (159 pp.).
Breesch, L., Swennen, R., Vincent, B., 2009. Fluid flow reconstruction in hanging and footwall carbonates: compartmentalization by Cenozoic reverse faulting in the Northern Oman Mountains (UAE). Mar. Pet. Geol. 26, 113–128.
Burbank, D.W., Puigdefàbregas, C., Muñoz, J.A., 1992a. The chronology of the Eocene tectonic and stratigraphic development of the Eastern Pyrenean Foreland Basin. NE Spain. Geol. Soc. Am. Bull. 104, 1101–1120.
Burbank, D.W., Vergés, J., Muñoz, J.A., Bentham, P., 1992b. Coeval hindward- and forward-imbricating thrusting in the south-central Pyrenees, Spain: timing and rates of shortening and deposition. Geol. Soc. Am. Bull. 104, 3–17.
Caja, M.A., Permanyer, A., 2008. Significance of organic matter in Eocene turbidite sediments (SE Pyrenees, Spain). Naturwissenschaften 9, 1073–1077.
Caja, M.A., Permanyer, A., Marfil, R., Al-Asm, I.S., Martín-Crespo, T., 2006. Fluid flow record from fracture-fill calcite in the Eocene limestones from the South-Pyrenean Basin (NE Spain) and its relationship to oil shows. J. Geochem. Explor. 89, 27–32.
Carrigan, J.H., Anastasio, D.J., Kodama, K.P., Parés, J.M., 2016. Fault-related fold kinematics recorded by terrestrial growth strata, Sant Llorenç de Morunys, Pyrenees Mountains, NE Spain. J. Struct. Geol. 91, 161–176.
Carrillo, E., 2012. The Evaporites of the Southeastern Pyrenean Basin (Late Cuisian–Lutetian): Sedimentology and Structure (PhD Thesis). University of Barcelona, Barcelona, Spain (192 pp.).
Carter, N.L., Kronenberg, A.K., Ross, J.V., Wiltschko, D.V., 1990. Control of fluids on deformation of rocks. In: Knipe, R.J., Rutter, E.H. (Eds.), Deformation Mechanisms, Rheology and Tectonics. Geological Society, London, Special Publicationspp. 1–13.
Casini, G., Gillespie, P.A., Vergés, J., Romaire, I., Fernández, N., Casciello, E., Saura, E., Mehl, C., Homke, S., Embry, J.-C., Aghajari, L., Hunt, D.W., 2011. Sub-seismic fractures in foreland fold and thrust belts: insight from the Lurestan Province, Zagros Mountains, Iran. Pet. Geosci. 17, 263–282.
Cerling, T.E., Quade, J., Wang, Y., Bowman, J.R., 1989. Carbon isotopes in soils and palaeosols as ecology and palaeoecology indicators. Nature 341, 138–139.
Choukroune, P., team, E, 1989. The ECORS Pyrenean deep seismic profile reflection data and the overall structure of an orogenic belt. Tectonics 8, 23–39.
Clavell, E., 1992. Geologia del petroli de les conques terciàries de Catalunya (PhD thesis). University of Barcelona (488 pp.).
Claypool, G.E., Kaplan, W.T., Kaplan, I.R., Sakai, H., Zak, I., 1980. The age curves of sulfur and oxygen isotopes in marine sulfate and their mutual interpretations. Chem. Geol. 28, 199–260.
Costa, E., Garcés, M., López-Blanco, M., Beamud, E., Gómez-Paccard, M., Larrasoaña, J.C., 2010. Closing and continentalization of the South Pyrenean foreland basin (NE Spain): magnetochronological constraints. Basin Res. 22 (6), 904–917.
Craig, H., Gordon, I.-I., 1965. Deuterium and oxygen-18 variations in the ocean and the marine atmosphere. In: Tongiorgi, E. (Ed.), Proceedings of a Conference on Stable Isotopes in Oceanographic Studies and Paleotemperatures. Consiglio Nazionale delle Richerche, Laboratorio di Geologia Nucleare, Pisa, Italy, pp. 9–130.
Crognier, N., 2016. Évolution thermique, circulation de fluides et fracturation associées à la structuration du bassin d'avant-pays sud-pyrénéen (PhD thesis). Universitéde Pau, Pau, France (329 pp.).
Crognier, N., Hoareau, G., Lacroix, B., Aubourg, C., Dubois, M., Lahfid, A., Labaume, P., Suarez-Ruiz, I., 2015. Thermicity and Fluid Flow Related to the Evolution of the South Pyrenean Foreland Basin (SPFB). EGU General Assembly, Vienna, Austria.
Crognier, N., Hoareau, G., Aubourg, C., Dubois, M., Lacroix, B., Branellec, M., Callot, J.P., Vennemann, T., 2017. Syn-orogenic fluid flow in the Jaca basin (south Pyrenean fold and thrust belt) from fracture and vein analyses. Basin Res. 1–30.
Cruset, D., Cantarero, I., Travé, A., Vergés, J., John, C.M., 2016. Crestal graben fluid evolution during growth of the Puig-reig anticline (South Pyrenean fold and thrust belt). J. Geodyn. 101, 30–50.
Dale, A., John, C.M., Mozley, P.S., Smalley, P.C., Muggeridge, A.H., 2014. Time-capsule concretions: unlocking burial diagenetic processes in the Mancos Shale using carbonate clumped isotopes. Earth Planet. Sci. Lett. 394, 30–37.
Dennis, K.J., Affeck, H.P., Passey, B.H., Schrag, D.P., Eiler, J.M., 2011. Defining an absolute reference frame for 'clumped' isotope studies of CO_2. Geochim. Cosmochim. Acta 75 (22), 7117–7131.
Dewaele, D., Muchez, P., Banks, D.A., 2004. Fluid evolution along multistage composite fault systems at the southern margin of the Lower Palaeozoic Anglo-Brabant fold belt, Belgium. Geofluids 4, 341–356.
Dewever, B., 2008. Diagenesis and Fluid Flow in the Sicilian Fold-and-Thrust Belt (PhD thesis). Katholieke Universiteit Leuven, Leuven, Belgium (183 pp.).
Dewever, B., Swennen, R., Breesch, L., 2013. Fluid flow compartmentalization in the Sicilian fold and thrust belt: implications for the regional aqueous fluid flow and oil migration history. Tectonophysics 591, 194–209.
Evans, M.A., Fischer, M.P., 2012. On the distribution of fluids in folds: a review of controlling factors and processes. J. Struct. Geol. 44, 2–24.
Evans, M.A., Bebeout, G.E., Brown, C.H., 2012. Changing fluid conditions during folding: an example from the central Appalachians. Tectonophysics 576-577, 99–115.
Ferket, H., Roure, F., Swennen, R., Ortuño, S., 2000. Fluid migration placed into the deformation history of fold-and-thrust belts: an example from the Veracruz basin (Mexico). J. Geochem. Explor. 69-70, 275–279.
Fischer, M.P., Kenroy, P.R., Smith, A.P., 2013. Fluid systems around salt diapirs. In: AAPG Annual Convention and Exhibition, Pittsburgh, Pennsylvania, May 19–22, 2013.
Fontana, S., Nader, F.H., Morad, S., Ceriani, A., Al-Aasm, I.S., Daniel, J.-M., Mengus, J.-M., 2014. Fluid–rock interactions associated with regional tectonics and basin evolution. Sedimentology 61 (3), 660–690.
Friedman, I., O'Neil, J.R., 1977. In: Fleischer, M. (Ed.), Compilation of stable isotope fractionation factors of geochemical interest. Data of Geochemistry, U. S. Gov. Print. Off, Washington D. C, pp. 1–12.
Froelich, P.N., Klinkhammer, G.P., Bender, M.L., Luedtke, N.A., Heath, G.R., Cullen, D., Dauphin, P., Hammond, D., Hartman, B., Maynard, V., 1979. Early oxidation of organic matter in pelagic sediments of the eastern equatorial Atlantic: suboxic diagenesis. Geochim. Cosmochim. Acta 43, 1075–1090.
Ge, S., Garven, G., 1989. Tectonically induced transient groundwater flow in foreland basin. In: Price, R.A. (Ed.), Origin and Evolution of Sedimentary Basins and Their Energy and Mineral Resources. American Geophysical Union, pp. 145–157.
Van Geet, M., Swennen, R., Durmishi, C., Roure, F., Muchez, P., 2002. Paragenesis of Cretaceous to Eocene carbonate reservoirs in the Ionian fold and thrust belt (Albania): relation between tectonism and fluid flow. Sedimentology 49, 697–718.
Gomez-Rivas, E., Corbella, M., Martín-Martín, J.D., Stafford, S.L., Teixell, A., Bons, P.D., Griera, A., Cardellach, E., 2014. Reactivity of dolomitizing fluids and Mg source evaluation of fault-controlled dolomitization at the Benicàssim outcrop analogue (Maestrat Basin, E Spain). Mar. Pet. Geol. 55, 26–42.
Guo, W., Mosenfelder, J.L., Goddard, W.A., Eiler, J.M., 2009. Isotopic fractionations associated with phosphoric acid digestion of carbonate minerals: insights from first-principles theoretical modeling and clumped isotope measurements. Geochim. Cosmochim. Acta 73 (24), 7203–7225.
Haines, S.H., 2008. Transformations in Clay-rich Fault Rocks: Constraining Fault Zone Processes and the Kinematic Evolution of Regions (PhD thesis). University of Michigan, Ann Arbor, U.S (295 pp.).
Hausegger, S., Kurz, W., Rabitsch, R., Kiechl, E., Brosch, F.-J., 2010. Analysis of the internal structure of a carbonate damage zone: implications for the mechanisms of fault breccia formation and fluid flow. J. Struct. Geol. 32 (9), 1349–1362.
Heydari, E., 1997. Hydrotectonic models of burial diagenesis in platform carbonates based on formation water geochemistry in North American sedimentary basins. In: Montañez, I.P., Gregg, J.M., Shelton, K.L. (Eds.), Basin-wide Diagenetic Patterns: Integrated Petrologic, Geochemical, and Hydrologic Considerations. Society of Economic Paleontologists and Mineralogists, Special Publication Vol. 57. pp. 53–79.
Huntington, K.W., Eiler, J.M., Affek, H.P., Guo, W., Boniface, M., Yeung, L.Y., Thiagarajan, N., Passey, B., Tripati, A., Daëron, M., Came, R., 2009. Methods and limitations of 'clumped' CO_2 isotope ($\Delta 47$) analysis by gas-source isotope ratio mass spectrometry. J. Mass Spectrom. 44 (9), 1318–1329.
Immenhauser, A., Dublyansky, Y.V., Verwer, K., Fleitman, D., Pashenko, S.E., 2007. Textural, elemental and isotopic characteristics of Pleistocene phreatic cave deposits (Jabal Madar, Oman). J. Sediment. Res. 77 (1–2), 68–88.
Irwin, H., Curtis, C., Coleman, M., 1977. Isotopic evidence for source of diagenetic carbonates formed during burial of organic-rich sediments. Nature 269, 209–213.
John, C.M., Bowen, D., 2016. Community software for challenging isotope analysis: first applications of "Easotope" to clumped isotopes. Rapid Commun. Mass Spectrom. 30 (21), 2285–2300.
Kim, S.T., O'Neil, J.R., 1997. Equilibrium and nonequilibrium oxygen isotope effects in synthetic carbonates. Geochim. Cosmochim. Acta 61 (16), 3461–3475.
Kluge, T., John, C.M., Jourdan, A.L., Davis, S., Crawshaw, J., 2015. Laboratory calibration of the calcium carbonate clumped isotope thermometer in the 25–250 °C temperature range. Geochim. Cosmochim. Acta 157, 213–227.
Labaume, P., Meresse, F., Joliver, M., Teixell, A., Lahfid, A., 2016. Tectonothermal history of an exhumed thrust-sheet-top basin: an example from the south Pyrenean thrust belt. Tectonics 35, 1280–1313.
Lacroix, B., Buatier, M., Labaume, P., Travé, A., Dubois, M., Charpentier, D., Ventalon, S., Convert-Gaubier, D., 2011. Microtectonic and geochemical characterization of thrusting in a foreland basin: example of the South-Pyrenean orogenic wedge (Spain). J. Struct. Geol. 33, 1359–1377.

Lacroix, B., Travé, A., Buatier, M., Labaume, P., Vennemann, T., Dubois, M., 2014. Syntectonic fluid-flow along thrust faults: example of the South-Pyrenean fold-and-thrust belt. Mar. Pet. Geol. 49, 84–98.
Lipsey, L., Pluymaekers, M., Goldberg, T., Oversteeg, K.v., Ghazaryan, L., Cloetingh, S., Wees, J.-D.V., 2016. Numerical modelling of thermal convection in the Luttelgeest carbonate platform, the Netherlands. Geothermics 64, 135–151.
López-Martínez, N., Fernández-Marrón, M.T., Valle, M.F., 1999. The succession of vertebrates and plants across the Cretaceous-Tertiary boundary in the Tremp Formation, Ager valley (south-central Pyrenees, Spain). Geobios 32 (4), 617–627.
Lyubetskaya, T., Ague, J.J., 2009. Modeling the magnitudes and directions of regional metamorphic fluid flow in collisional orogens. J. Petrol. 50 (8), 1505–1531.
Machel, H.G., Cavell, P.A., 1999. Low-flux, tectonically-induced sequeegee fluid flow ("hot flash") into the Rocky Mountain Foreland Basin. Bull. Can. Petrol. Geol. 47 (4), 510–533.
Marker, D., Burkhard, M., 1992. Fluid circulation, progressive deformation and mass-transfer processes in the upper crust: the example of basement-cover relationships in the External Crystalline Massifs, Switzerland. J. Struct. Geol. 14 (8–9), 1047–1057.
Mató, E., Saula, E., Martínez-Rius, A., Muñoz, J.A. and Escuer, J., 1994. Memoria de la Hoja n° 293 (Berga). Mapa Geológico de España E. 1:50.000 (MAGNA), Segunda Serie, Primera Edición. IGME, 66.
McArthur, J.M., Howarth, R.J., Bailey, T.R., 2001. Strontium isotope stratigraphy: LOWESS version 3: best fit to the marine Sr-isotope curve for 0–509 Ma and accompanying look-up table for deriving numerical age. J. Geol. 109, 155–170.
McCaig, A.M., 1988. Deep fluid circulation in fault zones. Geology 16, 867–870.
McCaig, A.M., Wayne, D.M., Marshall, J.D., Banks, D., Henderson, I., 1995. Isotopic and fluid inclusion studies of fluid movement along the Gavarnie Thrust, central Pyrenees: reaction fronts in carbonate mylonites. Am. J. Sci. 295, 309–343.
McCrea, J.M., 1950. On the isotopic chemistry of carbonates and a paleotemperature scale. J. Chem. Phys. 18, 849–957.
Mey, P.H.W., Nagtegaal, P.J.C., Roberti, K.J., Hartevelt, J.J.A., 1968. Lithostratigraphic subdivision of post-Hercinian deposits in the south-central Pyrenees, Spain. Leidse. Geol. Meded. 41, 21–228.
Meyers, W.J., Lohmann, K.C., 1985. Isotope geochemistry of regionally extensive calcite cement zones and marine components in Mississipian limestones, New Mexico. In: Harris, O.M., Schneidermann, N. (Eds.), Carbonate Cements SEPM, Special Publications, pp. 223–239.
Morrow, D.W., 1998. Regional subsurface dolomitization: models and constraints. Geosci. Can. 25, 57–70.
Moya, S., Ramos-Guerrero, E., Agustí, J., Checa, L., 1991. Depositos lacustre-palustres asociados a las zonas intermedias de la Fm. Bellmunt (Prepirineo catalán). In: I Congreso del Grupo Español del Terciatrio. Comunicaciones, pp. 225–228.
Muñoz, J.A., 1992. Evolution of a continental collision belt: ECORS–Pyrenees crustal balanced section. In: McClay, K.R. (Ed.), Thrust Tectonics. Chapman & Hall, London, pp. 235–246.
Muñoz, J.A., 2002. The Pyrenees. In: Gibbons, W., Moreno, T. (Eds.), The Geology of Spain. Geological Society, London, pp. 370–385.
Muñoz, J.A., Martínez, A., Vergés, J., 1986. Thrust sequences in the eastern Spanish Pyrenees. J. Struct. Geol. 8 (3–4), 399–405.
Oliver, J., 1986. Fluids expelled tectonically from orogenic belts: their role in hydrocarbon migration and other geologic phenomena. Geology 14, 99–102.
Oms, O., Dinarés-Turell, J., Vicens, E., Estrada, R., Vila, B., Galobart, À., Bravo, A.M., 2007. Integrated stratigraphy from the Vallcebre Basin (southeastern Pyrenees, Spain): new insights on the continental Cretaceous – Tertiary transition in southwest Europe. Palaeogeogr. Palaeoclimatol. Palaeoecol. 255, 35–47.
Person, M., Raffensperger, J.P., Ge, S., Garven, G., 1996. Basin-scale hydrogeologic modeling. Rev. Geophys. 34, 61–87.
Pollyea, R.M., Dusen, E.W.V., Fischer, M.P., 2015. Topography driven fluid flow within orogenic wedges: effects of taper angle and depth-dependent permeability. Geosphere 11 (5), 1–11.
Puigdefàbregas, C., Muñoz, J.A., Marzo, M., 1986. Thrust belt development in the Eastern Pyrenees and related depositional sequences in the Southern Foreland Basin. In: Allen, P.A., Homewood, P. (Eds.), Foreland Basins. Blackwell Publishing Ltd., Oxford, UK, pp. 229–246.
Puigdefàbregas, C., Muñoz, J.A., Vergés, J., 1992. Thrusting and foreland basin evolution in the Southern Pyrenees. In: McClay, K.R. (Ed.), Thrust Tectonics. Chapman & Hall, London, pp. 247–254.
Qing, H., Mountjoy, E., 1992. Large-scale fluid flow in the Middle Devonian Presqu'ile barrier, Western Canada Sedimentary Basin. Geology 20, 903–906.
Reynolds, S.J., Lister, G.S., 1987. Structural aspects of fluid-rock interactions in detachment zones. Geology 15, 362–366.
Rodríguez-Morillas, N., Playà, E., Travé, A., Martín-Martín, J.D., 2013. Diagenetic processes in a partially dolomitized carbonate reservoir: Casablanca oil field, Mediterranean Sea, offshore Spain. Geol. Acta 11 (2), 195–214.
Rosell, J., Linares, R., Llompart, C., 2001. El "Garumniense" prepirenaico. Rev. Soc. Geol. Esp. 14 (1–2), 47–56.
Roure, F., Choukroune, P., Berastegui, J., Muñoz, J.A., Villien, A., Matheron, P., Bareyt, M., Seguret, M., Camara, P., Deramond, J., 1989. Ecors deep seismic data and balanced cross sections: geometric constraints on the evolution of the Pyrenees. Tectonics 8 (1), 41–50.
Roure, F., Swennen, R., Schneider, F., Faure, J.L., Ferket, H., Guilhaumou, N., Osadetz, K., Robion, P., Vandeginste, V., 2005. Incidence and importance of tectonics and natural fluid migration on reservoir evolution in foreland fold-and-thrust belts. Oil Gas Sci. Technol. 60 (1), 67–106.
Roure, F., Andriessen, P., Callot, J.P., Faure, J.L., Ferket, H., Gonzales, E., Guilhaumou, N., Lacombe, O., Malandain, J., Sassi, W., Schneider, F., Swennen, R., Vilasi, N., 2010. The use of paleo-thermo-barometers and coupled thermal, fluid flow and pore-fluid pressure modelling for hydrocarbon and reservoir prediction in fold and thrust belts. In: Goffey, G.P., Craig, J., Needham, T., Scott, R. (Eds.), Hydrocarbons in Contractional Belts. Geological Society, London, Special Publicationspp. 87–114.
Sans, M., 2003. From thrust tectonics to diapirism. The role of evaporites in the kinematic evolution of the eastern South Pyrenean front. Geol. Acta 1 (3), 239–259.
Schneider, F., 2003. Basin modeling in complex area: examples from eastern Venezuelan and Canadian foothills. Oil Gas Sci. Technol. 58 (2), 313–324.
Séguret, M., 1972. Étude tectonique des nappes et séries décollées de la partie centrale du vesant sud des Pyrénées. Pub. USTELA, sér, Geol. Struct. n.2, Montpellier (155 pp.).
Serra-Kiel, J., Hottinger, L., Caus, E., Drobne, K., Ferràndez, C., Jauhri, A.K., Less, G., Pavlovec, R., Pignatti, J., Samsó, J.M., Schaub, H., Sirel, E., Strougo, A., Tamberau, Y., Tosquella, J., Zakrevskaya, E., 1998a. Larger foraminiferal biostratigraphy of the Tethyan Paleocene and Eocene. Bull. Soc. Geol. Fr. 169 (2), 281–299.
Serra-Kiel, J., Hottinger, L., Drobne, K., Ferràndez, C., Jauhri, A.K., Less, G., Pignatti, J., Samsó, J.M., Schaub, H., Sirel, E., Tamberau, Y., Tosquella, J., Zakrevskaya, E., 1998b. Larger benthic Foraminifera. In: Thierry, J., Farley, M.B., Jacquin, T., Graciansky, P.C., Vail, P.R. (Eds.), Mesozoic-Cenozoic Sequence Stratigraphy of European Basins. Society of Economic Paleontologist and Mineralogist, Special Publication (60 pp.).
Serra-Kiel, J., Travé, A., Mató, E., Saula, E., Ferràndez-Cañadell, C., Busquets, P., Tosquella, J., Vergés, J., 2003. Marine and Transitional Middle/Upper Eocene units of the Southeastern Pyrenean Foreland Basin (NE Spain). Geol. Acta 1 (2), 177–200.
Shackleton, J.R., Cooke, M.L., Sussman, A.J., 2005. Evidence for temporally changing mechanical stratigraphy and effects on joint-network architecture. Geology 33 (2), 101–104.
Sibson, R.H., Robert, F., Poulsen, K.H., 1988. High-angle reverse faults, fluid-pressure cycling, and mesothermal gold-quartz deposits. Geology 16, 551–555.
Swart, P.K., 2015. The geochemistry of carbonate diagenesis: the past, present and future. Sedimentology 62 (5), 1233–1304.
Swennen, R., Ferket, H., Benchilla, L., Roure, F., Ellam, R., team, S, 2003. Fluid flow and diagenesis in carbonate dominated foreland fold and thrust belts: petrographic inferences from field studies of late-diagenetic fabrics from Albania, Belgium, Canada, Mexico and Pakistan. J. Geochem. Explor. 78-79, 481–485.
Taylor, B.E., 1987. Stable isotope geochemistry of ore-forming fluids. In: Kyser, T.K. (Ed.), Short Course in Stable Isotope Geochemistry of Low Temperature Fluids. Mineral Association of Canada, pp. 337–418.
Tindall, J., Flecker, R., Valdes, P., Schmidt, D.N., Markwick, P., Harris, J., 2010. Modelling the oxygen isotope distribution of ancient seawater using a coupled ocean–atmosphere GCM: implications for reconstructing early Eocene climate. Earth Planet. Sci. Lett. 292, 265–273.
Travé, A., Labaume, P., Calvet, F., Soler, A., 1997. Sediment dewatering and pore fluid migration along thrust faults in a foreland basin inferred from isotopic and elemental geochemical analyses (Eocene southern Pyrenees, Spain). Tectonophysics 282 (1–4), 375–398.
Travé, A., Labaume, P., Calvet, F., Soler, A., Tritlla, J., Bautier, M., Potdevin, J.L., Séguret, M., Raynaud, S., Briqueu, L., 1998. Fluid migration during Eocene thrust emplacement in the south Pyrenean foreland basin (Spain): an integrated structural, mineralogical and geochemical approach. In: Mascle, A., Puigdefàbregas, C., LuterBacher, H.P., Fernàndez, M. (Eds.), Cenozoic Foreland Basins of Western Europe. Geological Society, Special Publicationspp. 163–188.
Travé, A., Calvet, F., Sans, M., Vergés, J., Thirlwall, M., 2000. Fluid history related to the Alpine compression at the margin of the south-Pyrenean Foreland basin: the El Guix anticline. Tectonophysics 321, 73–102.
Travé, A., Calvet, F., Salas, R., Playà, E., 2004. Fluid flow during Paleogene Compression in the Linking Zone Fold and Thrust Belt (Northeast Spain). In: Swennen, R., Roure, F., Granath, J.W. (Eds.), Deformation, Fluid Flow, and Reservoir Appraisal in Foreland Fold and Thrust Belts. AAPG Hedberg Seriespp. 215–243.
Travé, A., Labaume, P., Vergés, J., 2007. Fluid systems in foreland fold and thrust belts: an overview from the Southern Pyrenees. In: Lacombe, O., Lavé, J., Roure, F., Vergés, J. (Eds.), Thrust Belts and Foreland Basins: From Fold Kinematics to Hydrocarbon Systems. Springer, pp. 93–115.
Tucker, M.E., Wright, P.V., 1990. Carbonate Sedimentology. Blackwell, Oxford (482 pp.).
Valero, L., Garcés, M., Cabrera, L., Costa, E., Sáez, A., 2014. 20 Myr of eccentricity paced lacustrine cycles in the Cenozoic Ebro Basin. Earth Planet. Sci. Lett. 408, 183–193.
Vandeginste, V., Swennen, R., Allaeys, M., Ellam, R.M., Osadetz, K., Roure, F., 2012. Challenges of structural diagenesis in foreland fold-and-thrust belts: a case study on paleofluid flow in the Canadian Rocky Mountains west of Calgary. Mar. Pet. Geol. 35 (1), 235–251.
Vergés, J., 1993. Estudi geològic del vessant sud del Pirineu oriental i central. Evolució cinemàtica en 3D (PhD thesis). Universitat de Barcelona, Barcelona, Spain (203 pp.).
Vergés, J., Burbank, D.W., 1996. Eocene-Oligocene thrusting and basin configuration in the eastern and central Pyrenees (Spain). In: Friend, P., Dabrio, C. (Eds.), Tertiary Basins of Spain. Cambridge University, World and Regional Geology Vol. E11. pp. 120–133.
Vergés, J., Muñoz, J.A., 1990. Thrust sequences in the southern central Pyrenees. Bull. Soc. Geol. Fr. 8 (6), 265–271.
Vergés, J., Martínez, A., Muñoz, J.A., 1992. South Pyrenean fold and thrust belt: the role of foreland evaporitic levels in thrust geometry. In: McClay, K. (Ed.), Thrust Tectonics. Chapman & Hall, London, pp. 255–264.
Vergés, J., Millán, H., Roca, E., Muñoz, J.A., Marzo, M., Cirés, J., Bezemer, T.D., Zoetemeijer, R., Cloetigh, S., 1995. Eastern Pyrenees and related foreland basins: pre-, syn- and post-collisional cristal-scale cross-sections. Mar. Pet. Geol. 12 (8), 893–915.
Vergés, J., Marzo, M., Santaeulària, T., Serra-Kiel, J., Burbank, D.W., Muñoz, J.A., Giménez-Montsant, J., 1998. Quantified vertical motions and tectonic evolution of the SE Pyrenean foreland basin. In: Mascle, A., Puigdefàbregas, C., Luterbacher, H.P.,

Fernàndez, M. (Eds.), Cenozoic Foreland Basins of Western Europe. Geological Society Special Publicationspp. 107–134.
Vergés, J., Fernàndez, M., Martínez, A., 2002a. The Pyrenean orogen: pre-, syn-, and post-collisional evolution. In: Rosenbaum, G., Lister, G. (Eds.), Reconstruction of the Evolution of the Alpine-Himalayan Orogen. Journal of the Virtual Explorerpp. 55–74.
Vergés, J., Marzo, M., Muñoz, J.A., 2002b. Growth strata in foreland settings. Sediment. Geol. 146, 1–9.
Vilasi, N., 2010. Study of Reservoir Analogues in Foreland Fold-and-Thrust Belts: Sedimentology, Diagenesis, Deformation and Fracturing of the Upper Cretaceous-Eocene Carbonate Systems of the Ionian Zone (Southern Albania) (PhD thesis). Ecole des Mines de Paris, Paris, France (190 pp.).
Vilasi, N., Malandain, J., Barrier, L., Callot, J.P., Amrouch, K., Guilhaumou, N., Lacombe, O., Muska, K., Roure, F., Swennen, R., 2009. From outcrop and petrographic studies to basin-scale fluid flow modelling: the use of the Albanian natural laboratory for carbonate reservoir characterisation. Tectonophysics 474, 367–392.
Warren, J.K., 2006. Evaporites: Sediments, Resources and Hydrocarbons. Springer, Berlin Heidelberg.

Chapter 6

U-Pb geochronology applied to fracture-filling calcite cements to decipher emplacement and reactivation of SE Pyrenean thrust sheets

U-Pb geochronology applied to fracture-filling calcite cements to decipher emplacement and reactivation of SE Pyrenean thrust sheets

D. Cruset[1], J. Vergés[2], R. Albert[3], A. Gerdes[3], A. Benedicto[4], I. Cantarero[1], A. Travé[1]

[1] *Departament de Mineralogia, Petrologia i Geologia Aplicada, Facultat de Ciències de la Terra, Universitat de Barcelona (UB), Martí i Franquès s/n, 08028, Barcelona, Spain.*
d.cruset@ub.edu, i_cantarero@ub.edu, atrave@ub.edu

[2] *Institut de Ciències de la Terra Jaume Almera, ICTJA-CSIC, Lluís Solé i Sabaris s/n, 08028 Barcelona, Spain.*
jverges@ictja.csic.es

[3] *Department of Geosciences, Goethe University Frankfurt, 60438 Frankfurt am Main, Germany.*
gerdes@em.uni-frankfurt.de, albertroper@em.uni-frankfurt.de

[4] *UMR Geops, Université Paris Sud, 91405 Orsay, France.*
antonio.benedicto@u-psud.fr

Geology: In review

Abstract

Using U-Pb geochronology, we document 47 ages for the South Pyrenean fold and thrust belt. Results indicate that deformation migrated from the upper thrust sheets to the lower thrust units and to the foreland from 70.5 ± 1.1 Ma to 25 ± 17 Ma. These U-Pb ages also indicate that each of the thrust sheets registers its own deformational history as well as the history of the underlying thrust units emplaced during tectonic stacking. For instance, the Upper Pedraforca thrust sheet records the entire compressional history of the SE Pyrenees. Likewise, the wide distribution of U-Pb ages within each tectonic unit indicates that deformation was continuous rather than episodic. Calcite veins with Neogene ages ranging from 18.9 ± 0.8 Ma to 2.6 ± 1.3 Ma are interpreted as having been formed during the Neogene rift and post-rift Western Mediterranean events stretching across NE Iberia. These ages are the first evidence demonstrating deformation within the SE Pyrenees during these post-compressional events.

Introduction

Recent advances in geochronological techniques for dating fracture-filling minerals allow us to constrain their ages and therefore to date the activity of the fractures. Ar-Ar and Rb-Sr dating of authigenic illites formed in fault gouges are two of these dating methods (Van der Pluijm et al., 2001). However, these dating methods require the illites to have recrystallized at temperatures > 100 ºC and call for a complex process of clay fraction separation (Haines, 2008). Sm-Nd and U-

Th geochronology applied to calcites are also common dating methods, but samples need large Sm-Nd ratios, and in the case of the U-Th method, calcites must have formed in the last 6 $x10^5$ years (Flotté et al., 2001; Uysal., 2007; Pickering et al., 2017). U-Pb geochronology of fracture-filling calcites provides the best overall results for deciphering the timing of polyphasic tectonic deformation. Recent dating studies using U-Pb geochronology on calcites have been performed in both tectonic extensional settings (Ring and Gerdes, 2016; Roberts and Walker, 2016) and compressional settings (Beaudoin et al., 2018; Hansman et al., 2018; Parrish et al., 2018) and have been used as well to constrain the diagenetic history of sedimentary basins (Pagel et al., 2018).

In fold and thrust belts, long-lasting deformation results in the development of multistage fractures and calcite cements (Travé et al., 1997; 2000; 2007; Roure et al. 2005; Cosgrove, 2015), which record continuous or episodic deformation during the growth of orogens (Zhang et al., 2004; Fitz-Diaz et al., 2014). Therefore, U-Pb geochronology is an excellent method for dating the activity and emplacement of each tectonic unit, as well as later reactivation due to thrusting wedge propagation.

In this study we define the complete sequence of emplacement of the south Pyrenean thrust sheet stacking from a robust data set of 47 U-Pb ages obtained from the dating of 66 fracture-filling calcites for the first time. The results enable us to: 1) improve the accuracy of the sequence of deformation within the south Pyrenean thrust sheets by constraining the onset, duration and end of individual thrust motions; 2) decipher the potential overprinting of the Neogene extension affecting the NE of Iberia; and 3) determine if the south Pyrenean compression was continuous or episodic.

Geological setting

The south Pyrenean fold and thrust belt is a south-verging piggy-back thrust sequence emplaced from the Late Cretaceous through to the Oligocene, due to the collision between Iberia and Eurasia plates (Macchiavelli et al., 2017). In the SE Pyrenees, this sequence consists of the stacking of 3 thrust sheets north of the foreland basin (Fig. 1). From top-and-older to bottom-and-younger, these thrust sheets constitute the Bóixols-Upper Pedraforca (latest Cretaceous–Paleocene), the Lower Pedraforca (Paleocene–middle Eocene), and the Cadí (middle Eocene–late Oligocene) (e.g., Vergés et al., 2002a, b). These thrust sheets are composed of Mesozoic series and Paleogene syntectonic deposits. Upper Triassic evaporites at the base of the thrust sheets and syntectonic foreland evaporites constitute the detachment levels of these allochthonous units. The lowermost Cadí thrust sheet is linked to the Axial Zone antiformal stack formed by the Orri and Rialp basement thrusted units (Muñoz, 1992). The SE Pyrenean Eocene–Oligocene folded foreland basin was sampled in the Puig-reig anticline.

Calcite cements were collected from each thrust sheet and foreland basin (Fig. 1). The analyzed calcites precipitated in (Fig. 2): 1) N-S, NNW-SSE and NNE-SSW en-échelon vein

arrays, E-W folding-related veins, and normal faults associated with the internal deformation of thrust sheets and syn-orogenic sediments; 2) NW-SE and NE-SW strike-slip faults and E-W reverse faults formed within the main thrust fault zones; and 3) calcite cements precipitated between sedimentary breccia clasts. Fracture kinematic indicators are consistent with the N-S and NNW-SSE regional structural trends observed through the Pyrenees (Tavani et al., 2011; Cruset et al., 2016a; 2018; Nardini et al., 2019).

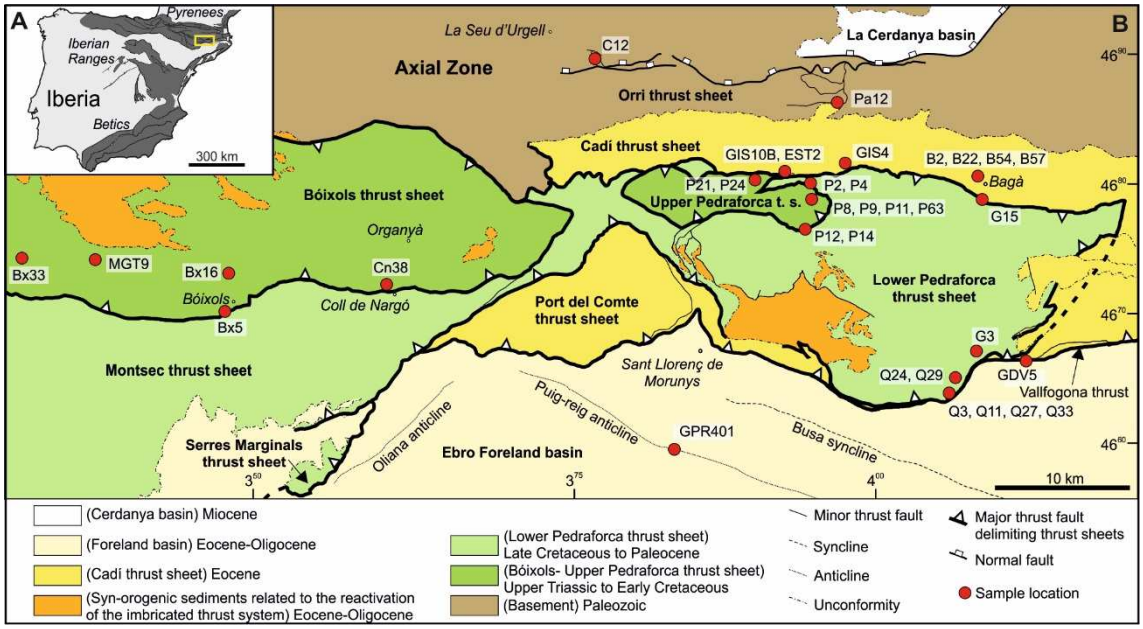

Fig.1. A) Simplified map of the Iberian Peninsula reporting the location of the Pyrenees and the studied area. B) Structural sketch of the studied area with the location of the studied structures and suitable samples for dating. For locations of samples which U-Pb dating failed refer to Table DR1 in the GSA Data repository[1].

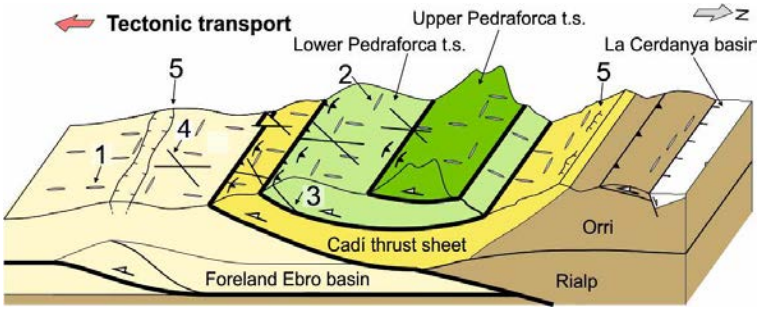

Fig.2 Sketch representing the fracture patterns targeted in this study: 1) En-échelon vein arrays; 2) Folding related veins; 3) Reverse faults; 4) Strike-slip faults; 5) Normal faults. For complementary details see Cruset et al., (2016a and 2018) and Nardini et al. (2019).

Methodology

The field work consisted of structural fracture network analysis (Cruset et al., 2016a; 2018; Nardini et al., 2019) and representative sampling of veins distributed within the internal part of thrust sheets and in folded syn-orogenic deposits, and veins belonging to damage zones of main reverse, strike-slip and normal faults. The textural characterization of fracture-filling calcites by means of petrographic observations shows that most of them precipitated coevally with fracturing (elongated sparite parallel or orthogonal to fracture walls). However, other textures, such as blocky sparite postdating elongated sparite, suggest late reactivation of fractures. 35 mounts from

66 samples were prepared for U-Pb geochronology, using a 193 nm ArF excimer laser coupled to an Element2 SF (sector field) ICP-MS. The laser parameters were: 213 µm spot, 12Hz and 2 J/cm2 of fluence. Data correction was done using an in-house VBA spreadsheet program (Gerdes and Zeh, 2009), and plotted using Isoplot 3.75 (Ludwig, 2012) in Tera-Wasserburg concordia plots (Fig. DR1 in GSA Data repository1). From these samples, 47 ages, represented with their 2σ errors, were obtained, four of them showing squared weighted deviates (MSWD) higher than 2.

Results

Using U-Pb geochronology, we documented 47 ages, ranging from 138 ± 12 Ma to 2.6 ± 1.3 Ma obtained from 43 fracture-filling calcites cements, two calcite cements precipitated between sedimentary breccia clasts, and one replacive dolomite (Fig. 3 and table DR2).

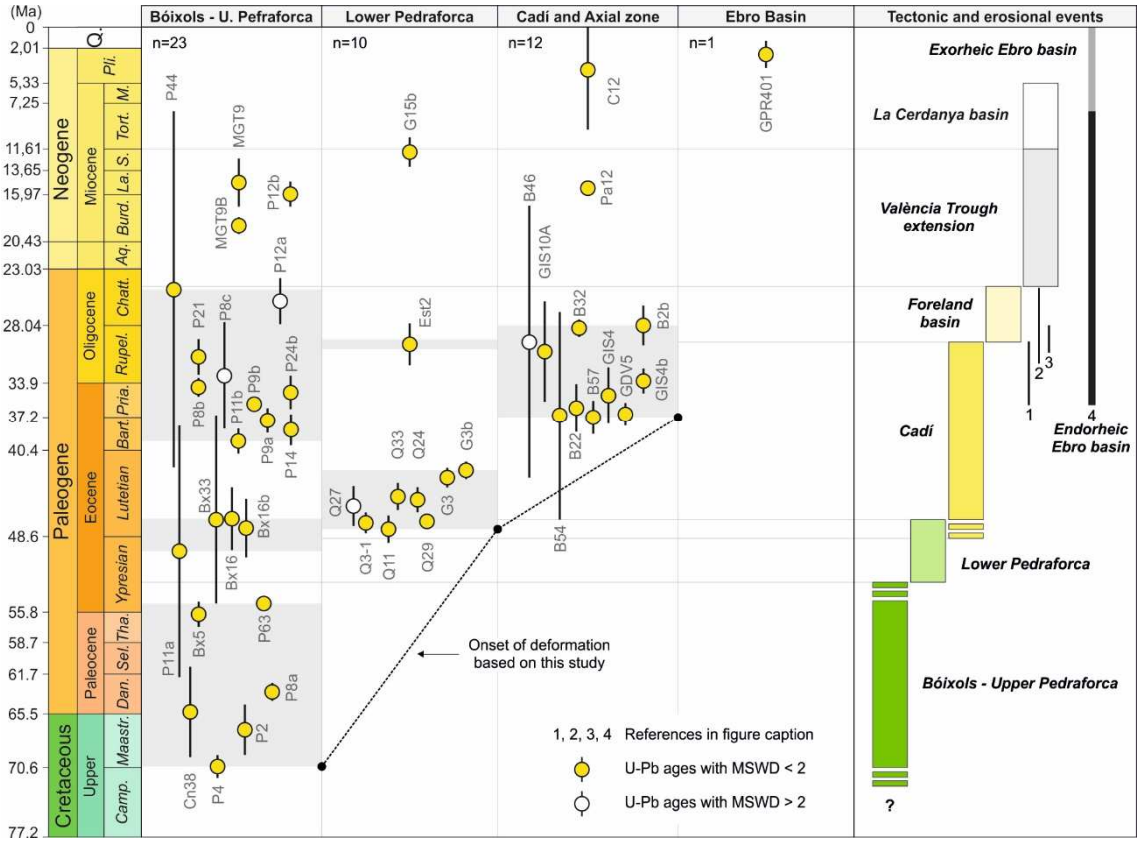

Fig.3. Diagram of U-Pb ages (in Ma) from the Bóixols-Upper Pedraforca, Lower Pedraforca and Cadí thrust sheets, Axial zone and foreland Ebro basin. The U-Pb age from the dolomitic host rock from sample P24 is reported in table DR2. Color bars on the right indicate the previous estimated ages of deformation in the Pyrenees and in the València trough based on Vergés et al. (2002). Ages for the Cadí thrust sheet and for the tectonic activity of the foreland Ebro basin are modified according to 1) Rushlow et al. (2013), 2) Meigs et al. (1996) and 3) Carrigan et al. (2016a). The timing of the development of the endorheic to exoreic foreland Ebro basin is based on 4) Garcia-Castellanos et al. (2003) and Costa et al. (2010).

In the Bóixols-Upper Pedraforca thrust sheet, the ages were divided in three clusters ranging from 70.5 ± 1.1 Ma to 54.9 ± 0.7 Ma, from 50 ± 12 Ma to 46.9 ± 3 Ma, and from 39.5 ± 1.2 Ma to 25 ± 17 Ma, with a higher density of data in the youngest cluster (Fig. 3). Three isolated ages ranging from 18.9 ± 0.8 Ma to 14.8 ± 2.3 Ma were also obtained. For the Lower Pedraforca thrust sheet, the results define a well-constrained group of ages ranging between 47.9 ± 1.3 Ma and

42.3 ± 0.8 Ma in addition to two isolated younger ages of 30.2 ± 2 Ma and 11.9 ± 1.4 Ma (Fig. 3). In the Cadí thrust sheet, only one cluster ranging from 37.9 ± 1.8 Ma to 28.4 ± 1.9 Ma and two younger ages of 15.3 ± 0.4 Ma and 3.9 ± 5.7 Ma were obtained (Fig. 3). In the Ebro foreland basin only one age of 2.6 ± 1.3 Ma was obtained (Fig. 3). The two middle-late Eocene ages of calcite cements precipitated between breccia clasts were obtained from Jurassic rocks of the Bóixols-Upper Pedraforca thrust sheet and range between 37.6 ± 0.84 Ma and 35.9 ± 1.2 Ma (samples P9a and P9b). In the same thrust sheet, a replacive dolomite was dated as Lower Cretaceous (138 ± 12 Ma). This value is reported in table DR2.

Four of the samples (B46, P8c, P12a and Q27) have MSWD values higher than 2 indicating either a mixing of calcite ages, or some dispersion of the data related to an underestimated analytical error, or an initial incomplete equilibration of the Pb isotopes (Rasbury and Cole, 2009). Consequently, the results from these four samples must be interpreted with caution.

Discussion

The exceptional robustness of our data set allowed us to define, for the first time, the sequential emplacement of the SE Pyrenean thrust sheets using U-Pb geochronology. Consequently, in fold and thrust belts where growth strata are scarce or completely eroded, this method is proven valid to determine the sequence of thrusting. The onset of the south Pyrenean deformation migrated to the foreland from the Late Cretaceous to the Oligocene, a timing which is in line with previously published estimates based on Meigs et al. (1996), Beamud et al. (2010), Rahl et al. (2011), Rushlow et al. (2013), Carrigan et al. (2016) and others (Fig. 3).

The total duration of the Bóixols-Upper Pedraforca thrust sheet displacement is of ~15.6 My. The oldest age obtained is 70.5 ± 1.1 Ma, which is younger than the proposed onset of thrust sheet movement by growth strata in the western end of the Bóixols thrust sheet (Mencos et al., 2015). The total duration of the Lower Pedraforca thrust sheet deformation is only ~5.6 My (47.9 ± 1.3 Ma to 42.3 ± 0.8 Ma). The oldest ages obtained, correspond to two samples (Q11 and Q33) from the growth strata along the tip line of the basal thrust of the Lower Pedraforca thrust sheet, representing the late tightening of these deposits at the end of the thrust sheet emplacement. It is interesting to note that no ages correspond to the initial displacement of the Lower Pedraforca thrust sheet. This apparent lack of internal deformation could be due to its low-angle footwall ramp geometry. Coeval U-Pb ages obtained within the Bóixols-Upper Pedraforca thrust sheet ranging from 47.8 ± 2.8 Ma to 46.9 ± 3 Ma (samples Bx16, Bx16b and Bx33) represent deformation during its transport above the underlying Lower Pedraforca thrust sheet. Nevertheless, the age of 50 ± 12 Ma (sample P11a) could also register the initial tectonic movement of this thrust sheet (Fig. 3). U-Pb ages for the Cadí thrust sheet record ~9.5 My of tectonic activity, and only correspond to the middle-late displacement of this unit. On the other hand, synchronous ages for the Bóixols-Upper Pedraforca (39.5 ± 1.2 Ma to 25 ± 17 Ma) and Lower Pedraforca (30.2 ± 2 Ma) thrust sheets reflect their out-of-sequence reactivation and therefore, could provide a longer period of deformation for the underlying Cadí thrust sheet as evidenced from geological observations (Fig.

3). In the folded Ebro foreland basin, no U-Pb ages were obtained related to its compressional history (Fig. 3). However, ages within the Cadí (28.7 ± 0.8 Ma to 28.4 ± 1.9 Ma) and Bóixols-Upper Pedraforca (26.1 ± 2.2 Ma to 25 ± 17 Ma) thrust sheets could be related to the folding and thrusting of the foreland basin strata as determined by Meigs et al. (1996) and Carrigan et al. (2016) (Fig. 3).

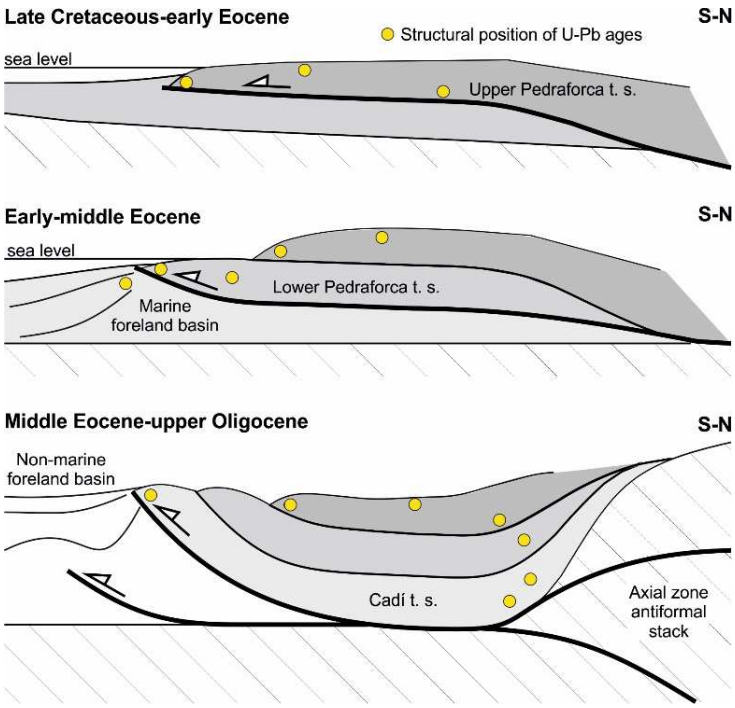

Fig.4. Simplified sketch of the southern Pyrenees based on U-Pb ages showing the sequence of deformation and its forelandwards propagation.

Based on its U-Pb ages, the Bóixols-Upper Pedraforca thrust sheet records the entire compressional history of the SE Pyrenees (70.5 ± 1.1 Ma to 25 ± 17 Ma), whereas the Lower Pedraforca and Cadí thrust sheets document younger ages and shorter periods of deformation (47.9 ± 1.3 Ma to 30.2 ± 2 Ma and 37.9 ± 1.8 Ma to 28.4 ± 1.9 Ma, respectively). The distinctive ages within the superposed thrust sheets, as well as their wide distribution within each tectonic unit, define a piggy-back thrust sequence for the SE Pyrenean allochthonous units and a relatively continuous rather than episodic deformation (Fig. 4).

Finally, U-Pb ages for the three superposed thrust sheets and the foreland basin ranging from 18.9 ± 0.8 Ma to 2.6 ± 1.3 Ma could be related to both the Neogene extension occurring in NE Iberia and concomitant erosion of the Ebro foreland basin after its opening to the Western Mediterranean at 8-11 Ma (Lewis et al., 2000; Garcia-Castellanos et al., 2003; Fillon and Van der Beek, 2012) (Fig. 3). These Neogene ages are the first evidence demonstrating deformation within the SE Pyrenees during these post-compressional events, since previous published studies only report the erosional exhumation of the orogen by applying apatite fission-track thermochronology to syn-orogenic sediments (Beamud et al., 2010; Rushlow et al., 2013).

Conclusions

U-Pb geochronology applied to fracture-filling calcite cements in the SE Pyrenean thrust system indicates that this method is a powerful tool to constrain the sequence of deformation in fold and thrust belts, especially in those in which syn-tectonic sediments are scarce or completely eroded. The results of our study indicate that: 1) the thrust front migrated towards de foreland from the Late Cretaceous to the late Oligocene (70.5 ± 1.1 Ma to 25 ± 17 Ma); 2) the Bóixols-Upper Pedraforca thrust sheet documents the entire compressional deformation, whereas the Lower Pedraforca and Cadí thrust sheets records younger ages and a shorter period of deformation; 3) the continuity over time of the different ages from each thrust sheet indicates continuous rather than episodic tectonic activity; and 4) Neogene U-Pb ages ranging from 18.9 ± 0.8 Ma to 2.6 ± 1.3 Ma indicate, for the first time, the extension of NE Iberia related to the formation of the Western Mediterranean. Results show that U-Pb geochronology is an effective method to define the sequence of thrust faulting in fold and thrust belts, especially where growth strata are scarce or totally eroded.

Acknowledgements

This research was performed within the framework of DGICYT Spanish Project CGL2015-6335-C2-1-R, Grup Consolidat de Recerca “Geologia Sedimentària” (2017SGR-824). U-Pb dating was performed in the Department of Geosciences of the Goethe University of Frankfurt.

References

Beamud, E., Muñoz, J. A., Fitzgerald, P. G., Baldwin, S. L., Garcés, M., Cabrera, L., and Metcalf, J. R., 2010, Magnetostratigraphy and detrital apatite fission track thermochronology in syntectonic conglomerates: constraints on the exhumation of the South-Central Pyrenees: Basin Research, v. 23, no. 3, p. 309-331.10.1111/j.1365-2117.2010.00492.x

Beaudoin, N., Lacombe, O., Roberts, N. M. W., and Koehn, D., 2018, U-Pb dating of calcite veins reveals complex stress evolution and thrust sequence in the Bighorn Basin, Wyoming, USA: Geology, v. 46, no. 11, p. 1015-1018.https://doi.org/10.1130/G45379.1

Carrigan, J. H., Anastasio, D. J., Kodama, K. P., and Parés, J. M., 2016, Fault-related fold kinematics recorded by terrestrial growth strata, Sant Llorenç de Morunys, Pyrenees Mountains, NE Spain: Journal of Structural Geology, v. 91, p. 161-176.http://dx.doi.org/10.1016/j.jsg.2016.09.003

Cosgrove, J. W., 2015, The association of folds and fractures and the link between folding, fracturing and fluid flow during the evolution of a fold–thrust belt: a brief review: Geological Society, London, Special Publications, v. 421, p. SP421.411.10.1144/sp421.11

Costa, E., Garcés, M., López-Blanco, M., Beamud, E., Gómez-Paccard, M., and Larrasoaña, J. C., 2010, Closing and continentalization of the South Pyrenean foreland basin (NE Spain): magnetochronological constraints: Basin Research, v. 22, no. 6, p. 904-917.10.1111/j.1365-2117.2009.00452.x

Cruset, D., Cantarero, I., Travé, A., Vergés, J., and John, C. M., 2016a, Crestal graben fluid evolution during growth of the Puig-reig anticline (South Pyrenean fold and thrust belt): Journal of Geodynamics, v. 101, p. 30-50.http://dx.doi.org/10.1016/j.jog.2016.05.004

Cruset, D., Cantarero, I., Vergés, J., John, C. M., Muñoz-López, D., and Travé, A., 2018, Changes in fluid regime in syn-orogenic sediments during the growth of the south Pyrenean fold and thrust belt: Global and Planetary Change, v. 171, p. 207-224.https://doi.org/10.1016/j.gloplacha.2017.11.001

Fillon, C., and Van der Beek, P., 2012, Post-orogenic evolution of the southern Pyrenees: constraints from inverse thermo-kinematic modelling of low-temperature thermochronology data: Basin Research, v. 23, p. 1-19.doi:10.1111/j.1365-2117.2011.00533.x

Fitz-Diaz, E., Hudleston, P., Tolson, G., and Pluijm, B. V. d., 2014, Progressive, episodic deformation in the Mexican Fold–Thrust Belt (central Mexico): evidence from isotopic dating of folds and faults: International Geology Reviewa, v. 56, no. 6, p. 734-755.doi: 10.1080/00206814.2014.896228

Flotté, N., Plagnes, V., Sorel, D., and Benedicto, A., 2001, Attempt to date Pleistocene normal faults of the CorinthPatras Rift (Greece) by U/Th method, and tectonic implications: Geophysical Research Letters, v. 28, no. 19, p. 3769-3772

García-Castellanos, D., Vergés, J., Gaspar-Escribano, J., and Cloetingh, S., 2003, Interplay between tectonics, climate, and fluvial transport during the Cenozoic evolution of the Ebro Basin (NE Iberia): Journal of Geophysical Research, v. 108, p. (B7), 2347

Gerdes, A., and Zeh, A., 2009, Zircon formation versus zircon alteration — New insights from combined U-Pb and Lu-Hf in-situ LA-ICP-MS analyses, and consequences for the interpretation of Archean zircon from the Central Zone of the Limpopo Belt: Chemical Geology, v. 261, p. 230-243, doi: 10.1016/j.chemgeo.2008.03.005.

Hansman, R. J., Albert, R., Gerdes, A., and Ring, U., 2018, Absolute ages of multiple generations of brittle structures by U-Pb dating of calcite: Geology, v. 46, no. 3, p. 207-210.https://doi.org/10.1130/G39822.1

Haines, S. H., 2008, Transformations in Clay-Rich Fault Rocks: Constraining Fault Zone Processes and the Kinematic Evolution of Regions: PhD thesis. University of Michigan, Ann Arbor, U.S., 295 p

Lewis, C. J., Vergés, J., and Marzo, M., 2000, High mountains in a zone of extended crust: Insights into Neogene-Quaternary topographic development of northeastern Iberia: Tectonics, v. 19, p. 86-102

Ludwig, K. R., 2012, User's Manual for Isoplot 3.75. A Geochonological Toolkit for Microsoft Excel Berkeley Geochronology Center Special Publication, v. 5, p. 1-75

Macchiavelli, C., Vergés, J., Schettino, A., Fernàndez, M., Turco, E., Casciello, E., Torné, M., Pierantoni, P. P., and Tunini, L., 2017, A new southern North Atlantic isochron map: Insights into the drift of the Iberian plate since the Late Cretaceous: Journal of Geophysical Research: Solid Earth, v. 122, p. 9603-9626.https://doi.org/10.1002/2017JB014769

Meigs, A. J., Vergés, J., and Burbank, D. W., 1996, Ten-million-year history of a thrust sheet: GSA Bulletin, v. 108, no. 12, p. 1608-1625

Mencos, J., Carrera, N., and Muñoz, J. A., 2015 Influence of rift basin geometry on the subsequent postrift sedimentation and basin inversion: The Organyà Basin and the Bóixols thrust sheet (south central Pyrenees): Tectonics, v. 34, p. 1452-1474.doi:10.1002/2014TC003692

Muñoz, J. A., 1992, Evolution of a continental collision belt: ECORS–Pyrenees crustal balanced section, in McClay, K. R., ed., Thrust Tectonics, Chapman & Hall, London, p. 235-246.

Nardini, N., Muñoz-López, D., Cruset, D., Cantarero, I., Martín-Martín, J. D., Benedicto, A., Gómez-Rivas, E., John, C. M., and Travé, A., 2019, From early contraction to post-folding fluid evolution in the frontal part of the Bóixols thrust sheet (southern Pyrenees) as revealed by the texture and geochemistry of calcite cements: Minerals, v. 9, no. 2, p. 117.http://dx.doi.org/10.3390/min9020117

Pagel, M., Bonifacie, M., Schneider, D. A., Gautheron, C., Brigaud, B., Calmels, D., Cros, A., Saint-Bezar, B., Landrein, P., Sutcliffe, C., Davis, D., and Chaduteau, C., 2018, Improving paleohydrological and diagenetic reconstructions in calcite veins and breccia of a sedimentary basin by combining Δ47 temperature, δ18Owater and U-Pb age: Chemical Geology, v. 481, p. 1-17.https://doi.org/10.1016/j.chemgeo.2017.12.026

Parrish, R. R., Parrish, C. M., and Lasalle, S., 2018, Vein calcite dating reveals Pyrenean orogen as cause of Paleogene deformation in southern England: Journal of the Geological Society, v. 175, p. 425-442.https://doi.org/10.1144/jgs2017-107

Pickering, R., 2017, U-Series dating, in Gilbert, A. S., ed., Encyclopedia of geoarchaeology: Dordrecht, Springer, p. 992-999.

Rahl, J. M., Haines, S. H., and Pluijm, B. A. v. d., 2011, Links between orogenic wedge deformation and erosional exhumation: Evidence from illite age analysis of fault rock and detrital thermochronology of syn-tectonic conglomerates in the Spanish Pyrenees: Earth and Planetary Science Letters, v. 307, no. 1-2, p. 180-190.https://doi.org/10.1016/j.epsl.2011.04.036

Rasbury, E. T., and Cole, J. M., 2009, Directly dating geologic events: U-Pb dating of carbonates: Reviews of Geophysics, v. 4, p. 1-27.https://doi.org/10.1029/2007RG000246

Ring, U., and Gerdes, A., 2016, Kinematics of the Alpenrhein-Bodensee graben system in the Central Alps: Oligocene/Miocene transtension due to formation of the Western Alps arc: Tectonics, v. 35, p. 1367-1391.https://doi.org/10.1002/2015TC004085

Roberts, N. M. W., and Walker, R. J., 2016, U-Pb geochronology of calcite-mineralized faults: Absolute timing of rift-related fault events on the northeast Atlantic margin: Geology, v. 44, no. 7, p. 531-534

Roure, F., Swennen, R., Schneider, F., Faure, J. L., Ferket, H., Guilhaumou, N., Osadetz, K., Robion, P., and Vandeginste, V., 2005, Incidence and Importance of Tectonics and Natural Fluid Migration on Reservoir Evolution in Foreland Fold-and-Thrust Belts: Oil & Gas Science and Technology, v. 60, no. 1, p. 67-106

Rushlow, C. R., Barnes, J. B., Ehlers, T. A., and Vergés, J., 2013, Exhumation of the southern Pyrenean fold-thrust-belt (Spain from orogenic growth to decay: Tectonics, v. 32, p. 843-860.doi:10.1002/tect.20030

Tavani, S., Mencos, J., Bausà, J., and Muñoz, J. A., 2011, The fracture pattern of the Sant Corneli Bóixols oblique inversion anticline (Spanish Pyrenees): Journal of Structural Geology, v. 33, p. 1662-1680.doi:10.1016/j.jsg.2011.08.007

Travé, A., Labaume, P., Calvet, F., and Soler, A., 1997, Sediment dewatering and pore fluid migration along thrust faults in a foreland basin inferred from isotopic and elemental geochemical analyses (Eocene southern Pyrenees, Spain): Tectonophysics, v. 282, no. 1-4, p. 375-398.10.1016/S0040-1951(97)00225-4

Travé, A., Calvet, F., Sans, M., Vergés, J., and Thirlwall, M., 2000, Fluid history related to the Alpine compression at the margin of the south-Pyrenean Foreland basin: the El Guix anticline: Tectonophysics, v. 321, p. 73-102.10.1016/S0040-1951(00)00090-1

Travé, A., Labaume, P., and Vergés, J., 2007, Fluid systems in Foreland Fold and thrust belts: an overview from the Southern Pyrenees, in Lacombe, O., Lavé, J., Roure, F., and Vergés, J., eds., Thrust Belts and Foreland Basins: From Fold Kinematics to Hydrocarbon Systems, Springer, p. 93-115.

Uysal, I. T., Zhao, J. X., Golding, S. D., Lawrence, M. G., Glikson, M., and Collerson, K. D., 2007, Sm–Nd dating and rare-earth element tracing of calcite: Implications for fluid-flow events in the Bowen Basin, Australia: Chemical Geology, v. 238, no. 1, p. 63-71.https://doi.org/10.1016/j.chemgeo.2006.10.014

Van der Pluijm, B. A. v. d., Hall, C. M., Vrolijk, P. J., Pevear, D. R., and Covey, M. C., 2001, The dating of shallow faults in the Earth's crust: Nature, v. 412, p. 172.10.1038/35084053

Vergés, J., Fernàndez, M., and Martínez, A., 2002, The Pyrenean orogen: pre-, syn-, and post-collisional evolution, in Rosenbaum, G., and Lister, G., eds., Reconstruction of the evolution of the Alpine-Himalayan Orogen. Journal of the Virtual Explorer, Volume 8, p. 55-74.

Zhang, P. Z., Shen, Z., Wang, M., Gan, W., Bürgmann, R., Molnar, P., Wang, Q., Wu, J., Sun, J., Hanrong, S., Xinzhao, Y., and Niu, Z., 2004, Continuous deformation of the Tibetan Plateau from global positioning system data: Geology, v. 32, no. 9, p. 809-812.10.1130/g20554.1

Chapter 7

From hydroplastic to brittle deformation: controls on fluid flow in the Lower Pedraforca thrust sheet (southern Pyrenees)

From hydroplastic to brittle deformation: controls on fluid flow in the Lower Pedraforca thrust sheet (southern Pyrenees)

David Cruset[1], Irene Cantarero[1], Antonio Benedicto[2], Cédric M. John[3], Jaume Vergés[4], Anna Travé[1]

[1] Departament de Mineralogia, Petrologia i Geologia Aplicada, Facultat de Ciències de la Terra, Universitat de Barcelona, (UB), Martí i Franquès s/n, 08028, Barcelona, Spain.
d.cruset@ub.edu, i_cantarero@ub.edu, atrave@ub.edu

[2] UMR Geops, Université Paris Sud, 91405 Orsay, France.
antonio.benedicto@u-psud.fr

[3] Department of Earth Science and Engineering, Imperial College London, SW7 2BP, UK.
cedric.john@imperial.ac.uk

[4] Institut de Ciències de la Terra Jaume Almera, ICTJA-CSIC, Lluís Solé i Sabaris s/n, 08028 Barcelona, Spain.
jverges@ictja.csic.es

Marine and Petroleum Geology: Submitted

Abstract

In this contribution we present a multidisciplinary study to decipher the controls of the style of deformation on the fluid flow regime using the Lower Pedraforca thrust sheet in the southern Pyrenees as an example.

The integration of field-based and petrographic observations, and geochemical data allowed us to differentiate up to eight types of calcite cements (Cc1 to Cc8) precipitated during the deformation stretching the Lower Pedraforca thrust sheet.

During syn-sedimentary hydroplastic normal faulting affecting poorly-consolidated Upper Cretaceous sediments and Eocene syn-orogenic sediments, calcite cements did not precipitate. During the burial and the layer parallel shortening, however, calcite cements Cc1 to Cc4 precipitated from fluids in a relatively paleohydrological system. Cc3 precipitated from high-salinity fluids (~+5.4 ‰ VSMOW) with $^{87}Sr/^{86}Sr$ ratios of 0.707922 and at temperatures around 70 ºC. Contrarily, during folding and thrusting, calcite cements Cc5 to Cc8 in a more open paleohydrological system. Cc6 precipitated from high-salinity fluids (~+5 ‰ VSMOW) with 87Sr/86Sr ratios 0.707817 and at temperatures around 75 ºC.

The controls of deformation on the paleohydrological system observed in the Lower Pedraforca thrust sheet have strong similarities with that observed other areas worldwide under both compressional and extensional regimes.

Introduction

The study of the evolution of the fluid regime reveals the degree of fluid-rock interaction and the input of exotic fluids into the system through time (Breesch et al., 2009; Beaudoin et al., 2014; Crognier et al., 2017; Cantarero et al., 2018; Cruset et al., 2018). In the shallow crust, brittle deformation is responsible for the formation of fractures (Marrett and Allmendinger, 1990), which act as preferential conduits or seals for the migration of fluids (Missenard et al., 2014; Ogata et al., 2014; Maher et al., 2017). However, the conduit or barrier behaviour is not steady-state and it can evolve trough time, especially due to: 1) variations in the stress field, forcing changes in the tectonic regime (Sibson, 1995; Wiprut and Zoback, 2000; Soumaya et al., 2015); 2) the increase of fluid pressure, which can produce seismically-induced slip and/or hydraulic fracturing (Aydin, 2000; Wiprut and Zoback, 2000¸ Rutqvist et al., 2013); 3) fracture sealing by cements due to fluid regime changes (temperature, pressure, composition), (Benedicto et al., 2008; Beaudoin et al., 2014); and 4) a combination of the previous factors.

The reactivation of faults can increase the heterogeneity of fractured reservoirs and the uncertainty during reservoir analysis (Roure et al., 2005; Khosravi et al., 2012). Moreover, these heterogeneities are also controlled by additional factors such as fault core composition and cementation, which also affect fault permeability (Egholm et al., 2008 Dimmen et al., 2017). To mitigate these issues, outcrop studies, together with fluid flow analysis, can reduce the uncertainty during the evaluation of reservoirs which are under exploration or production stages.

The southern Pyrenees is an exceptionally well-preserved fold and thrust belt in which the complete sequence of thrust sheets and the age of their related syn-tectonic deposits are well known (Vergés and Muñoz, 1990; Vergés, 1993; Cruset et al., in review). In this compressional belt, the relationships between fluid migration and deformation have been studied either in its Paleozoic basement (McCaig et al., 1995, 2000; Trincal et al., 2017), cover thrust sheets constituted of Mesozoic and Paleogene rocks (Travé et al., 1997, 1998; Beaudoin et al., 2015; Crognier et al., 2017; Cruset et al., 2018; Lacroix et al., 2014, 2018; Nardini et al., 2019) and in its foreland basin, constituted of Paleogene rocks (Travé et al., 2000; Cruset et al., 2016a). Other studies in the southern Pyrenees report the presence of fractures formed in hydroplastic (Soliva and Benedicto, 2004, 2005; Soliva et al., 2006, 2008) and brittle (Shackleton et al., 2005, 2011; Tavani et al., 2011; Gutmanis et al., 2017) regimes. However, the relationships between fluids and these styles of fractures, as well as their evolution through time, have not been studied yet.

In this contribution, we report, for the first time, a whole history of fluid flow evolution from syn-sedimentary hydroplastic deformation to later brittle fracturing, using the Lower Pedraforca cover thrust sheet in the SE Pyrenees as an example. To deal with the aim of this study, previous fracture and isotope preliminary data already presented in Cruset et al. (2018) are extended. Besides, the absolute timing of fluid migration has been well-constrained using U-Pb geochronology of the studied fracture-filling calcite cements (Cruset et al., in review). We focus on three meso-scale (metre-scale) fracture systems which are correlative through time: 1)

hydroplastic normal faults (as defined by Petit and Beauchamp (1986) and Petit and Laville (1987); 2) background fracture systems, which consist of stratabound bed-perpendicular en-échelon vein arrays and bed-parallel slip surfaces; and 3) non-stratabound fracture systems formed of reverse, strike-slip and normal faults. The fracture analysis is combined with petrographic observations and geochemical data (carbon, oxygen and strontium isotopes, clumped isotopes thermometry and elemental composition) of calcite cements precipitated in the fractures affecting the Lower Pedraforca thrust sheet. The results obtained shed light on the changes in fluid regime related to fracturing within this thrust sheet.

Geological setting

The Pyrenees (Fig. 1A) formed due to the continental collision that resulted from the partial subduction of the Iberian plate beneath the Eurasian plate from Late Cretaceous to Miocene (Choukroune et al., 1989; Roure et al., 1989; Muñoz, 1992, 2002; Vergés et al., 2002). As a result, the previous Mesozoic rift basins were inverted, and an antiformal stack of thrust sheets constituted of basement units (the Axial zone) developed in the center of the Pyrenean chain (Fig.1B), acting as a boundary between the north and south Pyrenean fold and thrust belts (Muñoz, 1992).

The south Pyrenean fold and thrust belt (Fig. 1B, C and 2A) consists of a piggy-back sequence of south-verging thrusts (Puigdefàbregas et al., 1992), detached predominantly above Upper Triassic (Séguret, 1972) and Eocene evaporites deposited in the foreland basin (Vergés et al., 1992; Sans, 2003). In this work, we study the Lower Pedraforca thrust sheet (LPTS) (Fig. 1C and 2A), which consists of an allochthonous klippe detached in the Upper Triassic Keuper facies and emplaced from Lower to Middle Eocene (Puigdefàbregas et al., 1986; Burbank et al., 1992a; Cruset et al., in review). The emplacement of this structural unit was under marine conditions, as attested by the syn-orogenic fan delta conglomerates of Queralt deposited at the thrust front (Vergés, 1993).

The stratigraphy of the LPTS ranges in age between the Upper Triassic and the Oligocene and consists of pre- to syn-orogenic rocks (Fig. 2B). Pre-compressive units consist of evaporites and red clays from the Keuper facies, Jurassic limestones and dolostones from the Bonansa Fm. and Coniacian to Lower Santonian limestones (Mey et al., 1968; Simó, 1985; Calvet et al., 1993). Syn-orogenic materials consist of Upper Santonian to Campanian marine sandstones and limestones from the Vallcarga Fm., Campanian-Maastrichtian coastal deposits of the Areny Fm., Maastrichtian-Thanetian continental deposits from the Garumnian facies, Ilerdian limestones from the Cadí Fm., Lutetian-Bartonian marine conglomerates of the Coubet Fm. deposited in the thrust front and Oligocene continental conglomerates deposited during the reactivation of the Lower Pedraforca thrust sheet (Moeri, 1977; Vergés, 1993; López-Martínez et al., 1999; Rosell et al., 2001; Oms et al., 2007).

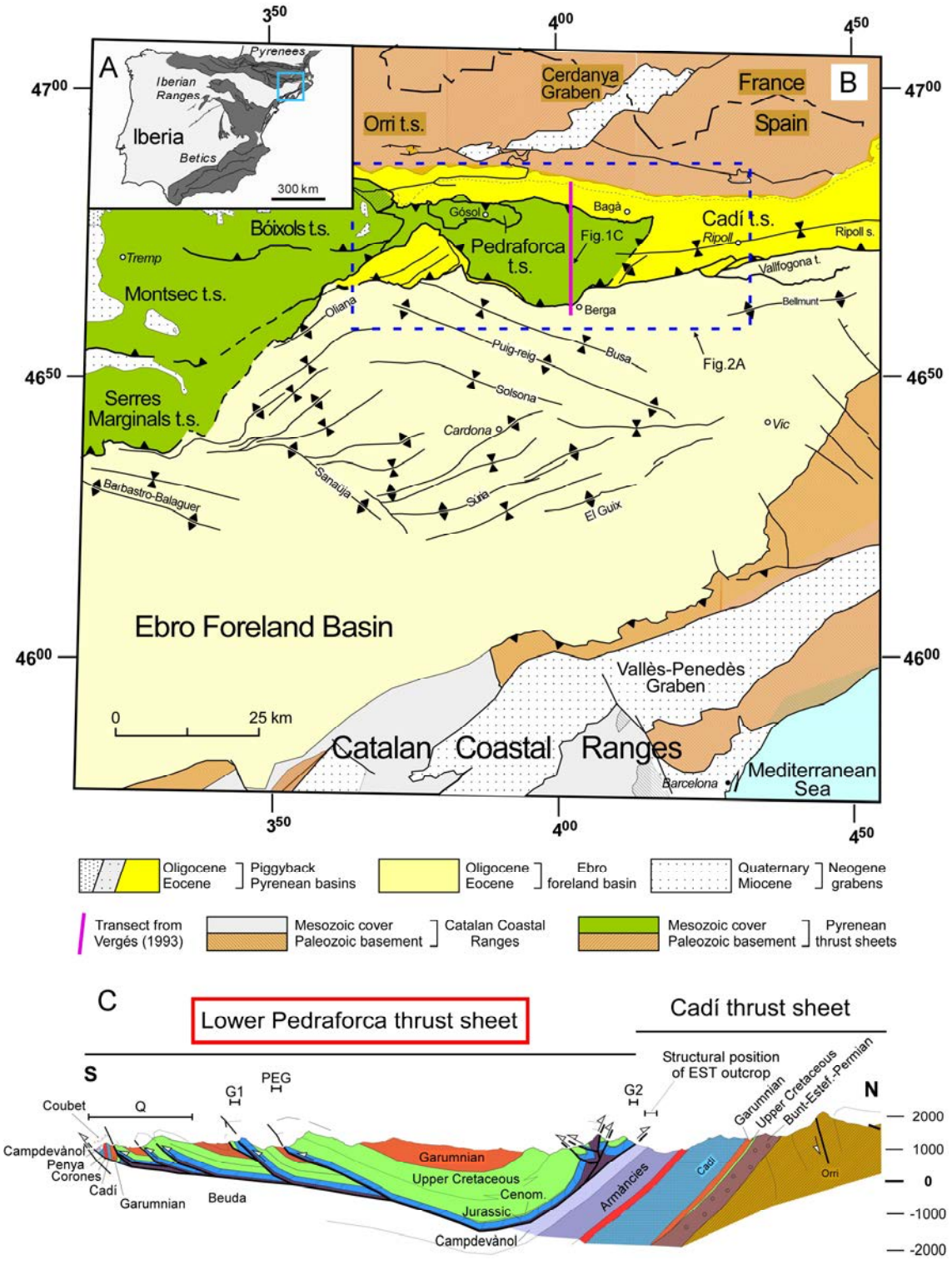

Fig. 1 A) Regional map of the Iberian Peninsula showing the location of the south Pyrenean fold and thrust belt (black box). B) Simplified geological map showing the main structural units forming the south Pyrenean fold and thrust belt (Vergés, 1993). The thick pink line indicates the location of the cross-section shown in Fig. 1C. The dashed blue box indicates the location of Fig. 2A. C) Geological cross section of the Lower Pedraforca thrust sheet from Vergés (1993) showing the structural position of the studied outcrops.

Methodology

Five outcrops (Q, G1, PEG, G2 and EST) located in the southern (Q, G1) and the northern (G2, EST) margins and in the internal nappes forming the LPTS (PEG) were chosen to study the structural controls on fluid flow during the formation of this structure (Fig. 2).

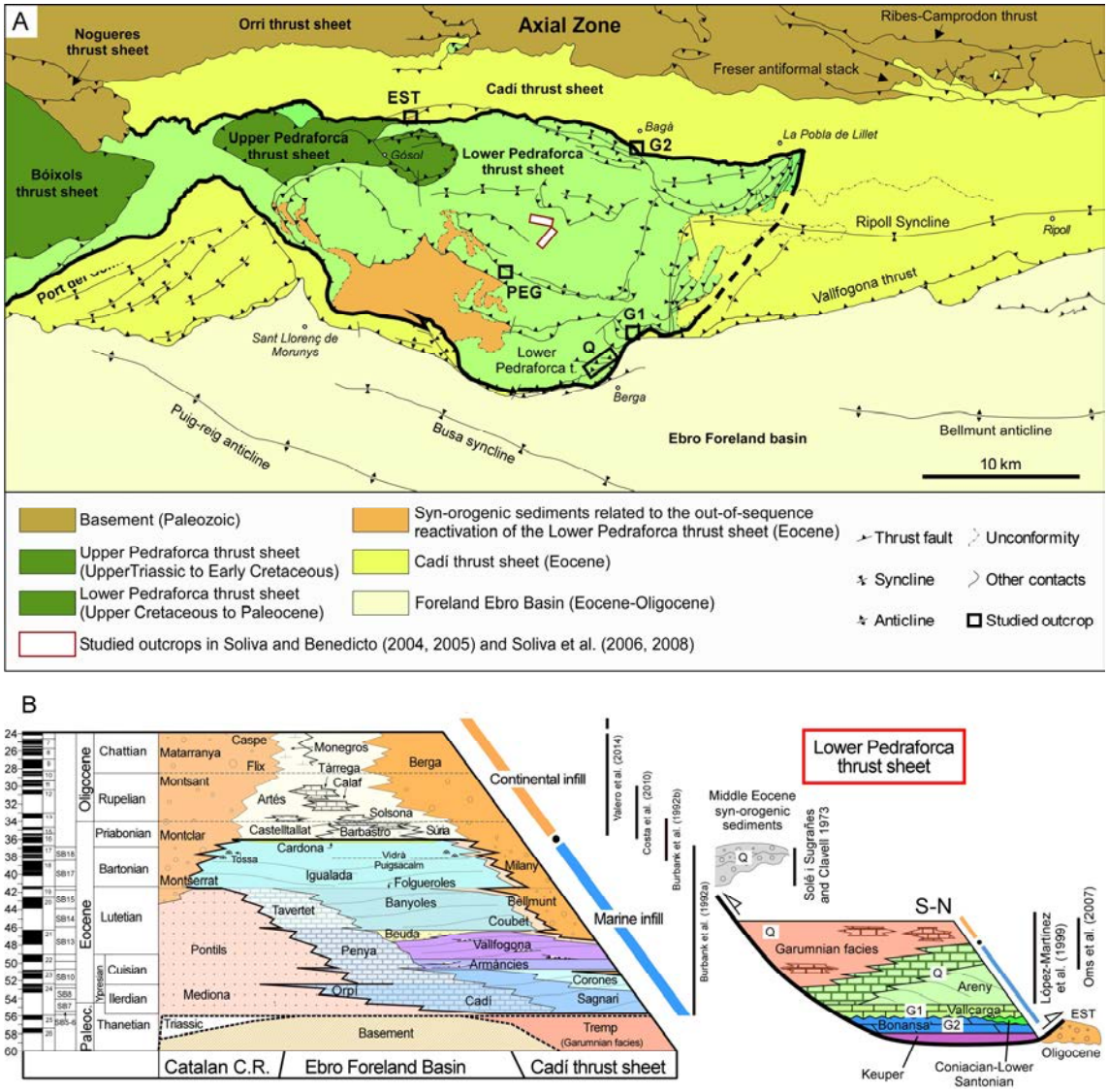

Fig. 2 A) Structural sketch of the studied area with outcrop locations. White boxes bounded by red lines indicate the areas studied by Soliva and Benedicto (2004, 2005) and Soliva et al. (2006, 2008) in the Lower Pedraforca thrust sheet. B) N-S stratigraphic panel of the Lower Pedraforca thrust sheet, Cadí thrust sheet and eastern Ebro Foreland Basin modified from Vergés et al. (1998). The age of sedimentary units has been defined according to Burbank et al. (1992a, b), López-Martínez et al. (1999), Oms et al. (2007), Costa et al. (2010) and Valero et al. (2014). Shallow Benthic Zones (SBZ) are from Serra-Kiel et al. (1998a and b). The white boxes with references Q, G1, PEG, G2 and EST indicate the stratigraphic location of the studied outcrops.

Bedding and fractures were measured on the field and crosscutting relationships between fractures were stablished. The fracture analysis was carried out using the program Win-Tensor (v5.8.8.) (Delvaux and Sperner, 2003). Each fracture system is plotted in Lower hemisphere Schmidt stereoplots and their associated stresses are calculated. Additionally, sampling of fracture-filling calcite cements and related host rocks was undertaken for petrographic observations and geochemical analyses.

Petrographic observations of 57 polished thin sections made from six different host rocks and eight fracture-filling calcite cements were made using optical and cathodoluminescence microscopy. A CL Technosyn cathodoluminescence device Model 8200 MkII operating at 23 kV and 350 µA gun current was used to distinguish the different types of cements.

For carbon- and oxygen-isotope analysis, a 400 µm-thick dental drill was employed to extract 60 ± 10 µg of powder from trims containing calcite cements and carbonate host rocks. The calcite powder was reacted with 100% phosphoric acid for 2 minutes at 70 °C. The resultant CO_2 was analyzed using an automated Kiel Carbonate Device attached to a Thermal Ionization Mass Spectrometer Thermo Electron (Finnigan) MAT-252 following the method of McCrea (1950). The results were corrected using the standard technique from Craig and Gordon (1965) and Claypool et al. (1980), expressed in ‰ with respect to the VPDB (Vienna Pee Dee Belemnite) standard. Standard deviation is ±0.02 ‰ for $\delta^{13}C$ and ± 0.05 ‰ for $\delta^{18}O$.

Clumped isotope thermometry was applied to two fracture-filling calcite cements to calculate temperatures of precipitation as well as the $\delta^{18}O$ values of the fluids from which these cements precipitated. This method has been applied to previous fluid flow studies with good results, avoiding problems related to fluid inclusion stretching during microthermometric analyses of carbonate cements (Swanson et al., 2012; Mangenot et al., 2018; Nardini et al., 2019). The two analyzed samples (Q2 and Q24) are representative of calcite cements Cc3 and Cc6. To analyze them, 2–3 mg aliquots from cements were measured with the Imperial Batch Extraction system (IBEX), an automated line developed at Imperial College of London. Each sample was dropped in 105% phosphoric acid at 90 ºC and reacted for 30 min. The reactant CO_2 was separated using a poropak-Q column and transferred into the bellows of a Thermo Scientific MAT 253 mass spectrometer (Thermo Fisher GmbH, Bremen, Germany). The characterization of a replicate consisted of 8 acquisitions in dual inlet mode with 7 cycles per acquisition. The post-acquisition processing was completed with a software for clumped isotope analysis named Easotope (John and Bowen, 2016). Δ_{47} values were corrected for isotope fractionation during phosphoric acid digestion employing a phosphoric acid correction of 0.069 ‰ at 90 ºC for calcite (Guo et al., 2009). The data were also corrected for non-linearity applying the heated gas method (Huntington et al., 2009) and projected into the absolute reference frame of (Dennis et al., 2011). Carbonate $\delta^{18}O$ values were calculated with the acid fractionation factors of (Kim et al., 1997). Samples were measured three times and the average result was converted to temperatures using the calibration method of (Davies and John, 2019). Calculated $\delta^{18}O$ values of the fluid are expressed in ‰ with respect to the VSMOW standard (Vienna Standard Mean Ocean Water).

One sample of carbonate host rock and three fracture-filling calcites were analyzed for $^{87}Sr/^{86}Sr$ isotopes. 100% calcite samples are fully dissolved in 5 ml of 10% acetic acid and introduced in an ultrasonic bath for 15 minutes. After this time, samples are dried after being centrifuged during 10 min at 4000 rpm. The resultant sample is digested in 1 ml of 3 M HNO_3 and dried. Finally, the resultant product is digested again in 3 ml of 3 M HNO_3 and introduced in chromatographic columns. The chromatographic separation of Sr was done using an extraction

resin type SrResinTM (Trisken International) (crown-ether (4.4' (5')-di-t-butylcyclohexano-18-crown-6). The Sr is recovered with HNO_3 0.05 M as eluent. The fraction where Sr is concentrated is dried, charged on a Re single filament with 1 µl of H3PO4 1 M and 2 µl of Ta_2O_5 and analyzed on a TIMS-Phoenix mass spectrometer. The method of acquisition of data consists of dynamic multicollection during 10 blocks of 16 cycles each one, with a beam intensity in the ^{88}Sr mass of 3 V. Analyses were corrected for possible interferences of ^{87}Rb. The $^{87}Sr/^{86}Sr$ ratios are normalized with respect to the measured mean value of the ratio $^{86}Sr/^{88}Sr$=0.1194 in order to correct possible mass fractionation during filament charge and instrumental analyses. The precision of the analytical standard error or internal precision is 0.000009.

Carbon-coated polished thin sections were used to analyse major, minor and trace element concentrations on a CAMECA SX-50 electron microprobe. The microprobe was operated using 20 kV of excitation potential, 15 nA of current intensity and a beam diameter of 10 µm. The detection limits were 135 ppm for Mn, 127 ppm for Fe, 101 ppm for Ca, 146 ppm for Na, 180 ppm for Mg and 390 ppm for Sr. Precision on major element analyses averaged 0.64% standard error at 2σ confidence levels.

Results

Outcrop description

Structural studies and sampling were carried out on five studied outcrops (Q, G1, PEG, G2 and EST, from south to north) belong to the imbricate thrust system forming the Lower Pedraforca thrust sheet (Fig. 1B and 2A).

The Q outcrop corresponds to the frontal part of the LPTS, a few hundreds of meters to the north of Berga village (Fig. 2A). The general structure of this outcrop consists of three imbricated thrust nappes in which the outcropping rocks are the Upper Cretaceous Areny Formation and the Paleocene Garumian facies (Fig. 1C). To the south, this structure is unconformably overlain by lower to middle Eocene syn-orogenic sediments showing growth strata geometries.

The G1 and PEG outcrops are located 3 km to the north and 10 km to the NW from Berga village, respectively (Fig. 2A). They consist of frontal thrust fault zones corresponding to the northern nappes of the LPTS (Fig. 1C and 2A). In the outcrop G1, the hangingwall is constituted of the Upper Triassic Keuper facies, which gradually change upwards to the Lower Jurassic rocks of the Bonansa Formation. These later are unconformably overlain by the Upper Cretaceous Vallcarga Formation. The footwall of the G1 outcrop is formed of rocks of the Upper Cretaceous Vallcarga Formation. The PEG outcrop consists of a thrust fault affecting the footwall of a major thrust nappe forming the LPTS (Fig. 1C and 2A). In this area, both the hangingwall and the footwall are formed of Paleocene Garumnian rocks.

The G2 outcrop is located in the northernmost part of the LPTS, 1 km to the south of Bagà village (Fig. 1 and 2A). In this area, the LPTS is tilted to the south due to the formation of the Ripoll syncline during the emplacement of the Cadí thrust sheet (Fig. 1C). The outcrop consists

of the thrust fault zone which is the boundary between the Lower Pedraforca thrust sheet (hangingwall) and the Cadí thrust sheet (footwall). The hangingwall is formed of Upper Triassic Keuper facies conformably overlain by Lower Jurassic rocks, whereas the footwall is formed of the middle Eocene Campdevànol Formation.

Finally, the EST outcrop is located 3 km to the NE of Gósol village (Fig. 1 and 2A). It consists of Oligocene conglomerates deposited in the footwall of the LPTS and related to its later reactivation. These conglomerates are unconformably overlying the middle Eocene Armàncies Formation from the Cadí thrust sheet (Fig. 2B).

Host rocks

The studied rocks in the LPTS involves sedimentary Jurassic, Upper Cretaceous, Paleocene, middle Eocene and Oligocene materials.

Jurassic rocks from the Bonansa Formation consist of millimeter-thick laminated mudstones. The Upper Cretaceous host rocks include the marine Vallcarga and Areny Formations. The Vallcarga Formation is formed of grainstones with up to 10% of detrital quartz. Microfauna includes Orbitoides and Hemicyclammina indicating an upper Santonian age (Pons and Caus, 1996). The Areny Formation is mainly composed of grainstones of peloids, miliolids, bryozoan and echinoid fragments and changes northwards to wackestones of gastropods, algae and scleractinian coral fragments.

The Paleocene Garumnian facies consist of continental detrital and carbonate rocks. Detrital rocks include red clays with orange and purple colorations, with abundant Microcodium that occasionally replaces the whole rock, and fine-grained sandstones formed of quartz (~10%) and carbonate clasts (~80-90%). These sandstones have a good sorting and are well-cemented. Regarding the Garumnian carbonate deposits, they are grey-brown mudstones and wackestones with charophyta.

Middle Eocene syn-orogenic sediments deposited in the Lower Pedraforca thrust front are formed of well-cemented, medium-grained grey sandstones with a good sorting. Detrital components consist of Microcodium fragments from the Garumnian (~5-10%), limestone clasts (~70%), quartz (~10%) and Nummulites (~10%).

Oligocene conglomerates are formed of centimeter- to meter-scale carbonate clasts supported by a matrix constituted of well-cemented and coarse-grained sandstones with a good sorting. Detrital components of the matrix are lithics derived from carbonates (>60%), metamorphic rocks and quartz.

Fracture analysis

Rocks forming the LPTS were affected by up to seven fracture sets (F1 to F7) summarized in Fig. 3.

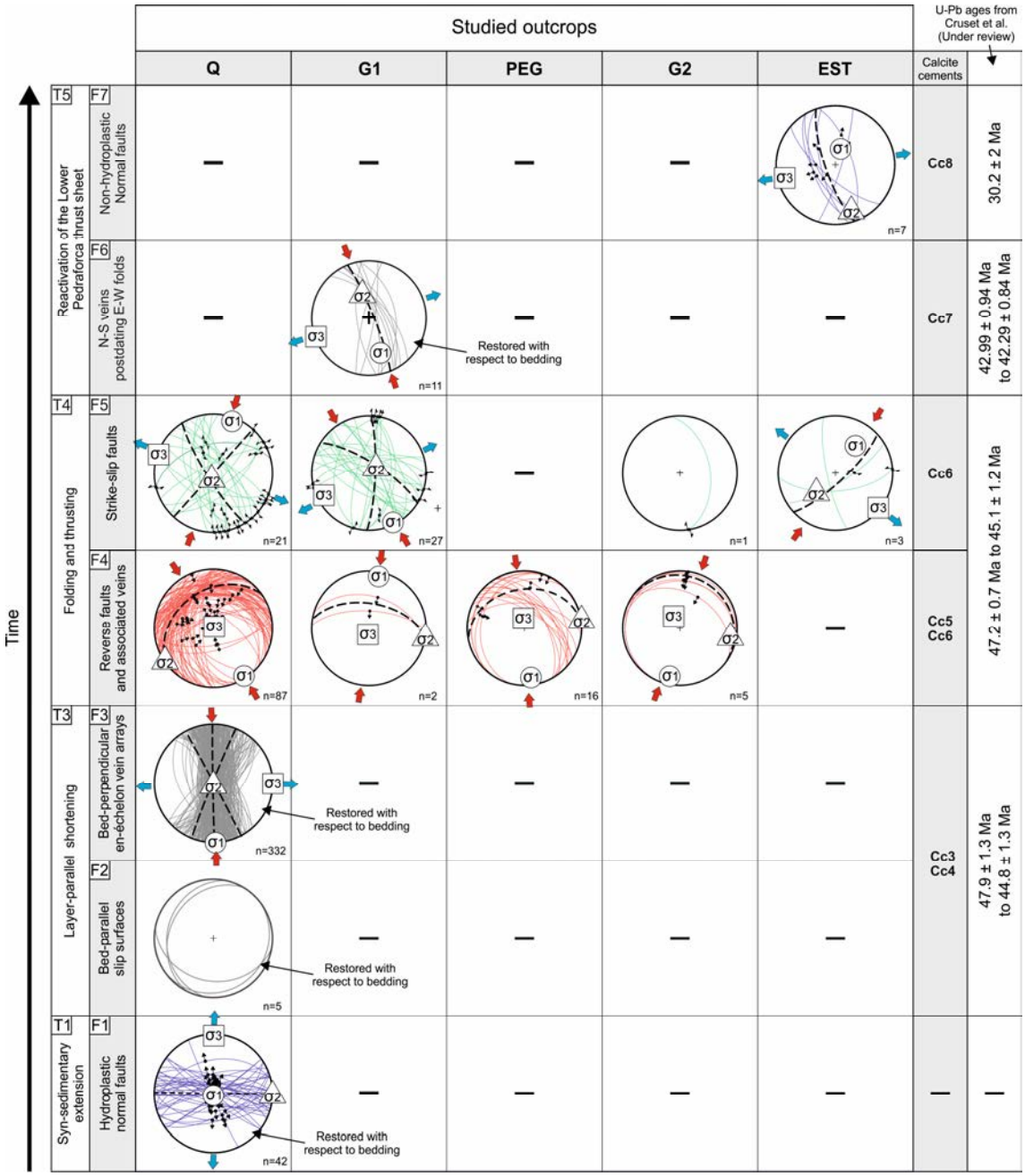

Fig. 3 Lower hemisphere Schmidt stereoplots representing fracture data from the different studied outcrops, their associated calcite cements and different stages of deformation. U-Pb ages from Cruset et al. (in review). Fracture systems F1, F3 and F6 are restored with respect to bedding. The grey boxes with references Q, G1, PEG, G2 and EST represent the outcrops location in Figs. 1 and 2. Thick dashed black lines represent mean planes for each fracture system.

Fracture set F1 consists of E-W stratabound normal faults affecting the Upper Cretaceous Areny Fm. and middle Eocene syn-orogenic sediments deposited in the thrust front (Fig. 3). These faults dip from 45º to 80º either towards the north or south, have a length of up to 2 m, millimeter thickness, show displacements up to 10 cm and soft, undulated grooves and striae sets (Fig. 4A and B). These features are indicative of hydroplastic deformation as defined by Petit and Beauchamp (1986) and Petit and Laville (1987). Calculated stress orientations indicate a N-S extension with vertical σ1 and horizontal σ2 and σ3 (Fig. 3). These fractures do not have calcite

cements, although occasionally calcite veins with reverse striae sets are present, resulted from a later reactivation. Fracture set F1 has been observed in outcrop Q. The second fracture set F2 consists of bed-parallel slip surfaces formed at the contact between clays and more competent layers of the Areny Fm (Fig. 3) and Garumnian facies in outcrop Q (Fig. 4C). F2 fractures have a thickness of up to 1 cm and a length of few centimeters.

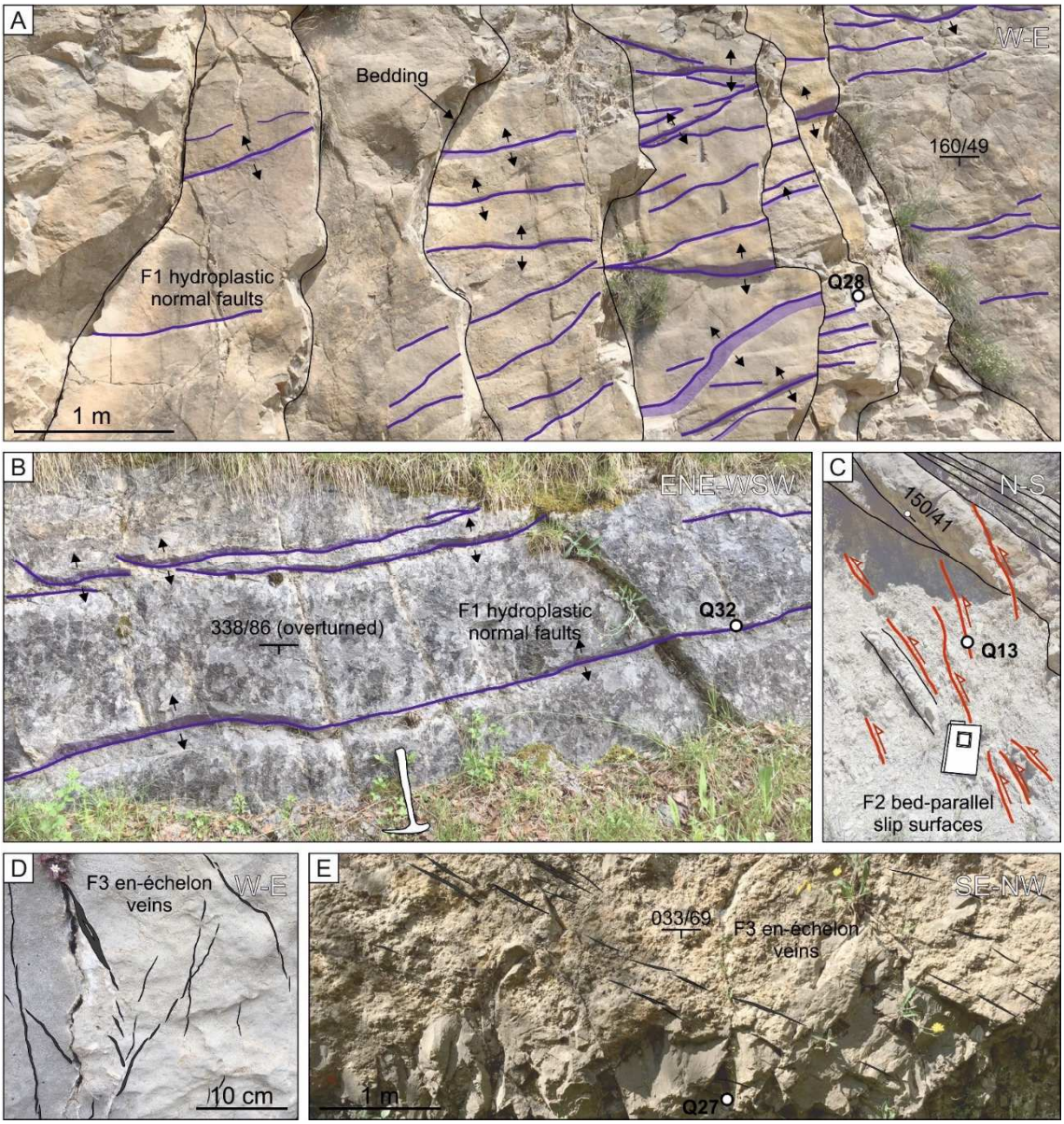

Fig. 4 Outcrop images showing the main features of fracture systems F1, F2 and F3 within the Lower Pedraforca thrust sheet. A-B) E-W hydroplastic normal faults F1 in the Upper Cretaceous Areny Formation and middle Eocene syn-orogenic sediments, respectively. C) Bed-parallel slip surfaces F2 affecting Paleocene sediments. D-E) N-S, NNW-SSE and NNE-SSW en-échelon vein arrays F3 affecting middle Eocene syn-orogenic sediments and the Upper Cretaceous Areny Formation, respectively. Bed dip directions and dips are given. White points indicate sample location.

Fracture set F3 consists of N-S, NNW-SSE and NNE-SSW en-échelon vein arrays (Fig. 3, 4D and E). F3 are bed-perpendicular, stratabound and show sub-vertical dips after restoring bedding to the horizontal (Fig. 3). F3 show openings of up to 2 cm and lengths of up to 30 cm. These fractures affect the Upper Cretaceous Areny Fm., the Paleocene Garumnian facies and

the middle Eocene syn-orogenic sediments. Calculated stress orientations for F3 indicate a N-S strike-slip motion, with vertical σ2 and horizontal σ1 and σ3 (Fig. 3). F3 has only been observed in outcrop Q.

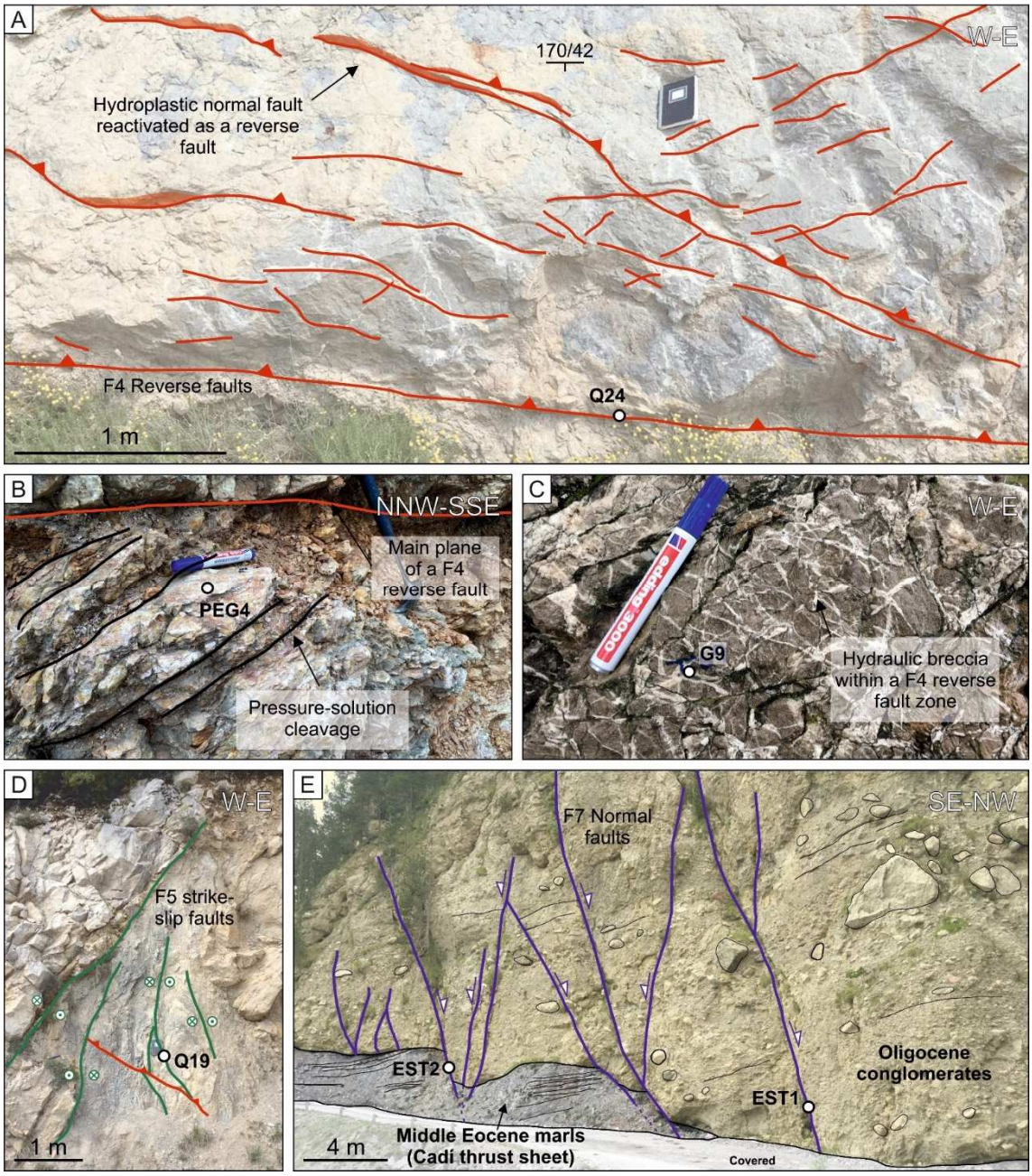

Fig. 5 Outcrop images showing the main features of fracture systems F4, F5 and F7 within the Lower Pedraforca thrust sheet. A) Reverse faults F4 and associated veins within the Upper Cretaceous Areny Formation. B) Pressure solution cleavage formed in the core of a F4 thrust fault. C) Hydraulic breccia formed in the damage zone of a F4 thrust fault. D) F5 strike-slip faults affecting the Upper Cretaceous Areny Formation. E) F7 normal faults affecting Oligocene conglomerates. Bed dip directions and dips are given. White points indicate sample location.

Fracture set F4 is constituted of E-W, NE-SW and NW-SE reverse faults zones and their associate veins affecting Jurassic and Upper Cretaceous rocks from the Bonansa, Areny and Vallcarga Formations (Fig. 3 and 5A). These faults dip between 15º and 75º towards the N and NW, are not stratabound, have a constant orientation regardless bed dips, are filled with calcite

and occasionally show hydrocarbon seeps. Fault cores are formed of thick S-C zones with development of pressure-solution cleavage (Fig. 5B) or thin discrete planes formed of up to 2 cm-thick shear veins. F4 show lengths from few centimeters to tens of meters. In thrust faults in which thick units of Upper Triassic evaporites are involved, however, hydraulic breccias are developed within the most competent rocks within the footwall (Fig. 5C). The calculated stress orientation for F4 indicates a N-S (outcrops G1, PEG and G2) and NW-SE (outcrop Q) reverse motion, with vertical σ3 and horizontal σ1 and σ2 (Fig. 3). In outcrop Q, some of the reserve faults formed due to the reactivation of hydroplastic normal faults F1.

The fifth fracture set (F5) consists of N-S, NW-SE, NNW-SSE and NE-SW strike-slip faults dipping between 45º and 90º and affecting Upper Triassic, Jurassic, Upper Cretaceous and Paleocene rocks. Fault planes are discrete, formed of shear veins with a thickness of up to 2 cm and show striae sets indicating dextral and sinistral motion (Fig. 3 and 5D). F5 faults have lengths of up to 5 meters. Calculated stress orientations for F5 indicate NW-SE, N-S and NE-SW strike-slip motion in outcrops Q, G1, G2 and EST, respectively (Fig. 3). Like F4, strike-slip faults have a constant angle regardless bed dips.

Fractures F6 consists of 1 cm-width and up to 5 cm-long N-S sub-vertical veins observed occasionally in thrust fault zones of the outcrop G1 (Fig. 3). These fractures affect folded Jurassic strata in a constant angle, indicating their post-folding formation. The stress orientation for F6 indicates NNW-SSE strike-slip motion (Fig. 3).

Fracture set F7 consists of normal faults affecting the Oligocene conglomerates related to the reactivation of the Lower Pedraforca thrust sheet studied in outcrop EST (Fig. 5E). These faults are NNW-SSE strike, dip between 60º and 80º either towards the SW and NE and show fault displacements from 1 to 2 m (Fig. 3). Fault planes are discrete, formed of up to 2 cm-thick extensional veins and show lengths of up to 20 meters. Calculated stress orientations for F7 indicate an ENE-WSW extension.

Petrology

The petrography of fracture, vug and moldic porosity, as well as for cements within in the LPS have allowed us to identify eight types of calcite cement (Cc1 to Cc8). The main features and crosscutting relationships of these cements are summarized in Figures 6 and 7. Some of the collected samples for this study are located in Fig. 5 for reference.

Cc1 consists of non-luminescent microsparite precipitated in the intergranular and moldic porosity of the Areny Formation in outcrop Q (Fig. 6A and B). Cc2 consists of blocky calcite crystals of more than 1 mm in size. This cement is non-luminescent and precipitated in vug porosity affecting the Garumnian facies in outcrop Q and in the intergranular porosity of breccias within the Jurassic limestones in outcrop G1 (Fig. 7). Cc3 consists of blocky calcite crystals ranging from 100 to 300 μm and fibrous calcite crystals parallel to fracture walls ranging from 200 μm to 2 mm long. This cement is orange luminescent and precipitated in F2 and F3 fractures and

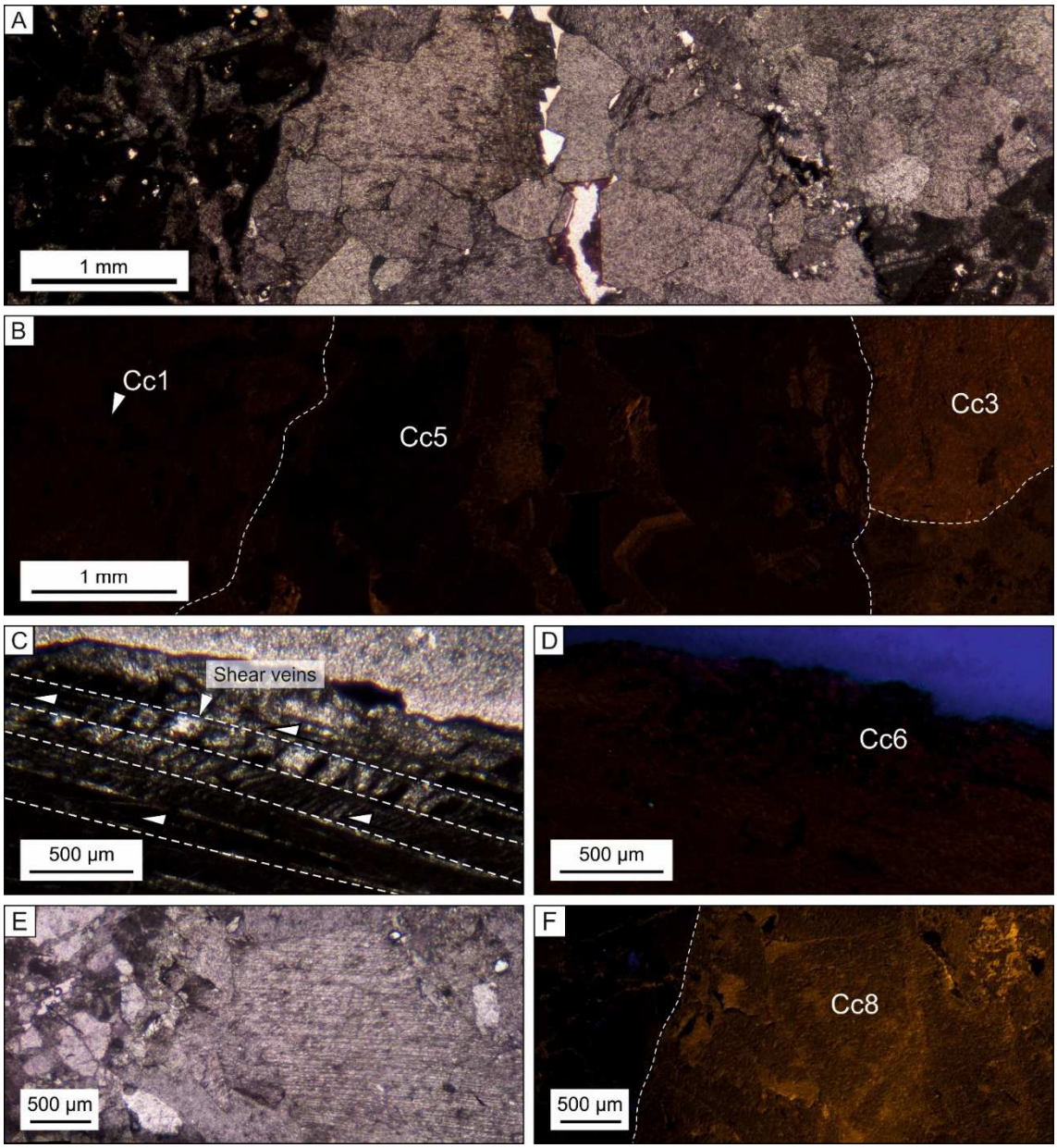

Fig. 6 Images from polarizing optical and cathodoluminescence (CL) microscopes of the main features of calcite cements and microstructures. A-B) Crosscutting relationships between intergranular porosity and veins filled with calcite cements Cc3 and Cc5. C-D) Image showing veins forming F4 reverse faults filled with calcite cement Cc6. E-F) Calcite cement Cc8 filling veins forming F7 normal faults.

in vug porosity postdating Cc1 and Cc2 in outcrop Q (Fig. 6A, B and 7). Cc4 consists of blocky and bladed crystals ranging between 250 µm and 2 mm and between 300 µm and 1 mm long, respectively. This cement is dull-orange to orange luminescent and precipitated in reactivated F1 fractures and in F3 veins affecting Eocene syn-orogenic sediments in outcrop Q (Fig. 7). Cc5 consists of sparite crystals ranging from 100 to 700 µm. This cement is zoned, from non-luminescent to dull orange and precipitated in vug porosities within the Areny Formation and in some fractures F4 postdating the previous cements in outcrop Q (Fig. 6A and B). Cc6 consists of blocky microsparite and from 200 µm to 2 mm long fibrous crystals parallel to fracture walls or blocky sparite filling rhomb-shaped veinlets formed by crack-seal mechanism (Fig. 6C and D). This cement is dull-brown and precipitated in vug porosities within the Areny Formation and in F4

and F5 fractures postdating Cc5 (Fig. 7). Cc6 has been observed in outcrops Q, G1, G2 and PEG. Cc7 consists of blocky calcite crystals ranging from 100 µm to 1mm (Fig.7). This cement is dull to bright orange and precipitated in F6 fractures. Cc7 is only observed in outcrop G1. Calcite cement Cc8 consists of blocky crystals ranging from 500 µm to more than 2 mm in size and shows orange luminescence (Fig. 6E and F). Cc8 has been only observed within fractures F7 in outcrop EST.

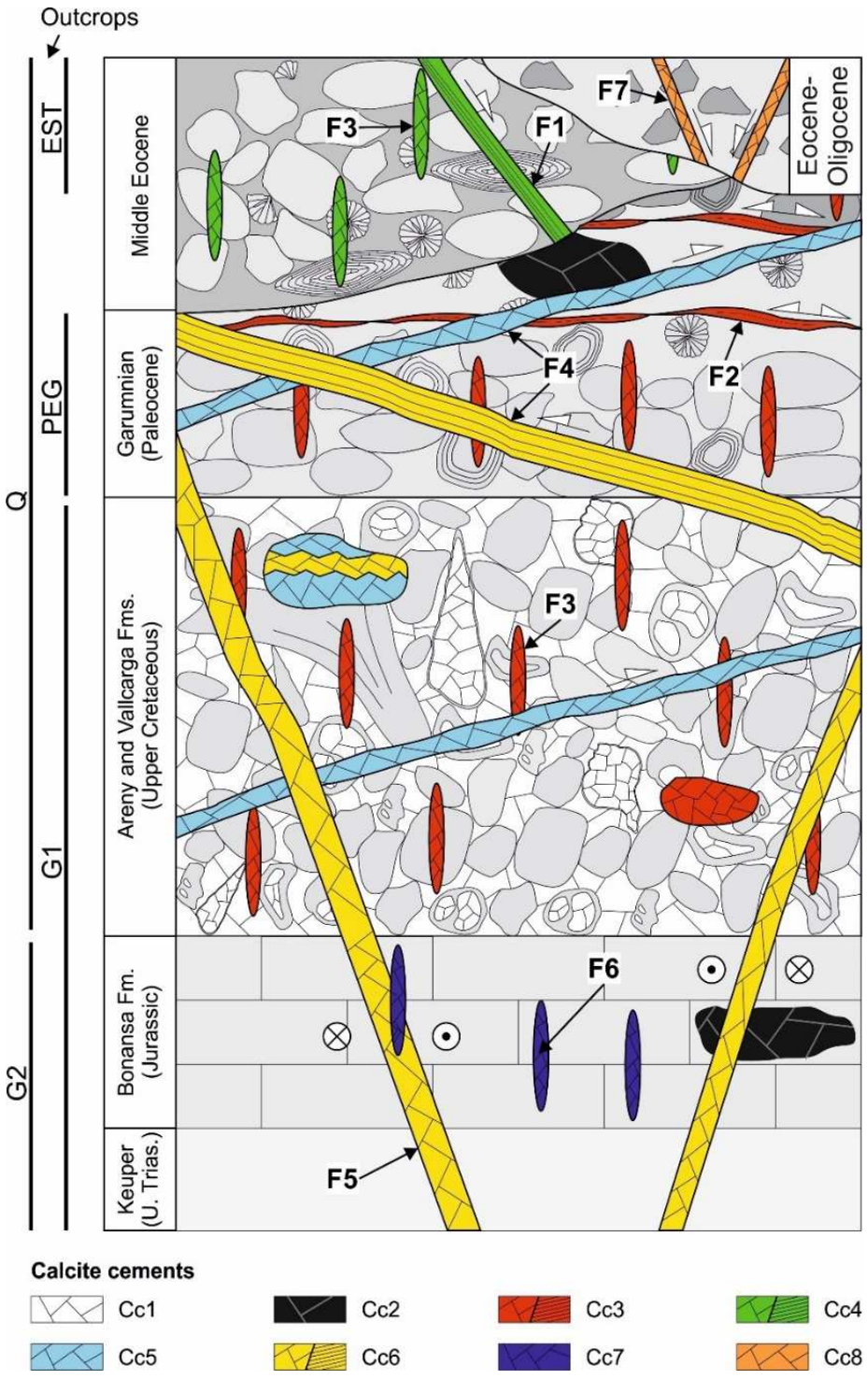

Fig. 7 Cross-cutting relationships between fractures and related calcite cements in the Lower Pedraforca thrust sheet.

Geochemistry

Carbon and oxygen isotopes

The carbon and oxygen isotopic composition of carbonate host rocks and calcite cements within the Lower Pedraforca thrust sheet is presented in Fig. 8 and Table S1.

Lower Jurassic marine limestones have $\delta^{13}C$ ranging from +1.5 to +4 ‰ VPDB and $\delta^{18}O$ between -5.2 and -3.6 ‰ VPDB (Fig. 8A). Marine carbonates from the Upper Cretaceous Vallcarga Formation have $\delta^{13}C$ values between +2.1 and +2.5 ‰ VPDB and $\delta^{18}O$ between -4.1 and -3.1 ‰ VPDB (Fig. 8A). Marine carbonates from the Upper Cretaceous Areny Formation have $\delta^{13}C$ between +1.5 and +1.7 ‰ VPDB and $\delta^{18}O$ between -4.5 and -3.2 ‰ VPDB (Fig.8). Paleocene palustrine limestones have $\delta^{13}C$ between -17.5 and -3.7 ‰ VPDB and $\delta^{18}O$ between -8.2 and -4.8 ‰ VPDB (Fig.8A). A carbonate clast from Oligocene conglomerates has a $\delta^{13}C$ of +1.1 ‰ VPDB and a $\delta^{18}O$ of -2.8 ‰ VPDB (Fig. 8A).

In order to simplify the discussion of the calcite cements, they have been grouped into: 1) calcite cements with $\delta^{18}O$ in equilibrium with their adjacent host rocks and 2) cements with $\delta^{18}O$ in disequilibrium with their adjacent host rocks (Fig. 8B).

Calcite cements from Cc1 to Cc5 show $\delta^{13}C$ and $\delta^{18}O$ values in equilibrium with their adjacent host rocks (Fig.8B). Cc1 has $\delta^{13}C$ of +1.5 ‰ VPDB and $\delta^{18}O$ of -5.2 ‰ VPDB (Fig.8A). Cc2 has $\delta^{13}C$ values between -10.1 and -6.6 ‰ VPDB and $\delta^{18}O$ values between -6.5 and -5 ‰ VPDB (Fig.8A). For Cc3, the $\delta^{13}C$ ranges between -10.8 and -0.4 ‰ VPDB and the $\delta^{18}O$ ranges between -6.4 and -3.9 ‰ VPDB (Fig.8A). Cc4 has $\delta^{13}C$ values between -5.9 and -3.7 ‰ VPDB and $\delta^{18}O$ between -6.9 and -2.6 ‰ VPDB and Cc5 has $\delta^{13}C$ values between +0.8 and +1.6 ‰ VPDB and $\delta^{18}O$ ranging between -5.7 and -4.4 ‰ VPDB (Fig. 8A).

On the other hand, calcite cements from Cc6 to Cc8 show $\delta^{18}O$ values in disequilibrium with their adjacent host rocks though their $\delta^{13}C$ values are in equilibrium with it (Fig. 8B). For Cc6, the $\delta^{13}C$ ranges between -8.9 and +3.7 ‰ VPDB and the $\delta^{18}O$ between -10.7 and -5.8 ‰ VPDB (Fig.8A). Cc7 has $\delta^{13}C$ values between -1.73 and -0.94 ‰ VPDB and $\delta^{18}O$ ranging between -11.3 and -9.58 ‰ VPDB (Fig.8A). The $\delta^{13}C$ for Cc8 ranges between -0.3 and -0.2 ‰ VPDB and the $\delta^{18}O$ between -7.3 and -6.2 ‰ VPDB (Fig.8A).

Clumped isotopes thermometry

For this study, clumped isotopes thermometry has been applied to calcite cements Cc3 and Cc6, since they represent a change in fluid regime during the evolution of the LPTS. The results are presented in a $\delta^{18}O_{fluid}$ vs clumped temperature cross-plot (Fig. 9) and in Table S2. Temperature in ºC and $\delta^{18}O_{fluid}$ in ‰ VSMOW of fluids are calculated from measured Δ_{47} in carbonate cements using the equation of Davies and John (2019) for clumped isotope temperature and Friedman and O'Neil (1997) for the $\delta^{18}O_{fluid}$.

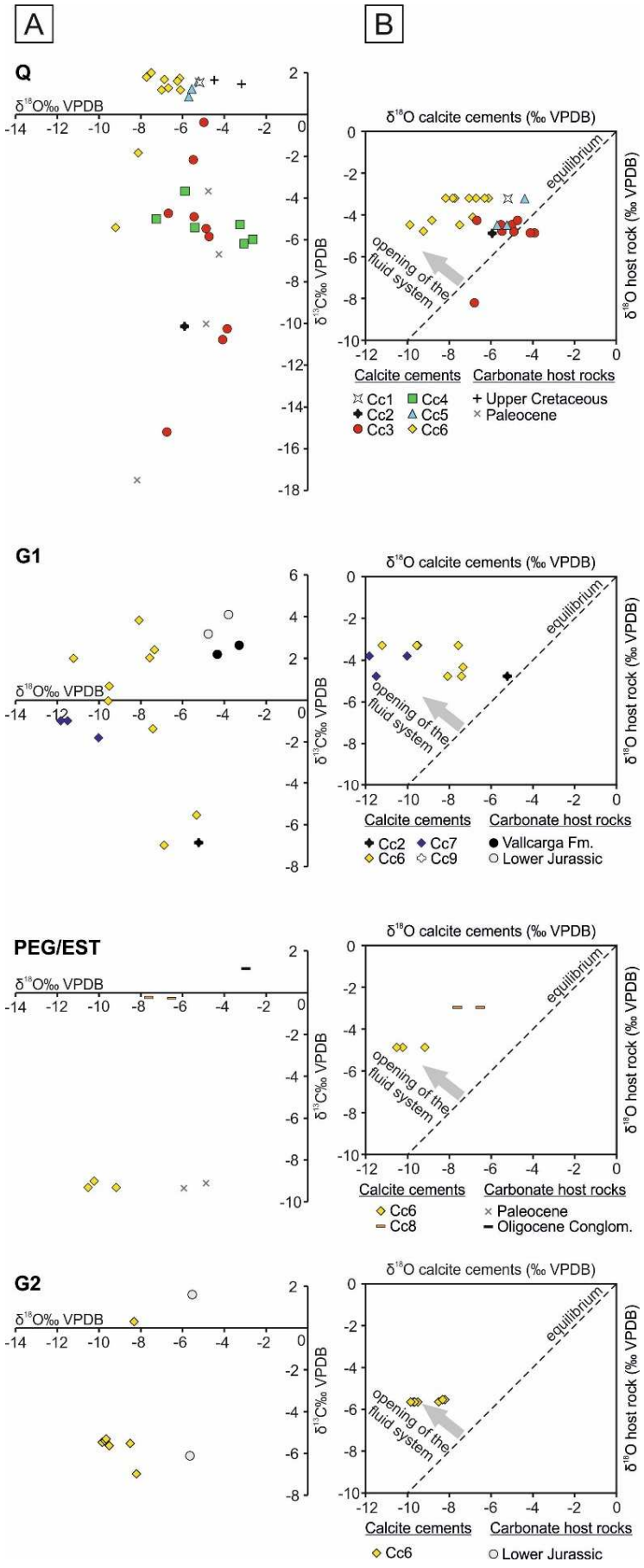

Fig. 8 $\delta^{18}O$ vs $\delta^{13}C$ and $\delta^{18}O_{calcite\ cements}$ vs $\delta^{18}O_{host\ rock}$ cross-plots from the Lower Pedraforca thrust sheet. The dashed black line represents the equilibrium between calcite veins and their adjacent host rocks.

For Cc3, the Δ_{47} is 0.579 ± 0.011 ‰, which translates into a temperature of 69.08 ± 5.34 ºC and a $\delta^{18}O_{fluid}$ of 5.42 ± 0.87 ‰ VSMOW. The analysed Δ_{47} for Cc6 is 0.579 ± 0.008 ‰, which translates into a temperature of 74.16 ± 4 ºC and a $\delta^{18}O_{fluid}$ of 5.08 ± 0.67 ‰ VSMOW.

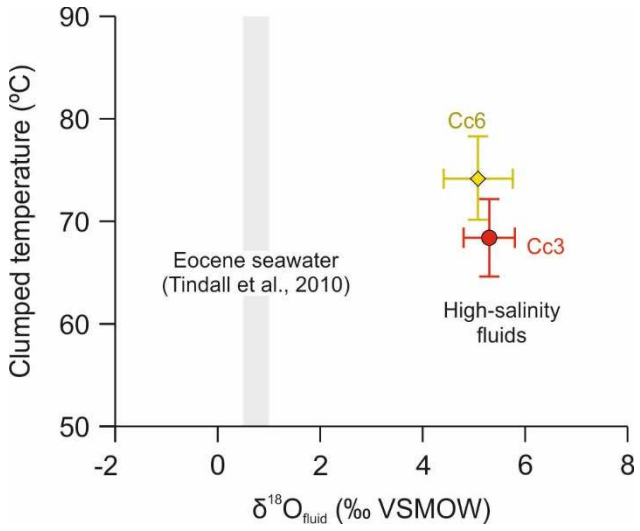

Fig. 9 Clumped isotopes temperatures in ºC vs calculated $\delta^{18}O_{fluid}$ (‰ VSMOW) for calcite cements Cc3 and Cc6 within the Lower Pedraforca thrust sheet. $\delta^{18}O$ of Eocene seawater in (‰ VSMOW is from Tindall et al. (2010).

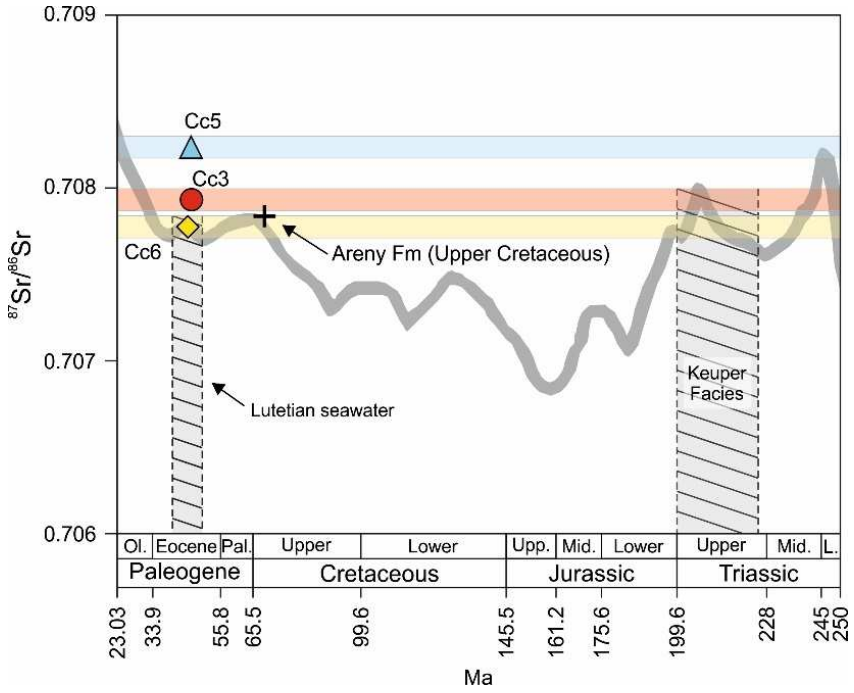

Fig. 10 $^{87}Sr/^{86}Sr$ composition of calcite cements and carbonate host rocks from the Lower Pedraforca thrust sheet. The $^{87}Sr/^{86}Sr$ ratios of the LOWESS curve from McArthur et al. (2001) are also plotted. The dashed grey areas indicate the $^{87}Sr/^{86}Sr$ ratios of middle Eocene seawaters and the Upper Triassic seawater.

Strontium isotopes

The Areny Fm. limestone has an $^{87}Sr/^{86}Sr$ ratio of 0.707841 (Fig.9, Table S2). Only calcite cements Cc3, Cc5 and Cc6 could be sampled, obtaining $^{87}Sr/^{86}Sr$ ratios of 0.707922, 0.708230 and 0.707817, respectively (Fig.10, Table S3).

Elemental composition

The Fe, Mg, Sr and Mn contents and Ca/Fe ad Mg/Ca molar ratios of calcite cements Cc1, Cc3, Cc4, Cc5 and Cc6 are presented in tables S4 and S5.

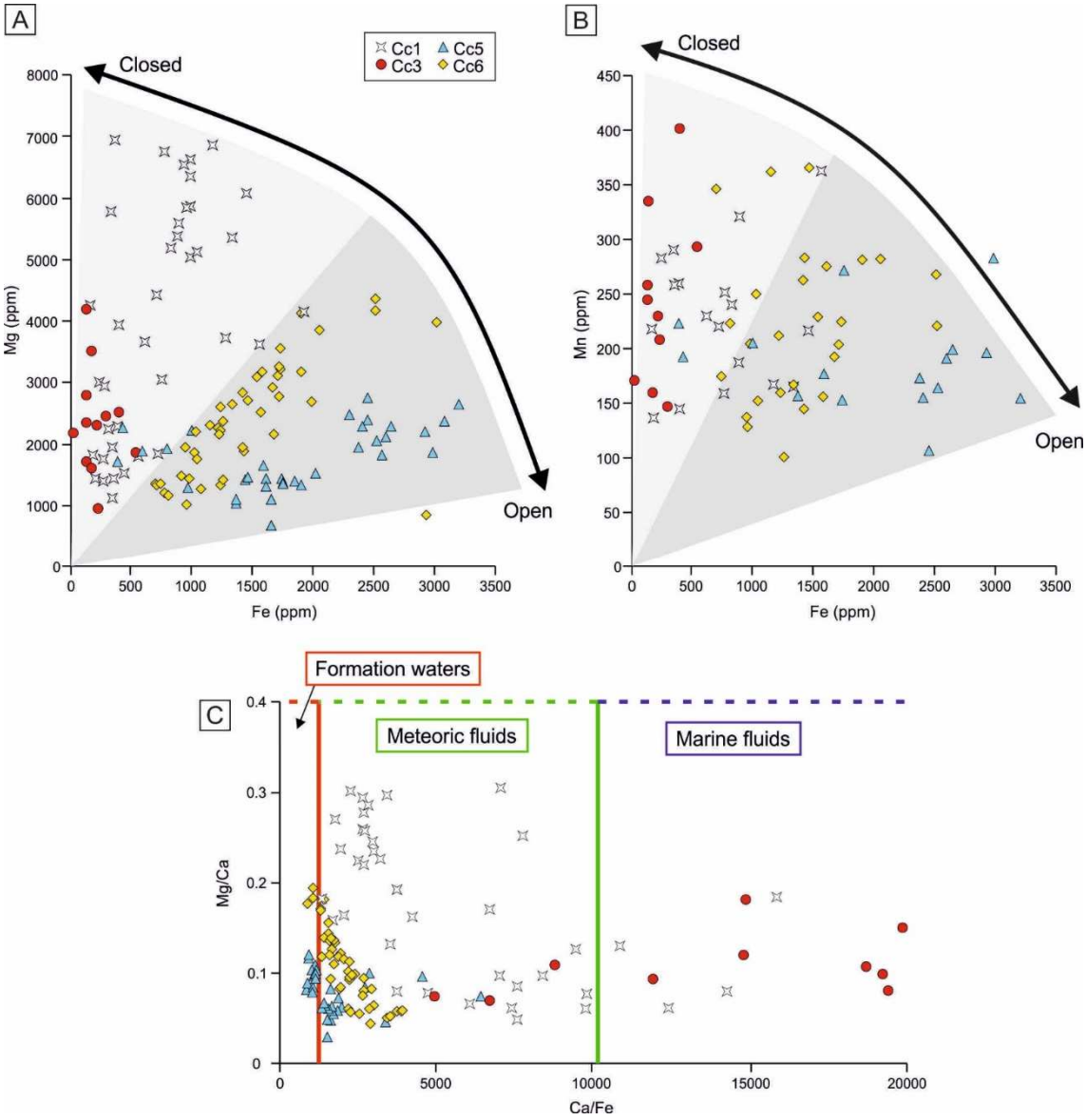

Fig. 11 Elemental composition of the calcite cements within the The Lower Pedraforca thrust sheet. A-B) Fe vs Mg and Fe vs Mn cross-plots of calcite cements Cc1, Cc3, Cc5 and Cc6. C) Ca/Fe vs Mn/Ca cross-plot of calcite cements Cc1-Cc3, Cc5 and Cc6. Areas bounded by blue, green and red thick lines represent the composition of marine, meteoric and formation fluids, respectively.

The elemental composition of calcite cement Cc1 shows values ranging from 172 to 1940 ppm in Fe and from 1096 to 6925 ppm in Mg. Sr and Mn contents range from below the detection limit to 3592 and 361 ppm, respectively. Calcite cement Cc3 has values ranging from below the detection limit to 548 ppm in Fe and from 289 to 4169 ppm in Mg. The Sr and Mn contents range from below the detection limit to 879 and 477 ppm, respectively. In calcite cement Cc4, the Fe

content is below the detection limit, whereas Mg shows values ranging from 801 to 4560 ppm. The Sr and Mn contents range from below the detection limit to 275 and 384 ppm, respectively. For calcite cement Cc5, Mg content ranges from 672 to 2765 ppm and the Fe, Sr and Mn contents range from below the detection limit to 3028, 1851 and 365 ppm, respectively. The Mg content of calcite cement Cc6 range from 679 to 4353 whereas its Fe, Sr and Mn contents range from below the detection limit to 3021, 656 and 362 ppm, respectively.

The distribution of results in a Fe vs Mg and Fe vs Mn cross-plot shows two different fields characterized by different slopes and defined by the envelope of the regression lines of the different cements (Fig. 11A and B). The first field (dashed line) includes calcite cements Cc1 and Cc3 and shows a high slope whereas the second one (dotted line) includes cements Cc5 and Cc6 and shows a lower slope with respect to that in the previous cements.

Molar ratios between Ca and Fe, Sr, Mn and Mg were calculated from the formula of McIntire (1963) and using K_{Mg}=0.097 at 70 ºC (Katz, 1973), K_{Fe}=5 (Tucker and Wright, 1990), K_{Mn}=8 at 25º C (Lorens, 1981), K_{Sr}=0.08 at 100ºC (Kinsman, 1969). The Ca/Fe molar ratio of cements Cc1, Cc3, Cc5 and Cc6 ranges from 1390 to 15903, from 4963 to 19934, from 836 to 6993 and from 880 to 3912, respectively. The Mg/Ca molar ratio ranges from 0.0474 to 0.30378 for Cc1, from 0.06884 to 0.1802 for Cc3, from 0.03428 to 0.19737 for Cc4, from 0.02966 to 0.12077 for Cc5 and from 0.04393 to 0.19532 for Cc6. The Ca/Fe and Mg/Ca ratios are plotted in Fig. 11C. The Sr/Ca molar ratios of cements Cc1, Cc3, Cc4, Cc5 and Cc6 range from 0.00599 to 0.052244, from 0.00557 to 0.01283, from 0.0065 to 0.0201, from 0.00518 to 0.02744 and from 0.0061 to 0.01917, respectively. The Mn/Ca ratios range from 0.0000317 to 0.0000848 for Cc1, from 0.0000319 to 0.000113 for Cc3, from 0.0000333 to 0.0000906 for Cc4, from 0.00025 to 0.0000859 for Cc5 and from 0.0000231 to 0.0000832 for Cc6.

Discussion

Timing of fracture development

The seven fracture sets F1 to F7 studied in the present work were formed in different stages of evolution of the Lower Pedraforca thrust sheet.

The hydroplastic behaviour of F1 normal faults indicate that they were formed when the sediments were still poorly consolidated (Petit and Beauchamp,1986; Petit and Laville, 1987) and therefore, we interpret that they formed at shallow depths soon after deposition of the Upper Cretaceous Areny Formation and Middle Eocene syn-orogenic sediments. Similar fracture patterns also affecting the Areny Formation have been observed in other areas of the LPTS (Soliva and Benedicto, 2004, 2005; Soliva et al., 2006, 2008) (Fig. 2A).

Fractures F2, F3, F4 and F6 were dated using U-Pb geochronology of calcite cements Cc3, Cc4, Cc6 and Cc7 (Cruset et al., in review). The obtained ages (from 47.9 ± 1.3 Ma to 42.29 ± 0.84 Ma) indicate that these fractures formed at the end of the LPTS emplacement. Additionally, crosscutting relationships between fractures and bedding allow us to differentiate the different

stages of deformation during this later emplacement. For instance, fracture systems F2 and F3 are arranged parallel and perpendicular to bedding respectively. These fracture patterns are observed at regional scale and are typical from the background deformation formed during layer-parallel shortening, during the first stages of compression in many fold and thrust belts (Casini et al., 2011; Tavani et al., 2015). Fracture systems F4, F5 and F6 have a constant orientation regardless of the beds dip, indicating that they formed during the main or late stages of folding, once strata were already tilted (Casini et al., 2011). The youngest ages were obtained in calcite cement Cc7 precipitated in fractures F6 (from 42.99 ± 0.94 Ma to 42.29 ± 0.84 Ma), revealing that they formed after F4 and F5. The presence in the thrust front of hydroplastic normal faults F1 with striae sets showing a reverse motion indicate that they were reactivated during this late stage as well as in other areas of the LPTS (Fig. 2A), where they show oblique and strike-slip striae sets (Soliva and Benedicto, 2004, 2005). F1 hydroplastic normal faults were reactivated probably to accommodate tilting and changes the orientation during folding or due to tectonically-induced increase of fluid pressure (Letouzey et al., 1990; Sibson, 1995; Aydin, 2000; Wiprut and Zoback, 2000; Chi et al., 2012; Cobbold et al., 2013; Rutqvist et al., 2013; Soumaya et al., 2015; Wiseall et al., 2018). The presence of hydraulic breccias in thrust fault zones and normal faults tilted to low angle or to 0º can be accounted for by a combination of both processes.

Normal faults F7 affect well-cemented Oligocene conglomerates. Their NNW-SSE orientation is not consistent with the E-W trend of the main south Pyrenean structures (Vergés and Muñoz, 1990). The U-Pb age obtained for cement Cc8 precipitated in F7 (30.2 ± 2 Ma) suggests that their formation could be related to an E-W extensional collapse of the Oligocene conglomerates deposited during the Eocene-Oligocene reactivation of the LPTS (Cruset et al., in review).

Evolution of the paleohydrological system

The evolution of the palaeohydrological system through time within the Lower Pedraforca thrust sheet is inferred from the geochemical data of calcite cements Cc1 to Cc8.

The $\delta^{13}C$ of all studied calcite cements is similar to their adjacent host rocks, indicating a high interaction between fluids and host rocks (Fig. 8). Therefore, the high dispersion in $\delta^{13}C$ values responds to fluids interacting with carbonate host rocks from different origins (Fig. 8). Likewise, the $\delta^{18}O$ values for calcite cements Cc1 to Cc5 are similar to their adjacent host rocks, reporting high fluid-rock interaction and a relatively closed fluid system (Fig. 8). For calcite cements Cc6 to Cc8 however, the $\delta^{18}O$ is progressively more depleted with respect to their adjacent host carbonates, suggesting an opening of the paleohydrological system to fluids (Fig. 8). Such depletion in $\delta^{18}O$, is interpreted in other areas of the southern Pyrenees and orogens worldwide as: 1) a change to hotter conditions during its precipitation; or 2) the input of meteoric waters which mixed at depth with hotter and more saline fluids (Travé et al., 1997; Immenhauser et al., 2007; Breesch et al., 2009; Vilasi, 2010; Vandeginste et al., 2012; Beaudoin et al., 2014; Lacroix et al., 2014; Cruset et al., 2016a; 2018; Nardini et al., 2019).

The two fields observed in the Fe/Mn and Mg/Fe cross-plots (Fig.11A and B) also indicate the behavior of the paleohydrological system during fluid migration within the LPTS. Thus, as the distribution coefficient of Mn (KMn) is higher than the distribution coefficient of Fe (KFe), in a closed paleohydrological system, Mn decreases faster in the fluid than Fe (Dromgoole and Walter, 1990). By opposition, if Fe decreases faster than Mn, the system is open. In the LPTS, calcite cements Cc1 and Cc3 fall in the field with a higher slope (Fig. 11B) that is with Mn decreasing faster than Fe, and thus, reflecting a relatively closed system and high fluid-rock interaction. Contrarily, cements Cc5 and Cc6 fall in the field with a lower slope, which denotes that Fe decreases faster than Mn, and therefore, that they precipitated in a more open paleohydrological fluid system in which fluid-rock interaction was low. However, this fact is in contrast with the evidence of equilibrium in $\delta^{18}O$ between cement Cc5 and its adjacent host rock (Fig. 8). However, low water-rock ratios could explain $\delta^{18}O$ through reequilibration of the fluid with host rock values (Banner and Hanson, 1990).

The elemental composition of the calcite cements also indicates the type of fluids migrating within the LPTS, since it is inherited from the former fluid. The Mn/Ca and Sr/Ca molar ratios of calcite cements Cc1, Cc3, Cc4, Cc5 and Cc6 (from 0.000231 to 0.0000906 for Mn/Ca and from 0.00518 to 0.05224 for Sr/Ca) are within the range of formation waters (McIntire, 1963; Howson et al., 1987; Tucker and Wright, 1990). The Mg/Ca and Ca/Fe ratios of calcite cements Cc1 and Cc3 (from 0.02966 to 0.30378 for Mg/Ca and from 1390 to 19934 for Ca/Fe) indicate the influence of marine, formation and meteoric waters (Tucker and Wright, 1990; Kolker and Chou, 1994; Steuber and Rauch, 2005; Ligi et al., 2013) (Fig. 11C), whereas in calcite cements Cc5 and Cc6 (from 0.02966 to 0.19432 for Mg/Ca and from 836 to 6993 for Ca/Fe) are within the range of meteoric and formation waters (Howson et al., 1987; Tucker and Wright, 1990; Kolker and Chou, 1994). These results suggest that during the evolution of the fluid system, the influence of marine waters is higher during the precipitation of cements Cc1 and Cc3, when the fluid system was relatively closed (Fig. 11C). In contrast, during the precipitation of calcite cements Cc5 and Cc6, the influence of meteoric and formation waters was higher, accounting for the opening of the fluid system to these fluids (Fig. 11C).

The $^{87}Sr/^{86}Sr$ ratios of calcite cements Cc3 (0.707922) and Cc5 (0.708230) are higher than expected for cements precipitated from Middle Eocene seawater (McArthur et al., 2001) and thus, fluids had to interact with a more radiogenic source. The values of Cc3 fall within the range of the Upper Triassic evaporites from Keuper (Fig. 10), indicating that fluids from which this cement precipitated may have interacted with the Upper Triassic evaporites. This interpretation is supported by the high $\delta^{18}O$ VSMOW of the fluid obtained from clumped isotopes thermometry (5.42 ± 0.68 ‰ VSMOW). For Cc5 however, the $^{87}Sr/^{86}Sr$ ratio indicates that the fluid interacted with an even more radiogenic source, which in this case could be the continental deposits from the Garumnian. On the other hand, calcite cement Cc6 shows the lowest $^{87}Sr/^{86}Sr$ ratio (0.707817, Fig. 10), which could indicate the influence of either middle Eocene seawaters or of brines from the Upper Triassic Keuper facies, which act as a detachment of the thrust system (McArthur et

al., 2001). However, like in Cc3, the $\delta^{18}O$ of the fluid from which Cc6 precipitated (5.08 ± 0.0.87 ‰ VSMOW) indicates the influence of Upper Triassic hot brines rather than seawater.

Relationships between deformation style and fluid flow

From the integration of fracture, petrological and geochemical data, a conceptual model divided in five stages (F1 to F5) showing the relationships between fluid flow and fracturing during the development of the LPTS is presented (Fig. 12).

During the first stage (T1, Fig.3 and 12A), hydroplastic normal faults formed soon after the deposition of the Upper Cretaceous Areny Formation at shallow conditions. During this event, there was no precipitation of cement within F1 faults. This fact could be due to that faulting of poorly consolidated sediments with internal heterogeneities occasionally form zones of low permeability (Caine and Minor, 2009; Loveless et al., 2011), or that calcite tend to precipitate within fractures in areas with elevated pressures and temperatures (Lee et al., 1996). Therefore, at surficial conditions fluids might not be saturated in calcite.

During T2 (Fig.12B), formation fluids with marine influence and in equilibrium with their adjacent host rocks precipitated as calcite cements Cc1 and Cc2 in the intergranular, moldic and vug porosities within the Jurassic Bonansa and Upper Cretaceus Areny Formations and Paleocene Garumnian facies. These cements precipitated previously to the compression related to the emplacement of the LPTS, as evidenced by crosscutting relationships between cements Cc1 and Cc2 and cement Cc3 (Fig. 6A and B and 7). Therefore, they probably precipitated during burial diagenesis of the Jurassic, Upper Cretaceous and Paleocene sediments.

At stage T3, during the layer-parallel shortening, fractures F2 and F3 formed in the studied area (Fig.3 and 12C). Hot brines (~70 ºC) derived from the Upper Triassic evaporites and in equilibrium with adjacent Upper Cretaceous and Paleocene host rocks (Fig. 8), migrated through fractures F2 and F3 and precipitated as calcite cements Cc3 and Cc4 in a relatively closed system (Fig. 11C). During T3, hydroplastic normal faults F1 in the Upper Cretaceous Areny Formation were cut by fractures F3, without being reactivated. In the thrust front however, hydroplastic normal faults developed within middle Eocene syn-orogenic sediments within Q outcrop were reactivated as they were tilted, allowing fluids to migrate and the precipitation of calcite cement Cc4.

During the fourth stage (T4), F4 reverse and F5 strike-slip faults and F6 veins developed during the folding and thrusting stage (T4, Fig.3 and 12D). During this event, recorded by cements Cc5, Cc6 and Cc7, the fluid system opened and the interaction between hot brines from the Keuper facies and host rocks decreased (Fig. 8, 10 and 11C). As deformation increased, F1 hydroplastic normal faults in the Upper Cretaceous Areny Formation were reactivated as reverse faults in the thrust front, whereas in other areas were reactivated as strike-slip faults, allowing fluid migration (Soliva and Benedicto, 2004, 2005; Soliva et al., 2006, 2008) (Fig. 2A). Such reactivations were induced by fluid pressure build-up and/or reorientation of pre-existing fractures

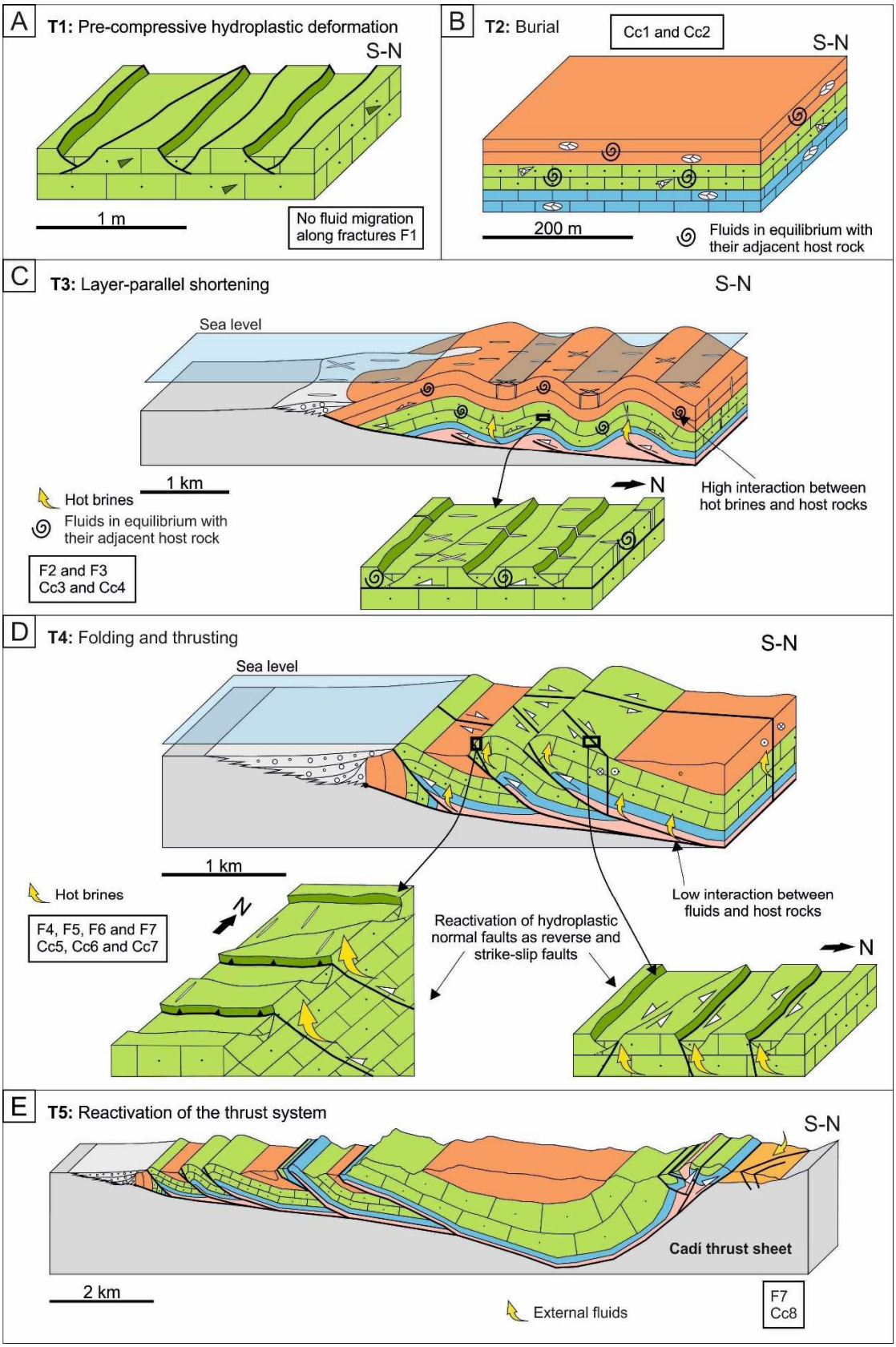

Fig. 12 Conceptual model of fluid flow evolution during the emplacement of the Lower Pedraforca thrust sheet. A) T1, pre-compressive hydroplastic deformation. B) T2, burial diagenesis. C) T3, early contraction. D) T4, late folding and thrusting. E) T5, reactivation of the thrust system. For each stage, the type of migrating fluids, associated calcite cements and fractures formed are given. Legend units are in Fig. 1C.

during folding (Letouzey et al., 1990; Sibson, 1995; Aydin, 2000; Wiprut and Zoback, 2000; Chi et al., 2012; Cobbold et al., 2013; Rutqvist et al., 2013; Soumaya et al., 2015; Wiseall et al., 2018). Fluids migrated along discrete fault planes or hydraulic breccias formed by fluid overpressures, which act as preferential paths in areas with low permeability (Aydin, 2000).

Finally, during the reactivation of the thrust system (T5, Fig. 3 and 12E) normal faults F7 formed, and fluids also in disequilibrium with their adjacent host rocks migrated through fractures where cement Cc8 precipitated in a relatively open system.

In our model, the differences in fluid flow behavior between the layer-parallel shortening and the late folding and thrusting have strong similarities with that observed in other fold and thrust belts worldwide. In all cases, fluid-related processes are controlled by the evolution of deformation patterns (Evans and Fischer, 2012). For instance, in the Bighorn Basin (Sevier thrust belt, USA), a closed paleohydrological system prevails during the layer-parallel shortening, whereas it opens to basement-derived fluids during the fracturing associated to folding and thrusting (Beaudoin et al., 2013). Likewise, in the Mexican fold and thrust belt and in the central Appalachians, fluids are stratigraphically segregated during the early deformation, whereas during fold tightening the fluid system is interconnected (Lefticariu et al., 2005; Fischer et al., 2009; Fitz-Diaz et al., 2011; Evans et al., 2012). Finally, in the Northern Oman Mountains, pre-burial fluids migrated through fractures in a rock-buffered system and deep-sourced fluids migrated through thrust faults during the main stage of compression (Breesch et al., 2009). In this last example, main thrust faults acted as barriers for transversal fluid flow, since evidences of migration of fluids were not observed in the hangingwall. These controls of deformation on the fluid regime in compressional settings are also observed in extensional regimes (Benedicto et al., 2008; Baqués et al., 2010; Cantarero et al., 2014). In these examples, during the first stages of the upwards propagation of normal faults, the paleohydrological system is relatively closed with high fluid-rock interaction. In contrast, during the final stages of deformation the system changes to a more open one, in which fluid-rock interaction is lower.

Conclusions

The integration of field-based and petrographic observations, together with geochemical data allow us to differentiate up to eight calcite cements (Cc1 to Cc8) revealing the evolution of the paleohydrological system during the emplacement of the Lower Pedraforca thrust sheet.

Calcite cements Cc1 to Cc4 precipitated from fluids in a relatively closed paleohydrological system in which the fluid-rock interaction was high. Calcite cement Cc3 precipitated from brines derived from the Upper Triassic evaporites acting as a detachment of the Lower Pedraforca thrust system ($\delta^{18}O_{fluid}$ ~+5.4 ‰ VSMOW) with $^{87}Sr/^{86}Sr$ ratios of 0.707922 and at temperatures around 70 ºC. Contrarily, calcite cements Cc5 to Cc8 precipitated from fluids in a more open paleohydrological system in which the interaction between fluids and host rocks was low. Cc6

also precipitated from brines derived from the Upper Triassic ($\delta^{18}O_{fluid}$ ~+5 ‰ VSMOW) with $^{87}Sr/^{86}Sr$ ratios of 0.707817 and at temperatures around 75 ºC.

Relationships between calcite cements and fractures indicate that: 1) during hydroplastic deformation related to the pre-folding stage within the Lower Pedraforca thrust sheet, there was no precipitation of calcite cements in fracture planes; 2) during the layer parallel shortening fluids migrated in a relatively closed system and fluid-rock interaction was high; and 3) during the folding and thrusting related to the emplacement of the Lower Pedraforca thrust sheet and during its late reactivation, the fluid-rock interaction decreased as the paleohydrological system opened.

Acknowledgements

The isotopic and electron microprobe analyses were carried out at “Centres Científics i Tecnològics” of the Universitat de Barcelona. Strontium analyses were done at the “CAI de Geocronología y Geoquímica Isotópica (UCM-CEI)” of the Universidad Complutense de Madrid. The clumped isotopes analyses were performed in the Qatar Stable Isotope Laboratory of Imperial College of London. This research was performed within the framework of DGICYT Spanish Project CGL2015-66335-C2-1-R, Grup Consolidat de Recerca ”Geologia Sedimentària” (2017SGR-824).

References

Aydin, A., 2000. Fractures, faults, and hydrocarbon entrapment, migration and flow. Marine and Petroleum Geology 17, 797-814.

Banner, J.L., Hanson, G.N., 1990. Calculation of simultaneous isotopic and trace element variations during water-rock interaction with applications to carbonate diagenesis. Geochimia et Cosmochimica Acta 54, 3123-3137.

Baqués, V., Travé, A., Benedicto, A., Labaume, P., Cantarero, I., 2010. Relationships between carbonate fault rocks and fluid flow regime during propagation of the Neogene extensional faults of the Penedès basin (Catalan Coastal Ranges, NE Spain). Journal of Geochemical Exploration 106, 24-33.

Beaudoin, N., Bellahsen, N., Lacombe, O., Emmanuel, L., Pironon, J., 2014. Crustal-scale fluid flow during the tectonic evolution of the Bighorn Basin (Wyoming, USA). Basin Research 26, 403-435.

Beaudoin, N., Huyghe, D., Bellahsen, N., Lacombe, O., Emmanuel, L., Mouthereau, F., Ouanhnon, L., 2015. Fluid systems and fracture development during syn-depositional fold growth: An example from the Pico del Aguila anticline, Sierras Exteriores, southern Pyrenees, Spain. Journal of Structural Geology 70, 23-38.

Beaudoin, N., Lacombe, O., Bellahsen, N., Emmanuel, L., 2013. Contribution of Studies of Sub-Seismic Fracture Populations to Paleo-Hydrological Reconstructions (Bighorn Basin, USA). Procedia Earth and Planetary Science 7, 57-60.

Benedicto, A., Plagnes, V., Vergély, P., Flotté, N., Schultz, R.A., 2008. Fault and fluid interaction in a rifted margin: integrated study of calcite-sealed fault-related structures (southern Corinth margin). Geological Society, London, Special Publications 299, 257-275.

Breesch, L., Swennen, R., Vincent, B., 2009. Fluid flow reconstruction in hanging and footwall carbonates: Compartmentalization by Cenozoic reverse faulting in the Northern Oman Mountains (UAE). Marine and Petroleum Geology 26, 113-128.

Burbank, D.W., Puigdefàbregas, C., Muñoz, J.A., 1992a. The chronology of the Eocene tectonic and stratigraphic development of the Eastern Pyrenean Foreland Basin. NE Spain. Geol. Soc. America Bull. 104, 1101-1120.

Burbank, D.W., Vergés, J., Muñoz, J.A., Bentham, P., 1992b. Coeval hinward- and forward-imbricating thrusting in the south-central Pyrenees, Spain: Timing and rates of shortening and deposition. Geological Society of America Bulletin 104, 3-17.

Caine, J.S., Minor, S.A., 2009. Structural and geochemical characteristics of faulted sediments and infewrences on the role of water in deformation, Rio Grande Rift, New Mexico. GSA Bulletin 121, 1325-1340.

Calvet, F., Porta, N.S.d., Salvany, J.M., 1993. Cronoestratigrafía (Palinología) del Triásico Sudpirenaico y del Pirineo Vasco-Cantábrico. Acta Geologica Hispanica 28, 33-48.

Cantarero, I., Alías, G., Cruset, D., Carola, E., Lanari, P., Travé, A., 2018. Fluid composition changes in crystalline basement rocks from ductile to brittle regimes. Global and Planetary Change 171, 273-292.

Cantarero, I., Travé, A., Alías, G., Baqués, V., 2014. Polyphasic hydrothermal and meteoric fluid regimes during the growth of a segmented fault involving crystalline and carbonate rocks (Barcelona Plain, NE Spain). Geofluids 14, 20-44.

Casini, G., Gillespie, P.A., Vergés, J., Romaire, I., Fernández, N., Casciello, E., Saura, E., Mehl, C., Homke, S., Embry, J.-C., Aghajari, L., Hunt, D.W., 2011. Sub-seismic fractures in Foreland fold and Thrust belts: insight from the Lurestan Province, Zagros Mountains, Iran. Petroleum Geoscience 17, 263-282.

Chi, G., Xue, C., Qing, H., Xue, W., Zhang, J., Sun, Y., 2012. Hydrodynamic analysis of clastic injection and hydraulic fracturing structures in the Jinding Zn-Pb deposit, Yunnan, China. Geoscience Frontiers 3, 73-84.

Choukroune, P., team, E., 1989. The ECORS Pyrenean deep seismic profile reflection data and the overall structure of an orogenic belt. Tectonics 8, 23-39.

Claypool, G.E., Kaplan, W.T., Kaplan, I.R., Sakai, H., Zak, I., 1980. The age curves of sulfur and oxygen isotopes in marine sulfate and their mutual interpretations. Chemical Geology 28, 199-260.

Cobbold, P.R., Zanella, A., Rodrigues, N., Løseth, H., 2013. Bedding-parallel fibrous veins (beef and cone-in-cone): Worldwide occurrence and possible significance in terms of fluid overpressure, hydrocarbon generation and mineralization. Marine and Petroleum Geology 43, 1-20.

Costa, E., Garcés, M., López-Blanco, M., Beamud, E., Gómez-Paccard, M., Larrasoaña, J.C., 2010. Closing and continentalization of the South Pyrenean foreland basin (NE Spain): magnetochronological constraints. Basin Research 22, 904-917.

Craig, H., Gordon, I.-I., 1965. Deuterium and oxygen-18 variations in the ocean and the marine atmosphere, in: Tongiorgi, E. (Ed.), Proceedings of a Conference on Stable Isotopes in Oceanographic Studies and Paleotemperatures. Consiglio Nazionale delle Richerche, Laboratorio di Geologia Nucleare, Pisa, Italy, pp. 9-130.

Crognier, N., Hoareau, G., Aubourg, C., Dubois, M., Lacroix, B., Branellec, M., Callot, J.P., Vennemann, T., 2017. Syn-orogenic fluid flow in the Jaca basin (south Pyrenean fold and thrust belt) from fracture and vein analyses. Basin Research, 1-30.

Cruset, D., Cantarero, I., Travé, A., Vergés, J., John, C.M., 2016a. Crestal graben fluid evolution during growth of the Puig-reig anticline (South Pyrenean fold and thrust belt). Journal of Geodynamics 101, 30-50.

Cruset, D., Cantarero, I., Vergés, J., John, C.M., Muñoz-López, D., Travé, A., 2018. Changes in fluid regime in syn-orogenic sediments during the growth of the south Pyrenean fold and thrust belt. Global and Planetary Change 171, 207-224.

Cruset, D., Vergés, J., Albert, R., Gerdes, A., Benedicto, A., Cantarero, I., Travé, A., in review. U-Pb Geochronology applied to fracture-filling calcite cements to decipher emplacement and reactivation of SE Pyrenean thrust sheets. Geology.

Davies, A.J., John, C.M., 2019. The clumped (13C18O) isotope composition of echinoid calcite: Further evidence for “vital effects” in the clumped isotope proxy. Geochimica et Cosmochimica Acta 245, 172-189.

Delvaux, D., Sperner, B., 2003. New aspects of tectonic stress inversion with reference to the TENSOR program, in: Nieuwland, D.A. (Ed.), New Insights into Structural Interpretation and Modelling. Geological Society, London, Special Publications, pp. 75-100.

Dennis, K.J., Affeck, H.P., Passey, B.H., Schrag, D.P., Eiler, J.M., 2011. Defining an absolute reference frame for ‘clumped’ isotope studies of CO2. Geochimia et Cosmochimica Acta 75, 7117-7131.

Dimmen, V., Rotevatn, A., Peacock, D.C.P., Nixon, C.W., Naerland, K., 2017. Quantifying structural controls on fluid flow: Insights from carbonatehosted fault damage zones on the Maltese Islands. Journal of Structural Geology 101, 43-57.

Dromgoole, E.L., Walter, L.M., 1990. Iron and manganese incorporation into calcite: effects of growth kinetics, temperature, and solution chemistry. Chemical Geology 81, 311-336.

Egholm, D.L., Clausen, R.O., Sandiford, M., Kristensen, M.B., Korstgård, J.A., 2008. The mechanics of clay smearing along faults. Geology 36, 787-790.

Evans, M.A., Bebeout, G.E., Brown, C.H., 2012. Changing fluid conditions during folding: An example from the central Appalachians. Tectonophysics 576-577, 99-115.

Evans, M.A., Fischer, M.P., 2012. On the distribution of fluids in folds: A review of controlling factors and processes. Journal of Structural Geology 44, 2-24.

Fischer, M.P., Higuera-Díaz, I.C., Evans, M.A., Perry, E.C., Lefticariu, L., 2009. Fracture-controlled paleohydrology in a map-scale detachment fold: Insights from the analysis of fluid inclusions in calcite and quartz veins. Journal of Structural Geology 31, 1490-1510.

Fitz-Diaz, E., Hudleston, P., Siebenaller, L., Kirschner, D., Camprubí, A., Tolson, G., Puig, T.P., 2011. Insights into fluid flow and water-rock interaction during deformation of carbonate sequences in the Mexican fold-thrust belt. Journal of Structural Geology 33, 1237-1253.

Friedman, I., O'Neil, J.R., 1977. Compilation of stable isotope fractionation factors of geochemical interest, in: Fleischer, M. (Ed.), Data of Geochemistry, U. S. Gov. Print. Off. Washington D. C., pp. 1-12.

Guo, W., Mosenfelder, J.L., Goddard, W.A., Eiler, J.M., 2009. Isotopic fractionations associated with phosphoric acid digestion of carbonate minerals: Insights from first-principles theoretical modeling and clumped isotope measurements. Geochimia et Cosmochimica Acta 73, 7203-7225.

Gutmanis, J., Oró, L.A.i., Díez-Canseco, D., Chebbihi, L., Awdal, A., Cook, A., 2017. Fracture analysis of outcrop analogues to support modelling of the subseismic domain in carbonate reservoirs, south-central Pyrenees, in: Ashton, M., Dee, S.J., Wennberg, O.P. (Eds.), Subseismic-Scale Reservoir Deformation. Geological Society, London, Special Publications, pp. 139-156.

Howson, M.R., Pethybridge, A.D., House, W.A., 1987. Synthesis and distribution coefficients of low-magnesium calcites. Chemical Geology 64, 79-87.

Huntington, K.W., Eiler, J.M., Affeck, H.P., Guo, W., Bonifacie, M., Yeung, L.Y., Thiagarajan, N., Passey, B., Tripati, A., Daëron, M., Came, R., 2009. Methods and limitations of 'clumped' CO2 isotope (Δ47) analysis by gas-source isotope ratio mass spectrometry. Journal of Mass Spectrometry 44, 1318-1329.

Immenhauser, A., Dublyansky, Y.V., Verwer, K., Fleitman, D., Pashenko, S.E., 2007. Textural, elemental and isotopic characteristics of Pleistocene phreatic cave deposits (Jabal Madar, Oman). Journal of Sedimentary Research 77, 68-88.

John, C.M., Bowen, D., 2016. Community software for challenging isotope analysis: First applications of "Easotope" to clumped isotopes. Rapid Communications in Mass Spectrometry 30, 2285-2300.

Katz, A., 1973. The interaction of magnesium with calcite during crystal growth at 25-90ºC and one atmosphere. Geochimia et Cosmochimica Acta 39, 486-508.

Khosravi, M., Rostami, B., Fatemi, S., 2012. Uncertainty Analysis of a Fractured Reservoir's Performance: A Case Study. Oil & Gas Science and Technology 67, 423-433.

Kim, S.T., O'Neil, J.R., 1997. Equilibrium and nonequilibrium oxygen isotope effects in synthetic carbonates. Geochimia et Cosmochimica Acta 61, 3461-3475.

Kinsman, D.J.J., 1969. Interpretation of Sr2+ concentrations in carbonate minerals and rocks. Journal of sedimentary Petrology 39, 486-508.

Kolker, A., Chou, C.L., 1994. Cleat-Filling Calcite in Illinois Basin Coals: Trace-Element Evidence for Meteoric Fluid Migration in a Coal Basin. The Journal of Geology 102.

Lacroix, B., Baumgartner, L.P., Bouvier, A.S., Kempton, P.D., Vennemann, T., 2018. Multi fluid-flow record during episodic mode I opening: Amicrostructural and SIMS study (Cotiella Thrust Fault, Pyrenees). Earth and Planetary Science Letters 503, 37-46.

Lacroix, B., Travé, A., Buatier, M., Labaume, P., Vennemann, T., Dubois, M., 2014. Syntectonic fluid-flow along thrust faults: Example of the South-Pyrenean fold-and-thrust belt. Marine and Petroleum Geology 49, 84-98.

Lee, Y.J., Morse, J.W., Wiltschko, D.V., 1996. An experimentally verified model for calcite precipitation in veins. Chemical Geology 130, 203-215.

Lefticariu, L., Perry, E.C., Fischer, M.P., Banner, J.L., 2005. Evolution of fluid compartmentalization in a detachment fold complex. Geology 33, 69-72.

Letouzey, J., Werner, P., Marty, A., 1990. Fault reactivation and structural inversion. Backarc and intraplate compressive deformations. Example of the eastern Sunda shelf (Indonesia). Tectonophysics 183, 341-362.

Ligi, M., Bonatti, E., Cuffaro, M., Brunelli, D., 2013. Post-Mesozoic Rapid Increase of Seawater Mg/Ca due to Enhanced Mantle-Seawater Interaction. Scientific Reports 3, 2752.

López-Martínez, N., Fernández-Marrón, M.T., Valle, M.F., 1999. The succession of vertebrates and plants across the Cretaceous-Tertiary boundary in the Tremp Formation, Ager valley (south-central Pyrenees, Spain). Geobios 32, 617-627.

Lorens, R., 1981. Sr, Cd, Mn and Co distribution coefficients in calcite as a function of calcite precipitation rate. Geochimia et Cosmochimica Acta 45, 553-561.

Loveless, S., Bense, V., Turner, J., 2011. Fault architecture and deformation processes within poorly lithified rift sediments, Central Greece. Journal of Structural Geology 33, 1554-1568.

Maher, H.D., Ogata, K., Braathen, A., 2017. Cone-in-cone and beef mineralization associated with Triassic growth basin faulting and shallow shale diagenesis, Edgeøya, Svalbard. Geological Magazine 154, 201-216.

Mangenot, X., Gasparrini, M., Rouchon, V., Bonifacie, M., 2018. Basin-scale thermal and fluid flow histories revealed by carbonate clumped isotopes (Δ47) – Middle Jurassic carbonates of the Paris Basin depocentre. Sedimentology 65, 123-150.

Marret, R., Allmendinger, R.W., 1990. Kinematic analysis of fault-slip data. Journal of Structural Geology 12, 973-986.

McArthur, J.M., Howarth, R.J., Bailey, T.R., 2001. Strontium Isotope Stratigraphy: LOWESS Version 3: Best Fit to the Marine Sr-Isotope Curve for 0–509 Ma and Accompanying Look-up Table for Deriving Numerical Age. Journal of Geology 109, 155-170.

McCaig, A.M., Tritlla, J., Banks, D.A., 2000. Fluid mixing and recycling during Pyrenean thrusting: evidence from fluid inclusion halogen ratios. Geochimia et Cosmochimica Acta 64, 3395-3412.

McCaig, A.M., Wayne, D.M., Marshall, J.D., Banks, D., Henderson, I., 1995. Isotopic and fluid inclusion studies of fluid movement along the Gavarnie Thrust, central Pyrenees: Reaction fronts in carbonate mylonites. American Journal of Science 295, 309-343.

McCrea, J.M., 1950. On the Isotopic Chemistry of Carbonates and a Paleotemperature Scale. Journal of Chemical Physics 18, 849-957.

McIntire, W.L., 1963. Trace element partition coefficients, a review of theory and applications to geology. Geochimia et Cosmochimica Acta 27, 1209-1264.

Mey, P.H.W., Nagtegaal, P.J.C., Roberti, K.J., Hartevelt, J.J.A., 1968. Lithostratigraphic subdivision of post-Hercinian deposits in the south-central Pyrenees, Spain. Leidse Geologische Mededelingen 41, 21-228.

Missenard, Y., Bertrand, A., Vergély, P., Benedicto, A., Cushing, M.-E., Rocher, M., 2014. Fracture-fluid relationships: implications for the sealing capacity of clay layers – Insights from field study of the Blue Clay formation, Maltese islands. Bulletin de la Société Géologique de France 185, 51-63.

Moeri, E.V., 1977. Oberkretazischen shelfsedimente in den zentralpyrenäen zwischen Rio Segre und Llobregat. Eclogae Geologicae Helvetiae 70, 193-235.

Muñoz, J.A., 1992. Evolution of a continental collision belt: ECORS–Pyrenees crustal balanced section, in: McClay, K.R. (Ed.), Thrust Tectonics. Chapman & Hall, London, pp. 235-246.

Muñoz, J.A., 2002. The Pyrenees, in: Gibbons, W., Moreno, T. (Eds.), The Geology of Spain. Geological Society, London, pp. 370-385.

Nardini, N., Muñoz-López, D., Cruset, D., Cantarero, I., Martín-Martín, J.D., Benedicto, A., Gómez-Rivas, E., John, C.M., Travé, A., 2019. From early contraction to post-folding fluid evolution in the frontal part of the Bóixols thrust sheet (southern Pyrenees) as revealed by the texture and geochemistry of calcite cements. Minerals 9, 117.

Ogata, K., Senger, K., Braathen, A., Tveranger, J., 2014. Fracture corridors as seal-bypass systems in siliciclastic reservoir-cap rock successions: Field-based insights from the Jurassic Entrada Formation (SE Utah, USA). Journal of Structural Geology 66, 162-187.

Oms, O., Dinarés-Turell, J., Vicens, E., Estrada, R., Vila, B., Galobart, À., Bravo, A.M., 2007. Integrated stratigraphy from the Vallcebre Basin (southeastern Pyrenees, Spain): New insights on the continental Cretaceous−Tertiary transition in southwest Europe. Palaeogeography, Palaeoclimatology, Palaeoecology 255, 35-47.

Petit, J.P., Beauchamp, J., 1986. Synsedimentary faulting and palaeocurrent patterns in the Triassic sandstones of the High Atlas (Morocco). Sedimentology 33, 817-829.

Petit, J.P., Laville, E., 1987. Morphology and microstructures of hydroplastic slickensides in sandstone. Geological Society, London, Special Publications 29, 107-121.

Pons, J.M., Caus, E., 1996. El Cretácico Superior en el Pirineo. Paleontología. Revista Española de Paleontología 11, 182-189.

Puigdefàbregas, C., Muñoz, J.A., Marzo, M., 1986. Thrust Belt Development in the Eastern Pyrenees and Related Depositional Sequences in the Southern Foreland Basin, in: Allen, P.A., Homewood, P. (Eds.), Foreland Basins. Blackwell Publishing Ltd., Oxford, UK. , pp. 229-246.

Puigdefàbregas, C., Muñoz, J.A., Vergés, J., 1992. Thrusting and Foreland Basin Evolution in the Southern Pyrenees, in: McClay, K.R. (Ed.), Thrust Tectonics. London, Chapman & Hall, pp. 247-254.

Rosell, J., Linares, R., Llompart, C., 2001. El "Garumniense" prepirenaico. Rev. Soc. Geol. España 14, 47-56.

Roure, F., Choukroune, P., Berastegui, J., Muñoz, J.A., Villien, A., Matheron, P., Bareyt, M., Seguret, M., Camara, P., Deramond, J., 1989. Ecors deep seismic data and balanced cross sections: Geometric constraints on the evolution of the Pyrenees. Tectonics 8, 41-50.

Roure, F., Swennen, R., Schneider, F., Faure, J.L., Ferket, H., Guilhaumou, N., Osadetz, K., Robion, P., Vandeginste, V., 2005. Incidence and Importance of Tectonics and Natural Fluid Migration on Reservoir Evolution in Foreland Fold-and-Thrust Belts. Oil & Gas Science and Technology 60, 67-106.

Rutqvist, J., Rinaldi, A.P., Cappa, F., Moridis, G.J., 2013. Modeling of fault reactivation and induced seismicity during hydraulic fracturing of shale-gas reservoirs. Journal of Petroleum Science and Engineering 107, 31-44.

Sans, M., 2003. From thrust tectonics to diapirism. The role of evaporites in the kinematic evolution of the eastern South Pyrenean front. Geologica Acta 1, 239-259.

Séguret, M., 1972. Étude tectonique des nappes et séries décollées de la partie centrale du vesant sud des Pyrénées. Pub. USTELA, sér, Geol. Struct. n.2, Montpellier.

Serra-Kiel, J., Hottinger, L., Caus, E., Drobne, K., Ferràndez, C., Jauhri, A.K., Less, G., Pavlovec, R., Pignatti, J., Samsó, J.M., Schaub, H., Sirel, E., Strougo, A., Tamberau, Y., Tosquella, J., Zakrevskaya, E., 1998a. Larger Foraminiferal Biostratigraphy of the Tethyan Paleocene and Eocene. Bulletin de la Societé Géologique de France 169, 281-299.

Serra-Kiel, J., Hottinger, L., Drobne, K., Ferràndez, C., Jauhri, A.K., Less, G., Pignatti, J., Samsó, J.M., Schaub, H., Sirel, E., Tamberau, Y., Tosquella, J., Zakrevskaya, E., 1998b. Larger benthic Foraminifera in: Thierry, J., Farley, M.B., Jacquin, T., Graciansky, P.C., Vail, P.R. (Eds.), Mesozoic-Cenozoic sequence stratigraphy of European basins., Society of Economic Paleontologist and Mineralogist, Special Publication, p. 60pp.

Shackleton, J.R., Cooke, M.L., Sussman, A.J., 2005. Evidence for temporally changing mechanical stratigraphy and effects on joint-network architecture. Geology 33, 101-104.

Shackleton, J.R., Cooke, M.L., Vergés, J., Simó, T., 2011. Temporal constraints on fracturing associated with fault-related folding at Sant Corneli anticline, Spanish Pyrenees. Journal of Structural Geology 33, 5-19.

Sibson, R.H., 1995. Selective fault reactivation during basin inversion: potential for fluid redistribution through fault-valve action, in: Buchanan, J.G., Buchanan, P.G. (Eds.), Basin Inversion, Geological Society Special Publication, pp. 3-19.

Simó, A., 1985. Secuencias deposicionales del Cretácico superior de la unidad del Montsec (Pirineo Central), Tesis Doctoral, Universitat de Barcelona. 325 pp.

Soliva, R., Benedicto, A., Maerten, L., 2006. Spacing and linkage of confined normal faults: Importance of mechanical thickness. Journal of Geophysical Research 111, B01402.

Soliva, R., Benedicto, A., Schultz, R.A., Maerten, L., Micarelli, L., 2008. Displacement and interaction of normal fault segments branched at depth: Implications for fault growth and potential earthquake rupture size. Journal of Structural Geology 30, 1288-1299.

Soumaya, A., Ayed, N.B., Delvaux, D., Ghanmi, M., 2015. Spatial variation of present-day stress field and tectonic regime in Tunisia and surroundings from formal inversion of focal mechanisms: Geodynamic implications for central Mediterranean. Tectonics 34, 1154-1180.

Steuber, T., Rauch, M., 2005. Evolution of the Mg/Ca ratio of Cretaceous seawater: Implications from the composition of biological low-Mg calcite. Marine Geology 217, 199-213.

Swanson, E.M., Wernicke, B.P., Eiler, J.M., Losh, S., 2012. Temperatures and fluids on faults based on carbonate clumped-isotope thermometry. American Journal of Science 312, 1-21.

Tavani, S., Mencos, J., Bausà, J., Muñoz, J.A., 2011. The fracture pattern of the Sant Corneli Bóixols oblique inversion anticline (Spanish Pyrenees). Journal of Structural Geology 33, 1662-1680.

Tavani, S., Storti, F., Lacombe, O., Corradetti, A., Muñoz, J.A., Mazzoli, S., 2015. A review of deformation pattern templates in foreland basin systems and fold-and-thrust-belts: Implications for the state of stress in the frontal regions of thrust wedges. Earth-Science Reviews 141, 82-104.

Tindall, J., Flecker, R., Valdes, P., Schmidt, D.N., Markwick, P., Harris, J., 2010. Modelling the oxygen isotope distribution of ancient seawater using a coupled ocean–atmosphere GCM: Implications for reconstructing early Eocene climate. Earth and Planetary Science Letters 292, 265-273.

Travé, A., Labaume, P., Calvet, F., Soler, A., 1997. Sediment dewatering and pore fluid migration along thrust faults in a foreland basin inferred from isotopic and elemental geochemical analyses (Eocene southern Pyrenees, Spain). Tectonophysics 282, 375-398.

Travé, A., Labaume, P., Calvet, F., Soler, A., Tritlla, J., Bautier, M., Potdevin, J.L., Séguret, M., Raynaud, S., Briqueu, L., 1998a. Fluid migration during Eocene thrust emplacement in the south Pyrenean foreland basin (Spain): an integrated structural, mineralogical and geochemical approach, in: Mascle, A., Puigdefàbregas, C., LuterBacher, H.P., Fernàndez, M. (Eds.), Cenozoic Foreland Basins of Western Europe. Geological Society, Special Publications, pp. 163-188.

Travé, A., Calvet, F., Sans, M., Vergés, J., Thirlwall, M., 2000. Fluid history related to the Alpine compression at the margin of the south-Pyrenean Foreland basin: the El Guix anticline. Tectonophysics 321, 73-102.

Trincal, V., Buatier, M., Charpentier, D., Lacroix, B., Lanari, P., Labaume, P., Lahfid, A., Venneman, T., 2017. Fluid–rock interactions related to metamorphic reducing fluid flow in meta-sediments: example of the Pic-de-Port-Vieux thrust (Pyrenees, Spain). Contributions to Mineralogy and Petrology 172, 78.

Tucker, M.E., Wright, P.V., 1990. Carbonate Sedimentology. Blackwell, Oxford.

Valero, L., Garcés, M., Cabrera, L., Costa, E., Sáez, A., 2014. 20 Myr of eccentricity paced lacustrine cycles in the Cenozoic Ebro Basin Earth and Planetary Science Letters 408, 183-193.

Vandeginste, V., Swennen, R., Allaeys, M., Ellam, R.M., Osadetz, K., Roure, F., 2012. Challenges of structural diagenesis in foreland fold-and-thrust belts: A case study on paleofluid flow in the Canadian Rocky Mountains West of Calgary. Marine and Petroleum Geology 35, 235-251.

Vergés, J., 1993. Estudi geològic del vessant sud del Pirineu oriental i central. Evolució cinemàtica en 3D. PhD thesis, Universitat de Barcelona, Barcelona, Spain, p. 203.

Vergés, J., Fernàndez, M., Martínez, A., 2002. The Pyrenean orogen: pre-, syn-, and post-collisional evolution, in: Rosenbaum, G., Lister, G. (Eds.), Reconstruction of the evolution of the Alpine-Himalayan Orogen. Journal of the Virtual Explorer, pp. 55-74.

Vergés, J., Martínez, A., Muñoz, J.A., 1992. South Pyrenean fold and thrust belt: The role of foreland evaporitic levels in thrust geometry, in: McClay, K. (Ed.), Thrust Tectonics. London, Chapman & Hall, pp. 255-264.

Vergés, J., Muñoz, J.A., 1990. Thrust sequences in the southern central Pyrenees. Bull. Soc. géol. France 8, 265-271.

Vilasi, N., 2010. Study of reservoir analogues in foreland fold-and-thrust belts: sedimentology, diagenesis, deformation and fracturing of the upper cretaceous-eocene carbonate systems of the ionian zone (Southern Albania). PhD thesis. Ecole des Mines de Paris, Paris, France, p. 190.

Wiprut, D., Zoback, M.D., 2000. Fault reactivation and fluid flow along a previously dormant normal fault in the northern North Sea. Geology 27, 595-598.

Wiseall, A.C., Cuss, R.J., Hough, E., Kemp, S.J., 2018. The role of fault gouge properties on fault reactivation during hydraulicstimulation; an experimental study using analogue faults. Journal of Natural Gas Science and Engineering 59, 21-34.

Chapter 8

Fluid flow evolution from the Mesozoic extension to the Alpine orogeny in the Upper Pedraforca thrust sheet (southern Pyrenees)

Fluid flow evolution from the Mesozoic extension to the Alpine orogeny in the Upper Pedraforca thrust sheet (southern Pyrenees)

David Cruset[1], Jaume Vergés[2], Antonio Benedicto[3], Enrique Gómez-Rivas[1], Irene Cantarero[1], Cédric M. John[4], Anna Travé[1]

[1] Departament de Mineralogia, Petrologia i Geologia Aplicada, Facultat de Ciències de la Terra, Universitat de Barcelona, (UB), Martí i Franquès s/n, 08028, Barcelona, Spain.
d.cruset@ub.edu, e.gomez-rivas@ub.edu, i_cantarero@ub.edu, atrave@ub.edu

[2] Institut de Ciències de la Terra Jaume Almera, ICTJA-CSIC, Lluís Solé i Sabaris s/n, 08028 Barcelona, Spain.
jverges@ictja.csic.es

[3] UMR Geops, Université Paris Sud, 91405 Orsay, France.
antonio.benedicto@u-psud.fr

[4] Department of Earth Science and Engineering, Imperial College London, SW7 2BP, UK.
cedric.john@imperial.ac.uk

Geofluids: In preparation

Introduction

Rifted margins are areas where diapirism occurs due to halokinetic movements (Sannemann, 1968; Jackson et al., 1990; Rowan and Vandeville, 2006; Hudec et al., 2013; Martín-Martín et al., 2016). Diapirs are structures that strongly control the palaeohydrology of salt-bearing basins, since fluids can migrate to salt bodies from adjacent areas and circulate through their boundaries, close to the weld zone (Reuning et al., 2009; Smith et al., 2012; Fischer et al., 2013). Resources like hydrocarbons and metalipherous ore deposits (i.e. Pb-Zn) associated with the migration of such fluids can accumulate below cap-rocks and structural traps related to the diapir growth (Rouvier et al., 1985; Sheppard et al., 1996; Davison, et al., 2000; Allen and Allen, 2005; Perona et al., 2018). Salt-bearing basins are often incorporated into orogens, and compressive deformation structures (e.g. new and reactivated fractures, folds) typically overprint the pre-existing fracture networks that formed during extension, thus resulting in complex crosscutting relationships between different structures (Salardon et al., 2017).

During compressive basin inversion, thrust faults can behave as paths for the vertical migration of overpressured fluids derived from sedimentary basins and/or the underlying basement (Sibson, 1995; Beaudoin et al., 2014; Frazer et al., 2014). These structures can also act as effective traps for hydrocarbons and become preferred sites for the formation of ore

deposits. Furthermore, previous hydrocarbon traps formed before orogenic compression can potentially be modified or jeopardized, allowing fluid re-mobilization (Roure et al., 2005; Cooper and Warren, 2010). Therefore, achieving a clear understanding of the different structures and fluid evolution between extensional and compressional phases before and during the formation of an orogen is key for basin analysis and for the exploration and production of georesources.

The southern Pyrenees is a well-known fold-and-thrust belt that developed due to the Late Cretaceous inversion of a series of extensional basins that developed during the Jurassic and Cretaceous rifting phases that affected the north of the Iberian plate (Vergés et al., 1995, 2002). Both the extensional and compressive structures are well-constrained and documented by several studies that deciphered the geometry of the precursor rift basins and the associated diapirism, as well as the later thrust sheet emplacement (Martínez et al., 2001; Vergés and García-Senz, 2001; García-Senz, 2002; Vergés et al., 2002; Lopez-Mir et al., 2014; Mencos et al., 2015; Saura et al., 2015). The evolution of fluid flow during the migration of the south Pyrenean thrust front is also well characterized, especially from the Early Eocene to the Oligocene (Cruset et al., 2018). Similar studies have also been carried out in the Axial zone (Grant et al., 1990; Banks et al., 1991; Trincal et al., 2017), in individual structures within cover thrust sheets (Travé et al., 1997, 1998, 2007; Caja et al., 2006; Lacroix et al., 2014, 2018; Beaudoin et al., 2015; Crognier et al., 2017; Nardini et al., 2019) and in the Ebro foreland basin (Travé et al., 2000; Cruset et al., 2016). The results of these works indicate that fluid flow during the Pyrenean compression phases was multiepisodic and report the progressive exhumation of the studied structures, as well as the influence on fluid composition of the underlying evaporitic units that acted as the detachment level for thrust sheets, the basement rocks and also of connate marine fluids trapped within sediments. Contrarily, the relationships between fluid flow and deformation during the Mesozoic extension that affected northern Iberia have received less attention. Most of the existing studies have been focused mainly on the Jurassic-Cretaceous rifting within the Catalan Coastal Ranges (Baqués et al., 2012, 2013; Cantarero et al., 2013, 2014). Other works studied the dolomitization events during the Late Jurassic-Early Cretaceous rift and the Late Cretaceous post-rift stages in the Iberian Chain (Nadal, 2001; Gomez-Rivas et al., 2014). In the Pyrenees and Cantabrian zones, however, few studies have been carried out about the fluid-rock interactions during the metamorphism associated with the hyperextension of the north Iberian margin (Boulvais, 2016; De Felipe et al., 2017; Salardon et al., 2017) and the origin of Pb-Zn deposits and dolomitizations during the Mesozoic extension (Munoz et al., 2016; Gasparrini et al., 2017). Hence, more data and an integrating study is needed to decipher the differences and similarities in fluid flow of post-Variscan extensional and compressional deformation affecting the north Iberian margin. In this study, we report the evolution of the fluid systems within the Upper Pedraforca thrust sheet, the oldest structural unit of the south Pyrenean fold-and-thrust belt. This structure consists of a rift basin affected by halokinetic deformation during the Jurassic-Cretaceous extension and incorporated into the Pyrenean orogen during the Late Cretaceous compression and inversion period. The aims of this study are: 1) to differentiate between deformative and fluid flow events related to the Mesozoic extension from those related to the

Alpine compression; 2) to characterize the origin and composition of fluids migrating along fractures during these two events; and 3) to propose a conceptual fluid flow model of the Upper Pedraforca thrust sheet. To achieve them, fracture orientation data, petrographic observations and geochemical analyses (REE+Y elements and Sr, C, O and clumped isotopes) are combined with published U-Pb ages of the study area (Cruset et al., in review). The comparison of the obtained model with other areas, such as the Cantabrian and north Pyrenean zone, the Catalan Coastal Ranges and the Iberian Chain enlightens about regional and local fluid flow events along rifted margins that later underwent compressional inversion.

Geological setting

The Pyrenees (Fig. 1A) are the result of the continental collision between Iberia and Eurasia from the Late Cretaceous to the Miocene, within the context of the Alpine orogeny (Choukroune et al., 1989; Roure et al., 1989; Muñoz, 1992, 2002; Vergés et al., 2002). Due to this collision, the Mesozoic Iberian margin was uplifted and incorporated into the Pyrenean orogen, whose central part is the Axial zone, an antiformal stack composed of basement-involved thrust sheets dominated by Paleozoic rocks (Fig. 1B) (Muñoz, 1992). This area acts as a boundary between the thick-skinned north Pyrenean zone and the south Pyrenean fold and thrust belt (Fig. 1B and C), which consists of a piggy-back sequence of south-directed thrust sheets detached above Upper Triassic and Eocene evaporites (Fig. 1C) (Séguret, 1972; Vergés et al., 1992; Sans, 2003).

Prior to the Alpine compression, the north Iberian margin was affected by lithosphere extension during the Late Triassic and Early Jurassic, which favored the deposition of extensive carbonate sediments in platforms during the Jurassic (Mey et al., 1968; Peybernès, 1976; Vergés and García-Senz, 2001; Aurell et al., 2002; Martín-Chivelet, 2002). During the Late Jurassic and Early Cretaceous, the reactivation of the Pyrenean rifting resulted in the opening of the Bay of Biscay, which induced diapirism by the flow of Upper Triassic evaporites and the formation of salt-related basins (Rios, 1948; Brinkmann and Lögters, 1968; Serrano and Martínez del Olmo, 1990; McClay et al., 2004; Canérot et al., 2005; López-Mir et al., 2014; Poprawski et al., 2014; Saura et al., 2015; Tavani et al., 2018). In the north Pyrenean zone, however, this extension produced the extreme thinning of the continental crust and the exhumation of upper mantle rocks during the Late Aptian and the Albian-Cenomanian (Lagabrielle et al., 2010; Clerc and Lagabrielle, 2014; Clerc et al., 2016). After this rifting event and prior to the Pyrenean compression, moderate subsidence associated with post-rift thermal contraction affected the area (Martín-Chivelet, 2002).

The studied structure in this work is the Upper Pedraforca thrust sheet (UPTS) (Fig. 1C), the oldest cover thrust sheet of the eastern sector of the south Pyrenean fold-and-thrust belt. It consists of an extensional basin affected by diapirism, incorporated into the Pyrenean orogen during the Late Cretaceous-Palaeocene compression (Puigdefàbregas and Souquet, 1986; Vergés, 1993; Saura et al., 2015) and reactivated during the Eocene-Oligocene (Cruset et al., in review). The UPTS emplaces Upper Triassic, Jurassic and Cretaceous pre-compressive rocks

over Upper Cretaceous to Palaeocene syn-orogenic sediments of the south Pyrenean foreland basin (Vergés, 1993; Martínez et al., 2001; García-Senz, 2002).

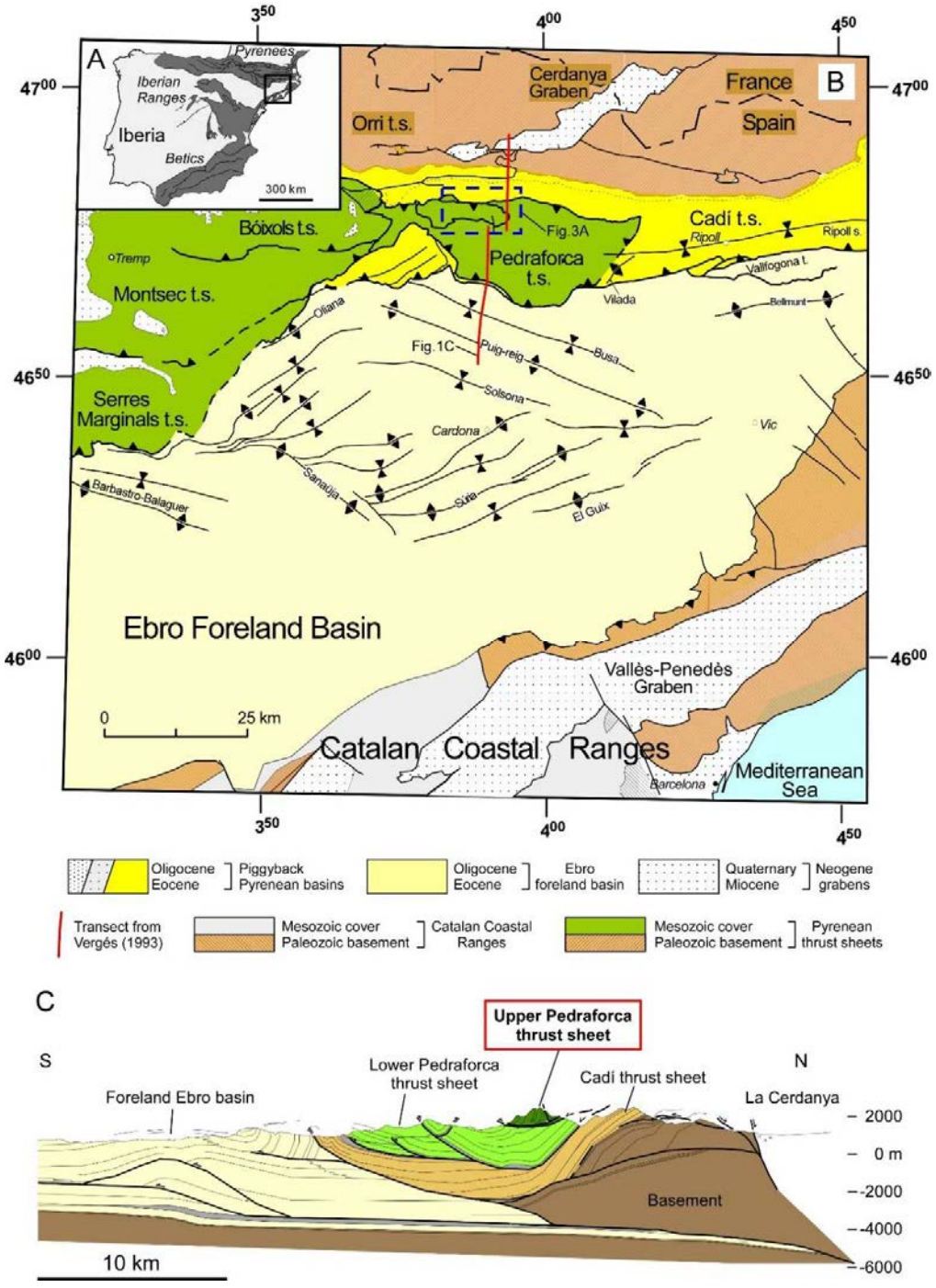

Fig. 1. A) Regional map of the Iberian Peninsula showing the location of the south Pyrenean fold-and-thrust belt (black box). B) Simplified geological map showing the main structural units forming the south Pyrenean fold-and-thrust belt (Vergés, 1993). The thick red lines indicate the location of the composite cross-section in Fig. 1C. The dashed blue box indicates the location of Fig. 3A. C). Geological cross section of the Lower Pedraforca thrust sheet, from Vergés (1993).

The stratigraphy of the UPTS is similar to that in its western equivalent, the Bóixols thrust sheet (García-Senz, 2002; Mencos et al., 2015) and is divided into pre-rift, syn-rift and post-rift marine sediments and marine to continental syn-orogenic sediments (Fig. 2). The pre-rift

sequence is composed of Triassic and Jurassic rocks. Triassic units consist of evaporites and clays from the Keuper facies, which constitute the main detachment level in the Pyrenees, and laminated dolostones from the Isàvena Formation (Séguret, 1972; Calvet et al., 1993; Arnal et al., 2002). The Jurassic is represented by the Bonansa Formation and in the studied area consists of Lower Jurassic dolomitic breccias, laminated limestones and dark marls with brachiopods and ammonoids and Middle and Upper Jurassic dolostones (Peybernès 1976; Aurell et al., 2002). The syn-rift sequence comprises Lower Cretaceous rocks and consists of Berriasian breccias and Valanginian to Albian limestones and marls (García-Senz, 2002). Post-rift sediments in the UPTS are represented by limestones of the Cenomanian-Turonian Santa Fe Formation and Lower Santonian limestones with Lacazina from the Sant Corneli Formation (Mey et al., 1968; Skelton et al., 2003; Ullastre and Masriera, 2004). The Syn-orogenic sequence is constituted of Upper Cretaceous to Palaeocene sediments. The Upper Cretaceous units consist of marine marls, limestones and carbonate breccias of the Late Santonian to Maastrichtian Areny Formation. This unit is conformably overlain by the Maastrichtian to Danian marine dark marls, coastal siltstones and continental sandstones and conglomerates of Garumnian Facies (Puigdefàbregas and Souquet, 1986; Vicente et al., 2015).

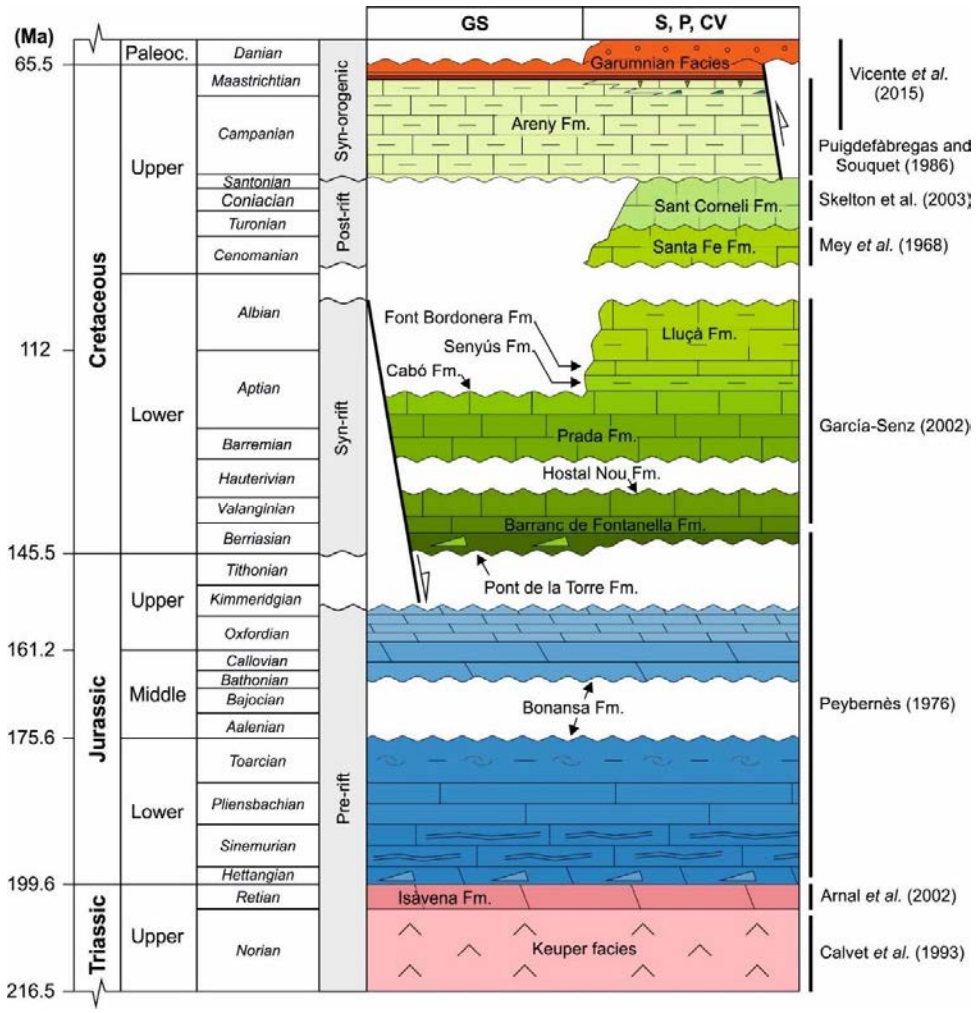

Fig. 2. Chronostratigraphic diagram showing the main sedimentary units of the Upper Pedraforca thrust sheet and their related tectonic events. The age of sedimentary units has been defined according to Mey et al. (1968), Peybernès (1976), Puigdefàbregas and Souquet (1986), Calvet et al. (1993), Arnal et al. (2002), García-Senz (2002), Skelton et al. (2003) and Vicente et al. (2015).

Methodology

Four outcrops located in the southern (Saldes outcrop - S) and northern margins (Gósol outcrop - GS, and Pedraforca outcrop - P), and in the internal part of the UPTS (Coll del Verdet outcrop - CV) were selected for the study of the evolution of fluid flow during the emplacement of this nappe (Fig. 3).

Field work consisted of fracture and bedding data acquisition to stablish their crosscutting relationships. In addition, sampling of fracture-filling calcite and dolomite cements and their adjacent host rocks was undertaken for petrographic observations and geochemical analyses. For the analysis of field data, fracture planes were plotted and restored with respect to bedding (when appropriate) using the software Win-Tensor (v5.8.8.) (Delvaux and Sperner, 2003). Additionally, for each fracture generation observed in this work, their associated stress orientations were also calculated with the same software.

Petrographic observations of 94 polished thin sections made from fracture-filling calcite and dolomite cements and host rocks were carried out using optical and cathodoluminescence microscopy. A CL Technosyn cathodoluminescence device Model 8200 MkII operating at 23 kV and 350 μA gun current was used to distinguish the different types of cements.

For carbon- and oxygen-isotope analysis, 134 microsamples were prepared using a 400 μm-thick dental drill to extract 60 ± 10 μg of powder from trims containing calcite and dolomite cements and carbonate host rocks. The carbonate powder was reacted with 100% phosphoric acid for two minutes at 70 °C for calcite and 15 minutes at 70 ºC for dolomite. The resultant CO_2 was analyzed using an automated Kiel Carbonate Device attached to a Thermal Ionization Mass Spectrometer Thermo Electron (Finnigan) MAT-252 following the method of McCrea (1950). The results were corrected using the standard technique from Craig and Gordon (1965) and Claypool et al. (1980), expressed in ‰ with respect to the VPDB (Vienna Pee Dee Belemnite) standard. Standard deviation is ±0.03 ‰ for $\delta^{13}C$ and ± 0.05 ‰ for $\delta^{18}O$.

For clumped isotopes thermometry, two dolomite cements and eight calcite cements were analyzed. This method is applied to calculate temperatures of cement precipitation as well as the $\delta^{18}O$ values of the fluids from which these they precipitated. To analyze the samples, 2–3 mg aliquots from cements were measured with the Imperial Batch Extraction system (IBEX), an automated line developed at Imperial College of London. Each sample was dropped in 105% phosphoric acid at 90 ºC and reacted for 30 min. The reactant CO_2 was separated using a poropak-Q column and transferred into the bellows of a Thermo Scientific MAT 253 mass spectrometer (Thermo Fisher GmbH, Bremen, Germany). The characterization of a replicate consisted of 8 acquisitions in dual inlet mode with 7 cycles per acquisition. The post-acquisition processing was completed with a software for clumped isotope analysis named Easotope (John and Bowen, 2016). Δ_{47} values were corrected for isotope fractionation during phosphoric acid digestion employing a phosphoric acid correction of 0.069 ‰ at 90 ºC for calcite (Guo et al., 2009).

The data were also corrected for non-linearity applying the heated gas method (Huntington et al., 2009) and projected into the absolute reference frame of (Dennis et al., 2011). Carbonate $\delta^{18}O$ values were calculated with the acid fractionation factors of (Kim et al., 1997). Samples were measured three times and the average result was converted to temperatures using the calibration method of (Davies and John, 2019). Calculated $\delta^{18}O$ values of the fluid are expressed in ‰ with respect to the VSMOW standard (Vienna Standard Mean Ocean Water).

For $^{87}Sr/^{86}Sr$ analyses, twenty-six samples of 100% calcite and dolomite cements and carbonate host rocks were analyzed. Samples were fully dissolved in 5 ml of 10% acetic acid and introduced in an ultrasonic bath for 15 minutes. After this time, samples were centrifuged during 10 min at 4000 rpm and dried. The resultant product was digested in 1 ml of 3 M HNO_3 and dried. Finally, the sample was digested again in 3 ml of 3 M HNO_3 and introduced in chromatographic columns. For chromatographic separation of Sr an extraction resin type SrResinTM (Trisken International) (crown-ether (4.4' (5')-di-t-butylcyclohexano-18-crown-6) was used. The Sr was recovered with HNO_3 0.05 M as eluent. The fraction where Sr is concentrated was dried, charged on a Re single filament with 1 µl of H_3PO_4 1 M and 2 µl of Ta_2O_5 and analyzed on a TIMS-Phoenix mass spectrometer. The method of data acquisition consisted of dynamic multicollection during 10 blocks of 16 cycles each one, with a beam intensity in the ^{88}Sr mass of 3 V. Analyses were corrected for possible interferences of ^{87}Rb. $^{87}Sr/^{86}Sr$ ratios are normalized with respect to the measured mean value of the ratio $^{86}/Sr/^{88}Sr=0.1194$ in order to correct for possible mass fractionation during filament charge and instrumental analyses. The precision of the analytical standard error or internal precision is 0.000009.

To determine the rare earth and yttrium contents (REE+Y) of calcite and dolomite cements and carbonate host rocks, 25 samples were analyzed by means of high-resolution inductively coupled plasma-mass spectrometry (HR-ICP-MS), using a Thermo Scientific model Element XR. Up to 100 mg of powder was sampled from trims using a 400/500 µm-diameter dental drill. Powdered samples were dried at 40ºC during 24 h and later 100 mg of sample were acid digested in closed PTFE vessels with a combination of HNO_3+HF+ $HClO_4$ (2.5 ml: 5 ml: 2.5 ml v/v). The samples were evaporated and, 1 ml of HNO3 was added to make a double evaporation. Finally, the sample was re-digested and diluted with MilliQ water (18.2 MΩcm-1) and 1 ml of HNO_3 in a 100 ml volume flask. In order to improve the sensitivity of the ICP-MS, a tuning solution containing 1 µg.l-1 Li, B, Na, K, Sc, Fe, Co, Cu, Ga, Y, Rh, In, Ba, Tl, U was used, and as internal standard, 20 mg.l-1 of a monoelemental solution of 115In. Reference materials are the BCS-CRM nº 393 (ECRM 752-1) limestone, JA-2 Andesite and JB-3 Basalt. The precision of the results was expressed in terms of two standard deviations of a set of eight reference materials measurements (reference material JA-2), whereas accuracy (%) was calculated using the absolute value of the difference between the measured values obtained during the analysis and the certified values of a set of eight reference material analysis (reference material BCS-CRM nº 393 for major oxides and JA-2 for trace elements). The analysed elements and their detection limits expressed in ppm are: La (0.21), Ce (0.32), Pr (0.04), Nd (0.15), Sm (0.03), Eu (0.01), Gd (0.02), Tb (0.003), Dy

(0.02), Y (0.20), Ho (0.003), Er (0.01), Yb (0.01) and Lu (0.01). The detection limit (DL) was calculated as three times the standard deviation of the average of ten blanks. A Multielemental Solution IV-CCS-1 Rare Earths Standard in HNO_3, 125ml (100 µg/ml) of Inorganic Ventures was used in order to perform the calibration curves. REE and Y data are normalized to the Post-Archean Australian Shale (PAAS) from McLennan (1989).

Results

Description of the outcrops

The studied outcrops (Gósol, Pedraforca, Coll del Verdet and Saldes) are taken as representative of the whole structure of the Upper Pedraforca Thrust Sheet (UPTS) (Fig. 3A and B). Structural studies and sampling were systematically carried out on each of them.

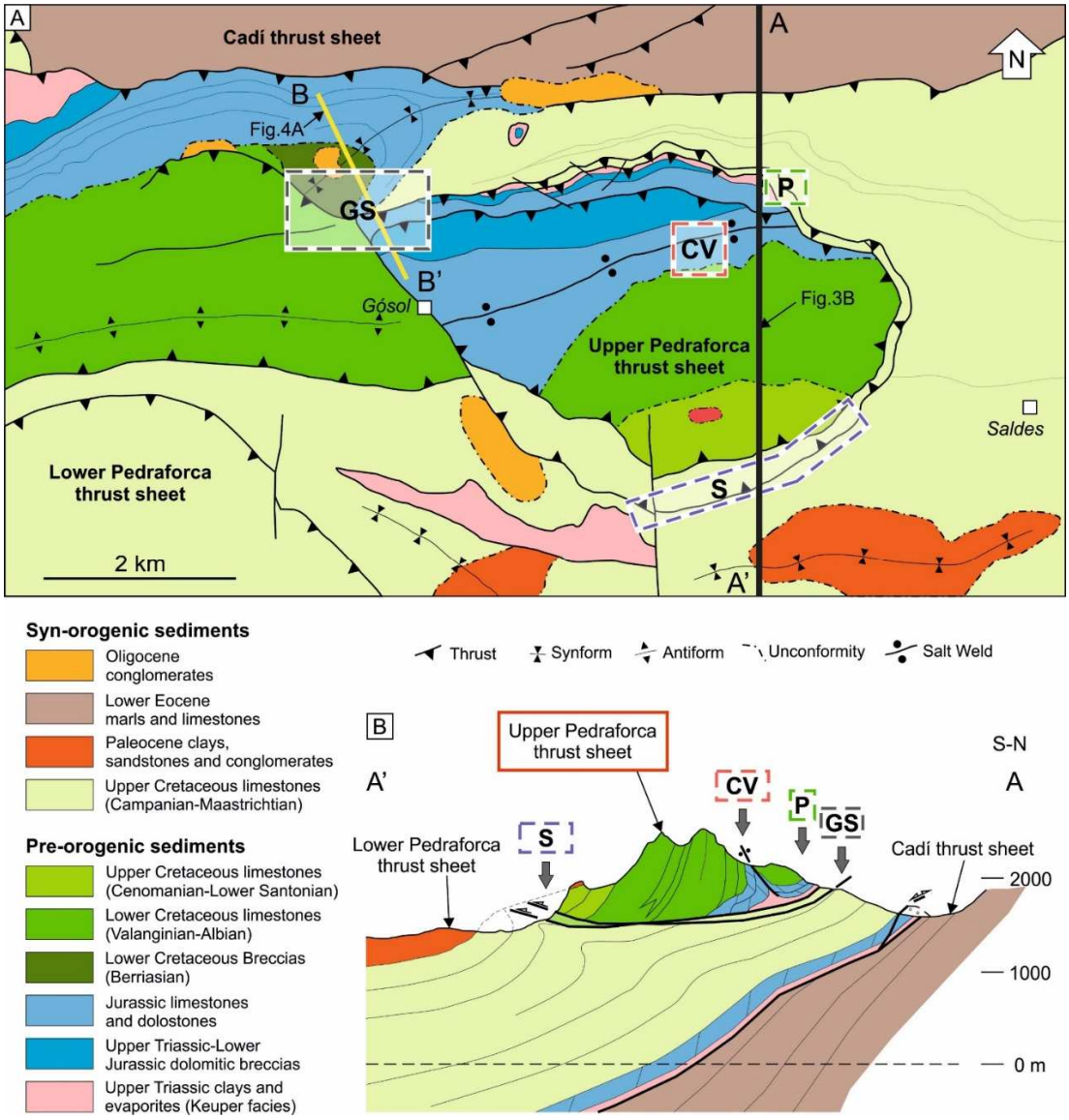

Fig. 3. A) Structural sketch with the location of the studied outcrops (transparent boxes bounded by dashed colored lines), Fig. 3B (Dark grey line) and Fig. 4A (yellow line). B) Detailed geological cross-section of the Upper Pedraforca thrust sheet from Vergés (1993) showing the structural position of the studied outcrops (grey arrows).

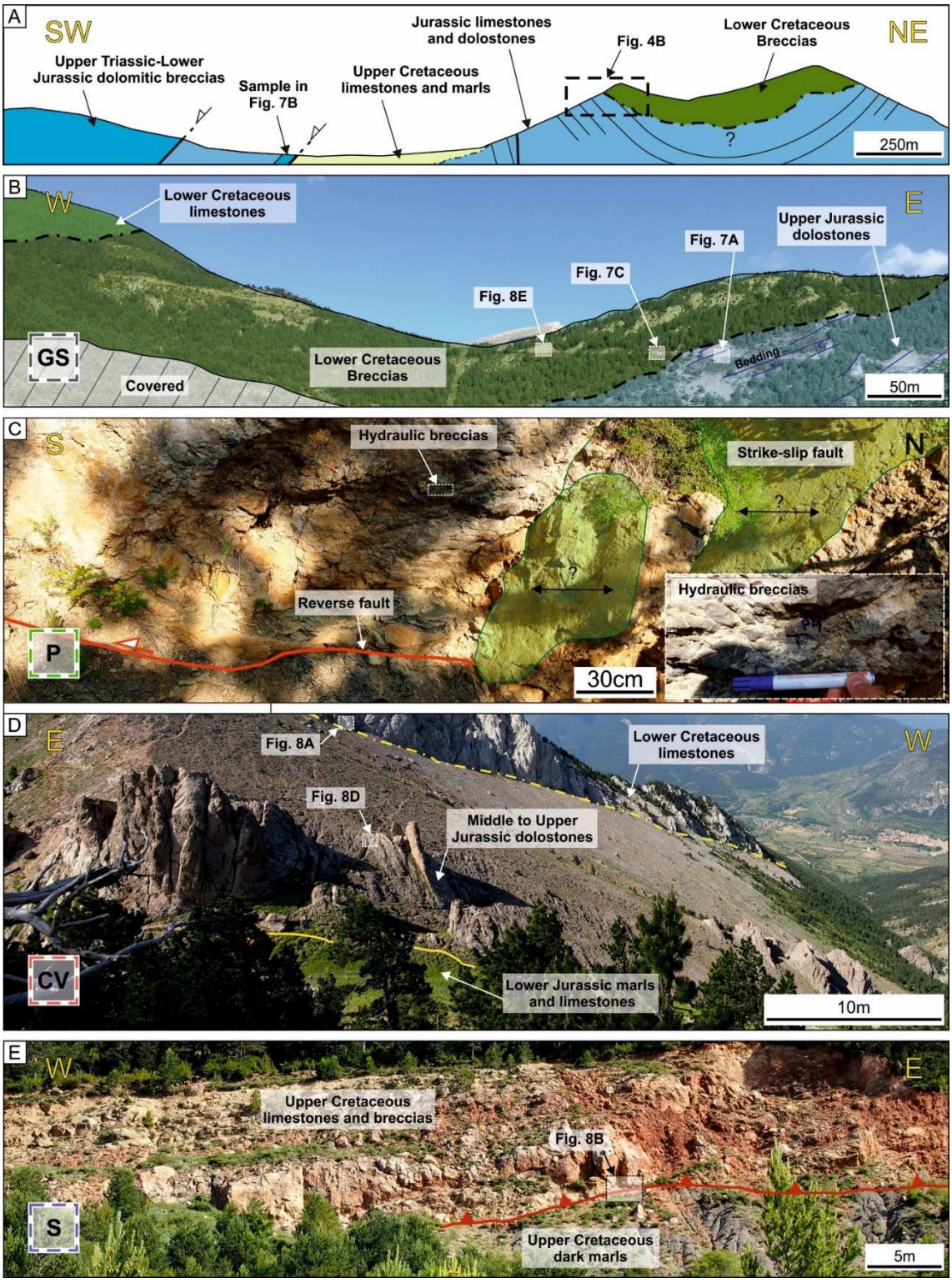

Fig. 4. Representative images of the studied outcrops in Fig. 3. A) Sketch of outcrop GS with the location of Figs. 4B and 7B. B) Interpreted image of the SE limb of the syncline in outcrop GS. The location of Figs. 7A, 7C and 8E is given. B) Interpreted image of a fault zone within the P outcrop. The white dashed box indicates the location of the image in the right lower corner. C) Image of the outcrop CV with the location of Figs. 8A and 8D. D) Image of the S outcrop where the Upper Cretaceous breccias are overthrusting Upper Cretaceous dark marls.

The Gósol (GS) and Pedraforca (P) outcrops correspond to the northernmost part of the UPTS (Fig. 3A and B). The GS outcrop is located at the north of the Gósol village. It consists of an ENE-WSW syncline composed of Jurassic limestones and dolostones within the hangingwall

of the UPTS (Fig. 4A). This structure is unconformably overlain by 1) syn-rift Lower Cretaceous breccias made of fragments of Jurassic dolostones and limestones in its western part and 2) Upper Cretaceous syn-orogenic marls and marly limestones in its eastern part (Fig. 3A and 4A and B). Towards the south, the Upper Cretaceous rocks are overthrusted by Jurassic limestones and dolostones. The described structures agree with halokinetic deformation, which has been already reported in the study area by Saura et al. (2015).

The P outcrop is located 3 km northwest of the Saldes village and corresponds to the damage zone of the main thrust of the UPTS. In this area, Campanian breccias made of mudstone fragments are affected by reverse and strike-slip faults (Fig. 4C). In the P outcrop, the UPTS is tilted to the south due to the later emplacement of the Cadí thrust sheet (Fig. 3B).

The Coll del Verdet outcrop (CV) corresponds to the internal part of the UPTS, close to the Coll del Verdet area in the Pedraforca massif (Fig. 3A and B). The structure of this outcrop consists of subvertical beds of Lower Jurassic limestones and marls and Middle Jurassic sucrose dolostones corresponding to a weld zone (Saura et al., 2015). These rocks are unconformably overlain by a thin layer of carbonate breccias partly replaced by dolomite and thick beds of limestones from the Lower Cretaceous (Fig. 4D).

The Saldes outcrop (S) corresponds to the frontal part of the UPTS and is located between the Gósol and Saldes villages (Fig. 3A and B). It is in an equivalent structural position than the P outcrop and consists of a thrust fault zone which acts as a boundary between Upper Cretaceous breccias, rudist limestones and yellowish siltstones and sandstones with dinosaur egg fragments in the hangingwall, and Upper Cretaceous dark marls with lignite beds in the footwall (Fig. 4E).

Host rocks

The Bonansa Formation comprises rocks from the Lower to the Upper Jurassic. Lower Jurassic rocks include: 1) Hettangian breccias completely replaced by dolomite with crystals ranging between 15 and 30 μm in size and exhibiting planar-s textures, as defined by Gregg and Sibley (1984) and Sibley and Gregg (1987), 2) Sinemurian mudstones, with mm-thick planar lamination and ripples (Fig. 5A) and 3) Toarcian dark marls and peloidal grainstones with echinoid fragments partly replaced by up to 60 μm-width euhedral dolomite crystals (Fig. 5B). Sinemurian mudstones are occasionally brecciated. These breccias are cemented by calcite and partly replaced by up to 2 mm-wide saddle dolomite crystals (Fig.5 C and D). Middle Jurassic rocks comprise sucrose dolostones made of subhedral crystals with sizes ranging from 200 to 400 μm and exhibiting planar-s textures (Fig. 5E). Occasionally, these dolostones are completely calcified and contain millimeter-size vugs filled with calcite cement. Upper Jurassic rocks include well-bedded dolostones showing planar-s textures, with moldic porosities filled with dolomite cement and centimeter-size vugs filled with calcite cement. The Lower Cretaceous rocks include 1) breccias from the Pont de la Torre Formation, composed of fragments of Lower to Upper Jurassic limestones and dolostones and Lower Cretaceous wackestones with Trocholina (with fragment sizes ranging from few millimetres to the metric scale) and 2) well-bedded dolostones with crystals

ranging between 15 and 30 μm in size and showing planar-s textures (Fig. 5F). In the CV outcrop (Fig. 3), the Lower Cretaceous breccias are partly replaced by this type of dolomite. Upper Cretaceous rocks are constituted of 1) Carbonate breccias from the Areny Formation with fragments of mudstones and wackestones with rudists locally cemented by red micrite, 2) dark marls with oysters and 3) yellow to reddish siltstones and sandstones with dinosaur eggs fragments from the Garumnian.

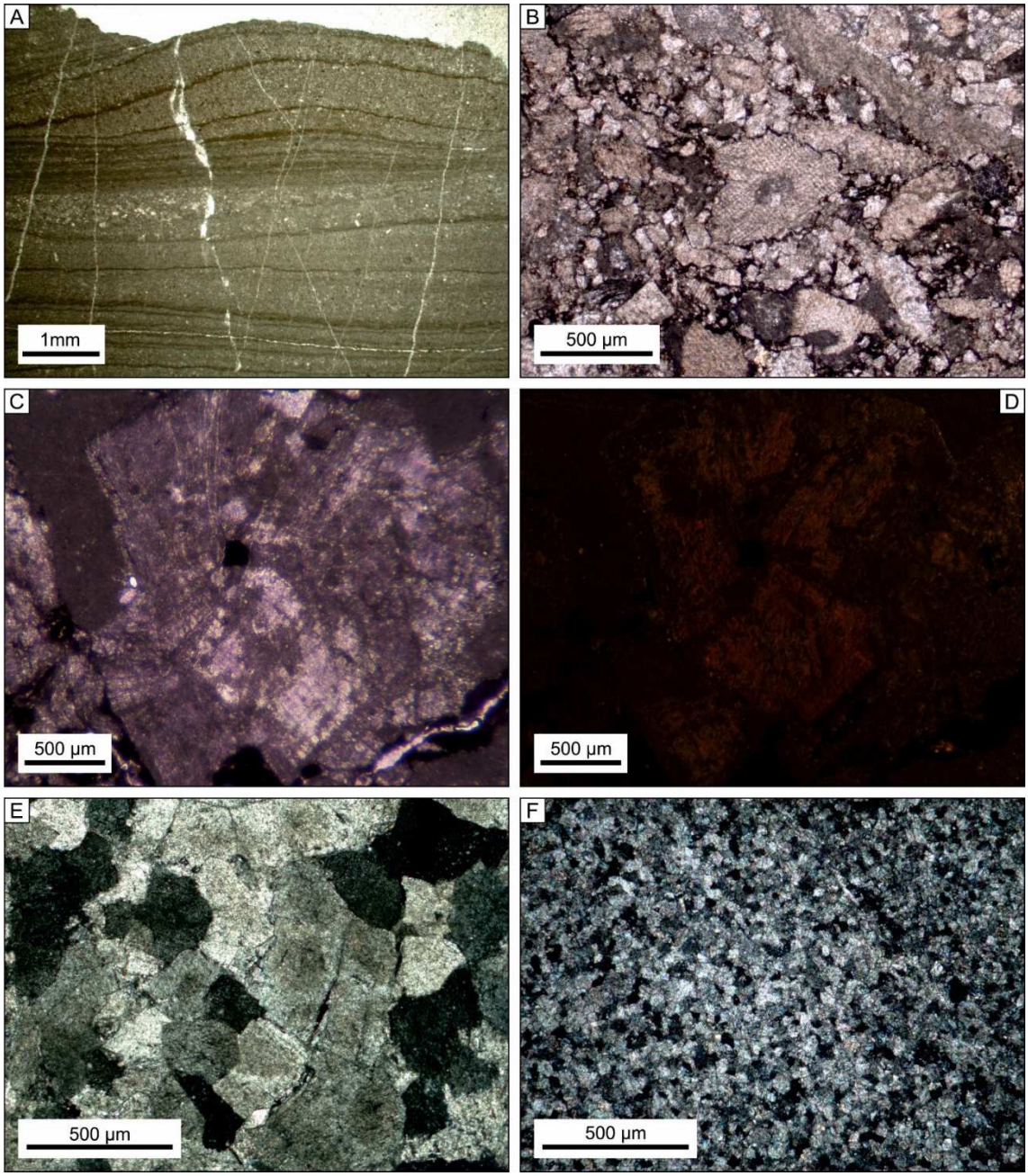

Fig. 5. Images from polarizing optical microscope and cathodoluminescence (CL) of the main textural features of the studied host rocks. A) Sinemurian mudstones with ripples and planar lamination. B) Toarcian grainstone partially replaced by euhedral crystals of dolomite. C-D) CL image of saddle dolomite replacing carbonate breccias made of Sinemurian mudstones. E) Middle Jurassic sucrose dolostones with planar-s texture (crossed nicols). F) Upper Cretaceous dolostones exhibiting planar-s texture.

Fracture analysis

The host-rocks that form the UPTS are affected by up to eight types of fractures: 1) bed-perpendicular veins, 2) randomly-oriented veins, 3) bed-parallel veins, 4) normal faults, 5) reverse faults, 6) strike-slip faults, 7) E-W-trending fractures and 8) N-S- and NNW-SSE-trending fractures. All these structures are summarized in Fig. 6. They are grouped into sixteen fracture generations (F1 to F15) according to well-stablished crosscutting relationships based on field and microstructural observations and U/Pb geochronology of fracture-filling cements (Cruset et al., in review).

The fracture system F1 consists of a conjugate system of two en-échelon vein arrays striking N-S and NNW-SSW, respectively (Fig.6). Fractures F1 are bed-perpendicular, finite apertures of up to 2 cm and are cemented by dolomite and calcite cements. Estimated stress orientations indicate N-S-directed strike-slip movement with horizontal σ1 and σ3 and vertical σ2. F1 is observed only affecting Lower to Upper Jurassic rocks of the GS outcrop (Fig.6 and 7A).

Fracture system F2 consists of randomly oriented veins filled with calcite and dolomite cements and apertures ranging from a few millimeters to up to 2 cm. These veins affect the lowermost part of the Lower Jurassic dolomitic breccias of the GS outcrop (Fig. 7B).

Fracture system F3 consists of bed-parallel slip veins and veins crosscutting bedding at low angles. They are associated with hydraulic breccias cemented by dolomite (Fig. 6). Fractures of this system affect Jurassic rocks, strike parallel to the axis of the syncline observed in the GS outcrop and appear concentrated in its SE limb (Fig. 3 and Fig. 6).

Fracture system F4 is represented by E-W-oriented normal faults dipping up to 50º predominantly to the south (Fig. 6 and 7C). The calculated stress orientations indicate N-S extension with vertical σ1 and horizontal σ2 and σ3. F4 has been observed affecting Lower Cretaceous breccias of the Pont de la Torre Formation in the GS outcrop.

Fractures F5 are reverse faults formed in the damage zone of large thrusts in the UPTS. These fault zones include discrete WNW-ESE reverse fault planes gently dipping to the north and filled with calcite cement (Fig.6), as well as hydraulic breccias made of centimeter-size limestone clasts cemented by calcite cement. Discrete fault planes postdate hydraulic breccias. The calculated stress orientations indicate N-S compression with vertical σ3 and horizontal σ1 and σ2. F5 has been only observed in the P outcrop affecting Upper Cretaceous breccias.

Fracture system F6 consists of NNW-SSE and ENE-WSW-oriented subvertical strike-slip faults formed in the same thrust fault zone than reverse faults F5. They also postdate the hydraulic breccias in the P outcrop. Estimated stress orientations for F6 indicate NW-SE-directed compression (Fig.6).

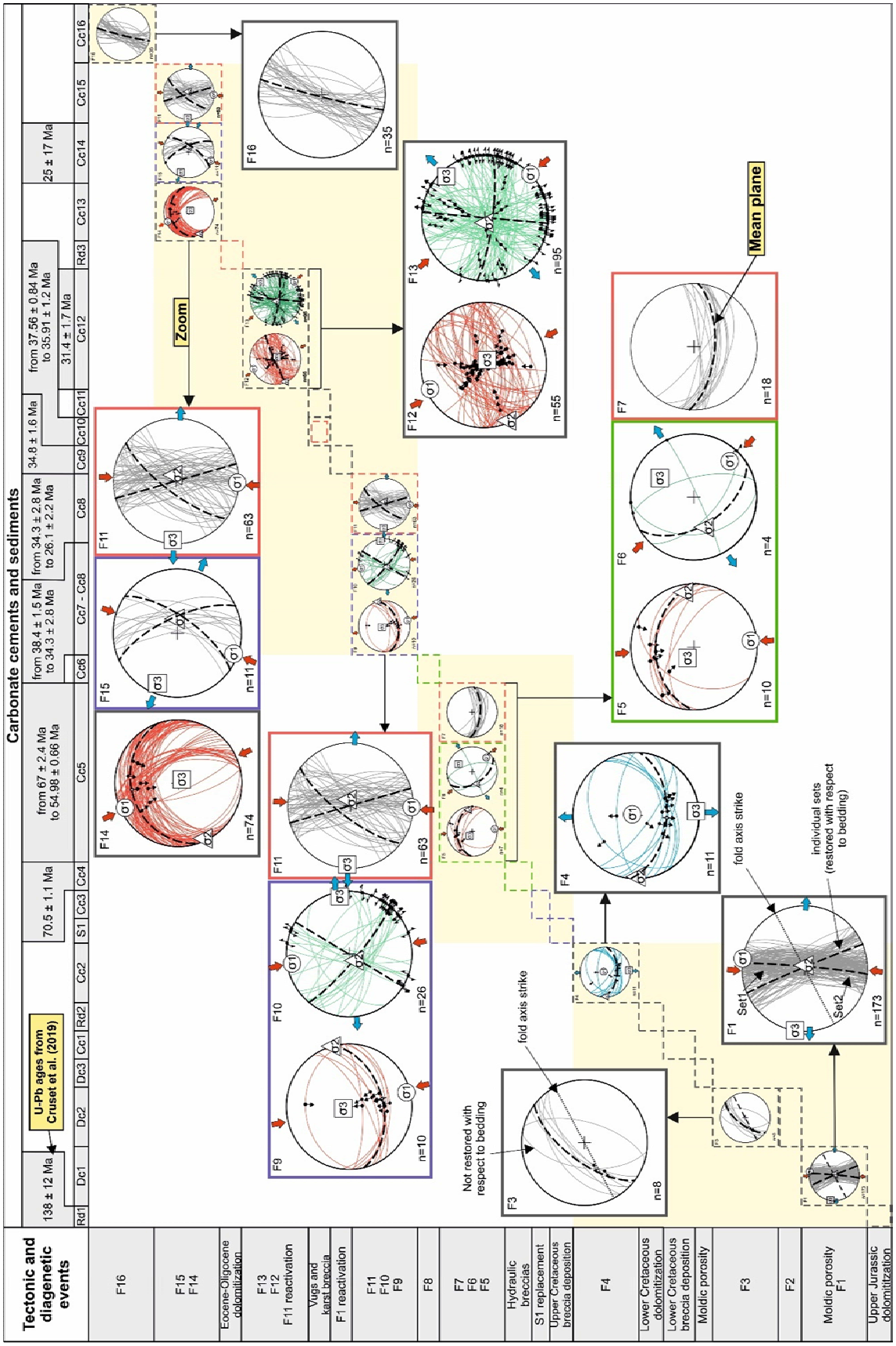

Fig. 6. Lower hemisphere Schmidt stereoplots representing fracture data from the different studied outcrops and their associated diagenetic and tectonic stages. Zooms of the stereoplots and the calculated stresses for each type of fracture are also represented. The dashed and continuous colored boxes represent each studied outcrop. Equivalent colors are used in Figs. 3, 11, 12, 13, 14 and 15. U-Pb ages from Cruset et al. (in review).

E-W fractures formed in the internal part of the UPTS and constitute the fracture system F7 (Fig. 6). These fractures crosscut bedding of Lower Jurassic to Lower Cretaceous rocks at a low angle. F7 structures have been only observed in the CV outcrop (Fig. 7A).

F8 consists of randomly oriented veins filled with calcite and postdating F5 and F6. They are formed of Mode I openings of up to 2 mm and have been only observed in outcrop P.

Fracture system F9 consists of E-W reverse faults formed in the fault zone of a major reverse fault in the footwall of the UPTS. They consist of discrete planes and dip between 30º and 70º to the south, although sporadically thrust fault planes dipping gently to the north are also observed (Fig. 8B). The calculated stress orientations indicate that they formed under N-S compression. F9 has been observed at the S outcrop (Fig. 6).

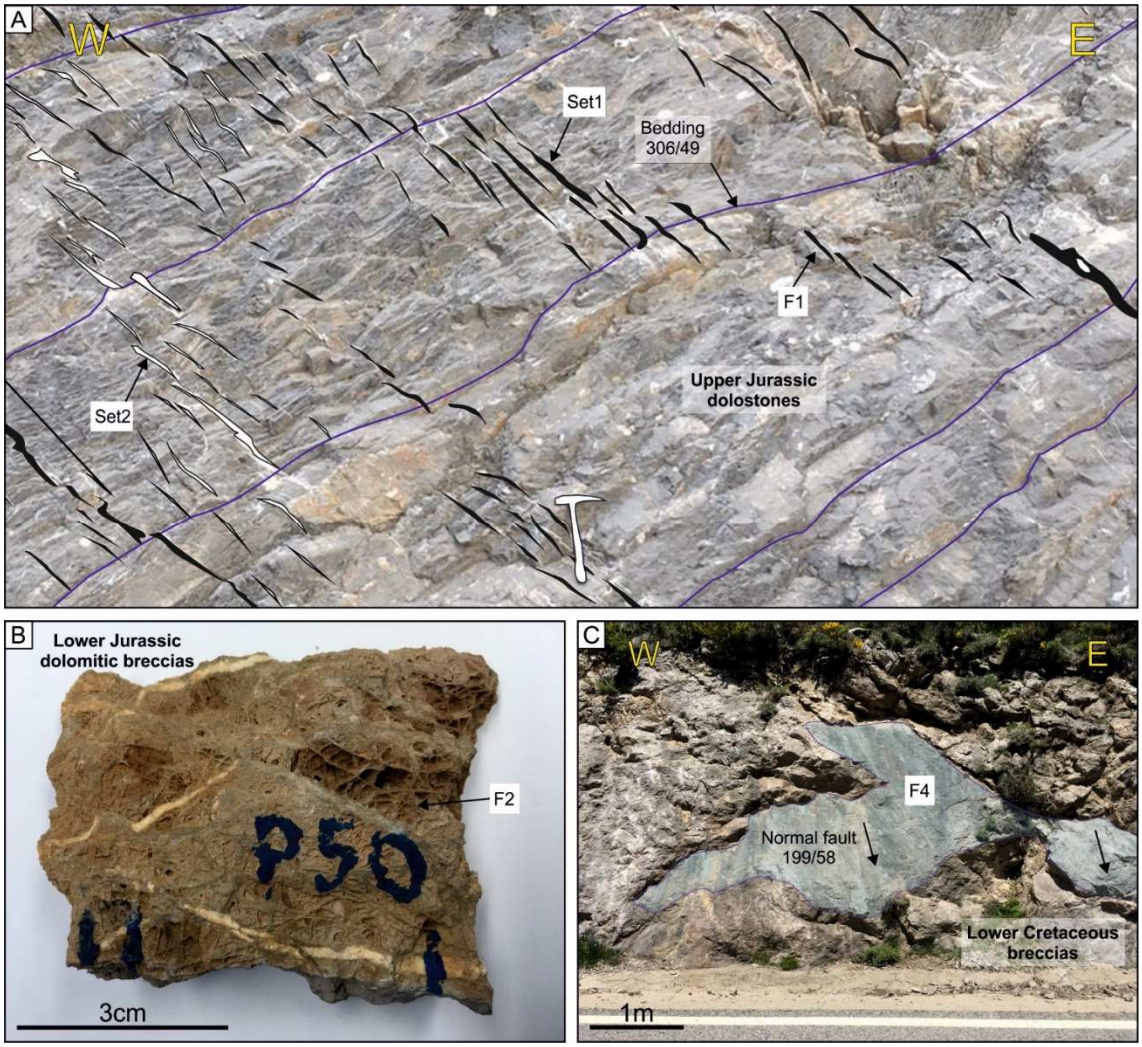

Fig. 7. Outcrop and laboratory images showing the main features of fracture systems F1, F2 and F4 within the Upper Pedraforca thrust sheet. A) F1 Bed-perpendicular N-S en-échelon vein arrays affecting Upper Jurassic dolostones (GS outcrop). B) Dolostones from the basal part of Lower Jurassic rocks affected by randomly oriented F2 fractures filled with dolomite and calcite cements (GS outcrop). C) E-W F4 normal faults affecting Lower Cretaceous breccias (GS outcrop).

F10 is defined by NE-SW and NW-SE strike-slip faults formed in the footwall of the UPTS, within the damage zones of large reverse faults (Fig. 6). These are sub vertical fractures (Fig. 8C) formed under N-S compression, according to stress inversion estimations (Fig. 6). F10 is affecting Upper Cretaceous breccias, marls and siltstones in the S outcrop.

F11 consists of NE-SW and NW-SE-striking veins occasionally showing strike-slip displacements. They developed in the internal part of the UPTS and show openings with lengths varying between a few centimeters and meters and appear associated with hydraulic breccias (Fig. 8D). These breccias expand tens of centimeters from the main fracture planes and are composed of millimeter-sized fragments of sucrose dolostones cemented by calcite cement. Stress orientations calculated for F11 indicate N-S strike-slip movement (Fig. 6). F11 has only been observed in the CV outcrop postdating F7.

The fracture system F12 consists of NE-SW reverse faults formed in the hangingwall of the UPTS. They are formed of discrete subvertical planes and are observed in the GS outcrop. The calculated stress directions reveal that they formed under NW-SE-oriented compression (Fig. 6).

F13 is formed of sub-vertical N-S and E-W strike-slip faults formed in the hangingwall of the UPTS (Fig. 6 and 8C). Their orientations reveal that they formed under NW-SE compression. F13 is affecting Upper Jurassic dolostones and Lower Cretaceous breccias at the GS outcrop.

Fracture system F14 is defined by low angle E-W and NE-SW-striking reverse faults dipping between 16º and 60º to the north and northwest, although occasionally can also be oriented N-S (Fig.6). They consist of discrete planes intermittently exhibiting dip-slip striae sets, and hydraulic breccias cemented by calcite cement. They formed under NW-SE compression (Fig.6). F14has only been observed in the GS outcrop postdating fractures of sets F12 and F13 (Fig. 8E).

F15 is composed of NNW-SSE and NE-SW-striking veins dipping between 50º and 90º towards the ENE and SSE, respectively (Fig. 6). F15 fractures are located at the damage zone of a large fracture postdating the major reverse fault in the frontal part of the UPTS in outcrop S (Fig. 3A). Their calculated stress orientations reveal that they formed under NNE-SSW-oriented compression with strike-slip movement.

F16 consists of isolated N-S-oriented fractures dipping between 60º and 90º and show constant orientation regardless of bed dip. These fractures are not generally filled by cements, although in certain cases they can appear filled with calcite cement. F16 structures affects Jurassic and Lower Cretaceous rocks and postdate fractures of the F14 set in the GS outcrop (Fig. 8E).

The integration of the fracture analysis, together with petrographic observations and geochemical data obtained from fracture-filling cements allows to identify up to nineteen carbonate cements which are described in the next sections.

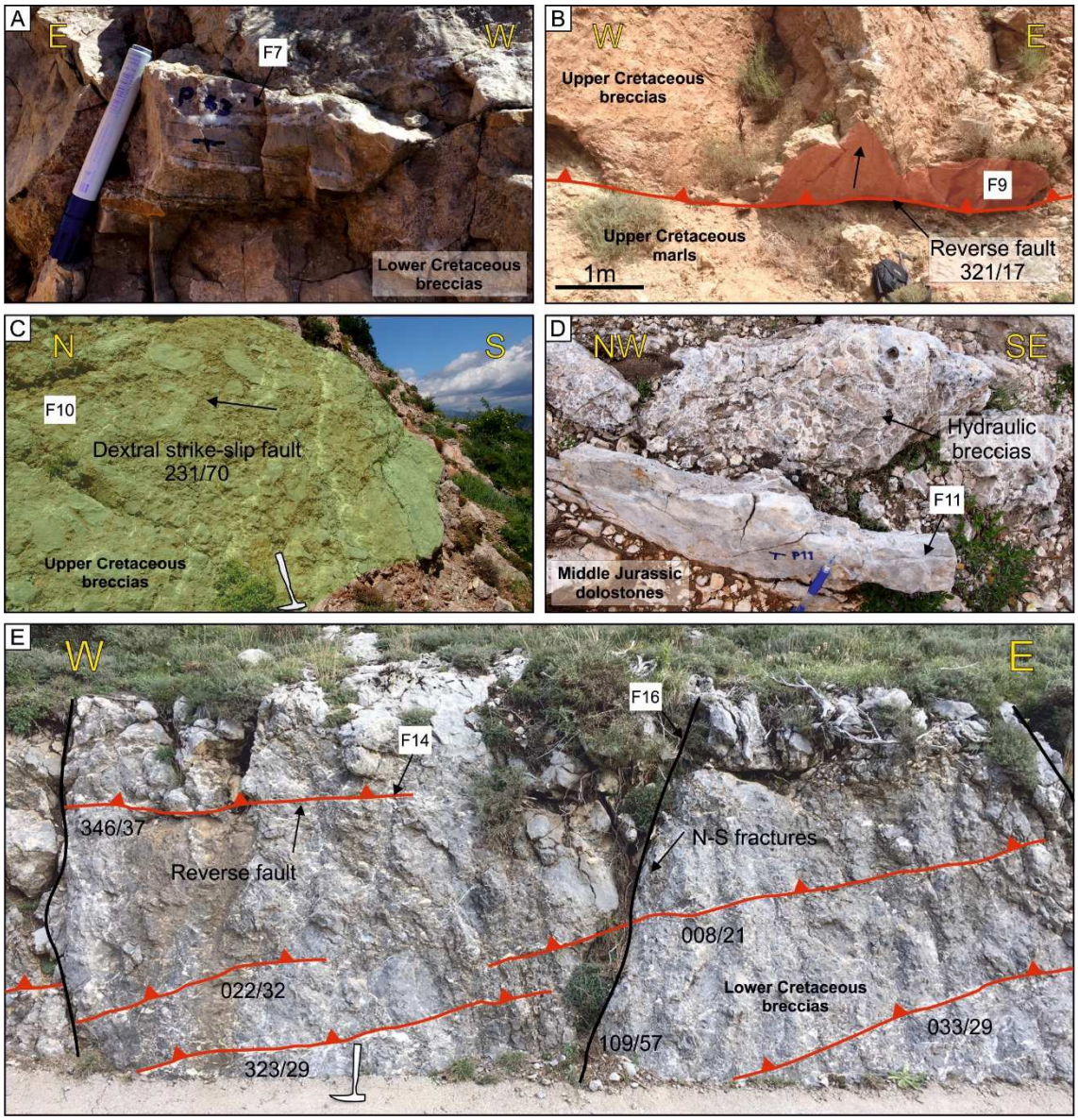

Fig. 8. Outcrop images showing the main features of reverse and strike-slip faults and E-W and N-S fractures within the Upper Pedraforca thrust sheet. A) E-W F7 fractures affecting Lower Cretaceous breccias (outcrop CV). B) F9 reverse fault emplacing Upper Cretaceous breccias of the Areny Formation over Upper Cretaceous dark marls of the Garumnian (outcrop S). C) F10 dextral strike-slip fault affecting Upper Cretaceous breccias (outcrop S). D) N-S F11 fractures and associated hydraulic breccias affecting Middle Jurassic dolostones (outcrop CV). E) F14 reverse faults and F16 N-S open fractures affecting Lower Cretaceous breccias (outcrop GS)

Petrology

Three generations of dolomite cement (Dc1 to Dc3), one type of carbonate sediment deposited between carbonate breccia clasts (S1) and sixteen generations of calcite cement (Cc1 to Cc16) have been observed in the UPTS. The chronology of these cements is summarized in Fig. 6, based on field and petrographic observations and on U-Pb dating of carbonate cements.

Dc1 consists of red luminescent saddle dolomite crystals ranging between 250 and 700 μm in size. This cement precipitated in bed-perpendicular veins F1 and moldic porosity within Upper Jurassic dolostones in outcrop GS (Fig. 9A and B). Dc2 is formed of non-luminescent saddle dolomite with crystal sizes ranging between 200 μm and 2 mm. This cement precipitated within

randomly oriented veins F2 and in bed-parallel veins F3 in outcrop GS. Dc3 is formed of red luminescent saddle dolomite crystals with sizes ranging between 200 µm and 1 mm and precipitated in the moldic porosity of the Upper Jurassic dolostones in outcrop GS. Calcite cement Cc1 is formed of up to 2 mm non-luminescent blocky crystals precipitated between Lower-Cretaceous breccia clasts in outcrop GS. Calcite cement Cc2 is formed of elongated sparite crystals ranging between 200 and 500 µm long and arranged parallel to fracture walls. This cement is non-luminescent to dull-brown and precipitated in normal faults F4 in outcrop GS.

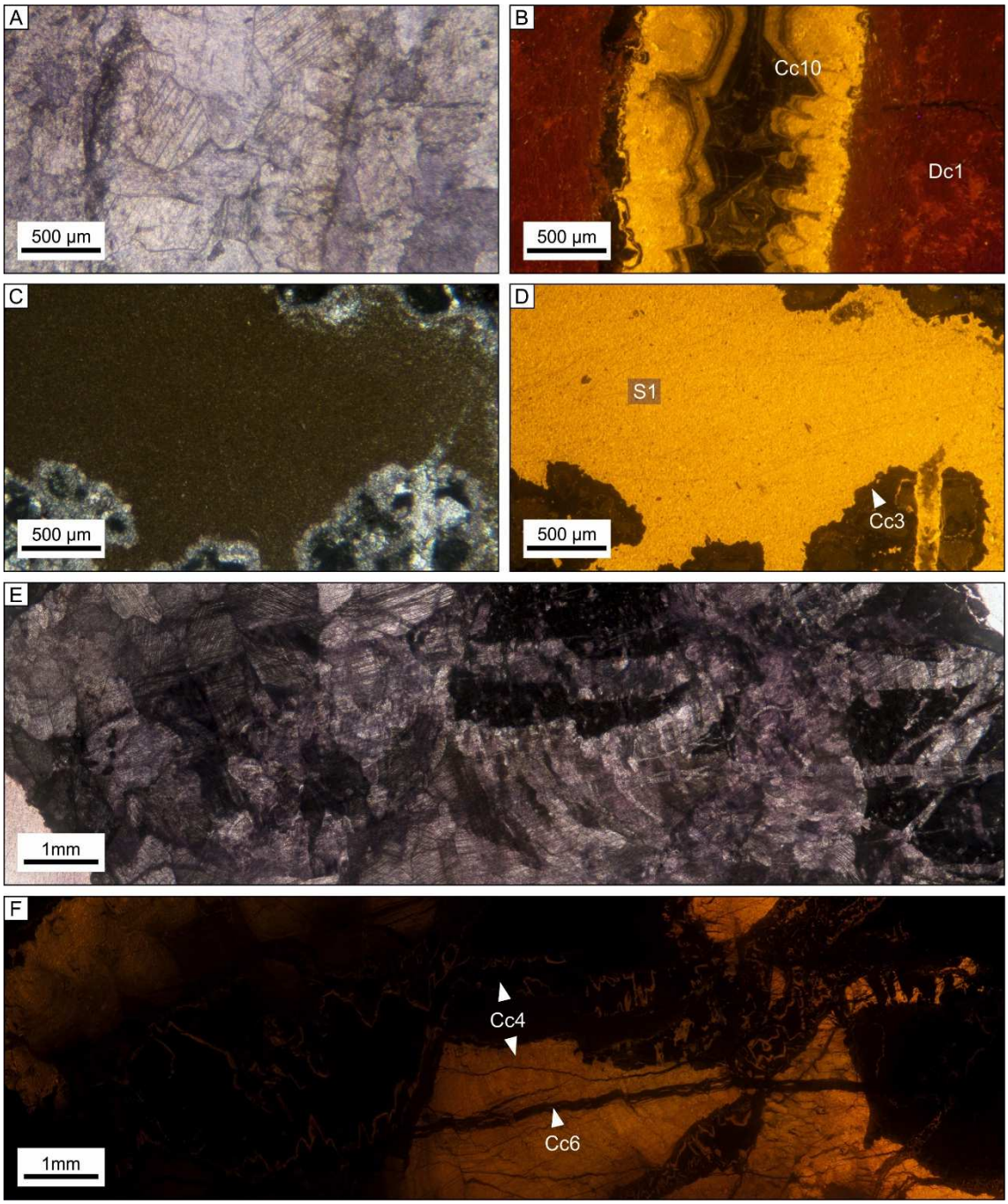

Fig. 9. Images from polarizing optical and cathodoluminescence microscope (CL) of the studied calcite and dolomite cements. A-B) CL image where are shown the crosscutting relationships between Dc1 and Cc10 in F1 fractures. C-D) Calcite Cc3 replacing S1 red micrite deposited between Upper Cretaceous Breccia clasts. E-F) Crosscutting relationships between Cc4 and Cc6 in hydraulic breccias formed in a thrust fault zone of the UPTS.

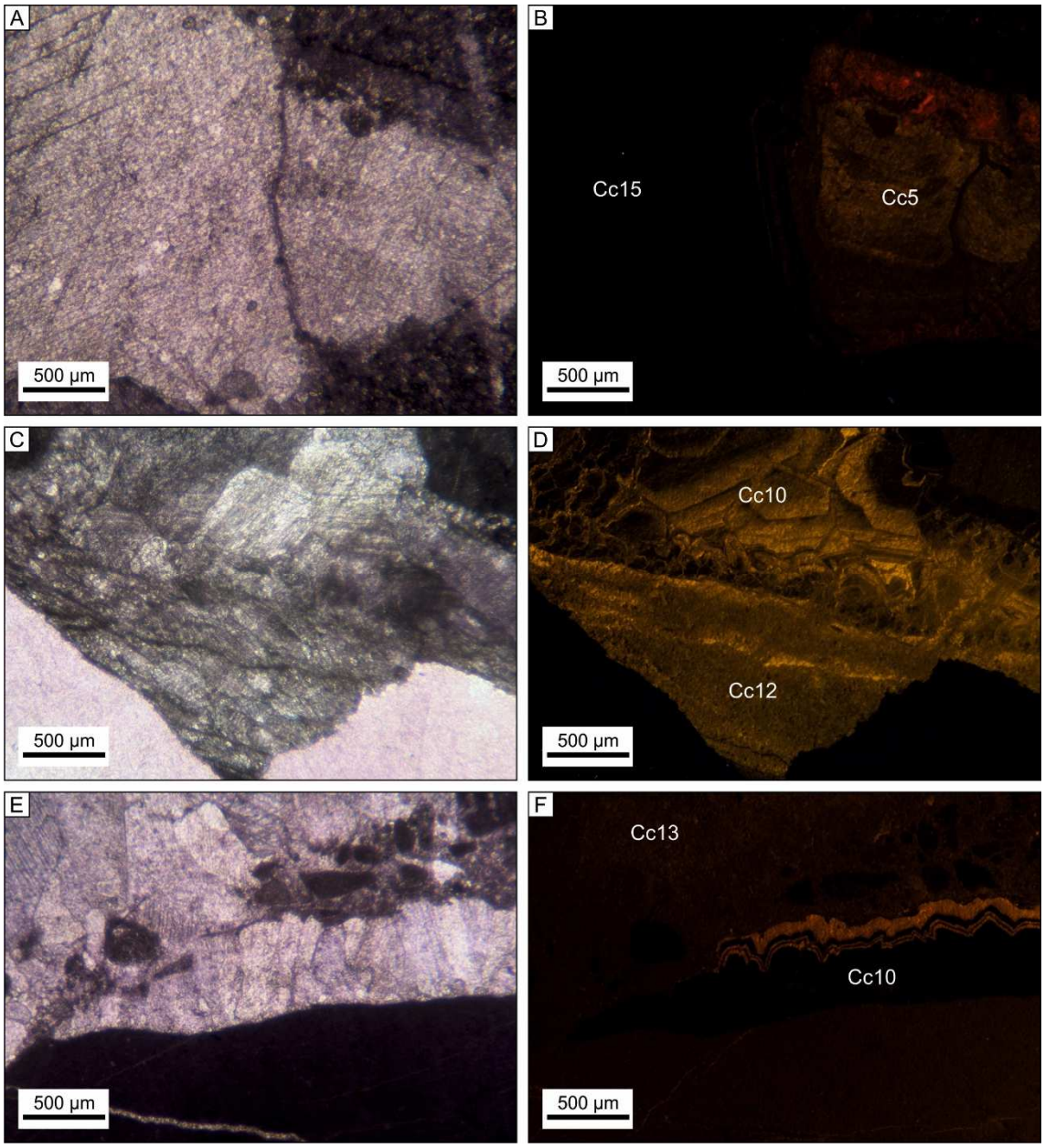

Fig. 10. Images from polarizing optical and cathodoluminescence microscope (CL) of the main features of studied calcite and dolomite cements. A-B) Crosscutting relationships between Cc5 in F7 fractures and Cc15 in F11 fractures. C-D) Calcite cement Cc12 from F13 fractures postdating Cc10 precipitated in vug porosity. E-F) Crosscutting relationships between Cc10 and Cc13 in F14 fractures.

Sediment S1 consists of micrite showing bright to yellow luminescence and deposited between clasts of Upper Cretaceous breccias from the Areny Formation in outcrop S (Fig.9B and C). Cc3 consists of non-luminescent microsparite. This cement is not filling fractures or the space between breccia clasts, but it is replacing sediment S1 as a recrystallization front (Fig.9B and C). Calcite cement Cc4 is formed of blocky crystals with sizes ranging between 400 µm and 1mm. This cement is orange luminescent to non-luminescent and precipitated in hydraulic breccias formed within the main thrust fault zone of the UPTS in outcrop P (Fig.9 E and F). Cc5 is formed of elongated calcite crystals arranged parallel to fracture walls and with a length of up to 3 mm. This cement is non-luminescent to dull-orange and precipitated in 1) F5 reverse faults and F6

strike-slip faults postdating hydraulic breccias cemented by Cc4 in the outcrop P (Fig.9 E and F) and 2) in E-W fractures F7 and punctually in N-S fractures F10 in outcrop CV (Fig.10A and B). Calcite cement Cc6 is formed of blocky crystals with sizes ranging between 20 and 100 μm. This cement is non-luminescent and precipitated within F8 veins post-dating Cc4 and Cc5 in outcrop P (Fig.9 E and F).

Calcite cement Cc7 is formed of up to 1 mm long elongated sparite crystals growing parallel to fracture walls and up to 2 mm long bladed crystals arranged perpendicular to fracture walls. This cement shows dull-orange luminescence and precipitated in vug porosities and strike-slip faults F10 affecting Upper Cretaceous carbonate breccias in outcrop S. Calcite cement Cc8 is formed of up to 2 mm long bladed crystals arranged perpendicular to fracture walls. This cement is dull-orange to orange luminescent and is observed in outcrops CV and S. In outcrop CV it precipitated within N-S fractures F11, which postdate fractures F7 filled with calcite cement Cc5. In outcrop S, Cc8 postdates Cc7. Calcite cement Cc9 consists of up to 100 μm blocky crystals, showing dull-orange luminescence and precipitated in reactivated veins F1 postdating Dc1 in outcrop GS. Calcite cement Cc10 is formed of blocky crystals ranging between 150 and 800 μm in size. This cement is non-luminescent to yellow luminescent or zoned dull-orange and precipitated in outcrops GS and CV. In outcrop GS, Cc10 precipitated in reactivated fractures F1 and in vug porosities affecting Upper Jurassic dolostones and Lower Cretaceous breccias (Fig.9A and B), and postdates cements Dc1, Dc2, Cc1, Cc2 and Cc9. In outcrop CV, Cc10 precipitated between breccia clasts made of Lower Jurassic limestones postdating Cc8. Calcite cement Cc11 is formed of up to 500 μm blocky calcite crystals. This cement is zoned, dull-brown to non-luminescent and precipitated within the vug porosity affecting Upper Jurassic dolostones in outcrop GS. Cc11 postdates Cc10. Cc12 is formed of 2 mm long elongated sparite crystals growing parallel to the walls of reverse faults F12 and strike-slip faults F13. This cement is dull-orange to orange luminescent postdates Cc10 and Cc11 precipitated in vug porosities within outcrop GS (Fig. 10C and D). Calcite cement Cc13 is formed of blocky crystals with sizes ranging between 100 μm and 1 mm. This cement is dull-orange and precipitated in outcrop GS in F14 reverse faults postdating Cc10 that precipitated in vug porosities and fractures F12 and F13 which are filled up with Cc12 (Fig.10E and F). Calcite cement Cc14 is formed of blocky crystals with sizes ranging between 200 μm and 4 mm. Cc14 shows dull-orange luminescence and precipitated in outcrop S within N-S fractures F15, which are postdating fractures F9 filled with Cc8. Cc15 is formed of blocky crystals with sizes ranging between 300 μm and 3 mm. This cement is orange luminescent to non-luminescent and precipitated within reactivated N-S fractures F11 and associated hydraulic breccias postdating Cc5 and Cc10 in outcrop CV (Fig.9A and B). Calcite cement Cc16 consists of mm-sized blocky crystals. This cement is non-luminescent and precipitated occasionally in N-S fractures F16 in outcrop GS.

Geochemistry

Carbon and Oxygen isotopes

The carbon and oxygen isotopic composition of carbonate host rocks, calcite and dolomite cements, and calcite sediment precipitated within fractures, between breccia clasts and vug porosity within the UPTS is presented in Fig. 11 and Table S1.

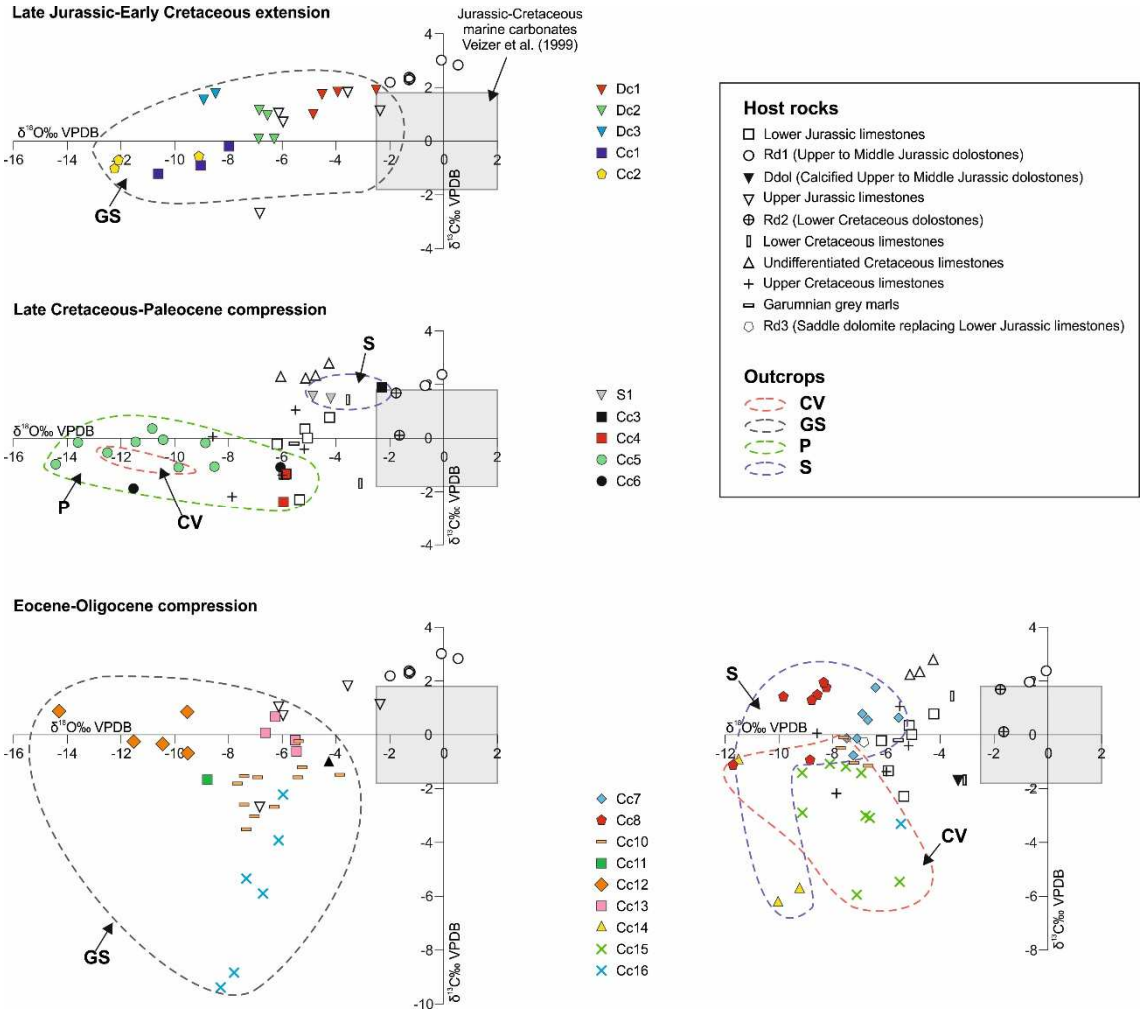

Fig. 11. $\delta^{18}O$ and $\delta^{13}C$ cross-plots of carbonate host rocks, dolomite and calcite cements and calcite sediment from the Upper Pedraforca thrust sheet. The dashed coloured boxes represent each studied outcrop. Equivalent colours are used in Figs. 3, 6, 12, 13, 14, and 15.

Lower Jurassic limestones have a $\delta^{13}C$ ranging between -2.3 and +0.8 ‰ VPDB and $\delta^{18}O$ between -6.2 and -4.2 ‰ VPDB. Middle to Upper Jurassic replacive dolostones (Rd1) have $\delta^{13}C$ ranging between +2 and +3.1 ‰ VPDB and $\delta^{18}O$ between -2 and +0.5 ‰ VPDB. Calcified dolostones from the Middle Jurassic have a $\delta^{13}C$ of -1.8 ‰ VPDB and a $\delta^{18}O$ of -3.3 ‰ VPDB. Upper Jurassic limestones have $\delta^{13}C$ values ranging between +0.7 and +1.9 ‰ VPDB and $\delta^{18}O$ values between -6.1 and -2.4 ‰ VPDB. Lower Cretaceous replacive dolostones (Rd2), have $\delta^{13}C$ ranging between +0.1 and +1.6 ‰ VPDB and $\delta^{18}O$ between -1.9 and -1.6 ‰ VPDB. Lower Cretaceous limestones have $\delta^{13}C$ values ranging between -1.7 and +1.4 ‰ VPDB and $\delta^{18}O$ between -3.6 and -3.1 ‰ VPDB. Upper Cretaceous limestones have $\delta^{13}C$ ranging between -2.2

and +1.1 ‰ VPDB and $\delta^{18}O$ between -8.6 and -5.2 ‰ VPDB. Undifferentiated Cretaceous limestones have $\delta^{13}C$ values ranging between +2.2 and +2.7 ‰ VPDB and $\delta^{18}O$ between -6.1 and -4.3 ‰ VPDB. The carbonate fraction of grey marls from the Garumnian have a $\delta^{13}C$ of -0.2 ‰ VPDB and $\delta^{18}O$ of -5.6 ‰ VPDB. Saddle dolomite replacing breccias made of fragments of Lower Jurassic limestones and Cc8 (Rd3), have a $\delta^{13}C$ of -0.3 ‰ VPDB and $\delta^{18}O$ of -6.8 ‰ VPDB.

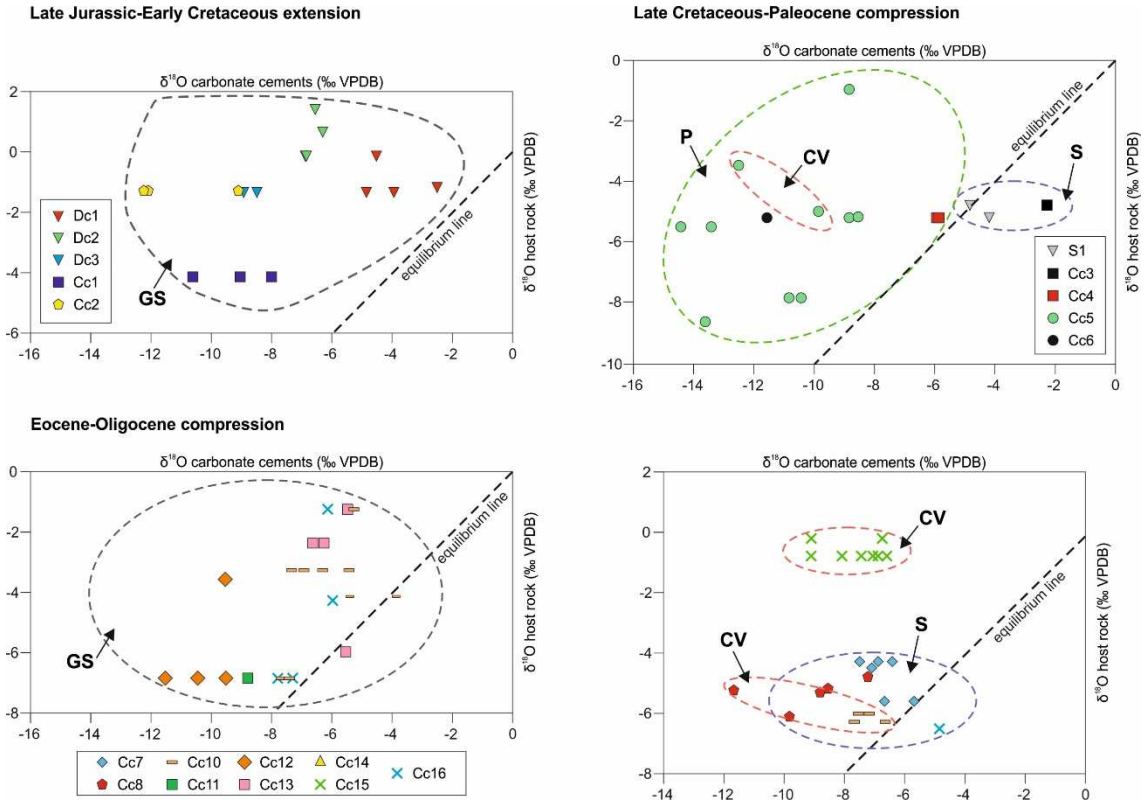

Fig. 12. $\delta^{18}O_{host\ rock\ cross\text{-}plot}$ vs $\delta^{18}O_{carbonate\ cement}$ cross-plots from the Upper Pedraforca thrust sheet. The dashed coloured boxes represent each studied outcrop. Equivalent colours are used in Figs. 3, 6, 11, 13, 14, and 15.

Dc1 has $\delta^{13}C$ values ranging between +1.1 and +1.9 ‰ VPDB and $\delta^{18}O$ values between -4.8 and -2.5 ‰ VPDB. For Dc2, the $\delta^{13}C$ ranges between +0.1 and +1.2 ‰ VPDB and the $\delta^{18}O$ between -6.9 and -6.3 ‰ VPDB. Dc3 has $\delta^{13}C$ values ranging between +1.6 and +1.8 ‰ VPDB and $\delta^{18}O$ values between -8.9 and -8.5 ‰ VPDB. Cc1 has $\delta^{13}C$ values ranging between -1.2 and -0.2 ‰ VPDB and $\delta^{18}O$ values between -10.6 and -7.9 ‰ VPDB, whereas for Cc2, the $\delta^{13}C$ ranges between -1.0 and -0.6 ‰ VPDB and the $\delta^{18}O$ between -12.2 and -9.1 ‰ VPDB. Dc1 has $\delta^{18}O$ values similar to its adjacent host rock, whereas Dc2, Dc3, Cc1 and Cc2 show a progressive depletion from older to younger carbonate cements (Fig.11).

S1 red micrite filling the intergranular porosity of Upper Cretaceous breccias have $\delta^{13}C$ values ranging between +1.5 and +1.6 ‰ VPDB and $\delta^{18}O$ between -4.8 and -4.2 ‰ VPDB. Cc3 has a $\delta^{13}C$ of +1.9 ‰ VPDB and a $\delta^{18}O$ of -2.3 ‰ VPDB. Cc4 has $\delta^{13}C$ values ranging between -2.4 and +1.3 ‰ VPDB and $\delta^{18}O$ values between -5.9 and -5.7 ‰ VPDB. Cc5 has $\delta^{13}C$ values ranging between -0.9 and +0.4 ‰ VPDB and $\delta^{18}O$ values between -14.4 and -8.5 ‰ VPDB. Cc6

has a $\delta^{13}C$ of -1.4 ‰ VPDB and a $\delta^{18}O$ of -6.1 ‰ VPDB. S1, Cc3 and Cc4 show $\delta^{18}O$ values close to the equilibrium with their adjacent host rocks, whereas Cc5 and Cc6 are in disequilibrium (Fig. 12).

Cc7 has $\delta^{13}C$ values ranging between -0.8 and +1.7 ‰ VPDB and $\delta^{18}O$ values between -7.5 and -5.5 ‰ VPDB. For Cc8, the $\delta^{13}C$ ranges between -1.1 and +1.9 ‰ VPDB and the $\delta^{18}O$ between -11.7 and -8.2 ‰ VPDB. Due to its small size, Cc9 was not sampled for carbon and oxygen isotopes. For Cc10, the $\delta^{13}C$ range between -3.5 and -0.1 ‰ VPDB and the $\delta^{18}O$ between -7.7 and -3.8 ‰ VPDB. Cc11 has a $\delta^{13}C$ of -1.3 ‰ VPDB and a $\delta^{18}O$ of -0.8 ‰ VPDB. For Cc12, the $\delta^{13}C$ ranges between -0.7 and +0.9 ‰ VPDB and the $\delta^{18}O$ between -14.3 and -9.6 ‰ VPDB Cc13 has $\delta^{13}C$ values ranging between -0.6 and + 0.7 ‰ VPDB and $\delta^{18}O$ values between -6.6 and -5.5 ‰ VPDB. Cc14 has $\delta^{13}C$ ranging between -6.2 and -0.9 ‰ VPDB and $\delta^{18}O$ values between -11.5 and -9.2 ‰ VPDB. For Cc15, the $\delta^{13}C$ ranges between -5.9 and -1.1 ‰ VPDB and the $\delta^{18}O$ between -9.1 and -5.5 ‰ VPDB. Finally, Cc16 has $\delta^{13}C$ values ranging between -9.3 and -2.2 ‰ VPDB and $\delta^{18}O$ values between -8.2 and -5.4 ‰ VPDB. In a $\delta^{18}O_{\text{host rock cross-plot}}$ vs $\delta^{18}O_{\text{carbonate cement}}$, calcite cements Cc10, Cc17 and Cc16 show values close to the equilibrium with their adjacent host rocks, whereas Cc11, Cc8, Cc13 and Cc15 are not in equilibrium (Fig. 12).

Clumped isotopes thermometry

Dolomite cements Dc1 and Dc2 and calcite cements Cc4, Cc5, Cc7, Cc8, Cc10, Cc12 and Cc14 where analysed for clumped isotopes thermometry (Fig. 13 and Table S2). Temperature in ºC and $\delta^{18}O_{fluid}$ in ‰ VSMOW of fluids are calculated from measured Δ_{47} in carbonate cements using the forms of Davies and John (2019) and Friedman and O'Neil (1997), respectively.

The measured Δ_{47} value for dolomite cement Dc1 is 0.458 ± 0.014 ‰ (n=4), which translates into a temperature of 149.4 ± 12.5 ºC and a $\delta^{18}O_{fluid}$ of +11.2 ± 1.1 ‰ VSMOW. For Dc2, the Δ_{47} value is 0.488 ± 0.008 ‰ (n=4) and the calculated temperature and $\delta^{18}O_{fluid}$ are 124.7 ± 6.2 ºC and +7.1 ± 0.7 ‰ VSMOW, respectively. Δ_{47} value for Cc4 is 0.556 (n=1), which translates into a temperature of 81± 21.7 ºC and a $\delta^{18}O_{fluid}$ of +6.6 ± 3 ‰ VSMOW. For Cc5, the Δ_{47} value is 0.558 ± 0.022 ‰ (n=3). The calculated temperature and $\delta^{18}O_{fluid}$ are 79.7 ± 12 ºC and +3.1 ± 1.7 ‰ VSMOW, respectively. For calcite cement Cc7, the Δ_{47} is 0.522 ± 0.007 ‰ (n=3). From this value, the calculated temperature and $\delta^{18}O_{fluid}$ are 100.78 ± 4.2 ºC and +9.4 ± 0.6 ‰ VSMOW, respectively. For Cc8 the measured Δ_{47} is 0.521 ± 0.008 ‰ (n=4), which translates into a calculated temperature and $\delta^{18}O_{fluid}$ of 101.4 ± 5 ºC and +3.9 ± 0.7 ‰ VSMOW, respectively. For Cc10, the Δ_{47} ranges between 0.675 ‰ (n=1) and 0.702 ± 0.01 ‰ (n=4). The calculated temperatures and $\delta^{18}O_{fluid}$ range between 21.6 ± 3 ºC and 30.3 ± 13.6 ºC and between -3.6 ± 2.7 ‰ and -4.84 ± 0.6 ‰ VSMOW, respectively. For Cc12 the measured Δ_{47} is 0.617 ± 0.017 ‰ (n=3), and the calculated temperature and $\delta^{18}O_{fluid}$ is 52.2 ± 7.1 ºC and -3.6 ± 1.2 ‰ VSMOW, respectively. Cc14 has a Δ_{47} of 0.58 ± 0.009 ‰ (n=4), which translates into a temperature and $\delta^{18}O_{fluid}$ of 67.27 ± 4.8 ºC and -0.33 ± 0.8 ‰ VSMOW, respectively.

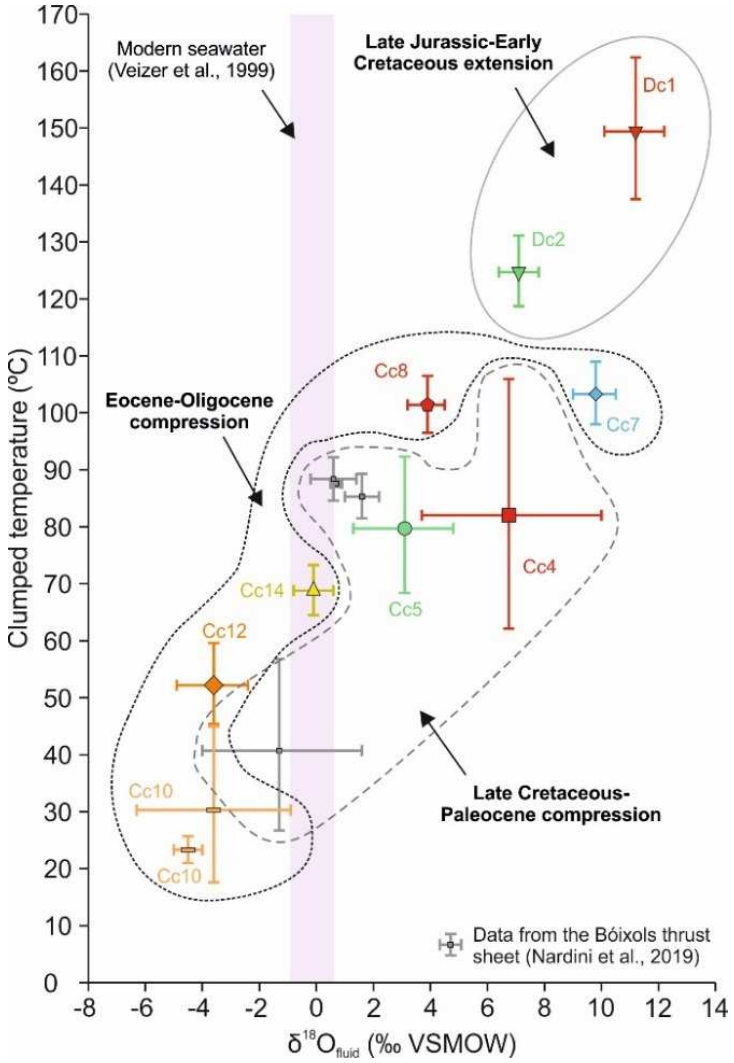

Fig. 13. Clumped isotopes temperatures (°C) vs calculated $\delta^{18}O_{fluid}$ (‰ VSMOW) for The Upper Pedraforca thrust sheet. Clumped isotopes data from Nardini et al. (2019) from the Bóixols thrust sheet is also plotted. $\delta^{18}O$ modern seawater in ‰ VSMOW is from Veizer et al. (1999).

Strontium isotopes

Lower Jurassic and Lower and Upper Cretaceous limestones, replacive dolostones Rd1 and Rd2, micrite S1, dolomite cements Dc1 and Dc2 and calcite cements Cc1, Cc3, Cc4, Cc5, Cc7, Cc8, Cc10, Cc12, Cc13 and Cc14 were analyzed for strontium isotopes (Fig.14 and Table S3).

Lower and Upper Jurassic limestones have $^{87}Sr/^{86}Sr$ ratios of 0.708301 and 0.707343, respectively. Replacive dolomite Rd1 has an $^{87}Sr/^{86}Sr$ ratio of 0.707816, whereas for Rd2 ranges between 0.707366 and 0.707604. For Upper Cretaceous limestones and micrite S1, this ratio ranges between 0.707850 and 0.708084 and between 0.707747 and 0.707951, respectively.

The $^{87}Sr/^{86}Sr$ ratio for Dc1 is 0.707425, whereas for Dc2 ranges between 0.708262 and 0.708354. Cc2 and Cc3 have ratios of 0.0707857 and 0.707720, respectively. The $^{87}Sr/^{86}Sr$ ratio of Cc4 ranges between 0.707563 and 0.707778, is 0.707707 for Cc5 and. For Cc7, this ratio is 0.707829, 0.709747 for Cc8, ranges between 0.707659 and 0.707919 for Cc10, is 0.708855 for Cc12, is 0.707933 for Cc13 and 0.707751 for Cc14.

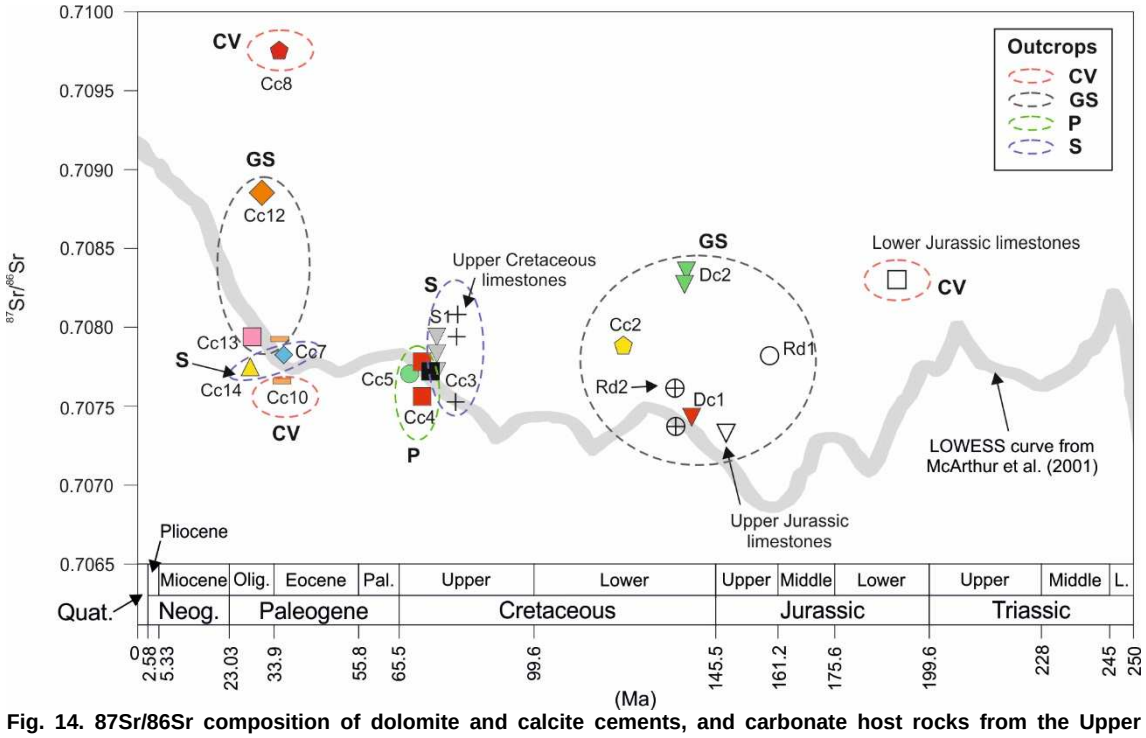

Fig. 14. 87Sr/86Sr composition of dolomite and calcite cements, and carbonate host rocks from the Upper Pedraforca thrust sheet. The ages of Dc1. Dc2, Cc2, Cc3, S1 and Cc13 are approximated, whereas for Cc4, Cc5, Cc8, Cc10 and Cc14 are based on U/Pb dating from Cruset et al. (in review). The LOWESS curve from McArthur et al. (2001) is also plotted. The dashed coloured boxes represent each studied outcrop. Equivalent colours are used in Figs. 3, 6, 11, 12, 13, and 15.

REE and Y composition

The REE and Y contents for Upper Jurassic and Lower Jurassic dolostones, Upper Cretaceous limestones, micrite S1, dolomite cements Dc1 and Dc2 and calcite cements Cc3, Cc5, Cc7, Cc8, Cc10, Cc12, Cc13 and Cc14 could be analyzed and results are presented in Table S4.

The highest REE and Y concentrations (in ppm) are observed in Rd1 (14.49), Dc1 (62.4), Upper Cretaceous limestones (between 2.64 and 19.71), S1 (between 12.57 and 30.23), Cc3 (13.38), Cc10 (12.79), Cc8 (between 11.45 and 13.34) and Cc14 (25.66). The lowest REE and Y concentrations (in ppm) are found in Rd2 (between 1.55 and 5.37), Dc2 (6.22), Cc5 (0.11), Cc10 (between 1.27 and 6.66) and Cc13 (1.04). All samples show light-REE+Y enrichments with respect to middle and heavy REE+Y contents.

Ce and Pr anomalies (Ce/Ce* and Pr/Pr*) were calculated using the formulas of Bau and Dulski (1996) and Lawrence et al. (2006), respectively (Fig. 15A and B and Table S5). For Rd1 the Ce and Pr anomalies are 0.85 and 1.04, respectively. For Dc1 the Ce anomaly is 0.75 and the Pr anomaly is 1.14. For Dc2 the Ce and Pr anomalies are 0.88 and 1.04, respectively. For Rd2 the Ce anomaly ranges between 0.90 and 1.07 and the Pr anomaly ranges between 0.96 and 1.05. The Ce anomaly of Upper Cretaceous limestones ranges between 0.70 and 0.75 whereas the Pr anomaly ranges between 1.15 and 1.17. For S1, the Ce anomaly ranges between 0.82 and 0.94 and the Pr anomaly ranges between 1.03 and 1.10. The Ce and Pr anomalies for Cc3 are 0.73 and 1.15, respectively. The Ce anomaly of Cc7 is 0.75 and the Pr anomaly is 1.13.

For Cc8 the Ce and Pr anomalies are 0.69 and 1.08, respectively. For Cc10 the calculated Ce anomaly is 0.69, whereas the Pr anomaly is 1.12. For Cc12, the Ce and Pr anomalies are 0.72 and 1.16, respectively. For Cc13 the calculated Ce and Pr anomalies are 0.86 and 1.07, respectively. For Cc14, the Ce anomaly is 0.84, whereas the Pr anomaly is 1.09.

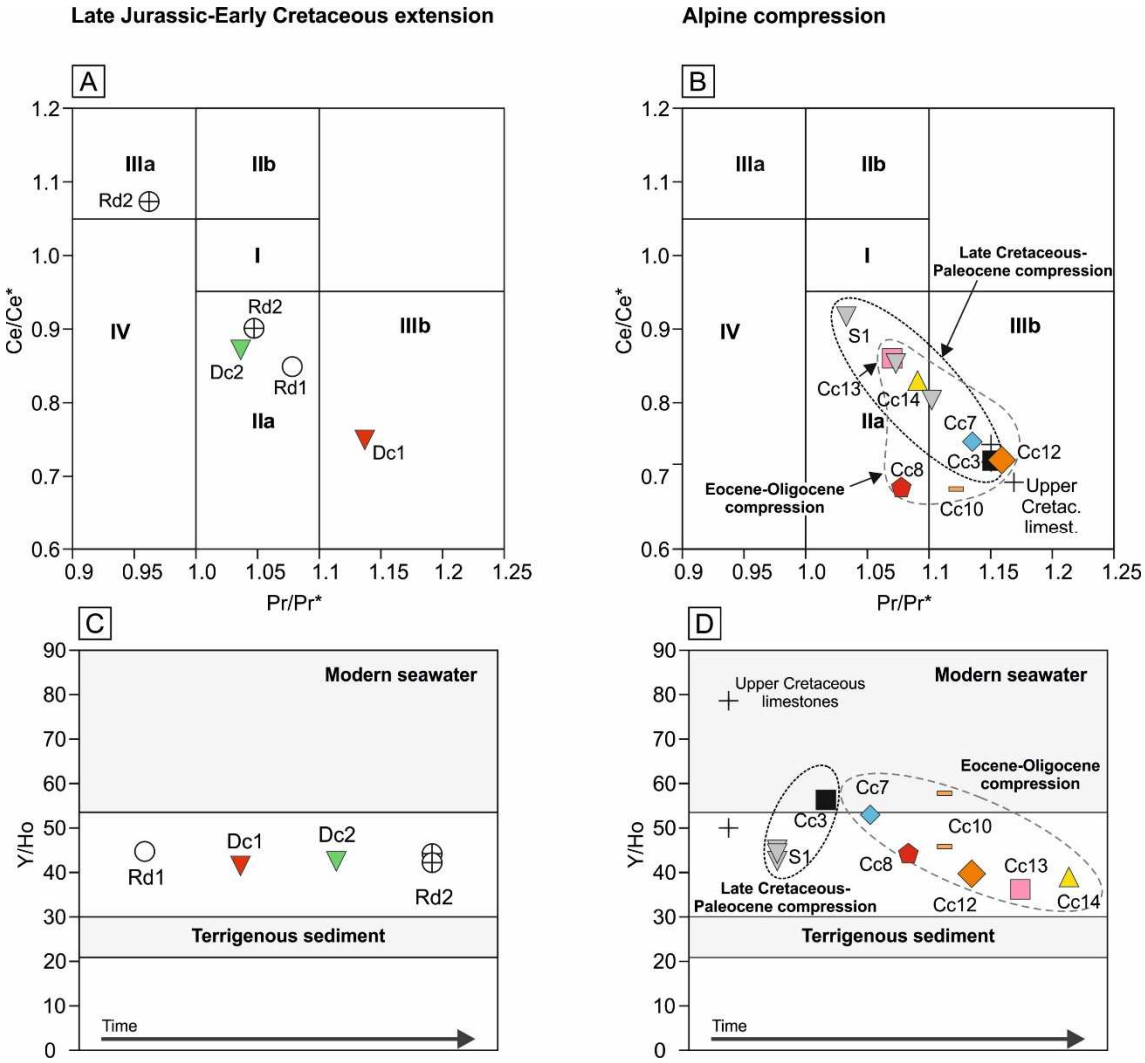

Fig. 15. A-B) PAAS-normalized Ce/Ce* vs Pr/Pr* cross-plot to analyse the Ce and Pr anomalies of carbonate host-rocks and dolomite and calcite cements. The method of Bau and Dulski (1996) as modified by Webb and Kamber (2000) is used. Field I: neither Ce nor La anomaly; field IIa: positive La anomaly and no Ce anomaly; field IIb: negative La anomaly and no Ce anomaly; field IIIa: positive Ce anomaly; field IIIb: negative Ce anomaly; field IV: positive Ce and La anomalies. C-D) Y/Ho ratios of carbonate host rocks and calcite and dolomite cements. Y/Ho limits for modern seawater and terrigenous sediments based on Bau and Dulski (1994) and Zhao et al. (2013).

The Y/Ho ratio is also calculated for Rd1 (44.91), Rd2 (between 42.75 and 44.38), Dc1 (42.07), Dc2 (42.83), S1 (between 43.49 and 45.80), Cc3 (56.34), Cc10 (between 45.89 and 57.78), Cc7 (52.87), Cc8 (between 39.88 and 44.34), Cc13 (36.35) and Cc14 (38.31). The calculated ratios do not show a clear trend from Rd1 to Rd2, with intermediate values between the composition of modern seawaters and terrigenous sediments (Fig. 15C). From Cc3 to Cc14, however, a progressive decrease of the Y/Ho ratio is observed, from values similar to modern seawaters to values similar to terrigenous sediments (Fig. 15D).

Discussion

Timing of deformation

Crosscutting relationships of the studied fracture systems completed with U/Pb ages of the studied fracture-filling carbonate cements from Cruset et al. (in review) allow to define the complete sequence of deformation within the UPTS (Fig.6).

Veins from F1 filled with Dc1 are perpendicular to bedding, indicating that this fracture system could have formed prior to the early folding of Jurassic rocks. F1 is restricted to the top of the Upper Jurassic dolostones, which are unconformably overlain by Lower Cretaceous breccias made of fragments of Jurassic limestones and dolostones including reworked F1 veins (Fig.3A) and therefore, before their deposition, during the Uppermost Jurassic-Lower Cretaceous. Lower Cretaceous breccias also include metric blocks of Upper Jurassic dolostones containing F3 fractures filled with Dc2, indicating that F3 and therefore, F2 (since they are filled with the same type of cement) formed before their deposition. Similar $\delta^{18}O$ and $\delta^{13}C$ values and $^{87}Sr/^{86}Sr$ ratios of Dc2 cement in veins within dolostone blocks and in-situ F2 veins support this interpretation. In the GS outcrop, fracture system F1 is sub-orthogonal to the axis of the syncline observed in this area (Figs.3A and 6), whereas the strike of F3 is axis-parallel. Furthermore, after restoring this fold to a position previous to the Pyrenean compression, F1 and F3 are concentrated exclusively in the vicinity of the overturned SE limb. The described deformation patterns for F1 and F3 fit well with that observed in diapiric provinces worldwide (Smith et al., 2012; Fischer et al., 2013; Coleman et al., 2018). In these areas, fractures perpendicular to salt walls and strike/Strike-oblique fractures formed due to folding are concentrated in the vicinity of salt welds. Such deformation in the study area could have been developed within the context of the Upper Jurassic-Lower Cretaceous reactivation of the Pyrenean rifting and associated diapirism (Vergés and García-Senz, 2001; García-Senz, 2002; Mencos et al., 2015; Saura et al., 2015). During this event, salt migrated due to the Upper Jurassic-Lower Cretaceous deformation and WNW-ESE salt-cored anticlines above pre-salt rocks formed (Canérot et al., 2005). F4 normal faults filled with Cc2 postdate Lower Cretaceous breccias and cement Cc1 precipitated within the intergranular porosity of these rocks. The quality of the outcrops does not allow to observe these fractures affecting younger rocks and therefore, they could have been formed at any time during the Lower Cretaceous extension or even during the Upper Cretaceous post-rift stage.

Calcite cements Cc4 precipitated in hydraulic breccias within damage zone of large reverse faults in the UPTS and Cc5 precipitated in F5, F6 and F7 fracture systems were aged by means of U/Pb geochronology (Cruset et al., in review). The ages (70.5 ± 1.1 Ma for Cc4 and between 67 ± 2.4 Ma and 54.98 ± 0.66 Ma for Cc5) indicate that these fractures formed during the Upper Cretaceous compression and inversion of the Pyrenean rift, and lasted to the end of the Palaeocene (Puigdefàbregas and Souquet, 1986; Vergés et al. 2002; Cruset et al., in review).

In outcrop S, calcite cement Cc7 precipitated in fracture systems F9 and F10 have a U/Pb age of 38.4 ± 1.5 Ma, whereas Cc8 precipitated in the same type of fractures has an age of 26.1

± 2.2 Ma (Cruset et al., in review). In outcrop CV for Cc8 precipitated in fractures F11 the age is 34.3 ± 2.8 Ma. In the outcrop GS, calcite cement Cc9, which is predating Cc10 has an age of 34.8 ± 1.6 Ma. In the internal part of the UPTS (outcrop CV), Cc10 precipitated between breccia clasts made of Lower Jurassic limestones has and U-Pb age ranging between 37.25 ± 0.5 Ma and 34.3 ± 1.6 Ma. In outcrop GS Cc12 precipitated in F12 and F13 fractures and postdating Cc11 has an age of 31.4 ± 1.7 Ma. F14 is filled with Cc13 is postdating F13 and F14 fractures filled with Cc12. F15 veins have a U/Pb age of 25 ± 17 Ma. Although the error range of this age is high, F15 is associated to a major fault which is crosscutting the main thrust fault plane of the UPTS containing Cc7 and Cc8 in the S outcrop (Fig. 3A). Therefore, we interpret that F15 formed after formation of F9 and F10 and the precipitation of the calcite cements mentioned before.

The U/Pb ages of calcite cements Cc7 to Cc15 and crosscutting relationships between fractures indicate that fracture systems F7 to F15 formed during the Eocene-Oligocene reactivation of the UPTS (Cruset et al., in review). This reactivation was the result of the emplacement of the Cadí thrust sheet and the basement units of Orri and Rialp (Burbank et al., 1992; Vergés, 1993; Beamud et al., 2010; Rushlow et al., 2013; Carrigan et al., 2016). Finally, F16 has a constant orientation regardless bedding dips, indicating that the probably formed during the post-compressional deformation which suffered the UPTS.

Chapter 9

Main Discussion

9. Main Discussion

In this chapter, the type of fluids and their evolution during the emplacement of each thrust unit, as well as the controls of the style of deformation on fluid flow will be considered to perform a fluid flow model of fold and thrust belts.

9.1. Timing of fluid migration and deformation

U-Pb geochronology applied to calcite cements presented in Chapters 4, 5, 7 and 8 confirms that the studied diagenetic products are related to the compressional history of the southern Pyrenees (Chapter 6; Fig. 3).

In the Upper Pedraforca thrust sheet, U-Pb ages obtained for calcite cements Cc4 and Cc5 (70.5 ± 1.1 Ma and from 67 ± 2.4 Ma to 54.98 ± 0.66 Ma, respectively) indicate that these cements precipitated during the Late Cretaceous-Paleocene compression (Puigdefàbregas and Souquet, 1986; Vergés et al. 2002; Cruset et al., in review). Calcite cement Cc7 has a U-Pb age of 38.4 ± 1.5 Ma, whereas for Cc8 the age ranges between 26.1 ± 2.2 Ma and 34.3 ± 2.8 Ma (Cruset et al., in review). Calcite cement Cc9, which is predating Cc10 has an age ranging from 37.25 ± 0.5 Ma to 34.8 ± 1.6 Ma. Calcite cement Cc12 is postdating Cc11 and has an age of 31.4 ± 1.7 Ma. Cc13 is postdating Cc12. Cc14 has a U-Pb age of 25 ± 17 Ma. Although the error range of this age is high, this cement postdates Cc7 and Cc8 in the Upper Pedraforca thrust front (Chapter 8). U-Pb ages of calcite cements Cc7 to Cc15 and crosscutting relationships between fractures indicate that these cements precipitated in fractures during the Eocene-Oligocene reactivation of the Upper Pedraforca thrust sheet (Cruset et al., in review; Chapter 8). This reactivation was the result of the emplacement of the Cadí thrust sheet and the basement units of Orri and Rialp (Burbank et al., 1992; Vergés, 1993; Beamud et al., 2010; Rushlow et al., 2013; Carrigan et al., 2016). Finally, Cc16 precipitated in F16 fractures, which have a constant orientation regardless bedding dips, indicating that the probably formed during the post-compressional deformation which suffered the Upper Pedraforca thrust sheet.

In the Lower Pedraforca thrust sheet, U-Pb geochronology applied to calcite cements Cc3, Cc4, Cc6 and Cc7 report ages ranging from 47.9 ± 1.3 Ma to 42.29 ± 0.84 Ma (Chapter 6). These ages indicate that these cemets precipitated in fractures at the end of the emplacement of this thrust unit. The youngest ages in the Lower Pedraforca thrust sheet were obtained in calcite cement Cc7 (from 42.99 ± 0.94 Ma to 42.29 ± 0.84 Ma). For Cc8 the obtained U-Pb age is 30.2 ± 2 Ma, suggesting that this cement precipitated in fractures formed during the Oligocene reactivation of the Lower Pedraforca thrust sheet (Cruset et al., in review).

In the Cadí thrust sheet, only one age for cements studied in this thesis has been obtained from U-Pb geochronology (Cc3 in sample GDV5; Cruset et al., in review). The obtained age (36.9 ± 1.1 Ma) is related to the activity of the Vallfogona thrust during the late Eocene. The other U-Pb obtained for the Cadí thrust sheet are obtained from calcite cements which have not been studied in this thesis.

Finally, U-Pb ages obtained in calcite cements within the three studied superposed thrust sheets and the foreland basin ranging from 18.9 ± 0.8 Ma to 2.6 ± 1.3 Ma could be related to both the Neogene extension occurring in NE Iberia and concomitant erosion of the Ebro foreland basin after its opening to the Western Mediterranean at 8-11 Ma (Lewis et al., 2000; Garcia-Castellanos et al., 2003; Fillon and Beek, 2012) (Chapter 6, Fig. 3). These Neogene ages are out of the scope of this thesis but indicate that fluid migration continued in the SE Pyrenees during these post-compressional events.

9.2. Type of fluids

The type of fluids migrating through fractures and intergranular and vug porosity affecting the southern Pyrenees can be determined by using the geochemical data from the studied calcite and cements.

The $\delta^{13}C$ of calcite cements precipitated in the Ainsa basin (Travé et al., 1997, 1998a), Castillo Mayor klippe and Jaca thrust (Lacroix et al., 2014, 2018), cements Dc1, Dc2, Dc3, Cc3, Cc4, Cc5, Cc6 , Cc7, Cc8 and Cc12 in the Upper Pedraforca thrust sheet (Chapter 8), Lower Pedraforca thrust sheet (Cruset et al., 2019; Chapter 7), Vallfogona thrust, (Cruset et al., 2016b, 2018), the Puig-reig anticline (Cruset et al., 2015, 2016a), as well as Cc2 in L'Escala thrust (Cruset et al., 2018) are similar to their adjacent host rocks. This similarity could indicate a rock-buffered system or the input of a CO_2 rich fluids, which generate acidic solutions that undergo modifications of the geochemical composition of host rocks (Gasparrini et al., 2013). In contrast, in the Abocador thrust, in cements Cc1, Cc2, Cc10, Cc14, Cc15 and Cc16 in the Upper Pedraforca thrust sheet, and in cements Cc1 and Cc3 in L'Escala thrust, the $\delta^{13}C$ of calcite cements shows depletion with respect to their adjacent host rocks. Such depletion is explained by the input of soil-derived or organogenic carbon into the fluid system (Irwin et al., 1977; Cerling et al., 1989).

The $\delta^{18}O$ calculated from clumped isotopes temperatures for the Vallfogona thrust (+12.12 ‰ VSMOW for Cc2, +6.3 7‰ VSMOW for Cc4 and +4.22‰ VSMOW for Cc5), calcite cements Cc3 and Cc6 in the Lower Pedraforca thrust sheet (+5.42 and +5.08 ‰ VSMOW, respectively), calcite cement Cc1 in Puig-reig anticline (between +4.7 and +9.2 ‰ VSMOW), calcite cement Cc2 in the Abocador thrust (+14.08 ‰ VSMOW) and El Guix anticline (+7.09 ‰ VSMOW) call for a composition within the range of magmatic, metamorphic and formation waters (Taylor, 1987). Similar values have been measured in the Upper Pedraforca thrust sheet from dolomite cements Dc1 and Dc2 (between +11.2 and +7.1 ‰ VSMOW, respectively) and calcite cements Cc4, Cc5, Cc7, Cc8, and Cc10 (between +3.1 and +9.8 ‰ VSMOW respectively) (Chapter 8, Fig. 13). In the Ainsa Basin, a fluid with a $\delta^{18}O$ ranging between +9.51 and +16 ‰ VSMOW is calculated from fluid inclusion data of celestite crystals formed within calcite cements precipitated in the Arro syncline (Travé et al., 1998a), and from the equation of Friedman and O'Neil (1977). Magmatic fluids are ruled out since magmatism did not develop during the formation of the Pyrenees, and

there are no evidences to differentiate between metamorphic and formation waters. On the other hand, in the frontal part of the Bóixols thrust sheet, $\delta^{18}O_{fluid}$ values calculated from clumped isotopes temperatures (between -1.3 and +1.6 ‰ VSMOW) highlight the influence of marine and meteoric fluids (Nardini et al., 2019). The same situation is observed in the Upper Pedraforca thrust sheet, which is the lateral equivalent of the Bóixols thrust sheet where $\delta^{18}O_{fluid}$ values ranging between -4.5 and -0.1 ‰ VSMOW are obtained from calcite cements Cc10, Cc12 and Cc14. In the Ainsa basin and in the Cotiella thrust sheet, which are structures formed below the sea level, the influence of marine connate waters trapped in the rock porosity has also been documented (Travé et al., 1997; Lacroix et al., 2014).

The temperatures obtained from clumped isotopes thermometry in the Vallfogona thrust (between 154 °C for Cc2, 101 °C for Cc4 and 105 °C for Cc5), Puig-reig anticline (between 92 °C and 129 °C for Cc1 and between 77 °C and 90 °C for Cc2) and Arro syncline (between 157 °C and 183 °C) were never reached by burial according to cross sections (Vergés, 1993; Labaume et al., 2016) and vitrinite reflectance data (Clavell, 1992; Vergés et al., 1998) assuming a geothermal gradient of 25 °C km−1, thus indicating a thermal anomaly. Preliminary temperature data from the Abocador thrust (177 °C) also call for the presence of high-temperature fluids. These results suggest hydrothermal fluid flow along fault zones in the Arro syncline, Vallfogona, Abocador and L'Escala thrusts and folding-related fractures and intergranular porosity within the Puig-reig anticline, which were connected at depth with basement-involved thrusts in the inner part of the Pyrenees, as has been already reported (Rye and Bradbury, 1988; Bradbury and Woodwell, 1987; McCaig et al., 1995, 2000; Travé et al., 2007; Trincal et al., 2017). Contrarily, clumped isotopes temperatures obtained in the frontal part of the Bóixols thrust sheet (between 40.7 and 88.4 ºC; Nardini et al., 2019), Upper Pedraforca thrust sheet ranging between 68.8 and 103.4 ºC (Chapter 8), Lower Pedraforca thrust sheet (69.08 ºC for Cc3 and 74.16 ºC for Cc6; Chapter 7), and in the El Guix anticline (117 ºC; Cruset et al., 2018), where reached by sediment burial rather than by the input of fluids in contact with the basement. Therefore, formation waters may have flowed through these structures instead of metamorphic fluids. The marine and meteoric origin of fluids in the Bóixols thrust sheet (Nardini et al., 2019), the presence of meteoric fluids that evolved to a formation water composition in the El Guix anticline (Travé et al., 2000), and the influence of Upper Triassic brines in calcite cements Cc3 and Cc6 in the Lower Pedraforca thrust sheet, and probably in the Upper Pedraforca thrust sheet, supports this interpretation. In these thrust sheets, evaporitic rocks may have acted as barriers for the input deep-sourced fluids, which only migrated through thrust sheets rooted at depth with basement units (e.g. Cadí thrust sheet, Puig-reig anticline). Dolomite cements Dc1 and Dc2 sampled in the Upper Pedraforca thrust sheet also precipitated from high-temperature fluids (149.4 and 124.7 ºC, respectively). However, these cements precipitated during the Late Jurassic-Early Cretaceous extension as we discussed in Chapter 8, and we have not geological data to determine if these temperatures were reached by sediment burial.

The progressive decrease in the Sr and Fe contents and the increase of the $^{87}Sr/^{86}Sr$ ratios in the thrust front from the lower Eocene to lower Oligocene, together with the depletion in $\delta^{18}O$ and decrease in temperature at outcrop scale in the Ainsa Basin, Vallfogona and L'Escala thrusts and Puig-reig anticline, accounts for the input of meteoric waters, which mixed at depth with the hydrothermal fluids (Cruset et al., 2016a, 2018). The depletion in Fe content and the decrease in $\delta^{18}O$ from older to younger calcite cements related to the progressive input of meteoric waters has also been observed in the Jaca thrust (Lacroix et al., 2014) and in the Upper Pedraforca thrust sheet (Chapter 8). However, in these thrust units meteoric fluids mixed at depth with formation waters. The progressive depletion in $\delta^{18}O$ is related to the mixing between meteoric waters and fluids with a higher temperature and salinity (Immenhauser et al., 2007), whereas the decrease in Fe content (Chapter 5, Fig. 6) could be related to the progressive input of oxidizing meteoric fluids into the system (Froelich et al., 1979; Tucker and Wright, 1990), which may have flowed downwards along faults and joints by topography-driven fluid flow (Bitzer et al., 2001). Likewise, the progressive decrease of the Y/Ho ratio in the Upper Pedraforca thrust sheet in calcite cements Cc7 to Cc14 (Chapter 8) accounts for the increasing influence of terrigenous sediment as this thrust sheet exhumed.

The geochemical trends observed in the structures described before are different than that observed in other areas of the southern Pyrenees. For instance, in the Abocador thrust, there is an enrichment in the $\delta^{18}O_{calcite}$ from older to younger cements. This trend is also observed in the Santo Domingo anticline (Sierras Exteriores, south western Pyrenees) with $\delta^{18}O_{fluid}$ values between −5 and 0 ‰ VSMOW in Bartonian-Priabonian veins and between +5 and +10 ‰ VSMOW in upper Priabonian-lower Rupelian veins (Crognier, 2016). This author interprets the highest $\delta^{18}O_{fluid}$ values as a strong interaction between meteoric waters and host rocks or by the input of strongly evaporated fluids. In the same area, in the Pico del Águila anticline, post-folding calcite veins precipitated from low-temperature meteoric waters (Beaudoin et al., 2015). From the $\delta^{18}O_{calcite}$ of these veins (from −2.2 to 0 ‰ VPDB) together with the temperatures reported by these authors (below 80 ± 20 °C) a $\delta^{18}O_{fluid}$ ranging between −4 and +11 ‰ VSMOW is calculated, suggesting that these fluids could be highly $\delta^{18}O$-enriched brines rather than meteoric waters. In the northern Jaca Basin, a positive correlation between the $\delta^{18}O_{fluid}$, temperature and salinity is observed from older to younger stages of fracturing without an enrichment in the $\delta^{18}O$ of calcite cements (Crognier et al., 2017). These authors suggest that hydrothermal fluids interacted with Triassic evaporites that acted as the detachment level of the south western Pyrenean thrust sheets. A positive correlation between the $\delta^{18}O_{calcite}$ and fluid salinity has also been observed in fracture-filling calcites precipitated in areas worldwide affected by salt tectonics (Fischer et al., 2013). The same scenario could be suggested for: 1) the Abocador thrust, where preliminary results on clumped isotopes thermometry (177 ± 40 °C and $\delta^{18}O_{fluid}$ of +14.1 ‰ VSMOW) and the presence of barite and celestite crystals formed within calcite cements favours the hypothesis of hydrothermal fluids interacting with brines released from the underlying Eocene evaporites of the Beuda Fm., which acted as the detachment of this structure; 2) the El Guix anticline, with calcite cements without systematic $\delta^{18}O$ variation, temperature around 117 ± 25 °C, a $\delta^{18}O_{fluid}$ of +7.1 ‰

VSMOW and halite precipitation in thrust zones also favours the hypothesis of a fluid interacting with the underlying Eocene Cardona Salt Formation (Travé et al., 2000); and 3) the Larra/Eaux chaudes thrust and Sierras Exteriores, with Triassic evaporites acting as the detachment level of the major thrust faults (Crognier et al., 2017). Consequently, we suggest that when evaporitic units are present, the presence of high-salinity fluids derived from them, highly controls the $\delta^{18}O$ of the calcite cements.

The presence of the thermal anomalies discussed above, with fluids in disequilibrium with their adjacent host rocks during millions of years, indicate the occurrence of thermal convection controlling fluid flow (Lipsey et al., 2016). According to this mechanism, large volumes of fluids are driven to the reaction site through fractures and permeable host rocks during long time periods (Person et al., 1996; Morrow, 1998). Other scenarios, which involve fluid release by heating or decompression of interstitial fluids by seal breaking are ruled out, since these mechanisms provide low volumes of fluids and they do not generate thermal anomalies (Gomez-Rivas et al., 2014).

9.3. Evolution of the paleohydrological system

The evolution of the palaeohydrological system through time within each thrust sheet forming the south eastern Pyrenees is inferred from fluid-rock relationships.

In those areas such as the Lower Pedraforca thrust sheet in which pre-compressive hydroplastic deformation is observed (Chapter 7), it is interesting to note that there is no precipitation of calcite cements between fracture planes. This fact could be due to that faulting of poorly consolidated sediments with internal heterogeneities occasionally form zones of low permeability (Caine and Minor, 2009; Loveless et al., 2011), or that calcite tend to precipitate within fractures in areas with elevated pressures and temperatures (Lee et al., 1996). Therefore, at surficial conditions fluids might not be saturated in calcite.

However, when compressional deformation stretched the structures studied in this thesis, calcite cements precipitated within fractures. For instance, during the layer-parallel shortening fluids tend to be in equilibrium with their adjacent host rocks, thus reporting a relatively closed paleohydrological system and high fluid-rock interaction. This equilibrium between calcite cements precipitated during the first stages of deformation and their adjacent host rocks has been observed in the Upper Pedraforca thrust sheet (Cruset et al., 2017; Chapter 8), Lower Pedraforca thrust sheet (Cruset et al., 2019; Chapter 7), Ainsa basin (Travé et al., 1997), Jaca thrust (Lacroix et al., 2014), Vallfogona and L'Escala thrusts (Cruset et al., 2016b, 2018) and in the Puig-reig anticline (Cruset et al., 2015, 2016a) based on $\delta^{18}O$ and elemental composition data. In contrast, during the folding and thrusting stage of these structures, the system opened, and the fluid-rock interaction decreased. In the Upper Pedraforca thrust sheet, Vallfogona and Jaca thrusts, and in the Puig-reig anticline this disequilibrium is related to the increasing influence of meteoric fluids as these structures emerged, inferred by the progressive decrease of the $\delta^{18}O_{fluid}$, fluid

temperature Fe content and Y/Ho ratios (Lacroix et al., 2014; Cruset et al., 2016a, 2017, 2018; Chapter 8). In the Lower Pedraforca thrust sheet, however, the opening of the fluid system does not reflect a significant change in the fluid composition (Chapter 7). Therefore, changes in the paleohydrology of this thrust sheet could be explained only by changes of fluid-rock ratio rather than the input of external fluids (Banner and Hanson, 1990).

9.4. Fluid flow evolution during the growth of the south Pyrenean fold and thrust belt

The results discussed in previous sections enable us to decipher the evolution of the fluid flow at the scale of the south Pyrenean fold and thrust belt from the Late Cretaceous to the Oligocene (Fig. 14).

From the Late Cretaceous to the Paleocene (Fig. 14), when the Upper Pedraforca thrust sheet emplaced, high-salinity fluids at temperatures between 79.7 and 81 ºC migrated through fractures affecting this structure (Chapter 8). These temperatures are similar to that documented in its lateral equivalent to the west, the Bóixols thrust sheet, in which connate marine fluids reached these temperatures by sediment burial (Nardini et al. 2019). As the Upper Pedraforca thrust sheet emerged, the salinity of fluids slightly decreased, indicating an increase of the influence of meteoric fluids. This decrease in the salinity related to the input of low-temperature meteoric waters into the fluid system, has also been documented in the Vallfogona and Jaca thrusts and in the Bóixols and Puig-reig anticlines (Lacroix et al., 2014; Cruset et al., 2016a, 2018: Nardini et al., 2019).

From the lower to the middle Eocene, the Lower Pedraforca thrust sheet emplaced (Fig. 14). At this time, brines derived from the underlying Upper Triassic evaporites acting as a detachment of the thrust sheet migrated through fractures during the layer-parallel shortening and later folding and thrusting (Chapter 7). Although the composition of fluids does not show strong differences during the evolution of the Lower Pedraforca thrust sheet, the decrease in $\delta^{18}O$ of calcite cements Cc6 to Cc8 with respect to Cc1 to Cc4 data indicates that the paleohydrological system changed from a relatively closed to a more open one. During the early Eocene, the Cotiella thrust sheet emplaced in the south wester Pyrenees, and deep-sourced fluids derived from the internal part of the orogen migrated through thrust faults and mixed with marine connate waters (Travé et al., 1997).

After the emplacement of the Lower Pedraforca thrust sheet, deformation was transferred to its related foreland basin and the Cadí thrust sheet emplaced from middle Eocene to the early Oligocene (Cruset et al. in review) (Fig. 14). During this period, deformation changed from thin-skinned, when the Upper and Lower Pedraforca thrust sheets detached above Upper Triassic units, to thick-skinned, when the Vallfogona thrust, the southern margin of the Cadí thrust sheet, rooted at depth with the basement units of Orri and Rialp (Vergés, 1993). This change had strong implications on the fluid regime in the south eastern Pyrenees, resulting in the development of

thermal anomalies within the Vallfogona and Abocador thrusts due to the migration of high-salinity hydrothermal fluids with temperatures ranging between 177 and 100 ºC (Cruset et al., 2018). As deformation in these structures advanced, the influence of meteoric waters which mixed at depth with hydrothermal fluids increased in thrust sheets not detached through thick evaporite units, and consequently, the salinity and temperature of the mixed fluid decreased. In contrast, in those structures such as the Abocador thrust and the Pico del Águila anticline, the fluid composition was controlled by thick evaporite units acting as a detachment of these thrust units (Cruset et al., 2018). As a result, high-salinity fluids migrated through fractures instead of low-salinity meteoric waters. In the Upper Pedraforca thrust sheet, during its middle Eocene to late Oligocene reactivation, the influence of meteoric fluids increased with respect to the initial emplacement of this thrust sheet from the Late Cretaceous to the late Paleocene (Chapters 6 and 8). This interpretation is based on clumped isotopes data and rare earth elements composition of calcite cements Cc7, Cc8, Cc10, Cc12 and Cc14, indicating a progressive exhumation of this thrust sheet above the Cadí and Lower Pedraforca units.

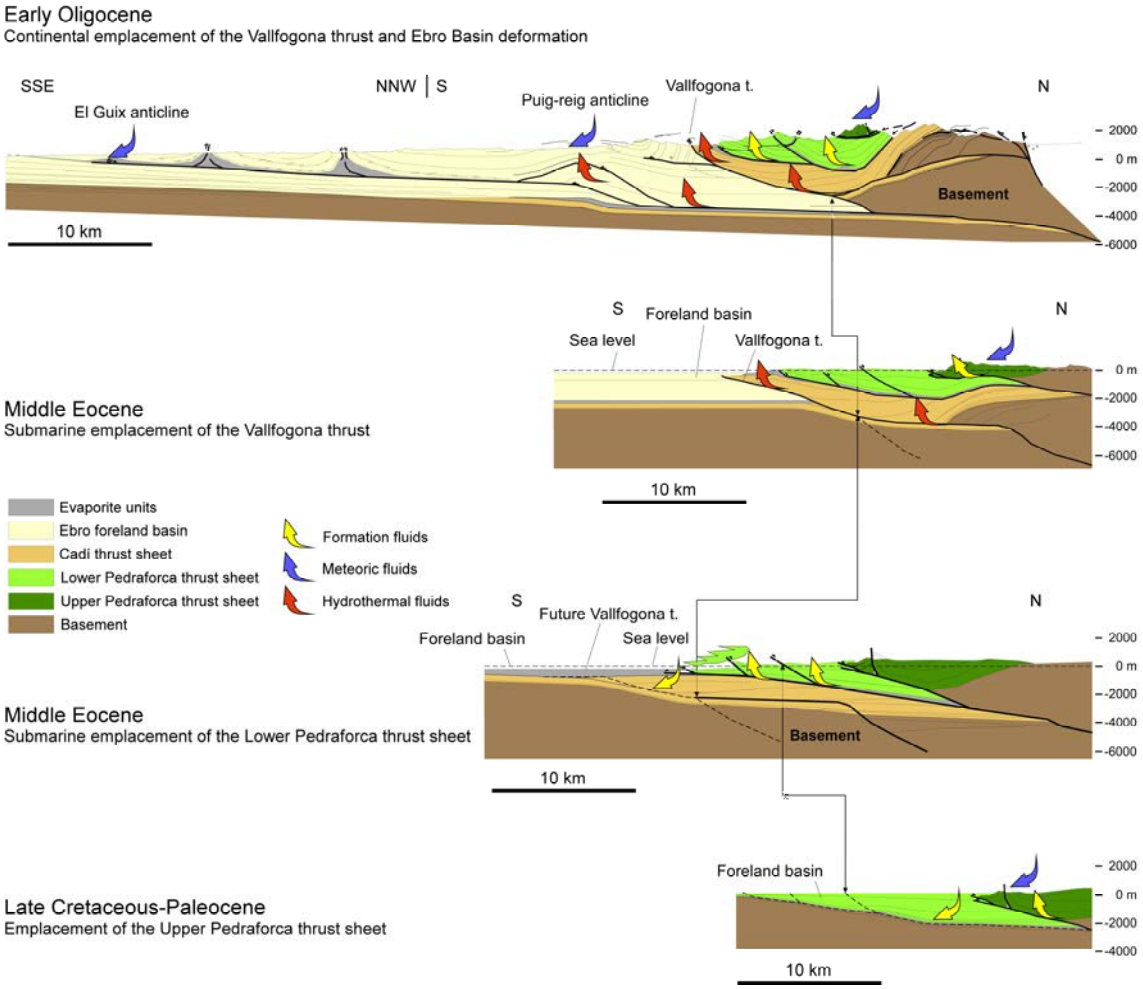

Fig.14. Fluid flow model during the growth of the south eastern Pyrenees from the Late Cretaceous to the Oligocene. Early Oligocene and middle Eocene cross sections from Vergés (1993) and Vergés et al. (1995), respectively.

The development of thermal anomalies related to the migration of deep-sourced fluids has also been documented in the south western Pyrenees in thrust faults rooted at depth with the

more internal parts of the orogen. For instance, Rye and Bradbury (1988) conclude that metamorphic fluids derived from the basement migrated through the Pineta thrust, a branch of the Monte Perdido thrust system. Travé et al. (1997, 1998a) reported that deep-sourced fluids mixed with local, and marine waters in the thrust front of the Ainsa basin. McCaig et al. (1995, 2000) documented the influence of brines derived from Triassic redbeds in their study of the Gavarnie thrust. Likewise, Trincal et al. (2017) document the recrystallization of mylonitized carbonate host-rocks due to the migration of high-salinity fluids derived from the Silurian in the Pic-de-Port-Vieux thrust fault zone. According to these authors, rock transformations took place under low-grade metamorphism conditions. Crognier et al. (2017) documented that thermal anomalies are related to the migration of hydrothermal fluids in contact with Triassic brines during the activity of the Gavarnie thrust, from late Eocene to early Oligocene. Labaume et al. (2016) suggest that thermal anomalies also could have developed at the base of the Eocene Hecho group due to the migration of high-temperature fluids (up to 240 ºC) through this sedimentary unit rather than burial heating. In the same area, similar temperatures of fluids were obtained in calcite and quartz veins within the Monte Perdido thrust system using fluid inclusions thermometry (Lacroix et al., 2011). Nevertheless, these authors discard the development of thermal anomalies in the thrust front, since $\delta^{18}O$ values of veins and host rocks are in equilibrium, thus suggesting that fluids were heated by burial of sediments. The $\delta^{13}C$ and $\delta^{18}O$ of deformed sediments within the Monte Perdido thrust fault zone reported by Lacroix et al. (2011) are lower than expected for Eocene marine carbonates (Veizer et al., 1999). These values indicate that the geochemical composition of the Eocene sediments changed probably due to the input of an external fluid enriched in CO_2, as has been observed in geothermal systems worldwide developed within carbonate rocks (Gasparrini et al., 2013). Therefore, the presence of thermal anomalies related to the migration hydrothermal fluids interacting with Eocene host rocks through the Monte Perdido thrust system should not be discarded.

During the final stages of evolution of the south eastern Pyrenean fold and thrust belt, deformation was transferred to the Ebro foreland basin, where the Puig-reig and El Guix anticlines formed (Fig. 14). Although in both anticlines high-salinity fluids migrated through fractures, they have a different origin. In the Puig-reig anticline, in the south Pyrenean thrust front, high-salinity fluids were deep-sourced and probably interacted with the Pyrenean basement (Cruset et al., 2016a). In contrast, in the El Guix anticline, which detached above the Cardona salt at the southern tip line of the south Pyrenean fold and thrust belt, these fluids are meteoric waters that evolved to a formation water composition when they interacted with the evaporites (Travé et al., 2000). Clumped isotopes temperatures obtained in this fold were achieved by burial within the Ebro foreland basin taking into account vitrinite reflectance data from Vergés et al. (1998) and a geothermal gradient of 25 °C km−1. These results suggest that hydrothermal fluids derived from deeper parts of the southern Pyrenees were probably diluted during their forward migration. A similar situation is observed in the southwestern Pyrenees during the Lutetian-Bartonian, taking into account the restored cross section of Labaume et al. (2016). During this period, hydrothermal fluids migrated in the Monte Perdido thrust system, which is located in the thrust front (Rye and

Bradbury, 1988; Travé et al., 1998a; Labaume et al., 2016). Contrarily, further south, in the Sierras Exteriores area, the Pico del Águila anticline detached above Upper Triassic evaporites, and the fluid system was dominated by meteoric and formation waters at temperatures below 100 ºC (Beaudoin et al., 2015). In the south eastern Pyrenees, the last stages of deformation within the Puig-reig anticline where characterized crestal graben collapse of this fold. During this stage, meteoric fluids percolated through crestal normal faults and mixed at depth with deep-sourced fluids (Cruset et al. 2016a). In the El Guix anticline these fluids have not been identified.

9.5. Conceptual model of fluid flow in fold and thrust belts.

The fluid flow behavior observed in the southern Pyrenees has strong similarities with that observed in other fold and thrust belts worldwide. In the following lines these similarities will be discussed.

The evolution of the paleohydrological system observed in the Upper Pedraforca, Lower Pedraforca and Cadí thrust sheets as well as in the Ebro foreland basin is common to that documented in many orogens worldwide. For instance, in the Bighorn Basin (Sevier thrust belt, USA), a closed paleohydrological system prevails during the layer-parallel shortening, whereas it opens during the fracturing associated to folding and thrusting (Beaudoin et al., 2013). Likewise, during the deformation stretching the Upper Pedraforca, Lower Pedraforca and Cadí thrust sheets the paleohydrological system evolves following this trend. In the Mexican fold and thrust belt and in the central Appalachians, fluids are stratigraphically segregated during the early folding, whereas during fold tightening the fluid system is interconnected (Lefticariu et al., 2005; Fischer et al., 2009; Fitz-Diaz et al., 2011; Evans et al., 2012). The same fluid flow behavior during folding has been documented in the Pico del Águila and the Puig-reig anticlines, in the southern Pyrenees (Beaudoin et al., 2015; Cruset et al., 2016a). Finally, in the Northern Oman Mountains, pre-burial fluids migrated through fractures in a rock-buffered system and deep-sourced fluids migrated through thrust faults during the main stage of compression (Breesch et al., 2009). In this last example, main thrust faults acted as barriers for transversal fluid flow, since evidences of migration of fluids were not observed in the hangingwall. The evolution of the paleohydrological system documented in compressional settings follows the same trend in extensional regimes (Benedicto et al., 2008; Baqués et al., 2010; Cantarero et al., 2014). In these examples, during the first stages of the upwards propagation of normal faults, the paleohydrological system is relatively closed with high fluid-rock interaction. In contrast, during the final stages of deformation the system changes to a more open one, in which fluid-rock interaction is lower.

The influence of the tectonic style of deformation on fluid flow observed in the southern Pyrenees (thin-skinned versus thick-skinned) is also documented in other fold and thrust belts worldwide. As an example, in the thin-skinned Sicilian fold and thrust belt, fluids are compartmentalized in the hangingwall of thrust sheets, above main detachments (Dewever et al., 2013). Likewise, according to fluid flow modelling done by Vilasi et al. (2009) in the Albanian thrust belt, thrust fault detachments constituted of Triassic evaporites could act as seals for

hydrocarbons trapped beneath these levels (Vilasi et al., 2009). Similarly, evaporitic detachments of the Bóixols, Lower and Upper Pedraforca thrust sheets, El Guix and the Pico del Águila anticlines and the Iberian Ranges were barriers for deep-sourced fluids. In all these structures only marine, meteoric and formation waters migrated above evaporitic detachments (Travé et al., 2000, 2004; Beaudoin et al., 2015; Nardini et al. 2019). In the Nuncios detachment fold complex, in the Mexican fold and thrust belt, fluids were confined within stratigraphic units during early deformation, and only were interconnected during fold tightening (Lefticariu et al., 2005; Fig. 15). In both stages of evolution, the fluid system was dominated by formation waters. In the Bighorn basin, in the Sevier thrust belt, formation fluids migrated through fractures during thin-skinned deformation (Beaudoin et al., 2014; Fig. 16). Contrarily, these authors also report that when the style of deformation evolved to thick-skinned, thrust faults connected with the crystalline basement allowed the input of hydrothermal fluids into the Bighorn basin (Fig. 16). The same situation is observed in the southern Pyrenees, with hydrothermal fluids migrating through the Gavarnie, Pic-de-Port-Vieux, Vallfogona and Abocador thrusts and fractures in the Puig-reig anticline, which are rooted at depth with basement units (Rye and Bradbury, 1988; McCaig et al., 1995; 2000) Trincal et al., 2017; Cruset et al., 2018). Likewise, in the western Alps, shear zones formed in the basement allowed the input of important amounts of basement-derived fluids into the sedimentary cover (Boutoux et al., 2014; Fig. 17). In the Anglo Brabant fold belt in Belgium, deep-sourced fluids migrating through reverse faults are the responsible of the formation of sulphide mineralizations (Piessens et al., 2002; Dewaele et al., 2004).

From the comparison of all the fold and thrust belts discussed above, it is interesting to note that whereas in detached thrust sheets, migrating fluids involved are marine, meteoric and/or formation waters, thick-skinned deformation allows the migration of hydrothermal fluids. As a result, based on the fluid flow evolution of the southern Pyrenees and other orogens worldwide, we present a conceptual model of fluid flow in fold and thrust belts in which are possible two situations (Fig. 18).

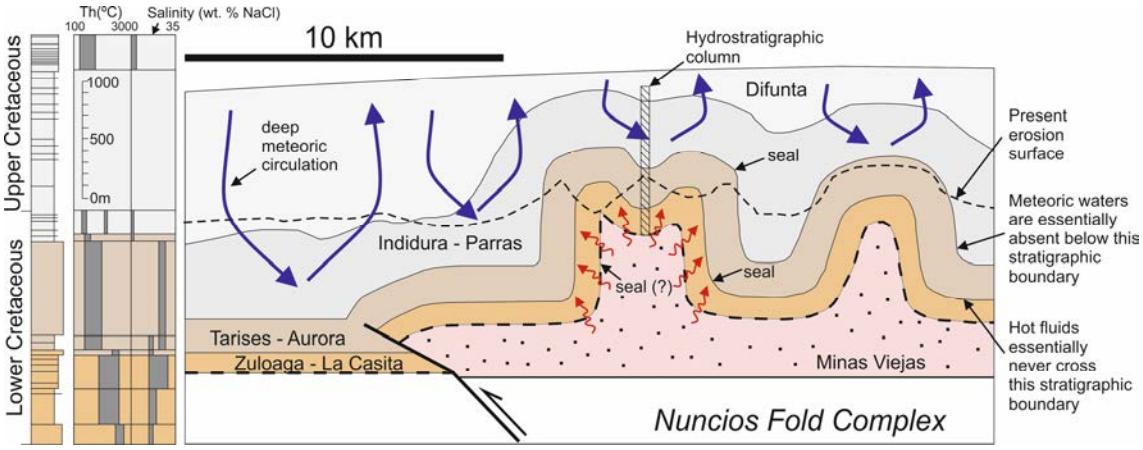

Fig. 15. Fluid system in the Nuncios Fold Complex showing four major hydrostratigraphic units, three stratigraphic seals, and fluid migration pathways. Note how the fluids involved in detachment folding are essentially meteoric waters. (Fischer et al., 2009).

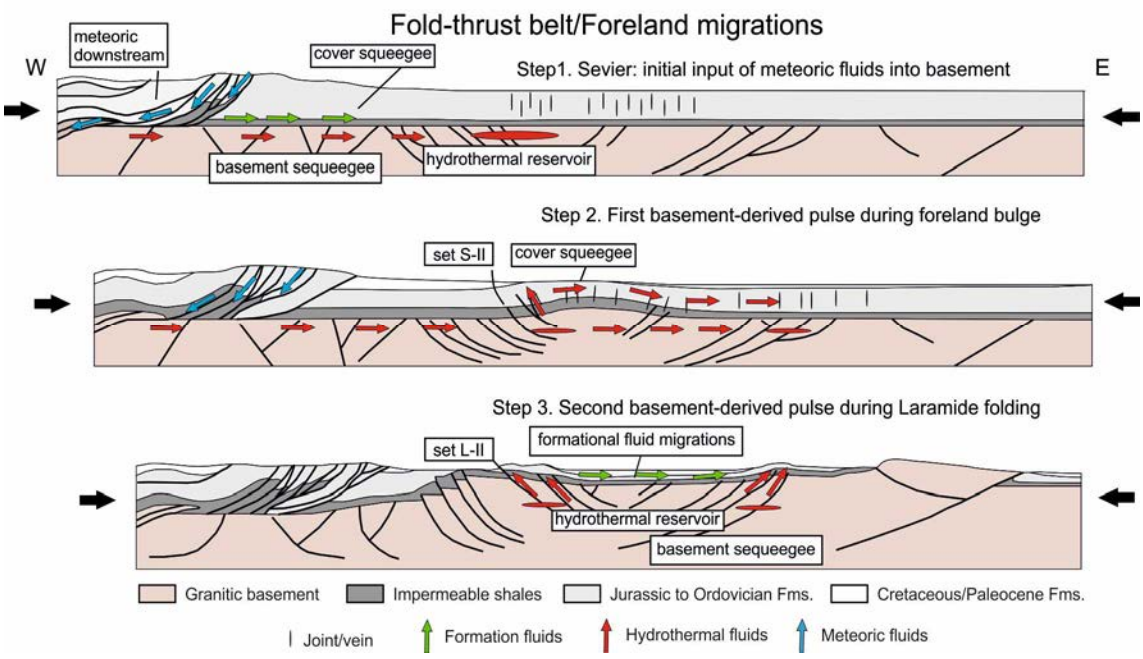

Fig. 16. Conceptual model of fluid flow of the Bighorn basin from Beaudoin et al. (2014). Note how in Step 1 hydrothermal fluids migrate through the basement below impermeable shales, whereas in Steps 2 and 3 hydrothermal fluids migrate into the sedimentary cover through thrust faults connected at depth with the basement.

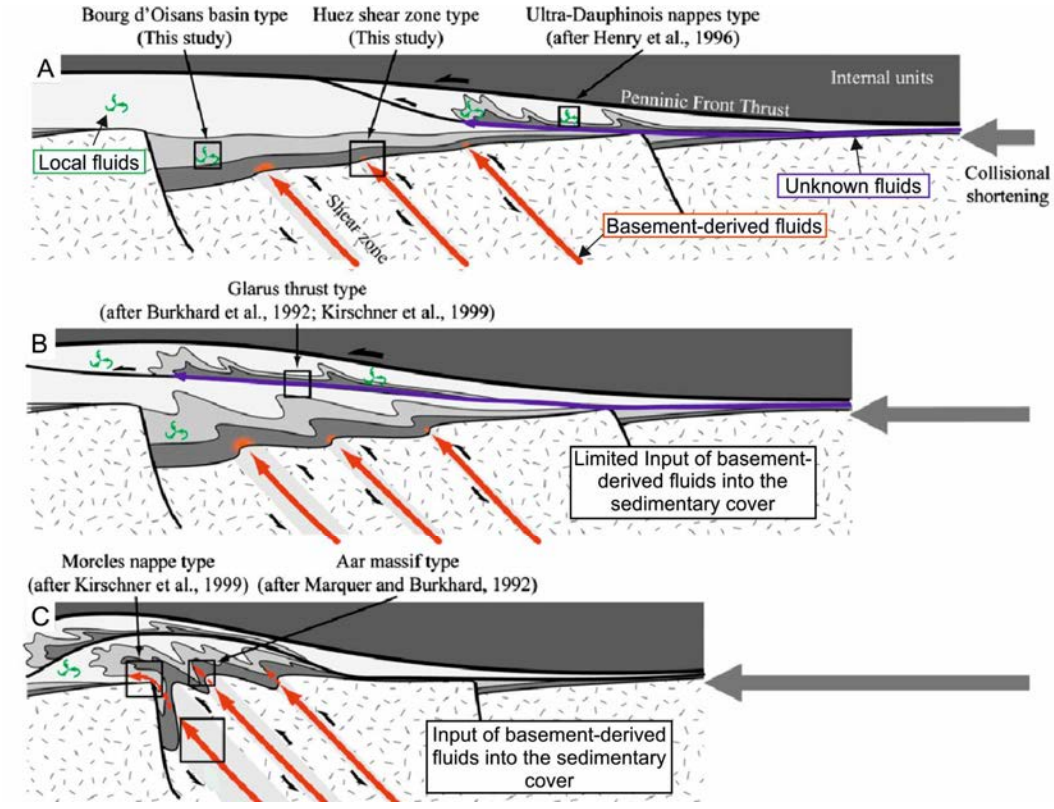

Fig. 17. Fluid evolution across the external Alpine Arc from Boutoux et al. (2014). A) Initial Alpine collisional shortening. The cover is detached from the basement and fluid circulation is restricted to lithologic unit scale above and under the thrusts. In the inherited basins, basement shear zones channelized large-scale fluid circulation although there is limited fluid percolation above shear zones. B) Higher amount of Alpine shortening. Cover thrust nappes overthrusted the inverted basins, allowing the channelization of large-scale fluid flow into thrusts. C) Late Alpine shortening. Local fluid circulation in the sedimentary nappes. Inverted basins were folded and strongly sheared by propagating basement shear zones favoring the input basement-derived fluids into the cover.

The first situation occurs in thin-skinned fold and thrust belts (Fig. 18A). During the layer-parallel shortening, formation, marine and/or meteoric fluids migrate through fractures above detachment levels. These levels act as barriers for transversal fluid flow that avoid the input of deep-sourced fluids. At this time, the paleohydrological system is relatively closed and therefore, fluid-rock interaction is low. Contrarily, during folding and thrusting affecting the detached structure, the paleohydrological system opened and the fluid-rock interaction decreased. During this period, these fluids are expelled into the foreland basin and as the thin-skinned thrust sheet emerge, the influence of meteoric fluids occasionally increases.

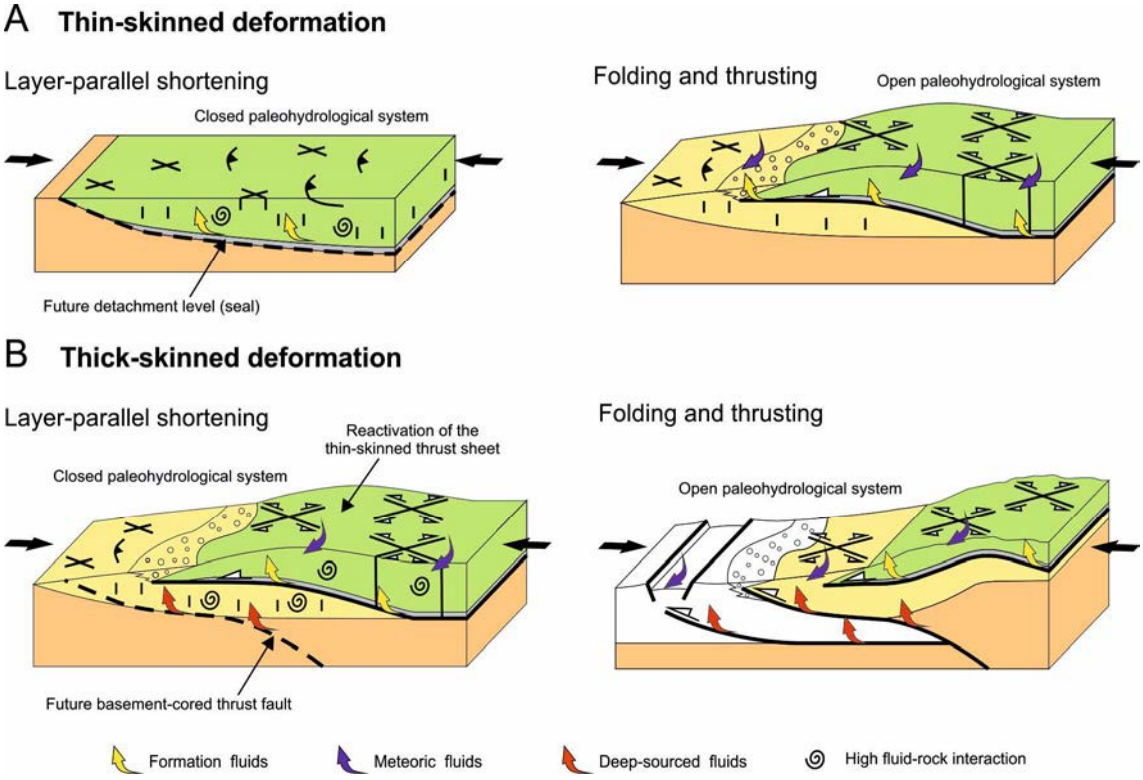

Fig.17. Conceptual model of fluid flow in fold and thrust belts. A) Fluid flow evolution in thin-skinned thrust sheets. B) Fluid flow evolution in thick-skinned thrust sheets.

The second situation develops in thick-skinned fold and thrust belts (Fig. 18B). Like in the first situation, during the layer-parallel shortening fluids migrated through fractures in a closed paleohydrological system. However, in this case fluids are hydrothermal, producing thermal anomalies in the deformed thrust sheet and foreland basin. Finally, during folding and thrusting stretching the deformed area, and as the thrust sheets emerge, the paleohydrological system opens to the input of external fluids, which in most cases consist of meteoric waters.

Chapter 10

Main Conclusions

10. Main Conclusions

In the following lines we present a summary of the main conclusions achieved in this thesis. The conclusions are organized according to: Chapter 4: Fluid flow during the late foreland stage in the Puig-reig anticline; Chapter 5: Fluid flow evolution in the south Pyrenean foreland basin; Chapter 6: U-Pb geochronology of fluid flow and deformation in the south Eastern Pyrenees; Chapter 7: Controls of deformation on the paleohydrological regime in the Lower Pedraforca thrust sheet; Chapter 8: Fluid flow evolution from the Mesozoic Extension to the Alpine orogeny in the Upper Pedraforca thrust sheet; and Chapter 9: Main discussion of this thesis.

In the Puig-reig anticline two fluid flow events related to the evolution of this fold have been identified: Cc1 related to the layer-parallel shortening and Cc2 linked to the anticline growth. Cc1 cement precipitated from an ascending hydrothermal fluid at temperatures between 92 and 130 ºC. This fluid had $\delta^{18}O_{fluid}$ between +4.7 and +9.2 ‰ VSMOW, relatively high $^{87}Sr/^{86}Sr$ ratio, and high Mn and Mg content and relatively low Sr and Fe content. Hydrothermal fluids migrated from around 4-5 km depth through the fracture system to reach the Berga and Solsona Formations during the layer-parallel shortening, partially replacing the host rocks by calcite. Cc1 precipitation was induced by p_{CO2} drop related to fracturing. Cc2 cement precipitated from a fluid in disequilibrium with its adjacent host rock at a temperature between 77 and 93 ºC. This fluid, with $\delta^{18}O_{fluid}$ between −1.7 ‰ and −0.7 ‰ VSMOW, relatively low $^{87}Sr/^{86}Sr$ and Mg, and high Sr and Fe content, resulted from the mixing at depth of the hydrothermal fluid from which Cc1 precipitated and low-temperature, probably meteoric, waters. Low-temperature fluids percolated through the crestal graben fault system according to the fault-valve model during the growth of the Puig-reig anticline. Fluid flow patterns between the Puig-reig and the El Guix anticlines along the same transect reveal that hydrothermal fluids migrated from N to S but did not reach the El Guix anticline along the tip line of the South Pyrenean fold and thrust belt. In this anticline, meteoric fluids that evolved to a formation water composition circulated above the Cardona salt Formation, which acted as a barrier for deep-sourced hydrothermal fluids.

In the south Pyrenean foreland basin, from Lower to Middle Eocene, ascending hydrothermal fluids migrated from the Axial zone to the foreland basin and mixed with connate marine waters trapped in rock porosity. The mixed fluid had temperatures up to 154 °C, enriched $\delta^{18}O$, $^{87}Sr/^{86}Sr$ slightly higher than Eocene seawater and high Fe and Sr contents. From Middle Eocene to Lower Oligocene, as the thrust front progressively emerged, meteoric waters migrated downwards the foreland basin by topography-driven fluid flow and mixed at depth with the hydrothermal fluids. The mixed fluid was progressively more depleted in $\delta^{18}O$, with temperatures between 77 and 129 °C, lower Fe and Sr contents and more radiogenic $^{87}Sr/^{86}Sr$ ratios than the former fluid. The comparison of southern Pyrenees to other orogens worldwide, suggests that the presence or absence of thick evaporitic units had a fundamental role in the fluid composition during fold and thrust belt evolution. In all cases, hydrothermal or formation fluids migrated along fractures within thrust sheets and mixed with low-temperature meteoric waters. When thrusts were not detached

through thick evaporite units, the resultant fluid was progressively more radiogenic, more depleted in $\delta^{18}O$ and had a lower temperature and lower Sr and Fe content, as the thrust front emerged. In contrast, when thrusts were detached along thick evaporitic units, the resulting fluid was enriched in $\delta^{18}O$.

U-Pb geochronology applied to fracture-filling calcite cements in the SE Pyrenean thrust system indicates that this method is a powerful tool to constrain the timing of fluid migration and sequence of deformation in fold and thrust belts, especially in those in which syn-tectonic sediments are scarce or completely eroded. The results of our study indicate that: 1) the thrust front migrated towards de foreland from the Late Cretaceous to the late Oligocene (70.5 ± 1.1 Ma to 25 ± 17 Ma); 2) the Bóixols-Upper Pedraforca thrust sheet documents the entire compressional deformation, whereas the Lower Pedraforca and Cadí thrust sheets records younger ages and a shorter period of deformation; 3) the continuity over time of the different ages from each thrust sheet indicates continuous rather than episodic tectonic activity; and 4) Neogene U-Pb ages ranging from 18.9 ± 0.8 Ma to 2.6 ± 1.3 Ma indicate, for the first time, the extension of NE Iberia related to the formation of the Western Mediterranean.

In the Lower Pedraforca thrust sheet, up to eight calcite cements (Cc1 to Cc8) reveal the evolution of the paleohydrological system during the emplacement of this thrust unit. Calcite cements Cc1 to Cc4 precipitated from fluids in a relatively closed paleohydrological system in which the fluid-rock interaction was high. Calcite cement Cc3 precipitated from brines derived from the Upper Triassic evaporites acting as a detachment of the Lower Pedraforca thrust system ($\delta^{18}O_{fluid}$ ~+5.4 ‰ VSMOW) with $^{87}Sr/^{86}Sr$ ratios of 0.707922 and at temperatures around 70 ºC. Contrarily, calcite cements Cc5 to Cc8 precipitated from fluids in a more open paleohydrological system in which the interaction between fluids and host rocks was low. Cc6 also precipitated from brines derived from the Upper Triassic ($\delta^{18}O_{fluid}$ ~+5 ‰ VSMOW) with $^{87}Sr/^{86}Sr$ ratios of 0.707817 and at temperatures around 75 ºC. Relationships between calcite cements and fractures indicate that: 1) during hydroplastic deformation related to the pre-folding stage within the Lower Pedraforca thrust sheet, there was no precipitation of calcite cements in fracture planes; 2) during the layer parallel shortening fluids migrated in a relatively closed system and fluid-rock interaction was high; and 3) during the folding and thrusting related to the emplacement of the Lower Pedraforca thrust sheet and during its late reactivation, the fluid-rock interaction decreased as the paleohydrological system opened.

In the Upper Pedraforca thrust sheet, high-salinity and high-temperature fluids migrated through diapir walls during the Early Cretaceous. From the Late Cretaceous to the Paleocene compression, during the first stages of the Pyrenean Orogeny, formation waters at temperatures around 80 ºC, $\delta^{18}O_{fluid}$ ranging between +6.6 and +3.1 ‰ VSMOW and $^{87}Sr/^{86}Sr$ ratios in equilibrium with Late Cretaceous marine waters migrated through main thrust fault zones. As the Upper Pedraforca thrust sheet emplaced, the paleohydrological system opened and the $\delta^{18}O_{fluid}$ decreased, thus indicating the increasing influence of meteoric fluids. Finally, during the Eocene-

Oligocene reactivation of the Upper Pedraforca thrust sheet, formation waters at temperatures between 100.78 and 70 ºC and $\delta^{18}O_{fluid}$ ranging from +9.34 to +3.9 ‰ VSMOW migrated trough main thrust fault zones. Coevally, in the internal part of the Upper Pedraforca thrust sheet, fluids at temperatures ranging between 50 and 20 ºC, $\delta^{18}O_{fluid}$ ranging from -4.84 and -3.6 ‰ VSMOW and decreasing Y/Ho ratios indicates the increasing influence of meteoric waters with respect to the Late Cretaceous-Paleocene compression as this thrust unit is exhumed.

The integration of the results obtained for each south eastern Pyrenean thrust sheet indicates that during the Late Cretaceous to Paleocene compression formation and marine fluids, both with an increasing meteoric influence, migrated through fractures affecting the Upper Pedraforca and Bóixols thrust sheets, respectively. Likewise, when the Lower Pedraforca thrust sheet emplaced during the middle Eocene, brines derived from Upper Triassic evaporites acting as detachment of this thrust unit migrated above this sealing unit. From the middle Eocene to the Oligocene, when the Cadí thrust sheet emplaced and deformation affected the Ebro foreland basin, hydrothermal fluids, probably in contact with the Pyrenean basement migrated to the south Pyrenean thrust front, inducing the development of thermal anomalies. Hydrothermal fluids did not reach the frontal part of the south eastern Pyrenean fold and thrust belt, the El Guix anticline. Instead, meteoric fluids which evolved to a formation water composition when interacted with the evaporitic Cardona Fm. dominated the fluid system during deformation. The same situation is observed in the thrust front of the south western Pyrenees, where the fluid system in the El Pico del Águila anticline was dominated by formation and meteoric waters, which probably interacted with Upper Triassic evaporites.

Relationships between the studied calcite cements and fractures enlighten on the evolution of the paleohydrological system during deformation in fold and thrust belts. The results indicate that: 1) during hydroplastic deformation related to the pre-folding stage within thrust sheets, there was no precipitation of calcite cements between fracture planes; 2) during the layer-parallel shortening fluids migrated in a relatively closed system and fluid-rock interaction was high; and 3) during later folding and thrusting the fluid-rock interaction decreased as the paleohydrological system opened.

The results obtained in the south Eastern Pyrenees and their comparison with studies developed in other orogens worldwide, allow us to perform a conceptual model of fluid flow in fold and thrust belts. In this model, whereas in thin-skinned thrust belts the fluid system is dominated by formation, marine and/or meteoric fluids migrating above detachment levels, thick-skinned thrust sheets allow the migration of hydrothermal fluids which produce thermal anomalies. In both situations, as these structures emerge, the influence of meteoric fluids increases progressively when the paleohydrological system opens.

Chapter 11

References

11. References

Allen, P.A., Allen, J.R., 2005. Basin Analysis: Principles and Applications. Blackwell Publishing, Malden, Massachusets.

Arnal, I., Calvet, F., Márquez, L., Márquez-Aliaga, A., Porta, N.S.d., 2002. The epeiric carbonate platform (Imón and Isábena Formations) of the Upper Triassic from the Northeastern Iberian Peninsula. Acta Geologica Hispanica 37, 299-328.

Aurell, M., Meléndez, G., Olóriz, F., 2002. Jurassic, in: Gibbons, W., Moreno, T. (Eds.), The Geology of Spain. The Geological Society of London, pp. 221-254.

Aydin, A., 2000. Fractures, faults, and hydrocarbon entrapment, migration and flow. Marine and Petroleum Geology 17, 797-814.

Banner, J.L., 1995. Application of the trace element and isotope geochemistry of strontium to studies of carbonate diagenesis. Sedimentology 42, 805-824.

Banner, J.L., Hanson, G.N., 1990. Calculation of simultaneous isotopic and trace element variations during water-rock interaction with applications to carbonate diagenesis. Geochimia et Cosmochimica Acta 54, 3123-3137.

Banks, D.A., Davies, G.R., Yardley, B.W.D., McCaig, A.M., Grant, N.T., 1991. The chemistry of brines from an Alpine thrust system in the Central Pyrenees: An application of fluid inclusion analysis to the study of fluid behavior in orogenesis. Geochimia et Cosmochimica Acta 55, 1021-1030.

Baqués, V., Travé, A., Benedicto, A., Labaume, P., Cantarero, I., 2010. Relationships between carbonate fault rocks and fluid flow regime during propagation of the Neogene extensional faults of the Penedès basin (Catalan Coastal Ranges, NE Spain). Journal of Geochemical Exploration 106, 24-33.

Baqués, V., Travé, A., Roca, E., Marín, M., Cantarero, I., 2012. Geofluid behaviour in successive extensional and compressional events: a case study from the southwestern end of the Vallès-Penedès Fault (Catalan Coastal Ranges, NE Spain). Petroleum Geoscience 18, 17-31.

Baqués, V., Travé, A., Cantarero, I., 2013. Development of successive karstic systems within the Baix Penedès Fault zone (onshore of the Valencia Trough, NW Mediterranean). Geofluids 14, 75-94.

Barrier, L., Proust, J.N., Nalpas, T., Robin, C., Guillocheau, F., 2010. Control of alluvial sedimentation at foreland basin active margins, case study from the north-eastern Ebro basin (south-eastern Pyrenees, Spain). Journal of Sedimentary Research 80, 728-749.

Bau, M., Dulski, P., 1994. Evolution of the yttrium-holmium systematics of seawater through time. Mineralogical Magazine 58, 61-62.

Bau, M., Dulski, P., 1996. Distribution of yttrium and rare-earth elements in the Penge and Kuruman iron-formations, Transvaal Supergroup, South Africa. Precambrian Research 79, 37-55.

Beamud, E., Muñoz, J.A., Fitzgerald, P.G., Baldwin, S.L., Garcés, M., Cabrera, L., Metcalf, J.R., 2010. Magnetostratigraphy and detrital apatite fission track thermochronology in syntectonic conglomerates: constraints on the exhumation of the South-Central Pyrenees. Basin Research 23, 309-331.

Beaudoin, N., Bellahsen, N., Lacombe, O., Emmanuel, L., 2011. Fracture-controlled paleohydrogeology in a basement-cored, fault-related fold: Sheep Mountain Anticline, Wyoming, United States. Geochemistry, Geophysics, Geosystems 12, 1-15.

Beaudoin, N., Lacombe, O., Bellahsen, N., Emmanuel, L., 2013. Contribution of Studies of Sub-Seismic Fracture Populations to Paleo-Hydrological Reconstructions (Bighorn Basin, USA). Procedia Earth and Planetary Science 7, 57-60.

Beaudoin, N., Bellahsen, N., Lacombe, O., Emmanuel, L., Pironon, J., 2014. Crustal-scale fluid flow during the tectonic evolution of the Bighorn Basin (Wyoming, USA). Basin Research 26, 403-435.

Beaudoin, N., Huyghe, D., Bellahsen, N., Lacombe, O., Emmanuel, L., Mouthereau, F., Ouanhnon, L., 2015. Fluid systems and fracture development during syn-depositional fold growth: An example from the Pico del Aguila anticline, Sierras Exteriores, southern Pyrenees, Spain. Journal of Structural Geology 70, 23-38.

Beaudoin, N., Lacombe, O., Roberts, N.M.W., Koehn, D., 2018. U-Pb dating of calcite veins reveals complex stress evolution and thrust sequence in the Bighorn Basin, Wyoming, USA. Geology 46, 1015-1018.

Benedicto, A., Plagnes, V., Vergély, P., Flotté, N., Schultz, R.A., 2008. Fault and fluid interaction in a rifted margin: integrated study of calcite-sealed fault-related structures (southern Corinth margin). Geological Society, London, Special Publications 299, 257-275.

Berástegui, X., García, J.M., Losantos, M., 1990. Structure and sedimentary evolution of the Organyà basin (Central South Pyrenean Unit, Spain) during the Lower Cretaceous. Bull. Soc. Géol. France 8, 251-254.

Bergman, S.C., Huntington, K.W., Crider, J.G., 2013. Tracing paleofluid sources using clumped isotope thermometry of diagenetic cements Along the Moab Fault, Utah. American Journal of Science 313, 490-515.

Bernasconi, S.M., Hu, B., Wacker, U., Fiebig, J., Breitenbach, S.F.M., Rutz, T., 2013. Background effects on Faraday collectors in gas-source mass spectrometry and implications for clumped isotope measurements. Rapid Communications in Mass Spectrometry 27, 603-612.

Bickle, M.J., Wickham, S.M., Chapman, H.J., Taylor, H.P., 1988. A strontium, neodynium and oxygen study of hydrothermal metamorphism and crustal anatexis in the Trois Seignerus Massif, Pyrenees, France. Contributions to Mineralogy and Petrology 100, 399-417.

Bitzer, K., Travé, A., Carmona, J.M., 2001. Fluid flow processes at basin scale. Acta Geologica Hispanica 36, 1-20.

Blenkinsop, T.G., 2008. Relationships between faults, extension fractures and veins, and stress. Journal of Structural Geology 30, 622-632.

Bons, P.D., Elburg, M.A., Gómez-Rivas, E., 2012. A review of the formation of tectonic veins and their microstructures. Journal of Structural Geology 43, 33-62.

Bons, P.D., Fusswinkel, T., Gómez-Rivas, E., Markl, G., Wagner, T., Walter, B., 2014. Fluid mixig from below in unconformity-related hydrothermal ore deposits. Geology 42, 1035-1038.

Booler, J., Tucker, M.E., 2002. Distribution and geometry of facies and early diagenesis: the key to accommodation space variation and sequence stratigraphy: Upper Cretaceous Congost Carbonate platform, Spanish Pyrenees. Sedimentary Geology 146, 225-247.

Boulvais, P., 2016. Fluid generation in the Boucheville Basin as a consequence of the North Pyrenean metamorphism. Comptes Rendus Geoscience 348, 301-311.

Boutoux, A., Verlaguet, A., Bellahsen, N., Lacombre, O., Villemant, B., Caron, B., Martin., E., Assayag, N., Cartigny, P., 2014. Fluid systems above basement shear zones during inversion of pre-orogenic sedimentary basins (External Crystalline Massifs, Western Alps). Lithos 206-207, 435-453.

Bowring, S.A., Grotzinger, J.P., Isachsen, C.E., Knoll, A.H., Pelechaty, S.M., Kolosov, P., 1993. Calibrating Rates of Early Cambrian Evolution. Science 261, 1293-1298.

Breesch, L., 2008. Diagenesis and fluid system evolution in the Northern Oman Mountains, United Arab Emirates. PhD thesis, Katholieke Universiteit Leuven, Leuven, Belgium, p. 159.

Bradbury, H.J., Woodwell, G.R., 1987. Ancient fluid flow within foreland terrains, in: Goff, J.C., Williams, B.P.J. (Eds.), Fluid flow in Sedimentary Basins and Aquifers. Geological Society Special Publication, pp. 87-102.

Breesch, L., Swennen, R., Vincent, B., 2009. Fluid flow reconstruction in hanging and footwall carbonates: Compartmentalization by Cenozoic reverse faulting in the Northern Oman Mountains (UAE). Marine and Petroleum Geology 26, 113-128.

Brinkmann, R.V., Lögters, H., 1968. Diapirs in Western Pyrenees and Foreland Spain. American Association of Petroleum Geologists Memory 8, 275-292.

Burbank, D.W., Puigdefàbregas, C., Muñoz, J.A., 1992a. The chronology of the Eocene tectonic and stratigraphic development of the Eastern Pyrenean Foreland Basin. NE Spain. Geol. Soc. America Bull. 104, 1101-1120.

Burbank, D.W., Vergés, J., Muñoz, J.A., Bentham, P., 1992b. Coeval hinward- and forward-imbricating thrusting in the south-central Pyrenees, Spain: Timing and rates of shortening and deposition. Geological Society of America Bulletin 104, 3-17.

Burisch, M., Gerdes, A., Walter, B.F., Neumann, U., Fettel, M., Markl, G., 2017. Methane and the origin of five-element veins: Mineralogy, age, fluid inclusion chemistry and ore forming processes in the Odenwald, SW Germany. Ore Geology Reviews 81, 42-61.

Caine, J.S., Minor, S.A., 2009. Structural and geochemical characteristics of faulted sediments and infewrences on the role of water in deformation, Rio Grande Rift, New Mexico. GSA Bulletin 121, 1325-1340.

Caja, M.A., Permanyer, A., 2008. Significance of organic matter in Eocene turbidite sediments (SE Pyrenees, Spain). Naturwissenschaften 9, 1073-1077.

Caja, M.A., Permanyer, A., Marfil, R., Al-Asm, I.S., Martín-Crespo, T., 2006a. Fluid flow record from fracture-fill calcite in the Eocene limestones from the South-Pyrenean Basin (NE Spain) and its relationship to oil shows. Journal of Geochemical Exploration 89, 27-32.

Caja, M.A., Permanyer, A., Marfil, R., Martín-Crespo, T., 2006b. Circulación de fluidos en fracturas en el miembro superior de la Fm. Armàncies (Eoceno, Pirineo oriental). Geogaceta 39, 103-106.

Caja, M.A., Permanyer, A., Munz, I.A., Johansen, H., 2007. Preliminary data on oil and aqueous fluid inclusions of the fracture-fill in the Corones and Armàncies Fms, Eocene, SE Pyrenees. Geogaceta 42, 127-129.

Calvet, F., Porta, N.S.d., Salvany, J.M., 1993. Cronoestratigrafía (Palinología) del Triásico Sudpirenaico y del Pirineo Vasco-Cantábrico. Acta Geologica Hispanica 28, 33-48.

Canérot, J., Hudec, M.R., Rockenbauch, K., 2005. Mesozoic diapirism in the Pyrenean orogen: Salt tectonics on a transform plate boundary. AAPG Bulletin 89, 211-229.

Cantarero, I., Lanari, P., Vidal, O., Alías, G., Travé, A., Baqués, V., 2013. Long-term fluid circulation in extensional faults in the central Catalan Coastal Ranges: P–T constraints from neoformed chlorite and K-white mica. International Journal of Earth Sciences 103, 165-188.

Cantarero, I., Travé, A., Alías, G., Baqués, V., 2014. Polyphasic hydrothermal and meteoric fluid regimes during the growth of a segmented fault involving crystalline and carbonate rocks (Barcelona Plain, NE Spain). Geofluids 14, 20-44.

Cantarero, I., Alías, G., Cruset, D., Carola, E., Lanari, P., Travé, A., 2018. Fluid composition changes in crystalline basement rocks from ductile to brittle regimes. Global and Planetary Change 171, 273-292.

Carrigan, J.H., Anastasio, D.J., Kodama, K.P., Parés, J.M., 2016. Fault-related fold kinematics recorded by terrestrial growth strata, Sant Llorenç de Morunys, Pyrenees Mountains, NE Spain. Journal of Structural Geology 91, 161-176.

Carrillo, E., 2012. The Evaporites of the Southeastern Pyrenean Basin (Late Cuisian – Lutetian): Sedimentology and Structure. PhD Thesis, University of Barcelona, Barcelona, Spain, p. 192.

Carrillo, E., Rosell, L., Ortí, F., 2014. Multiepisodic evaporite sedimentation as an indicator of palaeogeographical evolution in foreland basins (South-eastern Pyrenean basin, Early–Middle Eocene. Sedimentology 61, 2086-2112.

Carter, N.L., Kronenberg, A.K., Ross, J.V., Wiltschko, D.V., 1990. Control of fluids on deformation of rocks, in: Knipe, R.J., Rutter, E.H. (Eds.), Deformation Mechanisms, Rheology and Tectonics. Geological Society, London, Special Publications, pp. 1-13.

Casini, G., Gillespie, P.A., Vergés, J., Romaire, I., Fernández, N., Casciello, E., Saura, E., Mehl, C., Homke, S., Embry, J.-C., Aghajari, L., Hunt, D.W., 2011. Sub-seismic fractures in Foreland fold and Thrust belts: insight from the Lurestan Province, Zagros Mountains, Iran. Petroleum Geoscience 17, 263-282.

Cello, G., Invernizzi, C., Mazzoli, S., Tondi, E., 2001. Fault properties and fluid flow patterns from Quaternary faults in the Apennines, Italy. Tectonophysics 336, 63-78.

Cerling, T.E., Quade, J., Wang, Y., Bowman, J.R., 1989. Carbon isotopes in soils and palaeosols as ecology and palaeoecology indicators. Nature 341, 138-139.

Chandonais, D.R., Onasch, C.M., 2014. Fluid history of the Blue Ridge anticlinorium in the central Appalachians. Journal of Structural Geology 69, 415-427.

Chi, G., Xue, C., Qing, H., Xue, W., Zhang, J., Sun, Y., 2012. Hydrodynamic analysis of clastic injection and hydraulic fracturing structures in the Jinding Zn-Pb deposit, Yunnan, China. Geoscience Frontiers 3, 73-84.

Choukroune, P., team, E., 1989. The ECORS Pyrenean deep seismic profile reflection data and the overall structure of an orogenic belt. Tectonics 8, 23-39.

Chuhan, F., Kjeldstad, A., BjØrlykke, K., HØeg, K., 2002. Porosity loss in sand by grain crushing - experimental evidence and relevance to reservoir quality. Marine and Petroleum Geology 19, 39-53.

Clavell, E., 1992. Geologia del petroli de les conques terciàries de Catalunya. PhD thesis, University of Barcelona, p. 488.

Claypool, G.E., Kaplan, W.T., Kaplan, I.R., Sakai, H., Zak, I., 1980. The age curves of sulfur and oxygen isotopes in marine sulfate and their mutual interpretations. Chemical Geology 28, 199-260.

Clerc, C., Lagabrielle, Y., 2014. Thermal control on the modes of crustal thinning leading to mantle exhumation: Insights from the Cretaceous Pyrenean hot paleomargins. Tectonics 33, 1340-1359.

Clerc, C., Lagabrielle, Y., Labaume, P., Ringenbach, J.C., Vauchez, A., Nalpas, T., Bousquet, R., Ballard, J.F., Lahfid, A., Fourcade, S., 2016. Basement – Cover decoupling and progressive exhumation of metamorphic sediments at hot rifted margin. Insights from the Northeastern Pyrenean analog. Tectonophysics 686, 82-97.

Cobbold, P.R., Zanella, A., Rodrigues, N., Løseth, H., 2013. Bedding-parallel fibrous veins (beef and cone-in-cone): Worldwide occurrence and possible significance in terms of fluid overpressure, hydrocarbon generation and mineralization. Marine and Petroleum Geology 43, 1-20.

Coleman, A.J., Jackson, C.A.L., Duffy, O.B., Nikolinakou, M.A., 2018. How, where, and when do radial faults grow near salt diapirs? Geology 46, 655-658.

Conrad, R.E., Friedman, M., 1976. Microscopic feather fractures in the faulting process. Tectonophysics 33, 187-198.

Conti, S., Fontana, D., Mecozzi, S., Panieri, G., Pini, G.A., 2010. Late Miocene seep-carbonates and fluid migration on top of the Montepetra intrabasinal high (Northern Apennines, Italy): Relations with synsedimentary folding. Sedimentary Geology 231, 41-54.

Cooper, M., Warren, M.J., 2010. The geometric characteristics, genesis and petroleum significance of inversion structures, in: Law, R.D., Butler, R.W.H., Holdsworth, R.E., Krabbendam, M., Strachan, R.A. (Eds.), Continental Tectonics and Mountain Building: The Legacy of Peach and Horne. Geological Society, London, Special Publications, pp. 827-846.

Coplen, T.B., Hanshaw, B.B., 1973. Ultratitration by a compacted clay membrane-I. Oxygen and hydrogen isotopic fractionation. Geochimia et Cosmochimica Acta 37, 2295-2310.

Cosgrove, J.W., 2015. The association of folds and fractures and the link between folding, fracturing and fluid flow during the evolution of a fold–thrust belt: a brief review. Geological Society, London, Special Publications 421, SP421.411.

Costa, E., Garcés, M., López-Blanco, M., Beamud, E., Gómez-Paccard, M., Larrasoaña, J.C., 2010. Closing and continentalization of the South Pyrenean foreland basin (NE Spain): magnetochronological constraints. Basin Research 22, 904-917.

Craig, H., Gordon, I. I., 1965. Deuterium and oxygen-18 variations in the ocean and the marine atmosphere, in: Tongiorgi, E. (Ed.), Proceedings of a Conference on Stable Isotopes in Oceanographic Studies and Paleotemperatures. Consiglio Nazionale delle Richerche, Laboratorio di Geologia Nucleare, Pisa, Italy, pp. 9-130.

Crognier, N., 2016. Évolution thermique, circulation de fluides et fracturation associées à la structuration du bassin d'avant-pays sud-pyrénéen. PhD thesis, Universitéde Pau, Pau, France, p. 329.

Crognier, N., Hoareau, G., Lacroix, B., Aubourg, C., Dubois, M., Lahfid, A., Labaume, P., Suarez-Ruiz, I., 2015. Thermicity and fluid flow related to the evolution of the South Pyrenean Foreland Basin (SPFB), EGU General Assembly, Vienna, Austria

Crognier, N., Hoareau, G., Aubourg, C., Dubois, M., Lacroix, B., Branellec, M., Callot, J.P., Vennemann, T., 2017. Syn-orogenic fluid flow in the Jaca basin (south Pyrenean fold and thrust belt) from fracture and vein analyses. Basin Research, 1-30.

Cruset, D., Cantarero, I., Travé, A., Vergés, J., 2015. Evolución diagenética durante el crecimiento del anticlinal de Puig-reig (cinturón de pliegues y cabalgamientos surpirenaico). Geogaceta 58, 27-30.

Cruset, D., Cantarero, I., Travé, A., Vergés, J., John, C.M., 2016a. Crestal graben fluid evolution during growth of the Puig-reig anticline (South Pyrenean fold and thrust belt). Journal of Geodynamics 101, 30-50.

Cruset, D., Cantarero, I., Travé, A., Vergés, J., John, C.M., 2016b. Fluid migration during the Cadí thrust sheet emplacement (South Pyrenean fold and thrust belt), GEOFLUIDS VIII conference, Wuhan, Cgina. June 22-27, 2016.

Cruset, D., Cantarero, I., Vergés, J., Travé, A., 2017. Fluid rock relationships during the formation and inversion of an extensional basin (Upper Pedraforca thrust sheet, South Pyrenean fold and thrust belt), International Meeting of Sedimentology 2007. Toulouse, France, October 10-12, 2017.

Cruset, D., Cantarero, I., Vergés, J., John, C.M., Muñoz-López, D., Travé, A., 2018. Changes in fluid regime in syn-orogenic sediments during the growth of the south Pyrenean fold and thrust belt. Global and Planetary Change 171, 207-224.

Cruset, D., Vergés, J., Cantarero, I., Travé, A., 2019. From rock-buffered to open fluid system during emplacement of the Lower Pedraforca thrust sheet (South Pyrenees), in: Doronzo, D., Schingaro, E., Armstrong-Altrin, J., Zoheir, B. (Eds.), Petrogenesis and Exploration of the Earth's Interior. Proceedings of the 1st Springer Conference of the Arabian Journal of Geosciences (CAJG-1), Tunisia 2018, pp. pp 215-217.

Cruset, D., Vergés, J., Albert, R., Gerdes, A., Benedicto, A., Cantarero, I., Travé, A., in review. U-Pb Geochronology applied to fracture-filling calcite cements to decipher emplacement and reactivation of SE Pyrenean thrust sheets. Geology.

Cruset, D., Cantarero, I., Benedicto, A., John, C.M., Vergés, J., Travé, A., submitted. From hydroplastic to brittle deformation: controls on fluid flow in the Lower Pedraforca thrust sheet (southern Pyrenees). Marine and Petroleum Geology.

Cruset, D., Vergés, J., Benedicto, A., Gómez-Rivas, E., Cantarero, I., John, C.M., Travé, A., in preparation. Fluid flow evolution from the Mesozoic extension to the Alpine orogeny in the Upper Pedraforca thrust sheet (southern Pyrenees).

Dale, A., John, C.M., Mozley, P.S., Smalley, P.C., Muggeridge, A.H., 2014. Time-capsule concretions: Unlocking burial diagenetic processes in the Mancos Shale using carbonate clumped isotopes. Earth and Planetary Science Letters 394, 30-37.

David, C., Menendez, B., Bernabe, Y., 1998. The mechanical behavior of synthetic sandstone with varying brittle cement content. International Journal of Rock Mechanics and Mining Sciences and Geomechanics Abstracts 35, 759-770.

Davies, A.J., John, C.M., 2019. The clumped (13C18O) isotope composition of echinoid calcite: Further evidence for "vital effects" in the clumped isotope proxy. Geochimica et Cosmochimica Acta 245, 172-189.

Davison, I., Alsop, G.I., Evans, N.G., Safaricz, M., 2000. Overburden deformation patterns and mechanisms of salt diapir penetration in the Central Graben, North Sea. Marine and Petroleum Geology 17, 601-618.

De Felipe, I, Pereira, D., Pulgar, J.A., Iriarte, E., Mendia, M., 2017. Mantle exhumation and metamorphism in the Basque-Cantabrian Basin (N Spain): Stable and clumped isotope analysis in carbonates and comparison with ophicalcites in the North-Pyrenean Zone (Urdach and Lherz). Geochemistry, Geophysics, Geosystems 18, 631-652.

Delvaux, D., Sperner, B., 2003. New aspects of tectonic stress inversion with reference to the TENSOR program, in: Nieuwland, D.A. (Ed.), New Insights into Structural Interpretation and Modelling. Geological Society, London, Special Publications, pp. 75-100.

Dennis, K.J., Affeck, H.P., Passey, B.H., Schrag, D.P., Eiler, J.M., 2011. Defining an absolute reference frame for 'clumped' isotope studies of CO2. Geochimia et Cosmochimica Acta 75, 7117-7131.

Dewaele, D., Muchez, P., Banks, D.A., 2004. Fluid evolution along multistage composite fault systems at the southern margin of the Lower Palaeozoic Anglo-Brabant fold belt, Belgium. Geofluids 4, 341-356.

Dewever, B., 2008. Diagenesis and fluid flow in the Sicilian fold-and-thrust bellt. PhD thesis. Katholieke Universiteit Leuven, Leuven, Belgium, p. 183.

Dewever, B., Swennen, R., Breesch, L., 2013. Fluid flow compartmentalization in the Sicilian fold and thrust belt: Implications for the regional aqueous fluid flow and oil migration history. Tectonophysics 591, 194-209.

Diamond, L.W., 1994. Salinity of multivolatile fluid inclusions determined from clathrate hydrate stability. Geochimia et Cosmochimica Acta 58, 19-41.

Dimmen, V., Rotevatn, A., Peacock, D.C.P., Nixon, C.W., Naerland, K., 2017. Quantifying structural controls on fluid flow: Insights from carbonatehosted fault damage zones on the Maltese Islands. Journal of Structural Geology 101, 43-57.

Dromgoole, E.L., Walter, L.M., 1990. Iron and manganese incorporation into calcite: effects of growth kinetics, temperature, and solution chemistry. Chemical Geology 81, 311-336.

Egholm, D.L., Clausen, R.O., Sandiford, M., Kristensen, M.B., Korstgård, J.A., 2008. The mechanics of clay smearing along faults. Geology 36, 787-790.Evans, M.A., Bebeout, G.E., Brown, C.H., 2012. Changing fluid conditions during folding: An example from the central Appalachians. Tectonophysics 576-577, 99-115.

Eiler, J.M., 2007. "Clumped-isotope" geochemistry—The study of naturally-occurring, multiply-substituted isotopologues. Earth and Planetary Science Letters 262, 309-327.

Evans, M.A., Fischer, M.P., 2012. On the distribution of fluids in folds: A review of controlling factors and processes. Journal of Structural Geology 44, 2-24.

Evans, M.A., Bebeout, G.E., Brown, C.H., 2012. Changing fluid conditions during folding: An example from the central Appalachians. Tectonophysics 576-577, 99-115.

Fagereng, A., Harris, C., 2014. Interplay between flow and fault-fracture mesh generation within underthrust sediments: Geochemical evidence from the Chrystalls Beach Complex, New Zealand. Tectonophysics 612-613-147-157.

Fein, J.B., Walther, J.V., 1987. Calcite solubility in supercritical CO2-H2O fluids. Geochimia et Cosmochimica Acta 51, 1665-1673.

Ferket, H., Swennen, R., Arzate, S.O., Roure, F., 2006. Fluid flow evolution in petroleum reservoirs with a complex diagenetic history: An example from Veracruz, Mexico. Journal of Geochemical Exploration 89, 108-111.

Fillon, C., Van der Beek, 2012. Post-orogenic evolution of the southern Pyrenees: constraints from inverse thermo-kinematic modelling of low-temperature thermochronology data. Basin Research 23, 1-19.

Fischer, M.P., Higuera-Díaz, I.C., Evans, M.A., Perry, E.C., Lefticariu, L., 2009. Fracture-controlled paleohydrology in a map-scale detachment fold: Insights from the analysis of fluid inclusions in calcite and quartz veins. Journal of Structural Geology 31, 1490-1510.

Fischer, M.P., Kenroy, P.R., Smith, A.P., 2013. Fluid Systems around Salt Diapirs, AAPG Annual Convention and Exhibition, Pittsburgh, Pennsylvania, May 19-22, 2013.

Fitz-Diaz, E., Hudleston, P., Siebenaller, L., Kirschner, D., Camprubí, A., Tolson, G., Puig, T.P., 2011. Insights into fluid flow and water-rock interaction during deformation of carbonate sequences in the Mexican fold-thrust belt. Journal of Structural Geology 33, 1237-1253.

Fitz-Diaz, E., Hudleston, P., Tolson, G., Van der Pluijm, B., 2014. Progressive, episodic deformation in the Mexican Fold–Thrust Belt (central Mexico): evidence from isotopic dating of folds and faults. International Geology Reviewa 56, 734-755.

Flotté, N., Plagnes, V., Sorel, D., Benedicto, A., 2001. Attempt to date Pleistocene normal faults of the CorinthPatras Rift (Greece) by U/Th method, and tectonic implications. Geophysical Research Letters 28, 3769-3772.

Fontana, S., Nader, F.H., Morad, S., Ceriani, A., Al-Aasm, I.S., Daniel, J.-M., Mengus, J.-M., 2014. Fluid–rock interactions associated with regional tectonics and basin evolution. Sedimentology 61, 660-690.

Ford, M., Williams, E.A., Artoni, A., Vergés, J., Hardy, S., 1997. Progressive evolution of a fault-related fold pair from growth strata geometries, Sant Llorenç de Morunys, SE Pyrenees. Journal of Structural Geology 19, 413-441.

Frazer, M., Whitaker, F., Hollis, C., 2014. Fluid expulsion from overpressured basins: Implications for PbeZn mineralisation and dolomitisation of the East Midlands platform, northern England. Marine and Petroleum Geology 55, 68-86.

Friedman, M., Logan, J.M., 1977. Microscopic feather fractures Bull. Soc. Am. 81, 3417-3420.

Friedman, I., O'Neil, J.R., 1977. Compilation of stable isotope fractionation factors of geochemical interest, in: Fleischer, M. (Ed.), Data of Geochemistry, U. S. Gov. Print. Off. Washington D. C., pp. 1-12.

Froelich, P.N., Klinkhammer, G.P., Bender, M.L., Luedtke, N.A., Heath, G.R., Cullen, D., Dauphin, P., Hammond, D., Hartman, B., Maynard, V., 1979. Early oxidation of organic matter in pelagic sediments of the eastern equatorial Atlantic: suboxic diagenesis. Geochimia et Cosmochimica Acta 43, 1075-1090.García-Senz, 2002. Cuencas extensivas del Cretácico Inferior en los Pirineos centrales. Formación y subsecuente inversión, PhD thesis, Universitat de Barcelona, Spain, p. 310.

García-Castellanos, D., Vergés, J., Gaspar-Escribano, J., Cloetingh, S., 2003. Interplay between tectonics, climate, and fluvial transport during the Cenozoic evolution of the Ebro Basin (NE Iberia). Journal of Geophysical Research 108, (B7), 2347.

Garrido-Mejías, A., 1973. Estudio geológico y relación entre tectónica y sedimentación del Secundario y Terciario de la vertiente meridional pirenaica en su zona central (prov. de Huesca y Lérida). PhD thesis. Sciences Faculty of Granada, p. 395.

Gasparrini, M., Ruggieri, G., Brogi, A., 2013. Diagenesis versus hydrothermalism and fluid–rock interaction within the Tuscan Nappe of the Monte Amiata CO2-rich geothermal area (Italy). Geofluids 13, 159-179.

Gasparrini, M., López-Cilla, I., Blázquez-Fernandez, S., Rosales, I., Lerat, O., Martín-Chivelet, J., Doligez, B., 2017. A multidisciplinary modeling approach to assess facies-dolomitization-porosity interdependence in a Lower Cretaceous platform (northern Spain), in: Macneil, A.J., Lonnee, J., Wood, R. (Eds.), Characterization and Modeling of Carbonates–Mountjoy Symposium 1. SEPM (Society for Sedimentary Geology), p. 0.

Ge, S., Garven, G., 1989. Tectonically Induced Transient Groundwater Flow in Foreland Basin, in: Price, R.A. (Ed.), Origin and Evolution of Sedimentary Basins and Their Energy and Mineral Resources. American Geophysical Union, pp. 145-157.

Gerdes, A., Zeh, A., 2006. Combined U–Pb and Hf isotope LA-(MC-)ICP-MS analyses of detrital zircons: Comparison with SHRIMP and new constraints for the provenance and age of an Armorican metasediment in Central Germany. Earth and Planetary Science Letters 249, 47-61.

Gerdes, A., Zeh, A., 2009. Zircon formation versus zircon alteration – New insights from combined U-Pb and Lu-Hf in-situ La-ICP-MS analyses of Archean zircons from the Limpopo Belt. Chemical Geology 261, 230-243.

Ghosh, P., Adkins, J., Affek, H., Balta, B., Guo, W., Schauble, E.A., Schrag, D., Eiler, J.M., 2006. 13C–18O bonds in carbonate minerals: A new kind of paleothermometer. Geochimia et Cosmochimica Acta 70, 1439-1456.

Giménez-Monsant, J., 1993. Análisis de cuenca del Eoceno inferior de la unidad Cadí (Pirineo oriental). El sistema deltaico y de plataforma carbonática de la Formación Corones. PhD thesis, Universitat de Barcelona, Barcelona, Spain, p. 355.

Giménez-Montsant, J., Calvet, F., Tucker, M.E., 1999. Silica diagenesis in Eocene shallow-water platform carbonates, southern Pyrenees. Sedimentology 46, 969-984.

Goldstein, R.H., Reynolds, T.J., 1994. Sysematics of fluid inclusions in diagenetic minerals. SEPM Short Course Notes.

Gomez-Rivas, E., Corbella, M., Martín-Martín, J.D., Stafford, S.L., Teixell, A., Bons, P.D., Griera, A., Cardellach, E., 2014. Reactivity of dolomitizing fluids and Mg source evaluation of fault-controlled dolomitization at the Benicàssim outcrop analogue (Maestrat basin, E Spain). Marine and Petroleum Geology 55, 26-42.

Goffey, G.P., Craig, J., Needham, T., Scott, R., 2010. Fold–thrust belts: overlooked provinces or justifiably avoided?, in: Goffey, G.P., Craig, J., Needham, T., Scoot, R. (Eds.), Hydrocarbons in Contractional Belts. Geological Society, London, Special Publications, pp. 1-6.

Grant, N.T., Banks, D.A., McCaig, A.M., Yardley, B.W.D., 1990. Chemistry, Source, and Behavior of Fluids Involved in Alpine Thrusting of the Central Pyrenees. Journal of Geophysical Research 95, 9123-9131.

Guo, W., Mosenfelder, J.L., Goddard, W.A., Eiler, J.M., 2009. Isotopic fractionations associated with phosphoric acid digestion of carbonate minerals: Insights from first-principles theoretical modeling and clumped isotope measurements. Geochimia et Cosmochimica Acta 73, 7203-7225.

Gutmanis, J., Oró, L.A.i., Díez-Canseco, D., Chebbihi, L., Awdal, A., Cook, A., 2017. Fracture analysis of outcrop analogues to support modelling of the subseismic domain in carbonate reservoirs, south-central Pyrenees, in: Ashton, M., Dee, S.J., Wennberg, O.P. (Eds.), Subseismic-Scale Reservoir Deformation. Geological Society, London, Special Publications, pp. 139-156.Haines, S.H., 2008. Transformations in Clay-Rich Fault Rocks: Constraining Fault Zone Processes and the Kinematic Evolution of Regions. PhD thesis. University of Michigan, Ann Arbor, U.S. , p. 295.

Hansberry, R.L., Collins, A.S., King, R.C., Morley, C.K., Gize, A.P., Warren, J., Löhr, S.C., Hall, P.A., 2015. Syn-deformation temperature and fossil fluid pathways along an exhumed detachment zone, khao khwang fold-thrust belt, Thailand. Tectonophysics 655, 73-87.

Hanshaw, B.B., Coplen, T.B., 1973. Ultrafiltration by a compacted clay membrane II - Sodium ion exclusion at various ionic strengths Geochimia et Cosmochimica Acta 37, 2311-2327.

Hansman, R.J., Albert, R., Gerdes, A., Ring, U., 2018. Absolute ages of multiple generations of brittle structures by U-Pb dating of calcite. Geology 46, 207-210.

Hausegger, S., Kurz, W., Rabitsch, R., Kiechl, E., Brosch, F.-J., 2010. Analysis of the internal structure of a carbonate damage zone: Implications for the mechanisms of fault breccia formation and fluid flow. Journal of Structural Geology 32, 1349-1362.

Henderson, I.H.C., McCaig, A.M., 1996. Fluid pressure and salinity variations in shear zone-related veins, central Pyrenees, France: Implications for the fault-valve model Tectonophysics 262, 321-348.

Heydari, E., 1997. Hydrotectonic models of burial diagenesis in platform carbonates based on formation water geochemistry in North American sedimentary basins, in: Montañez, I.P., Gregg, J.M., Shelton, K.L. (Eds.), Basin-wide diagenetic patterns: integrated petrologic, geochemical, and hydrologic considerations. Society of Economic Paleontologists and Mineralogists, Special Publication 57, pp. 53-79.

Hoareau, G., Odonne, F., García, D., Debroas, D.J., Monnin, C., Dubois, M., Potdevin, J.L., 2015. Burial diagenesis of the Sobrarbe delta (Ainsa Basin, Spain) inferred from dolomitic concretions. Journal of Sedimentary Research 85, 1037-1057.

Howson, M.R., Pethybridge, A.D., House, W.A., 1987. Synthesis and distribution coefficients of low-magnesium calcites. Chemical Geology 64, 79-87.

Hudec, M.R., Norton, I.O., Jackson, M.P.A., Peel, F.J., 2013. Jurassic evolution of the Gulf of Mexico salt basin. AAPG Bulletin 97, 1683-1710.

Huntington, K.W., Eiler, J.M., Affek, H.P., Guo, W., Boniface, M., Yeung, L.Y., Thiagarajan, N., Passey, B., Tripati, A., Daëron, M., Came, R., 2009. Methods and limitations of 'clumped' CO2 isotope (Δ47) analysis by gas-source isotope ratio mass spectrometry. Journal of Mass Spectrometry 44, 1318-1329.

Husson, L., Moretti, I., 2002. Thermal regime of fold and thrust belts: an application to the Bolivian sub Andean zone. Tectonophysics 345, 253-280.

Immenhauser, A., Dublyansky, Y.V., Verwer, K., Fleitman, D., Pashenko, S.E., 2007. Textural, elemental and isotopic characteristics of Pleistocene phreatic cave deposits (Jabal Madar, Oman). Journal of Sedimentary Research 77, 68-88.

Irwin, H., Curtis, C., Coleman, M., 1977. Isotopic evidence for source of diagenetic carbonates formed during burial of organic-rich sediments. Nature 269, 209-213.

Jackson, M.P.A., Cornelius, R., Craig, C.H., Gansser, A., Stöcklin, J., Talbot, C.J., 1990. Salt Diapirs of the Great Kavir, Central Iran, Memoir. The Geological Society of America.

Jamtveit, B., Austrheim, H., 2010. Metamorphism: The Role of Fluids. Elements 6, 153-158.

John, C.M., Bowen, D., 2016. Community software for challenging isotope analysis: First applications of "Easotope" to clumped isotopes. Rapid Communications in Mass Spectrometry 30, 2285-2300.

Katz, A., 1973. The interaction of magnesium with calcite during crystal growth at 25-90ºC and one atmosphere. Geochimia et Cosmochimica Acta 39, 486-508.

Kendall, J., Vergés, J., Koshnaw, R., Louterbach, M., 2019. Petroleum Tectonic comparison of fold-thrust belts: the Sevier of the western US, the Pyrenees of Spain, the Zagros of Iraq and Iran, and the Beni Sub Andean of Bolivia. Geological Society, London, Special Publications 490, SP490-2018-2102.

Khosravi, M., Rostami, B., Fatemi, S., 2012. Uncertainty Analysis of a Fractured Reservoir's Performance: A Case Study. Oil & Gas Science and Technology 67, 423-433.

Kim, S.T., O'Neil, J.R., 1997. Equilibrium and nonequilibrium oxygen isotope effects in synthetic carbonates. Geochimia et Cosmochimica Acta 61, 3461-3475.

Kinsman, D.J.J., 1969. Interpretation of Sr2+ concentrations in carbonate minerals and rocks. Journal of sedimentary Petrology 39, 486-508.

Kirschner, D.L., Masson, H., Sharp, Z.D., 1999. Fluid migration through thrust faults in the Helvetic nappes (Western Swiss Alps). Contributions to Mineralogy and Petrology 136, 169-183.

Kluge, T., John, C.M., Jourdan, A.L., Davis, S., Crawshaw, J., 2015. Laboratory calibration of the calcium carbonate clumped isotope thermometer in the 25-250 ºC temperature range. Geochimia et Cosmochimica Acta 157, 213-227.

Knipe, R.J., McCaig, A.M., 1994. Microstructural and microchemical consequences of fluid flow in deforming rocks, in: Parnell, J. (Ed.), Geofluids: Origin, Migration and Evolution of Fluids in Sedimentary Basins. Geological Society, London, Special Publications, pp. 99-112.

Kolker, A., Chou, C.L., 1994. Cleat-Filling Calcite in Illinois Basin Coals: Trace-Element Evidence for Meteoric Fluid Migration in a Coal Basin. The Journal of Geology 102.

Labaume, P., Berty, C., Laurent, P., 1991. Syn-digenetic evolution of shear structures in superficial nappes: an example from the Northern Apennines (NW Italy). Journal of Structural Geology 13, 385-398.

Labaume, P., Moretti, I., 2001. Diagenesis-dependence of cataclastic thrust fault zone sealing in sandstones. Example from the Bolivian Sub-Andean Zone. Journal of Structural Geology 23, 1659-1675.

Labaume, P., Meresse, F., Joliver, M., Teixell, A., Lahfid, A., 2016. Tectonothermal history of an exhumed thrust-sheet-top basin: An example from the south Pyrenean thrust belt. Tectonics 35, 1280-1313.

Lacombe, O., Swennen, R., Caracausi, A., 2014. Fluid–rock–tectonics interactions in basins and orogens. Marine and Petroleum Geology 55, p. 332.

Lacroix, B., Buatier, M., Labaume, P., Travé, A., Dubois, M., Charpentier, D., Ventalon, S., Convert-Gaubier, D., 2011. Microtectonic and geochemical characterization of thrusting in a foreland basin: Example of the South-Pyrenean orogenic wedge (Spain). Journal of Structural Geology 33, 1359-1377.

Lacroix, B., Leclère, H., Buatier, M., Fabbri, O., 2013. Weakening processes in thrust faults: insights from the Monte Perdido thrust fault (southern Pyrenees, Spain). Geofluids 13, 56-65.

Lacroix, B., Travé, A., Buatier, M., Labaume, P., Vennemann, T., Dubois, M., 2014. Syntectonic fluid-flow along thrust faults: Example of the South-Pyrenean fold-and-thrust belt. Marine and Petroleum Geology 49, 84-98.

Lacroix, B., Baumgartner, L.P., Bouvier, A.S., Kempton, P.D., Vennemann, T., 2018. Multi fluid-flow record during episodic mode I opening: Amicrostructural and SIMS study (Cotiella Thrust Fault, Pyrenees). Earth and Planetary Science Letters 503, 37-46.

Lagabrielle, Y., Labaume, P., Blanquant, M.d.S., 2010. Mantle exhumation, crustal denudation, and gravity tectonics during Cretaceous rifting in the Pyrenean realm (SW Europe): Insights from the geological setting of the lherzolite bodies. Tectonics 29, TC4012.

Laubach, S.E., Olson, J.E., Gross, M.R., 2009. Mechanical and fracture stratigraphy. AAPG Bulletin 93, 1413-1426.

Lee, Y.J., Morse, J.W., Wiltschko, D.V., 1996. An experimentally verified model for calcite precipitation in veins. Chemical Geology 130, 203-215.

Lefticariu, L., Perry, E.C., Fischer, M.P., Banner, J.L., 2005. Evolution of fluid compartmentalization in a detachment fold complex. Geology 33, 69-72.

Letouzey, J., Werner, P., Marty, A., 1990. Fault reactivation and structural inversion. Backarc and intraplate compressive deformations. Example of the eastern Sunda shelf (Indonesia). Tectonophysics 183, 341-362.

Lewis, C.J., Vergés, J., Marzo, M., Heller, P.L., 1996. Youthful topography indicating active surface uplift in NE Iberia: Mantle upwelling along a leakly transform fault? Annales Geophysicae Suplement I, 14, C-204.

Lewis, C.J., Vergés, J., Marzo, M., 2000. High mountains in a zone of extended crust: Insights into Neogene-Quaternary topographic development of northeastern Iberia. Tectonics 19, 86-102.

Li, R., Dong, S., Lehrmann, D., Duan, L., 2013. Tectonically driven organic fluid migration in the Dabashan Foreland Belt: Evidenced by geochemistry and geothermometry of vein-filling fibrous calcite with organic inclusions. Journal of Asian Earth Sciences 75, 202-212.

Ligi, M., Bonatti, E., Cuffaro, M., Brunelli, D., 2013. Post-Mesozoic Rapid Increase of Seawater Mg/Ca due to Enhanced Mantle-Seawater Interaction. Scientific Reports 3, 2752.

Lipsey, L., Pluymaekers, M., Goldberg, T., Oversteeg, K.v., Ghazaryan, L., Cloetingh, S., Van der Wees, J., 2016. Numerical modelling of thermal convection in the Luttelgeest carbonate platform, the Netherlands. Geothermics 64, 135-151.

López-Martínez, N., Fernández-Marrón, M.T., Valle, M.F., 1999. The succession of vertebrates and plants across the Cretaceous-Tertiary boundary in the Tremp Formation, Ager valley (south-central Pyrenees, Spain). Geobios 32, 617-627.

Lopez-Mir, B., Muñoz, J.A., García-Senz, J., 2014. Restoration of basins driven by extension and salt tectonics: Example from the Cotiella Basin in the central Pyrenees. Journal of Structural Geology 69, 147-162.

Lorens, R., 1981. Sr, Cd, Mn and Co distribution coefficients in calcite as a function of calcite precipitation rate. Geochimia et Cosmochimica Acta 45, 553-561.

Losh, S., 1989. Fluid-rock interaction in an evolving ductile shear zone and across the brittle-ductile transition, central Pyrenees, France. American Journal of Science 289, 601-648.

Loveless, S., Bense, V., Turner, J., 2011. Fault architecture and deformation processes within poorly lithified rift sediments, Central Greece. Journal of Structural Geology 33, 1554-1568.

Lu, Y.C., Song, S.R., Wang, P.L., Wu, C.C., Mii, H.S., MacDonald, J., Shen, C.C., John, C.M., 2017. Magmatic-like fluid source of the Chingshui geothermal field, NE Taiwan evidenced by carbonate clumped-isotope paleothermometry. Journal of Asian Earth Sciences 149, 124-133.

Ludwig, K.R., 2009. Isoplot/Ex Ver 3.71: A geochronological toolkit for Microsoft Excel: Berkeley Geochronology Center Special Publications.

Lyubetskaya, T., Ague, J.J., 2009. Modeling the Magnitudes and Directions of Regional Metamorphic Fluid Flow in Collisional Orogens. Journal of Petrology 50, 1505-1531.

Macchiavelli, C., Vergés, J., Schettino, A., Fernàndez, M., Turco, E., Casciello, E., Torné, M., Pierantoni, P.P., Tunini, L., 2017. A new southern North Atlantic isochron map: Insights into the drift of the Iberian plate since the Late Cretaceous. Journal of Geophysical Research: Solid Earth 122, 9603-9626.

Machel, H.G., Cavell, P.A., 1999. Low-flux, tectonically-induced sequeegee fluid flow ("hot flash") into the Rocky Mountain Foreland Basin. Bulletin of Canadian Petroleum Geology 47, 510-533.

Maher, H.D., Ogata, K., Braathen, A., 2017. Cone-in-cone and beef mineralization associated with Triassic growth basin faulting and shallow shale diagenesis, Edgeøya, Svalbard. Geological Magazine 154, 201-216.

Mackay, P.A., 2015. The role of fluid pressure in contractional systems: examples from the Southern Canadian Rocky Mountains, in: Richards, F.L., Richardson, N.J., Rippington, S.J., Wilson, R.W., Bond, C.E. (Eds.), Industrial Sructural Geology: Principles, Techniques and Integration. Geological Society, London, Special Publications.

Mansurbeg, H., Caja, M.A., Marfil, R., Morad, S., Remacha, E., García, D., Martín-Crespo, T., El-Ghali, M.A.K., Nystuen, J.P., 2009. Diagenetic Evolution and porosity destruction of turbiditic hybrid arenites and siliciclastic sandstones of foreland basins: Evidence from the Eocene Hecho Group, Pyrenees, Spain. Journal of Sedimentary Research 79, 711-735.

Marker, D., Burkhard, M., 1992. Fluid circulation, progressive deformation and mass-transfer processes in the upper crust: the example of basement-cover relationships in the External Crystalline Massifs, Switzerland. Journal of Structural Geology 14 (8-9), 1047-1057.

Marret, R., Allmendinger, R.W., 1990. Kinematic analysis of fault-slip data. Journal of Structural Geology 12, 973-986.

Marshall, J.D., 1992. Climatic and oceanographic isotopic signals from the carbonate rock record and their preservation. Geological Magazine 129, 143-160.

Martín-Chivelet, J., 2002. Cretaceous, in: Gibbons, W., Moreno, T. (Eds.), The Geology of Spain. The Geological Society of London, pp. 264-292.

Martín-Martín, J.D., Vergés, J., Saura, E., Moragas, M., Messager, G., Vaqués, V., Razin, P., Grélaud, C., Malaval, M., Joussiaume, R., Casciello, E., Cruz-Orosa, I., Hunt, D.W., 2016. Diapiric growth within an Early Jurassic rift basin: the Tazoult salt wall (Central High Atlas, Morocco): Diapiric growth of the Tazoult salt wall. Tectonics 36, 2-32.

Martínez, A., Berástegui, X., Losantos, M., Schöllhorn, E., 2001. Estructura de los mantos superior e inferior del Pedraforca (Pirineos orientales). Geogaceta 30, 183-186.

Mató, E., Saula, E., Martínez-Rius, A., Muñoz, J.A., Escuer, J., 1994. Memoria de la Hoja nº 293 (Berga). Mapa Geológico de España E. 1:50.000 (MAGNA), Segunda Serie, Primera Edición. IGME, 66.

McCaig, A.M., 1988. Deep fluid circulation in fault zones. Geology 16, 867-870.

McArthur, J.M., Howarth, R.J., Bailey, T.R., 2001. Strontium Isotope Stratigraphy: LOWESS Version 3: Best Fit to the Marine Sr-Isotope Curve for 0–509 Ma and Accompanying Look-up Table for Deriving Numerical Age. Journal of Geology 109, 155-170.

McCaig, A.M., Wayne, D.M., Marshall, J.D., Banks, D., Henderson, I., 1995. Isotopic and fluid inclusion studies of fluid movement along the Gavarnie Thrust, central Pyrenees: Reaction fronts in carbonate mylonites. American Journal of Science 295, 309-343.

McCaig, A.M., Tritlla, J., Banks, D.A., 2000a. Fluid flow patterns during Pyrenean thrusting. Journal of Geochemical Exploration 69-70, 539-543.

McCaig, A.M., Tritlla, J., Banks, D.A., 2000b. Fluid mixing and recycling during Pyrenean thrusting: evidence from fluid inclusion halogen ratios. Geochimia et Cosmochimica Acta 64, 3395-3412.

McClay, K., Muñoz, J.A., García-Senz, J., 2004. Extensional salt tectonics in a contractional orogen: A newly identified tectonic event in the Spanish Pyrenees. Geology 32, 737-740.

McCrea, J.M., 1950. On the Isotopic Chemistry of Carbonates and a Paleotemperature Scale. Journal of Chemical Physics 18, 849-957.

McIntire, W.L., 1963. Trace element partition coefficients, a review of theory and applications to geology. Geochimia et Cosmochimica Acta 27, 1209-1264.

McLennan, S., 1989. Rare earth elements in sedimentary rocks; influence of provenance and sedimentary processes. Reviews in Mineralogy and Geochemistry 21, 277-290.

Meckler, A.N., Ziegler, M., Millán, M.I., Breitenbach, S.F., Bernasconi, S.M., 2014. Long-term performance of the Kiel carbonate device with a new correction scheme for clumped isotope measurements. Rapid Communications in Mass Spectrometry 28, 1705-1715.

Meigs, A.J., Vergés, J., Burbank, D.W., 1996. Ten-million-year history of a thrust sheet. GSA Bulletin 108, 1608-1625.

Mencos, J., Carrera, N., Muñoz, J.A., 2015 Influence of rift basin geometry on the subsequent postrift sedimentation and basin inversion: The Organyà Basin and the Bóixols thrust sheet (south central Pyrenees). Tectonics 34, 1452-1474.

Mey, P.H.W., Nagtegaal, P.J.C., Roberti, K.J., Hartevelt, J.J.A., 1968. Lithostratigraphic subdivision of post-Hercinian deposits in the south-central Pyrenees, Spain. Leidse Geologische Mededelingen 41, 21-228.

Meyers, W.J., Lohmann, K.C., 1985. Isotope geochemistry of regionally extensive calcite cement zones and marine components in Mississipian limestones, New Mexico, in: Harris, O.M., Schneidermann, N. (Eds.), Carbonate Cements SEPM, Special Publications, pp. 223-239.

Missenard, Y., Bertrand, A., Vergély, P., Benedicto, A., Cushing, M.-E., Rocher, M., 2014. Fracture-fluid relationships: implications for the sealing capacity of clay layers – Insights from field study of the Blue Clay formation, Maltese islands. Bulletin de la Société Géologique de France 185, 51-63.

Moeri, E.V., 1977. Oberkretazischen shelfsedimente in den zentralpyrenäen zwischen Rio Segre und Llobregat. Eclogae Geologicae Helvetiae 70, 193-235.

Moretti, I., Labaume, P., Sheppard, S., Boulègue, J., 2000. Compartmentalisation of fluid flow by thrust faults, Sub-Andean Zone, Bolivia. Journal of Geochemical Exploration 69-70, 493-497.

Morley, C.K., Warren, J., Tingay, M., Boonyasaknanon, P., Julapour, A., 2014. Comparison of modern fluid distribution, pressure and flow in sediments associated with anticlines growing in deepwater (Brunei) and continental environments (Iran). Marine and Petroleum Geology 51, 210-229.

Morrow, D.W., 1998. Regional Subsurface dolomitization: models and constraints. Geoscience Canada 25, 57-70.

Moya, S., Ramos-Guerrero, E., Agustí, J., Checa, L., 1991. Depositos lacustre-palustres asociados a las zonas intermedias de la Fm. Bellmunt (Prepirineo catalán). I Congreso del Grupo Español del Terciatrio. Comunicaciones, 225-228.

Mucci, A., Morse, J.W., 1983. The incorporation of Mg2+ and Sr2+ into calcite overgrowths: Influences of growth rate and solution composition. Geochimia et Cosmochimica Acta 47, 217-233.

Munoz, M., Baron, S., Boucher, A., Béziat, D., Salvi, S., 2016. Mesozoic vein-type Pb–Zn mineralization in the Pyrenees: Lead isotopic and fluid inclusion evidence from the Les Argentières and Lacore deposits. Comptes Rendus Geoscience 348, 322-332.

Muñoz, J.A., 1988. Estructura de las unidades surpirenaicas en la transversal del corte ECORS, in: Muñoz, J.A. (Ed.), Guía de campo, Reunión extraodinaria Ecors-Pirineos, p. 35.

Muñoz, J.A., 1992. Evolution of a continental collision belt: ECORS–Pyrenees crustal balanced section, in: McClay, K.R. (Ed.), Thrust Tectonics. Chapman & Hall, London, pp. 235-246.

Muñoz, J.A., 2002. The Pyrenees, in: Gibbons, W., Moreno, T. (Eds.), The Geology of Spain. Geological Society, London, pp. 370-385.

Muñoz, J.A., Martínez, A., Vergés, J., 1986. Thrust sequences in the eastern Spanish Pyrenees. Journal of Structural Geology 8, 399-405.

Nadal, J., 2001. Estudi de la dolomitització del Juràssic Superior-Cretaci inferior de la Cadena Ibèrica oriental i la Cadena Costanera Catalana: Relació amb la segona etapa de rift mesozoica, PhD Thesis, Universitat de Barcelona, Barcelona, Spain, p. 443pp.

Nardini, N., Muñoz-López, D., Cruset, D., Cantarero, I., Martín-Martín, J.D., Benedicto, A., Gómez-Rivas, E., John, C.M., Travé, A., 2019. From early contraction to post-folding fluid evolution in the frontal part of the Bóixols thrust sheet (southern Pyrenees) as revealed by the texture and geochemistry of calcite cements. Minerals 9, 117.

Oberhänsli, H., Allen, P.A., 1987. Stable isotopic signatures of tertiary lake carbonates, eastern Ebro Basin, Spain. Palaeogeography, Palaeoclimatology, Palaeoecology 60, 59-75.

Ogata, K., Senger, K., Braathen, A., Tveranger, J., 2014. Fracture corridors as seal-bypass systems in siliciclastic reservoir-cap rock successions: Field-based insights from the Jurassic Entrada Formation (SE Utah, USA). Journal of Structural Geology 66, 162-187.

Oliver, J., 1986. Fluids expelled tectonically from orogenic belts: their role in hydrocarbon migration and other geologic phenomena. Geology 14, 99-102.

Oms, O., Dinarés-Turell, J., Vicens, E., Estrada, R., Vila, B., Galobart, À., Bravo, A.M., 2007. Integrated stratigraphy from the Vallcebre Basin (southeastern Pyrenees, Spain): New insights on the continental Cretaceous−Tertiary transition in southwest Europe. Palaeogeography, Palaeoclimatology, Palaeoecology 255, 35-47.

Pagel, M., Bonifacie, M., Schneider, D.A., Gautheron, C., Brigaud, B., Calmels, D., Cros, A., Saint-Bezar, B., Landrein, P., Sutcliffe, C., Davis, D., Chaduteau, C., 2018. Improving paleohydrological and diagenetic reconstructions in calcite veins and breccia of a sedimentary basin by combining Δ47 temperature, δ18Owater and U-Pb age. Chemical Geology 481, 1-17.

Parrish, R.R., Parrish, C.M., Lasalle, S., 2018. Vein calcite dating reveals Pyrenean orogen as cause of Paleogene deformation in southern England. Journal of the Geological Society 175, 425-442.

Passchier, C.W., Trouw, R.A.J., 2005. Microtectonics, 2 ed. Springer Berlin Heidelberg.

Permanyer, A., Martín-Martín, J.D., Kihle, J., Márquez, G., Marfil, R., 2017. Oil shows geochemistry and fluid inclusion thermometry of Mid Cretaceous carbonates from the eastern Basque Cantabrian Basin (N Spain). Marine and Petroleum Geology 92, 255-269.

Perona, J., Canals, A., Cardellach, E., 2018. Zn-Pb Mineralization Associated with Salt Diapirs in the Basque-Cantabrian Basin, Northern Spain: Geology, Geochemistry, and Genetic Model Economic Geology 113, 1133-1159.

Person, M., Raffensperger, J.P., Ge, S., Garven, G., 1996. Basin-scale hydrogeologic modeling. Reviews of Geophysics 34, 61-87.

Petit, J.P., Beauchamp, J., 1986. Synsedimentary faulting and palaeocurrent patterns in the Triassic sandstones of the High Atlas (Morocco). Sedimentology 33, 817-829.

Petit, J.P., Laville, E., 1987. Morphology and microstructures of hydroplastic slickensides in sandstone. Geological Society, London, Special Publications 29, 107-121.

Petracchini, L., Antonellini, M., Billi, A., Scrocca, D., 2012. Fault development through fractured pelagic carbonates of the Cingoli anticline, Italy: Possible analog for subsurface fluid-conductive fractures. Journal of Structural Geology 45, 21-37.

Peybernès, B., 1976. Le Jurassique et le Crétacé inferieur des Pyrénées franco-espagnoles entre la Garonne et le Mediterranée., PhD thesis, Université de Toulouse, Toulouse, France, p. 459.

Pickering, R., 2017. U-Series dating, in: Gilbert, A.S. (Ed.), Encyclopedia of geoarchaeology: Dordrecht, Springer, pp. 992-999.

Piessens, K., Muchez, P., Dewaele, S., Boyce, A., Vos, W.D., Sintubin, M., Debacker, T.N., Burke, E.A.J., Viaene, W., 2002. Fluid flow, alteration and polysulphide mineralisation associated with a low-angle reverse shear zone in the Lower Palaeozoic of the Anglo-Brabant fold belt, Belgium. Tectonophysics 348, 73-92.

Pollyea, R.M., Dusen, E.W.V., Fischer, M.P., 2015. Topography driven fluid flow within orogenic wedges: Effects of taper angle and depth-dependent permeability. Geosphere 11, 1-11.

Poprawski, Y., Basile, C., Agirrezabala, L.M., Jaillard, E., Gaudin, M., Jacquin, T., 2014. Sedimentary and structural record of the Albian growth of the Bakio salt diapir (the Basque Country, northern Spain). Basin Research 26, 746-766.

Puigdefàbregas, C., Souquet, P., 1986. Tecto-sedimentary cycles and deposition sequences of the Mesozoic and Tertiary from the Pyrenees. Tectonophysics 129, 173-203.

Puigdefàbregas, C., Muñoz, J.A., Marzo, M., 1986. Thrust Belt Development in the Eastern Pyrenees and Related Depositional Sequences in the Southern Foreland Basin, in: Allen, P.A., Homewood, P. (Eds.), Foreland Basins. Blackwell Publishing Ltd., Oxford, UK. , pp. 229-246.

Puigdefàbregas, C., Muñoz, J.A., Vergés, J., 1992. Thrusting and Foreland Basin Evolution in the Southern Pyrenees, in: McClay, K.R. (Ed.), Thrust Tectonics. London, Chapman & Hall, pp. 247-254.

Qing, H., Mountjoy, E., 1992. Large-scale fluid flow in the Middle Devonian Presqu'ile barrier, Western Canada Sedimentary Basin. Geology 20, 903-906.

Rahl, J.M., Haines, S.H., Pluijm, B.A.v.d., 2011. Links between orogenic wedge deformation and erosional exhumation: Evidence from illite age analysis of fault rock and detrital thermochronology of syn-tectonic conglomerates in the Spanish Pyrenees. Earth and Planetary Science Letters 307, 180-190.

Ramsay, J.G., 1980. The crack-seal mechanism of rock deformation. Nature 284, 135-139.

Rasbury, E.T., Cole, J.M., 2009. Directly dating geologic events: U-Pb dating of carbonates. Reviews of Geophysics 4, 1-27.

Reif, D., Decker, K., Grasemann, B., Peresson, H., 2012. Fracture patterns in the Zagros fold-and-thrust belt, Kurdistan Region of Iraq. Tectonophysics 576-577, 46-62.

Reuning, L., Schoenherr, J., Heinmann, A., Urai., J.L., Littke, R., Kukla, P.A., Rawahi, Z., 2009. Constraints on the diagenesis, stratigraphy and internal dynamics of the surface-piercing salt domes in the Ghaba Salt Basin (Oman): A comparison to the Ara Group in the South Oman Salt Basin. GeoArabia 14, 83-120.

Reynolds, S.J., Lister, G.S., 1987. Structural aspects of fluid-rock interactions in detachment zones. Geology 15, 362-366.

Riba, O., 1973. Las discordancias sintectónicas del Alto Cardener (prepirineo catalán): ensayo de interpretación evolutiva. Acta Geologica Hispanica 8, 90-99.

Riba, O., 1976. Syntectonic unconformities of the Alto Cardener, Spanish Pyrenees: A genetic interpretation. Sedimentary Geology 15, 213-233.

Ring, U., Gerdes, A., 2016. Kinematics of the Alpenrhein-Bodensee graben system in the Central Alps: Oligocene/Miocene transtension due to formation of the Western Alps arc. Tectonics 35, 1367-1391.

Rios, J., 1948. Diapirismo. Boletiín del Instituto Geológico y Minero de España LX(20), 155-390.

Roberts, N.M.W., Rasbury, E.T., Parrish, R.R., Smith, C.J., Horstwood, M.S.A., Condon, D.J., 2017. A calcite reference material for LA-ICP-MS U-Pb geochronology. Geochemistry, Geophysics, Geosystems 18, 2807-2814.

Roberts, N.M.W., Walker, R.J., 2016. U-Pb geochronology of calcite-mineralized faults: Absolute timing of rift-related fault events on the northeast Atlantic margin. Geology 44, 531-534.

Rodríguez-Morillas, N., Playà, E., Travé, A., Martín-Martín, J.D., 2013. Diagenetic processes in a partially dolomitized carbonate reservoir: Casablanca oil field, Mediterranean Sea, offshore Spain. Geologica Acta 11, 195-214.

Rosell, J., Linares, R., Llompart, C., 2001. El "Garumniense" prepirenaico. Rev. Soc. Geol. España 14, 47-56.

Rosenbaum, G., Lister, G.S., Duboz, C., 2002. Relative motions of Africa, Iberia and Europe during Alpine orogeny. Tectonophysics 359, 117-129.

Roure, F., Choukroune, P., Berastegui, J., Muñoz, J.A., Villien, A., Matheron, P., Bareyt, M., Seguret, M., Camara, P., Deramond, J., 1989. Ecors deep seismic data and balanced cross sections: Geometric constraints on the evolution of the Pyrenees. Tectonics 8, 41-50.

Roure, F., Swennen, R., Schneider, F., Faure, J.L., Ferket, H., Guilhaumou, N., Osadetz, K., Robion, P., Vandeginste, V., 2005. Incidence and Importance of Tectonics and Natural Fluid Migration on Reservoir Evolution in Foreland Fold-and-Thrust Belts. Oil & Gas Science and Technology 60, 67-106.

Roure, F., Andriessen, P., Callot, J.P., Faure, J.L., Ferket, H., Gonzales, E., Guilhaumou, N., Lacombe, O., Malandain, J., Sassi, W., Schneider, F., Swennen, R., Vilasi, N., 2010. The use of paleo-thermo-barometers and coupled thermal, fluid flow and pore-fluid pressure modelling for hydrocarbon and reservoir prediction in fold and thrust belts, in: Goffey, G.P., Craig, J., Needham, T., Scott, R. (Eds.), Hydrocarbons in Contractional Belts. Geological Society, London, Special Publications, pp. 87-114.

Rouvier, H., Perthuisot, V., Mansouri, A., 1985. Pb-Zn Deposits and Salt-Bearing Diapirs in Southern Europe and North Africa Economic Geology 80, 666-687.

Rowan, M.G., Vandeville, B.C., 2006. Foldbelts with early salt withdrawal and diapirism: Physical model and examples from the northern Gulf of Mexico and the Flinders Ranges Australia. Marine and Petroleum Geology 23, 871-891.

Rushlow, C.R., Barnes, J.B., Ehlers, T.A., Vergés, J., 2013. Exhumation of the southern Pyrenean fold-thrust-belt (Spain from orogenic growth to decay. Tectonics 32, 843-860.

Rutqvist, J., Rinaldi, A.P., Cappa, F., Moridis, G.J., 2013. Modeling of fault reactivation and induced seismicity during hydraulic fracturing of shale-gas reservoirs. Journal of Petroleum Science and Engineering 107, 31-44.

Rye, D., Bradbury, H.J., 1988. Fluid flow in the crust: an example from a Pyrenean thrust ramp. American Journal of Science 288, 197-235.

Sáez, A., Riba, O., 1986. Depósitos aluviales y lacustres paleógenos del margen pirenaico catalán de la cuenca del Ebro, Libro guía Exc. XI Congreso Español de Sedimentología, Barcelona, pp. 1-6.

Sáez, A., Anadón, P., Herrero, M.J., Moscariello, A., 2007. Variable style of transition between Paleogene fluvial fan and lacustrine systems, southern Pyrenean foreland, NE Spain. Sedimentology 54, 367-390.

Salardon, R., Carpentier, C., Bellahsen, N., Pironon, J., France-Lanord, C., 2017. Interactions between tectonics and fluid circulations in an inverted hyper-extended basin: Example of mesozoic carbonate rocks of the western North Pyrenean Zone (Chaînons Bearnais, France). Marine and Petroleum Geology 80, 563-586.

Sannemann, D., 1968. Salt-rock families in northwestern Germany, in: Braunstein, J., O'Brien, D. (Eds.), Diapirism and Diapirs. AAPG Memoir, Boulder, Colo., pp. 261-270.

Sans, M., 2003. From thrust tectonics to diapirism. The role of evaporites in the kinematic evolution of the eastern South Pyrenean front. Geologica Acta 1, 239-259.

Sans, M., Vergés, J., 1995. Fold development Related to Contractional Salt Tectonics: Southeastern Pyrenean Thrust Front, Spain., in: Jackson, M.P.A., Roberts, D.G., Snelson, S. (Eds.), Salt tectonics: a global perspective. AAPG Memoir, pp. 369-378.

Sans, M., Muñoz, J.A., Vergés, J., 1996. Triangle zone and thrust wedge geometries related to evaporitic horizons (Southern Pyrenees). Canadian Petroleum Geology Bulletin 4, 375-384.

Sanz, P., Pollard, D.D., Allwardt, P.F., Borja, R.I., 2008. Mechanical models of fracture reactivation and slip on bedding surfaces during folding of the asymmetric anticline at Sheep Mountain, Wyoming. Journal of Structural Geology 30, 1177-1191.

Saura, E., Oró, L.A.i., Teixell, A., Vergés, J., 2015. Rising and falling diapirs, shifting depocenters, and flap overturning in the Cretaceous Sopeira and Sant Gervàs subbasins (Ribagorça Basin, southern Pyrenees). Tectonics 35.

Schneider, F., 2003. Basin Modeling in Complex Area: Examples from Eastern Venezuelan and Canadian Foothills. Oil & Gas Science and Technology 58, 313-324.

Schneider, J., Bakker, R.J., Bechstädt, T., Littke, R., 2008. Fluid Evolution During Burial Diagenesis and Subsequent Orogenetic Uplift: The La Vid Group (Cantabrian Zone, Northern Spain). Journal of Sedimentary Research 78, 282-300.

Schroyen, K., Muchez, P., 2000. Evolution of metamorphic fluids at the Variscan fold-and-thrust belt in eastern Belgium. Sedimentary Geology 131, 163-180.

Segnit, E.R., Holland, H.D., Biscardi, C.J., 1962. The solubility of calcite in aqueous solutions-I The solubility of calcite in water between 75” and 200º at CO2 pressures up to 60 atm Geochimia et Cosmochimica Acta 26, 1301-1331.

Séguret, M., 1972. Étude tectonique des nappes et séries décollées de la partie centrale du vesant sud des Pyrénées. Pub. USTELA, sér, Geol. Struct. n.2, Montpellier.

Serra-Kiel, J., Hottinger, L., Caus, E., Drobne, K., Ferràndez, C., Jauhri, A.K., Less, G., Pavlovec, R., Pignatti, J., Samsó, J.M., Schaub, H., Sirel, E., Strougo, A., Tamberau, Y., Tosquella, J., Zakrevskaya, E., 1998a. Larger Foraminiferal Biostratigraphy of the Tethyan Paleocene and Eocene. Bulletin de la Societé Géologique de France 169, 281-299.

Serra-Kiel, J., Hottinger, L., Drobne, K., Ferràndez, C., Jauhri, A.K., Less, G., Pignatti, J., Samsó, J.M., Schaub, H., Sirel, E., Tamberau, Y., Tosquella, J., Zakrevskaya, E., 1998b. Larger benthic Foraminifera in: Thierry, J., Farley, M.B., Jacquin, T., Graciansky, P.C., Vail, P.R. (Eds.), Mesozoic-Cenozoic sequence stratigraphy of European basins., Society of Economic Paleontologist and Mineralogist, Special Publication, p. 60pp.

Serra-Kiel, J., Mató, E., Saula, E., Travé, A., Ferràndez-Cañadell, C., Àlvarez-Pérez, G., Franquès, J., Romero, J., 2003a. An inventory of the marine and transitional Middle/Upper Eocene deposits of the Southeastern Pyrenean Foreland Basin (NE Spain). Geologica Acta 1, 201-229.

Serra-Kiel, J., Travé, A., Mató, E., Saula, E., Ferràndez-Cañadell, C., Busquets, P., Tosquella, J., Vergés, J., 2003b. Marine and Transitional Middle/Upper Eocene Units of the Southeastern Pyrenean Foreland Basin (NE Spain). Geologica Acta 1, 177-200.

Serrano, A., Olmo, W.M.d., 1990. Tectónica salina en el Dominio Cántabro-Navarro: Evolución, edad y origen de las estructuras salinas, in: Ortí, F., Salvany, J.M. (Eds.), Formaciones evaporíticas de la Cuenca del Ebro y cadenas periféricas, y de la zona de Levante, Enresa, Madrid, pp. 39-53.

Shackleton, J.R., Cooke, M.L., Sussman, A.J., 2005. Evidence for temporally changing mechanical stratigraphy and effects on joint-network architecture. Geology 33, 101-104.

Shackleton, J.R., Cooke, M.L., Vergés, J., Simó, T., 2011. Temporal constraints on fracturing associated with fault-related folding at Sant Corneli anticline, Spanish Pyrenees. Journal of Structural Geology 33, 5-19.

Shariatinia, Z., Haghighi, M., Feiznia, S., Alizai, A.H., Levresse, G., 2013. Hydrocarbon migration in the Zagros Basin, offshore Iran, for understanding the fluid flow in the Oligocene–Miocene carbonate reservoirs. Russian Geology and Geophysics 54, 64-81.

Sharp, I., Gillespie, P., Morsalnezhad, D., Taberner, C., Karpuz, R., Vergés, J., Horbury, A., Pickard, N., Garland, J., Hunt, D., 2010. Stratigraphic architecture and fracture-controlled dolomitization of the Cretaceous Khami and Bangestan groups: an outcrop case study, Zagros Mountains, Iran, in: Buchem, F.S.P.V., Gerdes, K.D., Esteban, M. (Eds.), Mesozoic and Cenozoic Carbonate Systems of the Mediterranean and the Middle East: Stratigraphic and Diagenetic Reference Models. Geological Society, London, Special Publications, pp. 343-396.

Sheppard, S.M.F., Charef, A., Bouhlel, S., 1996. Diapirs and Zn-Pb Mineralization: A General Model Based on Tunisian (N. Africa) and Gulf Coast (U.S.A.) Deposits, in: Sangster, D.F. (Ed.), Carbonate-Hosted Lead-Zinc Deposits: 75th Anniversary Volume. Society of Economic Geology, pp. 230-243.

Sibson, R.H., 1981. Fluid Flow Accompanying Faulting: Field Evidence and Models, in: Simpson, D.W., Richards, P.G. (Eds.), Earthquake prediction. American Geophysical Union, pp. 593-603.

Sibson, R.H., Robert, F., Poulsen, K.H., 1988. High-angle reverse faults, fluid-pressure cycling, and mesothermal gold-quartz deposits. Geology 16, 551-555.

Sibson, R.H., 1995. Selective fault reactivation during basin inversion: potential for fluid redistribution through fault-valve action, in: Buchanan, J.G., Buchanan, P.G. (Eds.), Basin Inversion, Geological Society Special Publication, pp. 3-19.

Sibson, R.H., 2005. Hinge-parallel fluid flow in fold-thrust belts: how widespread? Proceedings of the Geologists' Association 116, 301-309.

Sibson, R.H., Robert, F., Poulsen, K.H., 1988. High-angle reverse faults, fluid-pressure cycling, and mesothermal gold-quartz deposits. Geology 16, 551-555.

Simó, A., 1985. Secuencias deposicionales del Cretácico superior de la unidad del Montsec (Pirineo Central), Tesis Doctoral, Universitat de Barcelona. 325 pp.

Skelton, P.W., Gili, E., Vicens, E., Obrador, A., López, G., 2003. Revised lithostratigraphy of the Upper Cretaceous (Santonian) carbonate platform succession on the northern flank of Sant Corneli, southern Central Pyrenees Journal of Iberian Geology 29, 73-87.

Smith, A.P., Fischer, M.P., Evans, M.A., 2012. Fracture-controlled palaeohydrology of a secondary salt weld, La Popa Basin, NE Mexico. Geological Society, London, Special Publications 363, 107-130.

Soliva, R., Benedicto, A., 2004. A linkage criterion for segmented normal faults. Journal of Structural Geology 26, 2251-2267.

Soliva, R., Benedicto, A., 2005. Geometry, scaling relations and spacing of vertically restricted normal faults. Journal of Structural Geology 27, 317-325.

Soliva, R., Benedicto, A., Maerten, L., 2006. Spacing and linkage of confined normal faults: Importance of mechanical thickness. Journal of Geophysical Research 111, B01402.

Soliva, R., Benedicto, A., Schultz, R.A., Maerten, L., Micarelli, L., 2008. Displacement and interaction of normal fault segments branched at depth: Implications for fault growth and potential earthquake rupture size. Journal of Structural Geology 30, 1288-1299.

Soumaya, A., Ayed, N.B., Delvaux, D., Ghanmi, M., 2015. Spatial variation of present-day stress field and tectonic regime in Tunisia and surroundings from formal inversion of focal mechanisms: Geodynamic implications for central Mediterranean. Tectonics 34, 1154-1180.

Srivastava, D.C., Engelder, T., 1990. Crack-propagation sequence and pore-fluid conditions during fault-bend folding in the Appalachian Valley and Ridge, central Pennsylvania. Geol. Soc. America Bull. 102, 116-128.

Stephenson, B.J., Koopman, A., Hillgartner, H., McQuillan, H., Bourne, S., Noad, J., Rawnsley, K., 2007. Structural and stratigraphic controls on fold-related fracturing in the Zagros Mountains, Iran: implications for reservoir development, in: Lonergan, L., Jolly, R.J.H., Rawnsley, K., Sanderson, D.J. (Eds.), Fractured reservoirs. Geological Society, London, Special Publications, pp. 1-21.

Steuber, T., Rauch, M., 2005. Evolution of the Mg/Ca ratio of Cretaceous seawater: Implications from the composition of biological low-Mg calcite. Marine Geology 217, 199-213.

Suppe, J., Sábat, F., Muñoz, J.A., Poblet, J., Roca, E., Vergés, J., 1997. Bed-by-bed fold growth by kink-band migration: Sant Llorenç de Morunys, eastern Pyrenees. Journal of Structural Geology 19, 443-461.

Swanson, E.M., Wernicke, B.P., Eiler, J.M., Losh, S., 2012. Temperatures and fluids on faults based on carbonate clumped-isotope thermometry. American Journal of Science 312, 1-21.

Swart, P.K., 2015. The geochemistry of carbonate diagenesis: The past, present and future. Sedimentology 62, 1233-1304.

Swennen, R., Muskha, K., Roure, F., 2000. Fluid circulation in the Ionian fold and thrust belt (Albania): implications for hydrocarbon prospectivity. Journal of Geochemical Exploration 69-70, 629-634.

Swennen, R., Ferket, H., Benchilla, L., Roure, F., Ellam, R., team, S., 2003. Fluid flow and diagenesis in carbonate dominated Foreland Fold and Thrust Belts: petrographic inferences from field studies of late-diagenetic fabrics from Albania, Belgium, Canada, Mexico and Pakistan. Journal of Geochemical Exploration 78-79, 481-485.

Tavani, S., Mencos, J., Bausà, J., Muñoz, J.A., 2011. The fracture pattern of the Sant Corneli Bóixols oblique inversion anticline (Spanish Pyrenees). Journal of Structural Geology 33, 1662-1680.

Tavani, S., Storti, F., Lacombe, O., Corradetti, A., Muñoz, J.A., Mazzoli, S., 2015. A review of deformation pattern templates in foreland basin systems and fold-and-thrust-belts: Implications for the state of stress in the frontal regions of thrust wedges. Earth-Science Reviews 141, 82-104.

Tavani, S., Bertock, C., Granado, P., Piana, F., Salas, R., Vigna, B., Muñoz, J.A., 2018. The Iberia-Eurasia plate boundary east of the Pyrenees. Earth-Science Reviews 187, 314-337.

Taylor, B.E., 1987. Stable isotope geochemistry of ore-forming fluids, in: Kyser, T.K. (Ed.), Short Course in Stable Isotope Geochemistry of low Temperature Fluids. Mineral Association of Canada, pp. 337-418.

Tempest, S.A., 1991. Fluid-rock interaction in ductile shear zones, central-eastern Pyrenees. PhD thesis, Leeds University, 202 p.

Tilhac, R., Guillaume, D., Odonne, F., 2013. Fluid circulation and deformational gradient in north-Pyrenean flyschs: Example from the Saint-Jean-de-Luz basin (France). Tectonophysics 608, 832-846.

Tindall, J., Flecker, R., Valdes, P., Schmidt, D.N., Markwick, P., Harris, J., 2010. Modelling the oxygen isotope distribution of ancient seawater using a coupled ocean–atmosphere GCM: Implications for reconstructing early Eocene climate. Earth and Planetary Science Letters 292, 265-273.

Travé, A., Calvet, F., 2001. Syn-rift geofluids in fractures related to the early-middle Miocene evolution of the Vallès-Penedès half-graben (NE Spain). Tectonophysics 336, 101-120.

Travé, A., Labaume, P., Calvet, F., Soler, A., 1997. Sediment dewatering and pore fluid migration along thrust faults in a foreland basin inferred from isotopic and elemental geochemical analyses (Eocene southern Pyrenees, Spain). Tectonophysics 282, 375-398.

Travé, A., Labaume, P., Calvet, F., Soler, A., Tritlla, J., Bautier, M., Potdevin, J.L., Séguret, M., Raynaud, S., Briqueu, L., 1998a. Fluid migration during Eocene thrust emplacement in the south Pyrenean foreland basin (Spain): an integrated structural, mineralogical and geochemical approach, in: Mascle, A., Puigdefàbregas, C., LuterBacher, H.P., Fernàndez, M. (Eds.), Cenozoic Foreland Basins of Western Europe. Geological Society, Special Publications, pp. 163-188.

Travé, A., Calvet, F., Soler, A., Labaume, P., 1998b. Fracturing and fluid migration during Paleogene compression and Neogene extension in the Catalan Coastal Ranges, Spain. Sedimentology 45, 1063-1082.

Travé, A., Calvet, F., Sans, M., Vergés, J., Thirlwall, M., 2000. Fluid history related to the Alpine compression at the margin of the south-Pyrenean Foreland basin: the El Guix anticline. Tectonophysics 321, 73-102.

Travé, A., Calvet, F., Salas, R., Playà, E., 2004. Fluid Flow during Paleogene Compression in the Linking Zone Fold and Thrust Belt (Northeast Spain), in: Swennen, R., Roure, F., Granath, J.W. (Eds.), Deformation, fluid flow, and reservoir appraisal in foreland fold and thrust belts. AAPG Hedberg Series, pp. 215-243.

Travé, A., Labaume, P., Vergés, J., 2007. Fluid systems in Foreland Fold and thrust belts: an overview from the Southern Pyrenees, in: Lacombe, O., Lavé, J., Roure, F., Vergés, J. (Eds.),

Thrust Belts and Foreland Basins: From Fold Kinematics to Hydrocarbon Systems. Springer, pp. 93-115.

Trincal, V., Buatier, M., Charpentier, D., Lacroix, B., Lanari, P., Labaume, P., Lahfid, A., Venneman, T., 2017. Fluid–rock interactions related to metamorphic reducing fluid flow in meta-sediments: example of the Pic-de-Port-Vieux thrust (Pyrenees, Spain). Contributions to Mineralogy and Petrology 172, 78.

Treagus, S.H., 1988. Strain refraction in layered systems. Journal of Structural Geology 19, 551-566.

Tucker, M.E., Wright, P.V., 1990. Carbonate Sedimentology. Blackwell, Oxford.

Turner, J.P., Williams, G.A., 2004. Sedimentary basin inversion and intra-plate shortening. Earth-Science Reviews 65, 277-304.

Ullastre, J., Masriera, A., 2004. PEDRAFORCA: estratigrafía y estructura (Pirineo catalán, España). Treballs del Museu de Geologia de Barcelona 12, 11-52.

Uysal, I.T., Zhao, J.X., Golding, S.D., Lawrence, M.G., Glikson, M., Collerson, K.D., 2007. Sm–Nd dating and rare-earth element tracing of calcite: Implications for fluid-flow events in the Bowen Basin, Australia. Chemical Geology 238, 63-71.

Vajdova, V., Zhu, W., Chen, T.Z.N., Wong, T.F., 2010. Micromechanics of brittle faulting and cataclastic flow in Tavel limestone. Journal of Structural Geology 32, 1158-1169.

Valero, L., Garcés, M., Cabrera, L., Costa, E., Sáez, A., 2014. 20 Myr of eccentricity paced lacustrine cycles in the Cenozoic Ebro Basin Earth and Planetary Science Letters 408, 183-193.

Vandeginste, V., Swennen, R., Allaeys, M., Ellam, R.M., Osadetz, K., Roure, F., 2012. Challenges of structural diagenesis in foreland fold-and-thrust belts: A case study on paleofluid flow in the Canadian Rocky Mountains West of Calgary. Marine and Petroleum Geology 35, 235-251.

Vandeginste, V., Swennen, R., Gleeson, S.A., Ellam, R.M., Osadetz, K., Roure, F., 2005. Zebra dolomitization as a result of focused fluid flow in the Rocky Mountains Fold and Thrust Belt, Canada. Sedimentology 52, 1067-1095.

Van der Pluijm, B. A., Hall, C.M., Vrolijk, P.J., Pevear, D.R., Covey, M.C., 2001. The dating of shallow faults in the Earth's crust. Nature 412, 172.

Van Geet, M., Swennen, R., Durmishi, C., Roure, F., Muchez, P., 2002. Paragenesis of Cretaceous to Eocene carbonate reservoirs in the Ionian fold and thrust belt (Albania): relation between tectonism and fluid flow. Sedimentology 49, 697-718.

Veizer, J., Ala, D., Azmy, K., Bruckschen, P., Buhl, D., Bruhn, F., Carden, G.A.F., Diener, A., Ebneth, S., Godderis, Y., Jasper, T., Korte, C., Pawellek, F., Podlaha, O.G., Strauss, H., 1999. 87Sr/86Sr, d13C and d18O evolution of Phanerozoic seawater. Chemical Geology 161, 59-88.

Vergés, J., 1993. Estudi geològic del vessant sud del Pirineu oriental i central. Evolució cinemàtica en 3D. PhD thesis, Universitat de Barcelona, Barcelona, Spain, p. 203.

Vergés, J., Muñoz, J.A., 1990. Thrust sequences in the southern central Pyrenees. Bull. Soc. géol. France 8, 265-271.

Vergés, J., Burbank, D.W., 1996. Eocene-Oligocene thrusting and basin configuration in the eastern and central Pyrenees (Spain), in: Friend, P., Dabrio, C. (Eds.), Tertiary basins of Spain. Cambridge University, World and Regional geology, E11, pp. 120-133.

Vergés, J., Garcia-Senz, J., 2001. Mesozoic evolution and Cainozoic inversion of the Pyrenean Rift, in: Ziegler, P.A., Cavazza, W., Robertson, A.H.F., Crasquin-Soleau, S. (Eds.), Peri-Tethys Memoir 6: Peri-Tethyan Rift/Wrench Basins and Passive Margins. Mémoires du Muséum National d'Histoire Naturelle, Paris, pp. 187-212.

Vergés, J., Martínez, A., Muñoz, J.A., 1992. South Pyrenean fold and thrust belt: The role of foreland evaporitic levels in thrust geometry, in: McClay, K. (Ed.), Thrust Tectonics. London, Chapman & Hall, pp. 255-264.

Vergés, J., Millán, H., Roca, E., Muñoz, J.A., Marzo, M., Cirés, J., Bezemer, T.D., Zoetemeijer, R., Cloetigh, S., 1995. Eastern Pyrenees and related foreland basins: pre-, syn- and post-collisional cristal-scale cross-sections. Marine and Petroleum Geology 12, 893-915.

Vergés, J., Marzo, M., Santaeulària, T., Serra-Kiel, J., Burbank, D.W., Muñoz, J.A., Giménez-Montsant, J., 1998. Quantified vertical motions and tectonic evolution of the SE Pyrenean foreland basin, in: Mascle, A., Puigdefàbregas, C., Luterbacher, H.P., Fernàndez, M. (Eds.), Cenozoic Foreland Basins of Western Europe. Geological Society Special Publications, pp. 107-134.

Vergés, J., Fernàndez, M., Martínez, A., 2002a. The Pyrenean orogen: pre-, syn-, and post-collisional evolution, in: Rosenbaum, G., Lister, G. (Eds.), Reconstruction of the evolution of the Alpine-Himalayan Orogen. Journal of the Virtual Explorer, pp. 55-74.

Vergés, J., Marzo, M., Muñoz, J.A., 2002b. Growth strata in foreland settings. Sedimentary Geology 146, 1-9.

Vicente, A., Martín-Closas, C., Arz, J.A., Oms, O., 2015. Mastrichtian-basal Paleocene charophyte biozonation and its calibration to the Global Polarity Time Scale in the southern Pyrenees (Catalonia, Spain). Cretaceous Research 52, 268-285.

Vilasi, N., 2010. Study of reservoir analogues in foreland fold-and-thrust belts: sedimentology, diagenesis, deformation and fracturing of the upper cretaceous-eocene carbonate systems of the ionian zone (Southern Albania). PhD thesis. Ecole des Mines de Paris, Paris, France, p. 190.

Vilasi, N., Malandain, J., Barrier, L., Callot, J.P., Amrouch, K., Guilhaumou, N., Lacombe, O., Muska, K., Roure, F., Swennen, R., 2009. From outcrop and petrographic studies to basin-scale fluid flow modelling: The use of the Albanian natural laboratory for carbonate reservoir characterisation. Tectonophysics 474, 367-392.

Wacker, U., Fiebig, J., Schoene, B.R., 2013. Clumped isotope analysis of carbonates: comparison of two different acid digestion techniques. Rapid Communications in Mass Spectrometry 27, 1631-1642.

Warren, J.K., 2006. Evaporites:Sediments, Resources and Hydrocarbons. Springer Berlin Heidelberg.

Watkins, H., Butler, R.W.H., Bond, C.E., Healy, D., 2015. Influence of structural position on fracture networks in the Torridon Group, Achnashellach fold and thrust belt, NW Scotland. Journal of Structural Geology 74, 64-80.

Webb, G.E., Kamber, B.S., 2000. Rare earth elements in Holocene reefal microbialites: A new shallow seawater proxy. Geochimia et Cosmochimica Acta 64, 1557-1565.

Wickham, S.M., Taylor, H.P., 1985. Stable isotopic evidence for large-scale seawater infiltration in a regional metamorphic terrane; the Trois Seigneurs Massif, Pyrenees, France. Contributions to Mineralogy and Petrology 91, 122-137.

Wickham, S.M., Taylor, H.P., 1987. Stable isotope constraints on the origin and depth of penetration of hydrothermal fluids associated with Hercynian regional metamorphism and crustal anatexis in the Pyrenees. Contributions to Mineralogy and Petrology 95, 255-268.

Williams, E.A., Ford, M., Vergés, J., Artoni, A., 1998. Alluvial gravel sedimentation in a contractional growth fold setting, Sant Llorenç de Morunys, southeastern Pyrenees, in: Mascle, A., Puigdefàbregas, C., Luterbacher, H.P., Fernàndez, M. (Eds.), Cenozoic Foreland Basins of Western Europe., Geological Society Special Publications, pp. 69-106.

Wiseall, A.C., Cuss, R.J., Hough, E., Kemp, S.J., 2018. The role of fault gouge properties on fault reactivation during hydraulicstimulation; an experimental study using analogue faults. Journal of Natural Gas Science and Engineering 59, 21-34.

Wiprut, D., Zoback, M.D., 2000. Fault reactivation and fluid flow along a previously dormant normal fault in the northern North Sea. Geology 27, 595-598.

Worden, R.H., Benshatwan, M.S., Potts, G.J., Elgarmadi, S.M., 2015. Basin-scale fluid movement patterns revealed by veins: Wessex Basin, UK. Geofluids.

Zeng, L., 2010. Microfracturing in the Upper Triassic Sichuan Basin tight-gas sandstones: Tectonic, overpressure, and diagenetic origins. AAPG Bulletin 94, 1811-1825.

Zhang, P.Z., Shen, Z., Wang, M., Gan, W., Bürgmann, R., Molnar, P., Wang, Q., Wu, J., Sun, J., Hanrong, S., Xinzhao, Y., Niu, Z., 2004. Continuous deformation of the Tibetan Plateau from global positioning system data. Geology 32, 809-812.

Zhao, L., Chen, Z.Q., Algeo, T.J., Chen, J., Chen, Y., Tong, J., Gao, S., Zhou, L., Hu, Z., Liu, Y., 2013. Rare-earth element patterns in conodont albid crowns: Evidence for massive inputs of volcanic ash during the latest Permian biocrisis? Global and Planetary Change 105, 135-151.

Chapter 12

Annexes

Annex 1: Geochemical data from Chapter 4 (Cruset et al., 2016).

Table 1. $\delta^{18}O$ and $\delta^{13}C$ values of the host-carbonates and calcite cements Cc1 and Cc2.

Sample	Description	Type of cement	$\delta^{13}C$ VPDB	$\delta^{18}O$ VPDB
GP-R1	Calcite shear vein	Cc1	-1.51	-6.74
GP-R1	Calcite shear vein	Cc1	-1.51	-6.85
GP-R1	Calcite shear vein	Cc2	-1.44	-11.41
GP-R1	Calcite shear vein	Cc2	-1.52	-11.06
GP-R1	Calcite shear vein	Cc2	-1.34	-12.16
GP-R2	Calcite extension vein	Cc1	-1.93	-6.67
GP-R2	Calcite extension vein	Cc1	-1.91	-6.60
GP-R2	Intergranular cement	Cc1	-1.07	-6.25
GP-R4	Vug porosity	Cc1	-1.57	-6.37
GP-R4	Calcite shear vein	Cc1	-1.22	-6.30
GP-R4	Calcite shear vein	Cc1	-1.41	-6.25
GP-R4	Palustrine-lacustrine carbonate		-2.73	-7.26
GP-R5	Intergranular cement	Cc1	0.53	-5.93
GP-R5	Calcite shear vein	Cc2	-2.06	-10.67
GP-R5	Calcite shear vein	Cc2	-2.05	-9.96
GP-R7	Calcite shear vein	Cc1	-1.71	-6.29
GP-R7	Calcite shear vein	Cc1	-1.79	-7.76
GP-R7	Intergranular cement	Cc1	-0.62	-6.25
GP-R9A	Calcite extension vein	Cc1	-0.59	-6.54
GP-R9A	Calcite shear vein	Cc1	-0.78	-6.17
GP-R9A	Calcite shear vein	Cc1	-0.82	-6.26
GP-R9A	Intergranular cement	Cc1	-0.09	-6.72
GP-R9B	Calcite shear vein	Cc1	-0.85	-6.54
GP-R9B	Intergranular cement	Cc1	-0.02	-6.74
GP-R10	Calcite shear vein	Cc1	-0.11	-6.76
GP-R11	Calcite shear vein	Cc1	-1.08	-7.19
GP-R11	Calcite shear vein	Cc1	-1.08	-6.69
GP-R11	Intergranular cement	Cc1	-1.04	-6.69
GP-R11	Calcite shear vein	Cc2	-1.61	-9.67
GP-R12	Intergranular cement	Cc1	-1.31	-7.53
GP-R12	Calcite shear vein	Cc2	-1.95	-9.63
GP-R12	Calcite shear vein	Cc2	-1.99	-9.62
GP-R13	Calcite shear vein	Cc1	-1.37	-6.41
GP-R13	Calcite shear vein	Cc1	-1.42	-6.44
GP-R13	Intergranular cement	Cc1	-0.65	-6.23
302	Calcite extension vein	Cc1	0.21	-8.02
302	Calcite shear vein	Cc1	0.25	-8.02
302	Calcite shear vein	Cc1	-0.51	-9.39
302	Carbonate-derived clast		-3.22	-4.70
303	Calcite shear vein	Cc1	0.10	-7.81
303	Carbonate-derived clast		3.11	-3.12
309A	Calcite shear vein	Cc1	0.23	-7.29
309A	Calcite shear vein	Cc1	0.11	-7.37
309B1	Calcite shear vein	Cc1	-0.40	-7.36
309B1	Calcite shear vein	Cc1	-0.40	-7.65
310	Calcite shear vein	Cc1	0.96	-6.90
310	Calcite shear vein	Cc1	0.75	-7.12
311A	Calcite shear vein	Cc1	-0.69	-8.79
311A	Calcite shear vein	Cc2	-0.73	-12.68
311A	Calcite shear vein	Cc2	-2.13	-11.98
311B	Calcite shear vein	Cc1	-0.67	-7.21
311B	Calcite shear vein	Cc1	-1.30	-9.09
311D	Calcite shear vein	Cc2	-0.95	-13.07
311D	Calcite shear vein	Cc2	-0.51	-12.46
311F	Calcite shear vein	Cc1	0.74	-7.05
311F	Calcite shear vein	Cc1	0.74	-7.07
311F	Carbonate-derived clast		1.22	-7.19
311G	Calcite shear vein	Cc2	0.19	-12.99
311G	Carbonate-derived clast		-0.84	-8.91
312A	Calcite shear vein	Cc1	0.63	-7.57
312A	Calcite shear vein	Cc2	0.02	-13.11
312A	Carbonate-derived clast		0.59	-3.43
313A	Calcite shear vein	Cc2	-1.40	-12.88
313A	Calcite shear vein	Cc2	-1.80	-13.30
313A’	Calcite shear vein	Cc1	-2.34	-7.59
313A’	Calcite shear vein	Cc2	-2.30	-11.14

314A	Small fracture affecting clasts	Cc1	0.15	-7.50
314A	Calcite shear vein	Cc2	-1.60	-13.10
314A	Calcite shear vein	Cc2	-0.95	-10.64
314B	Calcite shear vein	Cc1	0.00	-7.23
314B	Calcite shear vein	Cc1	0.05	-7.23
314C	Calcite shear vein	Cc1	-0.22	-7.41
314C	Calcite shear vein	Cc1	-0.23	-7.83
314D1	Calcite shear vein	Cc1	-1.11	-7.85
314D1	Calcite shear vein	Cc2	-1.79	-12.80
314D2	Calcite shear vein	Cc1	-1.34	-9.27
314D2	Calcite shear vein	Cc2	-1.47	-13.95
314D2	Calcite shear vein	Cc2	-2.46	-12.21
317	Calcite shear vein	Cc1	-1.23	-8.09
317	Calcite shear vein	Cc1	-1.34	-7.50
EM-1	Palustrine-lacustrine carbonate		-2.44	-6.92
PR-1A	Palustrine-lacustrine carbonate		-3.3	-7.28
PR-1B	Palustrine-lacustrine carbonate		-2.52	-7.22

Table 2. $^{87}Sr/^{86}Sr$ values of palustrine-lacustrine host-carbonates and calcite cements Cc1 and Cc2.

Sample	Description	Type of cement	87Sr/86Sr
GP-R4	Eocene-Oligocene host-mudstone		0.708865
IP-R	Eocene-Oligocene host-marly limestone		0.708967
309A	Calcite shear vein	Cc1	0.709246
311A	Calcite shear vein	Cc2	0.708947
311D	Calcite shear vein	Cc2	0.709002
314C	Calcite shear vein	Cc1	0.709138

Table 3. Minimum, maximum and average temperatures of homogenization (T_h) and ice melting (T_m) of the fluid inclusions from the calcite cements Cc1 and Cc2. n represents the number of fluid inclusions analyzed.

Filling stage	Type of fluid inclusion	n		T_h (ºC)		T_m (ºC)
Calcite cement Cc1	Stretched secondary	37	Min. Max. Av.	130 218 154	Min. Max. Av.	-1 5 1.12
Calcite cement Cc2	Stretched primary	56	Min. Max. Av.	126 280 199	Min. Max. Av.	-2 1.7 0.44

Table 4. Calcite cement $\delta^{13}C$, $\delta^{18}O$, Δ_{47} and $\delta^{18}O_{fluid}$.

Sample	Description	n	$\delta^{13}C$ VPDB	$\delta^{18}O$ VPDB	Δ_{47}	T ºC	$\delta^{18}O_{fluid}$ VSMOW
309B1	Calcite cement Cc1	3	-0.44	-7.77	0.548 ± 0.009	92 ± 5	4.7 ± 0.6
317	Calcite cement Cc1	3	-0.99	-6.95	0.494 ± 0.010	129 ± 8	9.2 ± 0.7
311A	Calcite cement Cc2	3	-0.77	-12.32	0.574 ± 0.010	77 ± 5	-1.7 ± 0.7
311D	Calcite cement Cc2	3	-0.73	-12.85	0.551 ± 0.004	90 ± 3	-0.7± 0.3

Table 5. Minimum, maximum and average values of the elemental composition of the calcite cements Cc1 and Cc2 and calculated Mg/Ca, Sr/Ca, Mn/Ca and Ca/Fe molar ratios of the parent fluid applying the distribution coefficient equation of McIntire (1963).

Filling stage		Mg (ppm)	Ca (ppm)	Na (ppm)	Mn (ppm)	Fe (ppm)	Sr (ppm)	Molar ratio Mg/Ca[a]	Molar ratio Sr/Ca[b]	Molar ratio Mn/Ca[c]	Molar ratio Ca/Fe[d]
Calcite cement Cc1	Min.	600	381100	<d.l.	600	<d.l.	<d.l.	0.02136	-	0.00014	878.296
	Max.	4500	399200	500	2800	1100	600	0.16741	0.00876	0.00066	13829.573
	Av.	2171	391435	241	1406	544	537	0.07895	0.00324	0.00321	5864
Calcite cement Cc2	Min.	<d.l.	385000	<d.l.	300	300	<d.l.	-	-	0.00007	851.067
	Max.	2400	398000	300	2300	2300	3000	0.08606	0.04327	0.00054	9205.781
	Av.	1038	391553	238	1268	1080	886	0.03685	0.00764	0.00295	3548

[a] KMg Cc1= 0.1163 at 90 ºC (Katz, 1973)
KMg Cc2= 0.028 at 40 ºC (Mucci and Morse, 1983)
[b] KSr=0.08 at 100-150 ºC (Kinsman, 1969)
[c] KMn=8 at 50ºC (Dromgoole and Walter, 1990)
[d] KFe=5 at 50ºC (Dromgoole and Walter, 1990; Tucker and Wright, 1990)

Annex 2: Geochemical data from Chapter 5 (Cruset et al., 2018).

Table S1. Elemental composition of the calcite cements Cc1, Cc2, Cc3, Cc4, Cc5, Cc6 and Cc7 precipitated in the Vallfogona thrust.

Sample	Type of cement	Fe (ppm)	Mg (ppm)	Sr (ppm)	Mn (ppm)
GDV1	Cc1	3746	4461	d.l.	1665
GDV1	Cc1	1780	5590	509	852
GDV1	Cc1	2260	7187	422	616
GDV1	Cc1	1070	4310	1532	993
GDV1	Cc1	1294	4436	939	1958
GDV1	Cc2	5723	3481	d.l.	d.l.
GDV1	Cc2	2204	1891	d.l.	870
GDV1	Cc2	1658	1427	d.l.	932
GDV1	Cc2	2616	3347	d.l.	1016
GDV1	Cc2	1122	1683	d.l.	774
GDV1	Cc2	2334	2455	d.l.	1176
GDV1	Cc2	1654	1728	d.l.	890
GDV1	Cc2	1325	2036	d.l.	1176
GDV1	Cc2	1461	1232	d.l.	1170
GDV1	Cc2	2354	3099	d.l.	713
GDV1	Cc2	1567	2221	d.l.	946
GDV1	Cc2	1205	1529	d.l.	747
GDV1	Cc2	3499	3901	d.l.	1435
GDV1	Cc2	2486	2920	d.l.	952
GDV1	Cc2	4278	3921	d.l.	1104
GDV1	Cc2	2595	3356	d.l.	1221
GDV1	Cc2	4084	3707	d.l.	1100
GDV20	Cc2	5291	3876	d.l.	1160
GDV20	Cc2	5236	2953	d.l.	369
GDV20	Cc2	6010	4465	d.l.	716
GDV20	Cc2	2744	1600	d.l.	703
GDV20	Cc2	3461	2753	d.l.	595
GDV20	Cc2	3971	2309	d.l.	735
GDV20	Cc2	5074	2689	d.l.	1208
GDV20	Cc2	2582	1421	d.l.	344
GDV20	Cc2	6109	3739	d.l.	1191
GDV20	Cc2	329	3360	d.l.	236
GDV20	Cc2	4073	2207	d.l.	421
GDV26A	Cc2	5005	1821	d.l.	498
GDV26A	Cc2	4662	2806	d.l.	706
GDV26A	Cc2	5700	3563	d.l.	1023
GDV26A	Cc2	4826	3023	d.l.	854
GDV26A	Cc2	4857	3157	d.l.	1108
GDV26A	Cc2	3486	1700	d.l.	542
GDV26A	Cc2	4950	2776	d.l.	855

GDV26A	Cc2	5631	3318	d.l.	1584
GDV26A	Cc2	6731	2905	d.l.	1621
GDB13	Cc2	d.l.	3171	d.l.	d.l.
GDB13	Cc2	3217	1290	d.l.	551
GDB13	Cc2	4406	1780	d.l.	459
GDB13	Cc2	4330	1745	d.l.	577
GDB13	Cc2	5663	1806	d.l.	388
GDB13	Cc2	3579	1242	d.l.	211
GDB13	Cc2	3412	1187	d.l.	377
GDB15	Cc2	7349	4851	d.l.	913
GDB15	Cc2	3985	2887	d.l.	735
GDB15	Cc2	5703	3815	301	625
GDB15	Cc2	5839	3327	756	669
GDB15	Cc2	6096	2767	868	572
GDB15	Cc2	5029	2777	750	d.l.
GDB15	Cc2	6630	3389	526	828
GDB15	Cc2	5712	3436	749	502
GDB15	Cc2	5816	3112	1085	544
GDB15	Cc2	6326	3020	472	599
GDB15	Cc2	4372	1839	d.l.	550
GDB15	Cc2	4132	4460	d.l.	337
GDB15	Cc2	5462	7350	d.l.	869
GDB15	Cc2	3354	1455	848	586
GDB15	Cc2	7396	5187	d.l.	514
GDB15	Cc2	7377	4692	d.l.	423
GDB20	Cc3	1365	5035	628	1043
GDB20	Cc3	3480	2192	d.l.	940
GDB20	Cc3	7421	6023	d.l.	1482
GDB20	Cc3	9075	6862	d.l.	1418
GDB20	Cc3	4611	4660	d.l.	1288
GDB20	Cc3	7386	6674	d.l.	310
GDB20	Cc3	3261	1491	986	1255
GDB20	Cc3	7063	5675	178	1575
GDB20	Cc3	5020	2014	d.l.	1223
GDB20	Cc3	3616	1552	d.l.	1566
GDB20	Cc3	5170	2881	d.l.	1428
GDB20	Cc3	6217	2709	d.l.	1931
GDB20	Cc3	6937	3150	d.l.	2129
GDV1	Cc4	1668	1363	d.l.	1674
GDV1	Cc4	2883	3309	d.l.	1095
GDV1	Cc4	2972	4088	d.l.	1551
GDV1	Cc4	1302	1636	d.l.	1165
GDV1	Cc4	2598	3387	d.l.	1195
GDV1	Cc4	2245	2924	d.l.	585
GDV1	Cc4	2709	3213	d.l.	1249
GDV1	Cc4	1483	1630	d.l.	865
GDV26A	Cc4	4966	2143	d.l.	789

GDV26A	Cc4	4988	2681	d.l.	855
GDV26A	Cc4	5554	3348	d.l.	848
GDV26A	Cc4	3424	2397	d.l.	871
GDB7	Cc5	259	2848	d.l.	1461
GDB7	Cc5	240	2565	d.l.	1101
GDB7	Cc5	151	2675	d.l.	1141
GDB7	Cc5	89	956	506	1058
GDB7	Cc5	234	3018	d.l.	1367
GDB7	Cc5	205	1875	413	874
GDB7	Cc5	216	3254	d.l.	443
GDB7	Cc5	212	2324	371	d.l.
GDB7	Cc5	264	2097	543	903
GDB7	Cc5	d.l.	3483	d.l.	d.l.
GDB15	Cc6	3721	1239	d.l.	844
GDB15	Cc6	1999	d.l.	d.l.	673
GDB15	Cc6	1611	1549	d.l.	1236
GDB15	Cc6	2872	925	d.l.	d.l.
GDB15	Cc6	1428	602	d.l.	765
GDB15	Cc6	1089	1144	d.l.	3718
GDB15	Cc6	1504	1354	d.l.	3814
GDB15	Cc6	1527	1130	d.l.	4239
GDB15	Cc6	1017	857	d.l.	d.l.
GDB7	Cc7	d.l.	3523	d.l.	756
GDB7	Cc7	d.l.	2328	d.l.	d.l.
GDB7	Cc7	d.l.	2721	d.l.	d.l.
GDB7	Cc7	81	2489	d.l.	428
GDB7	Cc7	96	3587	d.l.	d.l.
GDB7	Cc7	99	2776	d.l.	d.l.

Table S2. Elemental composition of the calcite cements Cc1, Cc2 and Cc3 precipitated in the L'Escala thrust.

Sample	Type of cement	Fe (ppm)	Mg (ppm)	Sr (ppm)	Mn (ppm)
TES4	Cc1	588	1660	872	473
TES4	Cc1	1181	4411	315	793
TES4	Cc1	501	1470	1074	459
TES4	Cc1	424	1205	1033	378
TES4	Cc1	583	1061	1217	468
TES4	Cc1	974	1663	231	760
TES4	Cc1	501	1323	1157	368
TES4	Cc1	901	1332	208	511
TES4	Cc1	872	2009	499	373
TES4	Cc1	545	1041	516	421
TES4	Cc1	1518	3324	202	707
TES4	Cc1	1494	6140	231	1008
TES4	Cc1	1089	4846	487	851
TES4	Cc1	897	3067	558	507
TES4	Cc1	926	2626	338	688
TES4	Cc1	805	3191	510	755
TES4	Cc1	603	2623	623	550
TES4	Cc1	1287	5356	95	1042
TES4	Cc1	1128	6080	131	961
TES4	Cc1	1340	5258	95	870
TES4	Cc1	1060	3030	d.l.	674
TES4	Cc1	945	3624	12	884
TES4	Cc1	906	2508	d.l.	741
TES4	Cc1	786	1753	36	535
TES4	Cc1	574	2635	d.l.	612
TES4	Cc1	1374	3802	59	741
TES4	Cc1	1123	3880	83	726
TES4	Cc1	670	3194	12	545
TES4	Cc1	844	2479	d.l.	674
TES5	Cc1	2092	5520	125	851
TES5	Cc1	1364	3370	469	583
TES5	Cc1	1041	2300	997	368
TES5	Cc1	1422	3133	404	545
TES5	Cc1	1543	2153	47	669
TES5	Cc1	1234	3301	599	421
TES5	Cc1	1326	2926	469	540
TES5	Cc1	1355	3497	570	511
TES5	Cc1	1147	2767	552	382
TES5	Cc1	954	2306	718	368
TES5	Cc1	1808	4137	226	683
TES5	Cc1	1480	3580	368	444
TES9	Cc1	2140	3638	582	908
TES9	Cc1	2772	6685	303	1013

TES9	Cc1	2357	5739	261	1008
TES9	Cc1	2140	3987	516	913
TES9	Cc1	1191	1931	677	607
TES9	Cc1	1022	951	1181	492
TES9	Cc1	2401	5587	160	1252
TES9	Cc1	1552	2984	273	808
TES9	Cc1	2507	5506	214	1176
TES9	Cc1	2545	5601	47	1267
TES9	Cc1	1576	2664	582	889
TES9	Cc1	2025	3857	190	1109
TES9	Cc1	2261	4598	196	1061
TES9	Cc1	1215	2358	849	769
TES9	Cc1	1041	1193	d.l.	564
TES9	Cc1	1441	3863	95	1396
TES9	Cc1	1162	1300	303	856
TES9	Cc1	1446	2355	439	655
TES9	Cc1	1538	2842	178	918
TES9	Cc1	1306	2084	427	717
TES9	Cc1	1465	2447	475	784
TES9	Cc1	1745	3869	570	965
TES9	Cc1	1697	3384	303	731
TES9	Cc1	988	1444	1128	397
TES9	Cc1	2473	6051	137	1176
TES9	Cc1	2126	5284	30	1176
TES9	Cc1	1065	1317	594	631
TES9	Cc1	926	1315	297	497
TES9	Cc1	2401	6045	190	1008
TES9	Cc1	1567	1865	6	631
TES9	Cc1	926	2070	d.l.	540
TES11	Cc1	641	3191	457	822
TES11	Cc1	786	2871	d.l.	1138
TES11	Cc1	824	1560	617	813
TES11	Cc1	578	2208	611	602
TES11	Cc1	429	1061	1104	411
TES11	Cc1	675	3419	303	932
TES11	Cc1	689	2519	421	1051
TES11	Cc1	776	4457	d.l.	1004
TES11	Cc1	766	4338	18	1171
TES11	Cc1	405	2078	463	683
TES11	Cc1	815	2692	641	841
TES11	Cc1	660	2543	374	927
TES11	Cc1	824	4422	d.l.	999
TES11	Cc1	598	1701	516	674
TES11	Cc1	617	2485	427	841
TES11	Cc1	747	4471	380	903
TES11	Cc1	1036	3926	65	1152
TES11	Cc1	786	3370	463	875
TES11	Cc1	839	3915	119	1061
TES11	Cc1	699	3918	226	1051

TES11	Cc1	1306	7022	6	1697
TES11	Cc1	1017	4693	178	1104
TES11	Cc1	1239	6699	166	1816
TES11	Cc1	1186	7942	237	1558
TES11	Cc1	646	3445	142	1066
TES11	Cc1	694	4898	807	578
TES11	Cc1	844	5307	142	937
TES11	Cc1	578	1340	1080	516
TES11	Cc1	627	2462	421	765
TES11	Cc1	656	1548	706	674
TES11	Cc1	1046	4924	249	1094
TES11	Cc1	872	2963	6	975
TES11	Cc1	897	3713	148	798
TES11	Cc1	911	3329	243	1008
TES11	Cc1	603	2404	635	741
TES21	Cc2	6368	3272	487	922
TES21	Cc2	3109	1245	1371	392
TES21	Cc2	3321	1508	973	511
TES21	Cc2	5380	2488	718	683
TES21	Cc2	3827	1686	754	559
TES21	Cc2	4743	2081	558	760
TES21	Cc2	7496	3546	160	1094
TES21	Cc2	4319	2332	736	526
TES21	Cc2	4035	1934	700	459
TES21	Cc2	5910	2632	374	779
TES21	Cc2	7038	4183	249	1037
TES21	Cc2	3644	1242	872	411
TES21	Cc2	4782	1888	742	545
TES21	Cc2	8469	5030	166	1123
TES21	Cc2	7607	4347	190	832
TES21	Cc2	4261	1323	801	497
TES21	Cc2	6638	3698	255	937
TES21	Cc2	6382	3477	386	856
TES21	Cc2	3745	1649	1056	430
TES21	Cc2	7279	4725	202	937
TES23	Cc2	3827	1640	825	526
TES23	Cc2	8069	4889	184	1071
TES23	Cc2	7920	4454	154	1147
TES23	Cc2	7626	4589	255	980
TES23	Cc2	2916	885	1513	468
TES23	Cc2	8474	4419	77	1071
TES23	Cc2	4989	2649	694	574
TES23	Cc2	6594	4114	410	703
TES23	Cc2	4555	1562	178	813
TES23	Cc2	3418	1663	1490	363
TES23	Cc2	4526	2078	415	769
TES23	Cc2	3736	1459	932	569
TES23	Cc2	8783	5048	131	1047

TES23	Cc2	9106	5592	237	1008
TES23	Cc2	3572	1291	487	473
TES23	Cc2	8493	5716	154	1262
TES23	Cc2	3770	1277	1312	669
TES7	Cc3	34	646	1062	d.l.
TES7	Cc3	d.l.	1032	1733	38
TES7	Cc3	1210	1882	71	583
TES7	Cc3	1499	2831	279	688
TES7	Cc3	1644	3404	261	717
TES7	Cc3	1292	2574	350	683
TES7	Cc3	1620	3269	309	597
TES7	Cc3	1764	4396	d.l.	712
TES7	Cc3	2097	5754	196	894
TES7	Cc3	1099	1917	d.l.	545
TES7	Cc3	1567	3474	540	726
TES7	Cc3	2367	5339	166	1051
TES7	Cc3	1634	3295	487	717
TES7	Cc3	1740	3860	291	803
TES7	Cc3	1229	1268	83	545
TES7	Cc3	1461	3125	291	736
TES7	Cc3	1417	2920	463	636
TES7	Cc3	868	1265	1068	387

Table S3 Elemental composition of the calcite cements Cc1 and Cc2 precipitated in the Puig-reig anticline.

Sample	Type of cement	Fe (ppm)	Mg (ppm)	Sr (ppm)	Mn (ppm)
GP-R1	Cc1	700	1700	d.l.	1300
GP-R1	Cc1	700	1100	600	1400
GP-R1	Cc1	1100	2800	d.l.	1700
GP-R1	Cc1	400	600	500	900
GP-R1	Cc1	1000	1800	d.l.	1700
GP-R1	Cc1	300	1000	d.l.	1000
GP-R1	Cc1	600	1700	d.l.	1300
GP-R1	Cc1	400	800	d.l.	1100
GP-R1	Cc1	400	1000	d.l.	900
GP-R1	Cc1	500	1300	d.l.	1000
GP-R4	Cc1	d.l.	4500	d.l.	1700
GP-R4	Cc1	d.l.	1800	d.l.	1200
GP-R4	Cc1	d.l.	800	d.l.	900
GP-R4	Cc1	400	2100	d.l.	2200
GP-R4	Cc1	d.l.	4300	d.l.	1400
GP-R4	Cc1	d.l.	1600	d.l.	800
GP-R4	Cc1	d.l.	2100	d.l.	900
GP-R4	Cc1	d.l.	4100	d.l.	1500
GP-R4	Cc1	d.l.	4300	d.l.	1500
309A	Cc1	500	2000	600	d.l.
309A	Cc1	d.l.	1100	d.l.	1000
309A	Cc1	d.l.	1200	600	1200
309A	Cc1	0	1200	d.l.	800
309A	Cc1	d.l.	1900	d.l.	1500
309A	Cc1	200	2200	400	800
309A	Cc1	d.l.	800	d.l.	600
309A	Cc1	d.l.	3300	d.l.	1700
309A	Cc1	d.l.	2000	d.l.	1100
309A	Cc1	200	2300	d.l.	1600
311A	Cc1	900	2800	d.l.	1900
311A	Cc1	900	3200	d.l.	1500
311A	Cc1	700	3000	d.l.	1600
311A	Cc1	900	3500	d.l.	1900
311A	Cc1	700	2700	d.l.	2000
311A	Cc1	900	3300	d.l.	1900
311A	Cc1	d.l.	2500	d.l.	1500
311A	Cc1	300	1100	500	800
314D2	Cc1	400	3400	d.l.	2800
314D2	Cc1	300	3600	d.l.	1900
314D2	Cc1	400	2900	600	2200
314D2	Cc1	d.l.	1600	500	1800

314D2	Cc1	d.l.	1800	d.l.	1300
314D2	Cc1	d.l.	3000	d.l.	1700
314D2	Cc1	200	800	d.l.	1300
314D2	Cc1	700	1100	d.l.	1100
GP-R1	Cc2	600	900	1400	1500
GP-R1	Cc2	300	1600	600	1500
GP-R1	Cc2	300	d.l.	3000	1400
GP-R1	Cc2	400	900	2700	1300
GP-R1	Cc2	800	1700	700	1800
GP-R1	Cc2	1000	1700	d.l.	1700
GP-R1	Cc2	800	1200	800	1500
GP-R1	Cc2	600	1000	d.l.	1100
GP-R1	Cc2	600	1400	d.l.	900
GP-R1	Cc2	900	1800	500	1400
GP-R1	Cc2	400	1700	d.l.	300
GP-R1	Cc2	1000	2200	d.l.	1200
GP-R1	Cc2	1000	1900	d.l.	1600
GP-R1	Cc2	1100	1900	d.l.	1700
GP-R1	Cc2	800	2200	500	1200
GP-R1	Cc2	400	500	d.l.	700
311A	Cc2	1000	500	600	1300
311A	Cc2	1300	600	500	1400
311A	Cc2	1300	900	700	1300
311A	Cc2	1000	d.l.	d.l.	1700
311A	Cc2	1000	500	1100	1000
311A	Cc2	1200	d.l.	500	700
311A	Cc2	800	600	800	1100
311A	Cc2	500	2400	d.l.	1200
311A	Cc2	2300	1500	d.l.	2300
311A	Cc2	3200	1900	d.l.	1900
311A	Cc2	2200	1500	d.l.	1700
311A	Cc2	2000	1000	700	1000
311A	Cc2	2200	1400	500	1600
311D	Cc2	1600	900	d.l.	1100
311D	Cc2	1200	1200	d.l.	1000
311D	Cc2	1200	300	d.l.	1400
311D	Cc2	1300	300	d.l.	1400
311D	Cc2	700	500	d.l.	1300
311D	Cc2	1600	600	500	1000
311D	Cc2	1700	900	700	1100
311D	Cc2	1700	600	900	1000
311D	Cc2	1700	700	600	1400
314D2	Cc2	300	d.l.	d.l.	1200
314D2	Cc2	1100	500	d.l.	900
314D2	Cc2	400	800	d.l.	1300

314D2	Cc2	500	d.l.	700	1400
314D2	Cc2	700	d.l.	d.l.	600
314D2	Cc2	500	d.l.	500	700
314D2	Cc2	1400	1200	d.l.	1300

Carbon and oxygen isotopes

Table S4. $\delta^{18}O$ and $\delta^{13}C$ values of the carbonate host rocks and calcite cements Cc1, Cc2 and Cc3 precipitated in the Lower Pedraforca thrust sheet. For the third and fourth columns, the blank spaces represent host rocks which are not affected by fractures and do not contain calcite cement respectively.

Sample	Description	Fracture type	Type of cement	$\delta^{13}C$ PDB	$\delta^{18}O$ PDB
Q1c	Marine grainstone			1.68	-4.48
Q4b	Palustrine limestone			-10.02	-4.87
Q15b	Palustrine limestone			-17.47	-8.20
Q16c	Palustrine limestone			-3.65	-4.77
Q21d	Marine grainstone			1.45	-3.20
Q1b	Calcite shear vein	Strike-slip fault	Cc2	1.21	-5.55
Q3Bc	Calcite shear vein	Strike-slip fault	Cc2	1.58	-5.23
Q3Bb	Calcite shear vein	Strike-slip fault	Cc2	1.04	-9.86
Q8a	Vug Porosity		Cc2	0.84	-5.70
Q20a	Vug Porosity		Cc2	1.07	-4.39
Q20b	Vug Porosity		Cc2	1.17	-6.09
Q20c	Vug Porosity		Cc2	1.15	-7.01
Q21a	Calcite extension vein	Joint	Cc2	1.71	-6.15
Q21b	Calcite extension vein	Joint	Cc2	1.27	-6.69
Q21c	Calcite extension vein	Joint	Cc2	1.49	-5.17
Q3Ba	Calcite shear vein	Strike-slip fault	Cc3	-2.15	-5.50
Q4a	Calcite shear vein	Reverse fault	Cc3	-10.22	-3.87
Q6a	Calcite shear vein	Reverse fault	Cc3	-10.78	-4.06
Q6b	Calcite shear vein	Reverse fault	Cc3	-10.13	-5.95
Q11a	Calcite shear vein	Strike-slip fault	Cc3	-0.38	-4.98
Q11b	Calcite extension vein	Joint	Cc3	-5.97	-2.61
Q12a	Calcite extension vein	Joint	Cc3	-3.69	-5.89
Q13a	Calcite shear vein	Bed-parallel slip surface	Cc3	-4.89	-5.45
Q15a	Calcite shear vein	Strike-slip fault	Cc3	-15.18	-6.77
Q16a	Calcite extension vein	Joint	Cc3	-5.41	-9.21
Q16b	Calcite extension vein	Joint	Cc3	-5.46	-4.89
Q19Aa	Calcite shear vein	Strike-slip fault	Cc3	-1.85	-8.14

Table S5. $\delta^{18}O$ and $\delta^{13}C$ values of the carbonate host rocks and calcite cements Cc2, Cc3, Cc4 and Cc5 precipitated in Vallfogona thrust. For the third and fourth columns, the blank spaces represent host rocks which are not affected by fractures and do not contain calcite cement respectively.

Sample	Description	Fracture type	Type of cement	$\delta^{13}C$ PDB	$\delta^{18}O$ PDB
GDV1d	Marine Marl			-0.26	-6.60
GDV3c	Marine Marl			-2.56	-5.73
GDV26Ac	Marine Marl			-1.57	-4.82
GDV26Bc	Marine Marl			-1.35	-4.72
GDV30c	Marine Marl			-2.20	-6.94
GDB6a	Palustrine carbonate			-2.95	-7.19
GDV20a	Calcite extension vein	Joint	Cc2	-1.13	-5.74
GDV20b	Calcite extension vein	Joint	Cc2	-1.08	-5.75
GDV25a	Vug Porosity		Cc2	-2.64	-4.97
GDV26Aa	Vug Porosity		Cc2	-1.38	-5.49
GDV29Aa	Calcite shear vein	Bed-parallel slip surfacte	Cc2	-1.89	-5.26
GDV29Ab	Calcite shear vein	Bed-parallel slip surfacte	Cc2	-1.70	-4.74
GDB13A	Calcite shear vein	Bed-parallel slip surfacte	Cc2	-2.83	-5.61
GDB15a	Vug Porosity		Cc2	-3.86	-5.21
GDB15b	Calcite shear vein	Reverse fault	Cc2	-2.88	-6.24
GDV1b	Calcite shear vein	Reverse fault	Cc3	-0.70	-6.04
GDV1c	Calcite shear vein	Reverse fault	Cc3	-0.75	-6.83
GDV1e	Calcite shear vein	Reverse fault	Cc3	-0.90	-6.48
GDV5a	Calcite extension vein	Joint	Cc3	-0.80	-6.15
GDV5b	Calcite extension vein	Joint	Cc3	-0.16	-7.55
GDB20a	Calcite shear vein	Reverse fault	Cc3	0.21	-6.81
GDB20b	Calcite shear vein	Reverse fault	Cc3	-0.24	-6.89
GDV1a	Calcite shear vein	Reverse fault	Cc4	-1.54	-7.29
GDV1f	Calcite shear vein	Reverse fault	Cc4	-1.57	-7.34
GDV1g	Calcite shear vein	Reverse fault	Cc4	-1.43	-7.31
GDV3a	Calcite shear vein	Reverse fault	Cc4	-1.57	-6.93
GDV3b	Calcite shear vein	Reverse fault	Cc4	-1.52	-7.12
GDV26Ab	Calcite shear vein	Reverse fault	Cc4	-1.50	-6.79
GDV26Ba	Calcite shear vein	Reverse fault	Cc4	-1.44	-6.74
GDV26Bb	Calcite shear vein	Reverse fault	Cc4	-1.38	-6.91
GDV30a	Calcite shear vein	Strike-slip fault	Cc4	-1.65	-7.01
GDV30b	Calcite shear vein	Strike-slip fault	Cc4	-1.74	-7.03
GDV7a	Calcite shear vein	Strike-slip fault	Cc5	-2.37	-8.29
GDV7b	Calcite shear vein	Strike-slip fault	Cc5	-1.87	-7.79
GDV7c	Calcite shear vein	Strike-slip fault	Cc5	-2.08	-7.56

GDV9a	Calcite shear vein	Strike-slip fault	Cc5	-0.90	-9.08
GDv9b	Calcite shear vein	Strike-slip fault	Cc5	-1.14	-8.76
GDV13a	Calcite shear vein	Reverse fault	Cc5	-2.56	-8.98
GDV13b	Calcite shear vein	Reverse fault	Cc5	-2.33	-9.99
GDV13c	Calcite shear vein	Reverse fault	Cc5	-2.27	-9.49
GDV14a	Calcite shear vein	Reverse fault	Cc5	-2.32	-9.95
GDV14b	Calcite shear vein	Reverse fault	Cc5	-2.28	-9.94
GDV15a	Intergranular porosity		Cc5	-0.57	-7.90
GDV19a	Calcite shear vein	Reverse fault	Cc5	-1.24	-9.44
GDV19b	Calcite shear vein	Reverse fault	Cc5	-1.42	-9.63

Table S6. $\delta^{18}O$ and $\delta^{13}C$ values of the carbonate host rocks and calcite cements Cc1 and Cc2 precipitated in the Abocador thrust. For the third and fourth columns, the blank spaces represent host rocks which are not affected by fractures and do not contain calcite cement respectively.

Sample	Description	Fracture type	Type of cement	$\delta^{13}C$ PDB	$\delta^{18}O$ PDB
TAB7a	Carbonate clast			-1.67	-7.48
TAB7a	Carbonate clast			-1.69	-7.46
TAB11a	Carbonate clast			-0.31	-8.05
TAB11ab	Carbonate clast			-0.32	-7.95
TAB12a	Carbonate clast			0.45	-6.73
TAB16a	Carbonate clast			-0.77	-7.53
TAB16a	Carbonate clast			-0.59	-7.42
TAB17a	Carbonate clast			-0.47	-7.09
TAB17a	Carbonate clast			-0.42	-7.13
TAB1a	Calcite shear vein	Reverse fault	Cc1	-2.56	-8.60
TAB2a	Calcite shear vein	Reverse fault	Cc1	-2.72	-7.66
TAB4a	Calcite extension vein	Joint	Cc1	-2.17	-7.97
TAB6a	Calcite shear vein	Strike-slip fault	Cc1	-2.05	-7.61
TAB7b	Calcite shear vein	Reverse fault	Cc1	-1.81	-7.92
TAB7c	Calcite shear vein	Reverse fault	Cc1	-1.74	-7.84
TAB9b	Calcite shear vein	Reverse fault	Cc1	-1.61	-7.78
TAB9c	Calcite shear vein	Reverse fault	Cc1	-1.32	-8.12
TAB9c	Calcite shear vein	Reverse fault	Cc1	-2.28	-8.75
TAB11c	Calcite shear vein	Reverse fault	Cc1	-1.89	-8.34
TAB12b	Calcite extension vein	Joint	Cc1	-1.81	-7.80
TAB12b	Calcite extension vein	Joint	Cc1	-1.75	-7.85
TAB12c	Calcite shear vein	Reverse fault	Cc1	-0.42	-9.08
TAB13a	Calcite shear vein	Reverse fault	Cc1	-1.21	-7.93
TAB14a	Calcite shear vein	Reverse fault	Cc1	-1.09	-7.96
TAB14b	Calcite shear vein	Reverse fault	Cc1	-1.11	-7.88
TAB14c	Calcite shear vein	Reverse fault	Cc1	-1.08	-7.71
TAB15a	Calcite shear vein	Reverse fault	Cc1	-1.19	-8.01
TAB16b	Calcite extension vein	Joint	Cc1	-1.37	-7.97
TAB16c	Calcite extension vein	Joint	Cc1	-1.34	-8.11
TAB16c	Calcite extension vein	Joint	Cc1	-1.35	-8.19
TAB16d	Calcite extension vein	Joint	Cc1	-1.54	-8.44
TAB17b	Calcite extension vein	Joint	Cc1	-1.16	-7.79
TAB17c	Calcite extension vein	Joint	Cc1	-0.83	-7.41
TAB18Aa	Calcite shear vein	Strike-slip fault	Cc1	-1.19	-8.77
TAB18Ab	Calcite extension vein	Joint	Cc1	-1.08	-8.00
TAB18Ba	Calcite extension vein	Joint	Cc1	-1.11	-8.81
TAB18Bb	Calcite shear vein	Strike-slip fault	Cc1	-1.05	-8.01
TAB3a	Calcite shear vein	Reverse fault	Cc2	-4.19	-6.78
TAB3a	Calcite shear vein	Reverse fault	Cc2	-4.05	-6.90

TAB5a	Calcite shear vein	Reverse fault	Cc2	-2.14	-7.75
TAB8a	Calcite shear vein	Reverse fault	Cc2	-1.94	-4.98
TAB9a	Calcite shear vein	Reverse fault	Cc2	-1.54	-5.17
TAB10a	Calcite shear vein	Reverse fault	Cc2	-2.82	-6.34
TAB11b	Calcite shear vein	Reverse fault	Cc2	-1.46	-5.15
TAB11b	Calcite shear vein	Reverse fault	Cc2	-1.47	-5.20

Table S7. $\delta^{18}O$ and $\delta^{13}C$ values of the carbonate host rocks and calcite cements Cc1, Cc2 and Cc3 precipitated in the L'Escala thrust. For the third and fourth columns, the blank spaces represent host rocks which are not affected by fractures and do not contain calcite cement respectively.

Sample	Description	Fracture type	Type of cement	$\delta^{13}C$ PDB	$\delta^{18}O$ PDB
TES17b	Carbonate clast			0.00	-6.50
TES18b	Carbonate clast			-0.80	-7.40
TES19b	Carbonate clast			-0.70	-7.10
TES21b	Carbonate clast			-0.30	-6.70
TES1a	Calcite shear vein	Bed-parallel slip surface	Cc1	-2.10	-8.80
TES4a	Calcite shear vein	Reverse fault	Cc1	-3.10	-8.30
TES5a	Calcite extension vein	Joint	Cc1	-2.80	-8.50
TES7a	Calcite extension vein	Joint	Cc1	-1.90	-8.30
TES8a	Calcite shear vein	Reverse fault	Cc1	-2.30	-8.60
TES9a	Calcite shear vein	Reverse fault	Cc1	-2.20	-8.50
TES11a	Calcite shear vein	Bed-parallel slip surface	Cc1	-2.50	-8.50
TES12a	Calcite shear vein	Bed-parallel slip surface	Cc1	-2.40	-8.70
TES17a	Calcite shear vein	Strike-slip fault	Cc2	-0.60	-9.50
TES21a	Calcite shear vein	Strike-slip fault	Cc2	-0.50	-9.20
TES23a	Calcite shear vein	Strike-slip fault	Cc2	-0.60	-9.30
TES18a	Calcite extension vein	Joint	Cc3	-4.00	-12.60
TES19a	Calcite extension vein	Joint	Cc3	-3.10	-14.40

Strontium isotopes

Table S8. $^{87}Sr/^{86}Sr$ values of carbonate host rocks and calcite cements Cc2, Cc3, Cc4 and Cc5 precipitated in the Vallfogona thrust. For the third and fourth columns, the blank spaces represent host rocks which are not affected by fractures and do not contain calcite cement respectively.

Sample	description	Fracture Type	Type of cement	$^{87}Sr/^{86}Sr$
GDV1i	Marine marl			0.7086026
GDV22a	Marine marl			0.7080593
GDV20c	Calcite extension vein	Joint	Cc2	0.7081918
GDV25b	Vug porosity		Cc2	0.7081336
GDV26Ae	Vug porosity		Cc2	0.7080600
GDV1h	Calcite shear vein	Reverse fault	Cc3	0.7082869
GDV5c	Calcite extension vein	Joint	Cc3	0.7079360
GDV5d	Calcite extension vein	Joint	Cc3	0.7081716
GDV26Ad	Calcite shear vein	Reverse fault	Cc4	0.7081378
GDV7c	Calcite shear vein	Strike-slip fault	Cc5	0.7092587
GDV13d	Calcite shear vein	Reverse fault	Cc5	0.7093333

Table S9. $^{87}Sr/^{86}Sr$ values of carbonate host rocks and calcite cements Cc1, Cc2 and Cc3 precipitated in the L'Escala thrust. For the third and fourth columns, the blank spaces represent host rocks which are not affected by fractures and do not contain calcite cement respectively.

Sample	Description	Fracture Type	Type of cement	$^{87}Sr/^{86}Sr$
TES19b	Carbonate clast			0.708952
TES5	Calcite extension vein	Joint	Cc1	0.708179
TES4	Calcite shear vein	Reverse fault	Cc1	0.708165
TES9	Calcite shear vein	Reverse fault	Cc1	0.708171
TES11	Calcite shear vein	Bed-parallel slip surface	Cc1	0.708189
TES21	Calcite shear vein	Strike-slip fault	Cc2	0.708572
TES19a	Calcite extension vein	Joint	Cc3	0.708470

Annex 3: Data repository from Chapter 6.

GSA Data Repository

U-Pb geochronology applied to fracture-filling calcite cements to decipher emplacement and reactivation of south Pyrenean thrust sheets

D. Cruset[1], J. Vergés[2], R. Albert[3], A. Gerdes[3], A. Benedicto[4], I. Cantarero[1], A. Travé[1]

[1] Departament de Mineralogia, Petrologia i Geologia Aplicada, Facultat de Ciències de la Terra, Universitat de Barcelona (UB), Martí i Franquès s/n, 08028, Barcelona, Spain.
[2] Institut de Ciències de la Terra Jaume Almera, ICTJA-CSIC, Lluís Solé i Sabaris s/n, 08028 Barcelona, Spain.
[3] Department of Geosciences, Goethe University Frankfurt, 60438 Frankfurt am Main, Germany.
[4] UMR Geops, Université Paris Sud, 91405 Orsay, France.

U-Pb of calcite and dolomite method

The applied method is similar to that previously described by Ring and Gerdes (2016) and Burisch et al. (2017). U-Pb ages were acquired in situ in 35 polished mounds (2 cm thick) from 66 hand samples of calcite and dolomite by laser ablation-inductively coupled plasma-mass spectrometry (LA-ICP-MS) at Goethe University Frankfurt, using a modified method described in Gerdes and Zeh (2006, 2009). A ThermoScientific Element 2 sector field ICP-MS was coupled to a Resolution S-155 (Resonetics) 193nm ArF excimer laser (CompexPro 102) equipped with a two-volume ablation cell (Laurin Technic). Samples were ablated in a helium atmosphere (0.3 L min-1) and mixed in the ablation funnel with 0.9 L min-1 argon and 0.05 L min-1 nitrogen. Signal strength at the ICP-MS was tuned for maximum sensitivity while keeping oxide formation (monitored as $^{248}ThO/^{232}Th$) below 0.2% and no fractionation of the Th/U ratio. Static ablation used a spot size of 213 µm and a fluence of about 2 J cm^{-2} at 12 Hz. This yielded for National Institute of Standards and Technology Standard Reference Material-614 (NIST SRM-614) a depth penetration of ~0.6 $µms^{-1}$ and an average sensitivity of 350,000 c/s $µg^{-1}$ for ^{238}U. The detection limit for ^{206}Pb and ^{238}U was ~0.2 and 0.03 ppb, respectively.

Data were acquired in fully automated mode overnight in three sequences of 598 analyses each one. Each analysis consists of 20 s background acquisition followed by 20 s of sample ablation and 25 s washout. During 40 s of data acquisition, the signal of ^{206}Pb, ^{207}Pb. ^{208}Pb, ^{232}Th and ^{238}U were detected by peak jumping in pulse counting mode with a total integration time of 0.1s, resulting in 400 mass scans. Prior to analysis each spot was pre-ablated for 3 s to remove surface contamination. Soda-lime glass NIST SRM-614 was used as a reference glass together with two carbonate standards to bracket sample analysis.

Raw data were corrected offline using an in-house VBA spreadsheet program (Gerdes and Zeh, 2006, 2009). Following background correction, outliers (±2σ) were rejected based on the

time-resolved $^{207}Pb/^{206}Pb$ and $^{206}Pb/^{238}U$ ratios. The mean $^{207}Pb/^{206}Pb$ ratio of each analysis was corrected for mass bias 0.3% and the $^{206}Pb/^{238}U$ ratio for interelement fractionation (~5%), including drift over the sequence time, using NIST SRM-614. Due to the carbonate matrix, additional offset factors of 1.061 in seq1 and 0.963 in seq2 have been applied, which was determined using WC-1 carbonate reference material (Roberts et al., 2017). The $^{206}Pb/^{238}U$ fractionation during 20s depth profiling was estimated to be 3%, based on the common Pb corrected WC-1 analyses, and has been applied as an external correction to all carbonate analyses. Repeated analyses of a Zechstein dolomite (Gypsum pit, Tettenborn, Germany) used as secondary (in-house) standard yielded a lower intercept age of 259.5 ± 5.2 Ma (MSWD = 0.99 and n = 17) for sequence 1 and 255.3 ± 5.8 Ma (MSWD = 1.4 and n = 18) for sequence 2. A stromatolitic limestone from the Cambrian-Precambrian boundary in South-Namibia, analysed during sequence 2, yielded a lower intercept ages of 543.8 ± 5.3 Ma (MSWD = 1.4). This is within uncertainty identical to the U/Pb zircon age of 543 ± 1 Ma from the directly overlying ash layer (Spitskopf formation; Bowring et al., 1993). Altogether the data imply an accuracy and repeatability of the method of ~2% or better. The analytical results are presented in Table DR2. Data were plotted in Tera-Wasserburg diagrams Fig. DR2 and ages calculated as lower intercepts using Isoplot 3.71 (Ludwig, 2009). All uncertainties are reported at the 2σ level.

Repository data references

Bowring, S.A., Grotzinger, J.P., Isachsen, C.E., Knoll, A.H., Pelechaty, S.M., and Kolosov, P., 102 1993, Calibrating Rates of Early Cambrian Evolution: Science, v. 261, p. 1293–1298.

Burisch, M., Gerdes, A., Walter, B.F., Neumann, U., Fettel, M., and Markl, G., 2017, Methane and the origin of five-element veins: Mineralogy, age, fluid inclusion chemistry and ore forming processes in the Odenwald, SW Germany: Ore Geology Reviews, v. 81, p. 42–61.

Gerdes, A., and Zeh, A., 2006, Combined U–Pb and Hf isotope LA-(MC-)ICP-MS analyses of detrital zircons: Comparison with SHRIMP and new constraints for the provenance and age of an Armorican metasediment in Central Germany: Earth and Planetary Science Letters, v. 249, p. 47–61, doi: 10.1016/j.epsl.2006.06.039.

Gerdes, A., and Zeh, A., 2009, Zircon formation versus zircon alteration — New insights from combined U–Pb and Lu–Hf in-situ LA-ICP-MS analyses, and consequences for the interpretation of Archean zircon from the Central Zone of the Limpopo Belt: Chemical Geology, v. 261, p. 230–243, doi: 10.1016/j.chemgeo.2008.03.005.

Ludwig, K.R., 2009, Isoplot/Ex Ver 3.71: A geochronological toolkit for Microsoft Excel: Berkeley Geochronology Center Special Publications,.

Ring, U., and Gerdes, A., 2016, Kinematics of the Alpenrhein-Bodensee graben system in the Central Alps: Oligocene/Miocene transtension due to formation of the Western Alps arc: Tectonics, v. 35, p. 1367–1391, doi: 10.1002/2015TC004085.

Roberts, N.M.W., Rasbury, E.T., Parrish, R.R., Smith, C.J., Horstwood, M.S.A., and Condon,D.J., 2017, A calcite reference material for LA-ICP-MS U-Pb geochronology: Geochemistry, Geophysics, Geosystems, v. 18, p. 2807–2814.

Table DR1: Description and field images of samples

Bóixols – Upper Pedraforca thrust sheet

Sample	Location	Description	Host rock	Age
Bx1a	42° 9'55.90"N 1° 9'38.96"E	E-W sub-vertical calcite vein	Upper Cretaceous limestones	No

Sample	Location	Description	Host rock	Age
Bx5	42° 9'56.73"N 1° 9'39.25"E	Calcite within reverse fault	Upper Cretaceous limestones	Yes

Sample	Location	Description	Host rock	Age
Bx10	42°10'9.17"N 1° 9'47.38"E	Calcite within normal fault	Jurassic limestones	No

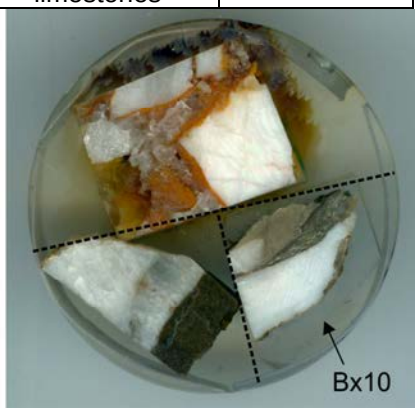

Sample	Location	Description	Host rock	Age
Bx11	42°10'25.48"N 1° 9'55.30"E	Calcite within strike-slip fault	Lower Cretaceous limestones	No

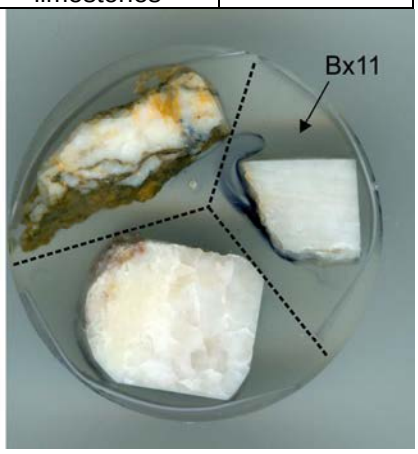

Sample	Location	Description	Host rock	Age
Bx16	42°10'24.90"N 1° 9'55.47"E	E-W calcite veins	Lower Cretaceous limestones	Yes

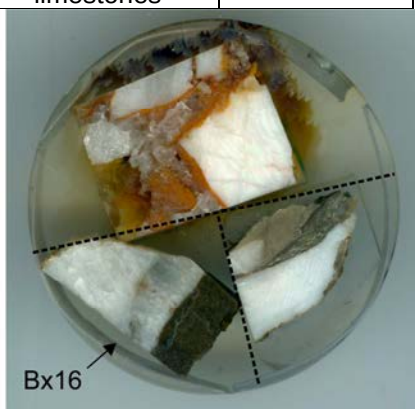

Sample	Location	Description	Host rock	Age
Bx33	42°11'29.08"N 0°57'27.28"E	Calcite within strike-slip fault	Upper Cretaceous marls and limestones	Yes

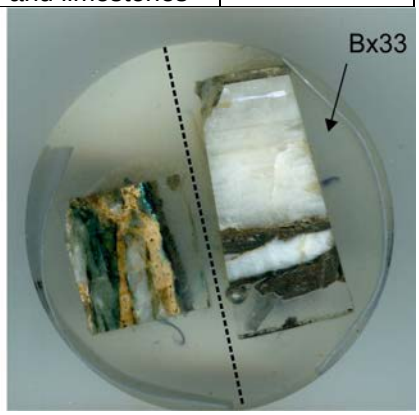

Sample	Location	Description	Host rock	Age
CN15	42°10'36.18"N 1°18'24.18"E	Calcite within strike-slip fault	Upper Cretaceous limestones	No

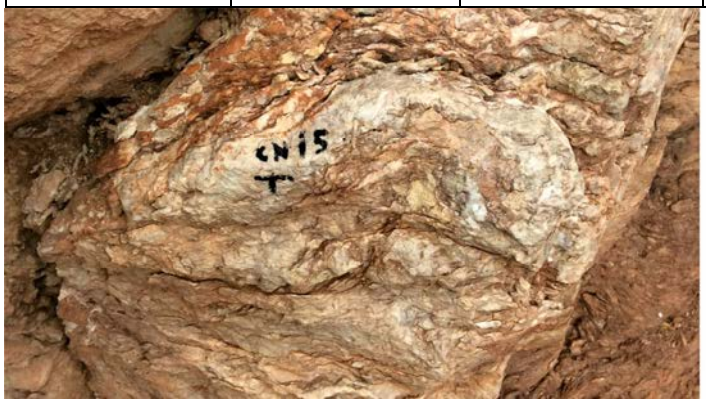

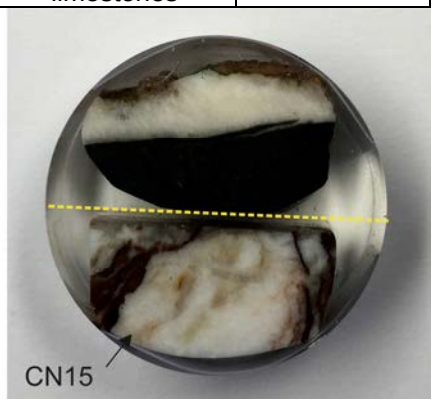

Sample	Location	Description	Host rock	Age
CN20	42°10'33.65"N 1°18'12.63"E	NW-SE calcite vein	Paleocene limestones	No

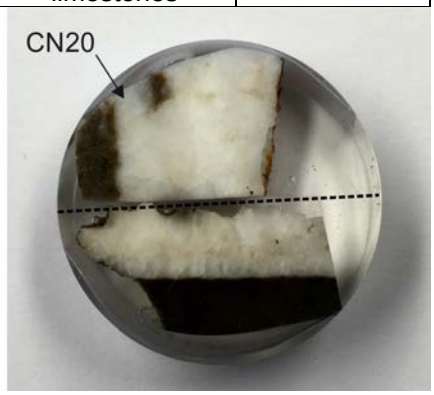

Sample	Location	Description	Host rock	Age
CN33	42°10'39.31"N 1°18'59.17"	NE-SW calcite vein	Lower Cretaceous limestones	No

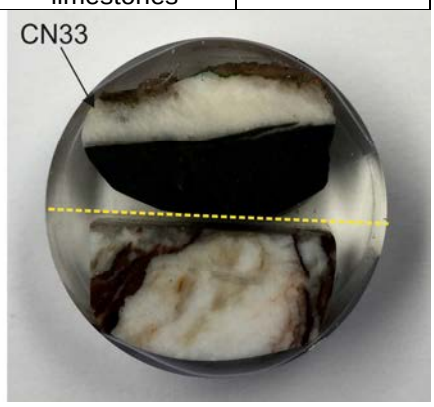

Sample	Location	Description	Host rock	Age
CN38	42°10'39.52"N 1°18'14.41"E	NW-SE calcite vein	Lower Cretaceous limestones	Yes

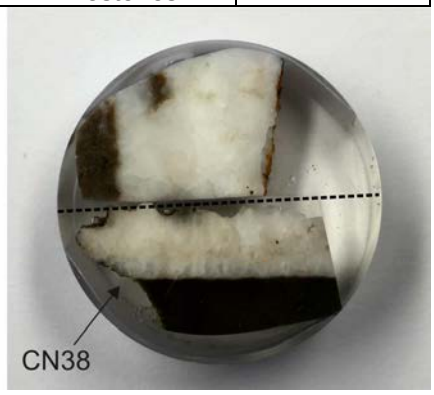

Sample	Location	Description	Host rock	Age
MGT9	42°11'53.57"N 1° 2'11.19"E	Calcite within normal fault	Lower Cretaceous limestones	Yes

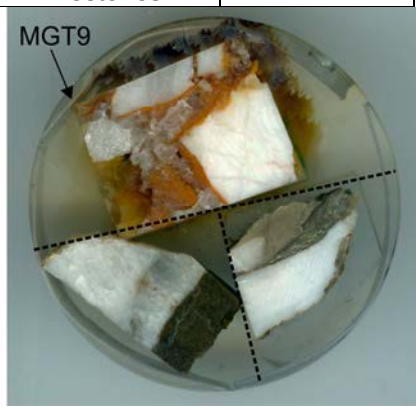

Sample	Location	Description	Host rock	Age
P2	42°14'50.15"N 1°42'18.21"E	Calcite within strike-slip fault	Upper Cretaceous limestones	Yes

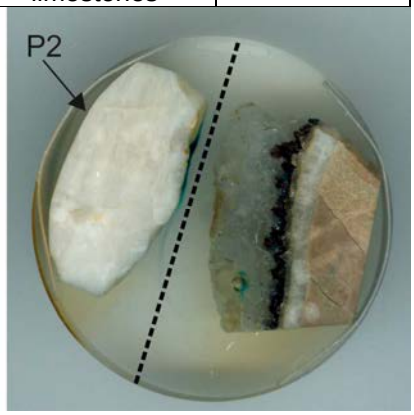

Sample	Location	Description	Host rock	Age
P4	42°14'50.15"N 1°42'18.21"E	Hydraulic breccia cemented by calcite	Upper Cretaceous limestones	Yes

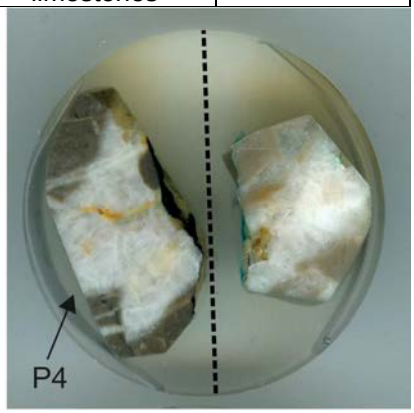

Sample	Location	Description	Host rock	Age
P8	42°14'39.87"N 1°41'52.75"E	N-S calcite vein	Lower Jurassic limestones	Yes

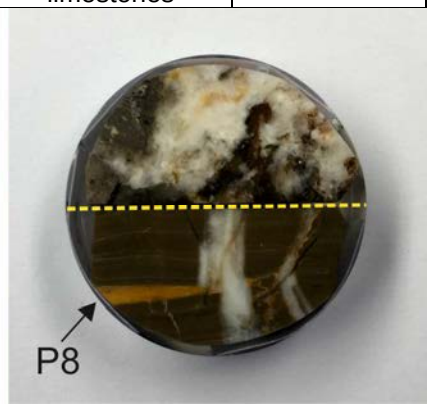

Sample	Location	Description	Host rock	Age
P9	42°14'39.62"N 1°41'52.82"E	Calcite within breccia	Lower Jurassic Breccias	Yes

Sample	Location	Description	Host rock	Age
P12	42°13'35.72"N 1°42'41.08"E	Calcite within strike-slip fault	Upper Cretaceous Breccias	Yes

Sample	Location	Description	Host rock	Age
P14	42°13'35.47"N 1°42'41.62"	Calcite within strike-slip fault	Upper Cretaceous marls	Yes

Sample	Location	Description	Host rock	Age
P44	42°13'14.60"N 1°41'12.57"E	N-S calcite vein	Upper Cretaceous siltstones	Yes

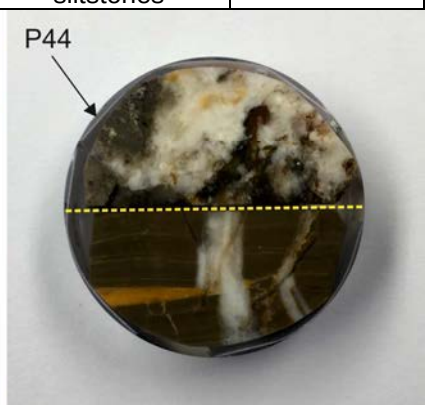

Sample	Location	Description	Host rock	Age
P21	42°14'59.03"N 1°39'5.60"E	Calcite within reverse fault	Lower Cretaceous breccias	Yes

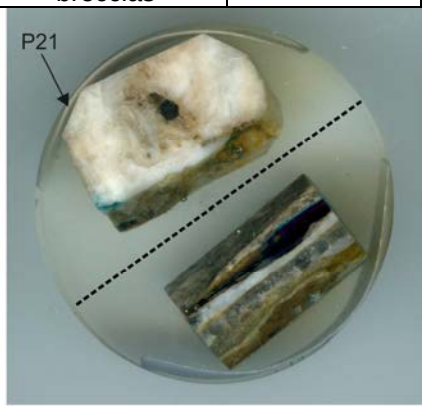

Sample	Location	Description	Host rock	Age
P24	42°14'58.92"N 1°39'14.55"E	N-S dolomite vein predating N-S calcite vein	Upper Jurassic dolostones	Yes

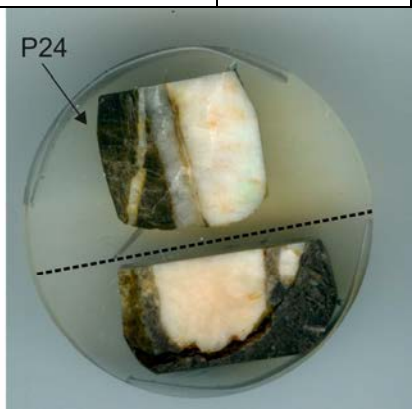

Sample	Location	Description	Host rock	Age
P63	42°14'31.10"N 1°41'55.27"E	Karst cavity	Lower Cretaceous breccias	Yes

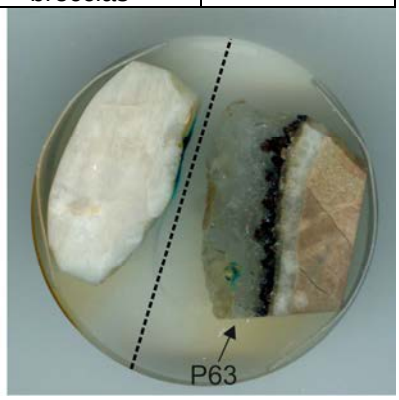

Sample	Location	Description	Host rock	Age
P69	42°14'59.09"N 1°39'6.44"E	Calcite within WSW-ENE reverse fault	Lower Cretaceous breccias	No

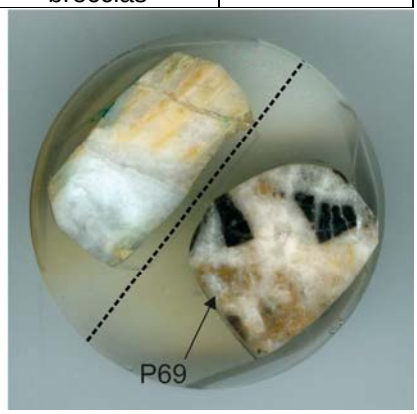

Sample	Location	Description	Host rock	Age
P75A	42°14'59.03"N 1°39'13.20"E	Bed-parallel dolomite vein	Upper Jurassic dolostones	No

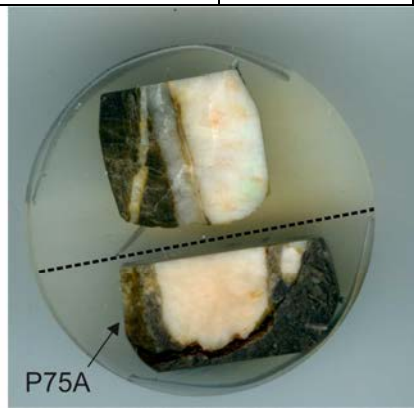

Sample	Location	Description	Host rock	Age
P82A and B	42°14'59.00"N 1°39'11.84"E	Calcite within E-W normal fault	Lower Cretaceous breccias	No

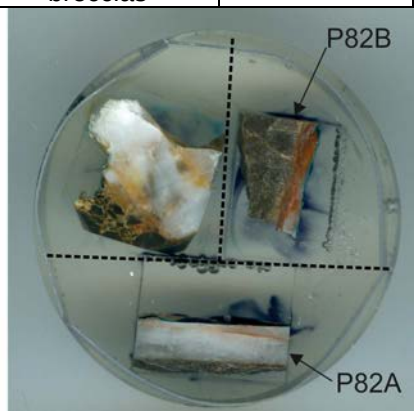

Sample	Location	Description	Host rock	Age
P86	42°14'54.16"N 1°38'52.10"E	Calcite within E-W reverse fault	Lower Cretaceous breccias	No

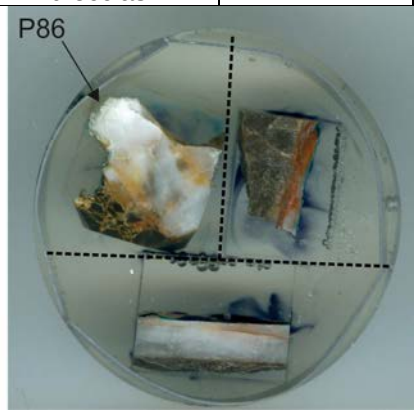

Lower Pedraforca thrust sheet

Sample	Location	Description	Host rock	Age
EST2	42°15'27.89"N 1°41'15.31"E	Calcite within NNW-SSE normal fault	Oligocene conglomerates	Yes

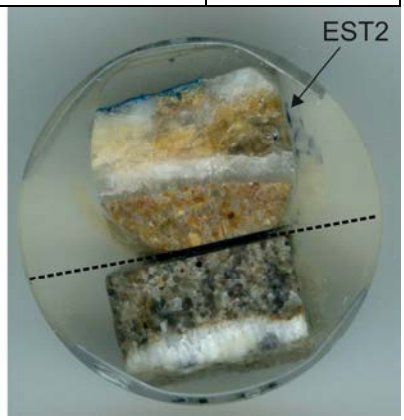

Sample	Location	Description	Host rock	Age
G3	42° 7'55.99"N 1°51'45.57"E	N-S calcite vein	Lower Jurassic limestones	Yes

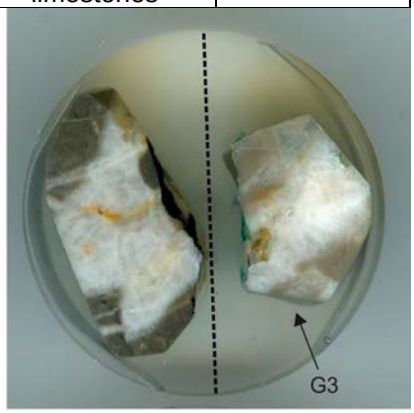

Sample	Location	Description	Host rock	Age
G4	42° 7'56.49"N 1°51'47.59"E	Calcite within strike-slip fault	Upper Cretaceous limestones	No

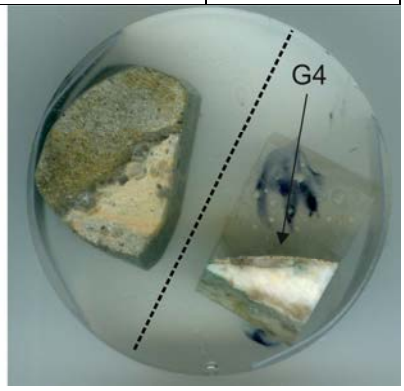

Sample	Location	Description	Host rock	Age
G15	42°14'16.70"N 1°51'55.89"E	Calcite within reverse fault	Lower Jurassic limestones	Yes

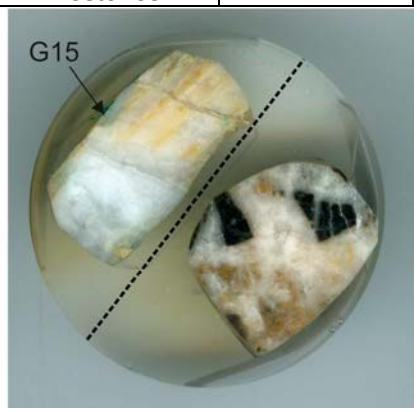

Sample	Location	Description	Host rock	Age
PEG1	42° 9'52.60"N 1°45'37.50"E	Calcite within reverse fault	Paleocene limestones	No

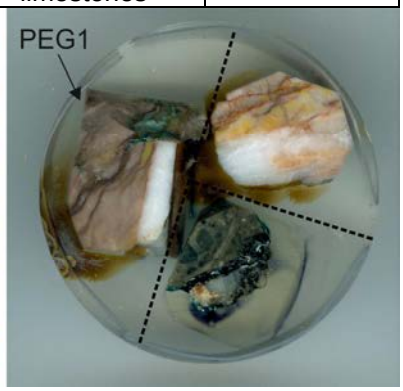

Sample	Location	Description	Host rock	Age
PEG4	42° 9'52.60"N 1°45'37.50"E	Calcite within reverse fault	Paleocene limestones	No

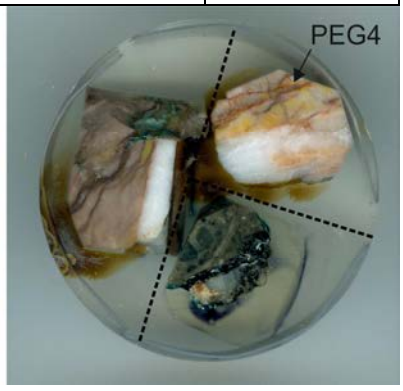

Sample	Location	Description	Host rock	Age
Q3-1 and Q3-2	42° 6'37.28"N 1°49'27.69"E	Calcite within reverse fault	Upper Cretaceous limestones	Q3-1 = Yes Q3-2 = No

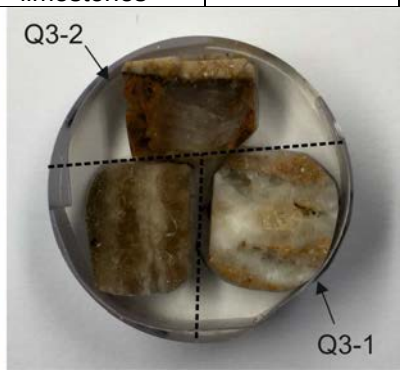

Sample	Location	Description	Host rock	Age
Q11	42° 6'26.46"N 1°49'35.42"E	E-W calcite vein	Middle Eocene sandstones	Yes

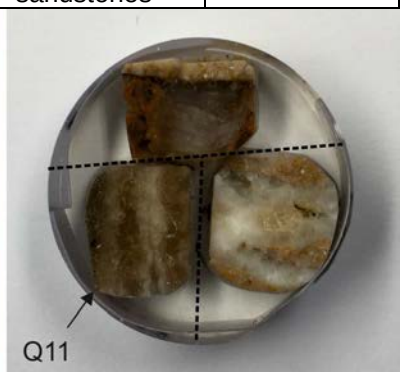

Sample	Location	Description	Host rock	Age
Q24	42° 7'0.88"N 1°50'34.71"E	Calcite within reverse fault	Upper Cretaceous limestones	Yes

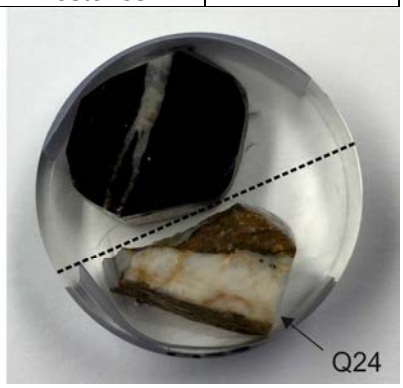

Sample	Location	Description	Host rock	Age
Q27	42° 6'38.01"N 1°49'26.53"E	N-S calcite vein	Upper Cretaceous limestones	Yes

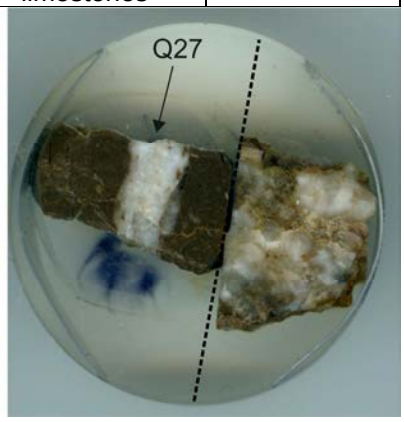

Sample	Location	Description	Host rock	Age
Q29	42° 7'5.30"N 1°50'38.26"E	Calcite within reverse fault	Upper Cretaceous limestones	Yes

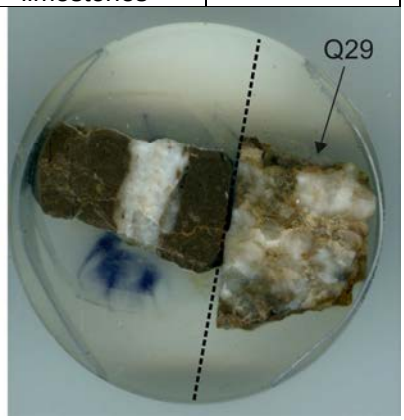

Sample	Location	Description	Host rock	Age
Q33	42° 6'26.26"N 1°49'35.74"E	N-S calcite vein	Middle Eocene sandstones	Yes

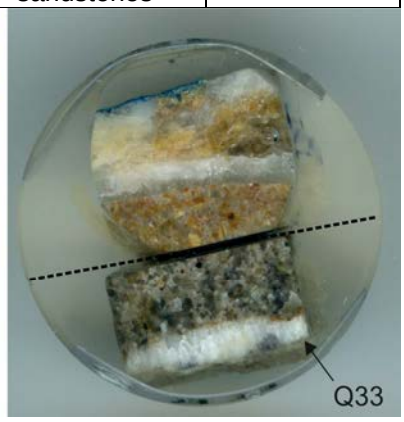

Cadí thrust sheet

Sample	Location	Description	Host rock	Age
B2	42°16'4.45"N 1°51'5.53"E	E-W calcite veins and vug porosity	Middle Eocene limestones	Yes

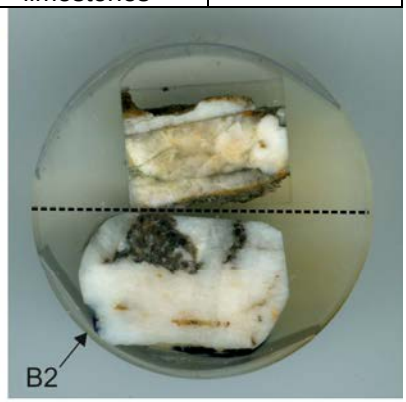

Sample	Location	Description	Host rock	Age
B1	42°16'4.45"N 1°51'5.53"E	N-S calcite vein	Lower Eocene limestones	No

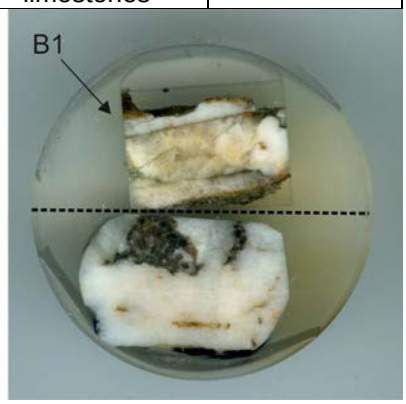

Sample	Location	Description	Host rock	Age
B22	42°15'43.66"N 1°52'24.92"E	E-W calcite vein	Lower Eocene limestones	Yes

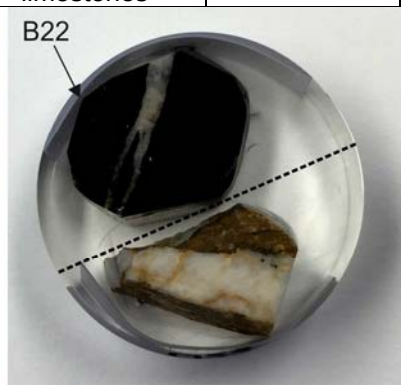

Sample	Location	Description	Host rock	Age
B24	42°15'43.67"N 1°52'24.47"E	E-W calcite vein	Lower Eocene limestones	No

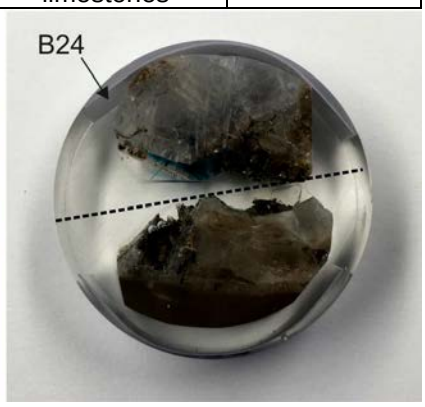

Sample	Location	Description	Host rock	Age
B32	42°15'34.75"N 1°51'59.95"E	N-S calcite vein	Lower Eocene limestones	Yes

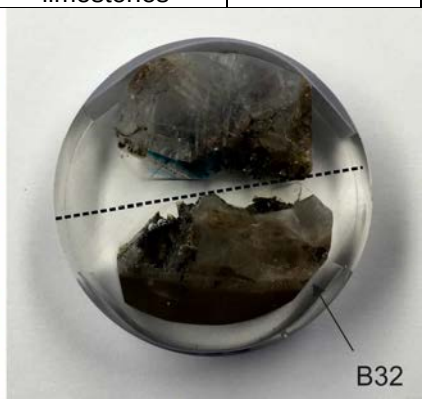

Sample	Location	Description	Host rock	Age
B45	42°16'3.65"N 1°51'5.22"E	Calcite within strike-slip fault	Lower Eocene limestones	No

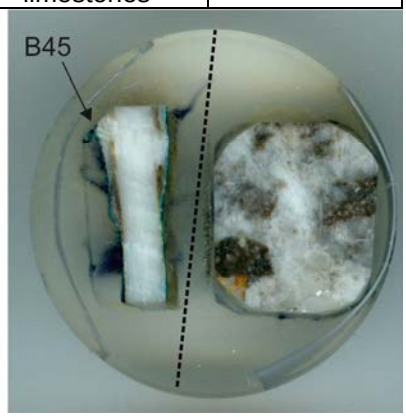

Sample	Location	Description	Host rock	Age
B46	42°15'55.18"N 1°51'1.34"E	N-S calcite vein	Lower Eocene limestones	Yes

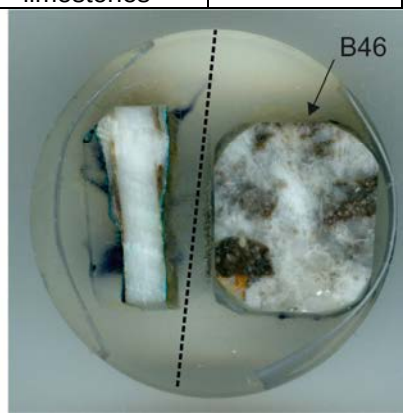

Sample	Location	Description	Host rock	Age
B54	42°15'52.14"N 1°51'4.54"E	N-S calcite vein	Lower Eocene limestones	Yes

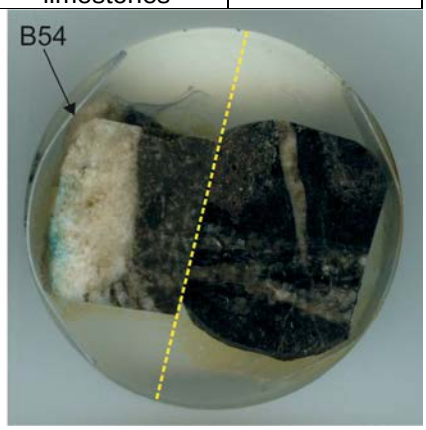

Sample	Location	Description	Host rock	Age
GDV5	42°7'49.04"N 1°54'1.88"E	Calcite within reverse fault	Lower Eocene marls	Yes

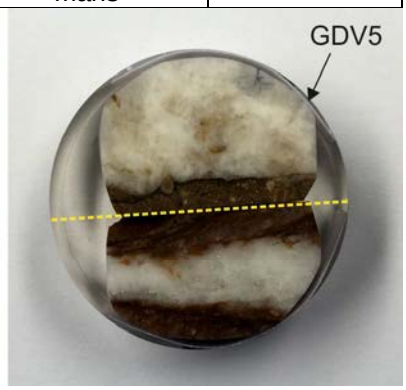

Sample	Location	Description	Host rock	Age
GDV13	42° 7'47.45"N 1°53'59.15"E	Calcite within reverse fault	Oligocene sandstones	No

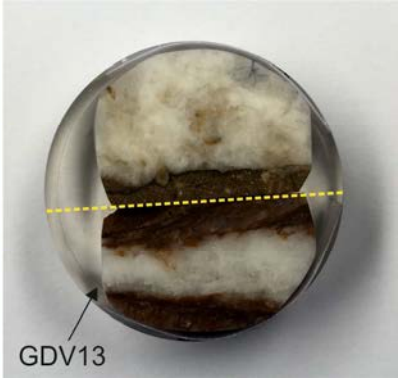

Sample	Location	Description	Host rock	Age
B57	42°15'43.95"N 1°52'24.76"E	N-S and E-W calcite veins	Lower Eocene limestones	Yes

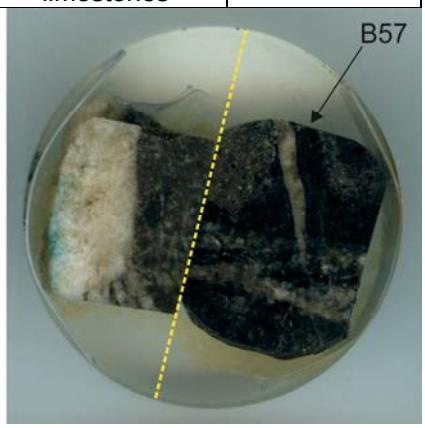

Sample	Location	Description	Host rock	Age
GDV26	42° 7'49.33"N 1°54'2.79"E	Calcite within strike-slip fault	Lower Eocene marls	No

Sample	Location	Description	Host rock	Age
GIS1	42°15'58.35"N 1°44'33.28"E	E-W calcite vein	Lower Eocene marls	Not analyzed

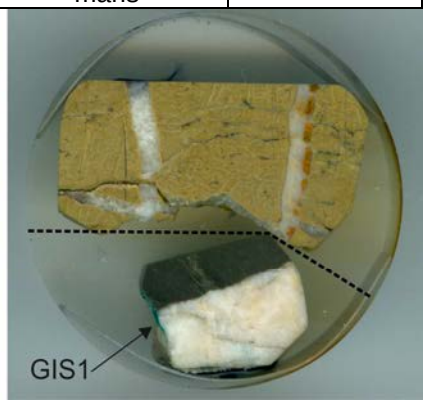

Sample	Location	Description	Host rock	Age
GIS4	42°16'10.42"N 1°42'29.96"E	N-S calcite vein	Lower Eocene marls	Yes

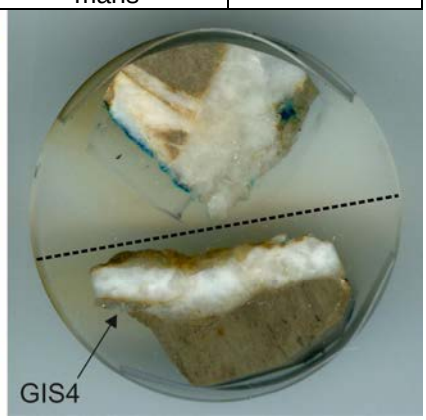

Sample	Location	Description	Host rock	Age
GIS10A	42°15'56.29"N 1°41'36.05"E	N-S and E-W calcite veins	Lower Eocene marls	Yes

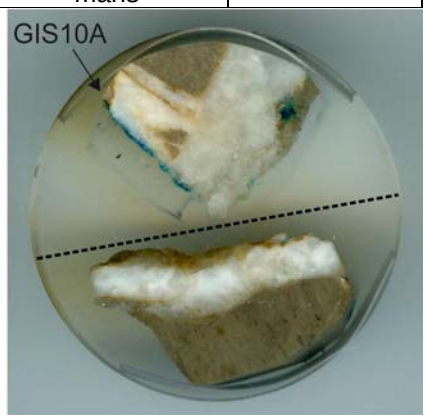

Sample	Location	Description	Host rock	Age
PA9	42°17'53.69"N 1°42'49.66"E	N-S and E-W calcite veins	Upper Cretaceous limestones	No

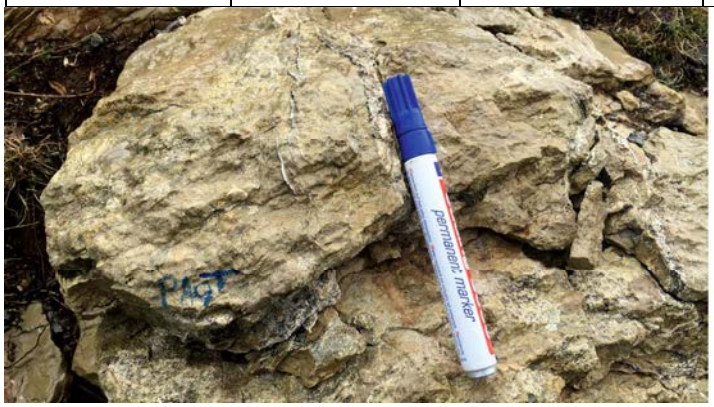

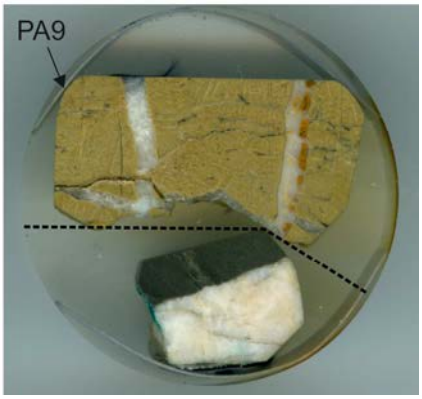

Sample	Location	Description	Host rock	Age
PA12	42°17'53.97"N 1°42'57.09"E	Calcite within reverse fault	Upper Cretaceous limestones	Yes

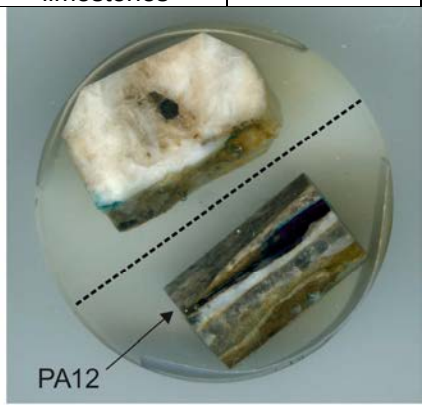

Ebro Basin

Sample	Location	Description	Host rock	Age
309B	42° 4'8.05"N 1°34'14.09"E	Calcite within strike-slip fault	Oligocene sandstones	No

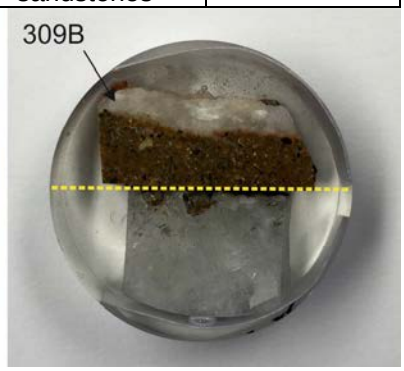

Sample	Location	Description	Host rock	Age
311A	42° 3'54.91"N 1°34'9.26"E	Calcite within strike-slip fault	Oligocene sandstones	No

Sample	Location	Description	Host rock	Age
GPR401	42° 3'54.91"N 1°34'9.26"E	Calcite within fault breccia	Oligocene sandstones	Yes

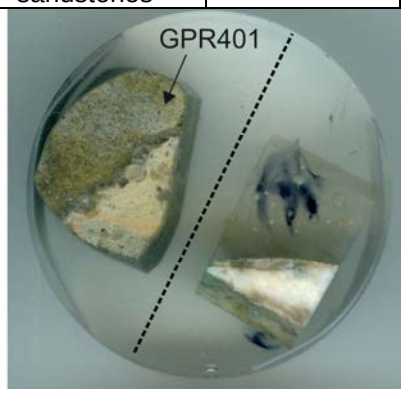

Axial Zone

Sample	Location	Description	Host rock	Age
C8	42°20'12.45"N 1°29'57.58"E	Calcite within reverse fault	Devonian limestones	No

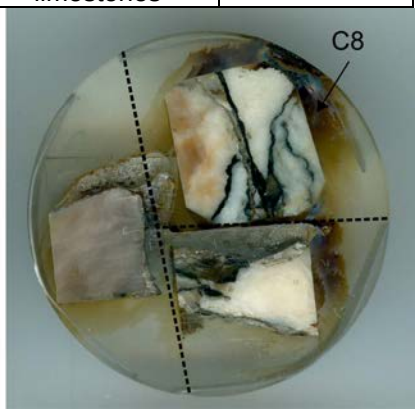

Sample	Location	Description	Host rock	Age
C9	42°20'12.45"N 1°29'57.58"E	Calcite within reverse fault	Devonian limestones	No

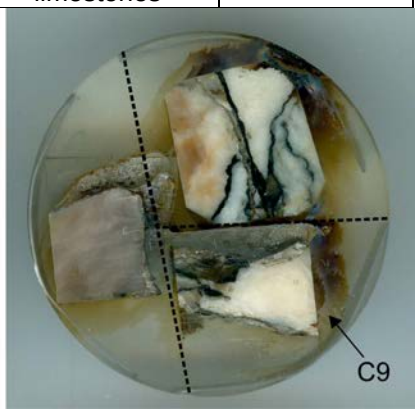

Sample	Location	Description	Host rock	Age
C10	42°20'12.45"N 1°29'57.58"E	N-S calcite vein	Permian volcanic rocks	No

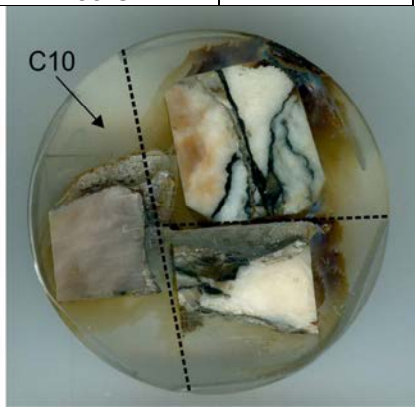

Sample	Location	Description	Host rock	Age
C12	42°20'12.45"N 1°29'57.58"E	E-W calcite vein	Permian volcanic rocks	Yes

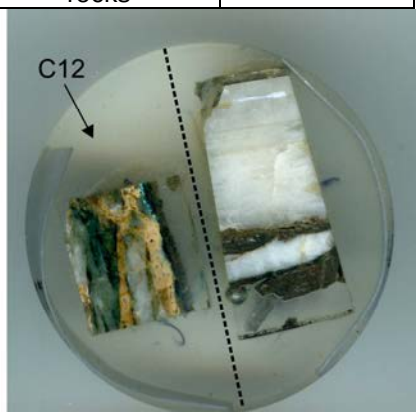

Sample	Location	Description	Host rock	Age
Est-2	42°21'37.16"N 1°31'5.31"E	Calcite within reverse fault	Permian¿? volcanic rocks	No

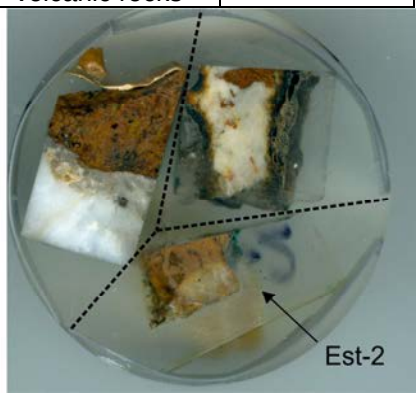

Sample	Location	Description	Host rock	Age
Est-8	42°21'34.91"N 1°31'8.19"E	Calcite within reverse fault	Devonian limestones	No

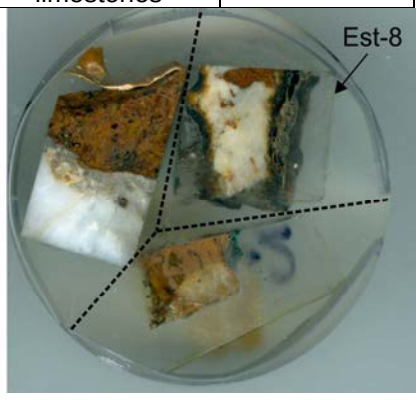

Sample	Location	Description	Host rock	Age
MAI2	42°32'43.83"N 1°43'11.37"E	Calcite within reverse fault	Devonian limestones	No

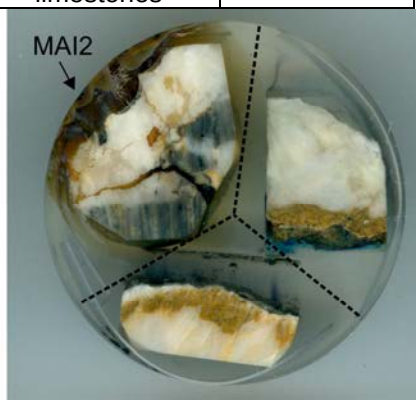

Sample	Location	Description	Host rock	Age
MAI3	42°32'43.91"N 1°43'11.58"E	Calcite within reverse fault	Devonian limestones	No

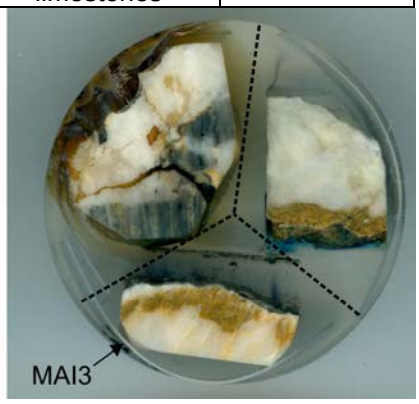

Sample	Location	Description	Host rock	Age
MAI4	42°32'43.69"N 1°43'11.01"E	Calcite within reverse fault	Devonian limestones	No

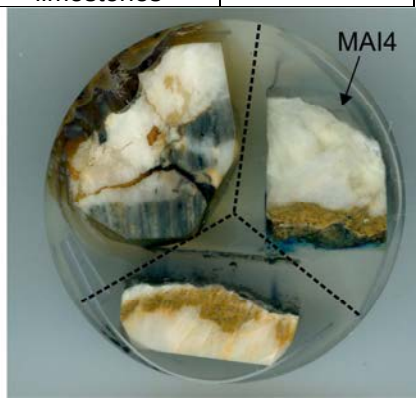

Table DR2: U-Pb calcite and dolomite ages

Sample	Structure	Age (Ma)	± 2σ	MSWD	Number of spots
Bx5	Bóixols-Upper Pedraforca	56.8	1.2	1.18	24
Bx16	Bóixols-Upper Pedraforca	46.9	3	0.93	23
Bx16b	Bóixols-Upper Pedraforca	47.8	2.8	1.5	23
Bx33	Bóixols-Upper Pedraforca	47	10	0.75	20
CN38	Bóixols-Upper Pedraforca	65.3	4.3	0.98	27
MGT9	Bóixols-Upper Pedraforca	14.8	2.3	1.09	23
MGT9b	Bóixols-Upper Pedraforca	18.9	0.8	1.6	27
P2	Bóixols-Upper Pedraforca	67	2.4	0.8	32
P4	Bóixols-Upper Pedraforca	70.5	1.1	1.08	20
P8a	Bóixols-Upper Pedraforca	63.4	0.85	1.07	59
P8b	Bóixols-Upper Pedraforca	34.3	2.8	0.89	12
P8c	Bóixols-Upper Pedraforca	33.2	5.1	2.2	28
P9a	Bóixols-Upper Pedraforca	35.9	1.2	1.5	24
P9b	Bóixols-Upper Pedraforca	37.6	0.84	0.69	26
P11a	Bóixols-Upper Pedraforca	50	12	1.8	13
P11b	Bóixols-Upper Pedraforca	39.5	1.2	1.3	34
P12a	Bóixols-Upper Pedraforca	26.1	2.2	3.8	14
P12b	Bóixols-Upper Pedraforca	14.9	1.2	0.66	15
P14	Bóixols-Upper Pedraforca	38.4	1.5	0.85	28
P21	Bóixols-Upper Pedraforca	31.4	1.7	1.8	24
P24a	Bóixols-Upper Pedraforca	138	12	1.4	21
P24b	Bóixols-Upper Pedraforca	34.8	1.6	1.5	14
P44	Bóixols-Upper Pedraforca	25	17	1.6	23
P63	Bóixols-Upper Pedraforca	54.9	0.66	0.99	25
EST2	Lower Pedraforca	30.2	2	1.8	21
G3	Lower Pedraforca	42.9	0.94	1.8	32
G3b	Lower Pedraforca	42.3	0.84	1.5	20
G15b	Lower Pedraforca	11.9	1.4	1.3	23
Q3-1	Lower Pedraforca	47.3	1	1.3	24
Q11	Lower Pedraforca	47.9	1.3	1.7	31
Q24	Lower Pedraforca	45.1	1.2	1.09	32
Q27	Lower Pedraforca	45.7	1.9	2.2	25
Q29	Lower Pedraforca	47.2	0.7	1.4	27
Q33	Lower Pedraforca	44.8	1.3	1.4	23
B2	Cadí	28.4	1.9	1.3	23
B22	Cadí	36.5	2.3	1.5	38
B32	Cadí	28.7	0.83	0.94	28
B46	Cadí	30	11.3	3.5	26
B54	Cadí	37	10	1.5	25
B57	Cadí	37.2	1.5	0.95	43

Sample	Structure	Age (Ma)	± 2σ	MSWD	Number of spots
GDV5	Cadí	36.9	1.1	0.82	21
GIS4	Cadí	35.1	2.2	1.3	30
GIS4b	Cadí	33.7	1.2	1.4	12
GIS10a	Cadí	30.1	4.8	1.2	15
Pa12	Cadí	15.3	0.4	1.7	21
C12	Axial zone	3.9	5.7	0.83	24
GPR401	Ebro basin	2.6	1.3	0.55	26

Fig. Dr1

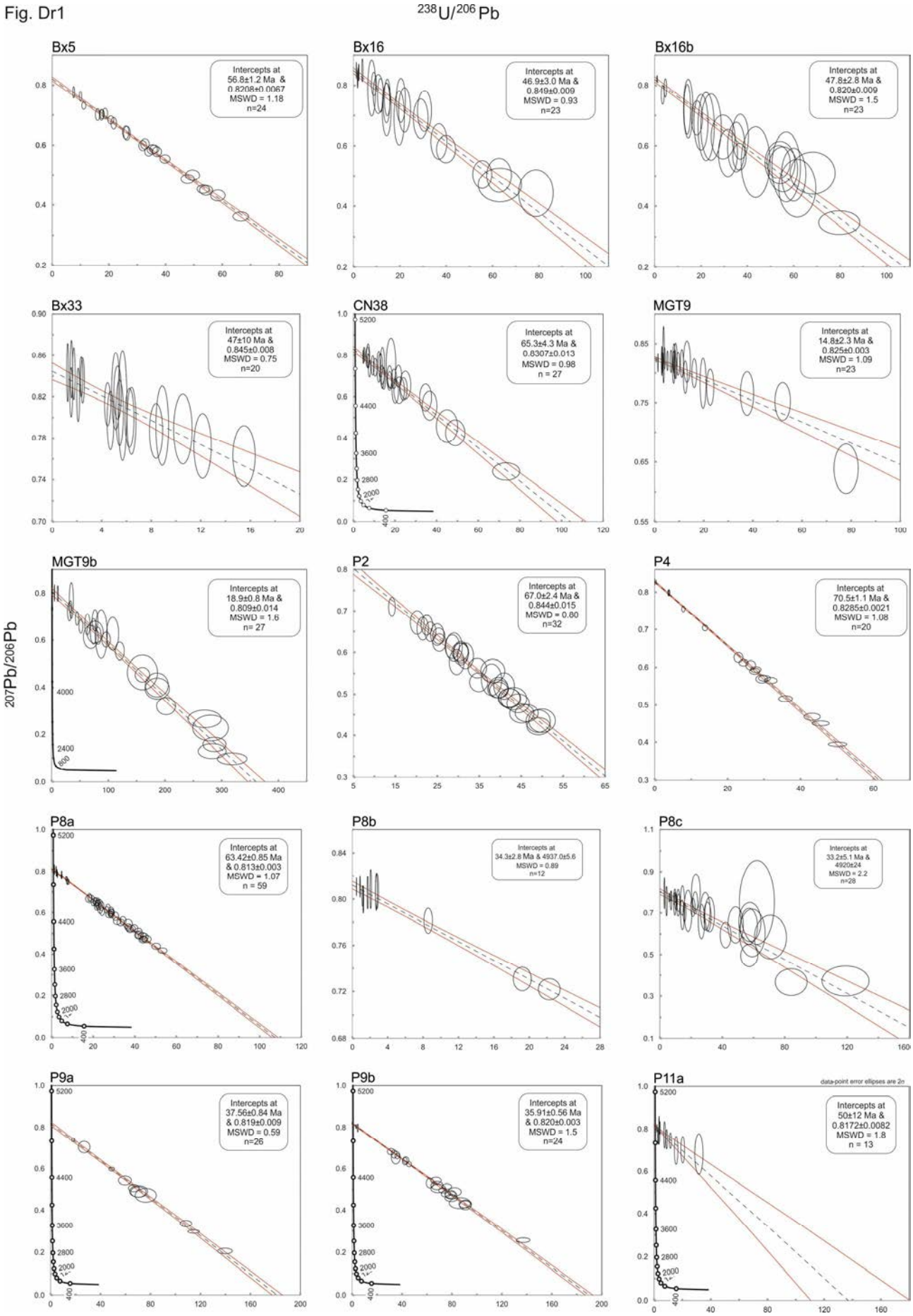
$^{238}U/^{206}Pb$
$^{207}Pb/^{206}Pb$
Bx5
Intercepts at 56.8±1.2 Ma & 0.8208±0.0067 MSWD = 1.18 n=24
Bx16
Intercepts at 46.9±3.0 Ma & 0.849±0.009 MSWD = 0.93 n=23
Bx16b
Intercepts at 47.8±2.8 Ma & 0.820±0.009 MSWD = 1.5 n=23
Bx33
Intercepts at 47±10 Ma & 0.845±0.008 MSWD = 0.75 n=20
CN38
Intercepts at 65.3±4.3 Ma & 0.8307±0.013 MSWD = 0.98 n = 27
MGT9
Intercepts at 14.8±2.3 Ma & 0.825±0.003 MSWD = 1.09 n=23
MGT9b
Intercepts at 18.9±0.8 Ma & 0.809±0.014 MSWD = 1.6 n= 27
P2
Intercepts at 67.0±2.4 Ma & 0.844±0.015 MSWD = 0.60 n=32
P4
Intercepts at 70.5±1.1 Ma & 0.8285±0.0021 MSWD = 1.08 n=20
P8a
Intercepts at 63.42±0.85 Ma & 0.813±0.003 MSWD = 1.07 n = 59
P8b
Intercepts at 34.3±2.8 Ma & 4937.0±5.6 MSWD = 0.89 n=12
P8c
Intercepts at 33.2±5.1 Ma & 4920±24 MSWD = 2.2 n=28
P9a
Intercepts at 37.56±0.84 Ma & 0.819±0.009 MSWD = 0.59 n=26
P9b
Intercepts at 35.91±0.56 Ma & 0.820±0.003 MSWD = 1.5 n=24
P11a
data-point error ellipses are 2σ
Intercepts at 50±12 Ma & 0.8172±0.0082 MSWD = 1.8 n = 13

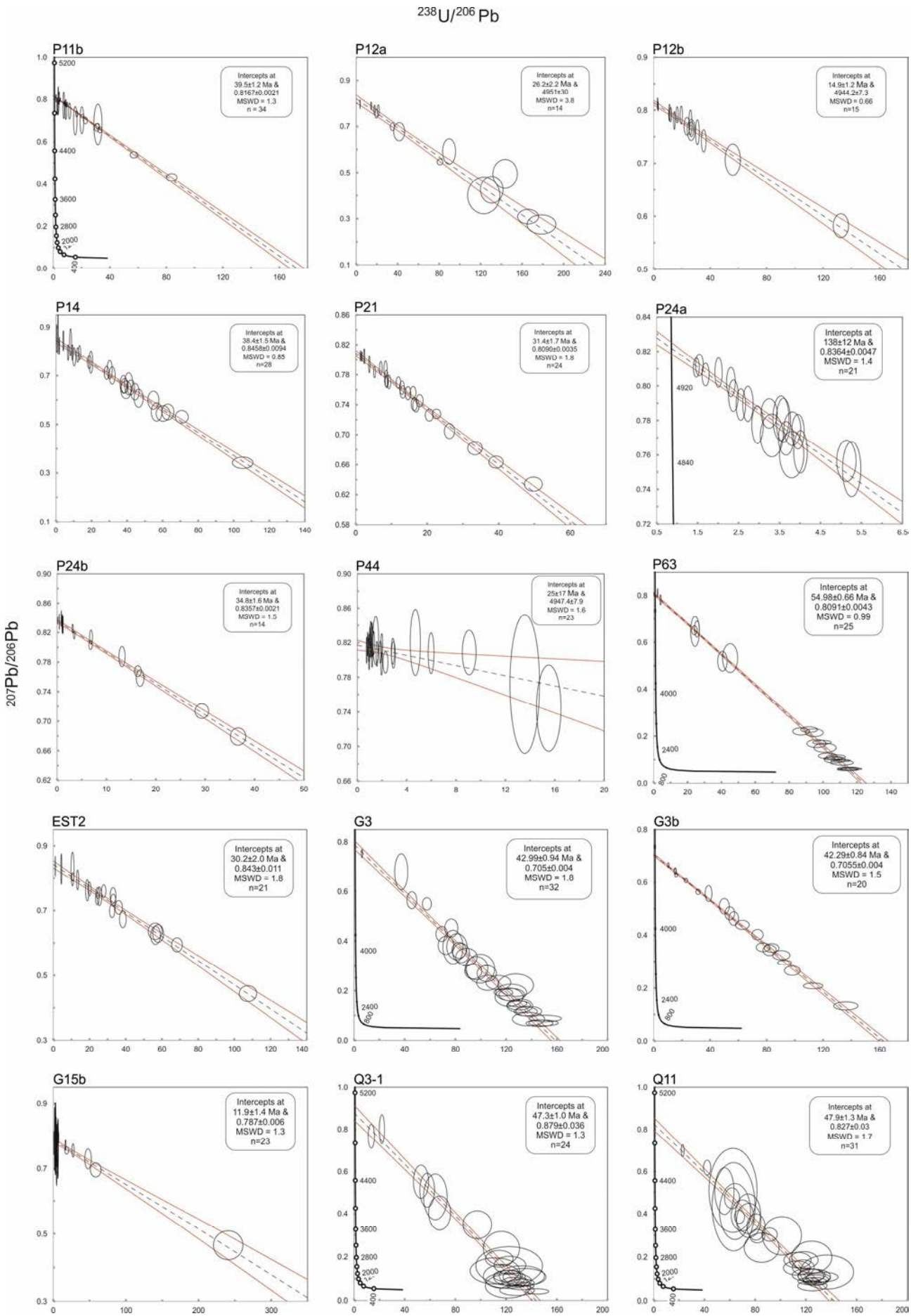
238U/206Pb
207Pb/206Pb
P11b
Intercepts at
39.5±1.2 Ma &
0.8167±0.0021
MSWD = 1.3
n = 34
P12a
Intercepts at
26.2±2.2 Ma &
4951±30
MSWD = 3.8
n=14
P12b
Intercepts at
14.9±1.2 Ma &
4944.2±7.3
MSWD = 0.66
n=15
P14
Intercepts at
38.4±1.5 Ma &
0.8458±0.0094
MSWD = 0.85
n=28
P21
Intercepts at
31.4±1.7 Ma &
0.8090±0.0035
MSWD = 1.8
n=24
P24a
Intercepts at
138±12 Ma &
0.8364±0.0047
MSWD = 1.4
n=21
P24b
Intercepts at
34.8±1.6 Ma &
0.8357±0.0021
MSWD = 1.5
n=14
P44
Intercepts at
25±17 Ma &
4947.4±7.9
MSWD = 1.6
n=23
P63
Intercepts at
54.98±0.66 Ma &
0.8091±0.0043
MSWD = 0.99
n=25
EST2
Intercepts at
30.2±2.0 Ma &
0.843±0.011
MSWD = 1.8
n=21
G3
Intercepts at
42.99±0.94 Ma &
0.705±0.004
MSWD = 1.8
n=32
G3b
Intercepts at
42.29±0.84 Ma &
0.7055±0.004
MSWD = 1.5
n=20
G15b
Intercepts at
11.9±1.4 Ma &
0.787±0.006
MSWD = 1.3
n=23
Q3-1
Intercepts at
47.3±1.0 Ma &
0.879±0.036
MSWD = 1.3
n=24
Q11
Intercepts at
47.9±1.3 Ma &
0.827±0.03
MSWD = 1.7
n=31

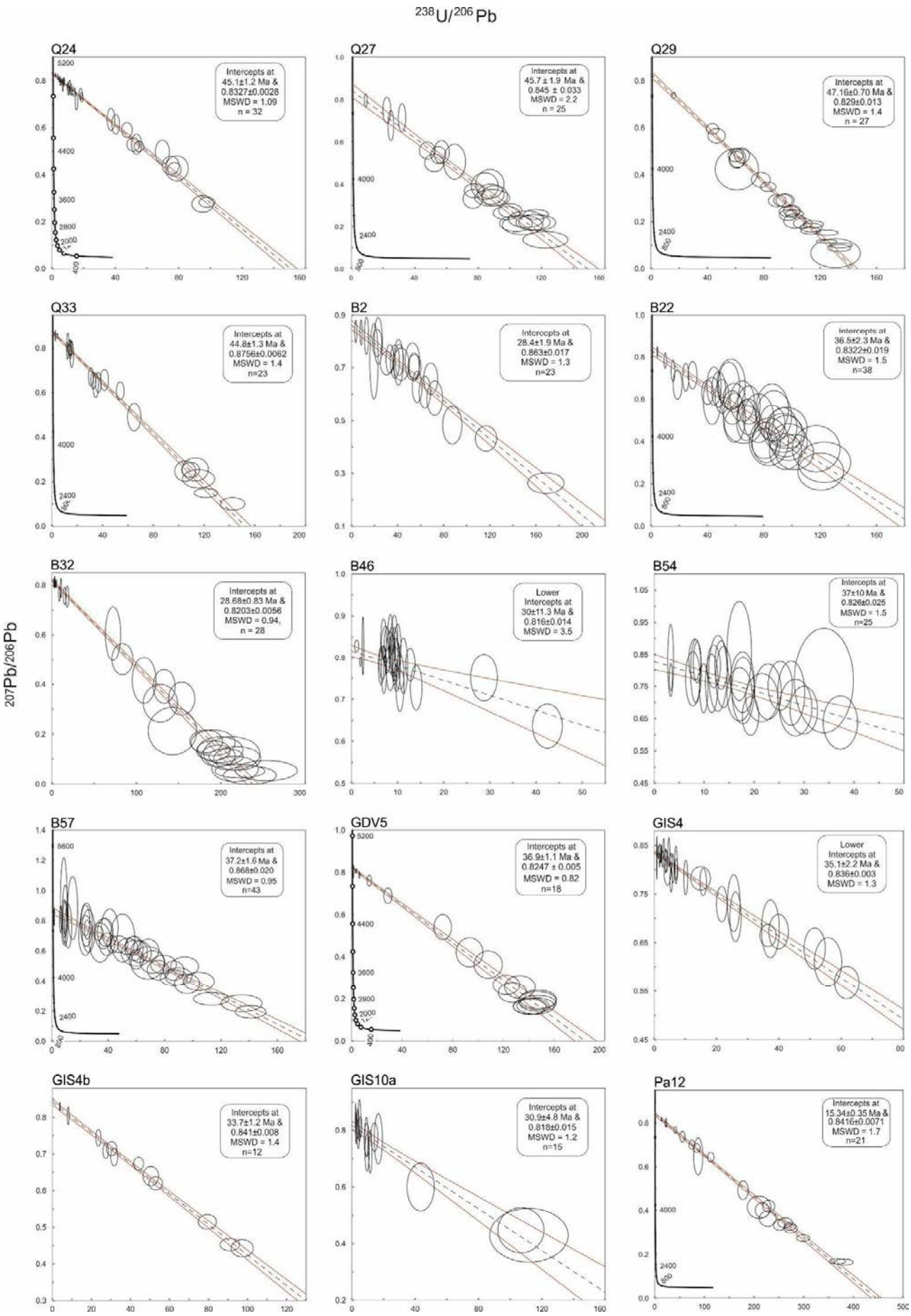
$^{238}U/^{206}Pb$
$^{207}Pb/^{206}Pb$
Q24
Intercepts at
45.1±1.2 Ma &
0.8327±0.0028
MSWD = 1.09
n = 32
Q27
Intercepts at
45.7 ± 1.9 Ma &
0.845 ± 0.033
MSWD = 2.2
n = 25
Q29
Intercepts at
47.16±0.70 Ma &
0.829±0.013
MSWD = 1.4
n = 27
Q33
Intercepts at
44.8±1.3 Ma &
0.8756±0.0062
MSWD = 1.4
n=23
B2
Intercepts at
28.4±1.9 Ma &
0.863±0.017
MSWD = 1.3
n=23
B22
Intercepts at
36.5±2.3 Ma &
0.8322±0.019
MSWD = 1.5
n=38
B32
Intercepts at
28.68±0.83 Ma &
0.8203±0.0056
MSWD = 0.94,
n = 28
B46
Lower
Intercepts at
30±11.3 Ma &
0.816±0.014
MSWD = 3.5
B54
Intercepts at
37±10 Ma &
0.826±0.025
MSWD = 1.5
n=25
B57
Intercepts at
37.2±1.6 Ma &
0.868±0.020
MSWD = 0.95
n=43
GDV5
Intercepts at
36.9±1.1 Ma &
0.8247 ± 0.005
MSWD = 0.82
n=18
GIS4
Lower
Intercepts at
35.1±2.2 Ma &
0.836±0.003
MSWD = 1.3
GIS4b
Intercepts at
33.7±1.2 Ma &
0.841±0.008
MSWD = 1.4
n=12
GIS10a
Intercepts at
30.9±4.8 Ma &
0.818±0.015
MSWD = 1.2
n=15
Pa12
Intercepts at
15.34±0.35 Ma &
0.8416±0.0071
MSWD = 1.7
n=21

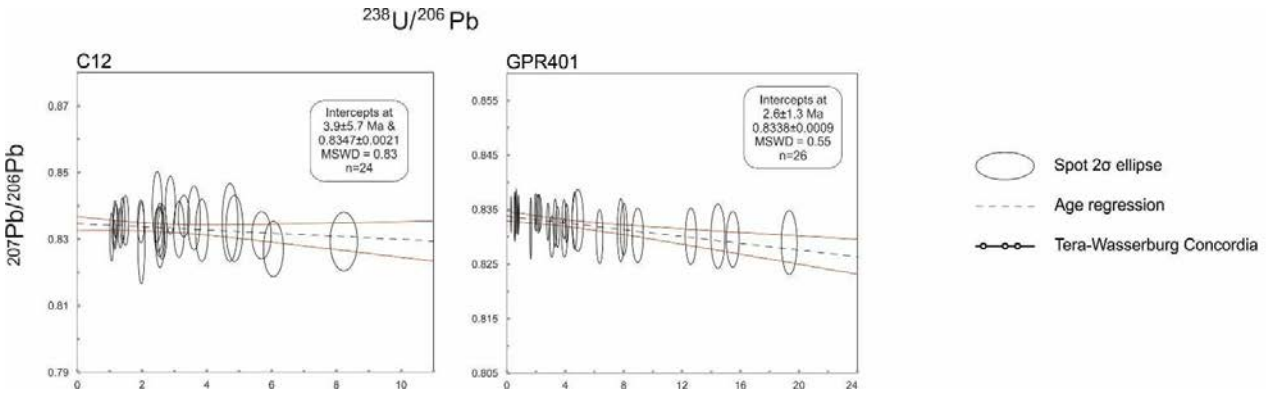
$^{238}U/^{206}Pb$
C12
GPR401
$^{207}Pb/^{206}Pb$
Intercepts at
3.9±5.7 Ma &
0.8347±0.0021
MSWD = 0.83
n=24
Intercepts at
2.6±1.3 Ma
0.8338±0.0009
MSWD = 0.55
n=26
Spot 2σ ellipse
Age regression
Tera-Wasserburg Concordia

Table DR3: LA-ICP-MS U-Th-Pb isotope data of calcite cements

spot	Sample	206Pb[a] (cps)	U[b] (ppm)	Pb[b] (ppm)	Th[b]/U	238U[c]/206Pb	± 2σ (%)	207Pb[c]/206Pb	± 2σ (%)
				Sequence 1					
A06	P12a	9805	0.171	0.074	0.00	3.745	3.0	0.796	2
A07	P12a	12378	1.022	0.093	0.00	17.683	3.2	0.7712	2.2
A07i	P12a	11387	1.110	0.084	0.00	21.349	3.6	0.7692	2.6
A08	P12a	14890	0.997	0.112	0.00	14.399	2.9	0.7893	1.7
A09	P12a	630	0.524	0.003	0.00	178.667	6.4	0.2751	12
A10	P12a	1906	0.364	0.013	0.00	41.477	10.5	0.6774	4.7
A11	P12a	270	0.155	0.002	0.00	122.986	10.3	0.401	16
A12	P12a	465	0.285	0.003	0.00	130.702	6.8	0.4257	11
A13	P12a	842	0.351	0.006	0.00	89.606	5.7	0.5919	7.6
A14	P12a	629	0.424	0.004	0.00	143.596	6.7	0.4945	10
A15	P12a	962	0.748	0.005	0.00	165.782	5.0	0.3089	8.3
A16	P12a	8866	3.364	0.059	0.01	80.841	2.8	0.5465	1.9
A17	P12a	10034	1.667	0.074	0.01	34.928	4.7	0.6988	2
A18	P12a	6986	0.642	0.053	0.00	19.482	5.7	0.7557	2.2
A19	P12b	5323	1.408	0.039	0.00	56.022	7.9	0.707	3.4
A20	P12b	8485	1.034	0.064	0.00	26.062	3.3	0.7772	2.5
A21	P12b	46712	0.708	0.362	0.08	3.206	3.0	0.8071	0.91
A22	P12b	17827	1.645	0.136	0.13	19.589	3.4	0.7909	1.8
A23	P12b	5601	3.505	0.038	0.02	132.591	3.3	0.5824	3.2
A24	P12b	19777	2.511	0.150	0.12	26.731	5.0	0.7644	1.5
A25	P12b	13899	1.782	0.107	0.07	26.596	8.5	0.7629	2.1
A26	P12b	30479	1.763	0.240	0.14	11.920	6.4	0.7918	1.4
A27	P12b	22672	1.783	0.174	0.11	16.656	3.9	0.7915	1.6
A28	P12b	13935	0.973	0.107	0.02	14.728	2.9	0.7808	1.8
A29	P12b	15208	0.813	0.118	0.05	11.236	4.3	0.7953	1.6
A30	P12b	12109	1.395	0.095	0.08	23.585	7.1	0.7699	1.8
A31	P12b	7735	1.141	0.059	0.01	30.979	3.5	0.7587	2.5
A32	P12b	37529	0.506	0.293	0.42	2.833	5.2	0.8123	1.1
A38	P12b	7898	1.341	0.060	0.01	35.448	3.9	0.7425	2.3
A94	B32	3247	0.300	0.026	0.24	18.165	8.6	0.7545	4.7
A95	B32	3587	0.157	0.028	0.29	8.905	8.5	0.766	3.2
A96	B32	11887	0.207	0.098	0.23	3.489	7.8	0.817	2
A97	B32	3003	0.231	0.024	0.18	15.161	8.6	0.757	3.8
A98	B32	19302	0.307	0.173	0.32	2.902	16.1	0.8083	2
A99	B32	75	0.053	0.000	0.01	142.816	16.5	0.2126	37
A100	B32	23936	0.467	0.226	0.58	3.385	17.4	0.809	1.4
A100i	B32	21045	0.573	0.168	0.62	5.574	6.6	0.806	1.5
A101	B32	2804	0.150	0.023	0.33	10.760	5.3	0.7886	4
A107	B32	10448	0.207	0.086	0.26	3.959	7.1	0.8062	1.7

spot	Sample	206Pb[a] (cps)	U[b] (ppm)	Pb[b] (ppm)	Th[b]/U	238U[c]/206Pb	± 2σ (%)	207Pb[c]/206Pb	± 2σ (%)
A108	B32	351	0.234	0.002	0.00	132.979	8.0	0.3921	14
A109	B32	257	0.258	0.001	0.00	199.402	11.0	0.1376	31
A110	B32	326	0.299	0.002	0.01	182.648	8.7	0.1713	21
A111	B32	792	0.326	0.005	0.01	83.612	12.3	0.5026	10
A112	B32	345	0.265	0.002	0.02	153.752	8.2	0.3431	16
A113	B32	343	0.187	0.002	0.01	109.206	10.5	0.4168	18
A114	B32	229	0.269	0.001	0.01	234.467	10.9	0.03493	84
A115	B32	140	0.150	0.001	0.01	212.947	12.8	0.1223	45
A116	B32	196	0.219	0.001	0.01	222.618	10.8	0.05182	43
A117	B32	164	0.180	0.001	0.01	216.826	10.3	0.06087	68
A118	B32	194	0.213	0.001	0.00	219.491	10.4	0.1024	38
A119	B32	260	0.257	0.001	0.01	196.967	8.4	0.1129	31
A120	B32	375	0.391	0.002	0.01	206.186	8.1	0.1105	23
A121	B32	312	0.299	0.002	0.01	191.095	8.5	0.1341	24
A122	B32	241	0.230	0.001	0.01	190.876	11.2	0.1658	25
A123	B32	179	0.229	0.001	0.00	253.872	11.8	0.05388	61
A124	B32	280	0.102	0.002	0.00	72.464	10.2	0.6053	15
A125	B32	298	0.191	0.002	0.00	128.502	12.9	0.3245	19
A130	GDV5	515	0.188	0.004	0.05	72.098	7.6	0.5413	9
A131	GDV5	303	0.225	0.002	0.16	146.757	8.2	0.1909	18
A132	GDV5	329	0.243	0.002	0.36	145.455	8.1	0.1654	19
A133	GDV5	352	0.238	0.002	0.15	133.014	7.2	0.2564	17
A134	GDV5	33056	0.285	0.271	0.66	1.702	5.9	0.7858	1.3
A135	GDV5	441	0.275	0.003	0.26	122.354	6.8	0.2663	14
A136	GDV5	32772	0.480	0.272	0.99	2.888	3.1	0.806	1.1
A137	GDV5	87678	0.914	0.735	2.34	2.050	3.0	0.8197	0.8
A138	GDV5	116992	0.782	0.979	1.29	1.315	4.1	0.8164	0.74
A139	GDV5	373	0.269	0.002	0.14	141.864	7.9	0.1641	19
A140	GDV5	7323	0.529	0.060	0.46	14.124	10.0	0.7618	2.8
A141	GDV5	19854	0.627	0.164	0.66	6.211	3.8	0.7885	1.7
A142	GDV5	27289	0.559	0.227	0.73	4.024	7.2	0.8077	1.1
A143	GDV5	100506	0.753	0.847	1.10	1.466	4.4	0.8207	0.76
A144	GDV5	680	0.379	0.004	1.16	108.038	8.2	0.3638	15
A145	GDV5	492	0.323	0.003	1.25	127.129	6.9	0.2299	17
A151	GDV5	451	0.325	0.002	0.36	140.885	7.3	0.1622	19
A152	GDV5	358	0.275	0.002	0.41	147.427	7.8	0.1976	18
A153	GDV5	1290	0.623	0.009	1.10	93.284	9.1	0.4216	13
A153i	GDV5	3750	0.549	0.029	0.98	28.827	9.1	0.6899	4.3
A154	GDV5	305	0.231	0.002	0.04	147.319	7.8	0.1778	17
A165	CN38	309	0.029	0.003	0.00	18.070	10.2	0.7616	13
A166	CN38	413	0.097	0.003	0.03	44.964	9.1	0.4585	14

spot	Sample	206Pb[a] (cps)	U[b] (ppm)	Pb[b] (ppm)	Th[b]/U	238U[c]/206Pb	± 2σ (%)	207Pb[c]/206Pb	± 2σ (%)
A167	CN38	3278	0.122	0.027	0.11	7.133	5.2	0.7711	3.7
A168	CN38	1748	0.158	0.014	0.00	17.416	4.3	0.6812	4.9
A169	CN38	663	0.120	0.005	0.03	34.686	6.5	0.5966	8.9
A170	CN38	1143	0.104	0.009	0.01	17.388	5.9	0.6903	7
A171	CN38	1608	0.122	0.013	0.04	14.550	5.0	0.6873	6.2
A172	CN38	859	0.090	0.007	0.05	20.129	6.1	0.6278	7.6
A173	CN38	813	0.060	0.007	0.09	13.945	6.1	0.7398	11
A174	CN38	1045	0.070	0.009	0.02	12.999	6.4	0.7506	6.2
A175	CN38	2701	0.097	0.023	0.15	6.807	10.3	0.7914	5.3
A176	CN38	2137	0.086	0.018	0.28	7.734	5.8	0.7354	4.5
A177	CN38	1845	0.090	0.015	0.15	9.294	6.2	0.7507	5.1
A178	CN38	2358	0.129	0.020	0.16	10.472	6.9	0.7419	4.8
A179	CN38	498	0.191	0.003	0.03	73.421	7.0	0.2392	14
A180	CN38	978	0.124	0.008	0.08	24.050	5.8	0.6379	7
A181	CN38	931	0.175	0.007	0.11	36.603	7.7	0.5567	10
A182	CN38	892	0.103	0.007	0.02	21.993	9.3	0.6315	8.2
A183	CN38	3868	0.105	0.033	0.60	5.171	5.4	0.8046	3.7
A184	CN38	952	0.109	0.008	0.03	21.650	5.5	0.699	6.3
A185	CN38	688	0.090	0.005	0.02	24.969	8.4	0.6564	8.3
A186	CN38	301	0.078	0.002	0.00	48.924	7.6	0.4259	12
A187	CN38	851	0.055	0.007	0.39	12.246	6.0	0.7449	8.3
A188	CN38	2660	0.067	0.023	0.08	4.792	4.3	0.7945	3.6
A189	CN38	1632	0.119	0.013	0.04	13.797	5.8	0.7049	5.3
A190	CN38	1298	0.134	0.011	0.07	19.489	4.8	0.6861	5.7
A191	CN38	1178	0.044	0.010	0.13	7.072	8.0	0.8	5.8
A231	Q24	7436	0.280	0.065	0.00	6.940	3.2	0.7795	2.5
A232	Q24	8681	0.890	0.074	0.00	18.822	3.6	0.7299	2.3
A233	Q24	1310	0.380	0.010	0.00	53.419	4.5	0.5303	6.6
A234	Q24	1495	0.305	0.012	0.00	37.313	5.0	0.6359	6
A235	Q24	2507	0.211	0.021	0.00	15.516	3.9	0.7105	4
A236	Q24	950	0.388	0.007	0.20	74.963	5.5	0.4396	7.3
A237	Q24	2291	0.589	0.018	0.01	47.371	5.6	0.5902	4.4
A243	Q24	5909	1.782	0.045	0.04	54.945	4.1	0.5206	3.5
A244	Q24	1918	1.029	0.012	0.00	97.847	3.8	0.2831	6
A245	Q24	798	0.419	0.005	0.00	95.147	5.6	0.2762	11
A246	Q24	3953	1.115	0.030	0.02	51.308	6.1	0.5297	4.5
A247	Q24	2121	0.898	0.015	0.00	77.280	4.2	0.4227	5.8
A248	Q24	40936	1.157	0.369	0.08	5.133	5.6	0.807	1.2
A249	Q24	608	0.264	0.004	0.03	78.864	7.2	0.4276	10
A250	Q24	834	0.319	0.006	0.17	69.735	5.0	0.4962	8.4
A251	Q24	23930	0.710	0.215	0.02	5.365	4.0	0.7945	1.5
A252	Q24	6033	0.348	0.053	0.01	10.461	3.8	0.7667	3

spot	Sample	206Pb[a] (cps)	U[b] (ppm)	Pb[b] (ppm)	Th[b] / U	238U[c] / 206Pb	± 2σ (%)	207Pb[c] / 206Pb	± 2σ (%)
A253	Q24	149572	0.912	1.387	0.57	1.088	5.5	0.8256	0.72
A254	Q24	16472	0.698	0.148	0.06	7.669	3.6	0.7978	1.7
A255	Q24	65942	0.872	0.602	1.03	2.395	4.6	0.8237	0.87
A256	Q24	29990	2.280	0.262	0.09	13.835	6.2	0.7501	1.6
A257	Q24	5557	0.371	0.049	0.00	12.066	3.5	0.7632	2.6
A258	Q24	4854	0.304	0.043	0.00	11.276	3.9	0.7736	3
A259	Q24	47054	0.982	0.429	0.34	3.765	3.0	0.8153	1.2
A260	Q24	30591	1.111	0.278	0.12	6.510	5.5	0.7969	1.4
A261	Q24	14870	1.121	0.132	0.08	13.602	6.6	0.7582	1.7
A262	Q24	12581	0.715	0.113	0.19	10.208	4.5	0.774	1.6
A263	Q24	1116	0.249	0.009	0.00	40.290	4.6	0.6152	5.6
A264	Q24	21183	0.896	0.192	0.14	7.587	2.9	0.7917	1.5
A265	Q24	53851	1.992	0.490	0.04	6.636	4.5	0.7996	1
A266	Q24	39279	1.010	0.359	0.12	4.613	3.2	0.805	1.1
A267	Q24	7003	0.710	0.062	0.07	18.198	3.9	0.7434	2.7
A268	P11b	2741	0.054	0.025	0.00	3.527	3.6	0.8204	4.2
A269	P11b	2870	0.065	0.026	0.00	4.060	5.8	0.8057	3.2
A270	P11b	3432	0.061	0.031	0.18	3.186	3.7	0.7646	3.7
A271	P11b	1734	0.086	0.015	0.01	8.897	4.4	0.7521	5.1
A272	P11b	5639	0.033	0.051	0.06	1.033	4.2	0.796	2.8
A273	P11b	2033	0.037	0.019	0.00	3.233	20.2	0.7671	4.4
A274	P11b	26862	0.126	0.251	0.22	0.833	4.1	0.8214	1.3
A275	P11b	937	0.039	0.009	0.00	7.396	6.3	0.7728	6.7
A276	P11b	100647	4.659	0.921	0.02	8.183	5.3	0.7813	0.88
A277	P11b	176369	0.941	1.634	0.03	0.946	3.1	0.8128	0.71
A278	P11b	17046	1.601	0.152	0.01	16.600	3.3	0.7316	1.6
A279	P11b	110819	2.225	1.024	0.02	3.550	3.2	0.8009	0.91
A280	P11b	63846	0.369	0.604	0.19	1.001	5.9	0.8064	1.1
A281	P11b	79322	0.303	0.744	0.17	0.667	3.8	0.8072	1
A282	P11b	547	0.097	0.005	0.05	31.606	7.3	0.6817	12
A288	P11b	1973	0.131	0.018	0.07	11.547	5.0	0.7452	4.1
A289	P11b	831	0.095	0.007	0.00	20.247	5.0	0.7018	7.3
A290	P11b	740	0.066	0.007	0.01	15.547	6.3	0.6992	7.8
A291	P11b	13603	0.161	0.129	0.03	2.046	5.0	0.8047	1.9
A292	P11b	13902	2.617	0.119	0.01	33.036	3.3	0.6564	1.8
A293	P11b	52585	2.964	0.484	0.00	9.881	2.8	0.7761	1.1
A294	P11b	91259	4.520	0.840	0.00	8.666	2.8	0.7745	0.81
A295	P11b	18236	3.270	0.159	0.00	31.299	3.1	0.6737	1.6
A296	P11b	77854	2.176	0.735	0.01	4.831	4.7	0.7986	0.93
A297	P11b	271773	1.639	2.601	0.07	1.036	4.7	0.8137	0.59
A298	P11b	131490	3.514	1.235	0.01	4.634	4.0	0.7954	0.66
A299	P11b	23367	3.056	0.208	0.01	22.691	4.9	0.7008	1.9

spot	Sample	206Pb[a] (cps)	U[b] (ppm)	Pb[b] (ppm)	Th[b]/U	238U[c]/206Pb	± 2σ (%)	207Pb[c]/206Pb	± 2σ (%)
A300	P11b	72787	3.902	0.673	0.01	9.328	3.1	0.7724	1.2
A301	P11b	68061	3.167	0.632	0.00	8.078	3.2	0.7761	1.1
A302	P11b	78312	3.664	0.736	0.00	8.045	6.9	0.7825	0.98
A303	P11b	49669	5.896	0.447	0.00	20.602	4.5	0.7208	0.98
A304	P11b	11886	2.123	0.105	0.01	30.826	4.6	0.6676	2.3
A305	P11b	8357	4.056	0.063	0.00	83.822	3.2	0.4318	3.3
A306	P11b	10865	3.583	0.088	0.00	57.110	3.4	0.5381	2.2
A307	P44	18048	0.119	0.172	0.68	1.142	2.8	0.8165	1.5
A308	P44	1378	0.124	0.013	0.18	15.511	5.2	0.7445	5.5
A309	P44	841	0.066	0.008	0.20	13.569	7.2	0.7724	8.5
A310	P44	2332	0.065	0.023	0.54	4.704	7.2	0.8206	3.8
A311	P44	6578	0.059	0.065	0.53	1.495	12.8	0.8227	2.8
A312	P44	20118	0.344	0.193	0.39	2.928	4.4	0.8062	1.6
A313	P44	17209	0.076	0.165	0.90	0.759	3.6	0.8115	1.5
A314	P44	23450	0.128	0.224	0.87	0.935	3.5	0.8118	1.4
A315	P44	26659	0.305	0.253	1.69	1.963	2.8	0.7961	1.4
A316	P44	18476	0.120	0.181	0.57	1.097	4.2	0.8289	1.6
A317	P44	13943	0.097	0.135	0.74	1.197	3.3	0.8236	2
A318	P44	17678	0.088	0.171	0.34	0.847	2.7	0.8185	1.4
A319	P44	8164	0.058	0.079	1.80	1.205	4.1	0.8156	2.4
A320	P44	17216	0.293	0.166	0.35	2.887	3.7	0.8103	1.5
A321	P44	7337	0.257	0.070	0.17	5.977	3.2	0.8081	2.4
A322	P44	8015	0.431	0.078	0.13	9.066	5.0	0.8089	2.6
A323	P44	25936	0.302	0.251	0.16	1.981	3.3	0.8171	1.4
A324	P44	20178	0.125	0.199	1.16	1.039	4.3	0.8213	1.8
A325	P44	22178	0.247	0.216	0.75	1.879	4.4	0.8093	1.3
A326	P44	26790	0.252	0.260	2.14	1.589	4.0	0.8072	1.5
A327	P44	34956	0.495	0.353	1.38	2.283	7.2	0.7974	1.3
A333	P44	22603	0.180	0.222	2.60	1.333	3.7	0.8199	1.3
A334	P44	37585	0.647	0.355	0.34	2.626	8.0	0.5774	2.4
A335	P44	9321	0.053	0.091	1.21	0.962	4.3	0.8095	2.1
A336	P8	14389	0.178	0.140	0.14	2.081	3.1	0.809	1.7
A337	P8	49493	5.692	0.466	0.01	19.212	4.3	0.7311	1.1
A338	P8	43726	5.881	0.413	0.01	22.267	4.5	0.7222	1
A339	P8	17490	0.294	0.173	0.19	2.784	5.4	0.8073	1.6
A340	P8	14893	0.242	0.146	0.19	2.717	3.2	0.8066	1.6
A341	P8	25324	0.263	0.248	0.19	1.733	2.9	0.8059	1.5
A342	P8	83805	0.238	0.824	0.30	0.474	3.1	0.8109	0.81
A343	P8	28124	0.209	0.274	0.26	1.243	2.9	0.7998	1.2
A344	P8	85394	0.448	0.839	0.55	0.876	2.7	0.8112	0.97
A345	P8	77467	0.555	0.779	0.45	1.165	6.3	0.8028	0.91
A346	P8	37119	1.934	0.364	0.03	8.576	4.6	0.7815	1.1

spot	Sample	206Pb[a] (cps)	U[b] (ppm)	Pb[b] (ppm)	Th[b]/U	238U[c]/206Pb	± 2σ (%)	207Pb[c]/206Pb	± 2σ (%)
A347	P8	1581	0.150	0.015	0.04	15.805	4.6	0.7031	5.3
A348	P8	12799	0.174	0.125	0.00	2.258	3.1	0.7897	1.7
A349	P8	1242	0.168	0.012	0.01	22.686	6.0	0.7485	5.8
A350	P8	2882	0.212	0.028	0.04	12.108	8.3	0.7482	4.5
A351	P8	2124	0.183	0.020	0.05	14.213	5.9	0.7256	4.1
A352	P8	2844	0.178	0.027	0.05	10.378	7.0	0.7526	4
A353	P8	3933	0.218	0.038	0.09	9.208	4.5	0.7684	3
A354	P8	6324	0.276	0.062	0.09	7.220	4.2	0.7806	2.5
A355	P8	9887	0.364	0.097	0.08	6.046	4.9	0.7737	2.2
A356	P8	5223	0.317	0.051	0.06	9.980	4.1	0.7754	2.5
A357	P8	694	0.244	0.006	0.00	57.274	7.8	0.4961	8.9
A358	P8	218	0.098	0.002	0.00	70.872	11.8	0.5844	15
A359	P8	824	0.049	0.008	0.00	9.597	6.5	0.7519	6.9
A360	P8	554	0.142	0.005	-0.03	42.159	6.8	0.5948	8.5
A361	P8	377	0.200	0.003	0.00	84.175	9.9	0.3674	14
A362	P8	367	0.041	0.004	0.00	18.083	11.4	0.7109	11
A363	P8	1707	0.222	0.016	0.03	21.177	5.5	0.7261	4.9
A364	P8	43346	0.246	0.437	0.00	0.922	3.6	0.8053	1.4
A365	P8	14384	0.228	0.144	0.00	2.581	3.2	0.7931	1.9
A366	P8	10474	0.311	0.104	0.00	4.829	3.0	0.7828	2.1
A367	P8	17142	0.231	0.174	0.00	2.176	3.6	0.8108	1.7
A368	P8	15040	0.211	0.152	0.00	2.263	3.4	0.792	1.7
A369	P8	14344	0.246	0.143	0.00	2.784	3.1	0.7848	1.8
A370	P8	16262	0.137	0.163	0.01	1.378	5.4	0.804	1.8
A371	P8	21975	0.176	0.225	0.01	1.289	4.4	0.8158	1.8
A372	P8	8738	1.462	0.080	0.00	27.078	2.9	0.6217	2.5
A373	P8	4845	0.680	0.045	0.00	22.497	3.7	0.6371	3.1
A374	P8	10332	1.172	0.098	0.00	18.175	3.9	0.673	2.4
A375	P8	8214	1.457	0.075	0.00	28.571	3.2	0.6093	2.3
A376	P8	8224	1.102	0.077	0.00	21.381	3.9	0.6508	2.7
A377	P8	9899	1.343	0.092	0.00	21.668	4.1	0.6295	2.3
A378	P8	8437	1.971	0.073	0.00	37.651	3.1	0.5202	2.4
A379	P8	6383	0.934	0.059	0.00	23.343	4.1	0.6209	3.2
A380	P8	10828	1.861	0.098	0.00	27.563	4.4	0.5915	2.3
A381	P8	8154	1.444	0.074	0.00	28.353	3.0	0.5935	2.2
A382	P8	10252	1.839	0.093	0.00	28.752	3.0	0.5898	2.2
A388	P8	10784	1.955	0.099	0.00	28.902	3.2	0.6004	2.3
A389	P8	5599	1.397	0.049	0.00	39.651	3.3	0.5253	2.9
A390	P8	8192	1.897	0.072	0.00	36.846	3.1	0.532	2.4
A391	P8	8277	1.149	0.078	0.00	21.925	3.0	0.6393	2.4
A392	P8	25466	1.315	0.255	0.00	8.170	2.9	0.7482	1.3
A393	P8	16004	0.766	0.161	0.01	7.582	3.7	0.7511	1.8
A394	P8	28137	1.266	0.285	0.00	7.112	2.8	0.7657	1.3

spot	Sample	206Pb[a] (cps)	U[b] (ppm)	Pb[b] (ppm)	Th[b] / U	238U[c] / 206Pb	± 2σ (%)	207Pb[c] / 206Pb	± 2σ (%)
A395	P8	878	0.016	0.009	0.00	2.950	6.6	0.7954	7.8
A396	P8	432	0.087	0.004	0.00	31.949	7.9	0.6931	9.7
A397	P8	240	0.181	0.002	0.00	118.991	10.4	0.3729	16
A398	P8	504	0.098	0.005	0.00	30.544	6.2	0.6829	8.2
A399	P8	364	0.112	0.003	0.00	48.567	8.3	0.643	11
A400	P8	594	0.102	0.006	0.00	26.674	6.2	0.6594	10
A401	P8	144	0.054	0.001	0.00	59.207	11.4	0.6045	15
A402	P8	281	0.103	0.003	0.00	57.670	10.0	0.6569	12
A403	P8	414	0.039	0.004	0.00	14.516	7.8	0.7261	12
A404	P8	1269	0.059	0.013	0.00	7.205	5.8	0.7601	5
A405	P8	840	0.064	0.009	0.00	11.770	7.5	0.749	7
A406	P8	913	0.027	0.010	0.00	4.335	8.8	0.7567	7.7
A407	P8	697	0.105	0.007	0.00	23.137	9.9	0.8018	8.8
A408	P8	376	0.071	0.004	0.00	29.121	8.7	0.709	10
A409	P8	298	0.111	0.003	0.00	57.078	7.9	0.6365	11
A410	P8	109	0.044	0.001	0.00	62.228	14.7	0.7518	22
A411	P8	3390	0.095	0.036	0.00	4.277	5.8	0.8068	3.3
A412	P8	4821	0.071	0.052	0.00	2.299	4.6	0.8335	3.1
A413	P8	10606	0.087	0.113	0.00	1.263	3.1	0.8191	1.8
A414	P8	7854	2.219	0.069	0.00	43.573	3.3	0.4887	2.8
A415	P8	8186	2.331	0.071	0.00	43.956	3.2	0.4701	2.7
A416	P8	7075	2.307	0.061	0.00	50.226	3.0	0.4388	2.7
A417	P8	11246	2.429	0.104	0.01	33.223	3.9	0.5531	2.3
A418	P8	4867	0.209	0.052	0.02	6.596	4.8	0.8016	2.9
A419	P8	5143	0.734	0.053	0.02	21.968	4.0	0.7393	3.2
A420	P8	12278	1.780	0.120	0.01	22.242	2.8	0.6469	2
A421	P8	10504	2.860	0.095	0.00	41.771	2.8	0.512	2.3
A422	P8	18968	2.362	0.194	0.03	18.443	9.5	0.6665	2.3
A423	P8	11468	3.997	0.097	0.00	53.305	2.8	0.4178	2.6
A424	P8	46001	2.135	0.483	0.03	7.077	3.5	0.7623	1.2
A425	P8	10819	2.683	0.099	0.01	37.836	4.7	0.5261	2.4
A426	P8	88950	1.581	0.953	0.07	2.699	2.9	0.7926	0.91
A427	P8	27982	1.405	0.291	0.05	7.675	3.3	0.7507	1.3
A428	P8	51622	1.593	0.547	0.03	4.690	3.4	0.7753	0.95
A429	P8	10749	3.126	0.095	0.01	44.170	2.8	0.4743	2.5
A430	P8	9531	2.307	0.089	0.00	36.738	4.4	0.5454	3.4
A431	P8	10961	2.292	0.104	0.00	31.516	4.4	0.561	2.5
A432	P8	58222	1.887	0.621	0.02	4.902	3.7	0.7776	0.93
A433	P8	11569	1.527	0.115	0.00	19.932	3.1	0.6497	2.1
A434	P8	81823	1.563	0.884	0.01	2.872	2.8	0.7907	0.92
A435	P8	6470	1.473	0.061	0.00	34.294	3.0	0.5626	2.7
A436	P8	5112	0.815	0.050	0.00	24.044	3.2	0.6313	2.9
A437	P8	8813	1.553	0.086	0.01	26.504	2.8	0.6126	2.1

spot	Sample	206Pb[a] (cps)	U[b] (ppm)	Pb[b] (ppm)	Th[b]/U	238U[c]/206Pb	± 2σ (%)	207Pb[c]/206Pb	± 2σ (%)
A438	P8	12547	1.557	0.127	0.00	18.685	2.8	0.6701	2.1
A444	P8	8990	1.248	0.091	0.00	20.721	3.0	0.6549	2.3
A445	P8	10535	1.638	0.106	0.00	23.175	3.4	0.6452	2.3
A446	P8	9646	1.445	0.098	0.01	22.232	3.3	0.6508	2.4
A447	P8	8233	1.346	0.081	0.01	24.295	3.3	0.6048	2.6
A448	P8	7608	1.463	0.075	0.00	28.580	3.3	0.5994	2.4
A449	P8	5627	1.737	0.051	0.00	45.683	3.3	0.4733	3.1
A450	P8	5962	1.794	0.055	0.00	44.543	3.0	0.4833	3.2
A451	P8	5717	1.631	0.053	0.00	42.212	3.1	0.4939	3.2
A452	P8	6324	1.784	0.058	0.00	41.701	3.0	0.4917	2.8
A453	P8	6725	1.398	0.066	0.01	30.694	3.5	0.5823	2.8
A454	Q3-1	228	0.101	0.002	0.01	64.185	11.7	0.4795	18
A455	Q3-1	117	0.096	0.001	0.00	121.448	11.8	0.06565	68
A456	Q3-1	325	0.116	0.003	0.02	52.826	9.1	0.5515	12
A457	Q3-1	410	0.272	0.003	0.01	97.276	9.3	0.3479	15
A458	Q3-1	162	0.128	0.001	0.02	116.293	9.9	0.2387	27
A459	Q3-1	229	0.209	0.002	0.00	134.499	10.1	0.1078	29
A460	Q3-1	657	0.589	0.004	0.00	131.441	6.3	0.06673	21
A461	Q3-1	1662	0.152	0.018	0.09	13.615	14.7	0.7677	6.1
A462	Q3-1	287	0.130	0.002	0.01	67.522	10.3	0.4033	16
A463	Q3-1	238	0.216	0.002	0.02	132.450	10.9	0.1122	34
A464	Q3-1	495	0.419	0.004	0.14	122.745	8.2	0.1039	27
A465	Q3-1	82	0.068	0.001	0.00	122.399	17.5	0.1581	46
A466	Q3-1	61	0.079	0.000	0.00	190.658	19.4	0.2812	36
A467	Q3-1	935	0.143	0.011	0.02	21.993	7.5	0.8009	7
A468	Q3-1	340	0.283	0.002	0.04	121.907	11.9	0.09094	32
A469	Q3-1	148	0.113	0.001	0.14	111.123	14.3	0.1351	36
A470	Q3-1	265	0.234	0.002	0.01	128.617	8.5	0.04649	41
A471	Q3-1	539	0.451	0.004	0.01	121.212	7.5	0.112	19
A472	Q3-1	816	0.815	0.005	0.08	144.363	4.9	0.04157	24
A473	Q3-1	789	0.721	0.006	0.01	131.752	6.2	0.08144	17
A474	Q3-1	559	0.448	0.004	0.06	114.561	7.6	0.1907	16
A475	Q3-1	603	0.531	0.004	0.01	126.534	6.2	0.08479	20
A476	Q3-1	191	0.155	0.001	0.01	116.645	10.1	0.1102	40
A477	Q3-1	308	0.125	0.003	0.01	57.737	8.0	0.5108	13
A478	Q3-1	16	0.005	0.000	0.09	21.459	60.5	0.4256	85
A479	Q3-1	297	0.257	0.002	0.05	123.001	8.1	0.1616	20
A506	Q11	172	0.156	0.001	0.01	124.642	10.2	0.1995	30
A507	Q11	875	0.731	0.007	0.03	113.379	7.5	0.1855	16
A508	Q11	4930	1.515	0.053	0.08	42.176	5.3	0.6188	4.6
A509	Q11	159	0.103	0.001	0.01	85.106	13.1	0.2426	23
A510	Q11	108	0.051	0.001	0.01	64.185	15.5	0.4117	26

spot	Sample	206Pb[a] (cps)	U[b] (ppm)	Pb[b] (ppm)	Th[b]/U	238U[c]/206Pb	± 2σ (%)	207Pb[c]/206Pb	± 2σ (%)
A511	Q11	6721	1.127	0.076	0.13	22.910	3.6	0.6992	3.3
A512	Q11	240	0.123	0.002	0.01	69.881	10.1	0.3922	15
A513	Q11	122	0.122	0.001	0.01	136.575	12.5	0.1313	48
A514	Q11	813	0.369	0.008	0.03	61.767	7.7	0.4735	8.5
A515	Q11	678	0.648	0.005	0.03	129.618	5.9	0.1039	16
A516	Q11	350	0.314	0.003	0.01	122.205	8.5	0.1177	20
A517	Q11	551	0.510	0.004	0.01	125.094	7.3	0.06845	27
A518	Q11	637	0.598	0.005	0.02	127.812	6.3	0.09592	18
A519	Q11	982	0.887	0.007	0.04	122.264	5.4	0.08929	14
A520	Q11	518	0.461	0.004	0.01	118.287	7.6	0.186	17
A521	Q11	201	0.111	0.002	0.01	74.963	10.3	0.3692	18
A522	Q11	618	0.612	0.005	0.02	133.014	7.4	0.1084	17
A523	Q11	47	0.022	0.000	0.01	62.578	24.6	0.5115	32
A524	Q11	464	0.426	0.004	0.02	123.839	6.5	0.1146	21
A525	Q11	427	0.364	0.003	0.02	112.918	7.5	0.1494	18
A526	Q11	159	0.119	0.001	0.01	101.092	12.3	0.2977	24
A527	Q11	47	0.023	0.000	0.00	63.052	21.8	0.4353	39
A528	Q11	375	0.359	0.003	0.02	126.662	8.0	0.1122	23
A529	Q11	1330	0.907	0.012	0.03	91.324	5.2	0.3025	8.2
A530	Q11	788	0.745	0.006	0.03	127.129	5.7	0.08819	16
A531	Q11	1166	0.712	0.010	0.37	81.699	5.6	0.2956	8.6
A532	Q11	168	0.070	0.002	0.02	55.835	10.9	0.5077	18
A533	Q11	1200	0.606	0.011	0.03	67.705	4.5	0.3861	6.8
A534	Q11	285	0.172	0.003	0.02	80.710	7.1	0.3383	15
A535	Q11	513	0.456	0.004	0.04	117.925	5.7	0.1529	18
A536	Q11	202	0.115	0.002	0.01	74.405	10.7	0.4005	19
A537	P9	5797	3.928	0.057	0.00	90.744	3.8	0.4244	4.2
A538	P9	14271	0.505	0.179	0.00	4.606	6.9	0.7987	2
A540	P9	4055	2.779	0.040	0.00	90.662	4.1	0.4303	3.5
A541	P9	9579	3.132	0.108	0.00	43.234	3.7	0.64	2.2
A542	P9	11097	3.543	0.125	0.00	42.230	3.1	0.6363	2.4
A543	P9	161124	0.969	2.021	0.00	0.791	3.1	0.8191	0.79
A544	P9	155446	3.801	1.916	0.00	3.247	7.1	0.8053	0.97
A545	P9	746910	0.014	9.421	0.03	0.002	3.9	0.821	0.54
A546	P9	8013	2.181	0.094	0.00	35.075	8.2	0.6537	3.8
A547	P9	5364	2.560	0.057	0.00	62.461	3.4	0.5311	3.6
A548	P9	6203	3.888	0.064	0.00	82.169	5.0	0.4892	3.4
A554	P9	18404	19.242	0.163	0.00	137.024	2.8	0.2563	3.5
A555	P9	20617	12.409	0.213	0.01	78.678	4.0	0.4779	3.3
A556	P9	12076	6.974	0.126	0.01	75.131	3.6	0.4801	2.6
A557	P9	18616	6.539	0.212	0.00	45.620	3.1	0.6213	1.7
A558	P9	26700	15.696	0.287	0.00	75.873	3.8	0.5149	2.1

spot	Sample	206Pb[a] (cps)	U[b] (ppm)	Pb[b] (ppm)	Th[b]/U	238U[c]/206Pb	± 2σ (%)	207Pb[c]/206Pb	± 2σ (%)
A559	P9	67167	16.773	0.823	0.00	31.201	7.4	0.6826	1.9
A560	P9	15770	8.188	0.172	0.00	67.249	4.8	0.543	2.4
A561	P9	23999	13.460	0.254	0.00	72.569	3.0	0.4967	2.2
A562	P9	23710	6.651	0.278	0.01	36.127	3.7	0.6607	1.6
A563	P9	13680	9.158	0.139	0.00	86.356	7.8	0.4348	5
A564	P9	11711	7.213	0.123	0.00	79.239	4.5	0.4734	3.2
A565	P9	17613	9.307	0.190	0.00	68.027	5.6	0.5194	3
A566	P9	11047	6.810	0.115	0.00	79.428	4.9	0.4594	3
A567	P9	12702	3.353	0.151	0.00	33.659	5.2	0.6706	2.4
A568	P9	3810	2.052	0.041	0.00	69.013	6.7	0.5052	3.2
A569	P9	45062	17.142	0.511	0.01	48.900	3.2	0.5979	1.3
A570	P9	29617	16.400	0.318	0.00	70.274	7.0	0.4888	4.2
A571	P9	92582	13.089	1.148	0.01	18.012	5.5	0.7399	1
A572	P9	41425	23.245	0.450	0.01	70.472	8.2	0.4915	4.6
A573	P9	24847	21.043	0.239	0.00	108.331	3.1	0.3352	3.6
A574	P9	54187	28.184	0.583	0.01	66.622	5.0	0.5072	2.8
A575	P9	15754	17.254	0.138	0.00	139.626	2.9	0.2053	5.3
A576	P9	30255	27.279	0.285	0.00	114.587	2.8	0.297	2.2
A577	P9	45648	21.383	0.506	0.00	59.524	6.9	0.5434	3.1
A578	P9	75952	15.816	0.913	0.00	26.853	14.1	0.7053	3.3
A579	P9	18930	11.286	0.200	0.00	76.161	8.9	0.4726	5.8
A580	P9	22820	0.500	0.295	0.39	2.768	3.7	0.7955	1.7
A581	P9	31370	2.000	0.403	0.02	8.078	5.7	0.7919	1.8
A582	P9	56099	2.132	0.730	0.05	4.771	3.6	0.8022	1.1
A583	P9	28063	1.722	0.365	0.04	7.669	5.2	0.7906	1.5
A584	P9	24732	3.638	0.308	0.06	18.515	4.0	0.7261	1.7
A585	P9	50445	3.055	0.642	0.04	7.710	5.0	0.787	0.95
A586	P9	80063	2.622	1.039	0.04	4.112	4.1	0.7967	0.92
A587	P9	43809	1.032	0.569	0.03	2.963	3.5	0.8005	1.1
A588	P9	39549	0.862	0.514	0.02	2.746	5.7	0.8063	1.2
A589	P9	37103	4.424	0.469	0.04	14.950	3.4	0.7469	1.1
A590	P9	40432	3.111	0.519	0.06	9.634	3.5	0.773	1.2
A591	P9	43824	1.088	0.573	0.03	3.101	3.6	0.7996	1
A592	P9	90806	1.145	1.195	0.04	1.570	11.5	0.8078	1.4
A593	P9	50308	1.112	0.660	0.03	2.755	3.6	0.8047	1
A594	P9	89803	2.443	1.187	0.04	3.370	3.2	0.8055	1.1
				WC-1 calcite reference (Roberts et al., 2017)					
P 03	WC-1	5960	6	0.27659244	0.00	22.401	2.5	0.1098	2.8
P 35	WC-1	5443	5	0.24345631	0.00	22.411	2.6	0.1187	2.9
P 69	WC-1	5287	5	0.24814146	0.00	22.852	2.6	0.1153	2.5
P 104	WC-1	4788	4	0.21027843	0.00	21.949	2.7	0.131	2.8
P 148	WC-1	3615	4	0.1787932	0.00	22.432	2.7	0.1144	2.6

spot	Sample	206Pb[a] (cps)	U[b] (ppm)	Pb[b] (ppm)	Th[b]/U	238U[c]/206Pb	± 2σ (%)	207Pb[c]/206Pb	± 2σ (%)
P 196	WC-1	4058	4	0.20482077	0.00	23.218	2.6	0.1159	2.9
P 240	WC-1	3779	4	0.20054314	0.00	23.132	3.0	0.1132	2.6
P 285	WC-1	3851	4	0.19615981	0.00	22.826	2.7	0.1257	3.3
P 330	WC-1	3289	4	0.18831887	0.00	23.414	2.6	0.1139	2.6
P 385	WC-1	3416	4	0.19407127	0.00	23.213	2.6	0.1261	3.5
P 441	WC-1	2720	4	0.17134958	0.00	22.999	2.9	0.1183	3.4
P 496	WC-1	3136	4	0.21059538	0.00	23.430	2.6	0.1206	3.8
P 551	WC-1	2592	4	0.17856733	0.00	22.356	2.7	0.1244	3.2
				Nama, stromatolitic limestone, Cambrian-Precambrian boundary, South Namibia					
B 04	NAMA	33218	2	0.72701275	0.03	5.348	4.2	0.4659	2.1
B 36	NAMA	18356	1	0.44097014	0.01	6.431	2.8	0.3972	1.7
B 70	NAMA	15638	1	0.39146974	0.01	6.892	2.7	0.3668	2.1
B 105	NAMA	11548	1	0.30318825	0.01	7.225	3.7	0.3478	2.2
B 149	NAMA	15971	2	0.42205988	0.02	6.925	3.8	0.3723	2.1
B 197	NAMA	19910	2	0.52390745	0.03	6.410	3.5	0.4006	2.3
B 241	NAMA	14612	1	0.3741792	0.02	5.365	4.0	0.4814	1.9
B 286	NAMA	18081	2	0.52018748	0.05	6.596	3.0	0.3948	1.6
B 331	NAMA	13915	1	0.40425221	0.02	6.281	3.2	0.4229	1.7
B 386	NAMA	22288	1	0.65405503	0.04	5.010	3.5	0.4821	2.1
B 442	NAMA	11295	1	0.38343061	0.01	6.614	3.8	0.3761	2.4
B 497	NAMA	8583	1	0.3202101	0.02	6.988	2.9	0.3555	2.1
B 552	NAMA	7391	1	0.29401884	0.01	7.267	3.5	0.3584	3.2
				Calgrun, inhouse calcite reference material					
9 5	Calgru	1505	7	0.04279431	0.00	234.5	4.9	0.2468	8.4
9 37	Calgru	3768	0	0.07606167	0.00	7.7	3.2	0.7451	3.1
9 71	Calgru	3822	1	0.08092124	0.00	50.8	4.6	0.6542	3.0
9 106	Calgru	1319	3	0.03427238	0.00	172.1	3.3	0.3748	4.5
9 150	Calgru	3442	1	0.07792698	0.00	47.3	3.0	0.6636	2.9
9 198	Calgru	384	7	0.02408513	0.00	299.9	3.3	0.08688	6.7
9 242	Calgru	2294	1	0.05524008	0.00	44.9	3.9	0.6535	3.3
9 287	Calgru	4545	0	0.10762331	0.00	6.8	4.2	0.7761	2.9
9 332	Calgru	2758	1	0.06873295	0.00	32.4	3.3	0.6983	3.2
9 387	Calgru	2264	1	0.06052375	0.00	49.9	3.2	0.6789	3.4
9 443	Calgru	2399	1	0.06891792	0.00	45.2	3.6	0.6571	3.9
9 498	Calgru	1510	3	0.05074196	0.00	131.8	3.2	0.468	3.6
9 553	Calgru	430	6	0.02772003	0.00	281.8	3.5	0.1447	9.4
				Sequence 2					
U007	GIS4	10790	169.45	51.65	<0.001	5.40	5.01	0.82	1.94
U008	GIS4	1216	102.85	6.10	0.03	26.10	5.67	0.70	5.93
U009	GIS4	4229	74.72	20.27	<0.001	6.03	5.28	0.80	3.01

spot	Sample	206Pb[a] (cps)	U[b] (ppm)	Pb[b] (ppm)	Th[b] / U	238U[c] / 206Pb	± 2σ (%)	207Pb[c] / 206Pb	± 2σ (%)
U010	GIS4	32948	128.03	155.10	1.05	1.37	12.34	0.84	1.27
U011	GIS4	635	133.41	3.51	0.02	55.80	6.44	0.61	6.71
U012	GIS4	9870	104.17	46.86	0.00	3.66	5.72	0.82	2.50
U013	GIS4	880	164.74	4.77	<0.001	51.51	5.42	0.64	5.43
U014	GIS4	1566	205.55	7.83	0.00	39.94	6.44	0.67	4.31
U015	GIS4	3013	359.04	14.89	0.07	36.53	5.81	0.67	2.81
U016	GIS4	8849	396.26	43.06	0.14	14.88	17.38	0.78	2.54
U017	GIS4	249836	702.17	1180.07	2.26	0.99	5.07	0.83	0.48
U018	GIS4	1730	143.38	8.84	<0.001	25.53	6.45	0.73	6.55
U019	GIS4	8694	102.61	41.50	0.12	4.07	5.39	0.82	2.21
U020	GIS4	37825	186.30	179.32	0.73	1.71	6.39	0.82	1.46
U021	GIS4	978	2.43	4.72	0.00	0.85	6.54	0.82	4.42
U022	GIS4	4320	132.25	21.14	<0.001	10.13	5.04	0.78	3.72
U023	GIS4	5440	72.76	25.61	0.01	4.73	5.15	0.84	2.93
U024	GIS4	519	61.55	2.52	0.00	37.31	6.25	0.68	7.16
U025	GIS4	15850	121.97	75.47	0.69	2.67	7.18	0.82	1.66
U026	GIS4	34967	213.43	165.65	0.38	2.13	5.31	0.83	1.27
U027	GIS4	11531	99.52	54.19	0.22	3.07	6.04	0.84	1.89
U028	GIS4	8379	177.06	40.52	<0.001	7.13	5.03	0.80	2.25
U029	GIS4	9916	65.03	46.80	0.00	2.31	4.58	0.83	1.73
U030	GIS4	6003	99.77	29.60	0.00	5.44	5.64	0.78	2.57
U031	GIS4	3627	74.28	17.40	0.03	7.01	4.90	0.81	3.90
U032	GIS4	791	192.83	4.46	0.01	61.81	5.20	0.57	4.84
U039	GIS4	2848	201.09	14.56	0.03	21.70	6.43	0.73	4.12
U040	GIS4	5202	250.52	25.68	0.02	15.72	5.49	0.78	2.97
U041	GIS4	8357	105.02	40.03	<0.001	4.28	21.56	0.80	2.98
U042	GIS4	15365	77.72	72.71	0.01	1.78	13.09	0.83	1.95
U043	GIS4b	6085	948.41	32.66	0.05	44.22	4.65	0.67	2.14
U044	GIS4b	22020	243.99	105.11	0.08	3.85	4.85	0.83	1.16
U045	GIS4b	2015	1050.17	14.27	0.07	97.27	4.77	0.44	4.36
U046	GIS4b	5158	966.18	28.60	0.03	50.45	6.48	0.64	3.39
U047	GIS4b	10421	786.64	52.86	0.03	23.58	4.67	0.74	2.51
U048	GIS4b	9913	996.97	51.12	0.07	30.39	7.13	0.71	2.20
U049	GIS4b	2879	1057.96	18.44	0.06	79.43	4.83	0.51	3.15
U050	GIS4b	7197	662.00	37.57	0.02	27.36	4.42	0.71	2.36
U051	GIS4b	4767	521.54	25.34	0.11	31.68	4.61	0.69	2.89
U052	GIS4b	7528	1527.36	42.54	0.04	53.00	5.38	0.62	2.39
U053	GIS4b	3245	1526.91	22.34	0.06	90.96	4.51	0.45	3.03
U054	GIS4b	6847	165.38	33.13	0.01	8.17	4.96	0.80	2.45
U055	Q29	555	566.56	6.61	0.01	97.35	5.25	0.23	8.15
U056	Q29	560	582.94	6.53	0.01	101.76	5.21	0.23	5.89

spot	Sample	206Pb[a] (cps)	U[b] (ppm)	Pb[b] (ppm)	Th[b]/U	238U[c]/206Pb	± 2σ (%)	207Pb[c]/206Pb	± 2σ (%)
U057	Q29	680	907.92	9.32	0.04	107.72	5.05	0.19	9.00
U058	Q29	641	1074.45	10.23	0.03	113.32	5.13	0.16	7.61
U059	Q29	585	449.40	5.70	0.02	93.73	5.85	0.29	7.32
U060	Q29	537	520.89	6.09	0.03	98.29	6.06	0.24	7.94
U061	Q29	621	489.12	6.11	0.03	95.21	5.56	0.29	7.92
U062	Q29	604	447.77	5.94	0.01	89.57	5.70	0.29	7.33
U063	Q29	972	304.33	6.71	0.01	60.80	7.18	0.46	6.38
U064	Q29	644	202.53	4.43	0.08	61.59	7.51	0.47	6.93
U065	Q29	835	269.45	5.66	0.02	64.57	6.75	0.48	5.51
U066	Q29	10443	3079.83	69.45	3.10	60.17	7.26	0.48	4.63
U073	Q29	11521	3253.01	69.64	3.20	60.98	20.61	0.42	17.00
U074	Q29	734	2374.07	18.01	1.79	134.99	4.87	0.10	8.00
U075	Q29	39349	2068.58	202.22	2.20	16.14	7.31	0.74	1.46
U076	Q29	14265	2492.58	82.94	1.73	43.69	8.23	0.59	3.17
U077	Q29	9734	1905.08	58.41	3.12	46.62	10.81	0.57	4.48
U078	Q29	15	76.80	0.58	<0.001	130.98	10.97	0.07	75.34
U079	Q29	1567	901.97	13.43	<0.001	83.26	5.37	0.35	4.57
U080	Q29	521	811.34	7.79	0.01	113.58	5.62	0.18	8.74
U081	Q29	311	380.09	4.15	0.01	102.01	6.24	0.20	12.27
U082	Q29	242	885.69	6.73	0.19	133.47	5.01	0.09	13.49
U083	Q29	684	1346.50	11.52	0.25	125.15	4.98	0.15	5.95
U084	Q29	643	946.65	9.05	0.01	115.30	5.03	0.19	6.38
U085	Q29	720	705.54	8.13	0.01	100.04	4.93	0.25	7.47
U086	Q29	4125	2017.53	32.77	0.02	77.97	7.01	0.38	6.78
U087	Q29	714	1848.17	15.40	<0.001	124.66	4.77	0.12	5.46
U088	Q27	75	166.86	1.44	0.03	122.40	9.47	0.14	23.14
U089	Q27	193	249.75	2.44	0.07	115.44	7.00	0.22	13.46
U090	Q27	877	224.17	5.89	0.08	52.27	9.57	0.50	6.75
U091	Q27	964	240.19	6.16	0.06	54.83	7.09	0.54	6.08
U092	Q27	1538	322.51	9.58	0.13	47.88	8.51	0.56	5.86
U093	Q27	678	346.60	5.63	0.05	77.47	6.64	0.37	7.26
U094	Q27	604	154.13	3.84	0.03	56.88	6.99	0.55	8.02
U095	Q27	311	283.10	3.37	0.03	97.85	7.01	0.26	9.78
U096	Q27	1049	94.90	5.81	0.04	24.90	5.93	0.68	8.68
U097	Q27	255	140.42	2.07	0.02	87.34	8.34	0.40	13.98
U098	Q27	1480	109.47	7.78	0.04	22.35	9.07	0.75	6.75
U099	Q27	149	199.60	1.93	0.07	116.32	8.80	0.22	14.34
U100	Q27	296	194.71	2.69	0.04	88.78	10.18	0.34	9.58
U101	Q27	511	306.87	4.34	0.03	87.89	7.82	0.35	11.02
U108	Q27	208	245.23	2.54	0.03	110.16	8.23	0.23	13.55
U109	Q27	575	370.21	5.07	0.11	90.39	7.27	0.35	11.34
U110	Q27	334	178.57	2.71	0.03	84.09	8.26	0.39	13.17

spot	Sample	206Pb[a] (cps)	U[b] (ppm)	Pb[b] (ppm)	Th[b] / U	238U[c] / 206Pb	± 2σ (%)	207Pb[c] / 206Pb	± 2σ (%)
U111	Q27	147	191.17	1.98	0.03	107.93	9.67	0.21	17.75
U112	Q27	3868	107.23	19.38	0.03	9.01	8.33	0.80	3.26
U113	Q27	314	180.00	2.88	0.03	76.58	6.62	0.33	10.97
U114	Q27	185	215.59	2.33	0.03	103.80	8.14	0.21	14.33
U115	Q27	1112	121.97	5.96	0.04	31.92	5.95	0.71	7.65
U116	Q27	304	99.98	2.12	0.03	65.07	8.71	0.51	13.34
U117	Q27	358	326.97	3.84	0.05	100.18	5.92	0.28	9.74
U118	Q27	218	244.52	2.44	0.02	116.42	5.60	0.26	7.49
U173	G3	261	230.99	2.84	0.01	96.64	7.53	0.29	13.17
U174	G3	236	414.34	3.65	0.03	124.39	6.59	0.18	11.13
U175	G3	773	633.83	7.55	0.05	99.78	9.14	0.29	16.42
U176	G3	450	711.89	6.68	0.02	117.78	5.19	0.19	6.21
U177	G3	234	711.10	5.45	0.03	135.49	5.50	0.12	12.32
U178	G3	118	175.38	1.55	0.01	127.55	9.00	0.22	16.81
U179	G3	216	1184.38	8.07	0.03	146.32	5.95	0.07	15.91
U180	G3	218	979.62	6.58	0.02	150.87	6.93	0.09	11.92
U181	G3	177	995.92	6.65	0.02	149.41	6.39	0.07	13.53
U182	G3	350	849.92	6.92	0.00	130.12	5.78	0.14	10.57
U183	G3	1176	522.26	9.06	0.02	76.73	5.52	0.45	6.60
U184	G3	2417	643.86	15.86	0.01	57.46	5.07	0.55	3.74
U185	G3	228	385.45	3.43	0.01	123.95	8.04	0.19	14.18
U186	G3	393	223.60	3.49	0.48	81.13	8.08	0.38	11.39
U187	G3	566	359.04	5.28	0.01	84.52	6.37	0.35	9.04
U188	G3	812	549.16	7.61	0.03	88.66	7.78	0.34	8.60
U189	G3	650	662.98	7.41	0.03	104.72	5.95	0.27	9.91
U190	G3	394	210.18	3.40	0.15	78.08	8.33	0.38	14.74
U191	G3	357	427.55	4.62	0.01	105.39	6.70	0.23	10.67
U192	G3	535	481.13	6.03	0.01	94.06	5.81	0.28	8.94
U193	G3	362	462.40	4.63	0.01	113.88	7.09	0.23	10.09
U200	G3	476	842.60	7.50	0.01	122.28	7.38	0.17	17.18
U201	G3	604	1391.94	11.51	0.08	128.86	4.77	0.15	6.97
U202	G3	1656	707.45	13.40	0.02	69.13	5.36	0.43	5.81
U204	G3	9078	158.80	40.18	0.10	6.29	6.63	0.75	1.84
U206	G3	95	405.28	2.98	0.01	137.64	7.57	0.09	25.81
U207	G3	1538	330.03	10.33	0.02	45.61	6.95	0.56	4.94
U208	G3	351	171.49	3.00	0.26	72.50	6.96	0.38	7.85
U209	G3	230	724.32	5.46	0.02	137.85	6.03	0.12	13.76
U210	G3	172	437.22	3.54	0.01	130.74	6.39	0.14	15.88
U211	G3	858	527.04	7.97	0.02	82.82	5.58	0.36	7.16
U213	G3	235	151.60	2.03	0.10	92.52	9.80	0.35	11.54
U214	G3	594	83.77	3.44	0.15	37.25	11.36	0.68	8.77

spot	Sample	206Pb[a] (cps)	U[b] (ppm)	Pb[b] (ppm)	Th[b]/U	238U[c]/206Pb	± 2σ (%)	207Pb[c]/206Pb	± 2σ (%)
U215	G3b	6584	5498.83	70.91	0.02	92.62	4.30	0.30	2.40
U216	G3b	5184	3831.03	51.67	0.02	90.37	5.54	0.32	4.44
U217	G3b	22835	2899.00	157.86	0.03	25.91	4.53	0.55	1.79
U218	G3b	44719	4515.68	288.86	0.02	22.89	4.36	0.61	1.08
U219	G3b	12647	4810.22	100.97	0.02	62.82	6.32	0.44	3.21
U220	G3b	54956	3498.68	342.88	0.07	15.26	4.72	0.64	1.05
U221	G3b	4493	6502.04	64.38	0.01	112.90	5.01	0.21	4.33
U222	G3b	556	1520.24	11.76	0.01	136.04	5.18	0.13	9.43
U223	G3b	3571	1072.82	26.99	0.01	53.94	5.21	0.48	4.19
U224	G3b	42590	1791.50	261.15	0.02	10.40	4.48	0.67	1.16
U225	G3b	21166	1346.37	132.46	0.01	15.21	4.32	0.64	1.63
U226	G3b	55003	3751.39	350.20	0.02	15.88	4.20	0.63	0.96
U227	G3b	26041	3926.17	177.77	0.02	31.53	4.23	0.56	1.43
U228	G3b	2157	1394.92	21.00	0.01	82.07	4.69	0.34	4.77
U229	G3b	5778	5729.82	68.18	0.02	98.19	4.64	0.27	5.48
U230	G3b	9292	3134.25	78.48	0.03	51.79	5.86	0.41	3.28
U231	G3b	2217	1317.97	21.17	0.02	77.50	5.13	0.35	3.84
U232	G3b	2554	679.13	18.74	0.01	50.01	5.74	0.51	4.71
U233	G3b	3252	618.65	22.63	0.00	38.87	5.04	0.56	4.47
U234	G3b	1579	1019.53	15.17	0.01	83.52	5.10	0.35	3.81
U235	G3b	2922	1450.47	25.38	0.01	73.53	4.46	0.40	3.98
U236	G3b	3189	1061.15	25.07	0.02	56.72	4.99	0.46	4.53
U237	P4	101842	1368.23	566.48	0.01	3.94	4.72	0.80	0.87
U244	P4	125232	1626.98	698.86	0.01	3.80	4.21	0.80	0.80
U245	P4	60593	3253.92	364.93	0.01	13.81	4.35	0.70	0.88
U246	P4	21240	5364.12	166.91	<0.001	43.19	4.26	0.47	1.66
U247	P4	77816	2226.49	450.89	0.01	7.87	4.60	0.76	0.86
U248	P4	32413	3543.79	213.32	0.00	24.41	4.27	0.61	1.15
U249	P4	27542	3991.64	189.94	0.00	30.13	4.40	0.57	1.09
U250	P4	26411	3154.96	175.26	0.00	26.35	4.14	0.61	1.66
U251	P4	35924	4589.83	242.54	0.00	27.44	4.15	0.59	1.12
U252	P4	28718	2897.56	186.85	<0.001	22.97	4.37	0.63	1.66
U253	P4	30419	4724.81	211.96	0.01	31.84	4.46	0.57	1.18
U254	P4	29459	4188.44	204.13	0.00	29.38	4.51	0.57	1.55
U255	P4	32896	11533.55	294.33	<0.001	50.15	4.16	0.39	1.20
U256	P4	41159	5303.99	277.87	<0.001	27.75	4.22	0.59	1.00
U257	P4	31172	8705.50	254.00	<0.001	45.54	4.21	0.45	1.18
U258	P4	25603	4913.12	189.75	0.00	35.89	4.29	0.52	1.24
U259	P4	142186	181.49	795.19	0.14	0.38	5.67	0.83	0.60
U260	P4	297431	21.56	1650.51	30.61	0.02	4.88	0.83	0.54
U261	P4	131947	14.80	733.83	7.91	0.03	4.53	0.83	0.61
U262	P4	156639	12.92	875.94	28.49	0.02	5.46	0.83	0.66

spot	Sample	206Pb[a] (cps)	U[b] (ppm)	Pb[b] (ppm)	Th[b]/U	238U[c]/206Pb	± 2σ (%)	207Pb[c]/206Pb	± 2σ (%)
U263	MGT9	13425	149.01	72.96	0.00	3.37	4.32	0.82	1.71
U264	MGT9	7296	73.48	40.96	<0.001	2.96	5.47	0.82	2.52
U265	MGT9	2259	104.14	13.03	<0.001	13.18	8.75	0.82	3.52
U266	MGT9	2734	215.75	15.35	<0.001	22.66	5.29	0.78	3.19
U267	MGT9	6221	165.50	34.72	<0.001	7.89	4.53	0.83	2.51
U268	MGT9	8536	152.96	48.29	0.00	5.23	4.36	0.82	1.71
U269	MGT9	5579	177.17	30.31	<0.001	9.62	5.31	0.82	1.98
U270	MGT9	11234	256.35	62.99	0.01	6.72	4.32	0.82	1.95
U271	MGT9	5079	223.97	29.15	0.00	12.50	5.20	0.79	2.84
U272	MGT9	2706	79.54	15.33	<0.001	8.56	5.92	0.82	3.05
U273	MGT9	10367	292.67	58.50	0.02	8.24	4.39	0.82	2.44
U274	MGT9	19148	264.65	107.92	0.09	4.06	5.28	0.83	1.88
U275	MGT9	7334	196.89	41.65	0.03	7.76	4.94	0.81	2.79
U276	MGT9	17298	180.19	97.51	<0.001	3.05	4.54	0.82	1.60
U277	MGT9	21116	100.68	119.44	0.00	1.39	4.85	0.82	1.59
U278	MGT9	2929	36.57	16.60	0.01	3.66	6.63	0.83	4.77
U279	MGT9	1873	128.62	10.55	<0.001	19.73	5.05	0.78	4.40
U280	MGT9	3136	421.70	17.96	0.00	37.64	5.85	0.77	3.92
U281	MGT9	1051	372.08	7.12	0.18	77.94	5.18	0.64	5.31
U282	MGT9	99555	215.25	554.29	25.82	0.64	4.58	0.82	0.42
U289	MGT9	4403	246.77	24.94	0.02	16.15	4.87	0.80	2.50
U290	MGT9	1139	235.97	7.20	<0.001	52.14	4.93	0.75	3.45
U291	MGT9	6750	260.71	38.63	0.05	11.12	4.52	0.82	2.39
U292	MGT9b	732	1291.01	7.77	<0.001	201.97	6.76	0.32	9.34
U293	MGT9b	112	1030.24	3.30	<0.001	318.48	6.69	0.10	20.99
U294	MGT9b	251	1304.18	4.87	<0.001	287.31	5.78	0.16	15.38
U295	MGT9b	6892	884.67	41.95	0.00	33.38	5.84	0.74	2.78
U296	MGT9b	2399	539.20	15.75	<0.001	51.67	5.40	0.66	3.68
U297	MGT9b	1726	791.54	12.02	<0.001	96.16	6.39	0.60	4.33
U298	MGT9b	1250	1266.47	10.53	<0.001	160.20	6.53	0.45	5.54
U299	MGT9b	482	62.39	2.88	0.00	34.82	8.52	0.77	8.20
U300	MGT9b	990	330.96	6.68	<0.001	73.85	6.22	0.64	6.99
U301	MGT9b	506	249.60	3.44	<0.001	107.68	8.09	0.63	9.12
U302	MGT9b	5680	223.55	33.31	0.01	10.95	6.10	0.80	3.46
U303	MGT9b	112	701.74	2.60	0.00	283.14	7.13	0.13	19.79
U304	MGT9b	133	456.60	1.85	<0.001	280.39	9.16	0.23	19.86
U305	MGT9b	190	554.03	2.40	<0.001	269.81	8.90	0.27	11.53
U306	MGT9b	2671	496.61	17.03	<0.001	44.86	5.18	0.69	3.49
U307	MGT9b	2895	790.80	18.98	<0.001	63.16	6.02	0.67	5.46
U308	MGT9b	1212	759.54	8.96	<0.001	120.28	5.36	0.55	5.60
U309	MGT9b	2346	901.71	16.20	<0.001	82.03	5.27	0.62	4.77
U310	MGT9b	3070	1086.74	21.11	<0.001	76.59	15.31	0.63	6.06

spot	Sample	206Pb[a] (cps)	U[b] (ppm)	Pb[b] (ppm)	Th[b]/U	238U[c]/206Pb	± 2σ (%)	207Pb[c]/206Pb	± 2σ (%)
U311	MGT9b	2342	759.23	15.17	<0.001	76.67	5.29	0.68	5.44
U312	MGT9b	1639	207.34	10.33	<0.001	31.40	8.72	0.72	4.57
U313	MGT9b	2700	48.11	15.88	<0.001	4.95	6.36	0.80	3.66
U314	MGT9b	529	717.55	4.93	<0.001	186.35	9.43	0.40	9.25
U315	MGT9b	222	92.21	1.56	<0.001	87.54	9.94	0.63	13.50
U316	MGT9b	418	400.58	3.35	<0.001	160.20	13.59	0.46	12.91
U317	MGT9b	394	509.17	3.55	<0.001	185.58	8.92	0.41	10.16
U318	MGT9b	769	251.11	5.33	<0.001	69.25	15.51	0.61	6.51
U319	BX16	432	83.00	3.01	0.10	39.94	8.36	0.59	6.24
U320	BX16	168	54.48	1.16	0.19	63.16	12.04	0.47	9.70
U321	BX16	123	53.74	0.90	0.12	78.70	7.74	0.44	14.26
U322	BX16	427	33.74	2.62	0.08	20.46	7.91	0.75	7.97
U323	BX16	286	79.70	1.74	0.08	62.80	6.96	0.50	9.21
U324	BX16	7475	59.10	43.14	0.13	2.29	5.53	0.84	2.67
U325	BX16	1236	69.56	7.61	0.10	14.60	7.07	0.76	6.58
U326	BX16	529	31.93	3.48	0.25	14.34	10.99	0.72	9.95
U327	BX16	2072	65.29	12.09	0.12	8.84	9.78	0.80	3.97
U334	BX16	6893	45.04	40.72	0.11	1.83	5.14	0.82	2.80
U335	BX16	11130	49.41	64.37	0.10	1.29	5.06	0.85	2.62
U336	BX16	808	45.50	5.05	0.13	14.26	8.28	0.74	7.30
U337	BX16	1690	69.93	10.46	0.18	10.74	16.97	0.77	6.88
U338	BX16	361	30.84	2.40	0.26	19.74	9.29	0.69	10.61
U339	BX16	679	61.98	4.39	0.10	22.06	9.55	0.72	8.42
U340	BX16	326	94.71	2.35	0.12	55.56	6.04	0.51	7.50
U341	BX16	10325	73.29	59.88	0.11	2.04	8.30	0.84	2.06
U342	BX16	1424	64.50	8.87	0.17	11.67	8.97	0.77	5.96
U343	BX16	772	23.18	4.78	0.06	7.89	17.62	0.79	9.61
U344	BX16	488	58.06	2.95	0.12	30.66	8.05	0.72	7.74
U345	BX16	3779	50.87	22.03	0.13	3.87	5.96	0.85	3.65
U346	BX16	522	65.60	3.47	0.11	29.03	8.94	0.69	7.74
U347	BX16	325	55.75	2.22	0.19	36.87	7.69	0.61	7.75
U348	BX16b	5029	67.30	30.74	0.41	3.51	14.95	0.77	3.31
U349	BX16b	254	80.80	2.03	0.13	55.33	9.40	0.52	11.73
U350	BX16b	128	84.47	1.31	0.10	79.66	9.09	0.35	9.11
U351	BX16b	165	49.57	1.29	0.25	54.10	9.73	0.54	10.58
U352	BX16b	355	55.26	2.15	0.14	36.61	6.45	0.56	6.40
U353	BX16b	252	63.33	1.67	0.13	53.46	7.63	0.55	8.20
U354	BX16b	155	48.74	1.20	0.19	56.73	8.91	0.53	17.83
U355	BX16b	921	72.86	6.14	0.23	18.27	10.64	0.69	6.74
U356	BX16b	523	30.63	3.40	1.18	14.09	8.30	0.72	9.46
U357	BX16b	382	67.40	2.79	0.67	35.21	8.65	0.60	11.20

spot	Sample	206Pb[a] (cps)	U[b] (ppm)	Pb[b] (ppm)	Th[b]/U	238U[c]/206Pb	± 2σ (%)	207Pb[c]/206Pb	± 2σ (%)
U358	BX16b	146	24.81	1.13	0.89	31.65	10.60	0.58	11.05
U359	BX16b	285	32.31	2.01	1.15	24.35	14.82	0.66	13.54
U360	BX16b	6476	114.39	39.82	0.51	4.67	9.63	0.79	3.19
U361	BX16b	44100	175.65	266.32	0.61	1.09	9.45	0.82	1.21
U362	BX16b	502	43.80	3.34	0.91	20.00	12.41	0.68	11.08
U363	BX16b	361	33.77	1.70	0.27	29.52	14.23	0.63	9.40
U364	BX16b	169	57.90	1.17	0.22	68.17	11.61	0.51	11.21
U365	BX16b	269	46.94	1.89	0.19	36.96	7.77	0.63	9.62
U366	BX16b	411	25.38	2.74	0.17	14.51	11.46	0.72	10.99
U367	BX16b	300	31.10	2.12	0.23	22.23	12.84	0.66	13.88
U368	BX16b	188	45.99	1.49	0.22	43.58	11.65	0.55	17.52
U369	BX16b	229	83.15	1.91	0.12	59.98	7.16	0.50	14.22
U370	BX16b	191	80.44	1.75	0.18	61.54	10.59	0.46	16.99
U402	B2	492	187.17	3.74	0.24	72.26	7.73	0.58	9.07
U403	B2	443	253.94	3.94	0.60	87.48	7.82	0.48	12.15
U404	B2	1203	288.45	8.22	0.52	54.35	6.77	0.70	6.20
U405	B2	163	321.97	2.23	0.79	168.61	7.64	0.26	12.05
U406	B2	3279	287.31	20.92	0.27	22.35	14.85	0.79	5.45
U407	B2	1669	402.83	11.39	0.19	54.77	8.38	0.70	5.31
U408	B2	996	330.36	7.59	0.19	63.72	6.37	0.61	8.14
U409	B2	492	413.23	4.64	0.13	116.76	6.51	0.43	9.09
U410	B2	1845	241.37	12.35	0.23	30.49	14.77	0.72	5.08
U411	B2	836	236.01	6.14	0.38	56.98	6.04	0.63	7.75
U412	B2	1166	218.13	7.86	0.26	43.17	13.08	0.71	7.07
U413	B2	1130	186.35	7.74	0.24	37.72	8.50	0.72	7.12
U414	B2	1451	206.74	9.75	0.47	33.37	8.44	0.73	6.00
U415	B2	679	222.76	4.89	0.41	68.75	7.24	0.66	7.38
U416	B2	614	140.58	4.16	0.19	52.90	9.89	0.72	8.01
U417	B2	998	50.90	6.43	0.33	13.07	11.29	0.82	7.13
U418	B2	2236	71.78	14.11	0.21	8.46	9.42	0.83	4.76
U419	B2	400	33.42	2.68	0.54	19.57	15.00	0.73	16.26
U420	B2	914	80.32	5.64	0.21	23.27	12.44	0.80	9.18
U421	B2	4064	57.85	25.56	0.50	3.77	19.67	0.84	4.27
U422	B2	727	128.86	4.94	0.43	40.80	8.14	0.72	9.83
U423	B2	101	363.39	1.62	0.64	252.64	10.32	0.21	31.81
U424	B2	1084	190.82	7.24	0.30	41.40	7.24	0.73	6.63
U425	P2	3327	640.94	26.46	<0.001	34.54	5.20	0.56	3.36
U426	P2	7050	878.91	51.76	<0.001	25.35	4.70	0.64	2.43
U427	P2	4769	454.84	34.25	<0.001	20.21	6.62	0.67	3.47
U428	P2	1847	458.15	15.54	<0.001	40.94	4.90	0.52	4.99
U429	P2	4076	657.72	31.25	<0.001	30.69	4.79	0.60	3.22

spot	Sample	206Pb[a] (cps)	U[b] (ppm)	Pb[b] (ppm)	Th[b]/U	238U[c]/206Pb	± 2σ (%)	207Pb[c]/206Pb	± 2σ (%)
U430	P2	2774	449.02	21.81	<0.001	29.62	4.85	0.58	4.25
U431	P2	6555	677.91	47.47	0.01	21.54	5.21	0.66	3.44
U432	P2	2533	906.64	24.30	0.00	49.05	4.82	0.43	5.12
U433	P2	4099	529.73	30.77	<0.001	25.47	5.05	0.62	2.76
U434	P2	4171	665.54	31.95	<0.001	30.41	5.26	0.60	2.87
U435	P2	3914	636.20	30.28	<0.001	30.62	4.86	0.60	3.81
U436	P2	4132	1130.97	36.55	<0.001	42.20	4.89	0.49	3.78
U437	P2	4665	576.82	34.53	<0.001	24.99	5.19	0.64	3.32
U438	P2	2821	426.33	21.63	<0.001	28.98	5.58	0.61	4.49
U445	P2	4721	510.72	34.41	<0.001	22.50	5.01	0.67	2.95
U446	P2	6585	422.60	46.33	<0.001	14.18	4.55	0.71	2.71
U447	P2	3774	564.19	29.03	<0.001	28.58	4.95	0.61	3.77
U448	P2	1890	535.41	16.88	<0.001	43.20	5.86	0.49	4.53
U449	P2	2199	499.97	18.47	<0.001	37.95	5.22	0.54	5.78
U450	P2	3675	916.08	31.87	<0.001	39.68	4.52	0.51	3.02
U451	P2	5822	671.12	43.18	<0.001	23.34	4.69	0.65	2.96
U452	P2	2934	874.35	26.71	<0.001	44.27	4.94	0.48	3.90
U453	P2	3559	615.56	28.18	<0.001	31.71	4.97	0.59	4.24
U454	P2	2652	591.87	21.98	<0.001	38.24	6.14	0.56	4.10
U455	P2	3174	786.13	27.54	<0.001	39.49	5.14	0.51	3.50
U456	P2	2394	766.62	22.60	<0.001	45.15	5.26	0.45	4.15
U457	P2	2517	829.06	23.84	<0.001	46.31	4.85	0.45	3.76
U458	P2	3933	838.87	33.60	0.00	34.88	5.07	0.53	3.49
U459	P2	2554	961.53	25.51	<0.001	49.15	4.65	0.42	4.01
U460	P2	2431	602.54	21.11	0.02	39.55	4.75	0.52	3.92
U461	P2	2041	762.54	20.07	0.00	49.98	5.18	0.44	5.34
U462	P2	2838	794.55	25.66	0.00	42.21	5.18	0.49	3.90
U463	P63	1568	2238.76	26.54	<0.001	94.78	4.55	0.21	6.29
U464	P63	610	155.79	5.33	0.00	40.59	5.63	0.52	6.62
U465	P63	2149	2811.55	34.79	0.00	91.71	4.43	0.23	4.30
U466	P63	92885	404.95	619.03	0.00	1.07	4.86	0.80	1.06
U467	P63	664	4083.86	34.72	<0.001	116.48	4.47	0.06	5.77
U468	P63	10571	1265.59	79.03	0.01	24.06	5.74	0.65	2.40
U469	P63	563	157.48	4.89	0.06	45.13	8.07	0.53	9.41
U470	P63	7451	126.97	50.34	0.01	4.08	7.78	0.78	2.31
U471	P63	3488	444.43	26.22	0.00	25.56	4.61	0.66	4.30
U472	P63	12642	118.60	83.71	0.02	2.33	4.55	0.81	1.93
U473	P63	392	1612.70	14.70	0.00	111.11	5.00	0.09	9.62
U474	P63	34060	83.46	226.47	0.03	0.60	4.38	0.81	1.30
U475	P63	58571	112.21	389.88	0.04	0.47	4.35	0.81	0.90
U476	P63	1213	3518.82	35.55	<0.001	102.71	4.42	0.12	8.33
U477	P63	1129	1470.87	19.06	0.01	87.06	4.69	0.22	5.74

spot	Sample	206Pb[a] (cps)	U[b] (ppm)	Pb[b] (ppm)	Th[b] / U	238U[c] / 206Pb	± 2σ (%)	207Pb[c] / 206Pb	± 2σ (%)
U478	P63	566	1955.93	18.73	<0.001	106.90	4.74	0.10	11.68
U479	P63	1605	6017.98	55.66	<0.001	110.38	4.28	0.10	4.19
U480	P63	1608	2974.87	33.53	0.02	96.10	4.84	0.17	8.10
U481	P63	1615	3039.87	33.29	0.00	99.34	4.53	0.17	3.88
U482	P63	786	5054.06	43.58	<0.001	114.57	4.39	0.06	7.00
U483	P63	1159	3676.52	35.35	<0.001	107.53	4.28	0.11	6.81
U484	P63	886	112.01	6.88	0.01	24.40	8.55	0.65	8.05
U485	P63	516	3112.07	26.86	<0.001	114.89	4.56	0.06	7.94
U486	P63	458	1009.04	10.65	<0.001	101.12	5.31	0.15	10.56
U487	P63	1496	4972.32	48.32	<0.001	105.82	4.29	0.11	4.90
U488	P21	77586	7985.50	554.68	<0.001	22.60	4.34	0.73	0.72
U489	P21	69647	2794.95	481.40	0.60	9.33	4.15	0.77	0.97
U490	P21	67107	1988.01	458.14	0.00	7.04	4.31	0.79	0.94
U491	P21	85126	845.28	574.77	<0.001	2.41	4.29	0.81	1.05
U492	P21	65026	2435.41	449.79	0.13	8.70	4.18	0.77	0.87
U493	P21	70252	4522.28	492.51	0.00	14.63	4.26	0.76	0.96
U500	P21	70482	3662.97	492.02	0.01	11.96	4.33	0.77	0.82
U501	P21	75859	1717.51	525.15	0.15	5.29	4.19	0.78	0.80
U502	P21	99860	562.09	680.79	0.02	1.35	4.32	0.81	0.74
U503	P21	52302	3720.91	369.68	0.04	16.05	4.13	0.76	0.89
U504	P21	164199	1187.37	1121.27	<0.001	1.73	4.31	0.80	0.69
U505	P21	84798	4971.19	600.72	0.02	13.20	4.78	0.76	0.89
U506	P21	52553	1879.54	364.73	0.00	8.36	4.37	0.79	1.16
U507	P21	55368	4479.81	396.95	<0.001	17.89	4.46	0.75	0.90
U508	P21	52309	849.61	361.59	0.06	3.82	4.36	0.79	1.13
U509	P21	49717	1856.94	349.17	0.02	8.57	4.75	0.78	1.16
U510	P21	57649	4444.98	416.35	<0.001	16.86	4.38	0.74	0.95
U511	P21	52735	3023.03	373.47	0.02	12.95	4.17	0.76	0.96
U512	P21	54926	4099.87	395.82	<0.001	16.38	4.20	0.74	0.97
U513	P21	52051	6551.86	387.14	<0.001	26.23	4.45	0.71	1.17
U514	P21	45907	12184.53	364.87	<0.001	49.70	4.11	0.63	1.22
U515	P21	58504	5628.95	428.59	<0.001	20.60	4.48	0.73	0.91
U516	P21	52224	10488.41	404.30	0.01	39.27	4.19	0.66	0.99
U517	P21	67258	11231.74	514.97	<0.001	33.37	4.96	0.68	1.06
U518	B46	3503	106.67	23.83	0.72	7.43	10.27	0.83	4.24
U519	B46	1790	52.42	12.58	1.19	6.76	8.75	0.79	4.19
U520	B46	1136	43.08	8.30	1.30	8.43	9.95	0.79	7.35
U521	B46	1356	52.79	9.41	2.57	9.30	6.81	0.83	7.25
U522	B46	2565	26.85	17.78	2.44	2.50	6.01	0.83	6.92
U523	B46	5973	86.77	13.10	0.60	10.51	6.56	0.75	2.45
U524	B46	1033	203.15	7.13	0.11	42.46	6.21	0.64	6.73

spot	Sample	206Pb[a] (cps)	U[b] (ppm)	Pb[b] (ppm)	Th[b]/U	238U[c]/206Pb	± 2σ (%)	207Pb[c]/206Pb	± 2σ (%)
U525	B46	1222	183.96	10.19	0.12	28.72	7.33	0.73	5.98
U526	B46	1196	81.70	9.13	0.67	14.04	5.89	0.83	5.50
U527	B46	45979	49.66	8.21	2.21	10.01	7.80	0.79	1.20
U528	B46	1597	402.34	330.96	0.42	1.97	6.21	0.83	4.70
U529	B46	1663	58.59	11.06	1.32	8.77	6.97	0.78	6.49
U530	B46	2491	72.14	11.91	1.20	9.79	7.51	0.78	4.77
U531	B46	1230	71.68	18.02	1.17	6.43	6.27	0.79	5.44
U532	B46	879	52.00	8.75	1.43	9.67	6.55	0.78	4.16
U533	B46	40773	47.86	6.08	1.56	12.75	31.86	0.83	1.38
U534	B46	2064	190.23	275.53	0.53	1.14	6.08	0.81	5.04
U535	B46	1329	79.16	14.59	1.24	8.88	6.17	0.80	6.93
U536	B46	2935	53.80	9.42	1.26	9.35	7.22	0.84	4.86
U537	B46	2870	84.04	20.15	0.56	6.97	7.36	0.82	5.42
U538	B46	4610	94.26	20.07	0.58	7.74	15.62	0.80	3.35
U539	B46	1929	183.37	33.67	0.09	8.87	6.60	0.77	6.18
U540	B46	2284	61.88	14.13	0.48	7.04	5.38	0.85	4.88
U541	B46	1381	78.72	15.64	0.78	8.45	6.73	0.78	7.03
U542	B46	770	70.07	10.05	2.45	11.26	7.01	0.74	7.71
U543	C12	119545	38.41	5.78	2.74	10.51	4.39	0.84	0.66
U544	C12	148272	694.06	824.66	1.58	1.40	4.18	0.83	0.38
U545	C12	173880	705.48	1035.95	2.12	1.13	4.44	0.83	0.71
U546	C12	171876	848.21	1207.97	1.66	1.17	4.46	0.83	0.71
U547	C12	324583	766.91	1198.25	1.92	1.06	4.68	0.84	0.50
U548	C12	166598	1618.94	2258.14	0.85	1.19	5.58	0.84	0.73
U555	C12	53141	1036.00	1160.53	0.73	1.49	4.99	0.84	1.03
U556	C12	107054	553.04	373.43	0.98	2.47	4.34	0.83	0.80
U557	C12	105075	1190.83	753.09	0.84	2.63	4.35	0.84	0.94
U558	C12	117930	1598.78	738.47	0.53	3.60	4.25	0.83	0.74
U559	C12	62681	1272.34	828.99	0.71	2.55	4.17	0.83	0.91
U560	C12	62477	1021.70	441.18	0.52	3.85	4.23	0.83	0.82
U561	C12	75369	832.31	440.45	0.50	3.14	4.58	0.83	0.95
U562	C12	49711	822.00	534.25	0.92	2.55	4.19	0.83	0.86
U563	C12	76597	1721.72	346.93	0.15	8.23	4.28	0.84	0.63
U564	C12	57245	644.19	545.35	1.21	1.96	4.32	0.84	0.84
U565	C12	77619	694.55	402.93	0.98	2.87	4.34	0.83	1.21
U566	C12	41836	658.13	551.54	1.22	1.98	4.20	0.84	1.15
U567	C12	45722	837.72	295.55	0.37	4.71	4.39	0.83	0.97
U568	C12	67208	949.37	325.02	0.31	4.85	4.28	0.83	0.69
U569	C12	48423	1594.28	465.07	0.29	5.69	4.15	0.83	0.82
U570	C12	72597	1260.13	344.68	0.20	6.05	4.28	0.84	0.61
U571	C12	192789	1016.50	514.25	0.33	3.29	4.21	0.83	0.59
U572	C12	96786	1096.55	1371.41	0.32	1.33	4.32	0.83	0.66

spot	Sample	206Pb[a] (cps)	U[b] (ppm)	Pb[b] (ppm)	Th[b]/U	238U[c]/206Pb	± 2σ (%)	207Pb[c]/206Pb	± 2σ (%)
U573	BX33	6538	1041.08	690.03	0.70	2.51	4.74	0.84	2.13
U574	BX33	6164	69.01	46.63	<0.001	2.46	4.50	0.81	2.09
U575	BX33	7770	121.58	44.63	0.00	4.48	4.93	0.85	2.71
U576	BX33	5026	51.51	55.26	0.00	1.56	4.71	0.80	2.90
U577	BX33	2873	141.03	36.86	0.03	6.25	4.73	0.77	2.96
U578	BX33	3943	207.02	21.35	0.00	15.54	4.77	0.82	2.55
U579	BX33	4317	90.30	28.24	<0.001	5.29	4.73	0.77	3.30
U580	BX33	3813	244.74	32.42	0.01	12.14	5.76	0.79	3.48
U581	BX33	4434	184.36	28.35	0.01	10.55	4.52	0.80	3.23
U582	BX33	3964	108.26	32.53	0.00	5.45	5.25	0.83	3.69
U583	BX33	3835	89.29	28.79	0.00	5.13	5.18	0.79	2.76
U584	BX33	2051	147.69	28.54	0.01	8.39	5.13	0.81	5.36
U585	BX33	7424	52.24	15.10	<0.001	5.68	4.84	0.84	2.74
U586	BX33	6151	40.04	53.38	0.01	1.25	4.85	0.84	2.45
U587	BX33	8973	46.27	44.22	0.03	1.75	6.09	0.82	2.36
U588	BX33	7601	60.55	65.18	0.36	1.54	4.58	0.82	2.56
U589	BX33	4417	70.61	55.48	<0.001	2.10	4.61	0.80	3.32
U590	BX33	3889	129.09	32.84	0.03	6.41	4.72	0.79	3.95
U591	BX33	5315	159.09	29.10	0.02	8.89	4.67	0.80	2.89
U592	BX33	6220	114.28	39.57	0.03	4.71	4.43	0.84	1.89
				Soda-lime glass NIST SRM-614					
A001	NIST	290623	0.85	2.79	0.93	1.22	0.59	0.87	0.47
A002	NIST	284547	0.86	2.73	0.94	1.26	0.54	0.87	0.42
A033	NIST	278502	0.81	2.68	0.95	1.21	0.47	0.87	0.37
A034	NIST	261572	0.80	2.52	0.95	1.27	0.41	0.87	0.42
A067	NIST	268583	0.79	2.61	0.96	1.21	0.60	0.87	0.46
A068	NIST	264484	0.80	2.58	0.97	1.23	0.40	0.87	0.52
A102	NIST	264427	0.80	2.64	0.96	1.21	0.55	0.87	0.44
A103	NIST	256512	0.82	2.56	0.95	1.28	0.44	0.87	0.38
A146	NIST	251301	0.81	2.58	0.96	1.25	0.48	0.87	0.36
A147	NIST	251716	0.82	2.59	0.95	1.27	0.69	0.87	0.44
A194	NIST	257030	0.83	2.75	0.96	1.21	0.51	0.87	0.34
A195	NIST	242489	0.82	2.59	0.96	1.25	0.68	0.87	0.51
A238	NIST	251683	0.82	2.78	0.97	1.18	0.49	0.87	0.40
A239	NIST	241638	0.84	2.67	0.95	1.25	0.37	0.87	0.53
A283	NIST	230326	0.82	2.64	0.96	1.24	0.64	0.87	0.40
A284	NIST	229149	0.82	2.62	0.96	1.26	0.45	0.87	0.55
A328	NIST	225180	0.83	2.67	0.96	1.25	0.52	0.87	0.40
A329	NIST	220174	0.81	2.61	0.97	1.24	0.45	0.87	0.39
A383	NIST	227452	0.84	2.82	0.97	1.21	0.51	0.88	0.60
A384	NIST	214023	0.84	2.65	0.96	1.27	0.55	0.87	0.54
A439	NIST	213330	0.82	2.76	0.97	1.20	0.55	0.87	0.37

spot	Sample	206Pb[a] (cps)	U[b] (ppm)	Pb[b] (ppm)	Th[b]/U	238U[c]/206Pb	± 2σ (%)	207Pb[c]/206Pb	± 2σ (%)
A440	NIST	200942	0.82	2.60	0.97	1.27	0.52	0.87	0.39
A494	NIST	190948	0.80	2.58	0.97	1.23	0.41	0.87	0.54
A495	NIST	191298	0.81	2.59	0.97	1.25	0.74	0.87	0.44
A549	NIST	187090	0.82	2.66	0.97	1.23	0.44	0.87	0.52
A550	NIST	181493	0.80	2.58	0.98	1.24	0.39	0.87	0.37
A593	NIST	182355	0.83	2.70	0.97	1.22	0.58	0.87	0.50
A594	NIST	178256	0.83	2.64	0.98	1.25	0.61	0.87	0.36
				WC-1 calcite reference (Roberts et al., 2017)					
B003	WC1	22262	6.59	0.40	<0.001	0.05	4.45	0.17	6.88
B004	WC1	12162	5.47	0.27	<0.001	0.04	4.31	0.12	4.46
B035	WC1	20733	5.95	0.37	<0.001	0.05	4.34	0.17	6.85
B036	WC1	9579	5.15	0.24	<0.001	0.04	4.36	0.10	6.05
B069	WC1	18979	7.08	0.38	<0.001	0.04	4.25	0.14	5.25
B070	WC1	10821	4.89	0.24	<0.001	0.04	4.45	0.12	9.90
B104	WC1	22794	7.08	0.42	<0.001	0.05	4.50	0.17	6.88
B105	WC1	9948	4.60	0.23	<0.001	0.04	4.21	0.12	3.58
B148	WC1	14977	8.02	0.38	<0.001	0.04	4.20	0.11	3.46
B149	WC1	13755	5.97	0.30	<0.001	0.04	4.38	0.13	6.39
B196	WC1	12556	6.74	0.32	<0.001	0.04	4.24	0.11	5.60
B197	WC1	14023	5.41	0.30	<0.001	0.05	4.62	0.15	10.57
B240	WC1	14284	6.95	0.35	<0.001	0.04	4.29	0.13	4.57
B241	WC1	11621	4.95	0.27	<0.001	0.05	4.53	0.14	7.89
B285	WC1	19784	6.47	0.41	<0.001	0.05	4.83	0.18	7.66
B286	WC1	13865	5.23	0.30	<0.001	0.05	4.47	0.16	5.00
B330	WC1	17944	6.88	0.41	<0.001	0.05	4.67	0.16	7.60
B331	WC1	8574	4.62	0.23	<0.001	0.04	4.27	0.12	5.12
B385	WC1	19217	7.28	0.44	<0.001	0.05	4.73	0.16	9.70
B386	WC1	9361	5.85	0.28	<0.001	0.04	4.30	0.11	7.17
B441	WC1	15083	8.46	0.44	<0.001	0.05	4.37	0.12	6.60
B442	WC1	21140	5.96	0.44	<0.001	0.05	4.83	0.22	7.11
B496	WC1	13690	6.34	0.37	<0.001	0.05	4.29	0.15	6.27
B497	WC1	18084	7.20	0.44	<0.001	0.05	4.94	0.18	7.97
B551	WC1	13625	6.67	0.38	<0.001	0.05	4.66	0.15	6.36
B552	WC1	13942	6.38	0.37	<0.001	0.05	4.70	0.17	7.66
				ASH15D calcite reference (Vaks et al., 2003)					
C005	ASH	2709	1.77	0.03	<0.001	0.00	10.20	0.79	5.19
C006	ASH	268532	1.30	2.48	<0.001	0.54	11.83	0.87	1.09
C037	ASH	179833	3.56	1.71	<0.001	0.14	8.77	0.87	0.74
C038	ASH	781250	2.82	7.34	<0.001	0.74	8.50	0.87	0.88
C071	ASH	486	2.38	0.01	<0.001	0.00	6.83	0.51	9.36
C072	ASH	383145	2.75	3.73	<0.001	0.38	7.22	0.87	0.82

spot	Sample	206Pb[a] (cps)	U[b] (ppm)	Pb[b] (ppm)	Th[b]/U	238U[c]/206Pb	± 2σ (%)	207Pb[c]/206Pb	± 2σ (%)
C106	ASH	10078	2.75	0.10	<0.001	0.01	7.69	0.83	1.75
C107	ASH	8403	2.19	0.08	<0.001	0.01	11.25	0.82	4.13
C150	ASH	5411	2.27	0.05	<0.001	0.01	7.64	0.83	2.46
C151	ASH	1583839	2.01	22.39	<0.001	2.47	16.23	0.92	38.60
C198	ASH	3610	2.29	0.04	<0.001	0.01	11.87	0.80	4.20
C199	ASH	312605	4.18	3.28	<0.001	0.23	12.45	0.87	0.58
C242	ASH	2363	3.22	0.03	<0.001	0.00	11.32	0.73	5.47
C243	ASH	428907	2.85	4.67	<0.001	0.47	15.07	0.87	1.41
C287	ASH	685	3.71	0.01	<0.001	0.00	10.03	0.50	8.73
C288	ASH	1210592	3.44	14.31	<0.001	1.13	5.07	0.88	1.14
C332	ASH	9218	3.22	0.11	<0.001	0.01	7.91	0.85	3.02
C333	ASH	543751	3.70	6.40	<0.001	0.49	12.91	0.88	0.73
C387	ASH	695606	1.84	8.49	<0.001	1.31	7.63	0.88	0.82
C388	ASH	669	6.54	0.01	<0.001	0.00	5.90	0.38	6.50
C443	ASH	984	1.77	0.01	<0.001	0.00	11.46	0.68	7.85
C444	ASH	11900	2.15	0.15	<0.001	0.02	15.19	0.86	2.51
C498	ASH	726	3.39	0.01	<0.001	0.00	6.10	0.54	5.77
C499	ASH	436	1.60	0.01	<0.001	0.00	8.47	0.59	10.29
C553	ASH	32340	1.94	0.45	<0.001	0.07	6.63	0.88	1.46
C554	ASH	432329	2.64	6.07	<0.001	0.65	17.97	0.88	0.89
				Sequence 3					
U088	BX5	9420	1306.86	53.92	0.00	35.05	3.65	0.59	2.18
U089	BX5	4695	1312.63	32.31	0.02	53.90	2.82	0.45	2.94
U090	BX5	4985	738.20	28.96	0.00	36.70	2.91	0.58	2.27
U091	BX5	6011	1640.29	41.26	0.01	52.88	2.64	0.45	2.48
U092	BX5	10180	625.09	52.28	0.02	18.53	3.30	0.70	2.07
U093	BX5	5571	523.14	30.33	0.00	25.79	2.97	0.64	2.69
U094	BX5	30170	1071.02	151.96	0.23	11.09	4.81	0.73	1.38
U095	BX5	7681	1048.54	44.65	0.02	33.81	2.67	0.58	2.02
U096	BX5	5545	416.83	29.41	0.01	21.57	3.12	0.67	2.35
U097	BX5	7002	1598.72	45.83	<0.001	47.44	3.48	0.49	2.61
U098	BX5	12511	381.08	61.51	0.01	9.91	2.53	0.76	1.81
U099	BX5	9737	1629.14	58.49	0.02	39.51	3.06	0.55	2.05
U100	BX5	7293	422.57	37.76	0.00	17.30	2.86	0.70	2.12
U101	BX5	9075	1145.56	51.54	0.01	32.50	3.16	0.60	2.33
U108	BX5	5328	1233.21	34.41	0.01	49.14	3.56	0.50	2.90
U109	BX5	4785	462.67	26.40	0.01	26.16	3.12	0.64	2.91
U110	BX5	4432	1904.47	36.09	0.01	66.03	2.68	0.36	3.41
U111	BX5	7862	180.21	38.56	0.00	7.53	2.75	0.78	2.02
U112	BX5	3523	1117.51	25.27	0.00	58.02	2.95	0.43	3.43
U113	BX5	9463	511.16	49.65	0.00	15.92	3.41	0.70	2.31
U114	BX5	10630	625.05	55.37	0.00	17.47	2.79	0.70	1.77

spot	Sample	206Pb[a] (cps)	U[b] (ppm)	Pb[b] (ppm)	Th[b]/U	238U[c]/206Pb	± 2σ (%)	207Pb[c]/206Pb	± 2σ (%)
U115	BX5	7621	957.26	43.98	0.00	31.72	2.85	0.60	2.27
U116	BX5	10757	1551.01	62.76	0.02	35.77	3.10	0.59	1.86
U117	BX5	16813	1201.68	89.62	0.08	20.53	3.66	0.68	1.62
U118	B22	124	59.81	0.95	0.04	80.02	9.04	0.39	15.07
U119	B22	58	60.63	0.60	0.04	122.20	12.22	0.30	25.71
U120	B22	162	67.78	1.08	0.06	85.48	8.27	0.49	14.09
U121	B22	108	52.49	0.83	0.03	81.19	9.80	0.40	19.64
U122	B22	113	72.30	0.95	0.02	94.85	9.57	0.35	19.55
U123	B22	124	59.53	0.86	0.03	92.98	8.47	0.47	15.76
U124	B22	591	39.45	3.20	0.12	18.75	13.36	0.67	8.47
U125	B22	126	46.34	0.84	0.07	75.79	11.47	0.51	18.42
U126	B22	72	54.15	0.58	0.03	116.40	11.61	0.37	24.33
U127	B22	53	59.30	0.58	0.03	119.60	10.80	0.26	27.70
U128	B22	121	65.43	0.90	0.07	95.11	10.77	0.43	18.66
U129	B22	254	62.52	1.55	0.10	57.41	10.26	0.56	11.57
U130	B22	84	43.39	0.62	0.17	93.11	11.56	0.44	17.10
U131	B22	151	48.01	0.98	0.15	67.02	8.01	0.50	15.79
U132	B22	127	74.85	0.99	0.19	96.94	10.94	0.40	17.85
U133	B22	218	63.06	1.31	0.18	69.09	9.13	0.57	12.95
U134	B22	362	59.61	2.03	0.19	44.44	9.06	0.66	11.15
U135	B22	318	56.97	1.79	0.13	47.68	8.20	0.65	10.56
U136	B22	1445	73.54	7.45	0.42	15.55	6.55	0.73	5.72
U137	B22	702	69.40	3.69	0.20	29.32	8.45	0.71	7.46
U138	B22	161	52.64	1.06	0.11	68.72	8.84	0.52	13.29
U139	B22	129	48.43	0.80	0.08	85.41	10.79	0.55	17.70
U140	B22	460	38.54	2.43	0.10	24.56	6.68	0.70	7.70
U141	B22	155	29.00	0.98	0.12	43.10	11.52	0.59	15.42
U142	B22	93	64.32	0.79	0.09	101.10	10.67	0.35	19.42
U143	B22	266	54.00	1.45	0.11	56.47	14.20	0.67	14.48
U144	B22	113	32.50	0.77	0.18	58.71	10.56	0.51	18.57
U145	B22	154	41.80	0.94	0.14	64.34	10.73	0.59	13.25
U152	B22	111	54.54	0.84	0.11	83.12	13.33	0.40	22.94
U153	B22	7399	100.47	35.99	0.20	4.62	4.53	0.82	2.45
U154	B22	2545	77.78	12.54	0.23	10.04	6.32	0.78	3.84
U155	B22	520	79.64	2.97	0.09	39.91	8.33	0.63	7.41
U156	B22	263	50.82	1.41	0.03	54.86	11.04	0.67	13.33
U157	B22	197	60.94	1.27	0.03	65.21	16.63	0.48	15.32
U158	B22	125	61.51	0.86	0.03	95.53	12.17	0.47	17.03
U159	B22	307	73.98	1.85	0.07	58.68	10.54	0.61	9.06
U160	B22	392	78.93	2.32	0.26	50.11	7.68	0.61	10.64
U161	B22	162	68.49	1.10	0.15	86.66	11.48	0.52	18.79
U162	GPR401	212761	4843.52	1037.07	0.02	7.75	2.47	0.83	0.57

spot	Sample	206Pb[a] (cps)	U[b] (ppm)	Pb[b] (ppm)	Th[b]/U	238U[c]/206Pb	± 2σ (%)	207Pb[c]/206Pb	± 2σ (%)
U163	GPR401	540733	1023.23	2629.61	0.09	0.65	2.45	0.83	0.40
U164	GPR401	204735	4807.73	896.11	0.04	8.90	3.49	0.83	0.49
U165	GPR401	772644	6351.47	3760.85	0.03	2.81	2.69	0.83	0.34
U166	GPR401	178934	7578.62	875.94	0.01	14.35	2.72	0.83	0.58
U167	GPR401	1840998	2966.52	9039.33	0.02	0.55	5.84	0.83	0.45
U168	GPR401	3507595	3020.32	17298.59	0.04	0.29	6.87	0.83	0.33
U169	GPR401	553461	5035.11	2732.16	0.03	3.06	4.12	0.83	0.37
U170	GPR401	529043	6079.43	2594.05	0.02	3.89	2.78	0.83	0.35
U171	GPR401	535338	5210.62	2633.18	0.02	3.29	3.16	0.83	0.42
U172	GPR401	495745	5048.75	2431.78	0.01	3.45	3.23	0.83	0.36
U173	GPR401	179746	866.67	883.53	0.05	1.63	2.51	0.83	0.55
U174	GPR401	267690	5004.05	1315.75	0.01	6.31	2.92	0.83	0.49
U175	GPR401	244681	3363.04	1211.54	0.05	4.61	3.00	0.83	0.51
U177	GPR401	367574	16776.09	1810.62	0.01	15.36	2.29	0.83	0.50
U178	GPR401	1582810	3725.85	7826.66	0.24	0.79	4.34	0.83	0.33
U179	GPR401	2378412	5400.31	11698.07	0.05	0.77	2.51	0.83	0.29
U180	GPR401	1060467	6893.91	5307.73	0.02	2.16	7.68	0.83	0.34
U181	GPR401	404697	5841.08	2010.48	0.02	4.83	6.42	0.83	0.56
U182	GPR401	1076146	6971.04	5307.19	0.03	2.18	2.40	0.83	0.32
U183	GPR401	110373	6374.68	550.39	0.01	19.20	2.27	0.83	0.58
U184	GPR401	228133	8527.86	1130.51	0.02	12.51	2.45	0.83	0.51
U185	GPR401	721736	8757.85	3569.45	0.03	4.08	2.31	0.83	0.35
U187	GPR401	782809	9212.99	3900.12	0.02	3.92	3.82	0.83	0.35
U188	GPR401	267296	6385.67	1333.25	0.04	7.95	2.30	0.83	0.47
U189	GPR401	1101025	6470.77	5466.64	0.02	1.97	3.63	0.83	0.33
U259	G15	352	7.89	1.99	<0.001	6.31	7.69	0.75	8.85
U260	G15	580	9.36	3.21	0.00	4.68	6.27	0.77	7.09
U261	G15	318	5.41	1.40	0.01	6.15	10.82	0.76	9.63
U262	G15	567	3.66	3.22	0.00	1.84	10.89	0.78	7.25
U263	G15	608	8.57	4.53	<0.001	3.00	21.04	0.75	7.17
U264	G15	678	8.87	3.66	0.00	3.94	6.96	0.79	6.71
U265	G15	878	4.98	3.89	0.01	2.08	10.83	0.79	5.69
U266	G15	492	5.55	2.88	0.01	3.10	10.38	0.77	8.26
U267	G15	949	10.11	5.27	<0.001	3.19	8.93	0.83	6.83
U268	G15	737	8.06	4.88	0.01	2.73	17.78	0.83	7.54
U269	G15	409	6.31	2.18	<0.001	4.53	10.34	0.72	8.72
U271	G15	454	10.23	2.56	<0.001	6.44	8.00	0.78	7.97
U272	G15	12608	1198.30	70.49	0.10	27.09	4.48	0.76	2.23
U273	G15	15076	344.15	81.52	0.13	6.87	9.46	0.80	2.19
U274	G15	2011	3.42	11.16	0.33	0.49	5.80	0.78	3.86
U275	G15	5960	33.97	33.12	0.01	1.66	5.02	0.78	2.64
U276	G15	29330	1879.47	164.07	0.06	18.25	11.58	0.76	1.25

spot	Sample	206Pb[a] (cps)	U[b] (ppm)	Pb[b] (ppm)	Th[b]/U	238U[c]/206Pb	± 2σ (%)	207Pb[c]/206Pb	± 2σ (%)
U277	G15	7696	1667.10	44.29	0.04	58.04	10.30	0.70	2.57
U278	G15	16360	949.30	90.82	0.21	16.81	2.87	0.77	1.70
U279	G15	2638	466.03	15.41	0.07	47.53	7.71	0.73	3.45
U280	G15	363	499.34	2.80	<0.001	239.10	6.88	0.47	7.54
U281	G15	672	3.92	3.67	<0.001	1.76	9.62	0.82	7.07
U282	G15	1191	7.46	6.93	0.00	1.70	7.98	0.74	5.64
U289	B54	524	48.20	3.06	1.86	25.06	7.60	0.75	8.27
U290	B54	356	55.36	2.23	1.92	37.01	7.28	0.64	10.55
U291	B54	403	44.11	2.40	1.16	28.11	9.19	0.68	10.52
U292	B54	669	54.32	4.28	2.00	19.15	6.64	0.66	7.50
U293	B54	459	38.13	2.66	1.82	22.61	9.39	0.73	9.56
U294	B54	450	53.77	2.76	1.44	29.74	7.26	0.68	8.96
U295	B54	688	54.66	3.98	1.85	21.39	12.16	0.72	8.49
U296	B54	527	25.88	3.03	2.85	13.79	8.99	0.78	10.08
U297	B54	361	36.73	2.12	2.47	27.23	7.82	0.73	11.19
U298	B54	563	20.34	3.27	3.04	9.85	6.54	0.74	8.38
U299	B54	533	32.82	3.03	2.02	16.97	11.86	0.73	9.31
U300	B54	815	21.11	4.34	2.59	8.09	12.04	0.83	6.25
U301	B54	779	30.88	4.28	2.55	11.85	8.82	0.81	6.71
U302	B54	682	18.87	3.96	2.65	7.68	15.06	0.77	9.06
U303	B54	899	25.42	4.92	2.44	8.54	7.08	0.83	6.38
U304	B54	379	24.68	2.21	2.40	17.66	10.07	0.74	11.50
U305	B54	174	21.78	1.04	2.38	33.73	14.08	0.77	17.32
U306	B54	395	4.39	2.22	0.70	3.28	14.31	0.83	11.01
U307	B54	625	17.67	3.48	1.63	8.29	10.28	0.80	10.09
U308	B54	363	14.96	2.09	0.04	11.44	8.69	0.76	9.86
U309	B54	654	29.20	3.61	1.85	13.31	7.51	0.82	7.62
U310	B54	505	32.06	2.92	1.79	17.55	10.69	0.76	10.18
U311	B54	1714	19.99	9.75	1.84	3.31	7.24	0.78	4.48
U312	B54	250	11.22	1.44	2.91	12.67	11.67	0.79	12.27
U313	B54	278	15.32	1.53	5.02	16.91	11.56	0.86	14.71
U314	B57	231	164.73	2.04	0.13	103.50	8.38	0.40	12.56
U315	B57	221	149.52	1.99	0.14	95.27	7.33	0.38	14.29
U316	B57	173	191.05	2.01	0.13	112.30	8.89	0.28	12.12
U317	B57	326	178.44	2.71	0.26	85.93	8.85	0.42	10.54
U318	B57	1456	134.70	8.55	0.23	24.93	6.41	0.74	7.04
U319	B57	879	174.06	5.52	0.20	47.26	10.72	0.65	7.00
U320	B57	430	34.62	2.39	0.06	23.72	10.31	0.80	10.40
U321	B57	569	140.13	3.65	0.26	57.23	7.52	0.64	7.94
U322	B57	260	135.31	1.98	0.25	93.57	8.35	0.50	10.11
U323	B57	377	159.62	2.80	0.28	78.63	9.25	0.51	9.82

spot	Sample	206Pb[a] (cps)	U[b] (ppm)	Pb[b] (ppm)	Th[b]/U	238U[c]/206Pb	± 2σ (%)	207Pb[c]/206Pb	± 2σ (%)
U324	B57	324	182.19	2.68	0.22	89.29	8.35	0.43	11.16
U325	B57	556	173.25	3.73	0.10	67.93	8.68	0.61	9.80
U326	B57	306	155.26	2.44	0.12	85.83	6.56	0.47	11.15
U327	B57	103	156.55	1.35	0.17	133.70	8.56	0.25	18.10
U334	B57	134	265.69	2.10	0.12	140.00	6.03	0.20	17.29
U335	B57	592	109.55	3.84	0.19	42.75	7.27	0.65	7.23
U336	B57	1402	178.47	8.47	0.11	32.91	8.06	0.72	5.34
U337	B57	578	136.79	3.80	0.14	53.44	10.42	0.63	6.91
U338	B57	428	187.18	3.37	0.08	74.91	8.14	0.47	11.03
U339	B57	551	158.69	3.75	0.16	61.50	7.62	0.60	9.71
U340	B57	443	135.80	3.22	0.07	59.44	6.56	0.55	9.75
U341	B57	487	128.13	3.26	0.16	58.00	8.68	0.62	10.70
U342	B57	139	6.77	0.79	<0.001	14.66	19.53	0.88	19.41
U343	B57	258	100.87	1.99	0.37	70.74	9.60	0.53	11.55
U344	B57	236	36.66	1.43	0.09	40.83	11.55	0.76	13.53
U345	B57	491	10.74	2.81	0.01	6.27	11.02	0.81	9.02
U346	B57	1129	6.61	6.48	0.13	1.69	10.53	0.83	5.87
U347	B57	144	52.86	1.09	0.11	67.59	14.24	0.52	16.85
U348	B57	314	91.39	2.22	0.15	59.48	14.44	0.59	11.96
U349	B57	312	53.79	2.07	0.12	38.90	11.24	0.65	9.33
U350	B57	332	48.54	2.02	0.06	37.66	11.86	0.73	10.38
U351	B57	363	52.61	2.25	0.05	36.40	13.46	0.72	11.47
U352	B57	198	27.11	1.20	0.03	34.05	18.31	0.66	16.07
U353	B57	212	20.70	1.35	0.05	23.73	16.56	0.70	15.28
U354	B57	163	34.88	1.07	0.02	49.83	13.96	0.69	18.81
U355	B57	127	3.54	0.74	0.00	8.40	22.58	0.93	25.13
U356	B57	127	4.23	0.74	<0.001	9.48	17.47	0.84	19.64
U357	B57	223	9.10	1.26	<0.001	11.52	17.51	0.76	15.46
U358	B57	348	11.51	2.00	0.00	9.48	12.79	0.82	11.22
U359	B57	246	21.73	1.44	0.03	24.34	14.14	0.78	15.11
U360	B57	157	15.40	0.94	<0.001	25.77	14.20	0.73	15.71
U361	B57	212	6.38	1.21	0.00	8.70	15.69	0.82	12.57
U362	B57	98	6.67	3.23	#¡DIV/0!	3.50	16.71	0.87	23.83
U363	Q33	1969	281.00	13.02	0.10	32.48	4.53	0.65	4.47
U364	Q33	174	399.02	3.53	0.10	120.60	5.92	0.15	11.06
U365	Q33	178	271.93	2.66	0.13	114.80	8.78	0.21	15.72
U366	Q33	550	205.19	4.34	0.20	64.49	6.29	0.49	10.24
U367	Q33	947	148.91	6.45	0.39	34.35	4.54	0.63	7.13
U368	Q33	1265	206.34	8.49	0.18	36.40	4.70	0.65	5.64
U369	Q33	3932	175.26	23.35	0.23	12.18	3.86	0.79	3.95
U370	Q33	209	256.04	2.83	0.10	104.40	6.06	0.25	15.03
U371	Q33	38569	166.50	217.42	0.33	1.30	3.54	0.87	1.33

spot	Sample	206Pb[a] (cps)	U[b] (ppm)	Pb[b] (ppm)	Th[b]/U	238U[c]/206Pb	± 2σ (%)	207Pb[c]/206Pb	± 2σ (%)
U372	Q33	4323	214.33	25.40	0.13	13.82	3.82	0.81	3.10
U373	Q33	349	429.90	4.58	0.10	108.70	4.83	0.25	10.82
U374	Q33	5909	307.74	35.14	0.08	14.23	6.81	0.79	2.85
U375	Q33	4001	218.92	23.76	0.16	15.03	4.31	0.80	3.27
U376	Q33	1979	261.68	13.03	0.12	30.54	4.66	0.67	4.97
U377	Q33	2529	135.56	15.29	0.34	14.44	8.08	0.80	4.37
U378	Q33	183	235.68	2.43	0.16	112.30	7.17	0.26	16.57
U379	Q33	2791	123.04	16.35	0.35	12.46	4.63	0.83	4.27
U380	Q33	1309	77.61	8.00	1.94	15.60	7.42	0.77	6.30
U381	Q33	1193	218.92	8.02	0.16	41.17	6.13	0.66	5.88
U382	Q33	10718	98.79	61.36	0.75	2.71	3.87	0.86	2.34
U389	Q33	19996	290.43	114.47	0.09	4.26	4.76	0.86	1.21
U390	Q33	1472	381.87	10.45	0.08	53.53	4.23	0.61	5.45
U391	Q33	85	339.35	2.46	0.15	141.50	5.17	0.10	23.12
U392	EST2	6090	907.60	39.35	<0.001	35.85	4.18	0.71	2.45
U393	EST2	7881	758.67	49.61	<0.001	24.12	2.64	0.74	2.13
U394	EST2	5238	877.09	34.99	<0.001	38.15	3.30	0.67	3.15
U395	EST2	6521	887.97	42.52	<0.001	32.25	2.92	0.70	2.41
U396	EST2	3886	159.98	25.13	0.03	10.55	6.14	0.83	5.17
U399	EST2	6070	23.13	35.70	<0.001	1.08	3.99	0.84	3.06
U402	EST2	6196	807.55	39.07	<0.001	32.78	3.36	0.75	2.67
U403	EST2	2544	1816.96	22.51	0.00	106.80	3.06	0.44	4.49
U404	EST2	3693	1002.98	25.89	<0.001	57.49	3.72	0.63	3.58
U405	EST2	5172	1367.63	36.45	<0.001	55.90	5.20	0.64	3.27
U406	EST2	6386	691.12	39.89	<0.001	27.68	2.83	0.76	2.17
U407	EST2	23886	940.08	144.35	0.12	10.65	4.20	0.80	1.38
U408	EST2	5077	253.51	30.98	<0.001	13.32	3.09	0.80	3.20
U409	EST2	1776	28.41	10.66	<0.001	4.42	4.51	0.83	4.71
U411	EST2	6958	933.44	44.69	<0.001	32.86	2.74	0.73	2.12
U412	EST2	3078	827.77	21.83	<0.001	56.08	3.32	0.62	3.69
U413	EST2	3965	1355.09	29.04	<0.001	67.84	2.89	0.59	2.98
U414	EST2	9940	965.02	62.88	<0.001	24.44	2.97	0.75	1.86
U415	EST2	11756	912.13	73.74	<0.001	19.83	2.73	0.77	2.28
U416	EST2	4043	297.08	25.53	<0.001	18.62	3.41	0.76	3.53
U417	EST2	4004	409.12	25.61	<0.001	25.30	3.50	0.74	3.15
U418	PA12	16354	5961.82	108.70	0.04	84.10	6.38	0.69	2.42
U419	PA12	1031	1685.36	9.63	0.03	228.00	3.84	0.42	5.39
U420	PA12	2062	4640.21	22.83	0.05	249.60	3.47	0.33	6.15
U421	PA12	8187	2617.81	54.47	0.04	74.30	6.02	0.70	2.42
U422	PA12	2713	6157.28	29.19	0.06	260.80	4.12	0.34	5.48
U423	PA12	2664	3926.94	24.42	0.10	208.70	9.02	0.42	10.04

spot	Sample	206Pb[a] (cps)	U[b] (ppm)	Pb[b] (ppm)	Th[b]/U	238U[c]/206Pb	± 2σ (%)	207Pb[c]/206Pb	± 2σ (%)
U424	PA12	1045	6815.64	20.21	0.03	365.40	3.03	0.17	5.98
U425	PA12	9043	4752.90	63.39	0.03	112.30	4.22	0.64	2.86
U426	PA12	831	1033.15	7.99	0.02	176.70	4.40	0.49	7.07
U427	PA12	858	1573.14	9.41	0.02	215.10	5.00	0.40	6.80
U428	PA12	534	250.29	4.32	0.03	86.99	8.34	0.65	10.66
U429	PA12	8819	858.05	62.20	0.08	22.54	3.83	0.80	2.01
U430	PA12	29461	2983.20	210.25	0.06	23.07	7.69	0.79	1.24
U431	PA12	8473	2196.91	62.44	0.03	55.53	7.32	0.74	2.68
U432	PA12	1778	5088.60	23.00	0.03	270.30	2.92	0.33	4.32
U433	PA12	41723	2406.29	292.95	0.08	13.53	5.54	0.82	0.89
U434	PA12	13687	2541.40	99.39	0.03	41.05	4.82	0.77	1.67
U435	PA12	2421	5114.73	28.33	0.04	226.10	5.74	0.36	7.87
U436	PA12	1707	6425.63	25.46	0.02	296.70	2.95	0.27	4.43
U437	PA12	699	5557.71	15.89	0.02	377.80	3.57	0.16	7.18
U438	PA12	1355	4017.24	17.94	0.02	271.80	3.56	0.32	4.91
U445	P14	1889	171.36	14.00	<0.001	19.51	3.84	0.76	4.94
U446	P14	1606	391.95	13.23	<0.001	44.11	3.79	0.63	4.37
U447	P14	2334	110.18	17.46	<0.001	10.18	6.54	0.78	4.01
U448	P14	1263	454.43	11.44	<0.001	56.24	3.89	0.55	5.57
U449	P14	1671	446.85	14.19	<0.001	46.15	4.00	0.61	5.00
U450	P14	1490	474.64	12.73	<0.001	54.39	4.21	0.60	5.05
U451	P14	4348	379.56	32.48	0.00	18.64	4.18	0.76	2.97
U452	P14	4128	225.57	30.11	<0.001	12.14	3.71	0.79	3.17
U453	P14	4601	187.83	33.37	0.00	9.17	3.46	0.80	3.26
U454	P14	1545	333.12	12.45	<0.001	40.58	4.23	0.67	5.55
U455	P14	1757	60.87	12.44	<0.001	8.15	4.83	0.84	5.51
U456	P14	2021	2.94	14.32	0.00	0.35	6.52	0.85	5.48
U457	P14	659	3.05	4.65	0.02	1.12	8.24	0.88	8.37
U458	P14	3223	26.29	23.04	<0.001	1.89	3.97	0.82	3.53
U459	P14	2187	37.68	15.33	<0.001	4.11	4.33	0.84	4.02
U460	P14	2117	454.96	17.39	<0.001	39.13	5.78	0.64	4.65
U461	P14	1796	723.92	16.40	<0.001	62.50	3.94	0.55	4.80
U462	P14	876	949.79	11.24	<0.001	104.30	4.02	0.34	5.58
U463	P14	2917	465.97	22.97	<0.001	31.37	3.83	0.70	4.20
U464	P14	3804	115.59	27.80	0.01	6.77	3.89	0.80	3.40
U465	P14	2390	495.44	19.51	0.01	38.33	3.71	0.66	3.75
U466	P14	3049	616.02	24.75	0.01	37.70	3.55	0.66	4.47
U467	P14	4161	246.89	30.51	<0.001	13.17	3.38	0.80	3.09
U468	P14	2341	535.89	19.27	0.00	41.81	3.48	0.65	3.79
U469	P14	3824	541.75	29.82	<0.001	28.27	3.23	0.71	3.13
U470	P14	2848	421.81	22.05	<0.001	29.98	3.29	0.73	4.27
U471	P14	2324	1101.04	21.92	<0.001	70.27	3.64	0.53	4.03

spot	Sample	206Pb[a] (cps)	U[b] (ppm)	Pb[b] (ppm)	Th[b]/U	238U[c]/206Pb	± 2σ (%)	207Pb[c]/206Pb	± 2σ (%)
U472	P14	1324	524.72	12.38	<0.001	59.79	4.86	0.55	4.77
U473	GIS10a	1315	56.90	9.78	0.44	9.33	14.30	0.77	6.28
U474	GIS10a	1204	78.90	9.01	0.20	14.12	12.91	0.78	5.35
U475	GIS10a	386	20.46	2.77	0.01	11.58	7.49	0.73	8.56
U476	GIS10a	863	17.84	6.20	0.65	4.78	14.92	0.83	7.26
U477	GIS10a	1624	26.79	11.55	0.41	3.84	14.18	0.82	5.36
U478	GIS10a	2732	49.96	20.08	0.80	4.04	16.54	0.79	5.50
U479	GIS10a	3948	95.76	29.20	0.67	5.39	13.39	0.81	3.78
U480	GIS10a	974	11.92	7.18	0.32	2.72	9.20	0.81	5.78
U481	GIS10a	472	37.05	3.58	0.12	16.61	12.46	0.77	9.51
U482	GIS10a	290	50.08	1.69	0.02	43.14	16.17	0.60	11.53
U483	GIS10a	475	21.92	3.59	0.33	9.56	10.98	0.72	7.50
U484	GIS10a	1086	46.09	8.15	0.64	9.12	9.07	0.78	7.26
U485	GIS10a	107	67.36	0.84	0.04	106.00	11.15	0.45	14.55
U486	GIS10a	59	30.49	0.36	0.03	111.10	18.10	0.43	18.04
U487	GIS10a	1136	12.13	8.34	0.28	2.42	7.32	0.84	6.04
U542	P24a	71317	763.29	543.51	0.93	2.30	3.12	0.80	0.87
U543	P24a	51225	988.86	419.23	2.36	3.77	6.04	0.76	1.45
U544	P24a	63022	759.32	485.95	0.98	2.54	3.07	0.79	0.95
U545	P24a	70360	784.82	542.21	1.07	2.36	3.53	0.79	0.94
U546	P24a	118144	838.65	899.70	1.00	1.53	4.66	0.81	0.63
U547	P24a	93240	6195.94	905.42	0.49	9.76	4.22	0.56	1.74
U548	P24a	85434	793.20	651.43	1.00	2.00	2.98	0.81	0.87
U558	P24a	110203	869.75	847.58	0.95	1.68	3.67	0.81	0.67
U559	P24a	136491	930.36	1048.01	1.00	1.46	3.50	0.81	0.57
U560	P24a	54709	707.41	424.14	1.08	2.71	3.22	0.79	1.06
U561	P24a	55502	794.45	435.74	0.96	2.94	3.28	0.78	1.14
U562	P24a	41329	663.31	324.53	1.28	3.29	6.59	0.77	1.31
U563	P24a	39612	675.87	311.37	1.05	3.51	4.02	0.78	1.36
U564	P24a	44417	693.39	348.21	1.07	3.22	4.51	0.78	0.89
U565	P24a	41089	760.73	323.88	1.07	3.78	3.92	0.78	1.03
U566	P24a	34718	602.42	272.76	1.02	3.57	3.38	0.78	1.34
U567	P24a	22911	585.90	183.41	1.11	5.10	3.15	0.76	1.29
U568	P24a	30920	613.44	246.34	1.11	3.98	2.70	0.76	1.32
U569	P24a	20239	533.73	162.56	0.93	5.22	2.82	0.75	1.74
U570	P24a	35154	676.19	277.65	1.11	3.92	2.42	0.77	1.06
U571	P24a	44043	790.43	349.68	1.10	3.63	3.61	0.77	1.03
U575	P24b	69393	5596.80	552.94	0.03	16.24	2.74	0.77	0.78
U576	P24b	26139	5322.33	223.31	0.03	36.41	2.81	0.68	1.41
U577	P24b	33031	5145.32	275.34	0.02	29.11	3.27	0.71	1.14

spot	Sample	206Pb[a] (cps)	U[b] (ppm)	Pb[b] (ppm)	Th[b]/U	238U[c]/206Pb	± 2σ (%)	207Pb[c]/206Pb	± 2σ (%)
U578	P24b	88194	2825.62	680.46	0.03	6.83	2.88	0.81	0.97
U579	P24b	33981	2851.48	272.62	0.02	16.70	3.18	0.76	1.21
U580	P24b	26231	1656.20	205.67	0.03	13.06	3.29	0.79	1.42
U581	P24b	34380	187.63	265.16	0.22	1.17	3.68	0.83	1.23
U582	P24b	27293	131.97	208.53	0.46	1.05	3.59	0.83	1.26
U583	P24b	60689	125.71	461.73	0.62	0.45	2.75	0.84	1.04
U584	P24b	36335	143.18	276.12	0.62	0.86	2.72	0.84	1.10
U585	P24b	121375	3914.60	949.43	0.08	6.74	3.83	0.80	0.63
U586	P24b	255002	3699.99	1952.39	0.09	3.14	2.40	0.83	0.58
U587	P24b	177337	2868.50	1372.09	0.19	3.44	3.18	0.82	0.51
U588	P24b	334135	180.08	2548.62	1.07	0.12	2.67	0.84	0.44
				Soda-lime glass NIST SRM-614					
A001	NIST	311162	856.22	2771.96	0.92	1.23	0.75	0.87	0.31
A002	NIST	308290	855.22	2751.92	0.94	1.24	0.69	0.87	0.32
A033	NIST	274989	775.13	2500.72	0.91	1.24	0.75	0.87	0.36
A034	NIST	289506	819.74	2631.25	0.94	1.24	0.65	0.87	0.45
A067	NIST	263235	752.42	2438.68	0.92	1.23	0.77	0.87	0.37
A068	NIST	294611	865.81	2730.97	1.00	1.26	0.49	0.87	0.21
A102	NIST	270170	780.45	2555.34	0.96	1.22	0.56	0.87	0.34
A103	NIST	268237	782.36	2541.46	0.96	1.23	0.92	0.87	0.42
A146	NIST	283305	851.76	2759.65	0.99	1.23	0.48	0.87	0.35
A147	NIST	287776	888.83	2801.50	1.01	1.26	0.53	0.87	0.33
A194	NIST	266427	831.86	2678.92	0.98	1.24	0.43	0.87	0.34
A195	NIST	261324	814.42	2635.32	0.97	1.23	0.69	0.87	0.34
A238	NIST	273213	900.19	2847.63	1.00	1.26	0.56	0.87	0.26
A239	NIST	244477	780.76	2537.97	0.94	1.23	0.65	0.87	0.36
A283	NIST	242735	808.16	2614.47	0.96	1.23	0.83	0.87	0.36
A284	NIST	232656	772.32	2510.72	0.94	1.22	0.85	0.87	0.38
A328	NIST	240408	840.64	2696.87	0.99	1.25	0.53	0.87	0.34
A329	NIST	228402	780.16	2563.45	0.95	1.22	0.61	0.87	0.45
A383	NIST	244403	905.93	2870.22	1.01	1.26	0.42	0.87	0.28
A384	NIST	217144	791.47	2560.25	0.96	1.24	0.69	0.87	0.42
A439	NIST	194845	837.31	2547.95	0.95	1.23	0.43	0.88	0.37
A440	NIST	197810	870.18	2601.42	0.97	1.26	0.38	0.87	0.39
A494	NIST	177323	799.78	2433.99	0.94	1.23	0.68	0.87	0.34
A495	NIST	189500	862.83	2592.51	0.99	1.25	0.53	0.87	0.36
A549	NIST	176891	822.10	2505.37	0.97	1.23	0.54	0.88	0.36
A550	NIST	164298	756.99	2326.86	0.94	1.22	0.62	0.88	0.40
A593	NIST	171024	822.64	2466.05	0.97	1.25	0.53	0.87	0.51
A594	NIST	171462	817.10	2474.91	0.97	1.24	0.40	0.87	0.43
				WC-1 calcite reference (Roberts et al., 2017)					

spot	Sample	206Pb[a] (cps)	U[b] (ppm)	Pb[b] (ppm)	Th[b]/U	238U[c]/206Pb	± 2σ (%)	207Pb[c]/206Pb	± 2σ (%)
B003	WC1	11806	5.25	0.26	<0.001	22.63	2.41	0.12	2.11
B004	WC1	13028	6.19	0.29	<0.001	23.36	2.26	0.11	3.19
B035	WC1	9527	4.92	0.22	<0.001	23.47	2.46	0.10	3.95
B036	WC1	14500	5.01	0.27	<0.001	22.04	2.44	0.14	2.47
B069	WC1	13153	5.52	0.28	<0.001	22.35	2.62	0.12	4.60
B070	WC1	11328	4.93	0.24	<0.001	22.61	2.31	0.12	2.41
B104	WC1	10696	4.20	0.22	<0.001	21.96	2.53	0.13	4.40
B105	WC1	11981	5.72	0.27	<0.001	23.14	2.37	0.11	4.18
B148	WC1	13191	4.76	0.27	<0.001	21.51	2.34	0.14	3.48
B149	WC1	12653	4.99	0.26	<0.001	22.19	2.58	0.14	3.25
B196	WC1	11407	7.25	0.32	<0.001	23.11	2.42	0.09	3.44
B197	WC1	15274	5.55	0.31	<0.001	21.49	2.42	0.15	2.94
B240	WC1	10280	6.39	0.29	<0.001	23.33	2.43	0.10	6.79
B241	WC1	15521	6.88	0.36	<0.001	22.51	2.32	0.13	3.87
B285	WC1	9106	5.25	0.24	<0.001	23.33	2.32	0.11	2.84
B286	WC1	11450	5.71	0.28	<0.001	22.83	2.36	0.12	2.49
B330	WC1	11695	6.06	0.30	<0.001	22.57	2.41	0.12	2.70
B331	WC1	10822	5.49	0.28	<0.001	22.19	2.29	0.12	4.83
B385	WC1	10810	5.84	0.29	<0.001	22.56	2.33	0.12	3.77
B386	WC1	9406	4.80	0.25	<0.001	22.35	2.42	0.13	2.92
B441	WC1	8332	5.49	0.26	<0.001	23.12	2.48	0.12	3.37
B442	WC1	7562	5.11	0.24	<0.001	22.99	2.77	0.11	3.10
B496	WC1	9176	7.03	0.32	0.00	23.43	2.51	0.11	3.89
B497	WC1	11312	6.15	0.32	<0.001	22.54	2.63	0.15	2.24
B551	WC1	7605	6.66	0.29	0.00	23.79	2.36	0.10	3.65
B552	WC1	7410	5.41	0.26	0.00	23.28	2.46	0.12	3.73
B595	WC1	6419	7.59	0.31	0.00	24.52	2.69	0.08	2.86
				ASH15D carbonate reference (Vaks et al., 2003)					
C005	ASH15D	1073	1.79	0.01	<0.001	499.60	6.75	0.67	5.97
C006	ASH15D	2273	2.53	0.02	<0.001	357.90	15.43	0.70	4.96
C037	ASH15D	539	1.96	0.01	<0.001	880.00	7.46	0.55	8.06
C038	ASH15D	852	1.04	0.01	<0.001	390.20	6.93	0.72	5.87
C071	ASH15D	1008	1.94	0.01	<0.001	569.80	6.48	0.68	5.65
C072	ASH15D	6701	3.72	0.06	<0.001	188.00	9.98	0.78	3.11
C106	ASH15D	566	1.82	0.01	<0.001	822.60	6.19	0.58	8.09
C107	ASH15D	317433	2.99	2.98	<0.001	3.50	7.35	0.87	1.38
C150	ASH15D	40733	2.87	0.39	<0.001	25.38	10.32	0.87	1.24
C151	ASH15D	1049	1.73	0.01	<0.001	479.00	6.10	0.71	7.03
C198	ASH15D	753	1.58	0.01	<0.001	669.30	8.12	0.62	6.17
C199	ASH15D	774	3.97	0.01	<0.001	1017.00	5.34	0.48	6.73
C242	ASH15D	510	5.06	0.01	<0.001	1359.00	6.82	0.35	7.79
C243	ASH15D	648	1.94	0.01	<0.001	697.10	8.12	0.60	7.34

spot	Sample	206Pb[a] (cps)	U[b] (ppm)	Pb[b] (ppm)	Th[b]/U	238U[c]/206Pb	± 2σ (%)	207Pb[c]/206Pb	± 2σ (%)
C287	ASH15D	817	4.13	0.01	<0.001	923.30	4.98	0.49	5.90
C288	ASH15D	797	2.27	0.01	<0.001	686.70	9.31	0.63	7.51
C332	ASH15D	1034	3.66	0.01	<0.001	748.20	4.26	0.59	4.93
C333	ASH15D	1705	2.94	0.02	<0.001	434.70	9.48	0.70	5.58
C387	ASH15D	1896	1.83	0.02	<0.001	259.90	7.57	0.79	5.10
C388	ASH15D	2664	2.14	0.03	<0.001	218.50	13.21	0.80	6.35
C443	ASH15D	1116	3.65	0.01	<0.001	847.40	4.80	0.55	6.15
C444	ASH15D	20518	2.75	0.25	<0.001	37.22	10.47	0.85	1.50
C498	ASH15D	633	1.75	0.01	<0.001	586.30	11.39	0.67	7.78
C499	ASH15D	3362	1.70	0.04	<0.001	135.20	17.04	0.84	4.43
C553	ASH15D	100009	3.11	1.31	<0.001	8.34	17.62	0.87	1.13
C554	ASH15D	4010	2.56	0.05	<0.001	158.70	34.91	0.80	5.45
C597	ASH15D	325	1.20	0.00	<0.001	695.40	8.59	0.64	8.66
C598	ASH15D	6877	2.46	0.09	<0.001	89.45	7.34	0.84	2.11
		Nama, stromatolitic limestone, Cambrian-Precambrian boundary, South Namibia							
D516	NAMA-dol	39761	1.39	0.59	0.03	5.50	6.65	0.50	3.70
D517	NAMA-dol	32238	1.45	0.50	0.01	6.34	3.54	0.46	2.66
D518	NAMA-dol	23819	1.25	0.37	0.02	6.91	3.11	0.42	2.55
D531	NAMA-dol	42985	1.73	0.65	0.01	6.06	4.05	0.49	2.61
D532	NAMA-dol	30556	1.58	0.49	0.02	6.76	3.22	0.43	1.59
D533	NAMA-dol	36126	1.94	0.57	0.01	6.97	3.00	0.42	1.92
D555	NAMA-dol	55567	2.39	0.86	0.05	6.19	4.57	0.46	3.09
D556	NAMA-dol	26732	1.15	0.41	0.02	6.25	2.76	0.48	1.45
D557	NAMA-dol	44444	1.60	0.67	0.01	5.59	6.47	0.50	4.00
D572	NAMA-dol	24936	1.52	0.46	0.01	7.47	2.97	0.40	2.07
D573	NAMA-dol	47519	1.26	0.69	0.03	4.69	5.62	0.58	2.78
D574	NAMA-dol	56334	1.86	0.84	0.02	5.30	3.31	0.53	1.55

Annex 4: Geochemical data from Chapter 7.

Carbon and oxygen isotopes

Table S1. $\delta^{18}O$ and $\delta^{13}C$ values of the carbonate host rocks and calcite cements Cc1, Cc2, Cc3, Cc4, Cc5, Cc6, Cc7 and Cc8 precipitated in the Lower Pedraforca thrust sheet. For the fourth column, the blank spaces represent host rocks which are not affected by fractures and do not contain calcite cement respectively.

Outcrop	Sample	Description	Type of cement	$\delta^{13}C$ PDB	$\delta^{18}O$ PDB
EST	EST3A	Oligocene Congl.		1,82	-5,04
Q	Q15B	Garumnian		-17,47	-8,20
Q	Q4B	Garumnian		-10,02	-4,87
Q	Q16C	Garumnian		-3,65	-4,77
PEG	PEG1B	Garumnian		-9,12	-4,86
PEG	PEG5A	Garumnian		-9,37	-5,94
Q	Q27B	Garumnian		-6,69	-4,26
Q	Q1C	Areny Fm.		1,68	-4,48
Q	Q21D	Areny Fm.		1,45	-3,20
G1	G4B	Vallcarga Fm.		2,62	-3,30
G1	G9B	Vallcarga Fm.		2,18	-4,34
G1	G3C	Lower Jurassic		4,10	-3,81
G1	G1A	Lower Jurassic		3,17	-4,78
G2	G16D	Lower Jurassic		-6,06	-5,65
G2	G14B	Lower Jurassic		1,65	-5,52
Q	Q21C	Moldic porosity	Cc1	1,49	-5,17
Q	Q6B	Vug Porosity	Cc2	-10,13	-5,95
Q	G7A	Breccia	Cc2	-6,86	-5,24
Q	Q13A	F2	Cc3	-4,89	-5,45
Q	Q1A	F3	Cc3	-0,38	-4,98
Q	Q3BA	F3	Cc3	-2,15	-5,50
Q	Q4A	F2	Cc3	-10,22	-3,87
Q	Q6A	F2	Cc3	-10,78	-4,06
Q	Q8A	Vug Porosity	Cc3	0,84	-5,70
Q	Q15A	F3	Cc3	-15,18	-6,77
Q	Q27A	F3	Cc3	-5,84	-4,73
Q	Q28A	F3	Cc3	-4,73	-6,68
Q	Q10A	F3	Cc4	-5,38	-5,4
Q	Q10B	F3	Cc4	-5,24	-3,24
Q	Q11A	F1	Cc4	-5,97	-2,61
Q	Q12A	F3	Cc4	-3,69	-5,89
Q	Q32A	F1	Cc4	-6,18	-3,06
Q	Q33A	F3	Cc4	-5,01	-7,26
Q	Q1B	F3	Cc5	1,21	-5,55

Q	Q3BC	F4	Cc5	1,58	-5,23
Q	Q20A	Vug Porosity	Cc5	1,07	-4,39
Q	Q19AA	F4	Cc6	-1,85	-8,14
Q	Q21A	F4	Cc6	1,71	-6,15
Q	Q21B	F4	Cc6	1,27	-6,69
Q	Q24A	F4	Cc6	1,60	-6,26
Q	Q24B	F4	Cc6	1,82	-7,70
Q	Q24C	F4	Cc6	1,76	-7,75
Q	Q20B	Vug Porosity	Cc6	1,17	-6,09
Q	Q20C	Vug Porosity	Cc6	1,15	-7,01
Q	Q23B	F5	Cc6	2,15	-8,16
Q	Q25A	F4	Cc6	1,79	-7,20
Q	Q29A	F4	Cc6	1,68	-6,87
Q	Q31A	F4	Cc6	2,01	-7,50
G1	G2A	F5	Cc6	3,81	-8,09
G1	G2B	F5	Cc6	-1,39	-7,42
G1	G4A	F5	Cc6	2,04	-7,59
G1	G5A	F5	Cc6	0,66	-9,51
G1	G5B	F5	Cc6	-0,03	-9,56
G1	G6A	F5	Cc6	-6,99	-6,89
G1	G6B	F5	Cc6	-5,56	-5,34
G1	G9A	F4	Cc6	2,41	-7,34
G1	G11A	F4	Cc6	1,99	-11,23
G2	G13A	F4	Cc6	0,39	-8,32
G2	G14A	F5	Cc6	-6,91	-8,20
G2	G15A	F4	Cc6	-5,55	-9,51
G2	G15B	F4	Cc6	-5,35	-9,68
G2	G16A	F4	Cc6	-5,42	-9,63
G2	G16B	F4	Cc6	-5,41	-9,85
G2	G16E	F4	Cc6	-5,46	-8,53
PEG	PEG1A	F4	Cc6	-9,03	-10,25
PEG	PEG4B	F4	Cc6	-9,32	-10,52
PEG	PEG4A	F4	Cc6	-9,33	-9,18
G1	G1B	F6	Cc7	-1,00	-11,50
G1	G3A	F6	Cc7	-1,81	-10,02
G1	G3B	F6	Cc7	-1,00	-11,85
EST	EST2A	F7	Cc8	-0,24	-7,62
EST	EST2B	F7	Cc8	-0,27	-6,52

Clumped isotopes thermometry

Table S2. Calcite cement $\delta^{13}C$, $\delta^{18}O$, Δ_{47} and $\delta 18O_{fluid}$ of the calcite cements Cc3 and Cc6 within the Lower Pedraforca thrust sheet. n represents the number of analyses per sample.

Sample	Outcrop	Type of cement	n	$\delta^{13}C$ VPDB	$\delta^{18}O$ VPDB	Δ_{47}	T ºC	$\delta^{18}O_{fluid}$ VSMOW
Q2	Q	Cc3	4	+0.33	-5.02	0.579 ± 0.011	69.08 ± 5.34	+5.42 ± 0.87
Q24	Q	Cc6	3	+1.6	-6.1	0.569 ± 0.008	74.16 ± 4	+5.08 ± 0.67

Strontium isotopes

Table S3. $^{87}Sr/^{86}Sr$ values of carbonate host rocks and calcite cements Cc3, Cc5 and Cc6 precipitated in the Lower Pedraforca thrust sheet. For the fourth column, the blank spaces represent host rocks which are not affected by fractures and do not contain calcite cement respectively.

Outcrop	Sample	Description	Type of cement	$^{87}Sr/^{86}Sr$
Q	Q1D	Areny Fm.		0,707841
Q	Q3BE	F3	Cc3	0,707922
Q	Q3BD	F4	Cc5	0,708230
Q	Q24D	F4	Cc6	0,707817

Elemental composition

Table S4. Mg, Sr, Fe, Mn and Ca content in ppm of calcite cements Cc1, Cc3, Cc5 and Cc6 precipitated in outcrop Q.

Sample	Type of cement	Mg (ppm)	Sr (ppm)	Fe (ppm)	Mn (ppm)	Ca (ppm)
Q21	Cc1	3648	1981	628	229	383932
Q21	Cc1	3706	d.l.	1287	d.l.	385862
Q21	Cc1	4234	1204	172	217	393080
Q21	Cc1	2236	534	327	d.l.	395724
Q21	Cc1	1508	541	447	d.l.	391150
Q21	Cc1	1096	649	359	257	392508
Q21	Cc1	1772	d.l.	571	d.l.	391079
Q21	Cc1	1813	d.l.	190	136	390007
Q21	Cc1	1420	d.l.	371	d.l.	395724
Q21	Cc1	1829	d.l.	730	219	395581
Q21	Cc1	1749	465	277	d.l.	390864
Q21	Cc1	1390	d.l.	281	d.l.	396153
Q21	Cc1	2983	d.l.	251	282	392794
Q21	Cc1	3925	d.l.	407	144	394152
Q21	Cc1	1412	d.l.	221	d.l.	395081
Q21	Cc1	2265	d.l.	394	259	398655
Q21	Cc1	1940	3593	358	290	391722
Q21	Cc1	2928	d.l.	290	d.l.	394938
Q21	Cc1	5574	d.l.	902	320	386791
Q21	Cc1	5355	1112	895	187	389149
Q21	Cc1	4129	d.l.	1940	d.l.	387291
Q21	Cc1	5097	407	1056	d.l.	388077
Q21	Cc1	6926	849	382	d.l.	387577
Q21	Cc1	5014	1070	997	d.l.	388792
Q21	Cc1	6524	d.l.	948	d.l.	388792
Q21	Cc1	5842	633	1001	d.l.	383717
Q21	Cc1	3036	1141	768	158	392794
Q21	Cc1	6612	941	998	d.l.	383646
Q21	Cc1	5817	666	972	d.l.	385147
Q21	Cc1	6047	758	1467	215	381859
Q21	Cc1	5330	753	1345	164	383289
Q21	Cc1	6830	d.l.	1180	167	385933
Q21	Cc1	6733	647	781	251	386648
Q21	Cc1	5173	1034	836	239	389864
Q21	Cc1	3600	414	1574	362	388935
Q21	Cc1	6339	615	997	d.l.	389435
Q21	Cc1	5748	1417	348	d.l.	388792
Q21	Cc1	4400	d.l.	718	d.l.	390078
Q3B	Cc3	2163	d.l.	29	170	396796
Q3B	Cc3	3025	d.l.	d.l.	139	392222

Q3B	Cc3	2909	d.l.	d.l.	212	393509
Q3B	Cc3	2690	d.l.	d.l.	d.l.	393509
Q3B	Cc3	2280	d.l.	229	229	393294
Q3B	Cc3	4169	387	142	257	393294
Q3B	Cc3	1715	d.l.	d.l.	d.l.	394223
Q3B	Cc3	1949	d.l.	d.l.	191	397868
Q3B	Cc3	3485	d.l.	185	159	395796
Q3B	Cc3	2803	d.l.	d.l.	d.l.	394509
Q3B	Cc3	2031	d.l.	d.l.	139	398083
Q3B	Cc3	2777	d.l.	139	d.l.	396582
Q3B	Cc3	3894	385	d.l.	d.l.	394581
Q3B	Cc3	3441	d.l.	d.l.	d.l.	397511
Q3B	Cc3	3905	d.l.	d.l.	205	397440
Q3B	Cc3	1599	467	186	d.l.	394938
Q3B	Cc3	2631	d.l.	d.l.	d.l.	400584
Q3B	Cc3	2342	d.l.	d.l.	208	397154
Q3B	Cc3	2175	d.l.	d.l.	187	396082
Q3B	Cc3	1448	d.l.	d.l.	d.l.	398369
Q6	Cc3	2073	d.l.	d.l.	477	391079
Q6	Cc3	937	494	240	208	392294
Q6	Cc3	2494	d.l.	405	400	391222
Q6	Cc3	2438	d.l.	307	146	388291
Q6	Cc3	1696	d.l.	146	335	392294
Q6	Cc3	289	d.l.	d.l.	d.l.	393366
Q6	Cc3	1844	d.l.	548	293	390507
Q6	Cc3	2322	d.l.	139	244	387291
Q6	Cc3	1189	879	d.l.	223	391651
Q11	Cc4	4391	656	d.l.	384	386505
Q11	Cc4	3378	478	d.l.	d.l.	390221
Q11	Cc4	1696	d.l.	d.l.	d.l.	391365
Q11	Cc4	1330	468	d.l.	d.l.	392008
Q11	Cc4	3562	756	d.l.	163	389864
Q11	Cc4	2325	446	d.l.	251	391793
Q11	Cc4	1172	1374	d.l.	d.l.	390864
Q11	Cc4	1172	d.l.	d.l.	165	393938
Q11	Cc4	1765	762	d.l.	143	392508
Q11	Cc4	802	d.l.	d.l.	190	397440
Q11	Cc4	1296	d.l.	d.l.	163	395796
Q11	Cc4	890	d.l.	d.l.	d.l.	394223
Q11	Cc4	1470	d.l.	d.l.	240	394581
Q11	Cc4	1277	d.l.	d.l.	207	396725
Q11	Cc4	3764	d.l.	d.l.	162	392151
Q11	Cc4	4561	d.l.	d.l.	d.l.	392794
Q11	Cc4	2986	d.l.	d.l.	164	392794
Q11	Cc4	4062	d.l.	d.l.	256	394581
Q11	Cc4	3799	d.l.	d.l.	198	393580

Q11	Cc4	4184	d.l.	158	209	391007
Q3B	Cc5	1344	d.l.	1902	281	387362
Q3B	Cc5	1537	934	2024	314	387505
Q3B	Cc5	1405	1302	1846	d.l.	386862
Q3B	Cc5	1466	674	1468	366	387934
Q3B	Cc5	1325	d.l.	1611	d.l.	385504
Q3B	Cc5	1438	934	1613	275	387577
Q3B	Cc5	1356	884	1756	d.l.	385004
Q3B	Cc5	1107	1269	1651	d.l.	388006
Q3B	Cc5	1096	1851	1361	d.l.	385647
Q3B	Cc5	1450	d.l.	1742	153	387791
Q3B	Cc5	1385	d.l.	1754	272	385361
Q3B	Cc5	672	1166	1655	d.l.	385433
Q3B	Cc5	2073	d.l.	d.l.	328	390507
Q3B	Cc5	1912	d.l.	d.l.	211	391293
Q3B	Cc5	1993	d.l.	d.l.	194	392008
Q3B	Cc5	1890	d.l.	595	d.l.	388720
Q3B	Cc5	2221	d.l.	1002	205	391651
Q3B	Cc5	1920	d.l.	792	d.l.	386004
Q3B	Cc5	1040	1385	1371	156	387577
Q3B	Cc5	1426	d.l.	1436	d.l.	389721
Q3B	Cc5	1662	d.l.	1588	177	391293
Q3B	Cc5	1303	d.l.	968	d.l.	397082
Q3B	Cc5	2289	d.l.	2404	155	390650
Q3B	Cc5	2487	d.l.	2305	d.l.	387219
Q3B	Cc5	2389	d.l.	2451	d.l.	391936
Q3B	Cc5	2289	d.l.	2647	199	389506
Q3B	Cc5	1835	549	2570	d.l.	389149
Q3B	Cc5	1943	d.l.	2379	173	391436
Q3B	Cc5	2122	d.l.	2603	191	386505
Q3B	Cc5	2367	d.l.	3089	d.l.	387863
Q3B	Cc5	2049	354	2531	164	390650
Q3B	Cc5	2204	d.l.	2927	196	387791
Q3B	Cc5	2640	d.l.	3209	154	385361
Q3B	Cc5	1867	d.l.	2985	283	389935
Q3B	Cc5	2765	d.l.	2447	107	389221
Q3B	Cc5	2260	808	427	192	393938
Q3B	Cc5	1720	1414	391	223	392794
Q24	Cc6	1414	581	1257	101	397297
Q24	Cc6	680	d.l.	d.l.	d.l.	403229
Q24	Cc6	2200	d.l.	1030	250	395438
Q24	Cc6	2318	d.l.	1151	362	396510
Q24	Cc6	2841	644	1415	263	394581
Q24	Cc6	2265	d.l.	1214	212	395153
Q24	Cc6	1333	837	1237	d.l.	398440
Q24	Cc6	2714	d.l.	d.l.	d.l.	399584

Q24	Cc6	682	d.l.	d.l.	147	405516
Q24	Cc6	1354	d.l.	743	174	399369
Q24	Cc6	1026	d.l.	956	129	397154
Q24	Cc6	1960	d.l.	1422	145	394652
Q24	Cc6	1437	d.l.	979	204	399869
Q24	Cc6	1949	d.l.	949	137	399083
Q24	Cc6	1177	d.l.	812	223	397368
Q24	Cc6	2225	d.l.	1233	d.l.	395867
Q24	Cc6	2374	d.l.	1254	d.l.	396010
Q24	Cc6	3173	d.l.	1584	156	394080
Q24	Cc6	1771	d.l.	1046	152	399083
Q24	Cc6	3211	d.l.	1736	d.l.	390078
Q24	Cc6	2714	d.l.	1458	d.l.	390436
Q24	Cc6	2613	640	1232	d.l.	395010
Q24	Cc6	1872	d.l.	1024	d.l.	394438
Q24	Cc6	2777	d.l.	1722	d.l.	393366
Q24	Cc6	2933	420	1662	d.l.	392866
Q24	Cc6	2162	638	1231	160	396082
Q21	Cc6	2528	956	1565	d.l.	388649
Q21	Cc6	1892	d.l.	1427	283	388935
Q21	Cc6	3272	d.l.	1723	d.l.	387291
Q21	Cc6	2644	d.l.	1329	167	388720
Q21	Cc6	3101	d.l.	1541	229	394366
Q21	Cc6	1333	d.l.	706	d.l.	391865
Q21	Cc6	1273	d.l.	1072	d.l.	393580
Q21	Cc6	1364	d.l.	700	346	393151
Q21	Cc6	1210	1320	779	d.l.	393509
Q21	Cc6	1495	851	913	d.l.	393723
Q21	Cc6	3106	d.l.	1711	204	389078
Q21	Cc6	4166	d.l.	2521	221	386290
Q21	Cc6	3986	d.l.	3021	d.l.	382002
Q21	Cc6	2155	d.l.	1675	192	391079
Q21	Cc6	3848	d.l.	2057	282	385433
Q21	Cc6	4124	d.l.	1901	d.l.	386862
Q21	Cc6	3558	d.l.	1732	225	387005
Q21	Cc6	2693	d.l.	1986	d.l.	386076
Q21	Cc6	3181	956	1904	d.l.	387077
Q21	Cc6	4354	d.l.	2516	268	380859
Q21	Cc6	3864	d.l.	2054	d.l.	383503

Table S5. Mg/Ca, Sr/Ca, Ca/Fe and Mn/Ca ratios for calcite cements Cc1, Cc3, Cc4, Cc5 and Cc6 precipitated in outcrop Q.

Type of cement	Mg/Ca		Sr/Ca		Ca/Fe		Mn/Ca	
Cc1	Max.	0.30378	Max.	0.052244	Max.	15903	Max.	0.0000848
	Min.	0.0474	Min.	0.00599	Min.	1390	Min.	0.0000317
	Mean	0.17503	Mean	0.01432	Mean	5570	Mean	0.0000532
Cc3	Max.	0.1802	Max.	0.01283	Max.	19934	Max.	0.0001113
	Min.	0.06884	Min.	0.00557	Min.	4963	Min.	0.0000319
	Mean	0.010724	Mean	0.00759	Mean	13357	Mean	0.000054
Cc4	Max.	0.19737	Max.	0.0201	Max.	-	Max.	0.0000906
	Min.	0.03428	Min.	0.0065	Min.	-	Min.	0.0000333
	Mean	0.10427	Mean	0.01033	Mean	-	Mean	0.000048
Cc5	Max.	0.12077	Max.	0.02744	Max.	6993	Max.	0.0000859
	Min.	0.02966	Min.	0.00518	Min.	836	Min.	0.000025
	Mean	0.07749	Mean	0.01533	Mean	1916	Mean	0.0000506
Cc6	Max.	0.19432	Max.	0.01917	Max.	3912	Max.	0.0000832
	Min.	0.04393	Min.	0.00611	Min.	880	Min.	0.0000231
	Mean	0.10701	Mean	0.0114	Mean	2149	Mean	0.0000485

Annex 5: Geochemical data from Chapter 8.

Carbon and oxygen isotopes

Table S1. $\delta^{18}O$ and $\delta^{13}C$ values of the carbonate host rocks and dolomite and calcite cements precipitated in the Upper Pedraforca thrust sheet.

Sample	Outcrop	Type of cement	Description	$\delta^{13}C$ PDB	$\delta^{18}O$ PDB
P6	CV		Lower Jurassic limestones	0.35	-5.15
P8	CV		Lower Jurassic limestones	0.01	-5.05
P9	CV		Lower Jurassic limestones	-0.22	-6.18
P54	S		Lower Jurassic limestones	0.75	-4.44
P10	CV		Rd1	1.96	-0.67
P10	CV		Rd1	-1.70	-3.33
P24	GS		Rd1	2.33	-1.21
P26	GS		Rd1	2.19	-1.95
P32	GS		Rd1	2.29	-1.25
P36	GS		Rd1	-0.50	-3.99
P38	GS		Rd1	3.00	-0.05
P61B	CV		Rd1	2.37	-0.09
P73	GS		Rd1	2.80	0.58
P63	CV		Rd2	0.11	-1.66
P64	CV		Rd2	1.70	-1.80
P71	GS		Upper Jurassic limestones	1.11	-2.35
P41	GS		Upper Jurassic limestones	1.79	-3.58
P63	CV		Lower Cretaceous limestones	-1.70	-3.14
P64	CV		Lower Cretaceous limestones	1.44	-3.59
P12A	S		Undifferentiated Cretaceous limestones	2.30	-6.05
P18B	S		Undifferentiated Cretaceous limestones	2.24	-5.12
P19C	S		Undifferentiated Cretaceous limestones	2.35	-4.75
P20A	S		Undifferentiated Cretaceous limestones	2.80	-4.25
P1	P		Upper Cretaceous limestones	0.06	-8.58
P4	P		Upper Cretaceous limestones	-0.41	-5.17
P7	CV		Upper Cretaceous limestones	-1.33	-5.92
P56	P		Upper Cretaceous limestones	1.04	-5.55
P57	P		Upper Cretaceous limestones	-2.19	-7.90
P14	S		Garumnian grey marls	-0.19	-5.55
P18	S		S1	1.53	-4.18
P19	S		S1	1.62	-4.85
P66D	CV		Rd3	-0.29	-6.89
P6	CV		Ddol	-2.32	-7.38
P39	GS		Ddol	-0.97	-4.28
P24	GS	Dc1	F1	1.86	-3.92
P25	GS	Dc1	F1	1.05	-4.83
P38	GS	Dc1	F1	1.78	-4.53
P76	GS	Dc1	Calcite within moldic porosity	1.93	-2.54
P32	GS	Dc2	F2	1.21	-6.86
P36	GS	Dc2	F2	0.11	-6.89
P73	GS	Dc2	F2	0.99	-6.56
P75A	GS	Dc2	F3	0.07	-6.29
P77	GS	Dc3	Calcite within moldic porosity	1.50	-8.98
P77	GS	Dc3	Calcite within moldic porosity	1.75	-8.55
P72	GS	Cc1	Cement clast	-1.19	-10.61
P87A	GS	Cc1	Cement clast	-0.93	-9.12
P87B	GS	Cc1	Cement clast	-0.21	-8.05
P80	GS	Cc2	F4	-0.55	-9.20
P82A	GS	Cc2	F4	-0.70	-12.18
P82B	GS	Cc2	F4	-1.08	-12.36

P19	S	Cc3	Calcite replacing S1	1.90	-2.28
P4	P	Cc4	F5	-1.32	-5.85
P4	P	Cc4	F5	-2.37	-5.95
P1	P	Cc5	F5	-0.15	-13.62
P2	P	Cc5	F6	-1.05	-8.52
P3	P	Cc5	F5	-0.17	-8.86
P8	CV	Cc5	F11	-1.12	-9.86
P56	P	Cc5	F5	-0.14	-11.50
P56	P	Cc5	F5	-0.97	-14.46
P57	P	Cc5	F5	0.34	-10.85
P59	P	Cc5	F5	-0.06	-10.47
P63	CV	Cc5	F7	-0.58	-12.54
P4	P	Cc6	F8	-1.86	-11.56
P59	P	Cc6	F8	-1.10	-6.12
P14	S	Cc7	F10	0.56	-6.69
P15	S	Cc7	F10	0.64	-5.56
P18	S	Cc7	F10	0.77	-5.21
P19	S	Cc7	F10	-0.76	-7.23
P20	S	Cc7	Calcite within vug porosity	-0.13	-7.47
P20	S	Cc7	Calcite within vug porosity	0.78	-6.90
P20	S	Cc7	Calcite within vug porosity	1.75	-6.40
P6	CV	Cc8	F11	-1.12	-11.71
P8	CV	Cc8	F11	-0.90	-8.87
P12	S	Cc8	F9	1.29	-8.78
P12	S	Cc8	F9	-0.93	-8.84
P13	S	Cc8	F9	1.95	-8.33
P13	S	Cc8	F9	1.76	-8.24
P18	S	Cc8	F9	1.49	-8.57
P7	CV	Cc10	Calcite within breccia clasts	-1.04	-7.20
P7	CV	Cc10	Calcite within breccia clasts	-0.09	-7.59
P9	CV	Cc10	Calcite within breccia clasts	-0.49	-7.71
P9	CV	Cc10	Calcite within breccia clasts	-1.15	-6.68
P21	GS	Cc10	Calcite within vug porosity	-2.58	-7.43
P21	GS	Cc10	Calcite within vug porosity	-1.79	-7.67
P24	GS	Cc10	Calcite within vug porosity	-3.50	-7.33
P26	GS	Cc10	Calcite within vug porosity	-1.54	-6.94
P29	GS	Cc10	Calcite within vug porosity	-2.66	-6.30
P32	GS	Cc10	Calcite within vug porosity	-1.20	-5.25
P35	GS	Cc10	Calcite within vug porosity	-1.53	-7.44
P74	GS	Cc10	Calcite within vug porosity	-1.57	-5.41
P87A	GS	Cc10	Calcite within vug porosity	-0.26	-5.51
P87B	GS	Cc10	Calcite within vug porosity	-1.55	-3.97
P26	GS	Cc11	Calcite within vug porosity	-1.66	-8.80
P21	GS	Cc12	F12	-0.34	-10.44
P22	GS	Cc12	F13	-0.21	-11.52
P41	GS	Cc12	F12	0.89	-9.55
P73	GS	Cc12	F12	0.87	-14.32
P79	GS	Cc12	F12	-0.69	-9.58
P25	GS	Cc13	Reactivated F1	-0.59	-5.48
P31	GS	Cc13	F14?	-0.18	-5.52
P69	GS	Cc13	F14	0.08	-6.64
P71	GS	Cc13	F14	0.68	-6.24
P43	S	Cc14	F15	-5.72	-9.23
P44	S	Cc14	F15	-6.22	-10.04
P45	S	Cc14	F15	-0.94	-11.52
P10	CV	Cc15	F11	-1.42	-6.93
P10	CV	Cc15	F11	-1.08	-8.11
P10	CV	Cc15	F11	-5.94	-7.10

P11B	CV	Cc15	F11	-1.41	-9.14
P11B	CV	Cc15	F11	-1.18	-7.51
P61B	CV	Cc15	F11	-2.91	-9.17
P61B	CV	Cc15	F11	-3.03	-6.80
P62	CV	Cc15	Calcite within vug porosity	-3.10	-6.66
P63	CV	Cc15	Calcite within vug porosity	-5.49	-5.55
P8	CV	Cc16	F11	-3.30	-5.47
P33B	GS	Cc16	Calcite within vug porosity	-8.80	-7.79
P33B	GS	Cc16	Calcite within vug porosity	-5.32	-7.33
P39	GS	Cc16	Calcite within vug porosity	-2.21	-5.96
P40	GS	Cc16	Calcite within vug porosity	-9.39	-8.28
P42	GS	Cc16	Calcite within vug porosity	-3.92	-6.11
P46	GS	Cc16	Calcite within vug porosity	-5.89	-6.73

Clumped isotopes thermometry

Table S2. Calcite cement $\delta^{13}C$, $\delta^{18}O$, Δ_{47} and $\delta 18O_{fluid}$ of the dolomite cements Dc1 and Dc2, and calcite cements Cc4, Cc5, Cc7, Cc8, Cc10, Cc12 and Cc14 within the Upper Pedraforca thrust sheet. n represents the number of analyses per sample.

Sample	Outcrop	Type of cement	n	$\delta^{13}C$ VPDB	$\delta^{18}O$ VPDB	Δ_{47}	T ºC	$\delta^{18}O_{fluid}$ VSMOW
P24	GS	Dc1	4	+1.82	-5.08	0.458 ± 0.014	149.4 ± 12.5	+11.2 ± 1.1
P32	GS	Dc2	4	+1.16	-6.86	0.488 ± 0.008	124.7 ± 6.2	+7.1 ± 0.7
P4	P	Cc4	1	-1.5	-5.61	0.556	81 ± 21.7	+6.6 ± 3
P2	P	Cc5	3	-0.97	-8.85	0.558 ± 0.022	79.7 ± 12	+3.1 ± 1.7
P15	S	Cc7	3	+0.65	-5.46	0.522 ± 0.007	100.78 ± 4.2	+9.4 ± 0.6
P6	CV	Cc8	4	-1.23	-10.94	0.521 ± 0.008	101.4 ± 5	+3.9 ± 0.7
P7	CV	Cc10	1	-0.77	-7.28	0.675	30.3 ± 13.6	-3.6 ± 2.7
P26	GS	Cc10	4	-1.43	-6.75	0.702 ± 0.01	21.6 ± 3	-4.84 ± 0.6
P22	GS	Cc12	3	-0.19	-11.6	0.617 ± 0.017	52.2 ± 7.1	-3.6 ± 1.2
P44	S	Cc14	4	-6.27	-10.27	0.58 ± 0.009	67.27 ± 4.8	-0.33 ± 0.8

Strontium isotopes

Table S3. $^{87}Sr/^{86}Sr$ values of carbonate host rocks, dolomite cements Dc1 and Dc2 and calcite cements Cc2, Cc3, Cc4, Cc5, Cc7, Cc8, Cc10, Cc12, Cc13, Cc14 within in the Upper Pedraforca thrust sheet. For the third column, the blank spaces represent host rocks which are not affected by fractures and do not contain calcite cement respectively.

Sample	Outcrop	Type of cement	Description	$^{87}Sr/^{86}Sr$
P24	GS		Rd1	0.707816
P64	CV		Rd2	0.707604
P73	GS		Rd2	0.707366
P6	CV		Lower. Jurassic lim.	0.708301
P71	GS		Upper Jurassic lim.	0.707343
P17	S		U. Cretaceous lim.	0.708084
P18	S		U. Cretaceous lim.	0.707940
P19	S		U. Cretaceous lim.	0.707526
P17	S		S1	0.707837
P18	S		S1	0.707951
P19	S		S1	0.707747
P24	GS	Dc1	F1	0.707425
P32	GS	Dc2	F2	0.708262
P75	GS	Dc2	F3	0.708354
P82	GS	Cc2	F4	0.707857
P19	S	Cc3		0.707720
P4	P	Cc4	F5	0.707778
P4	P	Cc4	F5	0.707563
P2	P	Cc5	F6	0.707707
P15	S	Cc7	F10	0.707829
P6	CV	Cc8	F11	0.709747
P7	CV	Cc10	Cement between breccia clasts	0.707829
P26	GS	Cc10	Vug porosity	0.707919
P22	GS	Cc12	F13	0.708855
P69	GS	Cc13	F14	0.707933
P44	S	Cc14	F15	0.707751

Rare earths and yttrium composition

Table S4. Rare earths and yttrium contents of carbonate host rocks, dolomite cements Dc1 and Dc2 and calcite cements Cc3, Cc5, Cc7, Cc8, Cc10, Cc12, Cc3 and Cc14 within the Upper Pedraforca thrust sheet.

Sample	Outcrop	Type of cement	Description	La (ppm)	Ce (ppm)	Pr (ppm)	Nd (ppm)	Sm (ppm)	Eu (ppm)	Gd (ppm)	Tb (ppm)	Dy (ppm)	Y (ppm)	Ho (ppm)	Er (ppm)	Yb (ppm)	Lu (ppm)
P24	GS		Rd1	2.44	4.41	0.59	2.33	0.46	0.10	0.51	0.059	0.36	2.69	0.060	0.20	0.23	0.04
P64	CV		Rd2	0.28	0.53	0.05	0.19	0.05	0.02	0.05	0.006	0.04	0.29	0.007	0.02	0.02	d.l.
P73	GS		Rd2	0.80	1.75	0.23	0.93	0.19	0.05	0.20	0.021	0.13	0.92	0.022	0.06	0.07	0.02
P17	S		Upper Cretaceous lim.	0.49	0.58	0.09	0.37	0.05	0.03	0.09	0.01	0.07	0.77	0.02	0.04	0.03	d.l.
P18	S		Upper Cretaceous lim.	0.55	0.56	0.09	0.37	0.08	0.02	0.11	0.01	0.07	0.89	0.01	0.05	0.04	d.l.
P19	S		Upper Cretaceous lim.	4.35	5.85	0.81	2.93	0.58	0.16	0.64	0.07	0.44	3.31	0.07	0.22	0.23	0.04
P17	S		S1	5.45	9.76	1.32	5.05	0.92	0.24	1.05	0.12	0.75	4.66	0.11	0.34	0.41	0.06
P18	S		S1	4.65	9.08	1.09	3.93	0.72	0.16	0.77	0.09	0.56	3.66	0.08	0.29	0.29	0.05
P19	S		S1	2.28	4.47	0.51	1.92	0.32	0.10	0.35	0.04	0.25	1.9	0.04	0.16	0.18	0.03
P24	GS	Dc1	F1	8.58	22.73	3.41	13.38	2.46	0.42	2.35	0.237	1.30	6.51	0.155	0.47	0.35	0.05
P32	GS	Dc2	F2	0.47	1.79	0.27	1.25	0.29	0.06	0.26	0.033	0.20	1.34	0.031	0.10	0.10	0.02
P19	S	Cc3	Calcite replacing S1	2.80	3.72	0.59	2.33	0.36	0.10	0.45	0.05	0.35	2.26	0.04	0.16	0.14	0.03
P2	P	Cc5	F6	d.l.	d.l.	d.l.	d.l.	d.l.	0.02	0.04	0.01	0.03	d.l.	0.01	d.l.	0.02	d.l.
P15	S	Cc7	F10	1.42	3.34	0.51	2.00	0.46	0.15	0.51	0.08	0.41	3.5	0.07	0.18	0.13	0.02
P6	CV	Cc8	F11	0.94	2.42	0.52	2.69	0.72	0.2	0.68	0.1	0.51	4.02	0.09	0.21	0.21	0.03
P7	CV	Cc10	Calcite between breccia clasts	0.81	1.10	0.22	1.02	0.26	0.07	0.29	0.05	0.24	2.28	0.05	0.14	0.13	0.02
P26	GS	Cc10	Calcite in vug porosity	0.23	0.33	d.l.	0.19	d.l.	0.03	0.05	0.006	0.03	0.36	0.006	0.02	0.02	d.l.
P22	GS	Cc12	F13	1.89	3.61	0.56	2.19	0.45	0.10	0.46	0.051	0.28	1.59	0.040	0.11	0.10	0.02
P69	GS	Cc13	F14	d.l.	0.38	0.05	0.20	0.05	0.02	0.05	0.006	0.03	0.23	0.006	d.l.	0.02	d.l.
P44	S	Cc14	F15	4.46	8.36	1.07	3.99	0.79	0.18	0.87	0.11	0.60	4.48	0.12	0.3	0.28	0.05

Table S5. Calculated cerium (Ce/Ce*) and praseodymium (Pr/Pr*) anomalies and Y/Ho ratios for carbonate host rocks, dolomite cements Dc1 and Dc2 and calcite cements Cc3, Cc5, Cc7, Cc8, Cc10, Cc12, Cc3 and Cc14 within the Upper Pedraforca thrust sheet.

Sample	Outcrop	Type of cement	Description	Ce/Ce*	Pr/Pr*	Y/Ho
P24	GS		Rd1	0.85	1.08	44.91
P64	CV		Rd2	1.07	0.96	44.38
P73	GS		Rd2	0.9	1.05	42.75
P17	S		Upper Cretaceous limestones	0.73	1.15	49.98
P18	S		Upper Cretaceous limestones	0.7	1.17	78.75
P19	S		Upper Cretaceous limestones	0.75	1.15	50.24
P17	S		S1	0.82	1.10	43.49
P18	S		S1	0.87	1.07	44.16
P19	S		S1	0.94	1.03	45.80
P24	GS	Dc1	F1	0.75	1.14	42.07
P32	GS	Dc2	F2	0.88	1.04	42.83
P19	S	Cc3	Calcite replacing S1	0.73	1.15	56.34
P2	P	Cc5	F6	d.l.	d.l.	d.l.-
P15	S	Cc7	F10	0.75	1.13	52.87
P6	CV	Cc8	F11	0.69	1.08	44.34
P7	CV	Cc10	Calcite between breccia clasts	0.69	1.12	45.89
P26	GS	Cc10	Calcite within vug porosity	d.l.	d.l.	57.78
P22	GS	Cc12	F13	0.72	1.16	39.88
P69	GS	Cc13	F14	0.86	1.07	36.35
P44	S	Cc14	F15	0.84	1.09	38.31

Annex 6: Other publications.

Cruset, D., Cantarero, I., Travé, A., Vergés, J. (2015). Evolución diagenética durante el crecimiento del anticlinal de Puig-reig (cinturón de pliegues y cabalgamientos surpirenaico). Geogaceta. 58, 27-30.

Evolución diagenética durante el crecimiento del anticlinal de Puig-reig (cinturón de pliegues y cabalgamientos surpirenaico)

Diagenetic evolution during the growth of the Puig-reig anticline (South Pyrenean fold-and-thrust belt)

David Cruset[1, 2], Anna Travé[2], Irene Cantarero[2] y Jaume Vergés[1]

[1] Institut de Ciències de la Terra "Jaume Almera", CSIC, 08028 Barcelona, España.
dcruset@ictja.csic.es, jverges@ictja.csic.es
[2] Departament de Geoquímica, Petrologia i Prospecció Geològica. Facultat de Geologia, Universitat de Barcelona, 08028 Barcelona, España.
atrave@ub.edu, i_cantarero@ub.edu

ABSTRACT

The Puig-reig anticline was generated since the Lower-middle Priabonian, due to the growth of a double thrust sheet buried by alluvial sediments affected by inverse and strike-slip faults that finally acted as normal faults. In these fractures two generations of calcite cement have been observed: The first one, with values of $\delta^{18}O$ between -9 and -6‰ VPDB and Mg, Mn, Fe and Sr consistent with meteoric waters, precipitated in surficial conditions. The second generation, with $\delta^{18}O$ values between -14 and -9,5‰ VPDB and Mg, Mn, Fe and Sr values consistent with meteoric to formation waters.

Key-words: *Anticline, faults, calcite cement, isotopic data, elemental composition.*

RESUMEN

El anticlinal de Puig-reig se generó a partir del Priaboniense Inferior-medio debido al crecimiento de un doble cabalgamiento enterrado por sedimentos aluviales, afectados por fallas inversas y direccionales que posteriormente actuaron como fallas normales. En estas fracturas se ha determinado la presencia de dos generaciones de cemento de calcita: La primera, con unos valores de $\delta 1^{8}O$ entre -9 y -6‰ VPDB y valores de Mg, Mn, Fe y Sr consistentes con su formación a partir de aguas meteóricas, en condiciones superficiales. La segunda generación, con valores de $\delta^{18}O$ entre -14 y -9,5‰ VPDB y valores Mg, Mn, Fe y Sr consistentes con su formación a partir de un fluido meteórico-de formación.

Palabras clave: *Anticlinal, fallas, cemento de calcita, datos isotópicos, composición elemental.*

Geogaceta, 58 (2015), 27-30
ISSN (versión impresa): 0213-683X
ISSN (Internet): 2173-6545

Fecha de recepción: 25 de junio de 2014
Fecha de revisión: 29 de abril de 2015
Fecha de aceptación: 15 de mayo de 2015

Introducción

Los cementos carbonáticos en las fracturas de los cinturones de pliegues y cabalgamientos nos informan sobre el tipo de fluidos en los diferentes estadios de su evolución. Su estudio, aplicado al sistema de pliegues surpirenaicos, ha sido ya tratado anteriormente, tanto en sedimentos marinos del Eoceno Inferior (Travé *et al*., 1997), como en sedimentos continentales del Eoceno Superior (Travé *et al*., 2000). Durante esta última etapa, a partir del Priaboniense Inferior-medio, se desarrollaron abanicos aluviales en el sector más meridional del cinturón de deformación surpirenaico, en condiciones de sedimentación endorreicas (Costa *et al*., 2009).

Estos sedimentos sintectónicos, evidenciados por la presencia de discordancias progresivas (Riba, 1973; Anadón *et al*., 1986), recubrieron en parte los mantos de corrimiento a la vez que se deformaban generando los anticlinales de Oliana y Puig-reig en el sector comprendido entre los ríos Cardener y Segre (Vergés, 1993).

El objetivo de este trabajo es caracterizar petrológica y geoquímicamente los cementos precipitados en las fallas inversas, direccionales y normales, generadas durante el crecimiento del anticlinal de Puig-reig, con el fin de discernir el origen de los fluidos mineralizantes y establecer su evolución.

Metodología

Para realizar este estudio se han muestreado los cementos precipitados en los diferentes planos de falla que afectan al anticlinal, así como los de las rocas sedimentarias encajantes.

Para la caracterización petrológica de las muestras se han estudiado 32 láminas delgadas mediante microscopía óptica, y microscopía de catodoluminiscencia. La caracterización geoquímica de las muestras se ha realizado mediante el análisis de los isótopos estables de carbono y oxígeno de los diferentes cementos muestreados y de rocas encajantes carbonatadas. La caracterización geoquímica de estos cementos se ha completado con el análisis de su composición elemental mediante microsonda electrónica.

Contexto geológico

El anticlinal de Puig-reig, con una dirección WNW-ESE es ligeramente oblicuo a las

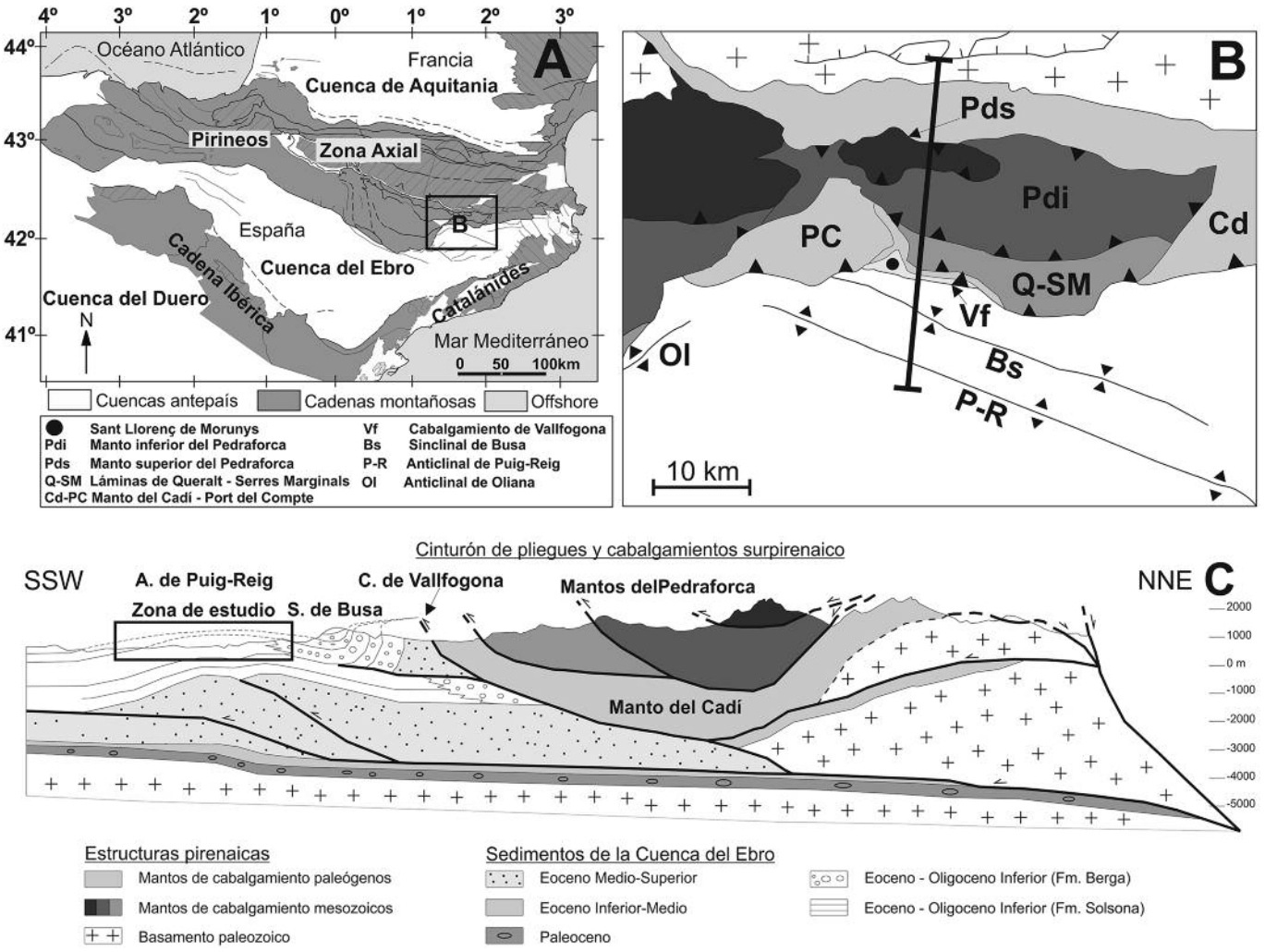

Fig. 1.- A) Mapa tectónico del NE de la Península Ibérica (Vergés, 1993). B) Esquema geológico simplificado de las principales unidades estructurales del cinturón de pliegues y cabalgamientos surpirenaico (CPCSP) a la altura del río Cardener (recuadro negro en A). La línea negra muestra la localización del corte geológico mostrado en C. C) Corte geológico de las principales estructuras de este sector del CPCSP. El recuadro negro indica la situación del anticlinal de Puig-reig. Simplificado de Vergés (1993).

Fig. 1.- A) Tectonic map of the north-eastern sector of the Iberian Peninsula (Vergés, 1993). B) Simplified geological scheme showing the main structural units of the South Pyrenean fold-and-thrust belt (SPFTB) along the Cardener river (black square in A). The black line indicates the location of the geological cross section. C) Geological cross section of the main structures of this sector of the SPFTB. The black square shows the Puig-reig anticline. Simplified from Vergés (1993).

estructuras principales pirenaicas y representa el primer anticlinal al sur del frente de cabalgamientos del Pirineo (Fig. 1A). El segmento estudiado se encuentra cerca de la localidad de Sant Llorenç de Morunys (Fig. 1B) y está constituido por los sedimentos continentales que comprenden los conglomerados de la Fm. Berga (Riba, 1973; Puigdefàbregas *et al*., 1986, 1992) y las areniscas y arcillas fluviales de la Fm. Solsona (Sáez, 1987). Estos sedimentos fueron depositados a partir del Priaboniense inferior-medio, en el momento en que la Cuenca del Ebro perdió toda conexión con el Océano Atlántico debido al levantamiento de los Pirineos occidentales. El levantamiento de esta región comportó una regresión marina a escala de cuenca y el paso a condiciones endorreicas (Sáez *et al*., 2007). El carácter sintectónico de estos depósitos aluviales con el cabalgamiento de Vallfogona (Vergés, 1993) está demostrado por las geometrías de crecimiento y las numerosas discordancias progresivas (Riba, 1973).

Desde el punto de vista estructural, el anticlinal de Puig-reig es un pliegue suave, de gran amplitud y ligera vergencia hacia el sur, resultado de un doble cabalgamiento en profundidad (Fig. 1C), producido por una rampa que conecta el nivel de despegue basal situado en la Fm. evaporítica de Beuda con el nivel de sales de la Fm. Cardona (Vergés *et al*., 1992). La actividad de esta doble estructura fue simultánea a la del cabalgamiento de Vallfogona, tal y como se demuestra por la geometría de doble cuña del sinclinal de Busa (Vergés, 1993). Numerosas fallas normales que actualmente muestran salto normal y desplazamiento métrico a decamétrico, inversas y direccionales se desarrollaron en la charnela y flancos del anticlinal de Puig-reig durante su formación. Estas fallas son el objeto de nuestro estudio.

Resultados

El estudio estructural de los afloramientos ha permitido determinar la presencia de fallas inversas, normales y direccionales. Las

fallas inversas muestran una orientación NE-SW y un buzamiento hacia el SE. Las fallas direccionales en general se orientan perpendicularmente a las fallas compresivas e indican un movimiento diestro en la mayoría de los casos. Finalmente, las fallas normales son paralelas y oblicuas al eje del pliegue y muestran indicios de haber actuado previamente como fallas direccionales.

El estudio petrológico de las muestras ha permitido diferenciar 2 generaciones de cemento de calcita (Fig 2). La primera de ellas (Cc1) se ha identificado en la porosidad de las rocas encajantes y en los planos de cizalla de fallas inversas, normales y direccionales. Está formado por cristales de esparita elongada y equidimensional de luminiscencia naranja brillante (Figs. 2B y 2D). Los cristales elongados, que pueden pasar lateralmente a equidimensionales con textura *blocky,* se encuentran únicamente en las fallas, donde se disponen paralelos a los planos de cizalla. El tamaño de los cristales elongados varía entre 1 y 1,5 mm de largo y 100 y 200 µm de ancho. Los cristales equidimensionales en las fallas a veces muestran zonación de crecimiento y miden entre 100 y 500 µm (excepcionalmente llegan hasta los 5 mm). Puntualmente, en los márgenes de algunas fallas, se observa un primer crecimiento de cristales *bladed* de hasta 100 µm de ancho. En las rocas encajantes, el cemento Cc1 está representado por cristales de esparita entre 5 y 10 µm en la porosidad intergranular de las rocas detríticas. En los *mudstones* lacustres forma estructuras geopetales en la porosidad vacuolar. El cemento Cc1 tiene valores entre -9 y -6 ‰ VPDB para el $\delta^{18}O$ y entre -2,5 y +1 ‰ VPDB para el $\delta^{13}C$ (Fig. 3). Los elementos traza (Mg, Mn, Fe y Sr) muestran valores medios y una desviación estándar de 2171 y 1085; 1406 y 464; 544 y 284; 537 y 74 ppm respectivamente.

La segunda generación de cemento de calcita (Cc2) solamente se encuentra en algunas fallas direccionales y en las fallas normales, que previamente actuaron como fallas direccionales. Este cemento consiste en cristales de esparita entre 100 y 500 µm y catodoluminiscencia rojo-naranja apagado (Figs. 2B y 2D) con textura tipo *blocky*. Cc2 tiene valores entre -14 y -9,5 ‰ VPDB para el $\delta^{18}O$ y entre -2 y +0,5 ‰ VPDB para el $\delta^{13}C$, estos últimos muy similares a los de Cc1 (Fig. 3). Los valores medios y la desviación estándar para el Mg, Mn, Fe y Sr son 1038 y 588; 1268 y 372; 1080 y 628; 886 y 674 ppm respectivamente. El contacto entre Cc1 y Cc2 puede ser gradual (Figs. 2A y 2B) o abrupto (Figs. 2C y 2D).

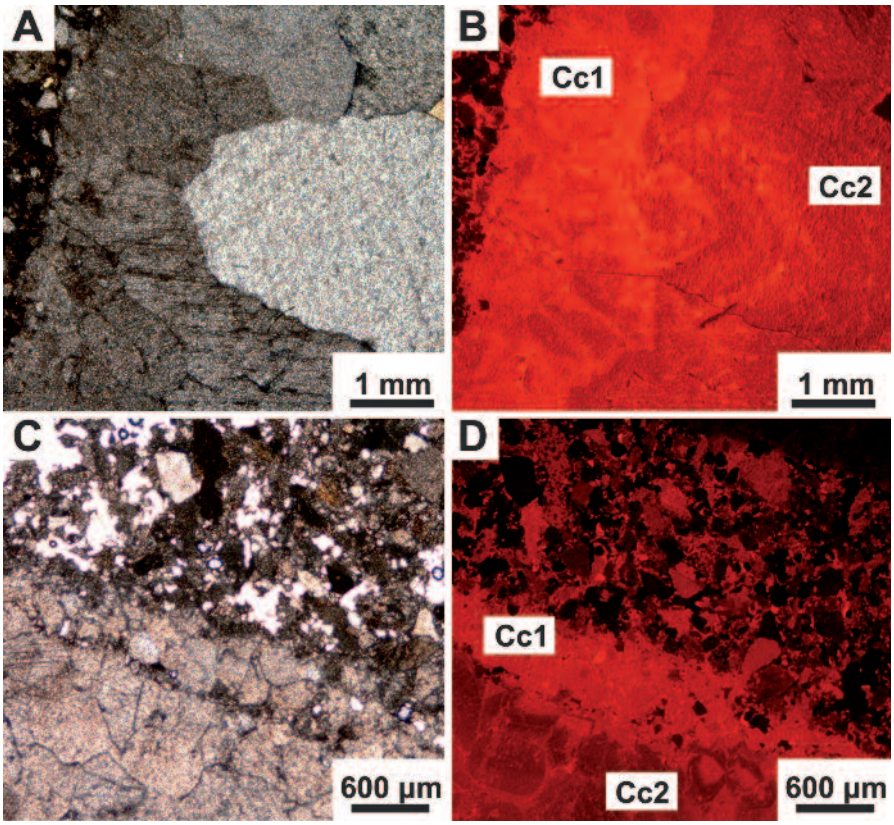

Fig. 2.- Imágenes de microscopio óptico de polarización (MOP) y catodoluminiscencia (CL) de algunos de los principales rasgos de los cementos estudiados. A-B) Imágenes de MOP y CL donde se ve el paso gradual entre Cc1 (más luminiscente) y Cc2 (rojo-naranja apagado). C-D) Imágenes de MOP y CL donde se ve el paso abrupto entre Cc1 y Cc2. (Ver figura en color en la Web).

Fig. 2.- Images from polarizing optical microscope and cathodolumiscence (CL) where are shown the main features of the studied cements. C-D) Plane light and CL images showing the gradual change between Cc1 (more luminiscent) and Cc2 (dull-red orange) cements. D) Plane light and CL images showing the sharp change from Cc1 and Cc2. (Sea colour figure on the Web).

Refiriéndose a los carbonatos encajantes, los valores isotópicos de oxígeno se encuentran entre -7,28 y -6,91‰ VPDB y los del carbono entre -3,3 y -2,44 ‰ VPDB (Fig. 3).

Discusión y conclusiones

Las relaciones molares de los elementos traza del cemento Cc1 son consistentes con su formación a partir de aguas meteóricas, mientras que para el cemento Cc2 son consistentes tanto con aguas meteóricas como con aguas de formación.

Los valores de $\delta^{18}O$ del cemento Cc1 se encuentran dentro del rango de los carbonatos lacustres y ligeramente empobrecidos respecto al de las aguas meteóricas actuales en esta área (entre -6,4 y -4,6‰ SMOW, Travé y Calvet, 2001). Esto podría indicar que el cemento precipitó en condiciones superficiales y/o durante las primeras etapas de enterramiento. Los valores de $\delta^{18}O$ de Cc2, más empobrecidos (Fig. 3), podrían responder a un incremento de la temperatura y/o a un cambio de la composición isotópica del fluido. Tanto la dispersión isotópica (Fig. 3) como el estudio de catodoluminiscencia (Figs. 2A y 2B) demuestran un cambio gradual entre los dos cementos. Además, en el caso de Cc2 se observa un empobrecimiento relativo en $\delta^{18}O$ del cemento según bajamos la serie estratigráfica. Esta distribución podría ser debida a 1) un incremento de la temperatura por enterramiento y 2) por la entrada gradual de aguas de formación a los niveles más profundos.

De este modo, se puede establecer una relación $\delta^{18}O$/tiempo, en la que los valores

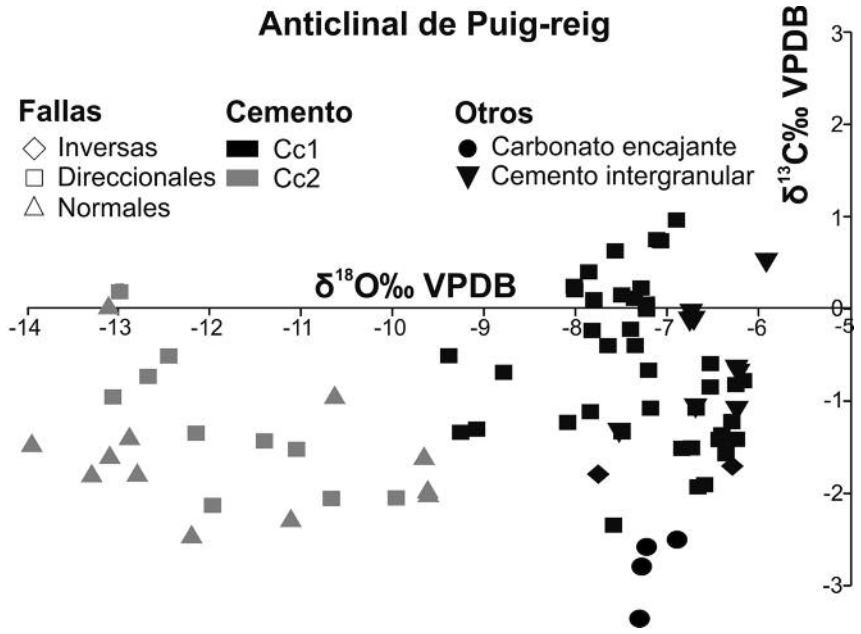

Fig. 3.- Valores de $\delta^{18}O$ y $\delta^{13}C$ de los cementos y carbonatos encajantes del anticlinal de Puig-reig.
***Fig. 3.- $\delta^{18}O$ and $\delta^{13}C$ cross-plot of cements* and carbonate host rocks *from the Puig-reig* anticline.**

más pesados son los más antiguos y los valores más ligeros los más modernos. Esta interpretación de posterioridad de Cc2 se demuestra por criterios petrográficos (Fig. 2A–D). También por el hecho de que este cemento solamente se encuentra en las fallas que han cambiado su campo de esfuerzos en las últimas fases de crecimiento de la estructura. En cambio, Cc1 se encuentra en todos los tipos de falla y en las rocas encajantes, habiendo precipitado durante los estadios iniciales de plegamiento.

Así, mediante la integración de datos petrológicos y geoquímicos, se puede explicar la evolución de los cementos que precipitaron en las fallas que afectan al anticlinal de Puig-reig en dos etapas. Una primera etapa, en la que precipitó un cemento Cc1 a partir de un fluido de origen meteórico y en condiciones superficiales. Gradualmente, en la segunda etapa precipitó un cemento Cc2 a partir de un fluido meteórico-de formación de mayor temperatura. Este incremento de la temperatura puede explicarse mediante el enterramiento progresivo del sistema de fallas durante el depósito de las formaciones Berga y Solsona o bien a la entrada de un fluido externo de mayor temperatura a los niveles que se encuentran a mayor profundidad.

Agradecimientos

Los autores agradecen los comentarios de las Dras. Rafaela Marfil y Mª Isabel Benito y de un revisor anónimo que han ayudado a mejorar el manuscrito. Esta investigación está financiada por el proyecto CGL2010- 18260, y el *Grup Consolidat de Recerca* "Geologia Sedimentària" *2014 SGR-251*.

Referencias

Anadón, P., Cabrera, L., Colombo, F., Marzo, M. y Riba, O. (1986). En: *Foreland Basins*. (P.A. Allen y P. Homewood, Eds.). IAS Special Publication 8, 259-271.

Costa, E., Garcés, M., López-Blanco, M., Beamud, E., Gómez-Paccard, M. y Larrasoaña, J.C. (2009). *Basin Research* 22, 904-917.

Puigdefàbregas, C., Muñoz, J.A. y Marzo, M. (1986). En: *Foreland Basins*. (P.A. Allen y P. Homewood, Eds.). IAS Special Publication 8, 229-246.

Puigdefàbregas, C., Muñoz, J.A. y Vergés, J. (1992). En: *Thrust Tectonics* (K.R. McClay, Ed.). London, Chapman & Hall, 247–254.

Riba, O. (1973). *Acta Geológica Hispánica* 8, 90-99.

Sáez, A. (1987). *Estratigrafía y sedimentología de las formaciones lacustres del tránsito Eoceno-Oligoceno del NE de la Cuenca del Ebro*. Tesis Doctoral, Univ. de Barcelona, 318 p.

Sáez, A., Anadón, P., Herrero, M.J. y Moscariello A. (2007). *Sedimentology* 54, 367-390.

Travé, A. y Calvet, F. (2001). *Tectonophysics* 336, 101-120.

Travé, A., Labaume, P., Calvet, F. y Soler, A. (1997). *Tectonophysics* 282, 375-398.

Travé, A., Calvet, F., Sans, M., Vergés, J. y Thirlwall, M. (2000). *Tectonophysics* 321, 73-102.

Vergés, J. (1993). *Estudi tectònic del vessant sud del Pirineu central i oriental. Evolució cinemàtica en 3D*. Tesis Doctoral, Univ. de Barcelona, 203 p.

Vergés, J., Muñoz, J.A. y Martínez, A. (1992). En: *Thrust Tectonics* (K.R. McClay, Ed.). London, Chapman & Hall, 255-264.

Cruset, D., Vergés, J., Cantarero, I., Travé, A. (2019) From rock-buffered to open fluid system during emplacement of the Lower Pedraforca thrust sheet (South Pyrenees). In: Doronzo D., Schingaro E., Armstrong-Altrin J., Zoheir B. (eds.) Petrogenesis and Exploration of the Earth's Interior. Proceedings of the 1st Springer Conference of the Arabian Journal of Geosciences (CAJG-1), Tunisia 2018. pp 215-217.

1ST CONFERENCE OF THE ARABIAN JOURNAL OF GEOSCIENCES (CAJG)
12–15 NOVEMBER 2018, HAMMAMET, TUNISIA

Springer
SPRINGER NATURE

From rock-buffered to open fluid system during emplacement of the Lower Pedraforca thrust sheet (South Pyrenees)

David Cruset[1]*, Jaume Vergés[2], Irene Cantarero[1] and Anna Travé[1]

[1] Departament de Mineralogia, Petrologia i Geologia Aplicada, Facultat de Ciències de la Terra, Universitat de Barcelona (UB), Martí i Franquès s/n, 08028, Barcelona.
[2] Institut de Ciències de la Terra Jaume Almera, ICTJA-CSIC, Lluís Solé i Sabaris s/n, 08028 Barcelona.
*Corresponding author: d.cruset@ub.edu

Abstract. The evolution of fluid flow during the emplacement of the Lower Pedraforca thrust sheet is inferred from fracture data, petrography and geochemistry of calcite cements.

The results show that during the earlier stages of compression, fluids migrating along fractures were in equilibrium with their adjacent host rocks. In contrast, external fluids in disequilibrium with their adjacent host rock migrated along fractures during the later stages of emplacement of the thrust sheet.
Similar evolution has been observed in other areas of the Pyrenees and other orogens worldwide.

Keywords: South Pyrenean fold and thrust belt, Fluids, Fractures.

1 Introduction

The cements precipitated in fractures record the composition and evolution of fluids during the tectonic history of fold and thrust belts [1].

In this work we define the evolution of fluids during the development of the Lower Pedraforca thrust sheet (South Pyrenees) integrating structural, petrographic and geochemical data. The results are compared with previous works done in the Southern Pyrenees (Jaca, Vallfogona and L'Escala thrusts, Ainsa Basin and Puig-reig anticline) and other orogens worldwide (Bighorn Basin and North Oman and Canadian Rocky Mountains) [2].

2 Geological setting

The south Pyrenean fold and thrust belt (SPFTB) consists of a south-directed thrust system emplaced from Late Cretaceous to Oligocene detached predominantly above Triassic and Eocene evaporites [3].

The studied structure is the Lower Pedraforca thrust sheet (LPTS), an imbricated thrust system emplaced during the Lutetian (Middle Eocene) [4]. It consists of an allochthonous klippe detached above Eocene sediments and constituted of Lower Triassic

evaporites, Lower Jurassic limestones and dolostones, Upper Cretaceous limestones (Areny Fm.), Paleocene continental deposits (Garumnian) and Eocene syn-orogenic sediments deposited in the thrust front [3].

3 Methodology

Field work consisted of fracture data acquisition (dip directions and dips) and sampling of calcite cements precipitated in fractures and host rocks for petrographic and geochemical studies. Fracture data were plotted in stereograms and restored with respect to host rock bedding to define different fracture sets. Petrographic observations of 26 polished thin sections were made using optical and cathodoluminescence microscopy to define different calcite cements and their crosscutting relationships. The Geochemical characterization of fluids consists of carbon- and oxygen-isotope analysis of fracture-filling cements and their adjacent carbonate host rocks.

4 Fractures and cements

Up to seven fracture sets have been identified in the studied area. F1 and F2 fractures comprise N-S and E-W bed-perpendicular veins, respectively. F2 is abutting F1, indicating a later time of formation. F3 fractures consist of bed-parallel slip surfaces. F4 consists of conjugated NW-SE and NE-SW bed-perpendicular veins abutting F1and F2. F5 consists of conjugated NNE-SSW and NW-SE veins associated to major thrusts cross-cutting bedding at high angle. F6 and F7 include small and major south-verging thrusts and strike-slip faults cross-cutting bedding at high angle, respectively.

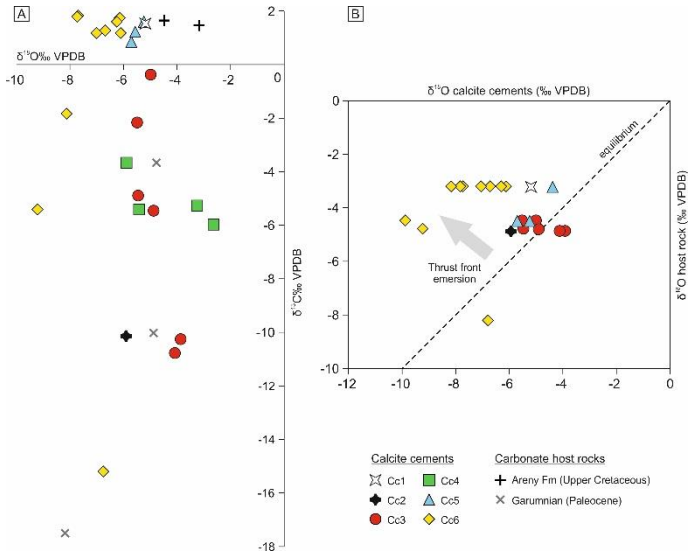

Fig. 1. A) $\delta^{18}O$ vs $\delta^{13}C$ cross-plot of calcite cements and host rocks and B) $\delta^{18}O_{calcite\ cement}$ vs $\delta^{18}O_{host\ rock}$ cross-plot from calcite cements of the LPTS.

The petrographic study of fracture fillings in the LPTS have allowed to identify six types of calcite cements. Cc1 consists of non-luminescent microsparite precipitated in the intergranular and moldic porosity of the Areny Fm. Cc2 consists of non-luminescent sparite precipitated in vug porosity affecting the Garumnian. Cc3 consists of orange luminescent sparite crystals, blocky or elongated parallel to fracture walls precipitated in F1, F2 and F3 fractures and vug porosity postdating Cc1 and Cc2. Cc4 consists of dull to orange luminescent sparite precipitated in F1, F2 and F4 affecting Eocene syn-orogenic sediments. Cc5 consists of zoned non-luminescent to dull orange cement precipitated in F1, F2 and F4 fractures postdating the previous cements. Cc6 consists of dull-brown sparite precipitated in F4, F5, F6 and F7 postdating Cc5.

Marine carbonates from the Areny Fm. have $\delta^{13}C$ between +1.5 and +1.7 ‰ VPDB and $\delta^{18}O$ between -4.5 and -3.2 ‰VPDB. Garumnian palustrine limestones have $\delta^{13}C$ between -17.5 and -3.7 ‰ VPDB and $\delta^{18}O$ between -8.2 and -4.8 ‰ VPDB (Fig. 1A). Cc1 has a $\delta^{13}C$ of +1.5 ‰ VPDB and $\delta^{18}O$ of -5.2 ‰ VPDB. Cc2 has a $\delta^{13}C$ of -10.1 ‰ VPDB and $\delta^{18}O$ of -6 ‰ VPDB. For Cc3, the $\delta^{13}C$ ranges between -10.8 and -0.4 ‰ VPDB and the $\delta^{18}O$ between -5.5 and -3.9 ‰ VPDB. Cc4 has $\delta^{13}C$ values between -5.9 and -3.7 ‰ VPDB and $\delta^{18}O$ between -5.9 and -2.6 ‰ VPDB. Cc5 has $\delta^{13}C$ values between +0.8 and +1.6 ‰ VPDB and $\delta^{18}O$ ranging between -5.7 and -4.4 ‰ VPDB. For Cc6, the $\delta^{13}C$ ranges between -15.2 and +1.8 ‰ VPDB and the $\delta^{18}O$ between -9.2 and -6.1 ‰ VPDB.

5 Discussion

Crosscutting relationships between fractures and bedding in the LPTS indicates that F1 to F4 formed during the first stages of compression, whereas F5 to F7 formed during the last stages of deformation once strata were already folded [5].

The $\delta^{13}C$ of all the calcite cements are similar to their host rocks, indicating a rock-buffered system. Likewise, the $\delta^{18}O$ values of Cc2 and Cc3 are also in equilibrium with their host rocks (Fig.1B), indicating a rock-buffered fluid system during calcite precipitation in the early vug porosity and also during formation of F1 to F3. In contrast, in calcite cements Cc5 and Cc6, the $\delta^{18}O$ is gradually more depleted with respect to their adjacent carbonate host rocks, indicating the opening of the system to exotic fluids as F4 to F7 formed (Fig.1B). This trend has already been reported in other areas of the SPFTB like the Jaca, Vallfogona and L'Escala thrusts, Ainsa Basin and Puig-reig anticline [2, 6, 7] as well as in other orogens worldwide such as the Bighorn Basin and North Oman and Canadian Rocky Mountains [2, 8, 9], were it has been interpreted as the input of upward migrating hot and saline fluids mixed at depth with progressively more abundant meteoric waters, probably linked to the emersion of the structure.

6 Conclusions

During the early compression of the LPTS, fluids in equilibrium with their adjacent host rock migrated along N-S and E-W bed-perpendicular veins and bed-parallel slip surfaces. The progressive precipitation of $\delta^{18}O$-depleted calcite cements in the faults

formed during the late stages of compression, indicate the input of external fluids into the system. This evolution of fluid behavior, also observed in other areas of the SPFTB and worldwide, is interpreted as the input of hot and saline fluids mixed at depth with progressively more abundant meteoric waters during the emersion of the structure.

Acknowledgements

The isotopes were carried out at CCiTUB of the Universitat de Barcelona. This research was funded by the projects CGL2015-66335-C2-1-R and 2017SGR-824.

References

1. Roure, F., Andriessen, P., Callot, J.P., Faure, J.L., Ferket, H., Gonzales, E., Guilhaumou, N., Lacombe, O., Malandain, J., Sassi, W., Schneider, F., Swennen, R. and Vilasi, N. The use of paleo-thermo-barometers and coupled thermal, fluid flow and pore-fluid pressure modelling for hydrocarbon and reservoir prediction in fold and thrust belts. In: G.P. Goffey, J. Craig, T. Needham and R. Scott (Eds.), Hydrocarbons in Contractional Belts. Geological Society, London, Spec. Pub., pp. 87-114 (2010).
2. Cruset, D., Cantarero, I., Vergés, J., John, C. M., Muñoz-López, D., Travé, A. Changes in fluid regime in syn-orogenic sediments during the growth of the south Pyrenean fold and thrust belt. Global & Planetary Change. https://doi.org/10.1016/j.gloplacha.2017.11.001 (2017).
3. Vergés, J. Estudi geològic del vessant sud del Pirineu oriental i central. Evolució 947 cinemàtica en 3D, PhD thesis, Universitat de Barcelona, 203 pp (1993).
4. Burbank, D.W., Vergés, J., Muñoz, J.A. and Bentham, P. Coeval hinward- and forward-imbricating thrusting in the south-central Pyrenees, Spain: Timing and rates of shortening and deposition. Geological Society of America Bulletin, 104, 3-17 (1992).
5. Casini, G., Gillespie, P.A., Vergés, J., Romaire, I., Fernández, N., Casciello, E., Saura, E., Mehl, C., Homke, S., Embry, J.-C., Aghajari, L. and Hunt, D.W. Sub-seismic fractures in Foreland fold and Thrust belts: insight from the Lurestan Province, Zagros Mountains, Iran. Petroleum Geoscience, 17, 263-282 (2011).
6. Lacroix, B., Travé, A., Buatier, M., Labaume, P., Vennemann, T. and Dubois, M. Syntectonic fluid-flow along thrust faults: Example of the South-Pyrenean fold-and-thrust belt. Marine and Petroleum Geology, 49, 84-98 (2014).
7. Travé, A., Labaume, P., Calvet, F., Soler, A. Sediment dewatering and pore fluid migration along thrust faults in a foreland basin inferred from isotopic and elemental geochemical analyses (Eocene Southern-Pyrenees, Spain). Tectonophysics, 282, 375-398 (1997).
8. Beaudoin, N., Bellahsen, N., Lacombe, O., Emmanuel, L. and Pironon, J. Crustal-scale fluid flow during the tectonic evolution of the Bighorn Basin (Wyoming, USA). Basin Research, 26 (3), 403-435 (2014).
9. Breesch, L., Swennen, R. and Vincent, B. Fluid flow reconstruction in hanging and footwall carbonates: Compartmentalization by Cenozoic reverse faulting in the Northern Oman Mountains (UAE). Marine and Petroleum Geology, 26, 113-128 (2009).

Annex 7: Oral presentations.

Cruset, D., Cantarero, I., Travé, A., Vergés, J., John, C. M. (2016b). *Fluid migration during the Cadí thrust sheet emplacement (South Pyrenean fold and thrust belt).* GEOFLUIDS VIII conference, Wuhan, China. June 22-27, 2016.

Fluid migration during the Cadí thrust sheet emplacement (South Pyrenean fold and thrust belt)

DAVID CRUSET [1, 2], IRENE CANTARERO [2], ANNA TRAVÉ [2], JAUME VERGÉS [1], CEDRIC M. JOHN [3]

[1] Institut de Ciències de la Terra Jaume Almera, ICTJA-CSIC, Lluís Solé i Sabaris s/n, 08028 Barcelona, Spain. dcruset@ictja.csic.es, jverges@ictja.csic.es

[2] Departament de Geoquímica, Petrologia i Prospecció Geològica, Facultat de Geologia, Universitat de Barcelona (UB), Martí i Franquès s/n, 08028, Barcelona, Spain. i_cantarero@ub.edu, atrave@ub.edu

[3] Qatar Carbonate and Carbon Storage Research Center and Department of Earth Science and Engineering, Imperial College London, SW7 2BP, UK. cedric.john@imperial.ac.uk

The South Pyrenean fold and thrust belt (NE Spain) is an excellent example to study the evolution of fluids during the progressive exhumation of a foreland basin.

This study is focused on the Cadí thrust sheet, emplaced from the middle Eocene to the lower Oligocene. The southern limit of the Cadí thrust sheet is the Vallfogona thrust, which places middle Eocene turbidites over upper Oligocene alluvial sediments. The main thrust fault, together with other minor fractures (inverse and strike-slip faults, bed-parallel and bed-perpendicular veins) acted as paths for fluids. Diverse generations of calcite cement precipitated in these fractures, recording two fluid flow stages during the emplacement of the Cadí thrust sheet.

During the first stage, calcite cement precipitated in small veins and vug porosity within the hanging wall of the main thrust fault from a fluid with a $\delta^{18}O$ of +12.12‰ SMOW at temperatures around 150 ºC. During the second stage, calcite cement precipitated in the main thrust fault and in minor thrusts and strike-slip faults affecting the hangingwall and footwall. This second calcite cement precipitated from a fluid with a $\delta^{18}O$ between +4.22 and +6.37‰ SMOW at temperatures around 100 ºC.

Keywords: Fluids, thrust faults, South Pyrenean fold and thrust belt

Cruset, D., Cantarero, I., Vergés, J., Travé, A. (2017) Fluid rock relationships during the formation and inversion of an extensional basin (Upper Pedraforca thrust sheet, South Pyrenean fold and thrust belt). International Meeting of Sedimentology 2007. Toulouse, France, October 10-12, 2017.

Fluid-rock relationships during the formation and inversion of an extensional basin (Upper Pedraforca thrust sheet, South Pyrenean fold and thrust belt)

David Cruset*†[1], Irene Cantarero[1], Jaume Vergés[2], and Anna Travé[1]

[1]Departament de Mineralogia, Petrologia i Geologia Aplicada, Universitat de Barcelona (UB). Grup Consolidat de Recerca "Geologia Sedimentària" (2014SGR-251) – Spain

[2]Group of Dynamics of the Lithosphere, Institute of Earth Sciences Jaume Almera ICTJA – CSIC – Spain

Abstract

The South Pyrenean fold and thrust belt (NE Spain) is an excellent example in which the relationships between fluids and sedimentary basins during the Mesozoic extension and Pyrenean orogeny can be studied.
This study is focused in the Upper Pedraforca thrust sheet, emplaced from Late Cretaceous to Paleocene. This structure consists of an extensional basin related to the diapirism affecting the Iberian Margin during Mesozoic times which was inverted during the Pyrenean compression. The main thrust places syn-rift Lower Jurassic to Upper Cretaceous limestones and dolostones over syn-orogenic Upper Cretaceous to Paleocene carbonates and clastic sediments.

Intergranular and vug porosity, joints, reverse and strike-slip faults acted as preferential paths for fluids during the Mesozoic extension and the Upper Cretaceous to Paleocene compression. The diverse generations of calcite cement precipitated recorded the geodynamic evolution of the Upper Pedraforca thrust sheet.

During the Mesozoic extension, calcite with a δ18O of -9.6 VPDB and δ13C of -3.1 VPDB precipitated in extensional fractures affecting laminated Lower Jurassic limestones. These veins are cut by bed-perpendicular joints filled with calcite (δ18O between -11.7 and -8.9 VPDB and δ13C between -1.1 and -0.9 VPDB), which precipitated from hot fluids. Within these veins, rhomb shaped dark crystals of calcite (δ18O of -7.4 VPDB and δ13C of -2.3) are observed. During the same period, carbonate breccias interbedded with Jurassic limestones and cemented with meteoric calcite (δ18O between -7.7 and -6.7 VPDB and δ13C between -1.2 and -0.5 VPDB) indicate that these sediments were periodically exposed during relative sea level falls.

During the Upper Cretaceous to Paleocene compression, hot fluids with increasingly meteoric influence migrated along vug porosity, joints and reverse and strike-slip faults from the Upper Pedraforca thrust sheet to its associated foreland basin, recording the progressive emersion of this structure. This evolution of fluids is evidenced by the progressive depletion

*Speaker
†Corresponding author: d.cruset@ub.edu

in δ18O and δ13C of calcite cements precipitated in reverse and strike-slip faults, from -5.5 to -13.6 VPDB and from +1.9 to -10.04 VPDB respectively.
Keywords: Fluids, extension, compression, South Pyrenean fold and thrust belt.